

Lecture Notes in Mechanical Engineering

Valentina Lopresto  
Ilaria Papa  
Antonio Langella *Editors*

# Dynamic Response and Failure of Composite Materials


DRAF 2022

 Springer

# Lecture Notes in Mechanical Engineering


## Series Editors

Fakher Chaari, *National School of Engineers, University of Sfax, Sfax, Tunisia*

Francesco Gherardini , *Dipartimento di Ingegneria “Enzo Ferrari”, Università di Modena e Reggio Emilia, Modena, Italy*

Vitalii Ivanov, *Department of Manufacturing Engineering, Machines and Tools, Sumy State University, Sumy, Ukraine*

## Editorial Board Members

Francisco Cavas-Martínez , *Departamento de Estructuras, Construcción y Expresión Gráfica Universidad Politécnica de Cartagena, Cartagena, Murcia, Spain*

Francesca di Mare, *Institute of Energy Technology, Ruhr-Universität Bochum, Bochum, Nordrhein-Westfalen, Germany*

Mohamed Haddar, *National School of Engineers of Sfax (ENIS), Sfax, Tunisia*

Young W. Kwon, *Department of Manufacturing Engineering and Aerospace Engineering, Graduate School of Engineering and Applied Science, Monterey, CA, USA*

Justyna Trojanowska, *Poznan University of Technology, Poznan, Poland*

Jinyang Xu, *School of Mechanical Engineering, Shanghai Jiao Tong University, Shanghai, China*

**Lecture Notes in Mechanical Engineering (LNME)** publishes the latest developments in Mechanical Engineering—quickly, informally and with high quality. Original research reported in proceedings and post-proceedings represents the core of LNME. Volumes published in LNME embrace all aspects, subfields and new challenges of mechanical engineering.

To submit a proposal or request further information, please contact the Springer Editor of your location:

**Europe, USA, Africa:** Leontina Di Cecco at [Leontina.dicecco@springer.com](mailto:Leontina.dicecco@springer.com)

**China:** Ella Zhang at [ella.zhang@springer.com](mailto:ella.zhang@springer.com)

**India:** Priya Vyas at [priya.vyas@springer.com](mailto:priya.vyas@springer.com)

**Rest of Asia, Australia, New Zealand:** Swati Meherishi at [swati.meherishi@springer.com](mailto:swati.meherishi@springer.com)

Topics in the series include:

- Engineering Design
- Machinery and Machine Elements
- Automotive Engineering
- Engine Technology
- Aerospace Technology and Astronautics
- Nanotechnology and Microengineering
- MEMS
- Theoretical and Applied Mechanics
- Dynamical Systems, Control
- Fluid Mechanics
- Engineering Thermodynamics, Heat and Mass Transfer
- Manufacturing
- Precision Engineering, Instrumentation, Measurement
- Tribology and Surface Technology

**Indexed by SCOPUS and EI Compendex.**

All books published in the series are submitted for consideration in Web of Science.

To submit a proposal for a monograph, please check our Springer Tracts in Mechanical Engineering at <https://link.springer.com/bookseries/11693>

Valentina Lopresto · Ilaria Papa ·  
Antonio Langella  
Editors

# Dynamic Response and Failure of Composite Materials

DRAF 2022

 Springer

*Editors*

Valentina Lopresto  
DICMaPI  
University of Naples Federico II  
Naples, Italy

Ilaria Papa  
DICMaPI  
University of Naples Federico II  
Naples, Italy

Antonio Langella  
DICMaPI  
University of Naples Federico II  
Naples, Italy

ISSN 2195-4356                      ISSN 2195-4364 (electronic)  
Lecture Notes in Mechanical Engineering  
ISBN 978-3-031-28546-2              ISBN 978-3-031-28547-9 (eBook)  
<https://doi.org/10.1007/978-3-031-28547-9>

© The Editor(s) (if applicable) and The Author(s), under exclusive license  
to Springer Nature Switzerland AG 2023

This work is subject to copyright. All rights are solely and exclusively licensed by the Publisher, whether the whole or part of the material is concerned, specifically the rights of translation, reprinting, reuse of illustrations, recitation, broadcasting, reproduction on microfilms or in any other physical way, and transmission or information storage and retrieval, electronic adaptation, computer software, or by similar or dissimilar methodology now known or hereafter developed.

The use of general descriptive names, registered names, trademarks, service marks, etc. in this publication does not imply, even in the absence of a specific statement, that such names are exempt from the relevant protective laws and regulations and therefore free for general use.

The publisher, the authors, and the editors are safe to assume that the advice and information in this book are believed to be true and accurate at the date of publication. Neither the publisher nor the authors or the editors give a warranty, expressed or implied, with respect to the material contained herein or for any errors or omissions that may have been made. The publisher remains neutral with regard to jurisdictional claims in published maps and institutional affiliations.

This Springer imprint is published by the registered company Springer Nature Switzerland AG  
The registered company address is: Gewerbestrasse 11, 6330 Cham, Switzerland

# Preface

Draf2022, “International Symposium on Dynamic Response and Failure of Composite Materials” organized in Ischia, Naples, from 21 to 24 June and now at its fourth edition, addressed current innovative research topics related to the dynamic behaviour of composite materials and sandwich structures. It had a strong emphasis on aerospace applications, as well as on automotive and naval ones in addition to more general topics. Particular attention was placed on failure modes, failure criteria, constitutive equations and damage investigations from experimental, theoretical and numerical points of view with the aim of providing the scientific basis for material and fabrication method selection and design of advanced structures.

The international conference saw the participation of renowned researchers from prestigious universities, academies, industries and research centres from all over the world, at the aim to meet people, share results of the scientific researches and create opportunities for collaborations. For the high level of the conference, each researcher was personally invited by the scientific committee. All the speakers positively answered to the invitation, and 140 contributions were presented.

This book is dedicated to the symposium and contains high-level papers presented by the scientific delegates. The papers reflect the main topic of the conference and highlight the effects of foreign object impacts, at low and high speed, explosions and crashes with applications to aircraft crash landings, road vehicle crashes, as well as the crucial problem of the damage, resulting in a clear view of the current state of the art in a specialized research field.

All the four editions of Draf conference were successful thanks to the precious help of Giovanni Belingardi from Politecnico of Torino.

During Draf2022, a special session was dedicated to Giovanni. The title of the session was “Composite materials for lightweighting and safety of vehicles”. It was very wide, and it included almost everything about composites because it was the best description of the research activities that Giovanni has carried out in all his career.

He has been and, actually, he still is a reference for many young researchers. He has several scientific merits that have permitted him to create a sound network with national and international collaborations on many aspects related to composites, in particular on their impact, fatigue, crashworthiness response and numerical modelling.

His best merit is that he has been able to create a network of friends that esteem him from a scientific point of view but also appreciate his human aspects: kind, honest and patient.

This is why the organizers of Draf2022 celebrated his retirement with the dedicated special session. And, finally, this is also the reason why this volume is dedicated to him as manifestation of gratitude.

His retirement is only from the academic career, not from the research because the scientific world always needs him.

# Organization

## Scientific Committee

V. Lopresto	University of Naples Federico II, Italy
A. Langella	University of Naples Federico II, Italy
A. Astarita	University of Naples Federico II, Italy
F. Memola Capece Minutolo	University of Naples Federico II, Italy
Z. Kazanci	Queen's University Belfast, Ireland
P. Russo	CNR, Italy
G. Belingardi	Polit. di Torino, Italy
P. Di Petta	MBDA, Italy
A. Riccio	University L. Vanvitelli, Italy
S. Cantoni	CIRA, Italy
G. Sabino	MBDA, Italy
L. Santo	University of Rome Tor Vergata, Italy
P. Navarro	University of Toulouse Paul Sabatier, France
F. Sarasini	University of Rome Sapienza, Italy
J. Tirillò	University of Rome Sapienza, Italy
F. Marulo	University of Naples Federico II, Italy
M. Ferraris	Polit. di Torino, Italy
M. Porfiri	New York University, USA
F. Ricci	University of Naples Federico II, Italy
I. Papa	University of Naples Federico II, Italy
F. Romano	CIRA, Italy
M. Guida	University of Naples Federico II, Italy

## Organizing Committee

Valentina Lopresto	University of Naples Federico II, Italy
Antonio Langella	University of Naples Federico II, Italy
Ilaria Papa	University of Naples Federico II, Italy
Claudio Cigliano	University of Naples Federico II, Italy
Chiara Cigliano	University of Naples Federico II, Italy

## Sponsors

Hexagon  
University of Naples Federico II  
DICMAPI  
Exemplar  
Evident - Olympus  
Instron  
MTS  
DAC, Distretto Aerospaziale Campano  
Alpha Star  
Megaride





# Contents

## Structural Integrity Assessment of Composite Structures

Uniaxial Fatigue Tests on Polyamide Reinforced with Short Glass Fibre .....	3
<i>Daniele De Caro, Stefano Plano, Davide Gabellone, Michele M. Tedesco, Carlo Boursier Niutta, Andrea Tridello, Giovanni Belingardi, and Davide S. Paolino</i>	
Numerical and Experimental Comparison of Impact Damage Detection by Using Piezoceramic Sensors/Actuators on a Stiffened Composite Panel .....	13
<i>Assunta Sorrentino and Fulvio Romano</i>	
Design, Numerical and Experimental Characterization of the Composite Rib for a Regional Aircraft .....	20
<i>Marco Esposito, Marco Gherlone, Massimiliano Mattone, Evangelos Karachalios, Vasilios Prentzias, Giorgio Fusco, Antonio Trinchese, Nicola Nola, and Fulvio Romano</i>	
Design, Numerical and Experimental Characterization of the Composite Spar for a Regional Aircraft .....	28
<i>Marco Esposito, Marco Gherlone, Massimiliano Mattone, Evangelos Karachalios, Vasilios Prentzias, and Fulvio Romano</i>	
Numerical and Experimental Comparison of Impact Damage Detection by Using Distributed Fiber Optics on a Stiffened Composite Panel .....	36
<i>Monica Ciminello, Salvatore Ameduri, Bernardino Galasso, Fulvio Romano, and Antonio Concilio</i>	
Equivalent Material Identification in Composite Scaled Hulls Vertical Impact Tests .....	43
<i>E. Cestino, G. Frulla, A. Polla, and G. Nicolosi</i>	
Design and Maintenance of Aircraft Composite Structures by Advanced Damage Inspection Techniques .....	51
<i>Fulvio Romano, Assunta Sorrentino, Monica Ciminello, Salvatore Ameduri, Michele Inverno, and Romualdo Sorrentino</i>	

Numerical Comparison of Damage Detection Methods Using Shm Distributed Fiber Optics (Fo) and Fibre Bragg Grating (Fbg) on a Full-Scale Wing Beam Test Article .....	58
<i>L. Pellone, M. Ciminello, B. Galasso, G. Apuleo, S. Shoham, U. Mercurio, A. Concilio, and I. Kressel</i>	
Design, Manufacturing and Testing of an Out-of-Autoclave Liquid Resin Infused Carbon-Epoxy Curved Stiffened Panel .....	67
<i>Daniele Fanteria, Evangelos Karachalios, Vincenzo Iannone, Ernesto Monaco, and Fulvio Romano</i>	
Mechanical Characterization of a Polymer-Metal Hybrid Structure for Automotive Applications: Quasi-static and Repeated Impact Tests .....	75
<i>D. Fiumarella, A. Canegrati, L. M. Martulli, A. Bernasconi, G. Mastinu, G. Belingardi, and A. Scattina</i>	
Numerical and Experimental Investigation on Single Lap Composite Joints .....	86
<i>A. Riccio, U. Merola, V. Acanfora, A. Russo, F. De Nicola, G. Giusto, and F. Di Caprio</i>	
<b>Innovative Manufacturing and Inspection Technologies</b>	
Sustainability of Fused Deposition Modeling: The Role of the Plate Material ...	99
<i>Ersilia Cozzolino, Francesco Napolitano, Antonello Astarita, Valentina Lopresto, Ilaria Papa, and Antonino Squillace</i>	
On the Mechanical Behaviour of Carbon Fibre Laminates Repaired with Hot Bonding Technology by Infusion .....	106
<i>Federica Donadio, Ilaria Papa, Antonio Viscusi, Luigi Carrino, Valentina Lopresto, Giancarlo Ingenito, Gabriella Caputo, and Antonio Langella</i>	
Damage Detection in Bio-Polyamide 11/Woven Basalt Fibres Composite Laminates Subjected to Dynamic Events .....	116
<i>Gabriella Epasto, Ilaria Papa, Valentina Lopresto, Libera Vitiello, and Pietro Russo</i>	
Approaching the Influence of Marine Environment Degradation on Impacted Carbon Fiber/Vinyl Ester Laminate with Electronic Speckle Pattern Interferometry Investigation .....	125
<i>Papa Ilaria, Lopresto Valentina, Russo Pietro, and Pagliarulo Vito</i>	

Speckle Interferometry Applied to the Detection of Defects in Stiffened Panel .....	135
<i>Russo Pietro, Ricci Fabrizio, Monaco Ernesto, Laurino Gianfranco, Paturzo Melania, D. 'Angelo Gennaro, and Pagliarulo Vito</i>	
Use of an Innovative Methodology for the Characterization of Polymers in the Analysis of the UV-Light Radiation Effects .....	142
<i>Andrea Genovese, Vincenzo Maria Arricale, Mario Barbaro, Luigi Marennna, Michele Sanfelice, and Guido Napolitano Dell'Annunziata</i>	
Double-Double Laminate Composites for Unmanned Aerial Vehicles .....	148
<i>F. Di Caprio, A. Riccio, S. W. Tsai, A. Russo, A. Braco, C. Leccia, and A. Sellitto</i>	
Numerical Study on the Compressive Behaviour of Repaired Composite Panels .....	156
<i>Aniello Riccio, Andrea Sellitto, Antonio Garofano, Giancarlo Ingenito, and Mauro Zarrelli</i>	
3D Printed Carbon PEEK - Influence of Printing Strategy on Tensile Performances .....	165
<i>Sara Varetti, Nicola Gallo, Ignazio Scavo, and Stefano Corvaglia</i>	
Influence of Process Parameters of 3D Printed PEEK on Crystallinity and Mechanical Performances .....	173
<i>Valentina Trimini, Sara Varetti, Gianluca Percoco, Stefano Corvaglia, Nicola Gallo, and Ignazio Scavo</i>	
Machining Approach for Recycling of CFRP Laminates .....	180
<i>Massimo Durante, Luca Boccarusso, Dario De Fazio, Antonio Formisano, and Antonio Langella</i>	
Thermo-mechanical Modelling of the Directed Energy Deposition (DED) Process for the Optimization of Deposition Strategies .....	186
<i>Marco Vallone, Massimo Damasio, Eleonora Atzeni, Mirna Poggi, and Alessandro Salmi</i>	
AM Part Qualification by Melpool, Material, and Grain Boundary Engineering .....	205
<i>Mallikharjun Marrey, Amirhossein Eftekharian, Guan-Cheng Chen, Dade Huang, and Frank Abdi</i>	

AF-Challenges-Synthetic Materials (Polymer and Ceramic) Lifting Model Blind Test Validation .....	217
<i>Harsh Baid, Amirhossein Eftekharian, Mohammedreza Bahadori, Dade Huang, Andrea Cantarutti, and Frank Abdi</i>	
Reduction of Slamming Damage on GFRP Panels in Dry/Wet Conditions in Hulls of High-Speed Boats .....	230
<i>A. Pollastro, V. Lopresto, P. Townsend, and J. C. Suarez-Bermejo</i>	
Characterization of the Viscoelastic Properties of Tires Through Non- Destructive Tests .....	237
<i>D. D.'agostinis Rinaldi, F. Farroni, and A. Genovese</i>	
<b>Dynamic Behaviour of Lightweighting and Natural Composites</b>	
OAK Wood Chemical Densification: Microstructure Changes and Perspectives .....	245
<i>L. Sansone, C. Cigliano, V. Lopresto, I. Papa, P. Russo, V. Antonucci, and M. R. Ricciardi</i>	
Hybridization of Thin Laminates with Natural Fibers: A Comparison Study Between Hemp and Flax .....	254
<i>L. Boccarusso, M. Durante, D. De Fazio, K. Myronidis, M. Meo, and F. Pinto</i>	
On the Damage Sensitivity of Guided Wave SHM System Under Different Loading Conditions .....	261
<i>Donato Perfetto, Alessandro De Luca, Giuseppe Lamanna, Aldo Minardo, Raffaele Vallifuoco, and Francesco Caputo</i>	
Impact Response of Carbon Fiber Composites: Comparison Between Epoxy and Bio-Based Epoxy Matrices .....	271
<i>R. Ciardiello, C. Boursier Niutta, A. Tridello, and D. S. Paolino</i>	
Analysis of the Behavior of Fiberglass Composite Panels in Contact with Water Subjected to Repeated Impacts .....	282
<i>A. C. Omaña, J. M. Arenas, and J. C. Suarez</i>	
Crash Testing of Polymer Matrix Composites Using Flat Specimens .....	290
<i>Lorenzo Vigna, Valentina Lopresto, Ilaria Papa, Pietro Russo, Andrea Calzolari, Giuseppe Galizia, Davide Salvatore Paolino, and Giovanni Belingardi</i>	

Green Composites Surface Modification Regarding Fibre/Resin Compatibility: An Approach from an Engineering and Chemistry Perspective .....	299
<i>Neffe A. Gomez, Martin Muscat, Claire DeMarco Muscat-Fenech, Duncan Camilleri, Emmanuel Sinagra, and Sandro Lanfranco</i>	
Strain-Rate Dependent FDEM Simulation of the Perforation Behaviour of Woven Composites Subjected to Low-Velocity Impact .....	307
<i>M. Rezasefat, A. A. X. da Silva, S. C. Amico, M. Giglio, and A. Manes</i>	
<b>Design and Manufacturing of New Generation Composite Materials for Aerospace Sector</b>	
On the Use of Double-Double Laminates to Improve and Innovate the Design of an All-Composite Wing Box .....	319
<i>Aniello Riccio, Francesco Di Caprio, Steven W. Tsai, and Andrea Sellitto</i>	
Thermal and Morphological Evaluation of the Composite Manufactured with Carbon Epoxy Prepreg via Hot Compression Molding .....	329
<i>Samia Danuta Brejão de Souza, Nicola Gallo, Ignazio Scavo, and Stefano Corvaglia</i>	
Application of Recycled Carbon Fibers in Aircraft Windows Frame .....	337
<i>S. Minosi, G. Buccoliero, M. Araganese, U. Raganato, A. Tarzia, S. Corvaglia, and N. Gallo</i>	
Experimental Investigation on Fracture Toughness of Open Hole Coupons Under Tension Load .....	343
<i>R. Cumbo and A. Baroni</i>	
Influence of Laser Texturing on Mechanical Performances of CFRP Single Lap Bonded Joint .....	351
<i>Gianluca Parodo, Wilma Polini, Luca Sorrentino, and Sandro Turchetta</i>	
Preliminary Sizing of a Hybrid-Electric Aircraft with Structural Batteries .....	357
<i>Salvatore Corcione, Gennaro Di Mauro, Vincenzo Cusati, Valerio Marciello, Michele Guida, and Fabrizio Nicolosi</i>	
Low-Velocity Impact Response of a Composite Structural Battery .....	364
<i>Gennaro Di Mauro, Pietro Russo, and Michele Guida</i>	
Impact Dynamics of Different Cabin Solutions of Small Airplanes .....	371
<i>Gennaro Di Mauro, Giuseppe Maurizio Gagliardi, Michele Guida, and Francesco Marulo</i>	

**Design of Controlled Rupture Structure for Safe Vector Ejection** ..... 377  
*Aniello Smarrazzo, Michele Guida, Francesco Marulo, M. Coppola, and R. Moliterno*

**Design of a VLA Vertical Control Surface with LRTM Technology** ..... 384  
*Massimo Viscardi*

**An Open Thinking for a Vision on Sustainable Green Aviation** ..... 391  
*Antonio Ficca, Francesco Marulo, and Antonio Sollo*

**On the Crashworthiness Behaviour of Additive Manufactured Sandwich Panels** ..... 401  
*V. Acanfora, F. Baldieri, A. Garofano, F. Fittipaldi, and A. Riccio*

**Author Index** ..... 413

# **Structural Integrity Assessment of Composite Structures**



# Uniaxial Fatigue Tests on Polyamide Reinforced with Short Glass Fibre

Daniele De Caro<sup>1</sup>(✉), Stefano Plano<sup>1</sup>, Davide Gabellone<sup>1</sup>, Michele M. Tedesco<sup>1</sup>, Carlo Boursier Niutta<sup>2</sup>, Andrea Tridello<sup>2</sup>, Giovanni Belingardi<sup>2</sup>, and Davide S. Paolino<sup>2</sup>

<sup>1</sup> Centro Ricerche FIAT, 10135 Torino, Italy  
daniele.de-caro@fcagroup.com

<sup>2</sup> Dipartimento di Ingegneria Meccanica e Aerospaziale, Politecnico di Torino,  
Corso Duca Degli Abruzzi 24, 10129 Torino, Italy

**Abstract.** In the automotive sector, composite materials are gaining greater interest, in particular for application to car body components, thanks to their lightweight potential, which can lead to significant fuel consumption reduction and performance enhancement. In order to be suitable for automotive applications, fatigue properties have to be carefully investigated to properly design structural components.

Having in mind the automotive application, a particular composite material, a polyamide reinforced with 18%wt short glass fibres, has been considered. Uniaxial fatigue tensile tests with load ratio  $R = 0.1$  were carried out on flat specimens made of the selected material. The experimental tests were performed using a hydraulic fatigue testing machine, in stress-controlled mode, with a loading frequency in the range of 0.5–3 Hz depending on the stress amplitude. P-S-N curves and endurance limit were determined according to the ISO standard 12107. Moreover, an innovative approach based on the Maximum Likelihood Principle (MLP) was used to estimate the P-S-N curves as well as the endurance limit. Obtained results showed that the estimation made with the MLP, reduces the total time of the test campaign and data fitting is more effective. Moreover, the material tested exhibits interesting properties for automotive applications.

**Keywords:** Composite materials · Uniaxial fatigue · Maximum likelihood method · Polyamide

## 1 Introduction

Composite materials nowadays are vastly used in many sectors like automotive, energy, aerospace, oil and gas. The use of composite materials is a compromise between cost and performance.

The automotive industry is one of the most important industries that has started using composite materials in a massive way. The main targets are finalised to performance improvement in sportive cars and light weighting to address the requirements related to the reduction of both energy consumption and CO<sub>2</sub> emissions.



The increasing use of composite materials in many fields and applications, led the designers to consider fatigue behaviour as a fundamental information for right component design.

However, the fatigue behaviour of composite materials is different from that of metallic materials, for this reason a different method and approach is used.

Investigations on composites fatigue behaviour are recently strongly increased in automotive field. The standard reference for fatigue tests on composite materials is the ISO 13003 European standard. The main difference with metallic material is the strong dependency of the fatigue behaviour of composite materials on the test frequency [1, 2]. Indeed the specimen temperature has to be controlled during the tests in order to limit the temperature rise of the sample surface (normally limited to 10 °C).

Moreover, the fatigue behaviour of composites material depends on a lot of parameters:

- Increasing the test frequency the fatigue strength tend to decrease like showed in many works. By increasing the frequency, the molecular motion will increase and self-heating phenomenon will occur, resulting from energy dissipation. Internal heat generation and consequent temperature rise may cause failure by thermal softening instead of fatigue [3–6].
- One of the most used manufacturing technologies for composite components is the injection moulding process that, due to its complexity, generate an anisotropic distribution of fibre or particle reinforcement in the final component. Many studies have been conducted on this topic, showing that the fatigue strength in transversal to flow direction is much lower than in parallel direction. This behaviour can be explained by the higher fibre percentage orientated along the flow direction [3–8].
- Many polymeric (for example Polyamide) matrix composites tend to adsorb water from the environment, this induces a change in their mechanical properties, including fatigue. The fatigue resistance of wet samples is much lower than with dried material. The water adsorption reduces the material fibre-interfacial strength of the composite [4, 6, 9].
- The effect of operating temperature is very detrimental on fatigue performances of composite material. The temperature effects have been investigated by many researchers. As a general trend it results that the fatigue strength decrease considerably in consequence of the increment of the operating temperature [7, 8].
- In short fibre reinforced composite, the fibre aspect ratio plays a fundamental role on the final material characteristics. Many works, carried out on different polymeric matrix composite, showed an increment of the fatigue strength in material with longer fibres [4].

Glass fibres reinforced polyamides is one of the most used materials in engineering plastics, especially for component requiring high strength, chemical and temperature resistance, in combination with excellent aesthetical finish; they have many applications in automotive parts like under hood, engine covers and intake ducts, cabin air intake manifolds, pedals and cooling modules [10].

The main aim of the present work is to investigate the uniaxial fatigue behaviour of polyamide reinforced with 18%wt short glass fibres. Other connected aims have been

the assessment of the suitability of an innovative approach based on the Maximum Likelihood Principle (MLP) to estimate the P-S-N curves as well as the endurance limit, both in terms of quality of the results and in terms of efficiency (i.e. reduction of the total time of the test campaign).

## 2 Material and Experimental Procedure

The composite matrix polyamide studied in this work, has been reinforced with 18%wt short glass fibres. Plates have been produced by injection moulding technique, with the dimensions 200mmx200mm 4mm thick.

The material has been produced by Solvay Engineering Plastics, the commercial name is TECHNYL® C 218 V18 BLACK; glass fibres with a length of 400  $\mu\text{m}$  and a diameter of 10  $\mu\text{m}$  have been used with a 18%wt. The final fibre length after the process was reduced to 250  $\mu\text{m}$  due to the process itself.

The material mechanical properties have been obtained by standard tests at the Fiat Research laboratory, and are summarized in the Table 1. The plates have been supplied in wet condition at hygroscopic saturation.

**Table 1.** Mechanical properties of the PA66 reinforced with 18%wt of short glass fibres.

Property	Value	Unit
Thickness	4	mm
Density (23 °C)	1.24	$\text{g/cm}^3$
Specific Young modulus	4065	$10^3 \frac{\text{m}^2}{\text{s}^2}$
Young modulus	5041	MPa
Ultimate tensile strength – UTS	96	MPa
Specific UTS	77	$10^3 \frac{\text{m}^2}{\text{s}^2}$
Tg	55	°C

The reported properties are related to the longitudinal direction with respect to the injection moulding. From the results of the mechanical tests carried out in FCA laboratories, it comes out that this material exhibits anisotropic behaviour, generally the mechanical strength and Young Modulus decrease in transversal direction. Mechanical properties are also affected by the strain rate, in particular the strengths increase at higher strain rates.

The material investigated in this work has been tested in fatigue in longitudinal direction and subjected to a load ratio  $R = 0.1$ . Only high cycle fatigue behaviour have been investigated.

The samples have been produced using milling machine, in order to have a better quality edges, and, before the tests, each specimen has been polished along the edge, to reduce the roughness at the minimum possible value.

The uniaxial fatigue tests have been carried out on a servo hydraulic machine, equipped with an axial load cell of 15 kN. All the samples were equipped with a thermocouple in order to monitor the temperature during the tests. The test frequency have been adapted to each specimen and applied load, to avoid that the temperature increases more than 10 °C respect to room temperature.

About the specimen geometry, dogbone shape have been used for the whole test campaign (Fig. 1).

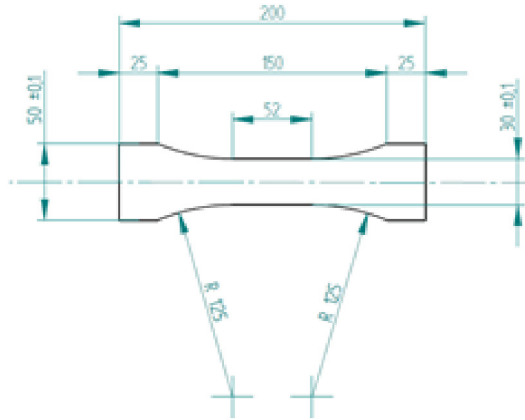


**Fig. 1.** Specimen geometry for fatigue test.

The test frequency applied during the tests, ranges from 0.5 Hz to 3 Hz (near the fatigue limit). The run out was imposed at  $1 \times 10^6$  cycles.

All tests have been conducted according to axial stress-controlled method. The failure criterion for each test has been identified with respect to the amount of cylinder displacement.

During the tests, cylinder displacement has been recorded, in order to study the evolution of hysteresis and elongation.

### 3 Results

In the first phase P-S-N curves and endurance limit were determined according to the ISO standard 12107. Different curves and endurance limit at different reliability are shown:

- R50, reliability of 50% (the highest)
- R90, reliability of 90% (in the middle)
- R90C90, reliability of 90% and a confidence level of 90% (the lowest)

A deeper analysis has been carried out to better understand the viscoelastic behaviour of this material. The cylinder displacement and hysteresis curve were recorded during

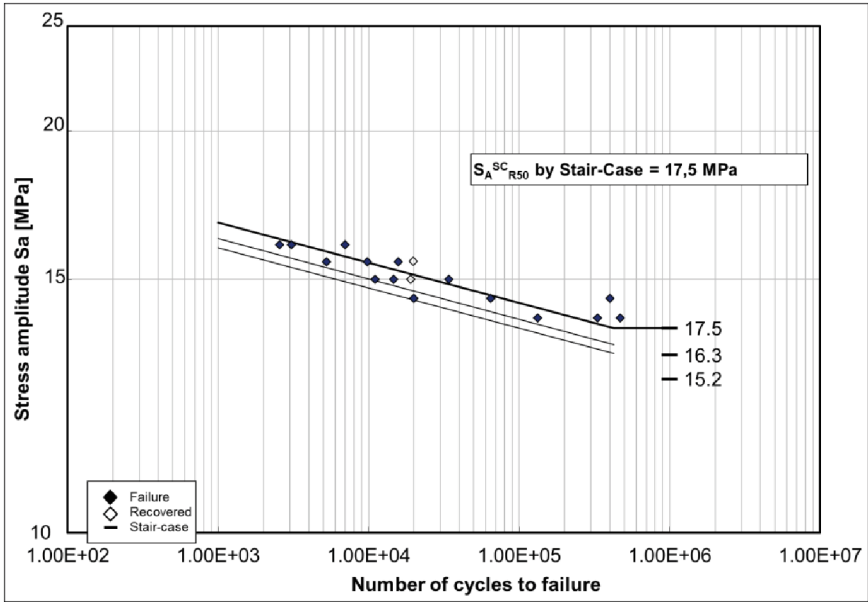


**Fig. 2.** P-S-N curve – PA66 reinforced with 18%wt of short glass fibers.

each fatigue cycle for all the tested specimens. From the testing machine cross head displacements at minimum and maximum loads, the elongation of the specimen during the test have been evaluated. A curve of the elongation versus the number of cycles has been obtained for each stress amplitude (Fig. 2).

From the results it is evident that for higher stress amplitudes the sample elongation increase during the test. Instead, at stress amplitudes near to the fatigue limit, the elongation remains quite constant for the whole sample life. The above reported analysis shows that the material stiffness for high stress amplitude decreases during the test; this means that some internal damage is taking place inside the sample: nucleates, propagates and leads to the final fracture (Fig. 3).

Hysteresis cycle analysis has been conducted for different samples loaded with a different stress amplitude, in order to see the energy dissipation evolution during the specimen life. The resulting graphs are summarized in the Fig. 4.

The hysteresis cycles at higher stress amplitude (compare the right diagram with the left one in Fig. 4) are wider. Moreover, looking at the results for the higher stress amplitude (Fig. 4a), there is an evolution of the hysteresis cycle during the test: the dimensions of hysteresis cycle tend to increase with the number of cycles, while the slope decreases. The material Young Modulus decreases progressively during the test (softening), this is clearly confirmed by the progressive increment in elongation. Also the hysteresis included area increases, this means that the energy dissipation spent in sample self-heating increases during the test. Instead, looking at the hysteresis cycles for a sample with a stress amplitude close to the fatigue limit (see Fig. 4b), they are quite constant during the specimen life, showing a lower self-heating effect on the material.

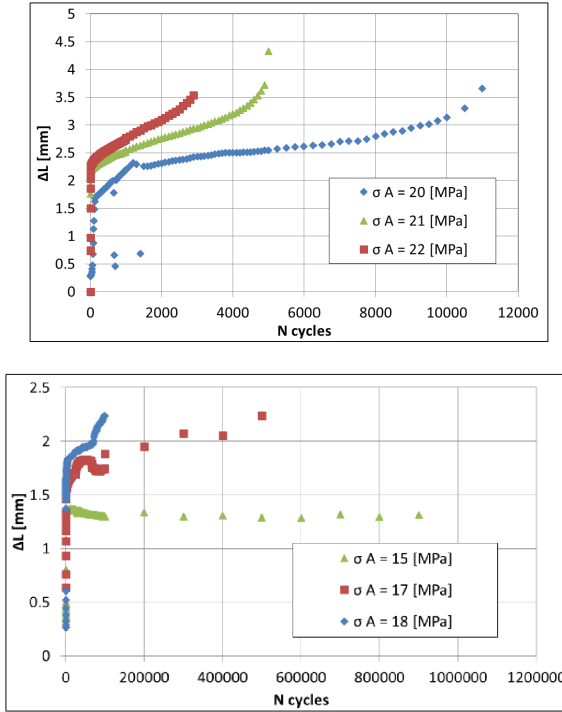


**Fig. 3.** Elongation vs number of cycles – PA66 reinforced with 18%wt of short glass fibers.

The short glass fibre reinforced polyamide exhibits a high degradation during the high cycle fatigue test. Moreover the polyamide samples have a high elongation and a high heat dissipation, not generally observed in metallic materials. This is the reason why the frequency applied during the test is very low in respect to that generally used for metallic material.

## 4 Maximum Likelihood Method

As usual in the high cycle fatigue curve it is possible to identify a finite life region (ruptures) and a part related to the fatigue limit (run outs); in the standard approach the two areas are evaluated separately. The maximum likelihood (ML) method permits to evaluate the high cycle fatigue curve using both rupture and run out specimens, giving the possibility to build a unified statistical model.

The ML statistic fatigue model is very well explained in the work of Paolino et al. [11, 12]. Here some notion will be reported considering the case of “one failure mode due to one cause with fatigue limit”.

Consider  $X_I$ , the fatigue limit, a random variable with a cumulative distribution function (cdf)  $F_{X_I}$  (e.g. normal or log normal distribution)

$$F_{X_I} = \Phi\left(\frac{S_a - \mu_{X_I}}{\sigma_{X_I}}\right) \quad (1)$$

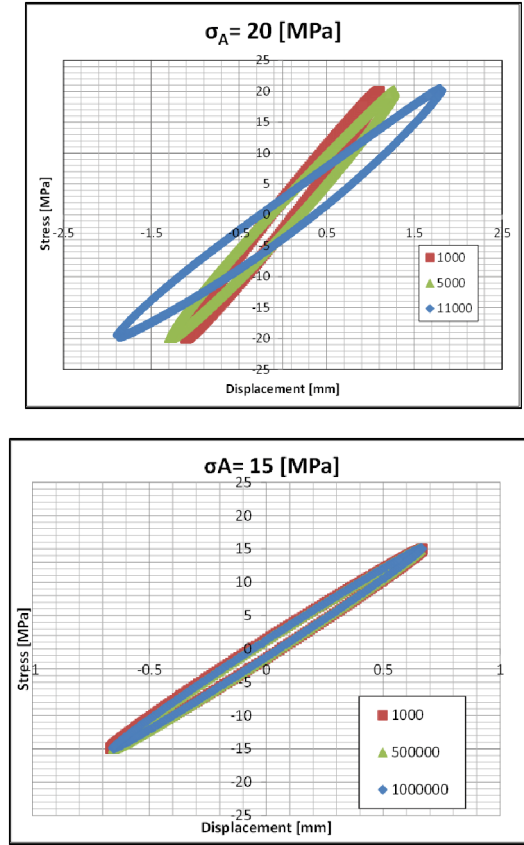


**Fig. 4.** Centred Hysteresis cycles – PA66 reinforced with 18%wt of short glass fibres.

where  $\mu_{X1}$  and  $\sigma_{X1}$  are respectively the location and scale parameters of the distribution, and  $S_a$  is the stress amplitude value. The cumulative distribution function (cdf) of the fatigue life  $Y$  (logarithm of the number of cycles to failure  $n_f$ ) can be expressed as:

$$F_Y = \Phi\left(\frac{Y - (a + x \cdot b)}{\sigma_Y}\right) \Phi\left(\frac{x - \mu_{X1}}{\sigma_{X1}}\right) \quad (2)$$

$Y = \log_{10}(n_f)$

$X = \log_{10}(S_a)$

$a, b$ : Basquin's law coefficients

$\sigma$ : standard deviation of the fatigue life

The maximum likelihood object function with sample data  $Y_1, \dots, Y_n$  at log stress level  $x_1, \dots, x_n$ , respectively, can be expressed as:

$$L(\theta; x, Y) = \prod_i^n [F'_Y(\theta; x_i, Y_i)]^{\delta_i} [1 - F_Y(\theta; x_i, Y_i)]^{1-\delta_i} \quad (3)$$

where

$$\theta = a, b, \sigma_Y, \mu_{Xl}, \sigma_{Xl}$$

$$\delta_i = \begin{cases} 1, & \text{if } Y_i \text{ is a failure} \\ 0, & \text{if } Y_i \text{ is a run out} \end{cases}$$

The ML estimate  $\hat{\theta}$  of  $\theta$  is the set of parameter values that maximize  $L(\theta)$ .

The analysis has been conducted by the Politecnico di Torino team, following the model described previously, developed by the Paolino and coworkers.

A reduced set of data has been used for the analysis (Stair case data randomly reduced to the half).

Below a comparison between the R50 and R90C90 P-S-N curves obtained by the standard and ML (Maximum Likelihood) methods are reported.

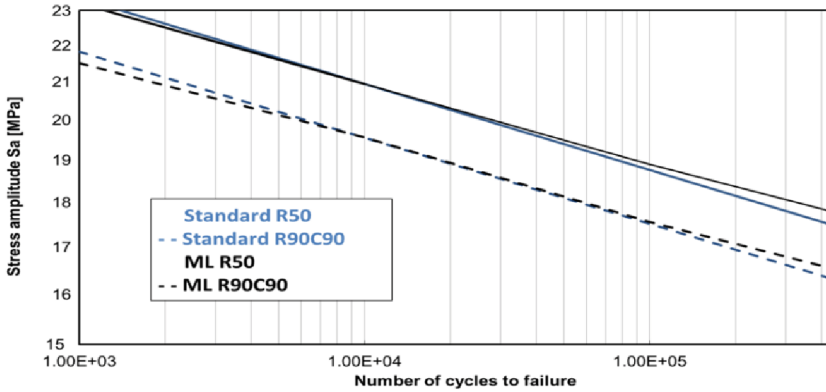


**Fig. 5.** P-S-N curves comparison – PA66 reinforced with 18%wt of short glass fibres

The P-S-N curves estimation using ML approach and the standard method are very similar (Fig. 5).

The new approach could allow reducing the number of specimens tested at lower stress amplitude (higher numbers of cycles at failure) cutting the total time for the high cycle fatigue characterization. Moreover, the new model implemented is more flexible, giving the possibility to use the best probabilistic approach based on the obtained experimental data.

Nevertheless, the ML method is more realistic in the fatigue behaviour representation of these materials, where the classic plateau observed in metals is not effective for composite materials design.

## 5 Conclusion

The current work was focused on fatigue behaviour investigation of short glass fibre reinforced polyamide PA66/GF18.

On polyamide the fatigue limit was about the 20% of the ultimate tensile stress, lower than what generally we found in metallic material (around the 50% of the yield strength).

The material exhibited a viscoelastic behaviour during the tests. This behaviour resulted in a degradation of the young modulus and heat generation increasing the number of cycle and the amplitude stress applied.

The investigation carried out in this work, showed that the standard approach described by international standard and here adopted, is not the most efficient for composite material like polyamide, where very low frequency was adopted to avoid self-heating effect. In order to reduce the total time of the test campaign to be useful for industrial field, a more efficient statistical approach was adopted to analyse fatigue raw data of polyamide composite. Maximum likelihood method was implemented in collaboration with Polytechnic of Turin, using a reduced set of data. The method showed a good agreement with raw data and with curves obtained by the conventional approach, both for fatigue limit estimation and in finite life region. The ML method could allow using less specimen than in standard approach, obtaining reliable results in shorter time.

The results obtained in this work are very important and useful for automotive world like FCA, where the composite material use will increase a lot in the future, in which an efficient, safety and intelligent design will be required. Moreover, the data obtained will be very useful for FCA design department, in order to better predict the composite component behaviour when cycling loads are applied, avoiding unexpected ruptures.

Finally, this work represents an important step forward for Group material laboratory in FCA, in the world of composite fatigue behaviour that was unexplored since few years ago, and that now it is leading to new more efficient and innovative statistical approach for raw data evaluation.

## References

1. Ing, D.S.: Application potential of composite materials in automotive. PhD (2015)
2. Pervaiz, M., Panthapulakkal, S., Sain, M., Tjong, J.: Emerging Trends in Automotive Lightweighting Through Novel Composite Materials (2016)
3. Zhou, Y., Mallick, P.K.: Fatigue performance of an injection-molded short E-glass fiber-reinforced polyamide 6,6: I. Effects of orientation, holes, and weld line. *Polym. Compos.* (2006)
4. Mortazavian, S., Fatemi, A.: Fatigue behavior and modeling of short fiber reinforced polymer composites: a literature review. *Int. J. Fatigue* (2015)
5. Zhou, Y., Mallick, P.K.: Fatigue performance of an injection molded talc-filled polypropylene. *Polym. Eng. Sci.* (2005)
6. Esmaeillou, B., Ferreira, P., Bellenger, V., Tcharkhtchi, A.: Fatigue behavior of polyamide 66/glass fiber under various kinds of applied load. HAL (2015)
7. Fatemi, M.: Fatigue behavior and modeling of short fiber reinforced polymer composites including anisotropy and temperature effects. *Int. J. Fatigue* (2015)
8. De Monte, M., Moosbrugger, E., Quaresimin, M.: Influence of temperature and thickness on the off-axis behaviour of short glass fibre reinforced polyamide 6.6 – cyclic loading. *Composites* (2010)
9. Fatikul: Damage mechanisms in short glass fiber reinforced polyamide-66 under monotonic and fatigue loading: effect of relative humidity and injection molding induced microstructure. *l'École Nationale Supérieure d'Arts et Métiers* (2014)



10. Mangino, E.: The research requirements of the transport sectors to facilitate an increased usage of composite materials (2004)
11. Paolino, D.S., Chiandussi, G., Rossetto, M.: A unified statistical model for S-N fatigue curves: probabilistic definition. *FFEMS* (2012)
12. Pascal, F.G., Meeker, W.Q.: Analysis of Fatigue Data with Runouts Based on a Model with Nonconstant Standard Deviation and a Fatigue Limit Parameter. *Statistics Preprints Iowa State University Digital Repository* (1996)



# Numerical and Experimental Comparison of Impact Damage Detection by Using Piezoceramic Sensors/Actuators on a Stiffened Composite Panel

Assunta Sorrentino<sup>(✉)</sup>  and Fulvio Romano 

CIRA-Italian Aerospace Research Centre, Via Maiorise snc, 81043 Capua, Caserta, Italy  
a.sorrentino@cira.it

**Abstract.** This work proposes a Structural Health Monitoring system for the detection and measurement of delamination areas in composite stiffened wing panels generated by low energy impacts, by using a network of sensors/actuators piezoceramics (PZT). This system is an offline system, pointing to be an alternative method to the current NDI/C-scan techniques.

The activities were performed in SMAF (SMart AirFrame) project of PRORA (the Italian Aerospace Research Program) and its promising reliability in the detection and measurement of the impact damage area was demonstrated.

The SHM algorithm is based on the elliptical triangulation method and high frequency Lamb waves. The network of PZT, placed on a composite stiffened panel, excites the structure with ultrasonic waves and, at the same moment, measures the perturbations induced by discontinuities present within the panel, like delamination. Through the calculation of the Time of Flight (ToF) of the signals and the knowledge of the actuator-sensor position, the method identifies location and dimension of the damage.

Many low energy impacts were performed on a full-scale stiffened panel and BVID (Barely Visible Impact Damage) was obtained in different positions.

The SHM-PZT system was applied to identify both the position and severity of the damage. The results were compared with the C-scan measurements and a good agreement was achieved.

**Keywords:** Impact detection · Composite structures integrity · Aircraft components · Structural Health Monitoring · Piezo-electrics · Lamb Waves

## 1 Introduction

This work was performed in the framework of the SMAF project, funded by PRORA (Italian Aerospace Research Program). It deals with the development of an SHM system based on high frequency piezoceramic sensors/actuators (PZT), able to detect, localize and measure, the delamination areas on a composite stiffened panel generated by low energy impacts. The algorithm presented is based on Elliptical Triangulation Method (ETM) based on the analysis of the ultrasonic waves. The comparison of the outputs

between the acquisitions in the undamaged and damaged structures gives the necessary information to the PZT SHM system. By the comparison with the C-scan, the proposed algorithm demonstrated the capability of this system to detect the impact areas, i.e. delamination, with a good accuracy.

## 2 Damage Detection Method

The damage detection method applied in this paper is the Elliptical Triangulation Method (ETM) based on the analysis of the ultrasonic waves. In order to verify the applicability of the method on increasingly complex structures, it was initially applied on flat plates [1–3] and then on stiffened composite panels affected by impact damage [4–7].

In this work, the ETM method is applied to an even more complex structure: a composite multi-stringer panel, representative of the upper skins of a typical wing box of a regional aircraft, subject to low velocity impact test.

The method is based on the concept that any discontinuity in the structure, if crossed by a wave, generates a disturbance. The practical scheme of the method applied on a flat plate is illustrated in Fig. 1. The Lamb wave is generated by actuator n.1 and it propagates in the structure going toward the damage ( $L_1$ ) and the sensor n.2 ( $L_S$ ). When the damage is reached, a perturbation is generated.

Both main and perturbation waves are acquired by sensor n.2. For each sensing-path can be written the following equations:

$$V_p = L_s * t_s \quad (1)$$

$$L_1 + L_2 = V_p * t_d \quad (2)$$

that allow to evaluate the perturbation path ( $L_1 + L_2$ ) by knowing the times of flight ( $t_s$  and  $t_d$ ) and the wave propagation velocity ( $V_p$ ).

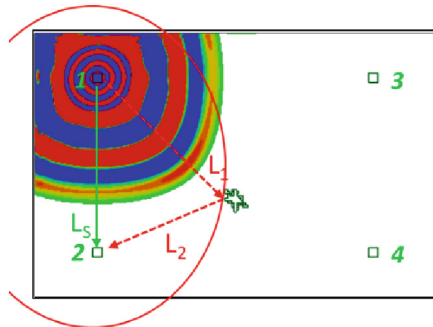


**Fig. 1.** Scheme of a panel with actuator-sensor path ( $L_S$ ) and actuator-damage-sensor path ( $L_1 + L_2$ ).

Three sensing-paths are necessary for a correct identification of the damage position, while at least four paths are required to evaluate the dimension of the damage, in fact each ellipse identifies the boundary on which the damage is located, so the damaged area can be obtained as the outer area enclosed between all the ellipses (Fig. 2).

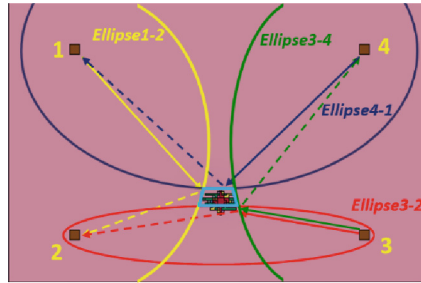


**Fig. 2.** Scheme for damage area evaluation.

### 3 Experimental Setup

A full size composite multi-stringer panel was sensorized with piezoelectric ceramic patch (DuraAct). In order to be able to detect the damage all over the panel, 16 sensors were placed on it (Fig. 3). Each area enclosed by 4 piezo has been independently scanned to check for damage (SHM subsystem). In Fig. 3 are underlined with a yellow dotted line some of these areas, while in Fig. 4 is shown a detail of them.

DuraAct Piezoelectric Patch Transducer, with dimensions of  $16 \times 13 \times 0.5$  mm, were used to achieve the SHM system.

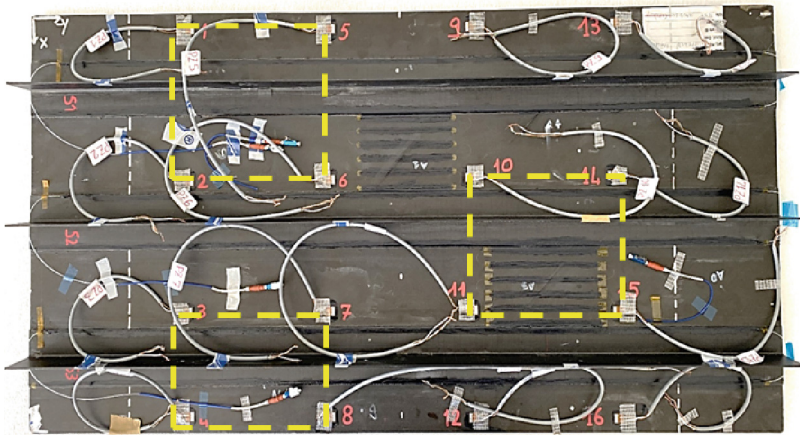


**Fig. 3.** Full sensorized wing box full size panel.

The devices have been used in both actuator-sensor features. National Instruments NI-USB Xseries device has been used to generate and record the Lamb wave signals. Controlling and analysis tools, written in Matlab environmental, have been used to drive NI device.

All the acquired information has been used by the analysis tool, that compares the files acquired before and after the damage, applies the elliptical triangulation method and gives out the information in terms of damage detection, positioning and dimensioning.

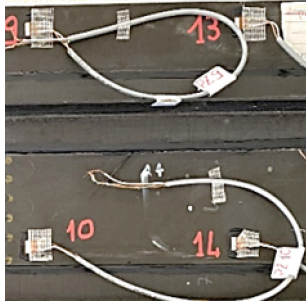
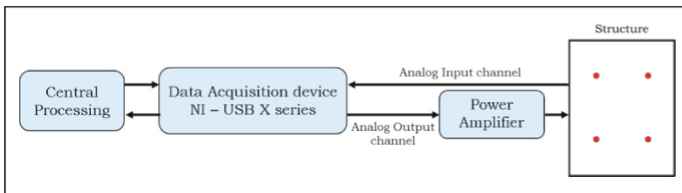


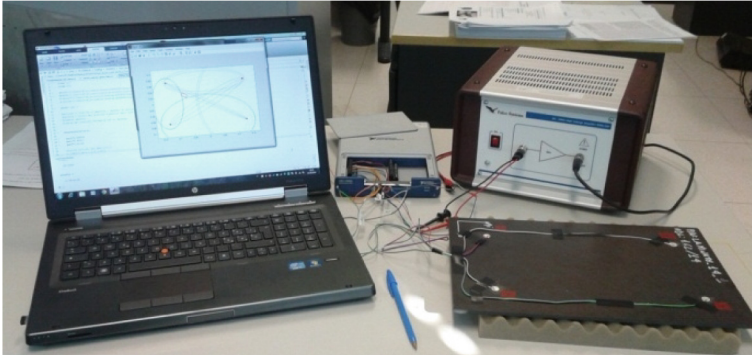
**Fig. 4.** Single area scanned by 4 piezo sensors.

Scheme and picture of whole experimental set-up are shown in Fig. 5.

The impacts have been realized by standardized drop weight impact machines and fixtures with energy impacts in the range 90 J–120 J. Structural element has then undergone ultrasonic NDI by Phased Array Ultrasonic Testing (PAUT) tests with an Olympus OmniScan SX flaw detector.



a)



b)

**Fig. 5.** Experimental set-up: scheme (a) and picture (b).

## 4 Experimental Results

In Fig. 6 (courtesy of University of Naples “Federico II”) are shown the NDI results with in evidence the delamination enclosed by green lines, while the yellow dotted lines identify the SHM subsystems.

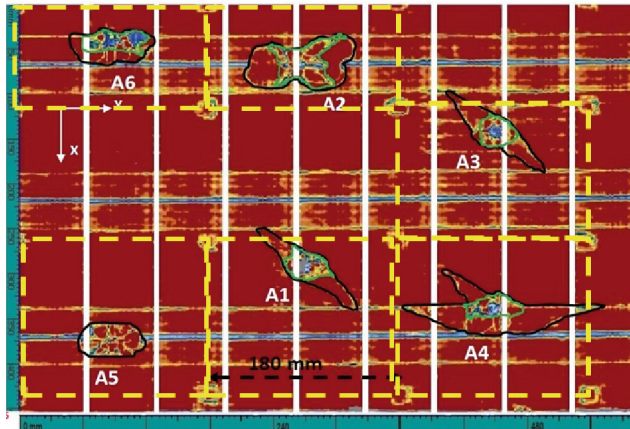


**Fig. 6.** Damage evidence in the C-Scan image (green line) and areas of SHM system detection (yellow dotted line)

The Piezo SHM system provides as output the position and dimension of the delamination. In Fig. 7, blue polygons indicate the position and their area gives an estimation of the damage area.

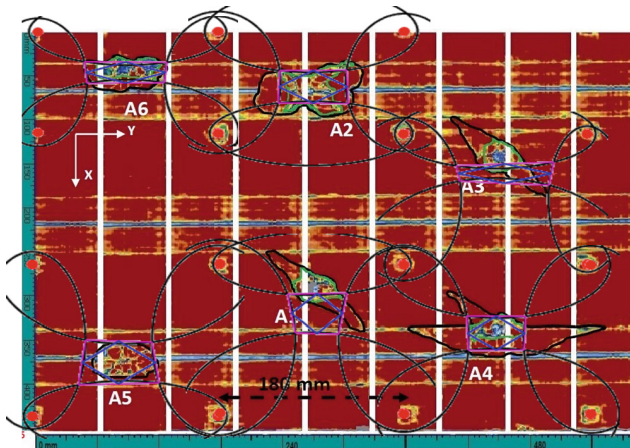


**Fig. 7.** Experimental results for damage detection

In order to have an estimation of the deviation from the reference data (NDI results) the percentage errors have been calculated; in particular regarding the position, the distance between the centers of the SHM and NDI areas has been expressed as a percentage of the diagonal of the relative SHM subsystem.

Results are shown in Table 1.

**Table 1.** SHM results error estimation

ID Danno	% Error (damage position)	% Error (area estimation)
A1	10%	7%
A2	2%	15%
A3	7%	18%
A4	3%	19%
A5	2%	11%
A6	3%	13%

## 5 Conclusions

The SHM PZT system, described in this work, has demonstrated its ability to identify and localize impact-induced damage. Experimental measurements were performed on a full size composite multi-stringer panel with many low energy impacts executed in different positions.

The SHM results have been compared with NDI ones and percentage errors in damage extension estimation were less than 20%, while in damage identification were less than 10%.

The bigger errors occur when the damage is very close to the sides of the quadrilateral of the four sensors/actuators.

## References

1. Lee, B.C., Staszewski, W.J.: Lamb wave propagation modelling for damage detection: II. Damage monitoring strategy. *Smart Mater. Struct.* **16**(2), 260–274 (2007). <https://doi.org/10.1088/0964-1726/16/2/004>
2. De Fenza, A., Sorrentino, A., Vitiello, P.: Application of artificial neural networks and probability ellipse methods for damage detection using lamb waves. *J. Compos. Struct.* **133**, 390–403 (2015)
3. Sorrentino, A., De Fenza, A.: Improved elliptical triangulation method for damage detection in composite material structures. *J. Mech. Eng. Sci.* **231**(16), 3011–3023 (2016)
4. Sorrentino, A., De Fenza, A., Romano, F., Mercurio, U.: Experimental application of Lamb wave based SHM system at complex composite material structures. In: *EWSHM 2018 – 9th European Workshop on Structural Health Monitoring*. Manchester, United Kingdom (2018)

5. Stawiarski, A., Muc, A., Kedziora, P.: Damage detection, localization and assessment in multi-layered composite structure with delaminations. *Key Eng. Mater.* **542**, 193–204 (2013)
6. Romano, F., Sorrentino, A., Pellone, L., Mercurio, U., Notarnicola, L.: New design paradigms and approaches for aircraft composite structures. *Multiscale Multidiscipl. Model. Exp. Des.* **2**(2), 75–87 (2018). <https://doi.org/10.1007/s41939-018-0034-8>
7. Romano, F., Ciminello, M., Sorrentino, A., Mercurio, U.: Application of structural health monitoring techniques to composite wing panels. *J. Compos. Mater.* (2019)








Co-funded by  
the European Union



# Design, Numerical and Experimental Characterization of the Composite Rib for a Regional Aircraft

Marco Esposito<sup>1</sup> , Marco Gherlone<sup>1</sup> , Massimiliano Mattone<sup>1</sup>,  
Evangelos Karachalios<sup>2</sup>, Vasilios Prentzias<sup>2</sup>, Giorgio Fusco<sup>3</sup>, Antonio Trinchese<sup>3</sup>,  
Nicola Nola<sup>3</sup>, and Fulvio Romano<sup>4</sup> 

<sup>1</sup> Department of Mechanical and Aerospace Engineering, Politecnico di Torino, Torino, Italy  
marco.gherlone@polito.it

<sup>2</sup> Hellenic Aerospace Industry, Research and Product Design, Schimatari, Greece

<sup>3</sup> Research and Development, AEROSOFT, Capua, Italy

<sup>4</sup> Aeronautics – Technologies Integration Office, CIRA – Italian Aerospace Research Centre,  
Capua, Italy

**Abstract.** As a key sub-component of the multilayered composite wing box for a regional aircraft, a rib has been designed (optimal stacking sequence), manufactured (using Liquid Resin Infusion) and tested in order to assess both the designing and manufacturing technologies.

**Keywords:** Rib · Composite materials · Liquid Resin Infusion · Experimental test

## 1 Introduction

The current effort is part of the Clean Sky 2 – AIRGREEN2 (AG2) project which aims at designing, analyzing, manufacturing and ground-testing a full-scale composite Outer Wing Box (OWB) demonstrator for a regional aircraft.

The work was funded by Clean Sky 2 Joint Undertaking, under the European's Union Horizon 2020 research and innovation Programme, under grant agreement No 807089 – REG GAM 2018 – H2020-IBA-CS2-GAMS-2017; WAL (Work Area Leader): Leonardo Aircraft.

The OWB has been designed in order to withstand stiffness, strength and stability requirements under critical loading conditions taken from the flight envelope. In particular, a minimum weight design has been obtained with an optimization based on genetic

algorithms that explored several thickness distributions and stacking sequences [1]. As important step of the project, a composite rib has been designed, manufactured and tested in order to validate the related technologies.

The rib, object of this work, corresponds to a middle section rib of the OWB. Static and non-linear finite element analyses have been performed in order to verify that the proposed rib test geometry would fail at the testing machine loading capacity. Moreover, a buckling analysis has completed the FE analyses as required by the design specifications.

The composite rib was manufactured by hand-layup and by using the Liquid Resin Infusion (LRI) method, an Out of Autoclave method (OoA), in which Dry Non Crimp Carbon Fabrics are impregnated by epoxy resin (high temperature cure) under the application of vacuum only [2–4]. The impregnated carbon fabric material was then cured in a standard oven. CATIA software was used for both the tool and part design. Respective material strength properties have been obtained by testing standard coupons manufactured by the same base materials (dry carbon fabrics and resin) and manufacturing method (LRI). Standard hand layup procedures were followed during the layup process of the fabrics. Appropriate auxiliary materials capable to withstand the respective LRI infusion and curing process specifications were used.

The rib has been tested up to failure under an in-plane shear loading condition [5]. The scope of the test was to validate the manufacturing process, as well as the design and FEM analysis in terms of strength properties and final failure.

## 2 Test Set-Up and Preliminary Rib FE Analysis

The rib has been tested at the LAQ-AERMEC Aeromechanical Structural Systems laboratory of Politecnico di Torino in order to assess the manufacturing process and to verify the load-carrying capacity of the sub-component. A supporting and loading structure, represented in Fig. 1, has been designed. The rib fixture is made of four steel frame segments, two short and two longer ones, shaped in order to follow the curved profile of the rib and connected by four hinges. One of the two short segments is clamped to the table hosting the test and the opposite short segment is pulled by an hydraulic jack in order to apply an in-plane shear loading to the rib. The connection between the rib and the frame segments has been obtained by using both epoxy adhesive and bolts on those edges where the rib is folded (i.e., the short edges and the top edge), whereas only the epoxy adhesive effect has been used along the unfolded long edge.

Based on the designed test set-up, a preliminary FEM buckling analysis has been performed (Nastran SOL105) in order to verify the feasibility of the experimental campaign. A load of 100 kN and material RTD pristine strength properties have been considered. Figure 2 presents the rib model with boundary and loading conditions and the 1st buckling mode corresponding to 46 kN.

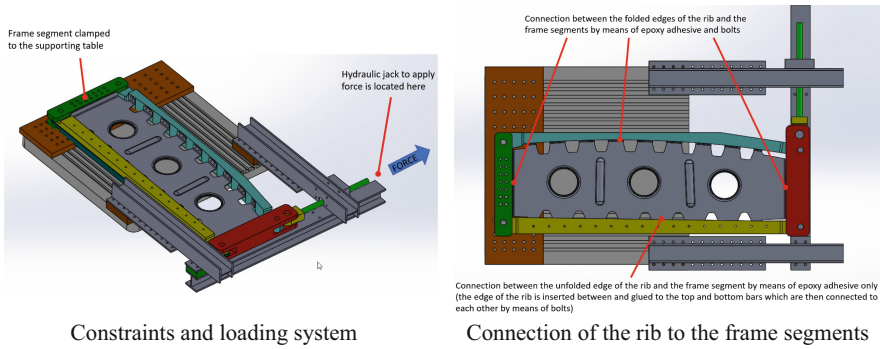


Fig. 1. Schematic overview of the rib test set-up.

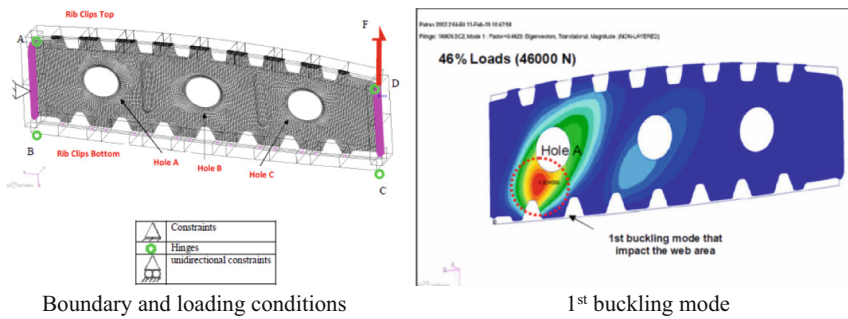


Fig. 2. Preliminary FE analysis of the rib.

### 3 Manufacturing

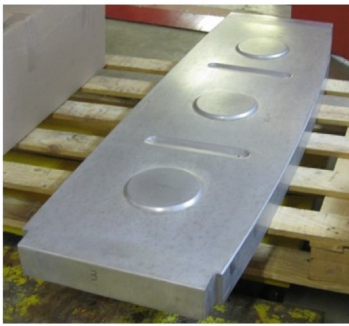
The following materials have been used for the RIB manufactured by HAI (HLU process): dry fiber: BNCF – 24 IMS – (0) – 196-600 by Cytec, resin for LRI impregnation: PRISM EP2400 resin by Cytec. Additionally, the following auxiliary fiberglass materials were used: dry Fiberglass HexForce® 01080 1280 TF970 by Hexcel (as internal layer for drill breakout protection & galvanic protection), dry biaxial Fiberglass X-E-PB-301 g/m<sup>2</sup>-1270 mm with Epikote binder by Saertex (as sacrificial external layer, covering only the area of the flanges).

The typical LRI process (steps/sequence) followed are briefly presented below.

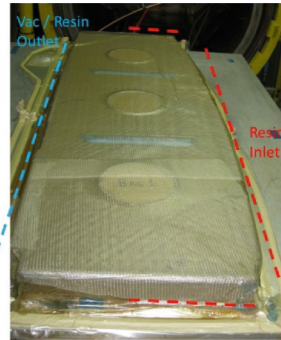
- Placement of dry fibers by HLU on the male tool. Pre-forming the dry fibers under vacuum and heat (binder activation) typically 15 min at 120 °C on the lay-up tool.
- Placement of LRI auxiliary materials (hoses, flow media & bagging materials) & connect inlet channels with resin container and outlet channels with vacuum.
- Full vacuum should be applied in both vacuum bags for the duration of the infusion and curing process.
- Preheat & degas the resin & tool at appropriate temperature defined by the resin characteristics (typically around 100 °C).

- Start the LRI process and allow sufficient time, under full vacuum to ensure complete fiber wetting.
- Curing the part under full vacuum @ 180 °C for 120 min. Allow tool to cool before releasing part from tool.

Figure 3 provides some details of the manufacturing process. A solid aluminum “male” tool, machined by CNC, was used as a layup and curing tool on which the dry fabrics were placed in order to perform the LRI process. As for the bagging and LRI setup, the inlet line is marked on the right side of the tool (around the flange bottom edges – red dashed line) while the outlet is on the left side of the tool (along the edge of the 4th flange – blue dashed line). Double bagging concept was applied.



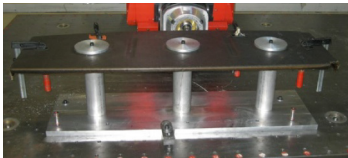
Aluminum “male” lay-up and curing tool



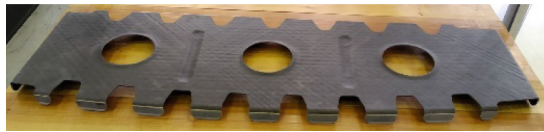
Dry preform bagging and LRI set-up

**Fig. 3.** Rib manufacturing process.

Following demolding of the part, machining/trimming by CNC 5-axis equipment using a custom made jig/fixture were performed (Fig. 4).



CNC machining



Manufactured rib

**Fig. 4.** Rib machining and final result.

## 4 Testing

The designed test-set up, once verified to be effective by means of the preliminary FE model, has been implemented by manufacturing the fixtures and assembling them at Politecnico di Torino (Fig. 5). A displacement transducer has also been connected to the edge of the rib that is moved by the applied force in order to measure the tip in-plane displacement. Figure 5 also provides a complete view of the test set-up, with the rib clamped on one short edge to the supporting table and the jack providing the load along the opposite edge.

A set of linear strain gauges and strain rosettes have been attached to the rib in order to provide measurements in some locations inspired by the results of the FE analysis (Fig. 6). In particular, 10 strain rosettes (5 back-to-back pairs) have been distributed in order to detect the buckling shapes corresponding to the first buckling modes (evaluated through the preliminary FE analysis), whereas 4 strain gauges (2 back-to-back pairs) have been added to monitor the rib close to the two folded short edges where damages are also expected to occur. The load has been increased according to a quasi-static procedure until failure of the rib.

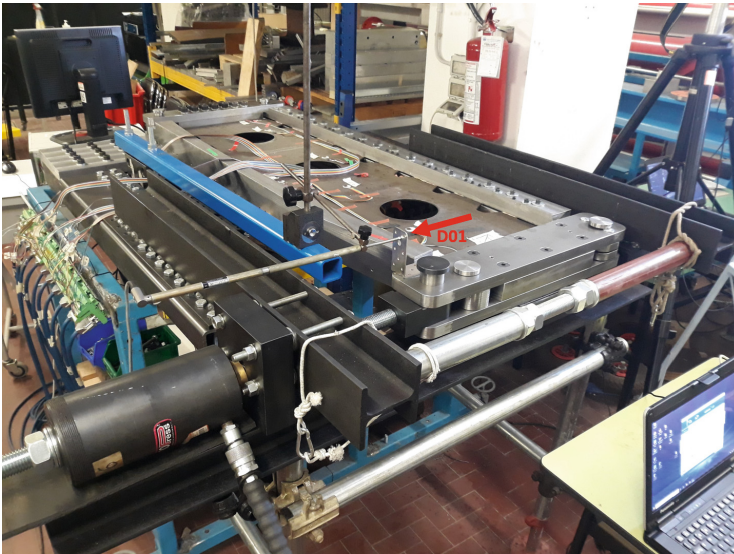


**Fig. 5.** Rib test set-up with fixtures to provide the boundary and loading conditions and a tip-displacement transducer (D01).

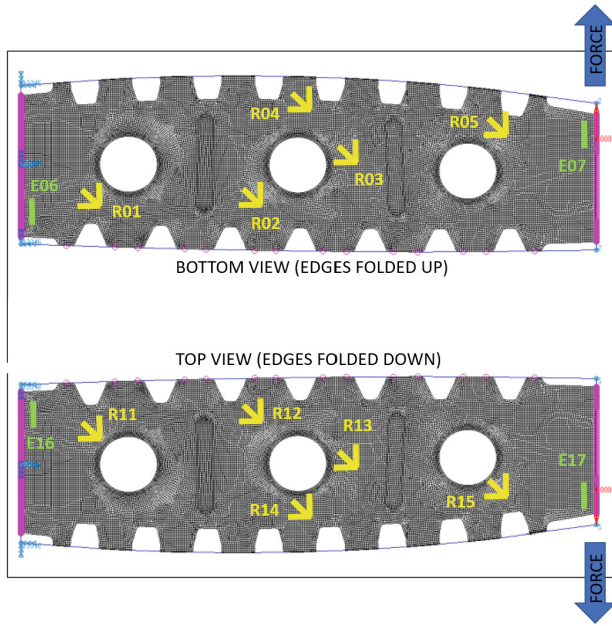


**Fig. 6.** Strain gauges and strain rosettes on both faces of the rib.

## 5 FEM vs Test Results Correlation

Considering with a higher accuracy the testing boundary and loading conditions and using the RTD HLU (Hand Lay-Up) material mechanical properties, the FEM has been updated in order to achieve a better compliance to experimental test results. An updated critical load of 32 kN (lower than the preliminary value of 46 kN) has been obtained through a linear buckling analysis (Nastran SOL105).

Moreover, a non-linear FE analysis has been performed (Nastran SOL106), thus leading to a further improved critical load of 31 kN (with a different critical shape) and providing strain vs load curves. The correlation between FEM & test results has then been investigated in terms of strain components, extracted in the finite element corresponding to the location of strain rosettes R05-R15 (Fig. 6) in the material directions X ( $0^\circ$ ), Y ( $90^\circ$ ) and XY ( $45^\circ$ ). Figure 7 shows, for example, the comparison between the experimental strains measured during the test along the  $45^\circ$  direction by rosettes R05 and R15 and those obtained by the linear buckling and non-linear static FE analyses. The experimental critical load is evaluated as 29 kN, the linear buckling analysis overestimates this value by 10% whereas the non-linear static analysis is more accurate (+7%). Numerical strain vs load curves also exhibit a good accuracy when compared with the experimental ones.

Moreover, a remarkable numerical-experimental match is obtained in terms of critical shape and corresponding damage considering the non-linear static FE analysis (Fig. 8).

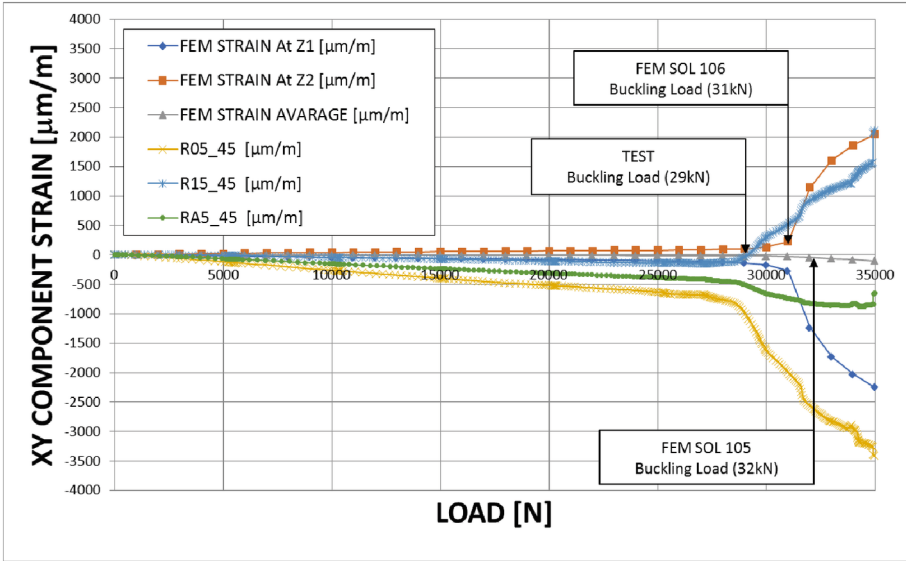


Fig. 7. Numerical vs test strain/load curves comparison.

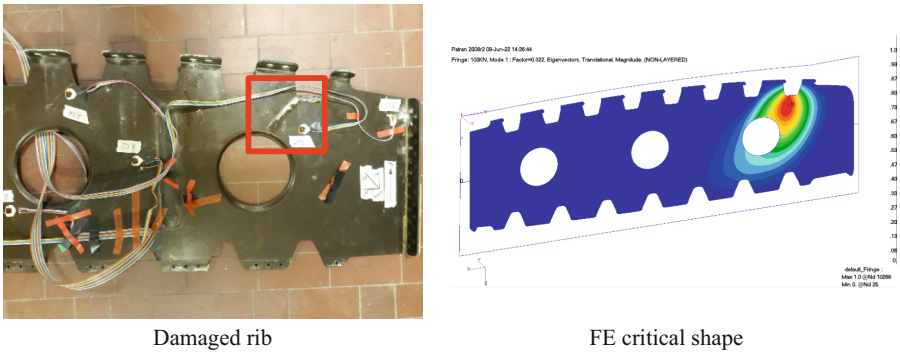


Fig. 8. Bucking/failure mode assessment, FEM (non-linear static) vs test.

## 6 Conclusions

The design of the composite multilayered rib for a regional aircraft wing has been performed, the sub-component has been manufactured using Liquid Resin Infusion and an experimental test has been conducted in order to assess both the analysis and the manufacturing technologies.

The manufacturing of the RIB by LRI has been performed using a standard oven and the quality of the manufactured part was acceptable. Only minor quality issues in non-structural glass plies have been identified, not affecting the structural performance of the final part. The capability to co-infuse sacrificial glass plies (which were then CNC machined to obtain the final part geometry) on top of the carbon plies has been verified

successfully. The experimentally evaluated failure mode and load are well predicted by the FE simulations. Strain vs load distributions provided by the FE analysis are in good agreement with the experimental results.




## References

1. Picchi Scardaoni, M., Izzi, M.I., Montemurro, M., Panettieri, E., Cipolla, V., Binante, V.: Multi-scale deterministic optimisation of blended composite structures: case study of a box-wing. *Thin-Wall. Struct.* **170**, 108521 (2022)
2. Karachalios, E., et al.: LRI-fabricated composite demonstrators for an aircraft fuselage on the basis of a Building Block design approach. *Compos. C: Open Access* **6**, 100178 (2021)
3. van Oosterom, S., Allen, T., Battley, M., Bickerton, S.: An objective comparison of common vacuum assisted resin infusion processes. *Compos. A: Appl. Sci. Manuf.* **125**, 105528 (2019)
4. Verma, K.K., Dinesh, B.L., Singh, K., Gaddikeri, K.M., Sundaram, R.: Challenges in processing of a cocured wing test box using vacuum enhanced resin infusion technology (VERITY). *Procedia Mater. Sci.* **6**, 331–340 (2014)
5. Singer, J., Arbocz, J., Weller, T.: *Buckling Experiments: Experimental Methods in Buckling of Thin-Walled Structures. Volume 2: Shells, Built-up Structures, Composites and Additional Topics.* Wiley (2002)





# Design, Numerical and Experimental Characterization of the Composite Spar for a Regional Aircraft

Marco Esposito<sup>1</sup> , Marco Gherlone<sup>1</sup> , Massimiliano Mattone<sup>1</sup>, Evangelos Karachalios<sup>2</sup>, Vasilios Prentzias<sup>2</sup>, and Fulvio Romano<sup>3</sup> 

<sup>1</sup> Department of Mechanical and Aerospace Engineering, Politecnico Di Torino, Torino, Italy  
marco.gherlone@polito.it

<sup>2</sup> Hellenic Aerospace Industry, Research and Product Design, Schimatari, Greece

<sup>3</sup> Aeronautics - Technologies Integration Office, CIRA - Italian Aerospace Research Centre, Capua, Italy

**Abstract.** As a key sub-component of the multilayered composite wing box for a regional aircraft, a spar segment has been designed (optimal stacking sequence), manufactured (using Liquid Resin Infusion) and tested (in a cantilevered configuration under tip shear load) in order to assess both the designing and manufacturing technologies.

**Keywords:** Spar · Composite materials · Liquid Resin Infusion · Experimental test

## 1 Introduction

The present work is part of the Clean Sky 2 – AIRGREEN2 (AG2) project which aims at designing, analyzing, manufacturing and ground-testing a full-scale composite Outer Wing Box (OWB) demonstrator for a regional aircraft. In order to achieve this objective, in the current development work, a small scale (in length) spar segment has been designed, manufactured and tested in order to validate the related technologies.

The work was funded by Clean Sky 2 Joint Undertaking, under the European's Union Horizon 2020 research and innovation Programme, under grant agreement No 807089 – REG GAM 2018 – H2020-IBA-CS2- GAMS-2017; WAL (Work Area Leader): Leonardo Aircraft.

The OWB has been designed in order to withstand stiffness, strength and stability requirements under critical loading conditions taken from the flight envelope. In particular, a minimum weight design has been obtained with an optimization based on genetic algorithms that explored several thickness distributions and stacking sequences [1]. A further analysis has been performed on the optimized front spar of the OWB. Focusing on the first two (root) bays, a spar segment (approx. 1100 mm long and 400 mm wide, constant section - no tapering) has been considered.

The spar segment was manufactured by using the Liquid Resin Infusion (LRI) method, an Out of Autoclave method (OoA), in which Dry Non Crimp Carbon Fabrics are impregnated by epoxy resin (high temperature cure) under the application of vacuum only [2–4]. The impregnated carbon fabric material is then cured in a standard oven or self-heated tool, heated internally by integrating electrical resistances and externally by heated blankets. In this work, a self-heated tool option was selected. The tool was designed as an egg-crate type construction in order to minimize both mass and thermal inertia. CATIA software was used for both the tool and part design.

A FEM analysis was performed by implementing progressive failure analysis using the MSC Marc software in order to predict the spar segment structural response during the experimental test. Respective material strength properties have been obtained by testing standard coupons manufactured by the same base materials (dry carbon fabrics and resin) and manufacturing method (LRI). Standard hand layup procedures were followed during the layup process of the fabrics. Appropriate auxiliary materials capable to withstand the respective LRI infusion and curing process specifications were used.

The spar segment has been tested up to failure in a cantilevered configuration and subjected to a tip in-plane pure shear force [5, 6]. The fixtures and loading system for the test have been designed in order to guarantee the correct clamped boundary conditions and to avoid any torsional effect. The scope of the test was to validate the manufacturing process, as well as the design and FEM analysis in terms of strength properties and final failure of the component. A numerical/experimental comparison is presented in terms of load vs displacement response curve and load vs strain (measured at some locations on the spar).

## 2 Test Set-Up and Preliminary Spar Segment FE Analysis

The spar segment has been tested at the LAQ-AERMEC Aeromechanical Structural Systems laboratory of Politecnico di Torino in a cantilevered condition with a tip shear force. A frame has been designed (Fig. 1) with the spar clamped between two steel plates and the gap between the web and the caps of the spar filled with aluminum plates. This fixture has been bolted on a T-slot cast steel plate anchored to the laboratory floor through bolts. The loading system has been designed in order to let the tip force be aligned with the cross-section shear center (torsion prevented). In particular, the load has been applied using an hydraulic jack.

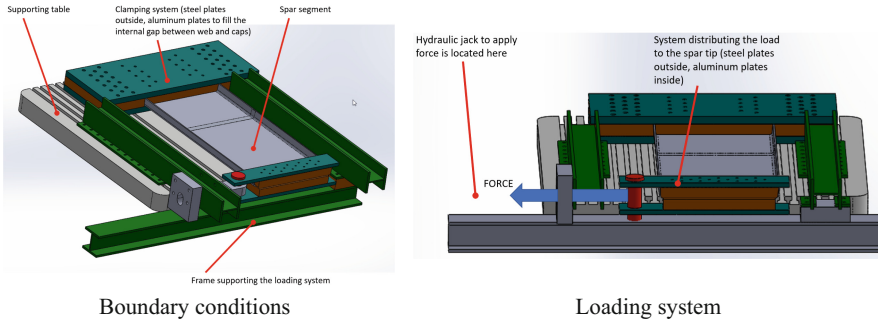


**Fig. 1.** Schematic overview of the spar test set-up.

Based on the designed test set-up, a FE analysis has been performed in order to verify the feasibility of the experimental campaign. Figure 2 presents the spar segment CAD model and the relevant FEM boundary conditions.

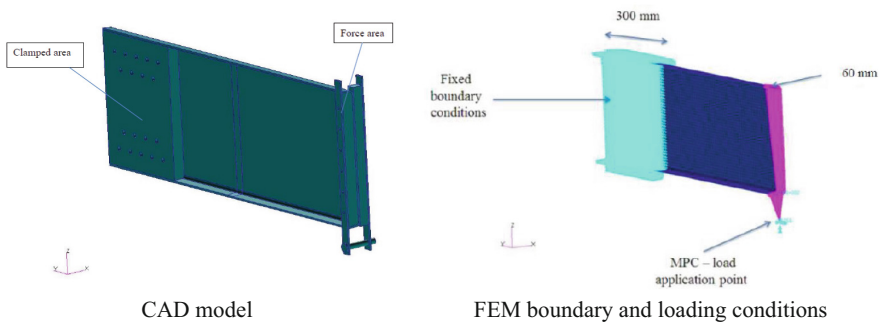


**Fig. 2.** Preliminary model of the spar test set-up.

### 3 Manufacturing

The following materials have been used for the spar segment manufactured by HAI (HLU process): dry fiber: BNCF – 24 IMS – (0) – 196–600 by Cytec, resin for LRI impregnation: PRISM EP2400 resin by Cytec. Additionally, the following auxiliary Dry Fiberglass HexForce® 01080 1280 TF970 by Hexcel was used as internal layer (for drill breakout protection & galvanic protection).

The typical LRI process (steps/sequence) followed are briefly presented below (Figs. 3 and 4).

- Placement of dry fibers by HLU on the male tool. Pre-forming the dry fibers under vacuum and heat (binder activation) typically 15 min at 120 °C on the lay-up tool.
- Placement of LRI auxiliary materials (hoses, flow media & bagging materials) & connect inlet channels with resin container and outlet channels with vacuum.
- Full vacuum should be applied in both vacuum bags for the duration of the infusion and curing process.
- Preheat & degas the resin & tool at appropriate temperature defined by the resin characteristics (typically around 100 °C).
- Start the LRI process and allow sufficient time, under full vacuum to ensure complete fiber wetting.
- Curing the part under full vacuum @ 180 °C for 120 min. Allow tool to cool before releasing part from tool.

The layup of the spar segment was performed on a male steel tool (egg-crate hollow type) and includes a drop off region on the tool surface (typical part thicknesses produced: 4,4–5,2 mm & 6–6,8 mm, tool radius for spar flanges: R8 mm, double bag concept performed, typical infusion times: 40 min).

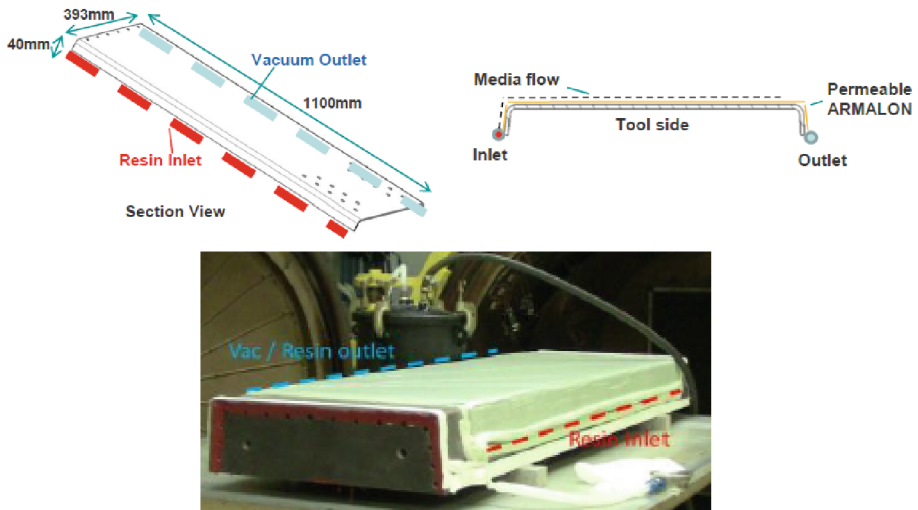


**Fig. 3.** Spar LRI process set-up. The inlet line is marked on the left side of the tool (red dashed line) while the outlet is on the right side of the tool (blue dashed line).



**Fig. 4.** Manufactured spar.

## 4 Testing

The designed test-set up, once verified to be effective by means of the preliminary FE model, has been implemented by manufacturing the fixtures and assembling them at Politecnico di Torino (Fig. 5).

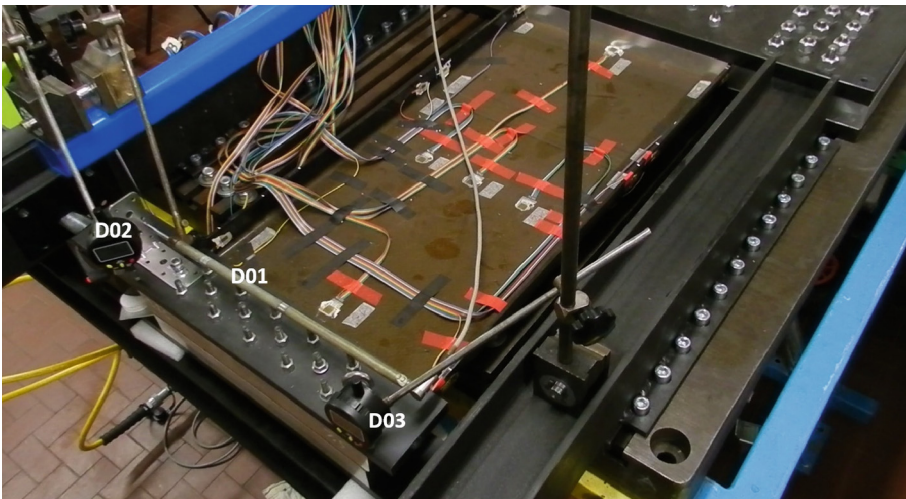


**Fig. 5.** Spar test set-up with fixtures to provide the boundary and loading conditions and strain and displacement sensors (D01, D02 and D03).

The spar segment has been equipped with a set of linear strain gauges and strain rosettes to monitor the strain distribution. Moreover, three displacement transducers have been connected to the spar segment in order to measure its tip deflection and to control that it was not experiencing any torsion (Fig. 5). The tip transverse load has been increased according to a quasi-static procedure until failure of the spar segment.

## 5 FEM vs Test Results Correlation

A progressive failure analysis (progressive stiffness reduction in the direction of relevant fiber – matrix damage) using Hashin damage initiation criterion in MSC Marc software has been performed. In Fig. 6, the load - displacement curve for both FEM and test is presented.

FEM – test deviation of stiffness is mainly due to material properties (stiffness & strength values defined in the model that may be slightly different from those in the manufactured part) and also the relevant boundary conditions (which in the FEM analysis are idealized). During manufacturing of demonstrator parts, typically minor imperfections occur, both in terms of material properties (i.e. from slight misalignment of fibers, minor gaps in plies between splices etc.) or even geometrical imperfections at the radiuses, thicknesses uniformity etc. This is especially true with a process such as LRI (compared to a more controlled prepreg manufacturing process).

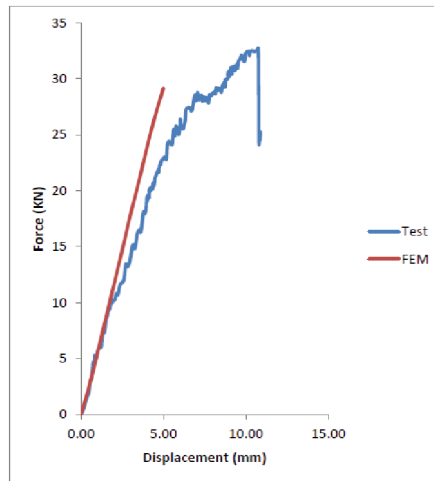


**Fig. 6.** Tip load – displacement curve (FEM vs test comparison).

Figure 7 shows the damaged areas (fiber and matrix) according to the FE analysis. Moreover, the damaged areas of the spar segment after the test are presented in Fig. 8. In comparison with the damaged regions of FEM results, they have occurred at the same position. They exist at the bottom flange of the spar segment due to compression during bending of the part when the load is applied.

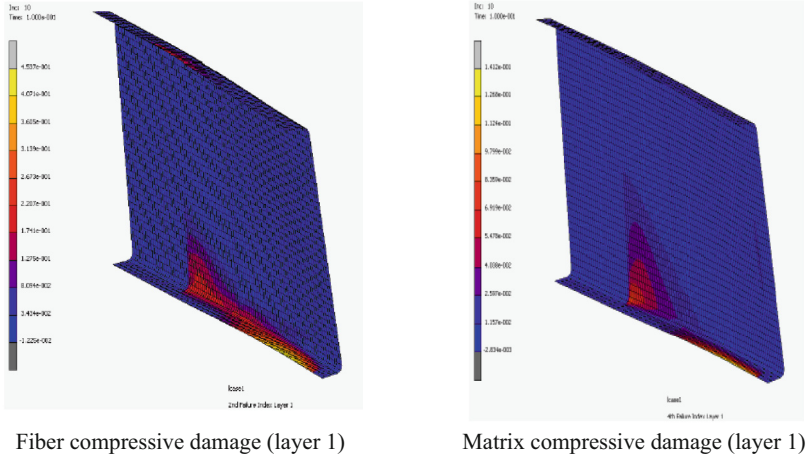


Fig. 7. Damaged areas (FEM).

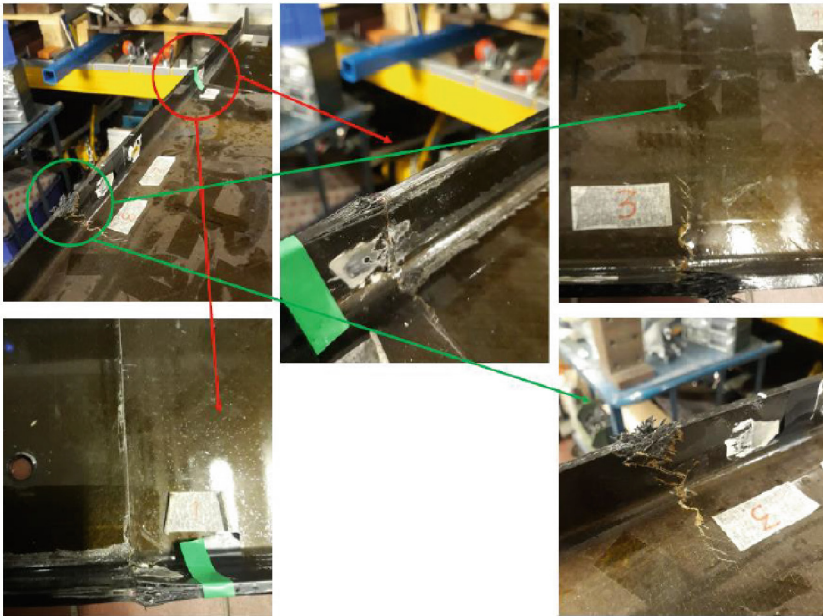


Fig. 8. Damaged areas (test).

## 6 Conclusions

The design of the composite multilayered spar segment for a regional aircraft wing has been performed, the sub-component has been manufactured using Liquid Resin Infusion

and an experimental test has been conducted in order to assess both the analysis and the manufacturing technologies.

The manufacturing of the spar segment by LRI has been performed on a self-heated tool and the quality of the manufactured part was acceptable. Only minor quality issues in non-structural glass plies have been identified, not affecting the structural performance of the final part. One of the advantages of the LRI manufacturing method has been verified, which is the capability to produce parts without the size limitation posed by the autoclave size. With the self-heated tool option, additional environmental benefits are expected, due to the minimization in the energy required to cure the part (as compared to curing the part in an equivalent size oven). Moreover, the experimentally evaluated stiffness, failure mode and location and failure load compare positively with the FE simulations.






## References

1. Picchi Scardaoni, M., Izzi, M.I., Montemurro, M., Panettieri, E., Cipolla, V., Binante, V.: Multi-scale deterministic optimisation of blended composite structures: case study of a box-wing. *Thin-Walled Structures* **170**, 108521 (2022)
2. Karachalios, E., et al.: LRI-fabricated composite demonstrators for an aircraft fuselage on the basis of a Building Block design approach. *Composites Part C: Open Access* **6**, 100178 (2021)
3. van Oosterom, S., Allen, T., Battley, M., Bickerton, S.: An objective comparison of common vacuum assisted resin infusion processes. *Compos. A Appl. Sci. Manuf.* **125**, 105528 (2019)
4. Verma, K.K., Dinesh, B.L., Singh, K., Gaddikeri, K.M., Sundaram, R.: Challenges in processing of a cocured wing test box using vacuum enhanced resin infusion technology (VERITY). *Procedia Materials Science* **6**, 331–340 (2014)
5. Singer, J., Arbocz, J., Weller, T.: *Buckling Experiments: Experimental Methods in Buckling of Thin-Walled Structures*, Vol. 2, Shells, Built-up Structures, Composites and Additional Topics. Wiley (2002)
6. Bino Prince Raja, D., Ramanan, G., Ishwara Gowda, V., Patil, Suganthi, P.: Static structural analysis and testing of aircraft wing spar using composite material. *Materials Today: Proceedings* **64**, 416–424 (2022)





# Numerical and Experimental Comparison of Impact Damage Detection by Using Distributed Fiber Optics on a Stiffened Composite Panel

Monica Ciminello<sup>(✉)</sup> , Salvatore Ameduri , Bernardino Galasso ,  
Fulvio Romano , and Antonio Concilio 

CIRA - Italian Aerospace Research Centre, Via Maiorise Snc, 81043 Capua, Caserta, Italy  
m.ciminello@cira.it

**Abstract.** The scope of the activity is the development of an SHM system based on distributed fiber optic sensors able to detect, localise and measure, the debonded skin/stringer extensions and delamination areas on a composite stiffened panel generated by low energy impacts.

The panel is sensorized with 1.2m long fiber optic interrogated with “Rayleigh Backscattering” technology. The fibers are bonded along the edge caps of each stringer and also on the skin according to a specific grid layout. The strain data are then processed by a proprietary SHM algorithm, developed in the SMAF (SMart AirFrame) project of PRORA (Italian Aerospace Research Program). The algorithm named LHEO is based on the identification of high local gradients correlation in time and space domain corresponding to post-impact residual strain discontinuities. Through the use of this tool, the algorithm allows to detect the size and position of damage occurred in the structure without the need of healthy reference. Then, in order to provide an estimation of the surface extension of the impact effect on the skin, a dedicated subroutine, named EB “Expanding Bubbles” is developed. This method uses as input the parts of the sensor network characterised by positive outcomes given by the LHEO algorithm and generates progressive circular regions around each sensor, computing the ratio of border points over total points falling inside the circle. The results were expressed in terms of deviation with respect to the NDI reference coming from C-SCAN measurements. A good agreement was achieved for both the kind of damages.

**Keywords:** Impact detection · Composite structures integrity · Aircraft components · Structural Health Monitoring · Fiber optics distributed sensing · SHM algorithms

## 1 Introduction

The research activity presented in this paper, has been carried out within the MIUR-funded National Aerospace Research Programme (PRORA). The project itself, named SMAF dealt with setting new methodology for composite structures design oriented to

low-weight constraints, by means of retrieved infos from SHM systems. The scope of the specific activity has been the development of an SHM system based on distributed fiber optic sensors (FOS), able to detect, localize and measure, the skin/stringer debonding extensions and delamination areas on a composite stiffened panel generated by low energy impacts. The method presented is based on cross-correlation analysis of strain data, retrieved by distributed fiber optics whose effectiveness has been demonstrated in several applications, [1]. In civil structures, that approach was applied to modal analysis for identifying faults insurgence, [2], or to data correlation in the discrete frequency domain to detect changes in stiffness and damping properties, irrespectively of the influence of hysteretic and non-linear responses, [3]. In [4], estimation of time of flight of wave packages by means of cross correlation signals was used to locate defects within a thin-plate. Proposed algorithm proves its capability to detect impact area and occurred skin-stringer debonding, without reference to applied loads or a certain baseline. A dedicated Matlab routine elaborates the output further, with the aim of visualizing and estimating impact region extension.

## 2 SHM System

Structural damage diagnosis algorithms include trade-off between diagnosis efficiency and accuracy. In general, the sensor system provides a signal signature describing the current state of the monitored structure. Features, exploited by classification, regression, or clustering algorithms, synthesize data collected to get sensible and concise representations of the phenomenon, aiming at identifying abnormal conditions as possible occurrences of damage. Based on experiences in several projects, CIRA has developed a specific SHM algorithm for FOS to detect damage size and location on the base of feature extraction and binary classification to be used with Distributed Fibers Optics strain data log.

### 2.1 Algorithm (L.H.E.O.)

Most of SHM robust systems are reference-driven, that means damage detection is based on the knowledge of the structure healthy signature. It is also known that in some applications, damage detection methods with unknown input force could be more desirable because real loading conditions are not always simple to reproduce. Thus, SHM should use the only measured readings. In this project the second approach is chased by FOS. The idea is to detect damage occurrences without any a-priori characterization of the component [5–7]. To do this, the main physical effect of the damage (that kind of) presence must be exploited in order to find out an effective identification procedure (features extraction). Damage is a structural discontinuity (Fig. 1). The transition onset is characterised by gradient peak of strain energy signal. This happen both in the space and in time domain [8, 9].

In-line distributed sensors network (high density) are able to detect such a profile. The sensors geometrically laying away from the discontinuity onset provide a quiet “linear” strain variation.

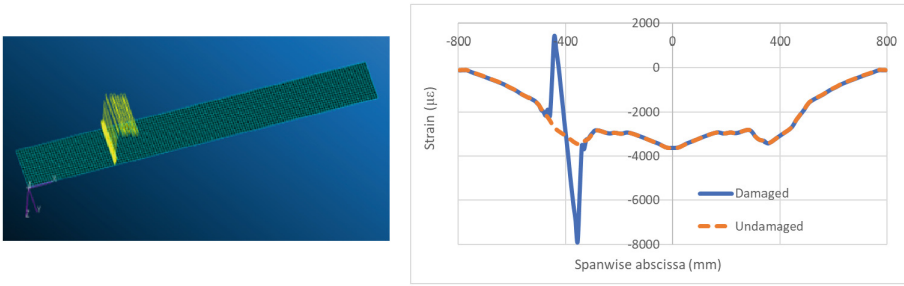


**Fig. 1.** Reference driven damage signature example.

LHEO process structural **damage as an edge discontinuity** along the strain energy signal. Edges onset can be tracked as non-linear event **in both the space and time correlating “current to next”**, by using “sliding window” proportional to the space resolution **ds** and sample rate **dt**.

- **Test statistic for DI (Damage Index):** if no jump/edge are present, the cross-correlation variance with respect to autocorrelation will be small. On the contrary, if data sample happens to be on the edge, then the two functions values will be quite different.
- **Hysteresis thresholding to filter eligible sensors:** the max envelope of the cross-correlation variance set the highest threshold (T), the mean value of the envelope set the low T. Any readout below LT (Low Threshold) are discarded, any readouts between LT and HT (High Threshold) are kept only if there is a “link” connecting them.

In addition, in order to provide an estimation of the impact surface, the algorithm generates progressive circular regions around each eligible sensor (previous readouts filtering), computing the ratio of positive sensors over total sensors falling inside. In this way it builds the coloured curves reported on the plots on the top. A mean curve is then estimated. Then, the 1st and 2nd derivatives of this curve are estimated. By using the first minima from both curves the delimiters of the estimated area of the damage are set. The area estimation is the average between the two minima (Fig. 2).

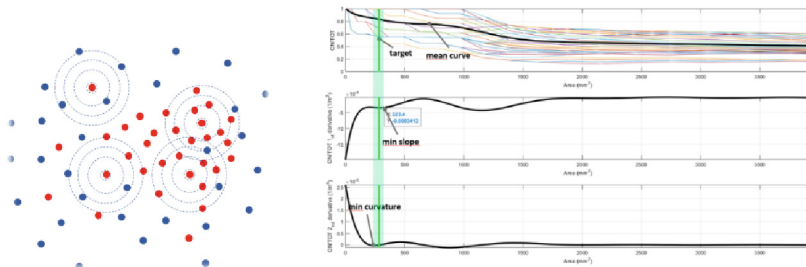


**Fig. 2.** Algorithm for impact area estimation.

### 3 Test Setup

A CFRP full size aeronautical panel, with three stringers, is sensorized with distributed fiber optics with a specific layout (Fig. 3) for impact area monitoring. The LUNA OFDR OdisiB, is the optical interrogator adopted to collect distributed sensor readouts. The regions of interest are the stringer edges cap for delamination detection and skin in between the stringers for impact detection (Fig. 4).

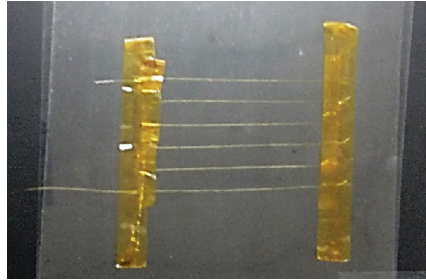


**Fig. 3.** Distributed FO with a sinusoidal path able to cover a skin region for impact detection

This high-resolution Rayleigh backscattering-based system can provide quasi-continuous strain data with a lower than  $1 \mu\epsilon$  resolution, and  $\pm 30 \mu\epsilon$  accuracy. In this work, a 2.6 mm space resolution and a 5 mm gauge length are selected. A single channel, 2 m long fiber, allowed then having more than 400 sensible points.

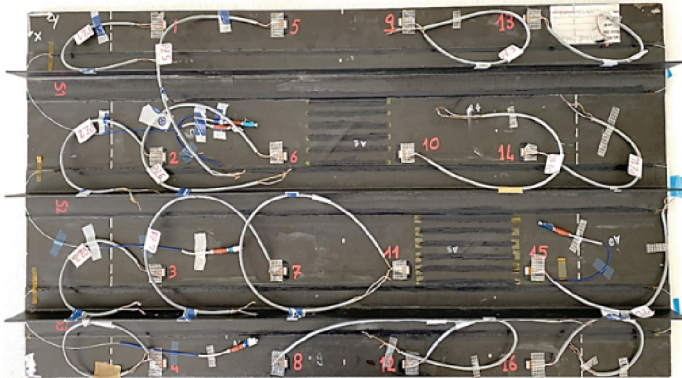


**Fig. 4.** Sensorized wing box full size panel

Damage are then realized by out-of-plane, concentrated low-medium energy impacts using a drop-weight device with a hemispherical impactor. Structural element has then undergone ultrasonic NDI by Phased Array Ultrasonic Testing (PAUT) tests with an Olympus OmniScan SX flaw detector. Both the cases of skin indentation and stringer debonding have been taken into consideration for validation and assessment of damage detection SHM algorithm.

## 4 Results

### 4.1 Experimental Results

In accordance with C-scan figures (courtesy of University of Naples “Federico II”), NDI imaging colours are associated to skin and stringers thicknesses. Healthy material is red, stringer web is blue, adhesive layer between stringer and skin is orange. As orange or red appears interrupted in the pattern, a damage occurred. White edges are used to identify the region of the impacts (Figs. 5 and 6). SHM output provides the position and dimension of the damage. Yellow lines indicate position and extension of fiber optics. Black line the eligible sensors from SHM algorithm, used to estimate the length of the disbonding, the pink area indicates the estimation of impact (Fig. 6). Results are collected in Table 1.

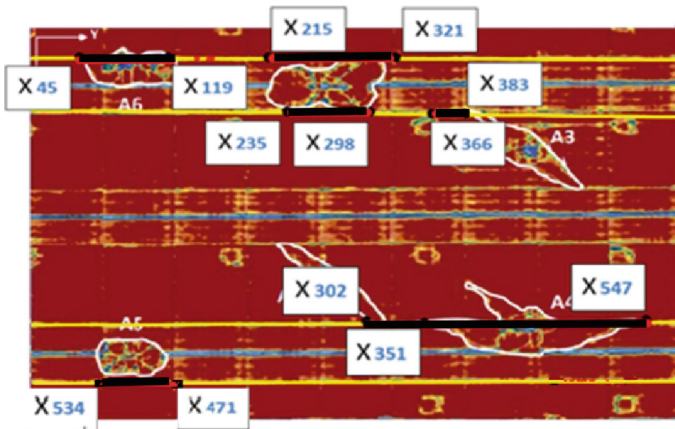


**Fig. 5.** Experimental Results for stringer cap delamination after impact.

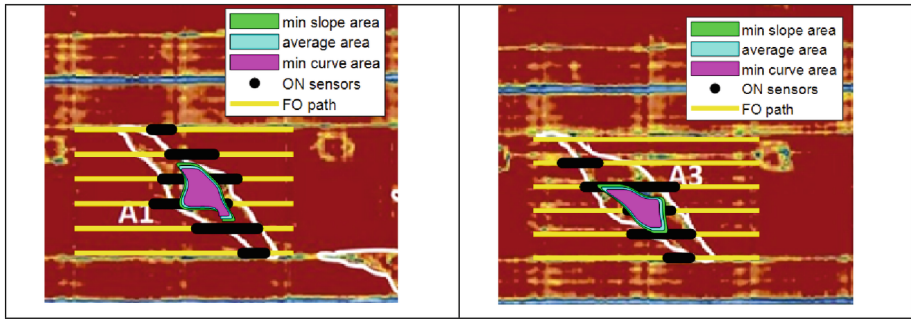


**Fig. 6.** Experimental Results for impact area estimation

**Table 1.** SHM results error estimation.

Fully impacted area	Target value (mm <sup>2</sup> )	Estimated value (mm <sup>2</sup> )	Deviation (%)
A1	1026,0	996,0	-2,9
A3	861,0	965,2	12,1

## 5 Conclusions

Experimental and Numerical measurements were performed on Test Article and a comparison with the C-scan of the damage detection method by means of Distributed Fiber Optics using LHEO algorithm has been shown.

The results of this work show that the LHEO algorithm provide reliable measurements for both position and size of disbonding passing from Distributed Fibers Optics.

The system appeared to be sensible at hundreds of microstrain signals (but it strongly depends by the instrumentation accuracy).

Errors in damage extension estimation confirmed to be in the region around 12%.

Lower boundary for damage length detection is 20 mm.

## References

1. Zhang, M., Schmidt, R., Markert, B.: Structural damage detection methods based on the correlation functions. In: Proceedings of the 9th International Conference on Structural Dynamics. Porto, Portugal (30 June–2 July 2014)
2. Huo, L.S., Li, X., Yang, Y.B., Li, H.N.: Damage detection of structures for ambient loading based on cross correlation function amplitude and SVM. *Shock Vib.* **2016**, 3989743 (2016)
3. Kouris, L.A.S., Penna, A., Magenes, G.: Seismic damage diagnosis of a masonry building using short-term damping measurements. *J. Sound Vib.* **394**, 366–391 (2017)
4. Yu, L., Bao, J., Giurgiutiu, V.: Signal processing techniques for damage detection with piezoelectric wafer active sensors and embedded ultrasonic structural radar. In: Proceedings of the Smart Structures and Materials, International Society for Optics and Photonics, pp. 492–503. San Diego, CA, USA (14–18 March 2004)

5. Ni, P., Xia, Y., Law, S.-S., Zhu, S.: Structural damage detection using auto/cross-correlation functions under multiple unknown excitations. *Int. J. Struct. Stab. Dyn.* **14**(05), 1440006 (2014)
6. Güemes, A., Fernández-López, A., Soller, A.: Damage detection in a stiffened curved plate by measuring the differential strains. In: Conference: ICCM 16th International Conference on Composite Materials (July 2007)
7. Muyu, Z., Rüdiger, S., Bernd, M.: Structural damage detection methods based on the correlation functions. In: Proceedings of the 9th International Conference on Structural Dynamics, EURO DYN 2014 Porto, Portugal (2014)
8. Fried, R.: On the robust detection of edges in time series filtering. *Comput. Stat. Data Anal.* **52**(2), 1063–1074 (2007)
9. Li, M., Ren, W.-X., Huang, T.-L., Wang, N.-B.: Experimental investigations on the cross-correlation function amplitude vector of the dynamic strain under varying environmental temperature for structural damage detection. *Journal of Low Frequency Noise, Vibration and Active Control* **39**(3), 631–649 (2020)



# Equivalent Material Identification in Composite Scaled Hulls Vertical Impact Tests

E. Cestino<sup>(✉)</sup>, G. Frulla, A. Polla, and G. Nicolosi

Politecnico di Torino DIMEAS, C.so Duca Degli Abruzzi 24, 10129 Torino, Italy  
enrico.cestino@polito.it

**Abstract.** The impact in water is a very complicated phenomenon due to the interaction between the hydrodynamic field and the structures and the possibility to investigate its characteristics by means of a scaled model seems straightforward. In general, the similarity procedure requires the scaling of different properties (mass, length, speed, etc.) to properly represent such a phenomenon. In the present case the fluid-dynamic phenomena are scaled thanks to the Froude similarity while the definition of specific material and its scaling rules for a complete similarity is required in several cases particularly when composites play a predominant role on the test response. The introduction of Trace parameter is proposed as a method orienting the designer for the right material selection in these situations. Numerical simulation using the LS-DYNA software and modified Von Karman theory is used to validate the procedure in predicting the maximum pressure in the first phases of impact. An experimental test is finally designed to calibrate the physical and numerical parameters.

**Keywords:** Impact tests · Flexible hulls · Physical similarity · Composite trace

## 1 Introduction

Airworthiness regulations require that aircraft should be proved to ensure the survivability of the ditching for the passengers. Seaplane aircrafts must be designed for water loads developed during take-off and landing with the seaplane in any attitude likely to occur in normal operation at appropriate forward and sinking velocities under the most severe sea conditions [1]. To make a stress analysis of seaplane floats, and especially of the members connecting the floats with the fuselage, it is of great importance to determine the maximum pressure acting on the floats during landing [2].

The research presented is in collaboration with the student team of the Polytechnic of Turin whose activities are centered around the S55 aircraft, a double-hulled flying seaplane designed and produced in Italy by Alessandro Marchetti, beginning in 1924. The S.55X featured many innovative design features and shortly after his entry into service, it began setting records for speed, payload, altitude and range and was the symbol of the aeronautical know how reached in Italy during the '20 s and '30 s. The S55 Student Team was born at the beginning of 2017 by a few students passionate about aeronautics and now has about 80 members.



Three main activities characterize the work of the Team. First a support for the design and verification of a 1:1 scale flying replica in collaboration with the Replica 55 group [2, 3]. In this context, the activity mainly concerns on simulation activities for the determination of aerodynamic and ditching loads and the construction of a complete FEM model of the aircraft which was manufactured of laminated wood [2]. The second activity was the design and manufacturing of a 1:8 scaled flying prototype propelled by two counter rotating propellers and electric motors powered by Lithium Polymer Batteries. This prototype is the basis for the third activity and the prototype which is under construction (S55-HERA), a long-range unmanned version with electric propulsion based on hydrogen fuel cells.

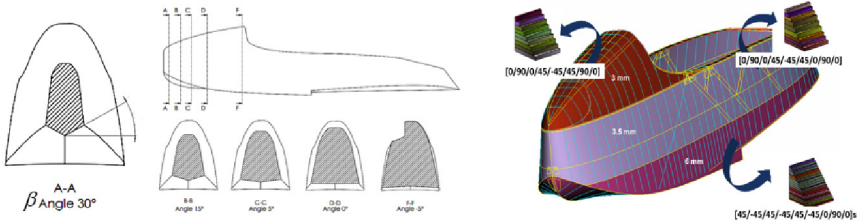


**Fig. 1.** Deadrise angle distribution and laminate layout for 1:1 S55 hull

As can be seen from Fig. 1, in the case of the 1:1 S55 hull have a wood composite structure in which the deadrise angles vary from 30° to 0° and take negative values in some sections. The research therefore concerns with the determination of ditching pressures in flexible hulls made of composite materials focusing on the difficulties associated with the creation of models in physical similarity and with the possibility of simulating such phenomena. The approach used has seen the definition of new analytical models including flexibility, experimental validation tests to validate the theoretical models and numerical simulation, starting from local models, global models with fixed deadrise angle up to models that represent the real geometry of the hull.

## 2 Theoretical Models

The first reason for this work is a limitation of current aeronautical regulations in determining ditching pressures when the dead-rise angles are very low. The regulation proposed formula is based on a treatment by Von Karman from 1929 [4] and is characterize on some fundamental assumptions: 1) calm water 2) rigid surface 3) water is considered as incompressible fluid 4) no Aerodynamic effects. Equation 1 reports the classic Von Karman expression for the maximum pressure observed over the wedge surface:

$$p_{max} = \frac{1}{2} \rho V_0^2 \pi \frac{1}{\text{tg}(\beta)} \quad (1)$$

A second theory used for comparison is the one developed by Wagner [5] in 1932.

This theory considers the local uprise of water along the wedge surface and the maximum pressure is calculated by Eq. 2:

$$p_{max} = \frac{1}{2} \rho V_0^2 \left[ 1 + \frac{\pi^2}{4 \tan(\beta^2)} \right] \quad (2)$$

## 2.1 Isotropic Flexible Wedge

Authors proposed a modification of the Von Karman formulation based on the idea that when dealing with a flexible hull the pressure itself generates an elastic component of the deadrise angle  $\beta_e$  which adds to the rigid one  $\beta_r$  as shown in Fig. 2.

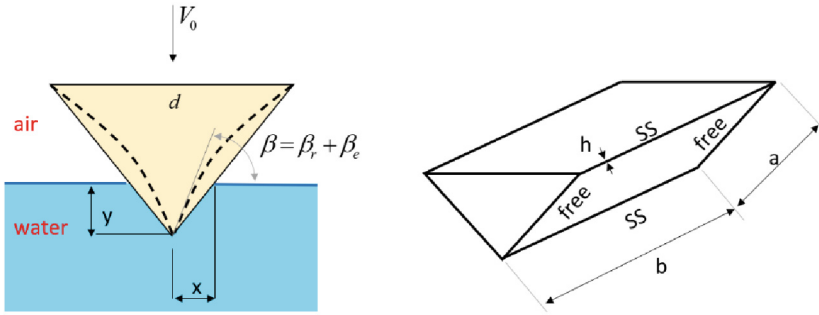


Fig. 2. Flexible edge notation

The elastic component depends on the stiffness of the structure and therefore on its deflection under load. The formula which describes the maximum pressure observed on the impacted surface is given here for the case of a flexible wedge made of isotropic material, simply supported on two sides and free on the other two as reported in Fig. 2.

$$p_{max} = \frac{1}{2} \rho V_0^2 \pi \left[ \frac{1 - \frac{5}{16} \frac{p_{max}(1-\nu^2)}{E} \left(\frac{a}{h}\right)^3 \text{ktg}(\beta_r)}{\frac{5}{16} \frac{p_{max}(1-\nu^2)}{E} \left(\frac{a}{h}\right)^3 k + \text{tg}(\beta_r)} \right] \quad (3)$$

where  $\beta_r$  is the rigid component of the deadrise angle and  $k$  is a parameter depending on system damping and representing the ratio between dynamic and static deflection. For the realization of a model in physical similarity it is necessary to consider that the rigid case is described by 5 different parameters, considering 3 fundamentals quantities reducible to two ( $g$ ;  $\rho$ ), three dimensionless parameters are to be reproduced between the real and the model scale.

:

$$f(p_{max}, \rho, V_0, d, \beta) = 0 \quad (4)$$

and therefore

$$\frac{V_0}{\sqrt{gd}} = Fr, \frac{p_{max}}{\rho gd}, \beta \quad (5)$$

On the other hand, in the flexible case we have 8 parameters, 3 fundamentals reducible to two ( $g$ ;  $\rho$ ):

$$f(p_{max}, \rho, V_0, d, \beta_r, h, \nu, E) = 0 \quad (6)$$

that means that 6 the dimensionless parameters must be reproduced between the real and the model scale:

$$\frac{V_0}{\sqrt{gd}} = Fr, \frac{p_{max}}{\rho gd}, \beta, \frac{h}{d}, \frac{p_{max}}{E}, \nu \quad (7)$$

Figure 3 shows some results relating to the maximum pressure as a function of the deadrise angle and vertical impact speed. Figure 3, on the left illustrates how the flexibility at low deadrise angles produce a reduction of the maximum pressure observed. Moreover, the second graph shows the same result reported as a function of the vertical impact speed. It can be noted that the effect of flexibility is more important as speed increases.

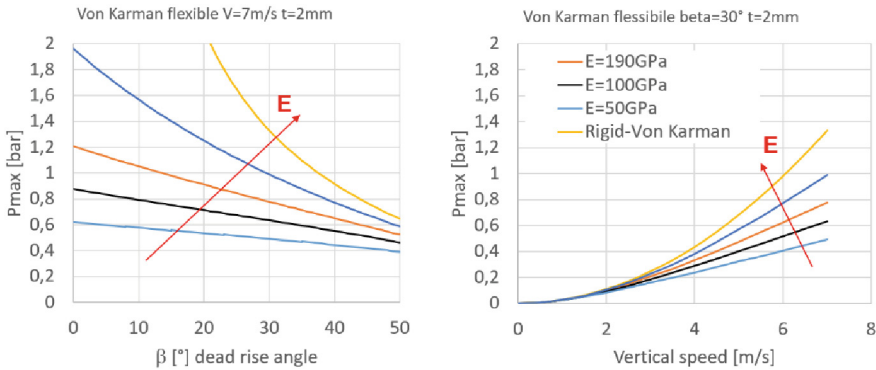


**Fig. 3.** Flexible & Rigid edge maximum pressure

## 2.2 Composite Flexible Wedge

In composite configurations it is possible to define a parameter (Trace) that is invariant with respect of the laminate lay-up. The stiffness tensor of a composite ply ( $Q_{ij}$ ):

$$Trace = Q_{11} + Q_{22} + 2Q_{66} = \frac{E_1 + E_2 + 2\left(1 - \nu_{12}^2 \frac{E_2}{E_1}\right)G_{12}}{1 - \nu_{12}^2 \frac{E_2}{E_1}} \quad (8)$$

or laminate (A, D) shares the same transformation and Trace:

$$Trace = \frac{1}{h}[A_{11} + A_{22} + 2A_{66}] = \frac{12}{h^3}[D_{11} + D_{22} + 2D_{66}] \quad (9)$$

In this way, all the information concerning stiffness is restrained in only one mechanical value. Therefore, Trace can be used to predict the mechanical behavior of different materials, isotropic and 2D orthotropic, by simple scaling. The trace includes three fundamental material parameters and the orthotropy ratio  $p_1 = E_1/E_2$  is characteristic of the material class. All materials with the same  $p_1$  belong to the same class as can be seen from the Fig. 4a in which the isotropic materials are on the black line, the fabrics on the dashed line and the unidirectional ones on the gray.

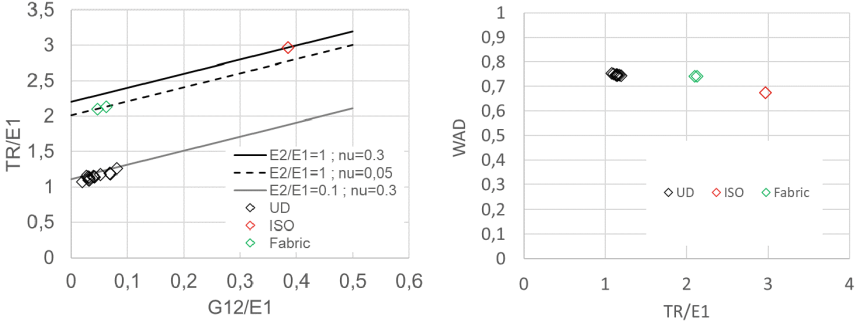


**Fig. 4.** a) material classes b) dimensionless deflection  $W_{AD}$

Considering the scaling procedure in a simple static problem concerning the deflection of a simply supported specially orthotropic plate loaded by a sinusoidal pressure, the equilibrium equation can be written in dimensionless form by making the trace appear [6]:

$$\bar{D}_{11} W_{,\xi\xi\xi\xi} + 2(\bar{D}_{12} + 2\bar{D}_{66})\lambda^2 W_{,\xi\xi\eta\eta} + \bar{D}_{22}\lambda^4 W_{,\eta\eta\eta\eta} - \frac{12p_z}{TR} \frac{a^4}{h^4} = 0 \quad (10)$$

where:

$$\xi = \frac{x}{a}; \quad \eta = \frac{y}{b}; \quad \zeta = \frac{h}{a}; \quad \lambda = \frac{a}{b}; \quad W = \frac{w}{h}; \quad [\bar{D}] = \frac{12}{h^3 TR} [D]; \quad \overline{TR} \frac{TR}{E_1} \quad (11)$$

Plate dimensionless displacement ( $W_{AD}$ ) can be expressed in terms of a load parameter and a stiffness parameter. By dividing the displacement by the load parameter, we get  $W_{AD}$  parameter

$$W_{AD} = \frac{W_{11}}{\frac{12}{\pi^4} \left(\frac{p_0}{TR}\right) \left(\frac{a}{h}\right)^4} = \left[ \frac{1}{\bar{D}_{11} + 2(\bar{D}_{12} + 2\bar{D}_{66})\lambda^2 + \bar{D}_{22}\lambda^4} \right] \quad (12)$$

Referring to Fig. 4b it is possible to say that with the same layout the materials of the same class have the same  $W_{AD}$  value. This means that it is possible to design a similitude structure by using a parameter that is the analogue of the  $p_{max}/E$  ratio in Eq. 7 of the isotropic case which in the case of composite structure become  $p_{max}/TR$ .

### 3 Experimental and Numerical Models

As regards the experimental tests, the first test carried out is on a wedge with a constant dihedral angle and made of steel ( $\beta_r = 30^\circ$ ,  $E = 190$  GPa,  $\nu = 0,3$ ). The wedge is equipped with two pressure sensors (P1, P2) and two accelerometers (A1, A2) and is released from different heights corresponding to different vertical speeds from 0.4 m corresponding to 2.8 m/s to 1.7 m corresponding to 5.77 m/s. Figure 5 reports the experimental set-up and the geometrical dimension of evaluated wedge configuration.

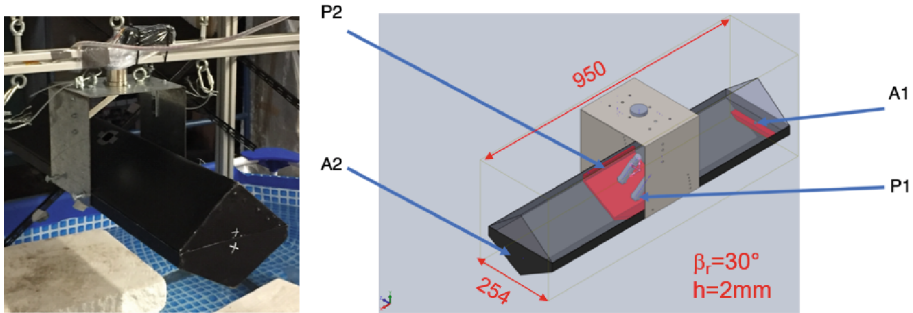


**Fig. 5.** Wedge for experimental vertical impact test

Once the wedge has been positioned to the desired height, it is released by means of an electromagnetic release system. Figure 6 shows some examples of accelerations (on the left) and pressures (on the right) measured at two different heights  $H = 0.7$  m and  $H = 1.3$  m. The results are reported both in the original form and also after the application of a Butterworth filter. For the pressure sensors the signal frequency is 93 Hz, a noise frequency at 2000 Hz and the cut-off frequency set at 500 Hz while for the acceleration sensors the frequency signal is 1000 Hz with 3000 Hz noise and 1200 Hz cutoff frequency.

Numerical models here proposed are based on the application of a general-purpose explicit finite element code. Explicit time integration scheme is used in LS-DYNA to solve dynamic equations that characterize FSI phenomenologies. SPH particles were used to simulate the fluid domain while Lagrangian shell elements have been used for the definition of the rigid wedge model. The simplest model here proposed is a local 2D approximation. The simulation takes advantage of the introduction of symmetry planes and with the definition of non-reflection walls. An example of pressure trend obtained with LS-DYNA in correspondence with the experimental sensors in a case in which the shell elements are imposed as a rigid structure are reported in Fig. 7. A comparison of the maximum pressures obtained for the different sensors position is reported in Fig. 8. Rigid LS-DYNA model gives a maximum pressure that lies within the range predicted by the theories of Von Karman and Wagner, both with the hypothesis of a rigid wedge. Black line reported in Fig. 8 shows the trend of the values predicted by the flexible wedge theory here proposed. Red crosses are the experimental values obtained during the test campaign. An excellent correlation between experimental data and proposed theory was obtained. LS-DYNA numerical solutions define higher pressure value for the

rigid wedge configuration. The null compliance of the structure defines higher pressure values as described by the analytical formulation here proposed and as reproduced in Fig. 8.

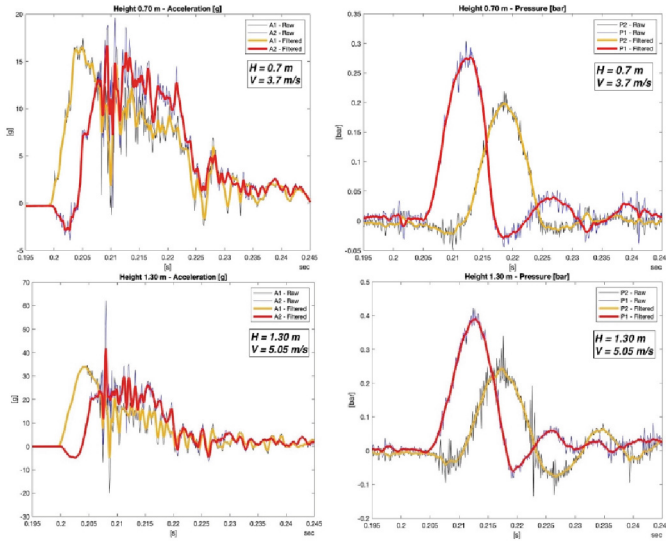


Fig. 6. Example of experimental data Accelerations (left) and pressures (right)

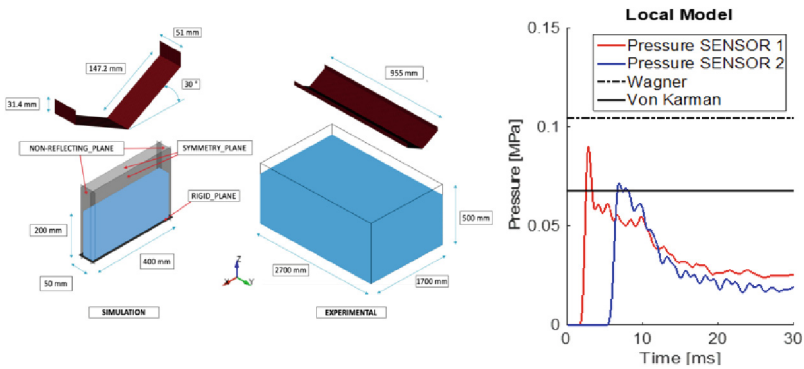
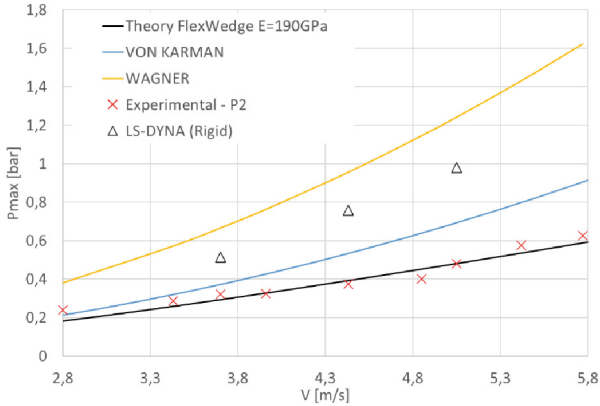


Fig. 7. LSDYNA model & results of Rigid Wedge

The future work will concern for the numerical part the simulation with the included flexibility and the transition to real geometry, while for the experimentation part a wedge is being designed that allows to install impact panels with different materials and different flexibilities. Trace will allow to identify the ideal material for a good physical similarity.



**Fig. 8.** Maximum pressure comparisons

## 4 Conclusions

The problem of designing models in physical similitude for the analysis of maximum ditching pressures is studied both in the rigid case and in the case of material flexibility. For composites, a structural parameter which represents the stiffness characteristics of the material with the same geometry, lay-up and boundary conditions is adopted. A simplified theoretical formulation is proposed for the isotropic case and its validity is demonstrated through vertical drop experimental tests. A numerical treatment is also proposed using the LS-DYNA software and SPH formulation.

## References

1. EASA: Certification Specifications for Normal, Utility, Aerobatic, and Commuter Category Aeroplanes CS-23. European Aviation Safety Agency (July 2012)
2. Cestino, E., et al.: Replica 55 Project: A Wood Seaplane in The Era of Composite Materials. In: Proc of 31st ICAS Congress. Belo Horizonte, Brazil (2018)
3. Nicolosi, G., et al.: Design of A Vertical Ditching Test. In: Proc. 32nd ICAS Congress 6–10 September 2021. Shanghai, China (2021)
4. Karman, V.: The impact on seaplane floats during landing. NACA (1929)
5. Wagner: Phenomena associated with impact and gliding on a liquid surface. *J. Appl. Mathema. Mecha.* **12**(4), 193-215 (1932)
6. Frulla, G., Cestino, E.: Equivalent material identification for complete similarity in scaled-model tests. In: proc. AIDAA XXV International Congress, pp. 282–288



# Design and Maintenance of Aircraft Composite Structures by Advanced Damage Inspection Techniques

Fulvio Romano<sup>(✉)</sup> , Assunta Sorrentino , Monica Ciminello ,  
Salvatore Ameduri , Michele Inverno , and Romualdo Sorrentino 

CIRA-Italian Aerospace Research Centre, Via Maiorise Snc, 81043 Capua, Caserta, Italy  
f.romano@cira.it

**Abstract.** This work summarises the outcome of the activities performed in the context of SMAF (Smart AirFrame) project, which is part of PRORA (the Italian Aerospace Research Program). The main goal of SMAF is the enhancement of an integrated offline SHM (Structural Health Monitoring) system, aimed to improve the maintenance and the design approaches of composite primary aircraft structures. The SHM system includes piezoceramic sensors/actuators (PZT) and distributed fiber optic sensors (FOS) for the detection, localisation and measurement, of both the lamination damage and the debonded skin-stringer line extension, induced by low energy impacts. The whole system has been developed and verified through a building block approach; through tests on structural subparts of intermediate and growing size and complexity: from small stiffened panels up to a full-scale stiffened wing panel. Experimental and numerical results are illustrated. Promising reliability of the integrated (PZT + FOS) SHM system has been demonstrated in detecting and measuring the area of the impact/delamination damage and skin-stringer debonding length. This should allow in the future the possibility to make more efficient composite structures, in terms of operating costs, also by improving their static strength with significant weight reduction.

**Keywords:** Stiffened Composite Panel · Damage · Design · Bonding · Impact Detection · Structural Health Monitoring

## 1 Introduction

The aircraft composite structures are characterised by a higher sensitivity to manufacturing defects and impact damage with respect to the metallic ones. The upper limit of the allowable manufacturing defects and in particular of the low energy impact damage, not detectable by the “visual inspection technique”, is the BVID (Barely Visible Impact Damage, [1, 2]). This damage, based exclusively on the sensitivity of the visual inspection technique, is that one used to provide the compressive design allowable of the airframe composite structures, determining therefore their final weight. The BVID is induced by tool drops, runway or ground debris, hailstones, etc., “barely” visible from a distance of about 1.5 m under ambient light conditions, and characterised by a



dent depth of about 0.8/1 mm. In SMAF (Smart AirFrame) project, funded by PRORA (Italian Aerospace Research Program), an integrated offline SHM (Structural Health Monitoring) system has been developed aiming at improving the current maintenance and the design approaches of aircraft primary structures in composite material. This system includes high frequency piezoceramic sensors/actuators (PZT, 100 kHz to 200 kHz) and distributed fiber optic sensors (FOS, 1 Hz to 250 Hz) for the detection, localisation and measurement, of the damage induced by low energy impacts and of the debonded skin-stringer line extension, in composite wing panels. The verification and validation of the SHM system has been achieved through the classical building block approach, by testing activities performed on structural sub-parts of intermediate and growing size (elements, details) and complexity (small-stiffened panels with different layups and damage scenarios), up to a full-scale stiffened wing panel. The experimental and numerical activities performed in this work have been addressed to demonstrate that the SHM system is potentially able to reduce the current operating costs for composite structures by a significant percentage: a) by replacing with it the current in service two-level inspection approach applied to these structures, that is visual inspection followed by NDI (Non-Destructive Inspection)/C-scan, if required; b) by improving their static strength with significant weight saving, thanks to the use of higher design allowables as result of the detection of impact damage with size and indentation smaller than the BVID.

## 2 SHM System

The SHM system has been conceived as an advanced non-destructive inspection system. It has been applied in this work to flat carbon-epoxy stiffened panels, representatives of upper wing box panels (loaded in compression) of a regional aircraft, subjected to low energy impacts (on the unstiffened skin, i.e. external side of the panels). The PZT subsystem is finalised to the detection, localisation and measurement of the delamination damage [3], while the FOS subsystem of both skin-stringer debonding and delamination damage [4]. Figure 1 shows small stiffened panels and examples of the impact damage and skin-stringer flange debonding.

Algorithms have been developed ad hoc for both types of the two subsystems.

The PZT algorithm is a triangulation analysis method based on the propagation of Lamb waves inside the structure [5]. The presence of a damage considerably disturbs the propagation of the wave on a panel compared to the undamaged panel, generating an additional wave that represents the perturbation (Fig. 2a). The detection area is delimited by a quadrilateral of four PZT patches; each PZT patch acts in turn as actuator and the other three as sensors. Three sensing paths are necessary for an accurate identification of the damage location, while the dimension of the damage (delamination area) is evaluated by a minimum of four sensing-paths.

The FOS subsystem uses distributed optical fiber sensors [6], Fig. 2b. It is based on time and spatial gradient features indicators extracted from a strain distribution provided by a Rayleigh backscattering optical monitoring system. Two algorithms have been developed; one, aimed at the localisation and measurement of the debonding length; the second (“expanding bubbles” method) aimed at the delamination area.

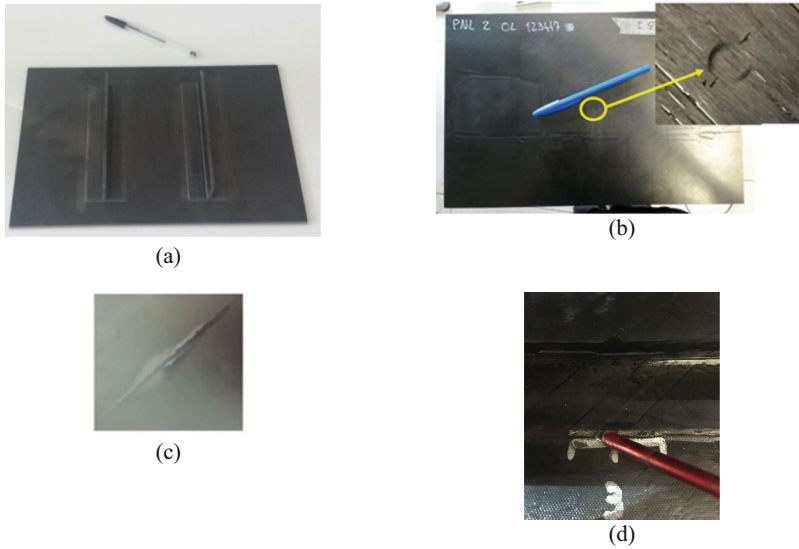


**Fig. 1.** Small stiffened panel, 350 mm × 230 mm: (a) stiffened skin; (b) impact in the middle of the stringer bay (on the external side/unstiffened skin); (c) damage on the opposite (on the internal side/stiffened skin); (d) skin-stringer flange debonding.

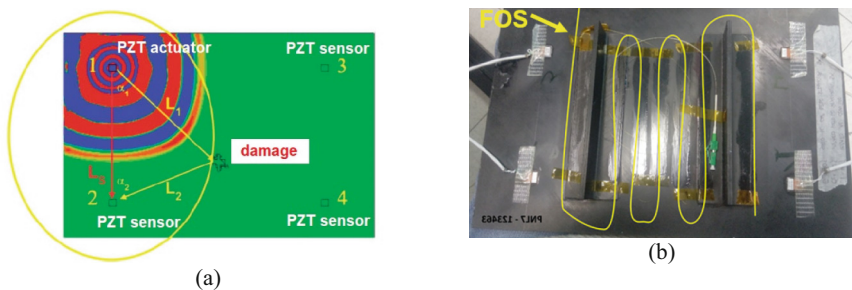


**Fig. 2.** (a) PZT subsystem: triangulation analysis method; (b) FOS subsystem: distributed optical fiber.

Figure 3 shows the impact scenario and the SHM hardware applied to small stiffened panels.



**Fig. 3.** Small stiffened panel, 350 mm  $\times$  230 mm: (a) damage scenario; (b) SHM system.

### 3 Verification and Validation Approach

The SHM system has been verified and validated through tests on CFRP panels of intermediate and growing size and complexity. In particular, starting from small panels (350 mm  $\times$  230 mm), unstiffened and then stiffened, to verify and tune the SHM algorithms, up to a full-scale stiffened wing panel for the final validation (see Fig. 4).

The small panels are characterized by different layups and thicknesses in agreement to a typical layup distribution over the wing of a regional aircraft.

The impact scenario applied to the panels is consisted for each panel in one or more impacts and in correspondence of the locations shown in the sketch of Fig. 5: in the middle of the stringer bay, i.e. centre of the panel (Fig. 5a), at the edge of the stringer flange, trying to provoke also the debonding between the skin and the stringer flange (Fig. 5b), under the stringer flange (Fig. 5c). The energy levels applied to the panels varies from 15 J to 120 J, depending on their thicknesses.

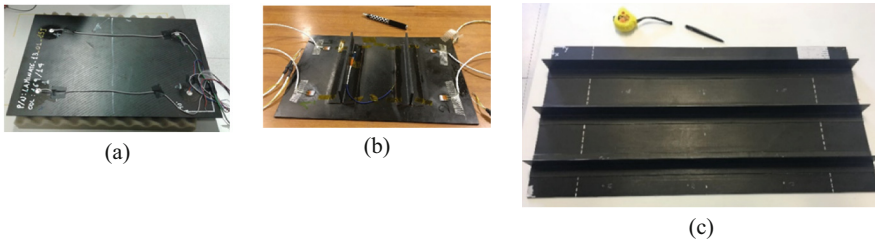


**Fig. 4.** (a) No.10 unstiffened panels (350 mm  $\times$  230 mm); (b) No.21 stiffened panels with 2 stringers (350 mm  $\times$  230 mm); (c) final demonstrator: No.1 stiffened panel with 3 stringers (470 mm  $\times$  940 mm).

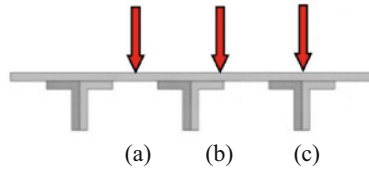


**Fig. 5.** Impact scenario.

Figure 6a shows the impact scenario applied to the final demonstrator (with  $A_i$  the impact sites) including the classified locations of Fig. 5.

The impacts have been executed by standardized drop weight impact machines and fixtures. After the impacts, C-scan have been executed in the impact locations, as for example that one shown in Fig. 6b. The estimation of the delamination area by C-scan is the reference data respect to which the capability of the SHM system is compared.

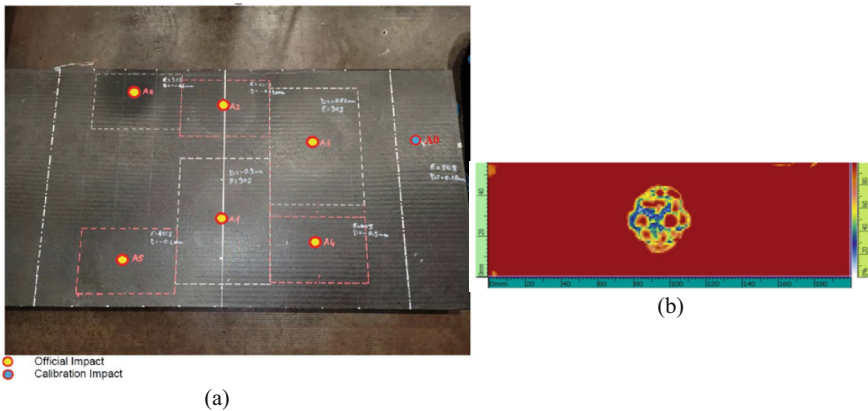


**Fig. 6.** (a) final demonstrator: impact scenario; (b) C-scan after impact on an impact location.

## 4 SHM Output

Figure 7 shows the SHM sensors/actuators bonded on the final demonstrator and some of the acquisitions and elaborations of the SHM system are reported in Fig. 8.

The results have shown an important capability of the system in the detection and measurement of both the delamination damage and skin/stringer debonding, with an average deviation, with respect to the C-scan output, of about 3% for their localization and of about 12% for the measurement of their size. This result satisfies the project requirements. On the other hand, the system has also demonstrated the capability to detect the impact damage with a dent depth lower than that one detectable with the standard visual inspection technique. A feasibility study, based on the possibility to resize the above stiffened panels, for the same design load, taking into account this

result, has implied therefore the use of a higher compressive design allowable, respect to that one associated to the classical BVID, with a consequent potential reduction in the structural weight of the new panels up to 20%.

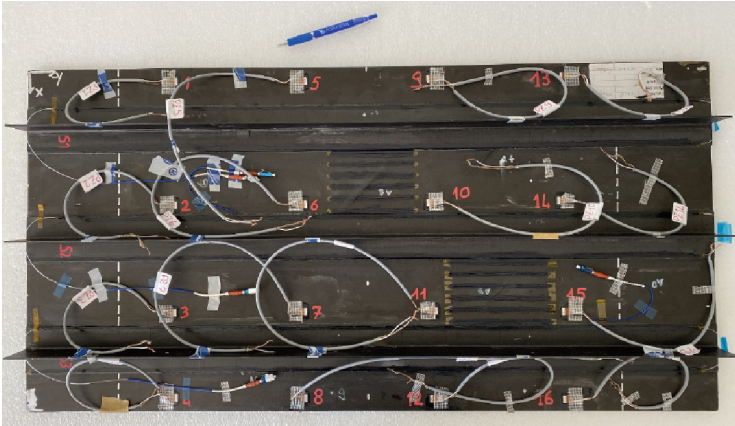


**Fig. 7.** PZT sensors/actuators and FOS applied to the final demonstrator.

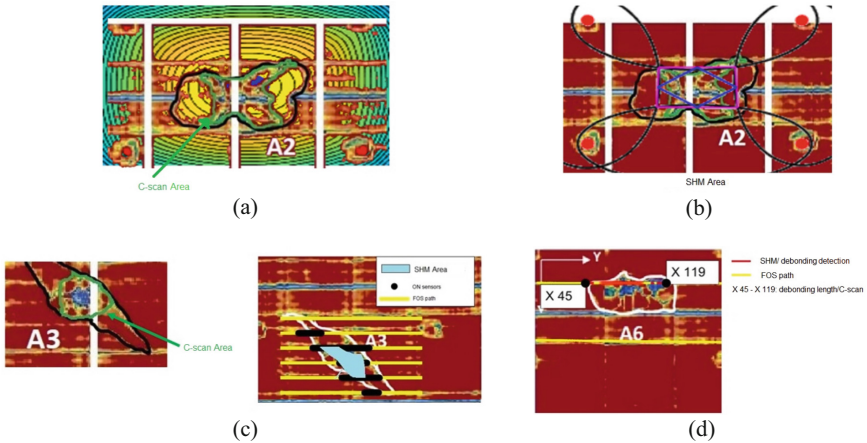


**Fig. 8.** (a, b) PZT subsystem: damage/delamination area. C-scan vs SHM output; (c) FOS subsystem: damage/delamination area. C-scan vs SHM output; (d) FOS subsystem: debonding detection. C-scan vs SHM output.

## 5 Conclusions

The SHM system developed in this work has demonstrated, within the limits of the planned technological development of the project, a promising reliability in detection and







localization of both delamination and debonding, as well as in the measurement of their dimensions. The two subsystems, PZT and FOS, have been proven to be complementary when one of the two subsystems is limited in detecting the damage due to technological constraints and restrictions. Additionally, the system is capable of detecting impact damage with a smaller indentation than the current one detected by traditional visual inspection technique. This paves the way in the future for the use of the SHM technology in place of the visual inspection technique and for the definition of a new damage threshold to be used in the design of the composite structures, allowing the application of higher design allowables and consequently obtaining lighter composite structures than the current ones.

## References

1. EASA AMC 20–29. Composite aircraft structure. <https://www.easa.europa.eu/downloads/1698/en>. Last Accessed 04 Sep 2022
2. Baaran, J.: Visual Inspection of Composite Structures. Institute of Composite Structures and Adaptive Systems DLR Braunschweig Lilienthalplatz 7, 38108 Braunschweig, Germany (9 July 2009)
3. Sorrentino, A., De Fenza, A., Romano, F., Mercurio, U.: Experimental application of Lamb wave based SHM system at complex composite material structures. In: EWSHM 2018 - 9th European Workshop on Structural Health Monitoring. Manchester, United Kingdom (2018)
4. Ciminello, M., Ameduri, S., Romano, F., Concilio, A.: Impact area and debonding line detection assessment by cross-correlation analysis and distributed sensing. *J. Opt. Fiber Technol.* **58**, article 102245 (2020)
5. Sorrentino, A., De Fenza, A.: Improved elliptical triangulation method for damage detection in composite material structures. *J. Mech. Eng. Sci.* **231**(16), 3011–3023 (2016)
6. Güemes, A., Fernández-López, A., Soller, A.: Optical fiber distributed sensing-physical principles and applications. *J. Struct. Health Monit.* **9**(3), 233–245 (2010)



# Numerical Comparison of Damage Detection Methods Using Shm Distributed Fiber Optics (Fo) and Fibre Bragg Grating (Fbg) on a Full-Scale Wing Beam Test Article

L. Pellone<sup>1</sup> (✉) , M. Ciminello<sup>1</sup> , B. Galasso<sup>1</sup> , G. Apuleo<sup>2</sup> , S. Shoham<sup>3</sup>,  
U. Mercurio<sup>1</sup> , A. Concilio<sup>1</sup> , and I. Kressel<sup>3</sup>

<sup>1</sup> CIRA-Italian Aerospace Research Centre, Capua, Italy  
l.pellone@cira.it

<sup>2</sup> Piaggio Aerospace Industries, Villanova d'Albenga, Italy

<sup>3</sup> Israel Aerospace Industries Ltd., Lod, Israel

**Abstract.** For the modern aeronautical industry, the search for cost reduction in the design, construction and maintenance of aeronautical structures represents a continuous challenge. There are many fields on which industries are focusing their activities; among the main ones there is certainly the use of innovative materials and new connection techniques for weight reduction, such as composite materials and bonding, and the use of techniques for monitoring structures (SHM). In particular, the latter would allow the state of the structure to be monitored throughout its operational life.

Among the most researched SHM monitoring techniques in the aviation field is the one using distributed fiber optics (FO) and Bragg grating (FBG) based technology. Through the use of these reading tools, CIRA has developed an algorithm that allows to detect the size and position of damages occurred in the structure due to possible impacts or variation of the connection conditions, with/without the need of deformation healthy references of the structure under load. This, in addition to allowing an enormous advantage in terms of both structure reliability and safety, would allow for longer maintenance times since the current state of the structure itself would be known.

In the framework of RESUME project funded by Italian Ministry of Defence (MOD) and in cooperation with Piaggio Aerospace (PAI) and Israel Aerospace Industry (IAI), the purpose of this paper is to present the results obtained using the SHM algorithm on a numerical and experimental analysis of a full-scale aircraft wing beam assuming the use of FOs or FBGs.

Finally, a comparison is made of the performance of the algorithm itself as a function of the monitoring technology used.

**Keywords:** Bonding detection · Composite structures integrity · Aircraft components · Structural health monitoring · Fiber optics distributed sensing · Fiber Bragg Grating · Integrated sensor networks · SHM algorithms

## 1 Introduction

The use of composite materials in aeronautical structures is gradually increasing due to new design and production techniques. They owe their use to the possibility of obtaining high performances in terms of strength and structural rigidity in relation to their weight. However, in view of the many advantages, composite structures are critical due to the high variation of mechanical properties depending on the type of their construction (layup) and the conditions of use (environmental and operating conditions).

One of the techniques that is most being explored is that of connecting structural parts by bonding.

Currently, the relevant normative FAA AC 20-107B [1] and EASA CS AMC 20-29 [2] do not exclude the certification of structures connected by bonding as long as certain conditions are met. Among these, certification may be possible if a reliable and repeatable non-destructive inspection methodology is available to ensure the integrity of the structure itself.

Currently, there is no suitable NDI method to meet the former requirement so, in order to certify a composite structural bonded joint, the use of additional fasteners is foreseen that must be able to withstand the relevant loads considering an overall failure of the connection line.

This work shows the preliminary activities related to develop of an SHM system that permit the onset damage detection in real-time of bonded structure by means of the use of Bragg Grating Fiber.

The aim of the activities is to develop a non-destructive inspection technique to detect the presence of damage in bonded structures and thus meet the requirement of current regulations.

## 2 RESUME Project

The **RE**al-Time Structural Health and Usage Monitoring Syst**EM**s (RESUME) for UAV is a joint Israeli-Italian project funded by the related Ministries of Defense (MOD), part of a larger program to increase collaboration and study in the field of aerostructure between the two sides.

The aim of the project is to detect structural anomaly's and damages (de-bonding) that may lead to catastrophic failure with optical Fiber Bragg Gratings (FBG) installed on a wing reference structure by means of a Health and Usage Monitoring System (HUMS) to observe the condition of the structural health status through real-time measurements.

### 2.1 Local High Edge Onset Algorithm (L.H.E.O.)

In the field of SHM for damage detection, many algorithms have been developed using different techniques for cross-correlation of data acquired with different types of sensors [3-8].

Based on experiences in several projects [8-11], CIRA has developed a specific SHM algorithm to detect damage size and location to be used with Distributed Fibers Optics. Compared to the classical SHM algorithm which use a "strain reference" approach based



on difference between a baseline set of measurements and current ones, in the **Local High Edge Onset** algorithm (L.H.E.O.) the difference is provided by using as reference set sensor and the corresponding next one. The measurements are acquired in the Space and Time domain, then a data Cross-correlation is performed and, based on dedicated threshold value, the damage identification is obtained in position and its length (Fig. 1).

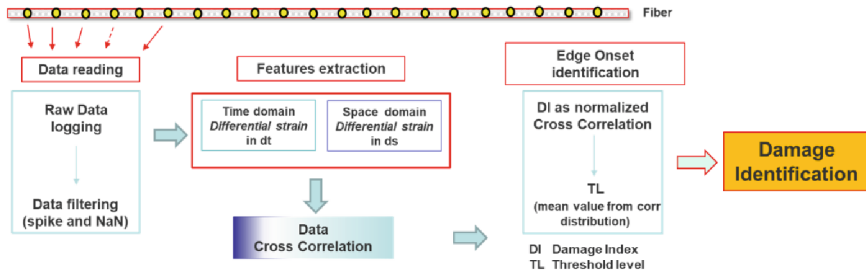


**Fig. 1.** L.H.E.O algorithm scheme

Since LHEO was developed primarily for use with distributed fiber optics (DFO), whereas one of the main requirements of the RESUME project is to use FBG, the main activity was the tuning of the algorithm on a discrete array data set.

So, passing from DFO to FBG, similar activities were expected due to different strain data reader system only. Specifically, these activities can be summarized as follows:

- ✓ Installation of Distributed Fiber Optics on Wing Beam
- ✓ Performed the Experimental Tests on Wing Beam
- ✓ Damage Identification by means of L.H.E.O. Algorithm
- ✓ Downsampling of experimental data for L.H.E.O. Algorithm tuning to FBG Array
- ✓ Comparison of experimental and numerical data

### 3 Wing Beam Test Article

The Wing Beam test article is a rectangular beam composed of two flat unidirectional carbon-epoxy tape skins and two C-shaped profile spars, both in unidirectional CFRP tape, bonded each other using a structural paste adhesive (Fig. 2-a).

In order to detect the debonding occurrences within the bonding line of the spar cap, Distributed Fiber Optic was integrated in the wing beam. The fiber position is sketched in the Fig. 2-b.

Three (3) different damage were artificially introduced along the bonding line of the spar cap. In the table below, the ID, nominal length and relative position are reported (Fig. 3).

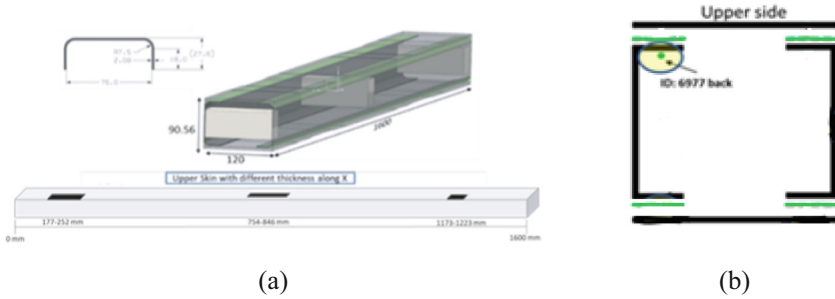


Fig. 2. Wing beam test article [9]

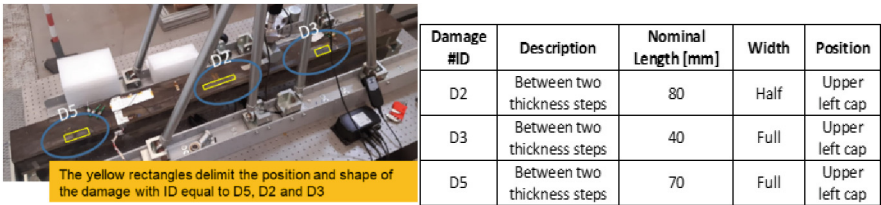


Fig. 3. Wing beam test article damages [10]

### 3.1 Wing Beam Test Rig

The test rig is made with steel tie rods and connected to an optical table thanks to two steel profiles. It consists of a special design “3-points bending” machine, with a linear actuator able to provide a load up to 10kN (LAI2-HIWIN). In the current test, external load was limited to 5kN.

The upper ends of the tie rods support a base, reinforced with ribs, for positioning a linear actuator. The Test rig is installed on an optical table equipped with a self-leveling system that uses the filling of tanks under the work surface thanks to the use of pressurized air in order to keep the actuator always in axis (Fig. 4-a).

The LUNA ODISI-B optical interrogator was used to retrieve distributed optical fibers strain data (Fig. 4-b).

### 3.2 Wing Beam Test Matrix

The tests involved two different positions of the force with respect to the axis (Fig. 5):

- Symmetrical load: Perpendicular force positioned at the center of the beam axis
- Asymmetrical load: Perpendicular force positioned in the vicinity of one of the supports.

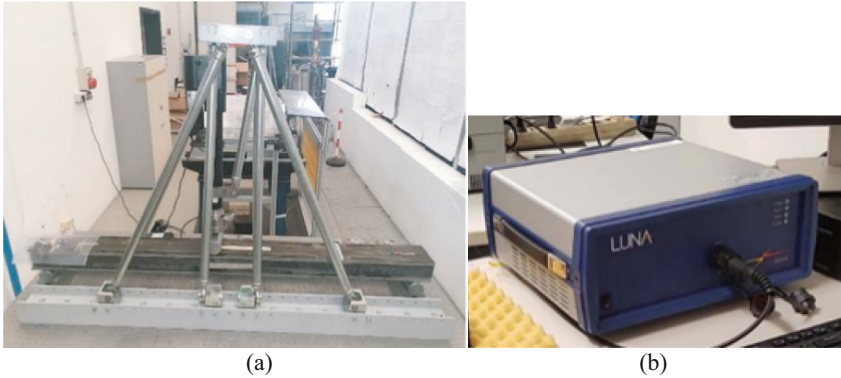


**Fig. 4.** Wing beam test rig

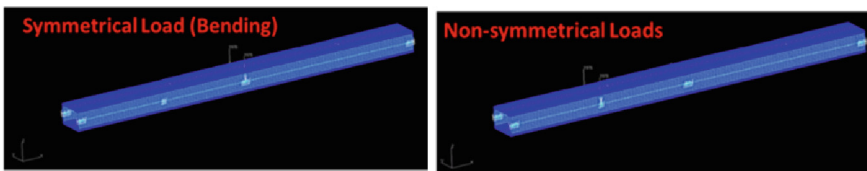


**Fig. 5.** Symmetric and non-symmetric loading scheme

When a symmetric load is considered, the application point is in the middle section of the spar, 800mm far from the spar ending edge, while when a Non-symmetric load is considered, the application point is at 1020mm far from the spar ending edge.

In this work the comparison between symmetrical load experimental data and related down-sampling ones are reported.



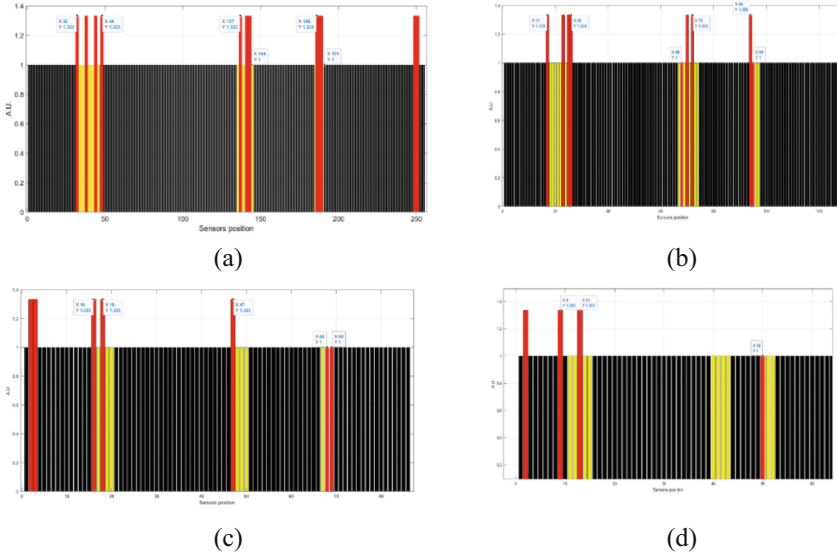


**Fig. 7.** LHEO Algorithm processing data results: downsampling at 5 mm (a), at 10 mm (b), at 15 mm (c) and 20 mm (d)

## 5 FO and FBG Data Results Comparison

The L.H.E.O. algorithm shows good capability in damage detection under different structural solicitation and different space resolution. The Table 1 shows the results comparison between experimental and downsampling results.

The dimension of damage, and its accuracy, depends to the loading and reading history of the data:

- ✓ Fiber optics are sensible to the strain energy so, the readout sensitivity increase with the inlet energy
- ✓ Decreasing the Array downsampling lead to decrease to spatial resolution so, the accuracy of the damage length estimation

**Table 1.** FO and FBG results comparison.

ERROR [%] #ID Fiber	symmetric			Downsampling/ Damage Error [%] @3kN	D5	D3	D2
	0.5kN	1kN	3kN				
6977	D5 = 100	D5 = 100	D5 = 10	2.5 (distributed)	10	7	6
	D2 = 70	D2 = 35	D2 = 6	5	10	15	10
	D3 = 100	D3 = 100	D3 = 7	10	15	35	25
				15	35	75	35
				20	50	No Detect	75

(a)

(b)

## 6 Conclusion

The present work is related to preliminary activities performed on a representative Composite Wing Beam related to apply on SHM Algorithm developed by CIRA in order to permit the detection of an onset damage.

Experimental and Numerical activities were performed on Test Article and a numerical comparison of damage detection methods by means of Distributed Fiber Optics and Fiber Bragg Grating using LHEO algorithm has been shown.

The results of this work show that the LHEO algorithm provide reliable measurements for both position and size of disbonding passing from Distributed Fibers Optics and FBG.

Obviously, the accuracy of damage detection, which makes the damage detectable by the UHMS system, depends on the applied load, the sensitivity of the type of sensors used and sensors spacing of FBG.

However, being a fiber optic sensor, the Bragg grid possesses all the advantages attributed to these types of transducers, namely: low loss (attenuation) compared to the length of the fiber, immunity to electromagnetic and radio frequency interference, small size and low weight, high sensitivity and long-term reliability.

## References

1. FAA - AC 20-107B. Composite Aircraft Structure (2010)
2. EASA. Composite Aircraft structures. AMC 20–29 (2010)
3. Ni, P., Xia, Y., Law, S.-S., Zhu, S.: Structural damage detection using auto/cross-correlation functions under multiple unknown excitations. In: International Journal of Structural Stability and Dynamics, vol. 14, no. 05, pp. 1440006 (2014)
4. Fernández-López, A., Menendez J.M., Güemes, A.: Damage detection in a stiffened curved plate by measuring the differential strains. In: Conference: ICCM 16th International Conference on Composite Materials (July 2007)
5. Muyu Zhang, Rüdiger Schmidt, Bernd Markert: Structural damage detection methods based on the correlation functions. In: Proceedings of the 9th International Conference on Structural Dynamics, EURO DYN 2014 Porto, Portugal (2014)

6. Fried, R.: On the robust detection of edges in time series filtering. *Computat. Stat. Data Anal.* **52**(2), 1063–1074 (2007)
7. Li, M., Ren, W.-X., Huang, T.-L., Wang, N.-B.: Experimental investigations on the cross-correlation function amplitude vector of the dynamic strain under varying environmental temperature for structural damage detection. *J. Low Freq. Noise Vib. Act. Control* **39**(3), 631–649 (2020). <https://doi.org/10.1177/1461348418820237>
8. Ciminello, M., et al.: Cross-Correlation Based Algorithm for SHM De-bonding Analysis of Typical Aeronautical Structures via OFDR. In: Rizzo, Piervincenzo, Milazzo, Alberto (eds.) *European Workshop on Structural Health Monitoring: EWSHM 2022 - Volume 1*, pp. 254–263. Springer International Publishing, Cham (2023). [https://doi.org/10.1007/978-3-031-07254-3\\_25](https://doi.org/10.1007/978-3-031-07254-3_25)
9. Concilio A., Ciminello M., Apuleo G., Kressel I., Shoham S., Bardenstein D.: Preliminary characterization of bonding defects in multi-element spars. In: *SPIE Smart Structures and NDE Conference 2019, Denver (CO-USA) (3–7 Marzo 2019)*. <https://doi.org/10.1117/12.2514297>
10. Concilio, A., et al.: De-Bonding Numerical Characterization and Detection in Aeronautic Multi-Element Spars. *Sensors* **22**(11), 4152 (2022). <https://doi.org/10.3390/s22114152>
11. Ciminello, M., Ameduri, S., Romano, F., Concilio, A.: Impact area and debonding line detection assessment by cross-correlation analysis and distributed sensing. *Opt. Fiber Technol.* **58**, 102245 (2020). <https://doi.org/10.1016/j.yofte.2020.102245>



# Design, Manufacturing and Testing of an Out-of-Autoclave Liquid Resin Infused Carbon-Epoxy Curved Stiffened Panel

Daniele Fanteria<sup>1</sup>(✉), Evangelos Karachalios<sup>2</sup>, Vincenzo Iannone<sup>3</sup>, Ernesto Monaco<sup>4</sup>,  
and Fulvio Romano<sup>5</sup>

<sup>1</sup> Department of Civil and Industrial Engineering, Aerospace Section, University of Pisa,  
Via Girolamo Caruso 8, 56122 Pisa, PI, Italy  
daniele.fanteria@unipi.it

<sup>2</sup> Hellenic Aerospace Industry, Research and Product Design, P.O. Box 23 GR 320 09,  
Schimatari, Greece

<sup>3</sup> Novotech Aerospace Advanced Technology S.r.l., Via G. Pascoli, 7, 80026 Casoria, Italy

<sup>4</sup> Department of Industrial Engineering, Aerospace Division, University of Naples “Federico  
II”, Via Claudio 21, 80125 Naples, Italy

<sup>5</sup> CIRA S.C.P.A, Italian Aerospace Research Centre, Aeronautics Technologies Integration  
Office, Via Maiorise, Snc, 81043 Capua, Italy

**Abstract.** The paper describes the development of design approaches and manufacturing procedures for a composite curved panel, reinforced by inverted “T” stringers, that is representative of the upper panel located at the wing tip of the regional aircraft taken as a reference within Clean Sky 2 research program.

The panel is manufactured from dry carbon preforms by means of Liquid (epoxy) Resin Infusion and an Out-of-Autoclave curing process.

The activity is a joint effort of some of AIRGREEN 2(AG2) consortium partners and Leonardo Aircraft (LDO) within Clean Sky 2 Regional Aircraft IADP: Novotech (NVT), Hellenic Aerospace Industries (HAI), University “Federico II” Napoli (UNINA), University of Pisa (UNIFI) and the Italian Aerospace Research Centre (CIRA). A SHM system is developed and installed to detect damages due to impacts. The panel is tested in compression with a test procedure compliant to aeronautical certification requirements for primary structures, to validate both the design and the manufacturing.

**Keywords:** AoA-Liquid Resin Infusion composites · Curved stiffened panel design · Curved Panel testing · Finite Element analysis

## 1 Introduction

The work presented in the paper is part of the Clean Sky 2 – AIRGREEN2 (AG2) project which aims at designing, manufacturing, and ground-testing a full-scale composite Outer Wing Box demonstrator for a regional aircraft. To achieve this objective a curved stiffened panel has been designed, manufactured and tested in order to validate the related technologies.



The work was funded by Clean Sky 2 Joint Undertaking, under the European’s Union Horizon 2020 research and innovation Programme, under grant agreement No 807089 – REG GAM 2018 – H2020-IBA-CS2- GAMS-2017; WAL (Work Area Leader): Leonardo Aircraft.

### 2 Design of the Curved Stiffened Panel

A curved panel (tool side radius of curvature equal to 2981 mm) has been designed that is stiffened by inverted “T” stringers having their general dimension as reported in the sketch shown in Fig. 1. FE model has been developed by Novotech to support a no-buckling design of a 3 ribs (spacing 320 mm) 3 stringers/4spacing width panel.

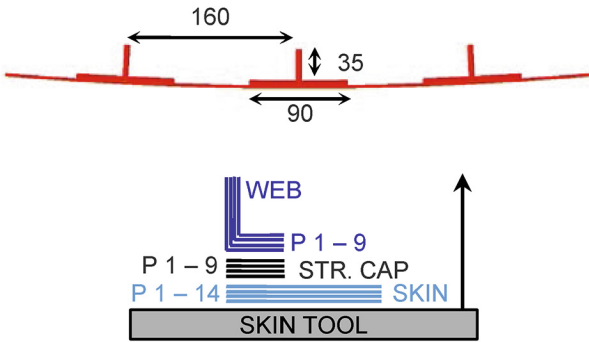


Fig. 1. Curved panel dimensions (mm) and stacking directions of the structural elements.

The general arrangement of the stiffening members layup is show scheme in Fig. 1 while the stacking sequence is given in Table 1.

FE analyses were carried out to determine buckling loads and first ply failure load according to material data and design allowables determined using CAI knock-down factors. Analyses with supported skin of the side and grounded skin in correspondence to rib feet showed failure load of 540 kN and a buckling load of 760 kN.

### 3 Manufacturing via LRI/OoA Process

The panel is manufactured from dry carbon preforms by means of vacuum assisted Liquid Resin Infusion and an oven (Out-of-Autoclave) curing process [1–3].

The curing tool consists of a formed steel sheet offering a layup surface with a 2981 mm curvature radius that is the OML of the curved panel. The tool surface is screwed to a steel framework supporting structure.

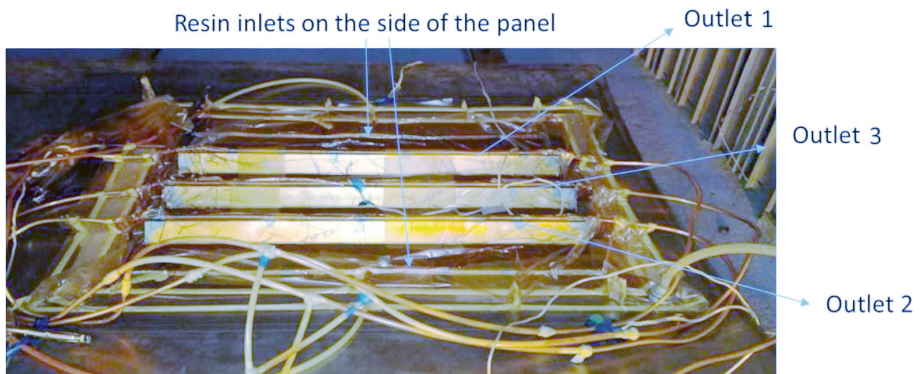
Appropriate mandrels for the forming of the stringers are connected to the skin tool via pins that allow relative sliding during the resin infusion and the curing process.

Dry non-crimp fabric is Hand lay up (HLU) and preformed (under vacuum and heat) prior to infusion. Then the internal and external vacuum bags are setup adding appropriate resin inlets and outlets for the resin infusion.

**Table 1.** Staking sequences.

Item	n. of plies	Stacking sequence
Skin	14	45/-45/0/0/90/-45/45/45/-45/90/0/0/-45/45
Stringer Cap	9	45/-45/0/0/90/-45/45/-45/45
Stringer web	9	45/-45/45/-45/90/0/0/-45/45

Prior to infusion the tool is preheated, and the resin (EP 24000) is preheated and degassed. Then infusion starts via inlets placed along the sides of the skin. Infusion proceeds until the resin reaches the outlet gates (placed along the webs of the stringers), then inlet gates are closed while the outlet gates remain connected to vacuum. The setup for the infusion process is shown in Fig. 2.

**Fig. 2.** Curved Panel LRI setup.

The curing process takes place in an oven at ambient pressure and includes the following steps: a temperature increase (at 2 °C/min) to 180 °C, dwell for 120 min, cooling (at <5 °C/min) to 60 °C or below. After debagging the panel is trimmed and drilled using a CNC milling equipment. Holes are drilled to allow the installation of dummy aluminium ribs that define the wing bays.

#### 4 Barely Visible Impact Damage Introduction

To evaluate the panel response, before and after the damage, through a SHM system, different impact damages have been introduced. The panel has been impacted using a pneumatic gun made available by Leonardo at Pomigliano d'Arco company premises. Some trials were conducted to decide the energy level to produce Barely Visible Impact Damage at mid-bay and under the stringer locations. The tests equipment and an overview of damage locations and relevant parameters are given in Fig. 3.

After the execution of impacts, a state-of-the-art US scanning has been carried out to assess delaminated areas and set a benchmark for SHM. An extended delamination,

separating the stringer cap from the skin, was detected in correspondence of the BVID impact under the central stringer.

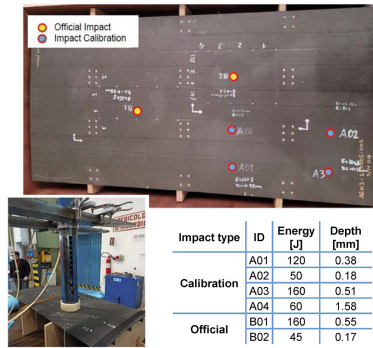


Fig. 3. Impact damage introduction.

### 5 SHM System for Multi-parameter Tomography

Two networks of piezoelectric transducers (PI PIC 255) have been installed by UNINA on the panel prior to impact execution. Piezo are used both as actuators and as sensors to measure wave signals on the pristine component; this defines baseline signals to be compared with ones measured after damage (see Fig. 4 for an example).

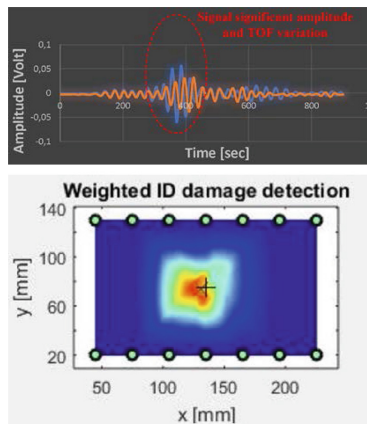


Fig. 4. Example of signals measured along an actuator-receiver path (top) and example of a damage combined contour plot obtained using different paths across a damaged area (bottom).

Signal comparison at the core of the SHM is carried out by a Parameter Statistical Tomography (MPT) [3–5]. Signal features in a sensor-actuator path are extracted, and

their differences used to define a Damage Index (DI): when DI exceeds a threshold, damage is detected (severity proportional to DI). Intersecting sensor-actuator paths that have higher than average DIs, allows the definition of a damaged area (see Fig. 4 for an example). Damage detected by the SHM system in the two scenarios present on the panel matched closely the measures carried out via US scanning.

## 6 Testing

The following general requirements are defined for the Curved Panel:

- The panel shall be compliant with the “no growth” approach for BVID damage, under fatigue loading in compression at constant amplitude. Strain surveys must be performed at intervals to detect changes in compliance due to possible damage growth
- A Design Service Goal (DSG) of 60000 flights, a 1.5 Life factor, and a 1.15 Load Enhancement Factor (LEF) shall determine the number of cycles and the maximum cyclic load. After the fatigue cycles the panel must retain a residual strength at least equal to the Design Ultimate Load (DUL).

The features of the Test Article, combined with such general requirements, lead to the following specific requirements for mechanical testing [6, 7]:

1. To have a uniform loading along panel width, potted ends with precision milled faces are needed.
2. Due to a 3 stringers/4 spacing width, design side support fixtures are needed to avoid premature skin buckling of the straight edges.
3. Design hypothesis for boundary conditions at ribs feet are hard to meet in practice; alternative supports for the dummy ribs are needed.
4. Effective UL of the test article must be re-evaluated according to buckling loads resulting from test boundary conditions

### 6.1 Test Set up Definition and Design of Test Fixtures

Non-linear FE analyses of the test set-up have been developed by UNIPI to support fixture design and panel tests, in particular different hypotheses for rib and side supports were studied and assessed. The selected solution (easier to manufacture and to mount on the testing machine) has the following key features: side supports are independent from rib supports and are stabilized laterally by composed section beams, rib edges are fixed to the frame of the testing machine through C section beams, the top potting frame is fixed to the upper head of the testing machine.

Drawings of the side supports and the manufactured fixtures ready to be mounted are shown in Fig. 5.

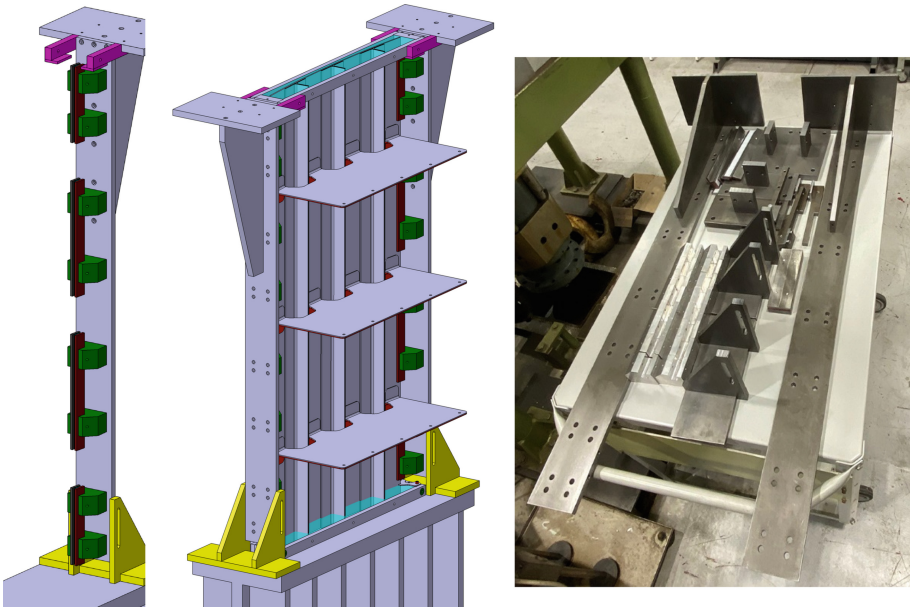


**Fig. 5.** Side support design and manufactured items ready to be installed.

## 6.2 Panel Preparation, Test Set-Up and Preliminary Loading

Potted ends were casted (UNUPI) using the frames supplied by HAI. The panel has been positioned with the stringers' axis orthogonal to a reference plane holding the end frame and equipped with columns restraining the panel during resin cast and cure.

Potted ends were precision milled to ensure planarity, reciprocal parallelism and orthogonality to the axes of the reinforcing stringers: this allows a uniform introduction of the load along the panel width. Then 44 uniaxial strain gauges (SG) and 4 rosettes have been installed in back-to-back configuration. The test article mounted on a 3 MN Servo-Hydraulic fatigue testing machine is shown in Fig. 6.

Due to testing boundary conditions at variance with design ones, the buckling load has been re-evaluated (ABAQUS non-linear analyses) for a pristine panel and found equal to 500 kN. Consequently, the Effective UL of the test article has been set at 440 kN (13.6% margin) with the Effective LL equal to 293.3 kN (EUL/1.5).

## 6.3 Fatigue Cycling Results

Following Leonardo indication about the max cyclic load for a single equivalent cycle per flight (producing the same damage as all cycles in an average flight, representative of AC life), the maximum fatigue cyclic load has been assumed equal to LL (including a 1.15 LEF), with  $R = 0.2$  (compression/compression cycles).

The total number of flights (and thus of Constant Amplitude cycles) is 90k (DSGx1.5). Fatigue test has been carried out at 0.5 Hz and stopped at 10k, 20k, 30k, 45k, 60k and 90k cycles for reading SGs and check possible compliance variations.



**Fig. 6.** Test set up completed and ready to start fatigue cycling.

Selected strain reading at LL after completion of different number of fatigue cycles is shown in Fig. 7, no appreciable variation of compliance is detectable so confirming that damage did not grow due to the fatigue cycles.

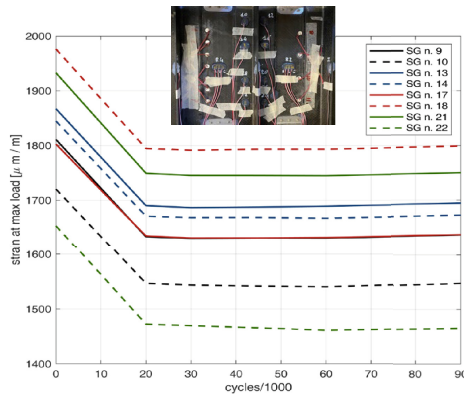


**Fig. 7.** Selected strain reading at LL after completion of different number of fatigue cycles.

## 7 Conclusions and Perspective

A curved panel, reinforced by inverted “T” stringers has been designed and manufactured from by LRI/OoA process.

An SHM System based on Multi-Parameter Tomography has been successfully used to detect delamination resulting from Barely visible impacts.

The panel has been completed with potted ends, instrumented with SGs and installed on the testing machine using specifically designed fixtures.

Fatigue testing has been completed and the “no growth” approach for Damage Tolerance demonstrated.

Demonstration of UL capability under static load and a final test up to Maximum load capability (Failure load) are to be completed soon.

## References

1. Karachalios, E., et al.: LRI-fabricated composite demonstrators for an aircraft fuselage on the basis of a Building Block design approach. *Compos. Part C: Open Access* **6**, 100178 (2021)
2. van Oosterom, S., Allen, T., Battley, M., Bickerton, S.: An objective comparison of com-mon vacuum assisted resin infusion processes. *Compos. A Appl. Sci. Manuf.* **125**, 105528 (2019)
3. Verma, K.K., Dinesh, B.L., Singh, K., Gaddikeri, K.M., Sundaram, R.: Challenges in processing of a cocured wing test box using vacuum enhanced resin infusion technology (VERITY). *Procedia Mater. Sci.* **6**, 331–340 (2014)
4. Beligni, A., et al.: Investigation on low velocity impact damage identification with ultrasonic techniques under different sensor network conditions. *IOP Conf. Ser.: Mater. Sci. Eng.* **1024**(1), 012027 (2021)
5. Memmolo, V., Maio, L., Monaco, E., Ricci, F.: Assessment of stringer debonding by guided wave inspection in composite structures. In: Rizzo, P., Milazzo, A. (eds.) *European Workshop on Structural Health Monitoring. EWSHM 2022. Lecture Notes in Civil Engineering*, vol. 270. Springer (2023)
6. Singer, J., Arbocz, J., Weller, T.: *Buckling Experiments: Experimental Methods in Buck-ling of Thin-Walled Structures*, vol. 2: Shells, Built-up Structures, Composites and Additional Topics. Wiley (2002)
7. Boni, L., Fanteria, D., Lanciotti, A.: Post-buckling behaviour of flat stiffened composite panels: experiments vs. analysis. *Compos. Struct* **94**(12), 3421–3433 (2012)



# Mechanical Characterization of a Polymer-Metal Hybrid Structure for Automotive Applications: Quasi-static and Repeated Impact Tests

D. Fiumarella<sup>1</sup>, A. Canegrati<sup>2</sup>, L. M. Martulli<sup>2</sup>, A. Bernasconi<sup>2</sup>, G. Mastinu<sup>2</sup>,  
G. Belingardi<sup>1</sup>, and A. Scattina<sup>1</sup> (✉)

<sup>1</sup> Department of Mechanical and Aerospace Engineering, Politecnico di Torino, Turin, Italy  
alessandro.scattina@polito.it

<sup>2</sup> Department of Mechanical Engineering, Politecnico di Milano, Milan, Italy

**Abstract.** Vehicle weight reduction is a core topic in the automotive industry, due to the growing demand for an emission abatement and for the design of sustainable products. This target is usually pursued by the car manufacturer by design lightweight structural and non-structural components. The vehicle suspension system draws particular attention due to its impact on the overall vehicle weight. In this square, in this work, a polymer metal hybrid (PMH) solution for the suspension system of a vehicle is proposed. PMH structures combines the high ductility of the metals with the high mechanical performance and lightweight of the composite materials. The proposed PMH demonstrator replicates, in a simplified geometry, the lower arm of a MacPherson suspension, that is usually subjected to bending loads. As the suspension arms must often withstand to dynamic stresses repeated over time, an experimental campaign was carried out to characterize the bending properties of a PMH demonstrator in repeated impact loads. The test configuration can be associated to a three-point bending. The demonstrator is produced by injection moulding, and it is made of an aluminium insert co-moulded in a short fibre reinforced polyamide main structure. The structure showed good performance when subjected to repeated dynamic impact test in terms of strength and stiffness. The metal insert provided a no-separation function avoiding catastrophic failure, confirming the goodness of the PMH solution for suspension arm applications.

**Keywords:** SFRP · Composite · Metal-Hybrid · Impact test · Suspension arm

## 1 Introduction

The lightening of vehicles is a key point in the automotive industry, in order to reduce the emissions of greenhouse and polluting gases. The European parliament has voted on a proposal to ban internal combustion cars starting from 2035 [1], in order to achieve a 100% reduction of CO<sub>2</sub> emissions. Designing vehicles with low environmental impact requires the use of lightweight and recyclable materials, which make vehicles ecologically sustainable not only during their useful life, but also throughout their entire life



cycle. The use of lightweight materials such as composites instead of conventional metallic materials for structural and non-structural purposes is therefore a fundamental step to achieve sustainability and efficiency targets.

The lightening design activities must be focused on the chassis, the body and the suspension elements, which together account for approximately 58% of the vehicle's entire weight [2]. An important challenge is represented by the lightening of the vehicle's suspension system due to its performance. A lightweight suspension system has a positive effect on the reduction of the overall vehicle weight and of the unsprung masses, improving the vehicle handling and the comfort of the occupants [3]. In literature, many authors propose suspension arms made carbon fiber reinforced thermosetting polymer (CFRTs) [4–7]. These solutions guarantee a lightening of the unsprung mass, and an increase in the stiffness of the suspension arms. Although an evident performance improvement, the fracture and failure mechanics of the CFRTs is still a critical point due to their uncontrolled and catastrophic failure mode [8–10]. In addition, the high production cost and the difficulty of a complete recycling of both the composite's initial constituents [11, 12] (resin and fibers) has restricted the use of CFRTs to a niche production.

A promising solution that combines good mechanical performance, recyclability and lightweight is represented by the PMH (Polymer Metal Hybrid) structures. The PMH structures are typically made of fiber reinforced thermoplastic polymer over-molded onto a thin metallic component. This technology combines in a singular component the ductility of the metals with the lightweight and mechanical properties of the polymer-based composites [13–16]. The PMH structures can be made with long fiber, short fiber, and thermoplastic or thermosetting matrices. The use of short fiber reinforced thermoplastic composites for the manufacturing of the PMH structure is preferable, as the separation, recovery and recycling of the two constituents results to be more efficient [17, 18]. However, as far as the authors are aware at the time of writing this article, the literature lacks proposals for suspension arms made of thermoplastic composite material.

This work aims to study the feasibility of a PMH structure made of metal-thermoplastic composite for a lower control arm of a McPherson suspension. A PMH demonstrator with a tapered I-beam-like structure was studied. This simplified geometry was defined because it replicates the portion of a suspension arm that undergoes to bending. The demonstrator is produced by injection molding and is made of a short glass fiber reinforced polyamide structure and an aluminum insert whose purpose is to give the structural integrity to the component even after the composite failure.

In order to verify the goodness of the proposed solution, the demonstrator was firstly tested to characterize its response in terms of static, fatigue and cyclic load conditions. A summary of the experimental campaign carried out is briefly proposed.

However, in normal use conditions, the suspension arms are often subjected to dynamic stresses repeated over time, and for this reason a special focus was given to the validation of the demonstrator in repeated impact loads.

## 2 Material and Method

### 2.1 The PMH Demonstrator

The Fig. 2 shows the CAD model and the dimensions of the PMH demonstrator. The composite part is made of 60% of short glass fiber reinforced PA6 provided by Radici High Performance Polymers and presents a I-like cross section, with two top and two bottom flanges. A curved housing surface was designed in the mid-span top-surface of the demonstrator whose aim is to maximize the contact area and avoid possible slips between the top surface and the loading head used during the test (see Sect. 2.2). From the housing two oblique ribs and one vertical rib run from the top to the bottom flanges in order to increase the stiffness of the structure and distribute the load (Fig. 1).

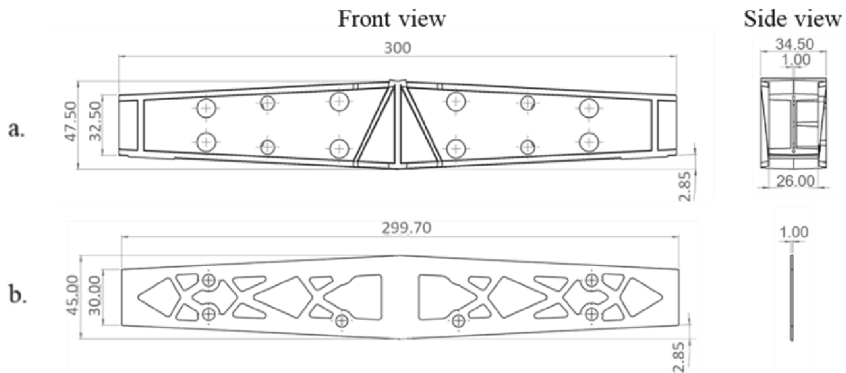


**Fig. 1.** PMH demonstrator: a) CAD model with dimensions; b) CAD model with dimensions of the aluminum insert.

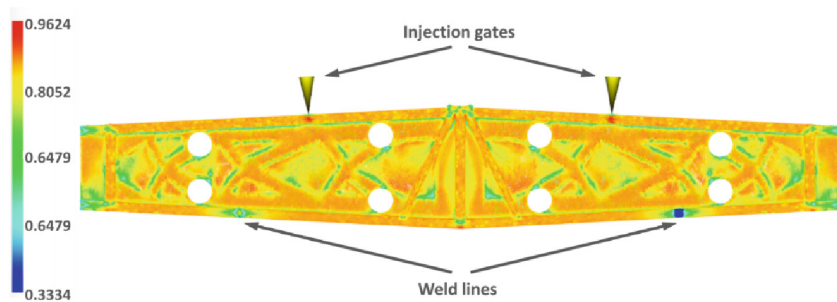


**Fig. 2.** Injection molding simulation. The results are in terms of maximum eigenvalue of the fiber orientation tensor.

The metal insert is made of a 6061-T6 aluminum, that is then embodied in the main structure, and present a truss-like tapered shape to reduce the weight of the component.

The demonstrator was produced by injection molding. The Fig. 2 shows the process simulation results in terms of the maximum eigenvalue of the orientation tensor,

highlighted by the colormap. The polymer injection gates are evidenced, where the fiber present a high degree of orientation. Conversely, in correspondence of the bottom flange two spot where the eigenvalue presents its minimum value can be appreciated (i.e., the fibers are randomly oriented). This region generates as a consequence of the meeting of two melt flow fronts and are commonly called weld-lines.

## 2.2 Test Description

The shape and geometry of the PMH demonstrator were designed to replicate a portion of the lower control arm of a McPherson suspension scheme (Fig. 3a). The wheel-side of the control arm is subjected to the load, while the chassis-side is constrained. Due to the difficulty to replicate in testing condition the chassis-side constrain and the material continuity, the demonstrator was mirrored about the vertical plane of the chassis-side, in order to test it in a three-point bending configuration (Fig. 3b).

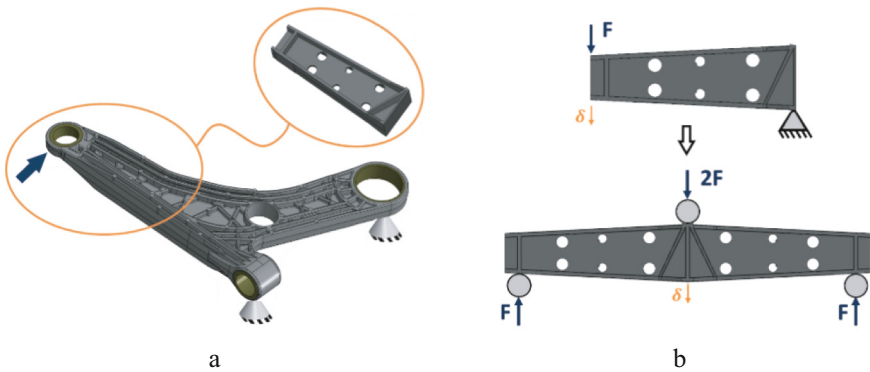


**Fig. 3.** a) detail of the lower control arm portion that the demonstrator replicates; b) loading condition and mirroring representation for the three-point bending test.

## 2.3 Preliminary Experimental Campaign

Before testing the impact response of the PMH demonstrator, an extensive experimental campaign was performed to validate the behaviour of the demonstrator, by reproducing all the loading scenarios that a suspension control arm normally faces during its working conditions.

Quasi-static tests, cyclic quasi-static tests, fatigue and creep tests were carried out to fully characterize the demonstrator's mechanical response. In all these test scenarios, the demonstrator was loaded in a three-point bending configuration.

Quasi-static tests were executed (Fig. 3b) at different temperature levels ( $-40$ ,  $23$  and  $85$  °C) and the effect of the moisture conditioning was evaluated too.

Furthermore, the specimen was tested in a cyclic quasi-static test configuration in order to analyze the permanent residual deformations on the coupons after each loading cycles.

Fatigue tests were run with a maximum force applied ranged from 2.45 kN to 4.2 kN and six load levels were investigated by incrementing the load of 0.35 kN each step.

Creep tests were performed to evaluate the extent of the specimen deformations when subjected to long-lasting static loads. The tests were performed at three temperature levels ( $-10$ ,  $23$ ,  $50$  °C) and two load levels (0.98 and 1.47 kN), using a testing machine designed by the authors from the Politecnico di Torino. Each creep test was run for approximately 500 h.

## 2.4 Repeated Impact Tests

Repeated impact tests were executed on the PMH demonstrator at different supplied energy levels  $E_0$  (5 J, 10 J, 15 J) in order to replicate real working conditions, such as a wheel shaking due to a pothole impact. 20 impacts were executed for the  $E_0$  equal to 5 J and 10 J, while only 3 impacts for the  $E_0$  equal to 15 J, due to the failure of the specimen after the third test. The tests were carried out at the Politecnico di Torino labs using a CEAST Fractovis Plus free-fall drop dart testing machine. A free fall impact mass of 15 kg was used, and the desired impact energy was adjusted by tuning the initial height of the falling mass. The impact dart had a hemispherical head tip with a diameter of 12 mm and its impacting location was set as shown in Fig. 3b.

A PCB piezoelectric load cell was used to acquire the load signal during the impact. The acquisition frequency was set to 1 MHz. The dart velocity  $v_0$  at the impact instant  $t_0$  was acquired by a photocell. The time  $t_f$  when the load firstly drops to zero (before a possible rebound of the dart on the specimen) was taken as the last instant of the test. The dart displacement during the impact was obtained by double integrating from  $t_0$  to  $t_f$  the dart acceleration, that was retrieved by the Newton's law. The energy history was evaluated by integrating the force over the displacement from  $d_0$  (i.e., the displacement at  $t_0$ ) to  $d_f$  (i.e., the displacement at  $t_f$ ).

A fastening device (Fig. 4) was specifically designed by the authors to keep the demonstrator in a fixed position and replicate the three-point bending configuration during the impact test. The fixture consists of two sliding span support that are leaning on a guideway, fixed on a plate. The upper part of the span support has two perforated lobes, where screws are inserted. These screws hold the specimen steady in its position, preventing it from moving or jumping off during the impact.

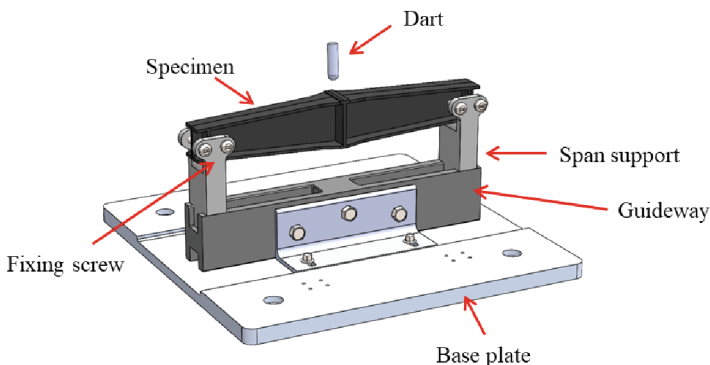


**Fig. 4.** Testing fixture used for the impact tests.

## 3 Results and Discussion

### 3.1 Preliminary Experimental Campaign Results

The quasi-static tests evidenced a satisfactory response of the PMH demonstrator, with a good repeatability of the demonstrator's stiffness. This aspect was confirmed also by the cyclic quasi-static tests, where the same specimen was subjected to multiple load-unload cycles. However, in this case, the specimen faced increasing residual deformation after each loading cycle. This was due to the permanent plastic deformation of the metal insert and the polymer fracture in correspondence of the welding lines. The welding lines resulted to be the critical region of the demonstrator, as will be discussed in detail in the Sect. 3.3.

Considering the quasi-static tests, the failure of the specimen was not characterized by a complete separation: firstly, the polymeric structure failed in a brittle way. In a second moment, the metal insert was still capable to carry the load and plastically deform, until a final drop of the load.

The failure of the metal insert did not occur during the fatigue tests, but at each load level tested, only the polymer structure failed in correspondence of the weld-lines.

The mechanical properties of the demonstrator proved to be temperature sensitive. The effect of the increase in temperature was to increase the compliance and the deformation at failure both for quasi-static tests and creep tests. In this last case, an increase in temperature from 23 °C to 50 °C led to a 64% increase of the deformation. An important aspect to be considered is that the PMH demonstrator is composed by two heterogeneous constituents (metal and polymer): this can lead to residual stresses due to the different thermal expansion coefficients of the demonstrator's materials.

### 3.2 Repeated Impact Test Results

Figure 5 shows the results of the repeated impact test in terms of force displacement and energy displacement curves at each supplied energy level. For all the curves a lowpass filter with a cutoff frequency of 1600 Hz was applied. At 5 J of supplied energy, the demonstrator was subjected to a maximum deflection of around 2.5 mm, then the absorbed energy was elastically released to the dart, that rebounded. A maximum force of around 4 kN was measured by the load cell in all the 20 repeated impacts. From the Fig. 5a it is possible to note that all the 20 curves are superimposed and there is not clear evidence of a degradation of the properties in terms of maximum load or stiffness. However, from the energy-displacement plot in Fig. 5b a slight increase in the displacement at the energy peak is appreciable, especially after the first impact. This trend is even more pronounced for the 10 J of supplied energy (Fig. 5d). Although also in this case the dart rebounded and the specimen elastically released the absorbed energy for all the 20 impacts, the deflection at maximum energy increased from 3.7 mm to 4.7 mm from the first to the last impact. From the Fig. 5c it is possible to notice that the force-displacement curves present almost all the same trend and shape, and there is no evidence of a sharp load drop due to crack initiation or fracture. However, after each impact the whole curve tends to move towards greater displacement due to the permanent residual deformation. The first part of the curve, before the force peak, shows

that the stiffness remained almost unchanged for all impacts, as well as the maximum load which lied between 5.2 kN and 5.3 kN.

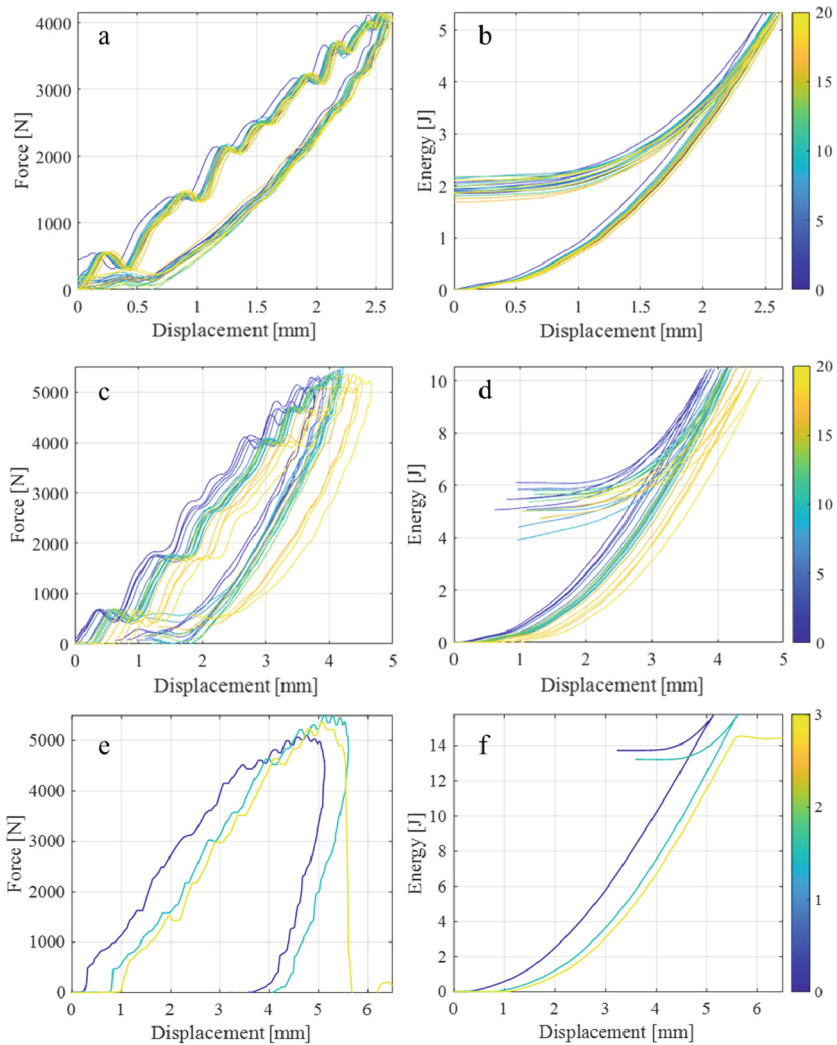


**Fig. 5.** Repeated impact test results at different levels of supplied energy: a–b) 5 J; c–d) 10 J; e–f) 15 J. The color bar indicates the number of test repetition.

The critical energy level (i.e., the  $E_0$  at which the specimen failed) resulted to be 15 J. The first two impacts at this energy level did not cause severe damage on the demonstrator that however was able to release just a small amount of elastic energy to the dart (Fig. 5f). During the third impact the specimen failed, and the dart did not rebound. From the force-displacement graph in Fig. 5e it is possible to notice that despite

the damage induced to the specimen (see Sect. 3.2), the slope of the curve until 3 mm of displacement is almost equal for all the three repeated impacts.

### 3.3 Discussion and Fracture Surface Analysis

The deformation and fracture modes of the PMH structure is influenced not only by the properties of its constituents, but also by the interaction between them. After the 20 impacts at  $E_0$  equal to 5 J, no markable damages were found on the polymer, except for a small fracture propagated only superficially in correspondence of the flange (region 2, Fig. 6a). The increase in the displacement at energy peak or at force peak suggests a plastic deformation of the metal insert after each impact.

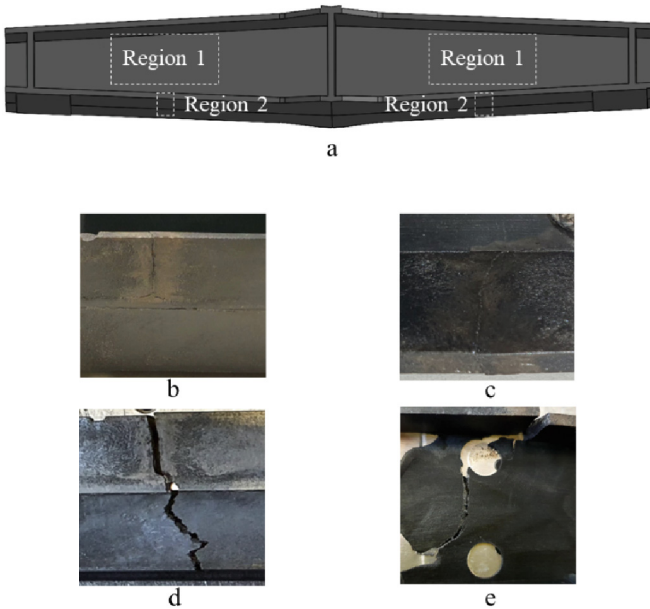


**Fig. 6.** Fracture surfaces: a) detail of the fracture locations; b-c) lower flange fracture (region 2) at 10 J of supplied impact energy; d) lower flange fracture at 15 J of impact energy (region 2); e) lateral surface fracture at 15 J of impact energy (region 1)

Considering the 10J energy level, two fractures were found on the bottom flange of the demonstrator after the repeated impacts. These fractures (Fig. 6 b–c) propagated also through the flange’s thickness, in correspondence of the region 2 as evidenced in the scheme in Fig. 6a. The regions 2 are the portion of the demonstrator where the weld-lines generated as predicted by the process simulation (Fig. 2). These fractures propagated transversally across half of the bottom flange, until the location of the metal insert. The residual permanent deformation after each impact can be thus associated both to the nucleation and propagation of these fractures and to the plastic deformation of the metal insert. However, as shown in the plot in Fig. 5c–d, although the presence of the fractures, no properties degradation was evident in terms of maximum load and stiffness.

Considering the 15 J level of supplied energy, after three impacts the specimen lost its load carrying capability. The fracture surfaces are shown in Fig. 6d–e. In this case, the fracture generated in correspondence of the weld-lines (region 2) and propagated across all the flange's width (Fig. 6d) and the demonstrator' side face (Fig. 6e). From this image, a relative sliding between the metal insert and the polymer can be appreciated: the heterogeneity of the properties of the polymer and the insert, led the structure to not deform uniformly: the polymer failed in a brittle way, while the metal insert plastically deformed, and no fractures were visually noted on it. However, the specimen kept its structural integrity: despite the high deflection at which the specimen undergone (between 5 and 5.5 mm) and loss of load-bearing capability, the metal insert guaranteed a no-separation function and avoided a catastrophic failure of the component.

## 4 Conclusion

The PMH technology for the production of a vehicle suspension arm was studied in this work. A demonstrator that replicates the portion of the lower control arm of a McPherson suspension was examined. The samples were made with an aluminum insert embedded in a short fiber reinforced thermoplastic polymer structure. The choice of a thermoplastic polymer was dictated by the need to make a fully recyclable component to accommodate the environmental issues. Due to the critical bending loads to which a suspension arm is subjected, a series of experimental tests in a three-point bending configuration were carried out to study the mechanical performance of the demonstrator.

The tests confirmed the good properties of the component in fatigue, creep and quasi-static conditions.

A series of repeated impact tests at different supplied energy levels were performed to verify the dynamic response of the demonstrator and thus replicate the real case loading condition of a suspension arm subjected to a pothole wheel shaking. The stiffness was repeatable as a function of the level of supplied energy and the test repetition. This aspect is of fundamental importance in the design of a lower control arm, as it guarantees the suspension to keep its kinematics and preserve the characteristic angle in all the working conditions. The critical point of the examined structure were the weld-lines generated on the lower flange during the injection molding manufacturing process. In these regions the presence of fractures was found even at low energy levels. On the other hand, considering the highest impact energy level (15 J), these regions resulted to be the nucleation spot from which the crack propagated leading the structure to lose its load-bearing capability. The structural function of the metal insert was fundamental to guarantee a residual structural integrity of the demonstrator, prevent catastrophic failure and therefore accomplishing the vehicle safety requirements for this type of components. In conclusion, the PMH technology confirmed to be a valuable solution for a vehicle suspension arm application in terms of weight, mechanical performance, safety, and recyclability.



## References

1. “Fit for 55 package: Council reaches general approaches relating to emissions reductions and their social impacts,” Council of the EU – Press Release (2022). <https://www.consilium.europa.eu/en/press/press-releases/2022/06/29/fit-for-55-council-reaches-general-approaches-relating-to-emissions-reductions-and-removals-and-their-social-impacts/>. Accessed 16 Aug 2022
2. Tisza, M., Czinege, I.: Comparative study of the application of steels and aluminium in lightweight production of automotive parts. *Int. J. Light. Mater. Manuf.* **1**(4), 229–238 (2018). <https://doi.org/10.1016/j.ijlmm.2018.09.001>
3. Carello, M., et al.: Composite control arm design: a comprehensive workflow. *SAE Tech. Pap.* **3**, 2355–2369 (2021). <https://doi.org/10.4271/2021-01-0364>
4. Anandakumar, P., Timmaraju, M.V., Velmurugan, R.: Development of efficient short/continuous fiber thermoplastic composite automobile suspension upper control arm. *Mater. Today: Proc.* **39**, 1187–1191 (2021). <https://doi.org/10.1016/j.matpr.2020.03.543>
5. Kim, D.H., Choi, D.H., Kim, H.S.: Design optimization of a carbon fiber reinforced composite automotive lower arm. *Compos. Part B Eng.* **58**, 400–407 (2014). <https://doi.org/10.1016/j.compositesb.2013.10.067>
6. Carello, M., Airale, A.G.: Composite suspension arm optimization for the city vehicle XAM 2.0. In: Öchsner, A., Altenbach, H. (eds.) *Design and Computation of Modern Engineering Materials*. ASM, vol. 54, pp. 257–272. Springer, Cham (2014). [https://doi.org/10.1007/978-3-319-07383-5\\_18](https://doi.org/10.1007/978-3-319-07383-5_18)
7. A. J. Banks: Composite lightweight automotive suspension system (CLASS). SAE Technical Paper 2019-01-11 (2019). <https://doi.org/10.4271/2019-01-1122>
8. Czél, G., Jalalvand, M., Wisnom, M.R.: Design and characterisation of advanced pseudo-ductile unidirectional thin-ply carbon/epoxy-glass/epoxy hybrid composites. *Compos. Struct.* **143**, 362–370 (2016). <https://doi.org/10.1016/j.compstruct.2016.02.010>
9. Ciampaglia, A., Fiumarella, D., Boursier Niutta, C., Ciardiello, R., Belingardi, G.: Impact response of an origami-shaped composite crash box: Experimental analysis and numerical optimization. *Composite Structures* **256**, 113093 (2021). <https://doi.org/10.1016/j.compstruct.2020.113093>
10. Boria, S., Scattina, A., Belingardi, G.: Axial energy absorption of CFRP truncated cones. *Compos. Struct.* **130**, 18–28 (2015). <https://doi.org/10.1016/j.compstruct.2015.04.026>
11. Abbate, E., Mirpourian, M., Brondi, C., Ballarino, A., Copani, G.: Environmental and economic assessment of repairable carbon-fiber-reinforced polymers in circular economy perspective. *Materials* **15**(9), 2986 (2022). <https://doi.org/10.3390/ma15092986>
12. Pimenta, S., Pinho, S.T.: Recycling carbon fibre reinforced polymers for structural applications: technology review and market outlook. *Waste Manag.* **31**(2), 378–392 (2011). <https://doi.org/10.1016/j.wasman.2010.09.019>
13. Eksi, S., Kaptı, A.O., Genel, K.: Buckling behavior of fiber reinforced plastic-metal hybrid-composite beam. *Mater. Des.* **49**, 130–138 (2013). <https://doi.org/10.1016/j.matdes.2013.02.029>
14. Eksi, S., Genel, K.: Bending response of hybrid composite tubular beams. *Thin-Walled Struct.* **73**, 329–336 (2013). <https://doi.org/10.1016/j.tws.2013.09.001>
15. Wang, Z., Jin, X., Li, Q., Sun, G.: On crashworthiness design of hybrid metal-composite structures. *Int. J. Mech. Sci.* **171**, 105380 (2020). <https://doi.org/10.1016/j.ijmecsci.2019.105380>
16. Zhu, G., Sun, G., Yu, H., Li, S., Li, Q.: Energy absorption of metal, composite and metal/composite hybrid structures under oblique crushing loading. *Int. J. Mech. Sci.* **135**, 458–483 (2018). <https://doi.org/10.1016/j.ijmecsci.2017.11.017>

17. Schweizer, S., Becker-Staines, A., Tröster, T.: Separation and reclamation of automotive hybrid structures made of metal and fibre-reinforced plastic. *Waste Manag.* **115**, 74–82 (2020). <https://doi.org/10.1016/j.wasman.2020.04.042>
18. Khalid, M.Y., Arif, Z.U., Ahmed, W., Arshad, H.: Recent trends in recycling and reusing techniques of different plastic polymers and their composite materials. *Sustain. Mater. Technol.* **31**, e00382 (2022). <https://doi.org/10.1016/j.susmat.2021.e00382>



# Numerical and Experimental Investigation on Single Lap Composite Joints

A. Riccio<sup>1</sup>, U. Merola<sup>1</sup>, V. Acanfora<sup>1</sup>, A. Russo<sup>1</sup>(✉), F. De Nicola<sup>2</sup>, G. Giusto<sup>2</sup>,  
and F. Di Caprio<sup>2</sup>

<sup>1</sup> Department of Engineering, University of Campania “L. Vanvitelli”, Via Roma, 29,  
81031 Aversa, (CE), Italy

angela.russo@unicampania.it

<sup>2</sup> Italian Aerospace Research Centre (CIRA), Capua, CE, Italy

**Abstract.** This work focuses on the study of reliable numerical models for the prediction of the mechanical behaviour of composite joints. When composite materials are adopted, proper joint designs need to be considered to obtain durable and safe assemblies. This study is aimed to better understand the damage initiation and propagation issues in composite joints for an efficient design with reduced overdimensioning. Several joint configurations are available and are dependent on the thickness of the components to be connected. In this study, the Single Lap Joint configuration has been examined, whose design provides the most cost-effective joint in terms of weight. Actually, single lap bonded, bolted and hybrid configurations have been analyzed to identify the best reliable solution to join composite parts. The numerical models have been validated by means of comparisons with experimental tests. The experimental/numerical comparisons shown that the proposed numerical procedure can be, effectively, adopted to predict the mechanical behaviour of composite joints.

**Keywords:** Composite Materials · Finite Elements Models · Mechanical tests · Bonded joints · Mechanical joints

## 1 Introduction

The construction of big-size complex systems, such as spacecraft and aircrafts, is possible only by assembling smaller components. When composite materials are adopted, proper joint designs need to be considered to obtain durable and safe assemblies.

A considerable research effort has been dedicated to the investigation of innovative techniques for the predictability of joints behaviour under service loads [1, 2]. The joints are usually the weakest elements in structures but also the most expensive; hence, the reduction of the number of joints is desirable to reduce, especially for composite mechanical joints, damages introduced during preparation and assemblies, thus increasing the reliability of the final product and reducing its costs.

In this paper, the configuration of Single Lap Joint has been analysed to investigate the advantages and disadvantages of bolting, bonding or hybrid joining techniques. Hence,

predictive numerical models, able to consider the damage initiation and propagation [3] in both composite and metallic regions, have been considered in this work.

For the bonding jointing technique, Davis and Bond [4] have investigated the physics and, in particular, the mechanical behavior of the adhesive layers. Sheppard et al. [5], on the other hand, have made an interesting study on singularities at the joint edges, pointing out the need of choosing adequate failure criteria. A considerable effort, in the literature, has been addressed to the development of several methods to improve the strength of single lap joints, Cooper et al. [6], as an example, have used finite elements with photoelastic analysis to demonstrate that, single lap joints configurations, geometrical non-linearity can have a remarkable influence on accurate prediction of stresses in the adhesive.

Bolted configurations, are largely used in aircrafts, have been also investigated in the frame of several studies, focusing on different key aspects of mechanically fastened joints, such as stress concentrations, clamping force and fastening patterns [7, 8]. Kim et al., in [9], have proposed four different types of finite element models to study bolted joints. The model with three-dimensional solid elements and surface-to-surface contact elements has revealed to provide the best agreement with experimental data. Chen et al., in [10], have studied, experimentally and numerically, the failure modes of bolted joints under tensile load. The basic failure modes in bolted joints: net tension, bearing and shear-out; and the secondary failure modes: cleavage and shear-out have been studied in [11]. Geometrical parameters have proved to have a significant influence on the failure modes of bolted joints [12].

Hybrid (bolted-bonded) joints have been partially investigated in the literature. Chan and Vedhagiri [13] have used the finite element method to calculate the stress distribution in bolted, bonded and hybrid composite laminated joints. Barut and Madenci [14] have proposed mathematical modelling to study creep and shear stress distributions in single lap hybrid joints. Bodjona et al. [15] have used finite element simulations and also experimental tests to investigate the mechanical behaviour of hybrid joints.

Based on these considerations, in the frame of the present work, the single lap joint configuration has been analyzed by comparing bolted, bonded and hybrid joining techniques. Starting from DCB and ENF tests, the characteristics of the adhesive, its stress limit and fracture energies have been obtained. Numerical tests have, also, been performed to evaluate the mechanical properties of the adhesive. These data have been used for the numerical study of bonded, bolted, and hybrid joints solutions. The comparison of the numerical results with experimental data from ad-hoc performed tests, has allowed the verification of the reliability of proposed numerical model in predicting the mechanical behaviour of single lap joints.

## 2 Geometrical Description of the Investigated Joints

The single lap joint configuration has been investigated in this work. **Single Lap Joints** (SLJ) consist of two partially overlapped composite laminates which can be connected each other by one or more rivets, can be bonded by a suitable adhesive or can be first bonded and then mechanically coupled (hybrid solution), as schematically shown in Fig. 1.

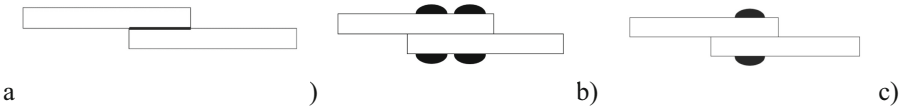


**Fig. 1.** Single lap joint. a) bonded joint; b) bolted joint; c) hybrid joint.

From the simple lap joint configuration, more complex solutions with double stepped lap with increasing thickness of the elements to be connected can be derived. However, the simple single lap joint configuration, is, usually, the most cost-effective one, in terms of production process. The single-lap joint configuration has been adopted, due to its simplicity and efficiency, in the frame of this study, for the standard mechanical test methods finalised to the determination of shear strength (ASTM D1002–72) and modulus (ASTM D3983-8) of adhesives. As already remarked, three connection types between composite parts have been studied:

- Bonded joints, which transfer the load through a cohesive surface by shear stresses, have no stress concentration, has high stiffness, good fatigue strength, is not subject to corrosion and has continuous surfaces. However, they are difficult to inspect, cannot be disassembled and have poor resistance to peeling.
- Bolted joints, which transfer the load through mechanical elements, such as bolts and rivets, can be easily disassembled and can be simply constructed, but have limited stiffness.
- Hybrid joints, involving both bonded and bolted characteristics, can be sometimes a compromise solution, which can reduce the limitations of bonded and bolted configurations.

### 3 Experimental Tests and Numerical Simulations

#### 3.1 Experimental Tests Setup

The mechanical properties of the laminate, shown in Table 1, have been obtained by standard experimental tests. The material system is a Carbon Fibers Reinforced polymer (CFRP) Fabric-type, with 24 plies ( $0^\circ$ ). The material fracture toughness has been experimentally determined according to DCB and ENF ASTM standards [16–18].

Single lap joints between composite plates with length  $L = 225$  mm, width  $W = 25$  mm and thickness  $T = 5$  mm, have been considered. Experimental tests have been performed for all the three joining typologies (bonded, bolted and hybrid). In the Fig. 2 the applied load and boundary conditions adopted during the tests are illustrated.

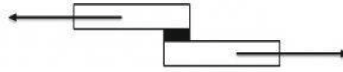
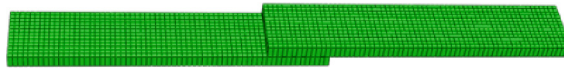
Five tensile tests for each configuration have been carried out.

#### 3.2 Numerical Model

Each joint configuration has been numerically investigated to determine the maximum achieved load, the debonding of the adherends, the ductile damage of the bolts, and the

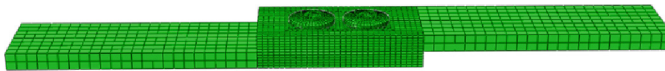
**Table 1.** Mechanical properties of laminates.

	Value	Units
$E_1$	65654.92	MPa
$E_2$	65654.92	MPa
$\sigma_{max,t}$	692.60	MPa
$\sigma_{max,c}$	595.14	MPa
$G$	3814.72	MPa
$\tau_{max}$	108.16	MPa

**Fig. 2.** Geometrical model**Fig. 3.** FE Model Bonded configuration

intra-laminar damage in the composite regions. Figure 3 shows the FE model [19] of Single Lap Bonded Joint.

Numerical analyses have been performed on the bolted joint configuration, whose numerical models are reported in Fig. 4. The contact zone between the two laminates has a length of 50 mm. The laminates have been split into two parts, the area not in contact with the rivet has elements with 2 mm size. In the contact area, 40 elements along the circumference of the hole and 6 elements along the thickness have been defined. The rivets are made of 3.5% magnesium aluminum.

**Fig. 4.** FE model-Bolted configuration

Finally, the hybrid configuration has been analysed. Figure 5 introduces the numerical FEM model for the hybrid joint configuration. The contact area between the two laminates has a size of 25 mm. The same discretize model as the bolted joint case has been used for the rivet, and the cohesive material has been taken from the bonded case.

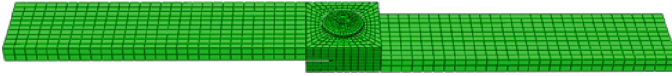


**Fig. 5.** FE model-Hybrid configuration

### 3.3 Comparison Between Numerical Results and Experimental Data

The obtained numerical results have been compared to experimental data in terms of load-displacement curves for each analysed configuration. In Fig. 6, the comparison between numerical results and experimental data for the bonded configuration is shown.

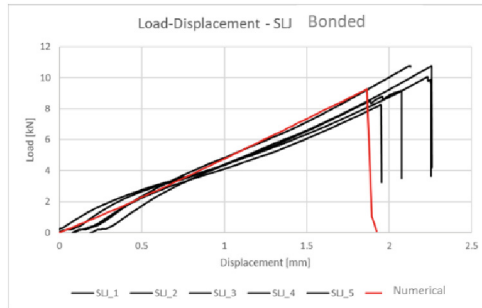


**Fig. 6.** Load-displacement curve-Numerical vs Experimental-Bonded configuration

The maximum load value achieved by the numerical model is 9.3 kN, which is 8% lower than the experimental average value. Actually the experimental curves' slope value changes between 4060 N/mm and 4790 N/mm, while the experimental failure load is between 8261 N and 10766 N with an averaged value of 10.12 kN.

Figure 7 shows the fibre tensile failure with the Hashin criterion, it can be seen that the critical areas still have a small value in terms of damage.

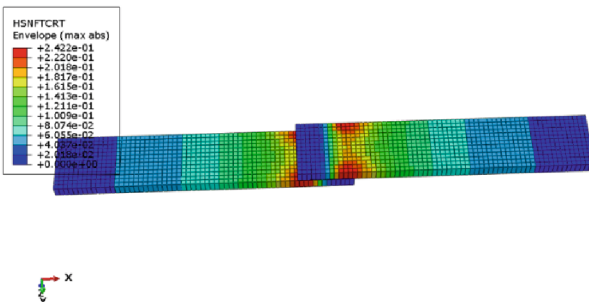


**Fig. 7.** Hashin criteria for fiber tensile failure-Bonded configuration.

For the Bolted configuration, the comparisons between numerical results and experimental data, in terms of load-displacements curve, are shown in Fig. 8. The maximum

load value reached by the numerical model is 3.5 kN, which is 1% lower than the experimental average value (3,55 kN). It can be observed that the values of the failure load are reduced if compared to the bonded configuration.

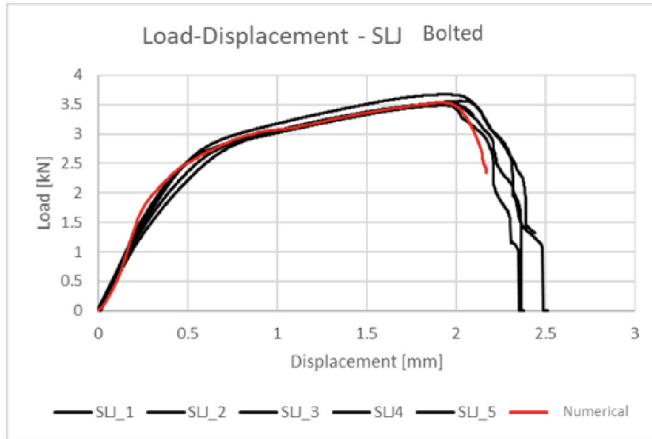


Fig. 8. Load-displacement curve-Numerical vs Experimental-Bolted configuration

Figure 9 shows the deformed shape at the beginning and at the end of the analysis, when the joint is no more able to sustain load.

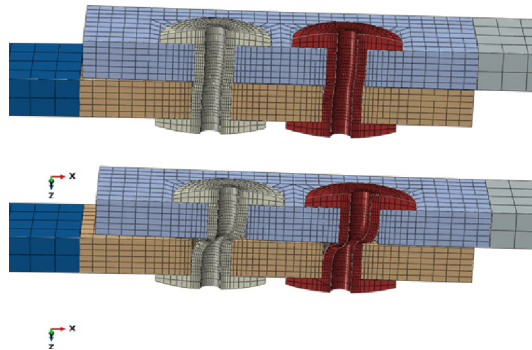


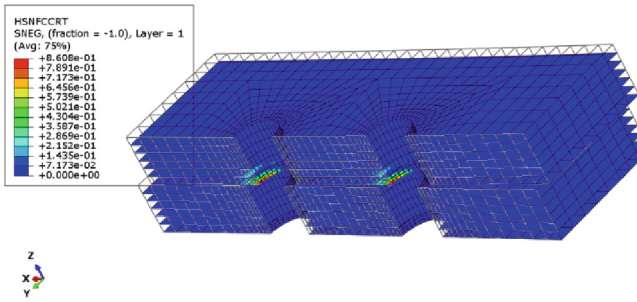
Fig. 9. Deformed at start and end of analysis.

At the end of the analysis, it can be noted that failure criteria contour plots show a concentration of damage in the rivets.

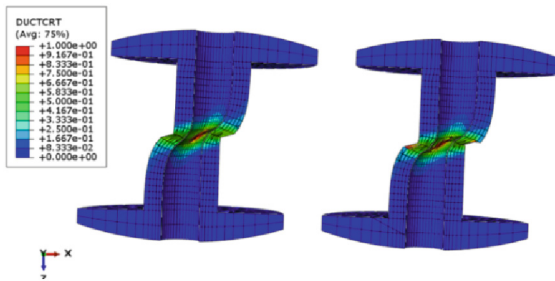
Figure 10 shows the Hashin Criteria values in the laminate for the most stressed (compression of fibres) mode, while Fig. 11 damage distribution in the rivet, is shown.

An excellent agreement between numerical predictions and experimental data can be noted from Fig. 11.



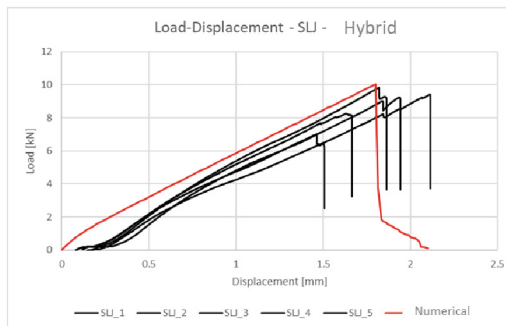


**Fig. 10.** Hashin criteria-composite structure-Bolted configuration.



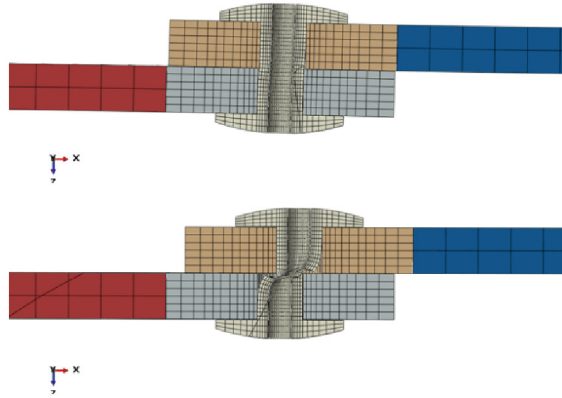
**Fig. 11.** Hashin criteria-Rivets-Bolted configuration.

Finally, for the Hybrid (bonded-Bolted) configuration, where an adhesive material has been used between the contact parts in addition to riveted joints, the comparisons between numerical results and experimental data, in terms of load-displacements curve, are shown in Fig. 12. The maximum load value achieved is 10 kN, which is 14% over the experimental average value (8,75 kN).



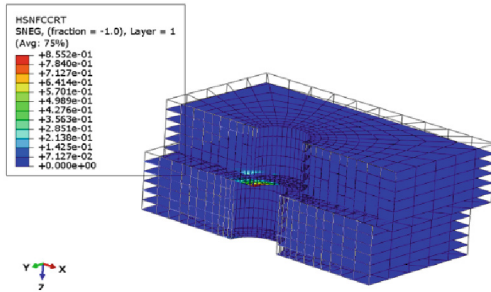
**Fig. 12.** Load-displacement curve-Numerical vs Experimental-Hybrid configuration

Figure 13 shows the deformed shape of the hybrid joint at the beginning and at the end of the analysis, where the joint is no more able to carry out its functions.



**Fig. 13.** Deformed at start and end of analysis.

Figure 14, shows the Hashin Criteria value (compression of fibres) in the laminates, while, Fig. 15 shows the damage of the rivet (in red the maximum tensile stress). At the end of the analysis the cohesive material and the rivet are completely damaged, while the laminate shows a very limited damaged area.



**Fig. 14.** Hashin criteria-composite structure-Hybrid configuration.

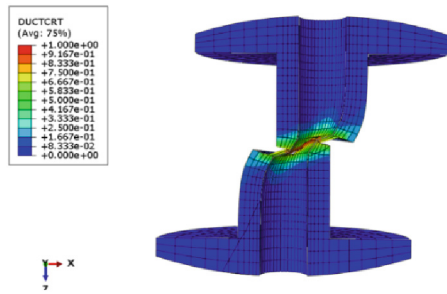


**Fig. 15.** Hashin criteria-Rivet-Hybrid configuration.

The agreement between numerical results and experimental data is still excellent for bolted configurations (bolted and hybrid) in terms of the maximum load (Fig. 8 and Fig. 12). The maximum load carrying capability, for these configurations, is influenced by the resistance of the bolts and by the debonding of the adherends. As observed in Fig. 11 and 15, the bolts experience catastrophic damages which strongly influenced the maximum load reached by each configuration. According to the numerical and experimental curves, resumed in Fig. 16, the bolted and hybrid configurations, due to the presence of rivets, have reduced strength surface for the single lap joint category. In terms of load difference, the bonded configuration has a higher maximum load.

According to the numerical analyses, a good agreement has been found between the experimental and numerical solutions for all the configurations, confirming the reliability of the introduced numerical models. Moreover, numerical results, integrated with experimental data, have provided useful information about the damage onset and evolution in joints components.

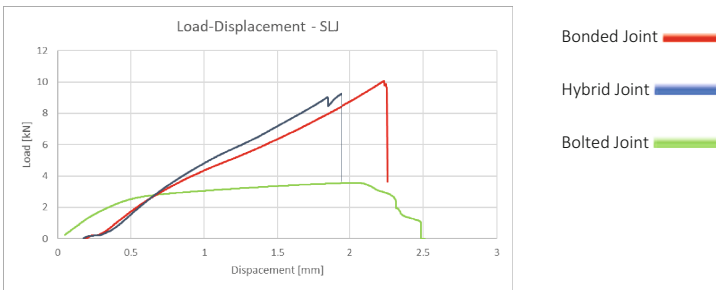


**Fig. 16.** Load-displacement curve-Single lap joint for Three configurations.

## 4 Conclusions

Bonded, bolted, and hybrid Composite Single Lap Joints have been numerically and experimentally investigated under tensile loading conditions. By comparing the numerical results and the experimental data obtained for the different joint configurations, the single lap bonded joint, as expected, has been found to be characterized by the higher failure loads. Hence, the single lap bonded joint, among the different types of joints, can be considered the preferred choice for the connection of composite materials, due to its peculiar mechanisms to transfer the tensile load. The proposed numerical models have been found able to correctly simulate the mechanical behaviour of the analysed joint configuration and to provide useful information about the damage development within joints components.

## References

1. Puchaáa, K., Szymczyk, E., Jachimowicz, J.: About mechanical joints design in metal-composite structure. *J. KONES Powertrain Transp.* **19**(3), 381–390 (2012)
2. Broughton, W.R., Crocker, L.E., Gower, M.R.L.: Design Requirements for Bonded and Bolted Composite Structures, NPL Report MATC(A) 65 (2002)
3. Sham Prasad, M.S., Venkatesha, C.S., Jayaraju, T.: experimental methods of determining fracture toughness of fiber reinforced polymer composites under various loading conditions. *J. Miner. Mater. Charact. Eng.* **10**(13), 1263–1275 (2011)
4. Davis, M., Bond, D.: Principles and practices of adhesive bonded structural joints and repairs. *Int. J. Adhes. Adhes.* **19**, 91–105 (1999)
5. Sheppard, A., Kelly, D., Tong, L.: A damage zone model for the failure analysis of adhesively bonded joints. *Int. J. Adhes. Adhes.* **18**, 385–400 (1998)
6. Cooper, P.A., Sawyer, J.W.: A critical examination of stresses in an elastic single lap joint, NASA Technical paper 1507 (1979)
7. Yan, Y., Wen, W.D., Chang, F.K., Shyprykevich, P.: Experimental study on clamping effects on the tensile strength of composite plates with a bolt-filled hole. *Compos. Part. A* **30**, 1215–1229 (1999)
8. Chakherlou, T.N., Oskouei, R.H., Vogwell, J.: Experimental and numerical investigation of the effect of clamping force on the fatigue behaviour of bolted plates. *Eng. Fail. Anal.* **15**, 563–574 (2008)
9. Kim, J., Yoon, J.C., Kang, B.S.: Finite element analysis and modelling of structure with bolted joints. *Appl. Math. Model* **31**, 895–911 (2007)
10. Chen, N., Luo, H., Wan, M., Chenot, J.: Experimental and numerical studies on failure modes of riveted joints under tensile load. *J. Mater. Process. Technol.* **214**, 2049–2058 (2014)
11. Hart-Smith, L.J.: Bolted joint analyses for composite structures—Current empirical methods and future scientific prospects. In: Kedward, K.T., Kim, H., (Eds.) Proceedings of the Joining and Repair of Composites Structures, West Conshohocken, PA, USA, 1 January 2004. ASTM international, West Conshohocken, PA, USA (2004)
12. Baker, A., Dutton, S., Kelly, D.: *Composite Material for Aircraft Structures*, 2nd edn. American Institute of Aeronautics and Astronautics, Reston, VA, USA (2004)
13. Chan, W.S., Vedhagiri, S.: Analysis of composite bonded/bolted joints used in repairing. *J. Compos. Mater.* **35**(12), 1045–1061 (2001)
14. Barut, A., Madenc, E.: Analysis of bolted–bonded composite single-lap joints under combined in plane and transverse loading. *Compos. Struct.* **88**(4), 579–594 (2009)
15. Bodjona, K., Raju, K., Lim, G.H., Lessard, L.: Load sharing in single-lap bonded/bolted composite joints, Part I: Model development and validation. *Compos. Struct.* **129**, 268–275 (2015)
16. ASTM D 5528–01 (2007)
17. O’Brien, T.K., Johnston, W.M., Toland, G.J.: Mode II Interlaminar Fracture Toughness and Fatigue Characterization of a Graphite Epoxy Composite Material, NASA/TM-2010-216838 (2010)
18. ASTM D 7905/M
19. Sellitto, A., Saputo, S., Di Caprio, F., Riccio, A., Russo, A., Acanfora, V.: Numerical experimental correlation of impact-induced damages in CFRP laminates. *Appl. Sci.* **9**(11), 2372 (2019)

# **Innovative Manufacturing and Inspection Technologies**



# Sustainability of Fused Deposition Modeling: The Role of the Plate Material

Ersilia Cozzolino<sup>(✉)</sup>, Francesco Napolitano, Antonello Astarita, Valentina Lopresto, Ilaria Papa, and Antonino Squillace

Dipartimento di Ingegneria Chimica, dei Materiali e Della Produzione Industriale, Università degli studi di Napoli Federico II, Piazzale Tecchio 80, 80125 Napoli, Italy  
ersilia.cozzolino@unina.it

**Abstract.** Fused deposition modelling (FDM) is an additive manufacturing technique providing numerous possibilities for producing complex geometries. In FDM, many heat sources make the layer-by-layer deposition mechanism a thermally driven process. Heat transfer is crucial in determining the temperature history and the interlayer adhesion of the FDMed parts. Thus, the relevance of this aspect linked to the concern about the increasing global warming leads to the investigation of solutions to reduce the environmental impact of the process. The results in the literature show that the greatest contribution in terms of power consumption during the FDM process is associated with heating the bed and keeping it warm. Thus, this study aims to provide guidelines for a better choice in the plate material of the 3D printer to reduce the energy consumption required by the process of heating the plate without renouncing to print parts that meet the industrial quality requirements.

**Keywords:** Sustainability · Fused Deposition Modeling · PLA · Aluminum · Steel

## 1 Introduction

Nowadays, the importance of the manufacturing processes from a green perspective and the growing diffusion of 3D printing devices have led to the study of a strategy for energy consumption reduction. Rapid prototyping and domestic use of 3D printers increase these machines' energy daily. Considering that the plate absorbs the main quantity of energy [1] it was assumed to investigate this aspect to pursue an energy consumption reduction strategy.

Commercial 3D printers are equipped with a steel plate with a very low thermal conductivity coefficient, so it requires a large amount of energy input to reach the target temperature and keep it constant. In this study the replacement was proposed with an Aluminum plate, in particular made of AA2024 which has 193 W/m-K thermal conductivity that is about 8 times higher than steel value.

Beyond the energetic performance, the mechanical properties of the workpieces was also evaluated because the new surface heating could generate thermal distortions and

then a geometrical error in the workpiece [2]. Moreover, during the on/off heating cycles, it could reach temperature peaks which can cause a rapid polymer degradation of the lowest layer in contact with the plate surface [3].

In summarizing, in this experimental study were used two different plates. The energy consumption was evaluated by monitoring it during the printing process. It was carried out through tensile tests and ultrasonic inspection on the workpieces produced, using the same experimental printing strategy. The final aim is to study the best compromise between printing setup and mechanical properties from an energy-saving perspective.

## 2 Materials and Methods

A Polyactic Acid (PLA) sample having the dimensions  $50 \times 50 \times 3$  mm was printed by means of the 3D printer called Sharebot 42. Its printing volume is  $250 \times 220 \times 220$  mm, and its Z resolution is  $50 \mu\text{m}$ . The plate temperature was fixed at  $90^\circ\text{C}$  to keep the material fluid and reduce the voids. A  $-45^\circ/+45^\circ$  raster orientation, an infill density of 100%, a line infill pattern and a layer thickness of 0.2 mm were chosen. The number of shells was chosen equal to two, according to the best results in literature in terms of good mechanical properties obtained [4]. The filament adopted for this study is Black PLA ICE having a diameter of 1.75 mm. Table 1 contains the speed and extrusion temperature adopted to print the sample.

**Table 1.** Experimental plan of PLA sample manufactured by FDM.

Configuration	Speed (mm/s)	Extrusion Temperature ( $^\circ\text{C}$ )
1	110	215

All the process conditions for 3D printing were chosen according to the best results in literature [4–6]. The sample mass was measured three times by means of the Gibertini ETERNITY 200 CAL balance, having an accuracy of  $\pm 0.05$  mg. Also, 3 tensile specimens having the ASTM standard geometry were printed and tested for the configuration adopted in this study using Galdabini QUASAR 50, equipped with a 50kN load cell and testing speed 3 mm/min.

During the printing process, power and energy consumption were measured by a device called Quality Analyser CA8331 (Chauvin Arnoux), which gives records of power and energy consumption as the output of the current and tension measurements. Figure 1 shows a schematization of the experimental setup adopted in this study.

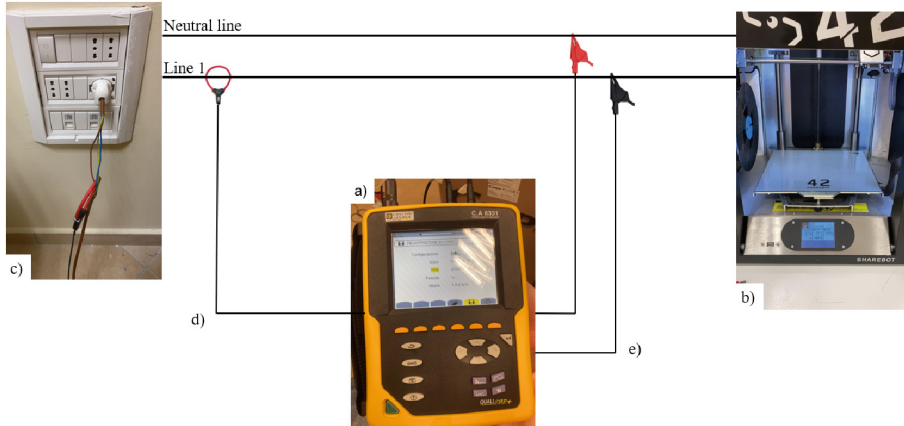


**Fig. 1.** Experimental setup: (a) the power and the energy analyzer Chauvin Arnoux CA 8331, b) the 3D printer (Sharebot 42), c) the electrical cabinet, d) the current sensor, e) the tension cables.

Two samples, having the same geometrical dimensions, of the same configuration were printed: one by using a 2024 aluminum plate and another by using a AISI 430 stainless steel plate to compare the results obtained in terms of energy consumption and mechanical properties.

The Specific Energy Consumption (SEC) was calculated to evaluate the efficiency of the energy consumption strategy. The formula of the SEC is the following:

$$SEC = E/m \quad (1)$$

where  $E$  is the energy consumption during 3D printing and  $m$  is the mass of the sample.

### 3 Results and Discussion

As mentioned in the previous section, power consumption was measured during printing the samples by using both the steel and aluminum plates. The power trends are observable in Fig. 1 and Fig. 2.



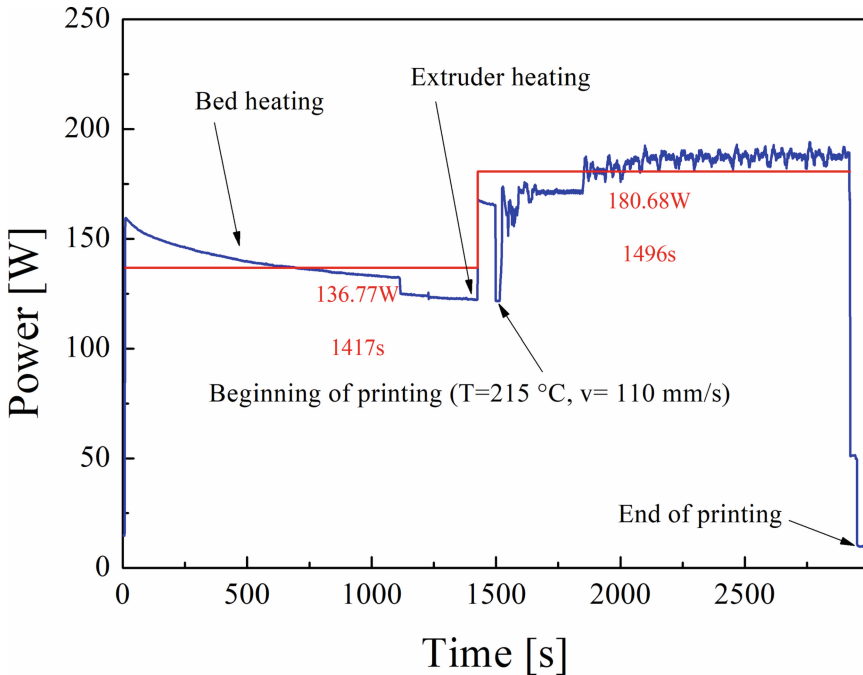


**Fig. 2.** Power trend over time during the FDM process of the configuration 1 in Table 1 by using the steel plate.

The red lines in Fig. 2 and Fig. 3 indicate the power average during the main subphases of the FDM process: bed heating and printing. During the printing subphase, the power average is very similar by comparing steel and aluminium plate. However, it lasts less time using the aluminium plate due to its higher thermal conductivity. Thermal conductivity of the aluminium is  $k = 235 \text{ W/m K}$  while that of the steel is  $k = 45 \text{ W/m K}$ . For the same reason, the bed heating subphase lasts less time by using the aluminium plate than by using the steel plate.

For better visualization of the results obtained, the percentages in terms of energy consumption for each subphase of the FDM process by using both the steel and aluminium plates are represented in the pie charts in Fig. 4 and Fig. 5.

It can be observed in Fig. 4 and Fig. 5 that a great amount of energy from the whole FDM process is consumed for heating the bed, agreeing with the literature [1]. Moreover, according to the results observed in the power trend graphs (Fig. 2 and Fig. 3), by fixing the process conditions, a higher energy consumption to heat the bed is required by using the steel plate because of the higher thermal conductivity of the aluminium plate.

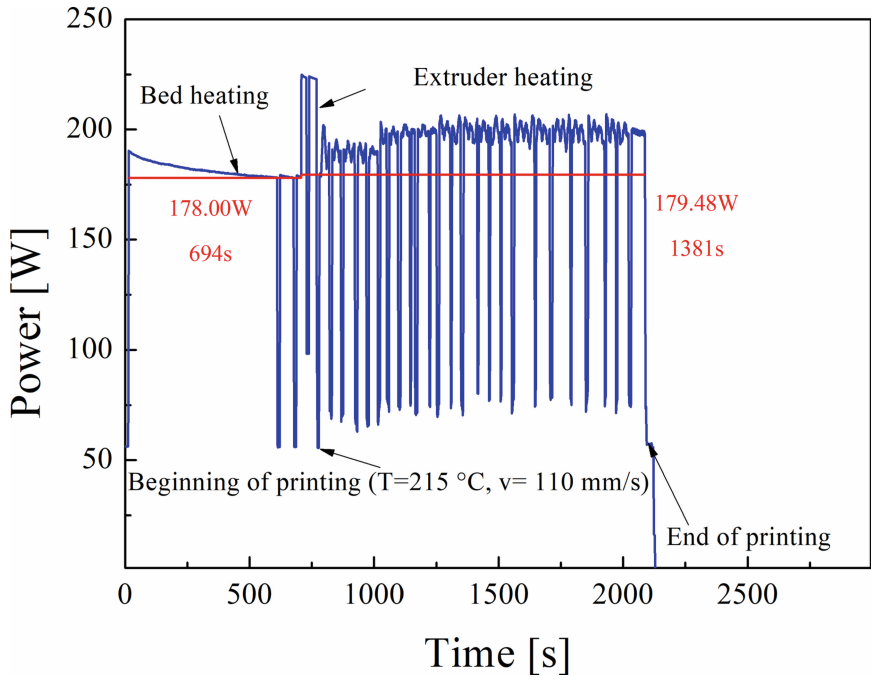


**Fig. 3.** Power trend over time during the FDM process of the configuration 1 in Table 1 by using the aluminum plate.

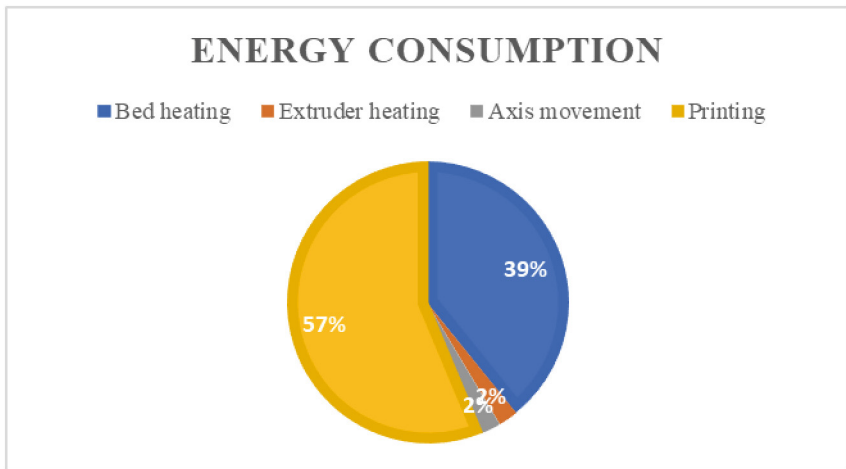


**Fig. 4.** Pie chart of the energy consumption during the main subphases of FDM process by using the steel plate

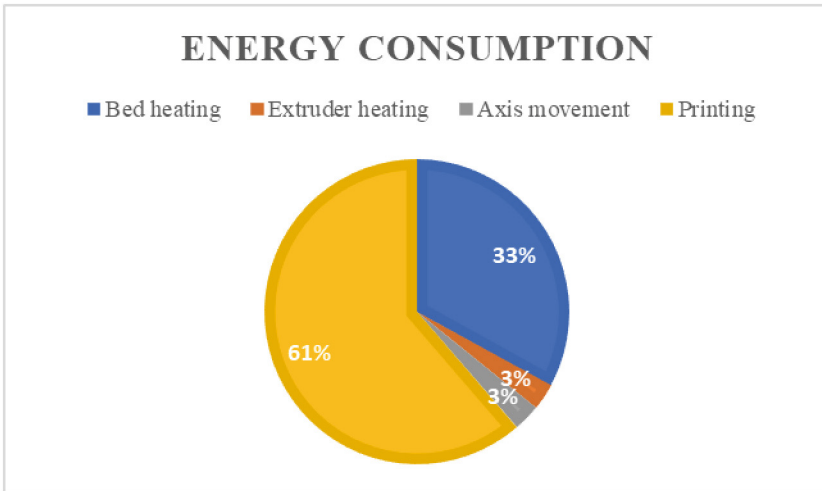


**Fig. 5.** Pie chart of the energy consumption during the main subphases of FDM process by using the aluminum plate

Finally, the results obtained in terms of SEC, calculated by Eq. 1, and UTS are contained in Table 2.

**Table 2.** Experimental plan of PLA samples manufactured by FDM.

Plate material	SEC (kJ/g)	UTS (MPa)	UTS/SEC
steel	29.8	50.6	1.7
aluminum	25.5	48.3	1.8

It can be seen that by fixing all the process conditions and by only varying the plate material of the 3D printer, more energy is required for each unit mass (1 g) to be printed by using the steel plate. In fact, specific energy consumption of 29.8 kJ/g is required by using the steel plate, while specific energy consumption of 25.5 kJ/g is required by using an aluminum plate. Concerning the UTS, very similar results are obtained in two conditions (Table 2). A joint analysis of the results obtained introduced an efficiency index given by the ratio between the SEC and the UTS.

As observable by the results in Table 2, the choice of the plate material hangs in the direction of aluminum rather than steel since the efficiency index is higher by using an aluminum plate.

## 4 Conclusions

This article deals with the study of the effect of the plate material on both the energy consumption and mechanical properties obtained. One configuration of process conditions particularly extrusion temperature and speed was adopted among the best technological results in literature by using two plate materials, steel and aluminum. The main conclusions of this study are the following:

- The greatest contribution in terms of power consumption during the FDM process is heating the bed and keeping it warm.
- The aluminum plate takes less time than the steel plate to reach the desired temperature. This result allows for saving energy during the bed heating subphase of the FDM process.
- The average power during the printing subphase is lower by using the aluminum plate than the steel plate. This result allows for saving energy even during the printing subphase of the FDM process.
- Using the aluminum plate rather than the steel plate saves up to 20% energy consumption for the entire FDM process.

Therefore, it is recommended to choose an aluminum plate under the same process conditions. Further investigation of this study may include the thermal imaging camera analysis to study the heat transfer between the plate and the material and between the layers and ultrasonic inspection to detect the quality of the printed PLA parts for better optimization of the FDM process conditions from an energy-saving perspective.

## References

1. Napolitano, F., Cozzolino, E., Papa, I., Astarita, A., Squillace, A.: Experimental integrated approach for mechanical characteristic optimization of FDM-printed PLA in an energy-saving perspective. *The Int. J. Adv. Manuf. Technol.* **121**, 3551–3565 (2022). <https://doi.org/10.1007/s00170-022-09535-z>
2. Choi, Y.-H., Kim, C.-M., Jeong, H.-S., Youn, J.-H.: Influence of bed temperature on heat shrinkage shape error in FDM additive manufacturing of the ABS-engineering plastic. *World J. Eng. Technol.* **04**(03), 186–192 (2016). <https://doi.org/10.4236/wjet.2016.43d022>
3. Luzanin, O., Movrin, D., Stathopoulos, V., Pandis, P., Radusin, T., Guduric, V.: Impact of processing parameters on tensile strength, in-process crystallinity and mesostructure in FDM-fabricated PLA specimens. *Rapid Prototyp. J.* **25**(8), 1398–1410 (2019). <https://doi.org/10.1108/RPJ-12-2018-0316>
4. Dey, A., Yodo, N.: A systematic survey of FDM process parameter optimization and their influence on part characteristics. *J. Manuf. Mater. Process.* **3**(3), 64 (2019). <https://doi.org/10.3390/jmmp3030064>
5. Wang, L., Gramlich, W.M., Gardner, D.J.: Improving the impact strength of Poly(lactic acid) (PLA) in fused layer modeling (FLM). *Polymer (Guildf)* **114**, 242–248 (2017). <https://doi.org/10.1016/j.polymer.2017.03.011>
6. Tsouknidas, A., Pantazopoulos, M., Katsoulis, I., Fasnakis, D., Maropoulos, S., Michailidis, N.: Impact absorption capacity of 3D-printed components fabricated by fused deposition modelling. *Mater. Des.* **102**, 41–44 (2016). <https://doi.org/10.1016/j.matdes.2016.03.154>



# On the Mechanical Behaviour of Carbon Fibre Laminates Repaired with Hot Bonding Technology by Infusion

Federica Donadio<sup>1</sup>(✉), Ilaria Papa<sup>1</sup>, Antonio Viscusi<sup>1</sup>, Luigi Carrino<sup>1</sup>,  
Valentina Lopresto<sup>1</sup>, Giancarlo Ingenito<sup>2</sup>, Gabriella Caputo<sup>2</sup>, and Antonio Langella<sup>1</sup>

<sup>1</sup> Department of Chemical, Materials and Production Engineering, University of Naples Federico II, Piazzale V. Tecchio 80, 80125 Napoli, Italy  
federica.donadio@unina.it

<sup>2</sup> Metitalia Srl, R&D Department, Via Delle Fontane 17, 84012 Angri, SA, Italy

**Abstract.** Humans have been using composite materials for several years. Still, their development is relatively recent and connected particularly to aeronautic and aerospace applications because of their exceptional strength, stiffness-to-density ratio and superior physical properties. Composites provide several advantages compared to traditional metallic counterparts for high-performance products that need to be lightweight but strong enough for tough loading conditions. However, these materials are sensitive to both high and low-speed impacts that frequently occur in the automotive and aerospace fields. Due to the high production costs for every single component in carbon fiber reinforced polymer, CFRP, further repair techniques have been developed to repair damaged components of a complex structure on-site without disassembling any element. This work investigated the goodness of the hot bonding repair technique by ultrasound technique and mechanical tests. An experimental study was carried out to determine the characteristics of carbon fiber-reinforced plastic at the open hole tension and open hole compression tests.

**Keywords:** Composite · repairing · mechanical properties · hot bonding technology

## 1 Introduction

Composite materials are among the most innovative materials in the aeronautical sector for their excellent characteristics of resistance, rigidity and lightness that allow the creation of significantly reduced weight structures, with the same performance, compared to those built with conventional materials.

Aeronautical industry requires regular inspections to maintain structural integrity, efficiency and safety of the aircraft [1]. Cause their typical anisotropy, composite materials are particularly sensitive to dynamic loads such as low and high-speed impacts due, for example, to accidental loads on the structure during the production and maintenance phases. The impact produces important damages inside the structure, affecting the stability and the service performance [2, 3].

The use of finite element (FE) methods has also increased to simulate the behaviour of composites to determine the stress distribution and to estimate the peak loads and the impact response. [4, 5].

The impacts are generally not worrying for the metal structures because of their inherent ductility and their energy-absorbing mechanisms, while composite materials are more brittle and are sensitive to impact damage [6]. Impact damage can cause an important reduction in compressive, tensile, shear and impact strength [7–9], depending on the impact energy, the impactor geometry and the composite design.

It's a common practice to assess the damage on composite structures using non-destructive techniques to choose for the repair or the replacement of the damaged component. If damage is limited, replacing the entire piece is not cost-effective and the reparation in situ is the only possible solution [10].

The growing demand for more reliable and repeatable repair procedures for composite components has driven the research to develop a repair process that is able to achieve these objectives. The repair techniques used in the aeronautical industry are methods based on the adhesive bonding of composite patches.

The kind of composite repair is a function of the type and the location damage, it can be injection, doubler or scarf-based [11]. The resin injection is a temporary solution to stop the spreading of damage. With the doubler repair is possible to keep the initial strength but not an aerodynamically smooth surface. At last, with a scarf reparation, the structure can maintain strength as well as a flush surface. Scarf repair is the better solution for aircraft composite structures, especially for external skin repair.

Composite repair methods involve either mechanically fastened repairs, not suitable for thin laminates or sandwich structures because of the high-stress concentrations [12, 13], or adhesively bonded patches that provide better joint efficiency and a smoother surface [14]. To obtain a good scarf repair, many factors need attention, such as accurate damage evaluation, precise scarfing, clean and active scarf surfaces, temperature and pressure controlled.

To meet this challenge the Metitalia s.r.l, an aeronautical company has developed an innovative repair technique that restores the structure directly in situ. The hot bonding process is an innovative technique that consists of removing damaged plies by scarfing step by step, applying an adhesive film and then a repair patch made by pre-infused plies uncured [15]. The composite patch applied on the laminate being repaired was finally cured with a heat blanket and with the pressure applied by the vacuum bag.

This research aimed to implement a repair procedure to be carried out on-site, directly on the aircraft. Using dry plies impregnated on-site, there is no need to freeze the material, which involves a significant economic savings of the transport costs compared to repairs with prepreg. Repaired and unrepaired carbon fiber-reinforced (CFRP) panels were manufactured and tested. Mechanical behaviour of specimens prepared by hot bonding technique was evaluated to measure the ability of the repair to maintain the initial mechanical performance. Both types of samples panels were analyzed with ultrasound technology to detect the presence of defects and porosity before being cut to obtain the specimens. Then the specimens were subjected to open hole tensile and compression tests to evaluate the mechanical behaviour in the maximum stress conditions caused by the presence of holes on the structure.

## 2 Materials and Experimental Setup

Unidirectional carbon woven 1,77 ÷ 1,83 fiber pre-impregnated, Cycom NTA62470, and Cycom OMS/977-2A glass fabric for the first and the last plies were used. The specimens were made inside the ISO 8 cleanroom. The previously cut plies are superimposed and arranged according to the directions in Table 1, to obtain 2 symmetrical laminates of dimensions 1062x674 mm.

**Table 1.** Stacking sequence of the laminates.

Ply	Orientation	Material
P1	0/90	OMS/977-2A-GLASS FABRIC
P2	0°	NTA-62470
P3	90°	NTA-62470
P4	+45°	NTA-62470
P5	-45°	NTA-62470
P6	0°	NTA-62470
P7	90°	NTA-62470
P8	0°	NTA-62470
P9	-45°	NTA-62470
P10	+45°	NTA-62470
P11	90°	NTA-62470
P12	0°	NTA-62470
P13	0/90	OMS/977-2A-GLASS FABRIC

The laminate was located inside the vacuum bag and subjected to the curing process in the autoclave.

Two laminates have been obtained, they have been named as:

- Pristine, that will be the unrepaired panel
- Infusion, that will be repaired with infused patches.

It was been supposed that a defect was located near the seventh ply, whereas the area involved in the repair operation is a strip along the laminate length.

The first operation of the repair is scarfing, which is the process of removing material to reach the damaged area. A 97 mm wide area that affects the layer of glass fibers, placed to avoid scratches on the surface, was eliminated at first. Subsequently, the removed zone decreases by 12 mm for every single ply until it reaches the defect, at the seventh ply, which instead has a size of 25 mm.

After the scarfing operation, the laminate was subjected to an accurate visual inspection to identify the formation of new defects like the excessive material removal in an unwanted point that could lead to a decrease of the mechanical properties after repair. Then, manually impregnated cloths were used to make the repair patch. Dry carbon fibers plies were infused with a two-component resin for the realization of the cloths. The repair patch contains the same weight of the material scarfed and the new plies maintain the same orientation of fibers as the removed plies.

The material used for the patch was a unidirectional carbon fiber fabric with 300, areal weight produced by Saertex. The RTM6-2, a two-component epoxy resin designed for molding and infusion processes produced by Hexcel, was used to impregnate the cloths. The amount of resin to be used will be calculated by the following equation where  $V_r\%$  and  $V_f\%$  are the volume fraction of the resin and the fiber, respectively.

$$Q_{\text{resin}} = \frac{V_r\%}{V_f\%} + 10\% \quad (1)$$

To avoid the cooling of the resin during the impregnation process, the impregnated cloths were placed on a plate and heated by an infrared lamp. The temperature was controlled thanks to a thermocouple positioned on the plate and it was maintained constant at 80 °C. The patch has been joined to the laminate using the adhesive FM309-1 after cleaning and preparing the surface. Every ply of the patch has a specific dimension and orientation explained in the following table (Table 2).

**Table 2.** Lay-up repair

Ply n°	Length (mm)	Width (mm)	Orientation (°)
7	All laminate's length	25	90
8	=	37	0
9	=	49	-45
10	=	61	45
11	=	73	90
12	=	85	0

After the impregnation and the placement of the clothes on the scarfing zone, the laminate is cured in a bag with an infrared lamp for 120 min at 180 °C under vacuum pressure.

The specimens 300 × 36 mm<sup>2</sup> cut from the original panels and used for the Open hole compression (OHC), and tension (OHT) test samples showed a nominal thickness of  $t_h = 3$  mm. The repair zone is located in the center of the specimen and the diameter hole was  $D = 6$  mm. The OHC and OHT tests were performed according to the standards ASTM D6484 [16] and ASTM D3878, respectively [17], using the MTS 810 Material Testing



Systems equipped with an advanced test design application software, Multi-Purpose Testware (MPT).

A loading capacity of 100KN characterizes it, a clamping pressure of  $2,0684e+7$  Pa, and the range of frequency 0–100 Hz and permits all different types of mechanical testing such as tension, compression, flexure, interlaminar shear strength, fatigue, fracture etc. Strain gauges were applied on 3 Pristine and 3 Infusion specimens for the OHT tests to evaluate the deformation during the tests, record the trend of the  $\sigma$ - $\epsilon$  curve, and consequently calculate Young's modulus (E). For the Infusion specimens, 2 strain gauges, one for each side, were positioned near the hole. The strain gauges were also connected with a Vishay model 7000 control unit, that acquires the data directly obtained from the strain gauges and processes them with the relative data processing software.

Ultrasound (US) measurements were carried out using a Multi2000 Pocket  $16 \times 64$  system by M2M using a Linear phased array Probe, 5 MHz, 64 Elements [18]. The reflection method is used for the analysis: a single probe emits and receives the ultrasonic waves that penetrate the piece.

The signal obtained by the internal reflections is examined according to the Echo Max (abs) procedure. It provides information about the presence of any defects representing a discontinuity in the material in which it propagates. The depth of a reflecting discontinuity is deduced from the delay between pulse transmission and echo reception [19]. Depending on the amplitude of the signal, the recorded image shows several colours. The laminates were subjected to ultrasonic analysis before cutting to produce the OHC and OHT specimens.

## 3 Results and Discussion

### 3.1 Ultrasonic C-scanning Analysis

Ultrasonic C-scanning provides an in-plain view of the damage inside the specimens. Different colour reflects the sample homogeneity. The more the image tends to red the more the signal is not attenuated while the images in black denoting a discontinuity completely absorbs the signal.

Each of the laminates, pristine and infusion, were subjected to ultrasonic C-scanning analysis before testing. Figure 1 shows the C-Scan image of the two laminates. For the pristine laminate, the image is totally red, which means there is no inhomogeneity; for the infusion laminate in the central zone interested by repair there is a considerable variation in colour due to the porosities or the no-adherence of the patch, probably caused by the absence of pressure during the cure.

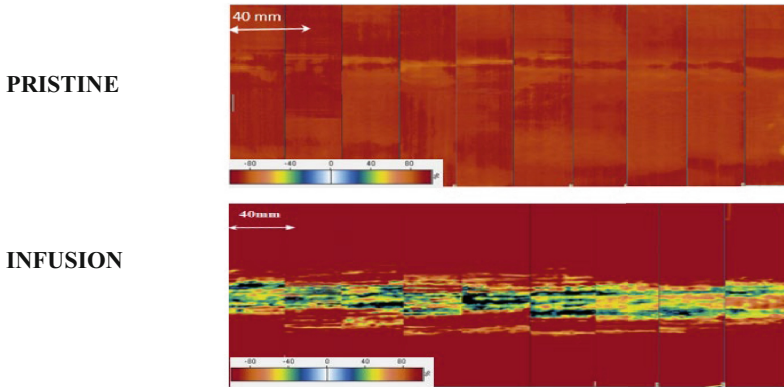


**Fig. 1.** Ultrasound C-Scan Analysis

### 3.2 Confocal Microscope Analysis

The cross-sectional area of the two samples was analysed with the confocal laser microscope. The pristine sample results compact and without defects, it is possible to individuate clearly the plies arrangement. Whereas, the infusion shows many irregularities, in particular the plies not affected by the repair have a linear and compact arrangement such as the pristine sample, while from the seventh ply, where the repair starts, there is not the same order and a lot of voids are concentrated in correspondence with the adhesive film.

From the analysis of the image, the percentages of voids shown in table 3 were obtained.

**Table 3.** Percentages of voids

Sample	Total Area [mm <sup>2</sup> ]	Void Area [mm <sup>2</sup> ]	% Voids
Pristine	26,8	0,4	1,49
Infusion	26,8	2,2	8,18

### 3.3 Open Hole Compression (OHC) and Open Hole Tension (OHT) Test

In this section, the open hole compression and open hole tension test results are reported. The only acceptable failure mode for ultimate open-hole tensile and compressive strength passes through the hole in the test specimen. All the tests were valid in fact, in all the specimens tested the failure occurred at the hole. In particular, the OHC tests reported the lateral gage middle failure mode, laminate fails laterally across the center of the hole. In contrast, for the OHT test the dominant failure mode was the multimode gage middle, the laminate fails in tension at the hole and exhibits multiple modes of failure in various



**Fig. 2.** Failure mode OHC and OHT tests

plies. The different failure modes are evident in Fig. 2, which shows some samples after the test.

Three samples of each laminate, pristine and infusion, were tested. Table 3 shows the maximum load before failure,  $F_{\max}$ , the ultimate open hole compression and tensile strength,  $\sigma_{\max}$ , and the total cross-sectional area disregarding hole A calculated during the tests.

**Table 4.** Open hole compression and tensile test parameters

	OHC			OHT		
	$F_{\max}$ [N]	A[mm <sup>2</sup> ]	$\sigma_{\max}$ [MPa]	$F_{\max}$ [N]	A[mm <sup>2</sup> ]	$\sigma_{\max}$ [MPa]
Pristine	20071,71	66	304,11	40006,62	66	606,16
	21385,53	65,9	324,5	37892,44	66,2	572,39
	20930,14	66	317,12	40171,99	66,1	607,73
Infusion	20387,82	72	283,16	36609,65	71,9	509,17
	23174,53	72,3	320,52	31568,88	71,9	439,06
	21249,41	72,1	294,72	33914,58	72	471,03

**Table 5.** Open hole tensile test with strain gauges parameters

	OHT					
	$F_{\max}$ [N]	A[mm <sup>2</sup> ]	$\sigma_{\max}$ [MPa]	$\epsilon_{\max}$	$\epsilon_{\max}$ NR	E [GPa]
Pristine	41155	66	623,56	0,005036	–	121,53
	42775	66,2	646,14	0,005432	–	117,5
	42190	66	639,24	0,005687	–	121,8
Infusion	35275	71,7	491,98	0,0041	0,0045	105,1
	34490	72	479,02	0,0046	0,0047	102,35
	35875	72,1	497,57	0,0048	0,0043	101,77

The average data of pristine and infusion OHC and OHT results were compared (Fig. 3). About the OHC test, the increase in thickness due to repair and the presence of

defects in the infusion specimens did not drastically affect the mechanical performance. The deformation of the specimen during the compression test tends to reduce the volume of the voids, consequently increasing the resistant section of the specimen, which tends to return to the initial conditions of the pristine sample.

Unlike the OHC test, lower breaking values are achieved in the infusion specimens compared to the initial conditions because the reduced resistant section of the specimen caused by the presence of voids at the inter-laminar interfaces and the stress concentrations around the voids.

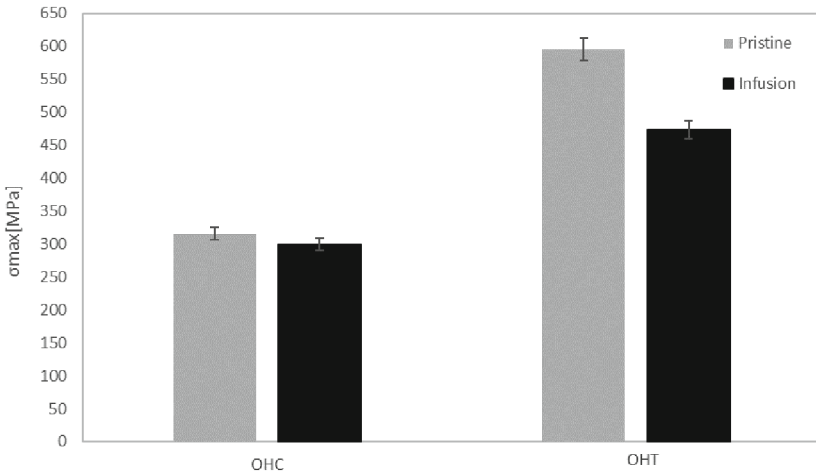


**Fig. 3.** Comparison between pristine and infusion OHC and OHT test results.

### 3.4 Open Hole Tension (OHT) Test with Strain Gauges

The maximum load before failure,  $F_{\max}$ , the ultimate open hole tensile strength,  $\sigma_{\max}$ , and the total cross-sectional area disregarding hole A, the strain,  $\epsilon_{\max}$ , and Young's modulus E registered during the test are reported in Table 4. For the Infusion specimens, strain gauges were applied on both sides,  $\sigma_{\max}$  NR is the strain calculated on the not repaired side. The failure mode of the specimens results the same as found in the OHT tests without strain gauge, a failure according to the MGM method described in the ASTM D387 standard.

Figure 4 shows the stress-strain curves relating to the OHT tests carried out on one Pristine sample, one Infusion sample on the repaired side and the unrepaired side. Analyzing the graph the same trend was found for every kind of specimen, the behaviour in the elastic range is the same in the three specimens, Pristine sample shows a break for a value of  $\sigma_{\max} = 646$  MPa while for the Infusion sample the breaking occurs for a  $\sigma_{\max} = 479$  MPa.

The comparison of the curves shows that the behaviour in the elastic range of the two types is similar. In accordance with the OHT test without strain gauges, the breaking

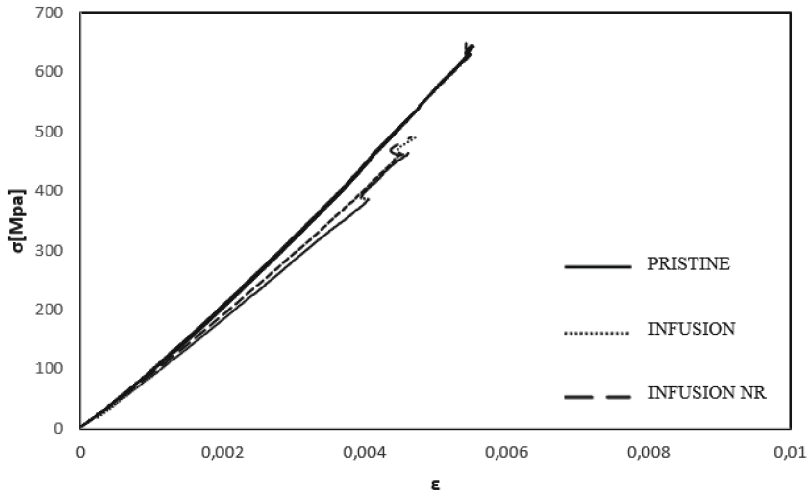


**Fig. 4.** Stress-strain curves relating to the OHT tests on pristine and infusion samples

load occurs for lower values in the infusion specimens compared to the pristine. The pristine specimen shows a higher deformation before breaking.

## 4 Conclusions

The work aims to investigate CFRP structures' behaviour for aeronautical applications repaired by using a hot bonding repair technique with infused cloths.

Ultrasound C-scan analysis conducted before the tests have revealed defects and porosity in the repaired area.

Open hole compression and tension tests were conducted to compare the mechanical behaviour of the repaired and unrepaired material. All the specimens tested showed the failure mode according to the standards, confirming the correct execution of the tests. The OHC results are similar for pristine and infusion samples, while about OHT with the repair there is an ultimate tensile strength lowering, the infusion sample breaks down before.

Even if the results obtained by this study show a tensile mechanical response unreliable about the infusion specimens, the hot bonding repair technique is very innovative, and it can be improved. It can develop the cycle cure under vacuum and the layering process of the repair.

Future tests at low-velocity impact can be conducted to characterize the dynamic behaviour and complete the study of the repair method.

This technique can be compared with other repair techniques used in the aeronautical industry.

## References

1. Bazargan, M.: *Airline Operation and Scheduling*. Ashgate Publishing Limited, Farnham (2010)

2. Papa, I., Ricciardi, M.R., et al.: Comparison between different NDT methods to detect and characterize impact damage on composite laminates. *J. Compos. Mater.* **54**, 617–631 (2020)
3. Cantwell, W.J., Morton, J.: The significance of damage and defects and their detection in composite materials: a review. *J. Strain Anal. Eng. Design* **27**(1), 29–42 (1992)
4. Bruno, M., et al.: A numerical investigation about temperature influence on thermoplastic hot-formed reinforced composites under low-velocity impact. In: ESAFORM 2021 - 24th International Conference on Material Forming, Art. no. 524 (2021)
5. Chowdhury, N., Chiu, W.K., Wang, J., Chang, P.: Finite element studies of thick bolted, bonded and hybrid carbon fibre step lap joints used in aircraft structures (2015, in process)
6. Davies, G.A.O., Zhang, X.: Impact damage prediction in carbon composite structures. *Int. J. Impact Eng* **16**(1), 149–170 (1995)
7. Abrate, S.: Impact on laminated composite materials. *Appl. Mech. Rev.* **44**(4), 155–190 (1991)
8. Prichard, J.C., Hogg, P.J.: The role of impact damage in post-impact compression testing. *Composites* **21**(6), 503–511 (1990)
9. Lopresto, V., Langella, A., Papa, I.: Residual strength evaluation after impact tests in extreme conditions on CFRP laminates. *Procedia Eng.* **167**, 138–142 (2016)
10. Armstrong, K.B., Cole, W., Bevan, G.: Care and Repair of Advanced Composites. SAE International, London (2005)
11. Soutis C, Hu FZ. Design and performance of bonded patch repairs of composite structures. *Proc. Inst. Mech. Eng. Part G: J. Aerosp. Eng.* **211**(4), 263–271 (1997)
12. Camanho, P.P., Lambert, M.: A design methodology for mechanically fastened joints in laminated composite materials. *Compos. Sci. Technol.* **66**(15), 3004–3020 (2006)
13. Camanho, P.P., Matthews, F.L.: A progressive damage model for mechanically fastened joints in composite laminates. *J. Compos. Mater.* **33**(24), 2248–2280 (1999)
14. Wang, C.H., Gunnion, A.J.: Optimum shapes of scarf repairs. *Compos. A Appl. Sci. Manuf.* **40**(9), 1407–1418 (2009)
15. Katnam, K.B., Da Silva, L.F.M., et al.: Bonded repair of composite aircraft structures: a review of scientific challenges and opportunities. *Progr. Aerosp. Sci.* **61**, 27–39 (2013)
16. ASTM Designation: D6484/D6484M – 14: Standard test method for open-hole compressive strength of polymer matrix composite laminates, pp. 1–16 (2014)
17. ASTM Designation: D5766/D5766M-11: Standard test method for open-hole tensile strength of polymer matrix composite laminates, pp. 1–7 (2018)
18. Papa, I., Lopresto, V., Langella, A.: Ultrasonic inspection of composites materials: application to detect impact damage. *Int. J. Lightweight Mater. Manuf.* **4**(1), 37–42 (2021)
19. Busse, G.: Optoacoustic phase angle measurement for probing a metal. *Appl. Phys. Lett.* **35**(10), 759–760 (1979). <https://doi.org/10.1063/1.90960>



# Damage Detection in Bio-Polyamide 11/Woven Basalt Fibres Composite Laminates Subjected to Dynamic Events

Gabriella Epasto<sup>1</sup>(✉), Ilaria Papa<sup>2</sup>, Valentina Lopresto<sup>2</sup>, Libera Vitiello<sup>2</sup>, and Pietro Russo<sup>3</sup>

<sup>1</sup> Department of Engineering, University of Messina, C.da Di Dio, Vill. Sant'Agata, 98166 Messina, Italy

[gabriella.epasto@unime.it](mailto:gabriella.epasto@unime.it)

<sup>2</sup> Department of Chemical, Materials and Production Engineering, University of Naples Federico II, 80125 Naples, Italy

<sup>3</sup> Institute for Polymers, Composites and Biomaterials – National Council of Research, 80078 Pozzuoli, Naples, Italy

**Abstract.** In this research paper, the low velocity impact behaviour was carried out on bio-polyamide 11/woven basalt laminates, produced with two different manufacturing procedures. The impact damage, obtained at  $U = 20J$ , was investigated by ultrasonic phased array techniques in order to propose an application field for such laminate. In addition, failure mechanisms were detected and evaluated to study the start and propagation of impact damage.

**Keywords:** green composites · wettability · impact damage · non-destructive evaluation

## 1 Introduction

Developing bio-based laminates with high mechanical properties and reduced weight is a great challenge which requires consistent research and innovation [1–3]. On the other hand, the thermoplastic matrix-based composites have great potential in a green design procedure, thanks to the possibility of being recycled after their use and their compatibility with basalt fibers, which can be chosen as reinforcement [4].

Among the mineral fibres, basalt ones are attracting significant interest due to good sound insulating properties, good heat resistance (superior to glass), excellent protection from chemical attack and low water absorption properties [5]. Therefore, basalt fibers [6] represent a valid alternative to synthetic ones as reinforcement of composite materials and are currently being investigated by several authors.

This contribution paid special attention to environmentally friendly composite plates based on a bio-polyamide 11 (PA11) and plain weave basalt fibre fabrics, obtained by film stacking and hot pressing. Previous studies [7–9] have demonstrated a rapid increase in viscosity of molten PA11 under isothermal conditions over time, due to post-condensation phenomena. Thus, two different compaction procedures, simply identified

as “fast” and “slow”, were explored by varying the pressure conditions and the duration of the process. In particular, the first one, ensuring a better impregnation of the reinforcement, with a substantially reduced volume of voids, allows significant enhancement in flexural properties and a good reduction in impact damage extension.

Given the strong anisotropic component of composite materials, it is difficult to evaluate the damage mechanisms triggered by impacts to which they are commonly subjected during their use [10]. Usually simulated with low-velocity dynamic impact tests, these events give rise to dissipative mechanisms interacting and, therefore, complex to be evaluated in depth.

In this context, the use of non-destructive inspection techniques (NDT) provides a valuable aid in studying the damage behaviour of composite structures [11, 12]. In particular, the complexity of these aspects, further aggravated for thermoplastic composites due to the plasticity of the matrix, can be overcome by comparing the results obtained with NDTs based on different principles.

This work is focused on the damage of impacted specimens carefully analysed by visual inspections, and phased ultrasonic array. In addition, accurate measurements of the damaged area, as well as of the damage depth, were performed by ultrasonic technique.

## 2 Experimental

### 2.1 Materials and Manufacturing Description

The research considered composite laminates based on Polyamide 11 (PA11, Rilsan® P40 TL,  $\rho = 1.04 \text{ g cm}^{-3}$ , MFI@235 °C/2.16 kg =  $4.06 \pm 0.61 \text{ g/10 min}$ ,  $T_m = 195 \text{ °C}$ ), kindly supplied by Arkema S.A. (Puteaux, France), as matrix. The reinforcement was a plain weave basalt fibre fabric (areal weight:  $210 \text{ g/m}^2$ , nominal thickness: 0.19 mm, yarn count of 10 ends/cm in warp and 9.5 ends/cm in weft) purchased at Incotology GmbH.

85  $\mu\text{m}$ -thick films of PA11 were obtained using a flat die extruder (mod. Teach-Line E20T by Collin GmbH, Ebersberg, Germany) equipped with a calendar (mod. CR72T by Collin GmbH, Ebersberg, Germany). The polymer, preliminarily dried in a vacuum oven at  $T = 70 \text{ °C}$  overnight, was filmed setting a screw speed of 60 rpm and the following temperature profile: 170–210–220–220–200 °C from the hopper to the slit die. Afterwards, the composite laminates were obtained by alternately overlapping, according to a pre-identified sequence, PA11 film and reinforcement layers and then subjecting the assembled system to hot compression with the aid of a lab hydraulic press (mod. P400E by Collin GmbH, Ebersberg, Germany). In detail, twenty layers of basalt fabric were alternated with PA11 films and compacted according to two moulding procedures on the base of rheological considerations reported elsewhere [15].

Specifically, two typologies of laminates were considered by operating at the same temperature but considering as many pressure cycles, designed to limit inevitable structural changes of the polymer melt (increase in viscosity) and identified as “fast” and “slow” by Vitiello et al. [7].



## 2.2 Impact Testing

The experimental characterization of the laminated samples was first examined in terms of surface appearance by wetting and profilometric tests. In this regard, optical contact angle measurements have been conducted by data physics Contact Angle System OCA15E. At the same time, the specimens were observed by visual inspection to investigate the damage, whereas a confocal microscope, Leica DCM3D, was used to measure the indentation depth obtained.

Impact tests were carried out by a falling weight machine, Ceast Fractovis Mk4 [13]. Rectangular specimens, 100x150 mm, cut by a diamond saw from the original panels, were centrally loaded by an instrumented cylindrical impactor with a hemispherical nose, 19.8 mm in diameter. Tests were conducted using an impactor with a mass equal to 3.640 kg placed at specific heights to obtain the selected impact energy  $U = 20J$ . Three measurements for each sample were reported.

## 2.3 Non Destructive Evaluation

Non-destructive evaluation was performed with PAUT. In addition, ultrasonic phased array tests were performed with the Olympus Focus PX 16/128 system, equipped with FocusPC software and a 64 elements linear probe @ 3.5 MHz (3.5 L64-NW1, 64 mm aperture, 1 mm pitch, 7 mm elevation). The wedge SNW1-0-L-IHC and the VersaMOUSE encoder were used for the analyses, which were performed in water.

# 3 Results

## 3.1 Optical Contact Angle and Roughness Surface Data

In Fig. 1 a and b, two examples of contact angle (CA) measurements are reported for the higher and the lower CA detected.

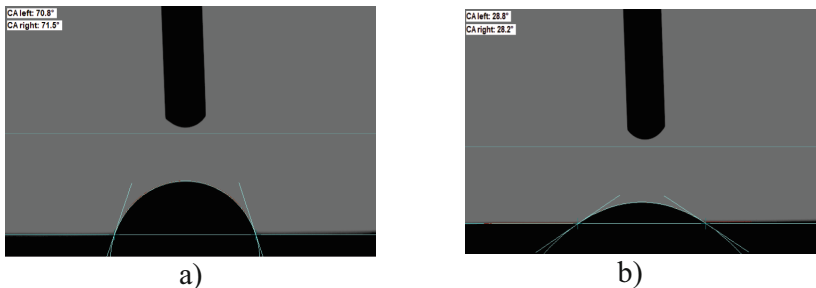


**Fig. 1.** Contact angle measurement

Each sample has been examined twenty times to verify superficial homogeneity of the composite. Figures 2 and 3 summarize the results and evidence the effect of two different manufacturing procedure (slow and fast).

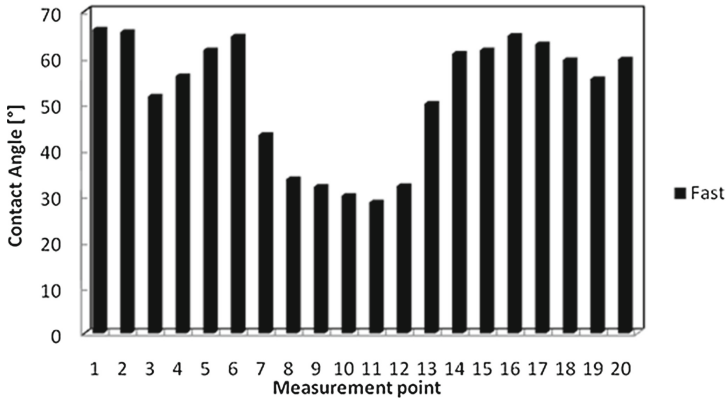


**Fig. 2.** Contact angle measurement fast procedure

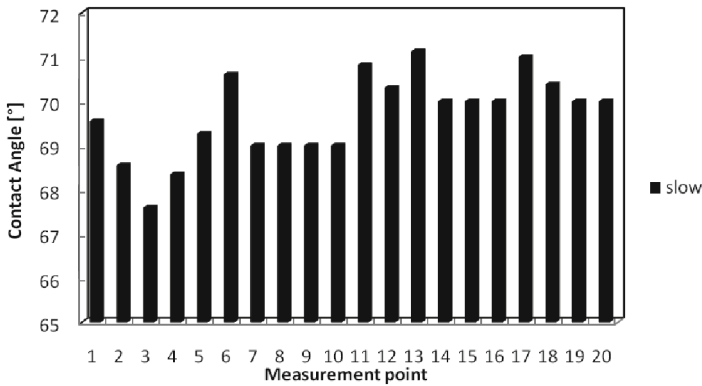


**Fig. 3.** Contact angle measurement slow procedure

Clearly, the investigated laminates show a significant variation of the contact angle, depending on the surface point at which the test is performed. The average value of this parameter is quite different between the “fast” sample and the “slow” one. In particular, the highest average contact angle for the “slow” sample has been found ( $CA = 72^\circ$ ) resulting similar to the neat PA11 CA [14], while the lowest average CA has been detected for the “fast” material ( $CA = 51^\circ$ ). Taking into account that preliminary profilometric measurements did not show significant variations in their surface roughness, the different levels of hydrophilicity found with the contact angle measurements can be attributed to the rheological behaviour of the resin. The process conditions strongly influence this latter aspect and probably determines a different distribution of the matrix on the surfaces examined. [15].

### 3.2 Impact Tests

Starting from considerations already discussed in a previous paper [9], “slow” and “fast” samples have shown the same impact stiffness and a maximum force value of contact ( $F_{\max}$ ) almost identical even if greater displacements have been detected for the “fast” procedure. The indentation test confirms this result carried out at impact energy level  $U = 20\text{J}$  on both “fast” and “slow” samples indicated in Fig. 4, in terms of comparison between the force-displacement curves.

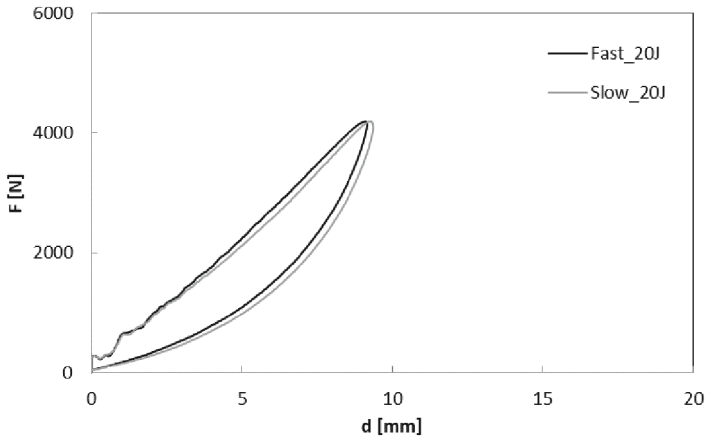


**Fig. 4.** Force displacement curves of indentation tests for three different impact energies.

The effects of the compaction procedure do not show a clear differentiation of the dynamic behaviour of the examined samples characterized by almost overlapping representative force-displacement curves. In other words, laminated samples studied have the same impact performances and absorbed energy as evaluated by the area enclosed in the curves of Fig. 4 (see Fig. 5). Reminding that the absorbed energy is an index of damage to the material, it can be assumed that the reference samples suffer a similar amount of damage for the same impact energy.

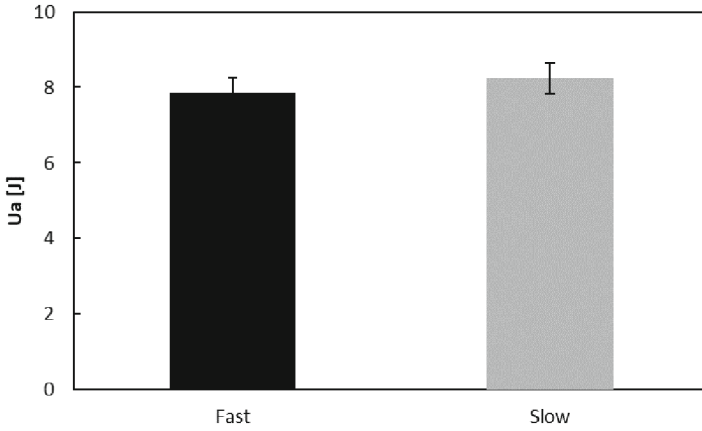


**Fig. 5.** Absorbed energy,  $U_a$ , for slow and fast procedure

To better understand the damage evolution, in Fig. 6, the measure of the footprint (Indentation,  $I$ ) impressed by the impactor on the tested samples was reported for  $U = 20\text{J}$ . The indentation depths are lower for the fast procedure sample, confirming their greater compactness, as reported in [9]. Given the similar values of absorbed energy with the same impact energy, the difference in indentation depth detected between the samples examined can be attributed to the different contributions of the dissipative phenomena triggered by the impact, as confirmed by the non-destructive tests in the next paragraph.

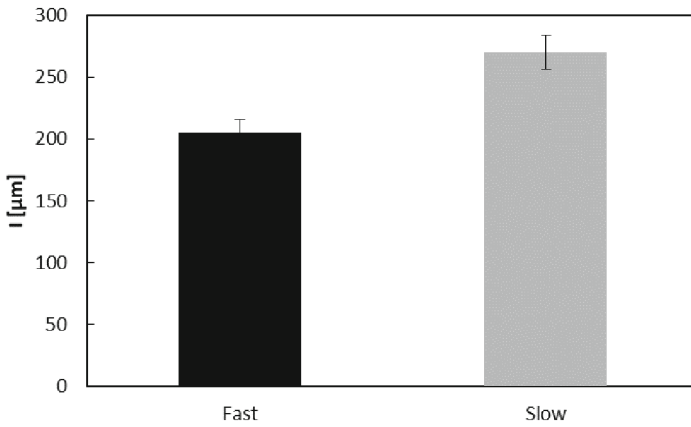


**Fig. 6.** Indentation depth,  $I$ , for slow and fast procedure

### 3.3 Non-destructive Evaluation

In Fig. 7 the C-scans of the gated signal in amplitude are reported. The results allow the measurements of the damage extension and the colour depending on the colour palette selected. The “fast” specimens experienced higher damage than “slow” ones at the same energy level (Fig. 8).

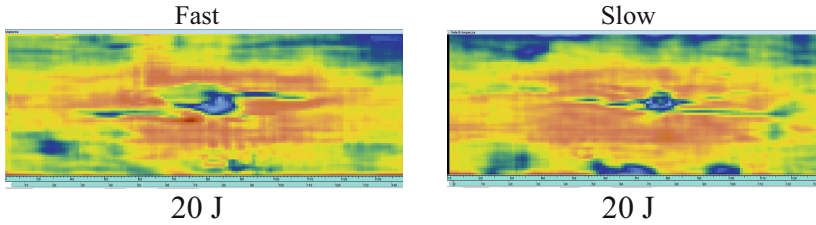


**Fig. 7.** C-scans of the impacted specimens' front wall gated signal (in amplitude).

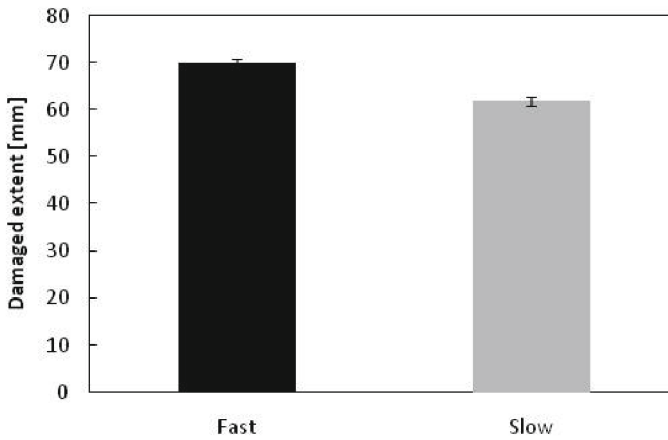


**Fig. 8.** Linear damage extent for both tested samples calculated by phased array UT

C-scans of the amplitude gated signal can provide other considerations, referred to the sound path between front and back walls.

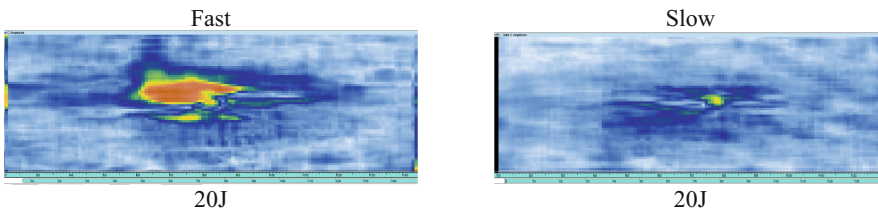


**Fig. 9.** C-scans of the impacted specimens gated sound path (in amplitude).

The barely visible impact damage cannot be detected by visual inspection, while PAUT allowed the assessment of the extent of the delaminated area (Fig. 9). By the results, “fast” specimens exhibited a larger amount of damaged area and higher sensitivity to such a kind of damage mechanism.

The B-scans can detect through-thickness damage mechanisms in the area below the contact between the impactor and the specimen (Fig. 10). At 20 J, primary bending cracks were evaluated, which cause fiber breakage, debonding and delamination. However, interlaminar cracks were detected.

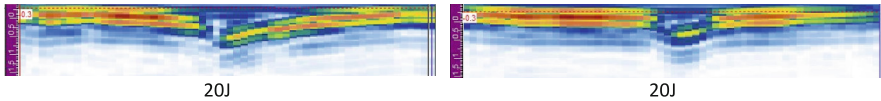


**Fig. 10.** B-scans of the impacted specimens a) “fast”; b) “slow”

## 4 Conclusions

The analysed specimens show interesting impact properties if compared to some categories of natural, synthetic and hybrid fibers laminates. Although the samples obtained by means of the two used procedures show a similar impact behaviour, the analysis of the damage evaluated using the ultrasound technique shows that the “Fast” specimens exhibited a larger amount of damaged area and higher sensitivity to such a kind of damage mechanism. To better evaluate the different damage mechanisms and try to improve the performance of the biocomposite, the comparative use of other non-destructive techniques could be useful to assess the improvement strategy to be applied.

**Acknowledgements.** The authors sincerely thank Prof. Annalisa Acquesta for the contact angle evaluation on the tested samples.

## References

1. Russo, P., Simeoli, G., Vitiello, L., Filippone, G.: Bio-Polyamide 11 hybrid composites reinforced with basalt/flax interwoven fibers: a tough green composite for semi-structural applications. *Fibers* **7**, 41 (2019). <https://doi.org/10.3390/fib7050041>
2. Bazan, Patrycja, Nosal, Przemysław, Wierzbicka-Miernik, Anna, Kuciel, Stanisław: A novel hybrid composites based on biopolyamide 10.10 with basalt/aramid fibers: mechanical and thermal investigation. *Compos. Part B: Eng.* **223**, 109125 (2021). <https://doi.org/10.1016/j.compositesb.2021.109125>
3. Akampumuza, O., Wambua, P.M., Ahmed, A., Li, W., Qin, X.-H.: Review of the applications of biocomposites in the automotive industry. *Polym. Compos.* **38**, 2553–2569 (2017). <https://doi.org/10.1002/pc.23847>
4. Boccardi, S., Boffa, N., Carlomagno, G.M., Del Core, G., Meola, C., Monaco, E., et al.: Lock-in thermography and ultrasonic testing of impacted basalt fibers reinforced thermoplastic matrix composites. *Appl Sci* **9**, 3025 (2019). <https://doi.org/10.3390/app9153025>

5. Russo, P., Simeoli, G., Cimino, F., Papa, I., Ricciardi, M.R., Lopresto, V.: Impact damage behavior of vinyl ester-, epoxy-, and nylon 6-based basalt fiber composites. *J. Mater. Eng. Perform.* **28**(6), 3256–3266 (2019). <https://doi.org/10.1007/s11665-019-04037-8>
6. Thorhallsson, E.R., Snaebjornsson, J.T.: Basalt fibers as new material for reinforcement and confinement of concrete. *Solid State Phenom.* **249**, 79–84 (2016)
7. Vitiello, L., Russo, P., Papa, I., Lopresto, V., Mocerino, D., Filippone, G.: Flexural properties and low-velocity impact behavior of polyamide 11/basalt fiber fabric laminates. *Polymers (Basel)* **13**, 1055 (2021). <https://doi.org/10.3390/polym13071055>
8. Militello, C., Bongiorno, F., Epasto, G., Zuccarello, B.: Low-velocity impact behaviour of green epoxy biocomposite laminates reinforced by sisal fibers. *Compos. Struct.* **253**, 112744 (2020). <https://doi.org/10.1016/j.compstruct.2020.112744>
9. Vitiello, L., Papa, I., Lopresto, V., Mocerino, D., Filippone, G., Russo, P.: Manufacturing of bio-polyamide 11/basalt thermoplastic laminates by hot compaction: the key-role of matrix rheology. *J. Thermoplast. Compos. Mater.* 089270572110702 (2022). <https://doi.org/10.1177/08927057211070232>
10. Muneer, A.M., Dhakal, H.N., Zhang, Z.Y., Barouni, A., Zahari, R.: Enhancement of impact toughness and damage behaviour of natural fibre reinforced composites and their hybrids through novel improvement techniques: a critical review. *Compos. Struct.* **259**, 113496 (2021). <https://doi.org/10.1016/j.compstruct.2020.113496>
11. Fischer, B., Sarasini, F., Tirillò, J., Lopresto, V., Ecault, R.: Impact damage assessment in bio-composites by micro-CT and innovative air-coupled detection of laser-generated ultrasound. *Compos. Struct.* **210**, 922–931 (2019)
12. Militello, C., Epasto, G., Bongiorno, F., Zuccarello, B.: First lamina hybridization of high performance CFRP with Kevlar fibers: effect on impact behavior and nondestructive evaluation. *Mech. Adv. Mater. Struct.* 1–16 (2022). <https://doi.org/10.1080/15376494.2022.2029639>
13. Papa, I., El Hassanin, A., Langella, T., Lopresto, V.: Experimental and analytical model for the penetration and indentation prediction on BFRP laminates under low velocity impacts. *J. Compos. Mater.* **55**, 1331–1338 (2021). <https://doi.org/10.1177/0021998320969790>
14. Rashmi, B.J., Loux, C., Prashantha, K.: Bio-based thermoplastic polyurethane and polyamide 11 bioalloys with excellent shape memory behavior. *J. Appl. Polym. Sci.* **134** (2017). <https://doi.org/10.1002/app.44794>
15. Lau, K., Hung, P., Zhu, M.-H., Hui, D.: Properties of natural fibre composites for structural engineering applications. *Compos. Part B Eng.* **136**, 222–233 (2018). <https://doi.org/10.1016/j.compositesb.2017.10.038>



# Approaching the Influence of Marine Environment Degradation on Impacted Carbon Fiber/Vinyl Ester Laminate with Electronic Speckle Pattern Interferometry Investigation

Papa Ilaria<sup>1</sup>, Lopresto Valentina<sup>1</sup>, Russo Pietro<sup>2</sup>, and Pagliarulo Vito<sup>3</sup>(✉)

<sup>1</sup> Department of Chemical, Materials and Production Engineering, University of Naples Federico II, Piazzale V. Tecchio 80, 80125 Napoli, Italy

<sup>2</sup> CNR National Research Council, IPCB Institute for Polymers, Composites and Biomaterials, Via Campi Flegrei 34, 80078 Pozzuoli, NA, Italy

<sup>3</sup> CNR National Research Council, ISASI, Institute of Applied Sciences and Intelligent Systems, Via Campi Flegrei 34, 80078 Pozzuoli, NA, Italy  
vito.pagliarulo@isasi.cnr.it

**Abstract.** This work considered the influence of water absorption aging on the impact damage of wet carbon fiber/vinyl ester laminate. In detail, low-velocity impact tests were systematically performed before and after conditioning the composite in dry and water-saturated states in a saline environment at 3%, respectively. In addition, Electronic Speckle Pattern Interferometry analyzed the damage of the impacted specimens, and the results were compared to the absorbed energy according to three impact energy levels: 10J, 20J, and 30J.

**Keywords:** ESPI · Low-velocity impact · Vinyl ester resin · Seawater ageing

## 1 Introduction

Composite materials' high mechanical performance and specific properties make them an attractive solution for structural parts in numerous industrial applications [1–3]. Over the last decades, their unconventional properties have meant a growing diffusion of composite materials in the aerospace, naval sector, and more, including parts of the primary structures, requiring satisfying stringent requirements [4]. On the other hand, their control and monitoring, to guarantee the structure's safety, often represent a challenge to the application of traditional control techniques due to the intrinsic complex nature of composites. In addition, since the failure happens quickly and abruptly, the monitoring plan has to be done frequently. Non-destructive techniques (NDT) are ideal for this purpose because they can be conducted on-site without disassembling the structure and increasing the number of inspections. Hence, the development of innovative NDT is becoming more consistent to ensure a quick, effective and efficient control check without giving up safety factors.



In particular, a damaging event can produce more severe damage if the component itself has been exposed to an aggressive environment for a longer operating time [5–8]. In this context, a critical aspect of fundamental importance is the sensitivity of composites to water which can significantly limit their use given prolonged exposure in humid environments, especially for those intended for application in the naval sector [9, 10]. Several studies have discussed the polymeric composite's resistance in various environmental conditions [6, 11, 12], but very few researches show the influence of moisture absorption on low-velocity damage [13–18].

Establishing the correlation between the damage and the deterioration state would mean having greater control over the lifetime with more confidence. So, suppose we can boost the number of inspections by NDT at the same time. In that case, we extend the components' life by preventing their early replacement at the expense of the same exposure to environmental conditions for a more extended period [19, 20].

This work intends to expand the literature by carrying out a non-destructive technique study on the effect of moisture absorption on a low-velocity impact event on laminates. Although glass-fibre composites are widely used in the naval sector, they degrade in the presence of water. Considering these drawbacks, the interest has recently been directed towards carbon fiber composites. In this case, the vinyl ester resin represents an attractive solution to be used as a matrix since the ester groups are less susceptible to water degradation by hydrolysis. In addition, this resin has good abrasion resistance and can guarantee higher values of toughness and elongation at break than other resins used in the reference application field. So, the degradative effect induced by exposure in seawater of vinyl ester-based composites reinforced with carbon fibers was considered according to the subsequent impact test. In detail, dry and water-saturated specimens impacted with three energy levels (10J, 20J and 30J) were investigated with speckle interferometry (ESPI) technique. Results will be compared to the absorbed energy to relate the consequent effect of water absorption in the laminates with its influence on the impact damage.

## 2 Experimental

### 2.1 A Materials and Manufacturing Description

The composite laminates are composed of the T700 carbon fiber fabric with a plain weave architecture 0–90, supplied by Toray Inc. (Tokyo, Japan) as the reinforcement, and a vinyl ester resin provided by Ashland (Kentucky, USA), under the trade name Derakane 510 A-40 (VE510A) as the matrix. Table 1 and Table 2 report the specifications of the two components.

Each laminate was obtained by vacuum-assisted resin transfer moulding (VARTM) at room temperature. The vinyl ester resin was formulated with 1.0 phr of methyl ethyl ketone peroxide (MEKP) as a catalyst and 0.20 phr of cobalt naphthenate (CoNap) promoter to obtain 50–60 min gel time. The cure and post-cure conditions for the resin lasted for 24 h at room temperature and 2 h at 120 °C, respectively. At the end of the manufacturing process, laminates were featured with a fiber volume content of 55.6%, per the ASTM D3171 Standard, and a void content approximately equal to 1.3 vol%.

The thickness of the composite laminates was equal to 3 mm with a lay-up sequence [(0/90)6]<sub>S</sub>, and a surface area of 150 × 100 mm<sup>2</sup>.

**Table 1.** Manufacturer specification of T700 carbon fiber.

Areal weight [g/m <sup>3</sup> ]	Density [g/cm <sup>3</sup> ]	Tensile Strength [MPa]	Elastic Modulus [GPa]	Strain to failure [%]
300	1.8	4900	230	2.1

**Table 2.** Manufacturer specification of Derakane 510 A-40 (VE510A) resin.

Density [g/cm <sup>3</sup> ]	Dynamic viscosity [MPa * s]	Tensile Strength [MPa]	Tensile Modulus [GPa]	Flexural Strength [MPa]	Flexural Modulus [GPa]	Styrene content [%]
1.23	400	86	3.40	150	3.6	38

## 2.2 Water Absorption Ageing

Laminates were dried in a vacuum oven at 70 °C overnight to prepare the specimens for the absorption test. Then, the immersion of pre-dried specimens was prolonged until their saturation, according to the following procedure. Finally, three dried samples were immersed for 30 days in an aqueous solution containing 3% by weight of NaCl (common cooking salt) to simulate seawater exposure. The state of the specimens at the beginning and the end of the conditioning in water, i.e. “dry” and “wet” respectively, were established by the weight constancy between two successive weightings. Precisely, the saturation of the specimens corresponded to the absorption of a quantity of water equal to about 0.7% by weight.

## 2.3 Mechanical Testing

Mechanical tests were carried out within 48 h of pre-drying and after the saturation in salty water for dry and wet samples, respectively. In previous work [21], the reproducibility of the results was verified based on at least five measurements and quasi-static tests were conducted to monitor the quality of the structural composite. In detail, inter-laminar shear strength (ILSS) and three-point flexural tests were carried out according to ASTM D2344 and ASTM D790 standards, respectively, on specimens cut from the laminates by means of a diamond saw.

To reproduce damage with an out-of-plane component, low-velocity impact tests were performed using a Ceast Fractovis instrumented drop-weight machine, centrally loaded by a cylindrical impactor with a hemispherical head of 19.8 mm diameter and a mass of 3.6 kg. Both dry and wet laminates (150 × 100 mm<sup>2</sup>) were impacted with three

different impact energies ( $U$ ) levels: 10 J, 20 J and 30 J. The energy levels were chosen according to the full penetration curve (load versus deflection), indicating the damage evolution up to the complete failure. Considering the curve (Fig. 1), it is possible to identify some characteristic values (changes in slope or small load drops as indicated by red arrow) corresponding to different damage phenomena, i.e. the initiations of delaminations, fiber debonding and breaking and matrix failure up to the catastrophic collapse of the material. In detail, the energy levels correspond approximately to 25%, 50% and 75% of the maximum absorbed energy and they were set by varying the height of the drop-weight.



**Fig. 1.** Generic load-displacement curve

The impactor was instrumented to draw the whole load-deflection curves, providing useful information about the impact response briefly discussed in the following section based on previous analysis.

#### 2.4 Electronic Speckle Pattern Interferometry

This work used the ESPI non-destructive system to identify the impact damage through a green laser source (532 nm) on dry and wet specimens after the mechanical tests. The holographic technique is based on a coherent light source's scattering phenomena to analyze the out-of-plane displacements, e.g. deformations or vibrations of the detected specimen's surface. With this methodology, it is possible to detect any defects in the material, such as welding defects, inhomogeneity or void gaps, as long as the displacement is comparable with the laser wavelength. However, any defect is an obstacle to the internal stress path induced by an external perturbation (thermal, mechanical, etc.), interrupting it and provoking a discontinuity in the fringe pattern [22–24].

The ESPI equipment must be installed on an optical table to isolate the entire system (equipment and specimen) from the surrounding environment's vibration. The entire setup is described in previous work [20]. In short, the laser source generates a reference beam (RB) light and object one (OB), which is reflected by the investigated surface. Then, the light waves of the RB and the reflected OB are coupled into a CMOS camera using an optical fiber. Next, they are processed into a speckle pattern by an image-processing

computer due to the mathematical calculations based on interferometric phenomena. Finally, the intensity of the unperturbed speckle pattern is recorded with the intensity  $I_1$ , mathematically expressed as follows:

$$I_1 = I_0 + I_r + 2\sqrt{I_0 I_r} \cos[\vec{f}_0](\theta) \quad (1)$$

where  $I_0$  is the light intensity scattered from the object,  $I_r$  is the reference beam's light intensity, and  $\theta$  is the phase angle.

Then, an external thermal perturbation produces stress on the specimen, and the deformation of the sample surface brings a new speckle pattern. Thus, the reflected wavefront is slightly modified and recorded with a new perturbed speckle pattern intensity  $I_2$ :

$$I_2 = I_0 + I_r + 2\sqrt{I_0 I_r} \cos[\vec{f}_0](\theta + \phi) \quad (2)$$

where  $\phi$  is the angle is related to the displacement, i.e. the deformation.

Comparing the recorded undisturbed and disturbed speckle patterns leads to a correlation between fringe pattern time by time. Analytically, the subtraction of the fringe patterns is governed by the following equation:

$$I_{(1-2)} = 2\sqrt{I_0 I_r} [\cos[\vec{f}_0](\theta) - \cos(\theta + \phi)] \quad (3)$$

The computer-aided subtraction of the deformed and the non-deformed patterns represents the out-of-plane displacement, i.e. the deformation that travels along with the sample. Any discontinuity in the fringe pattern can identify a discontinuity in the investigated material. Then, the correlation fringe pattern can be processed for contrast enhancement and noise removal, so the final phase-contrast map can be used to measure the displacement field with high accuracy.

### 3 Results

In previous work [18, 25], dry and wet samples' mechanical performance was tested to assess the phenomena that influence most of the flexural and impact properties. Moreover, consideration of the damage growth showed a preferential direction of the propagation in the laminate. Figure 2 shows the front and rear side images of dry and wet specimens after low-velocity impact tests at 20J.

For the sake of brevity, the discussion is focused only on the specimens impacted at this energy level, and these results will be taken as a reference in subsequent analyzes. No helpful information can be detected by visual inspection of the visible damage. However, it seems possible to note a larger damage extension for the wet samples.

This consideration is in accordance with a reduction of the average flexural strength values of about 12.5% attributed to plasticization phenomena caused by the absorbed water as reported in [25]. In addition, an increase in the flexural stiffness of the saturated specimens was found compared to the dry ones, determined by swelling phenomena. Even if the naked eye inspection is complex due to the opaque material, it is possible to notice an increase of the damage extension on the surface in the case of the wet sample (see the circled zones) and any evident damage on the rear side.

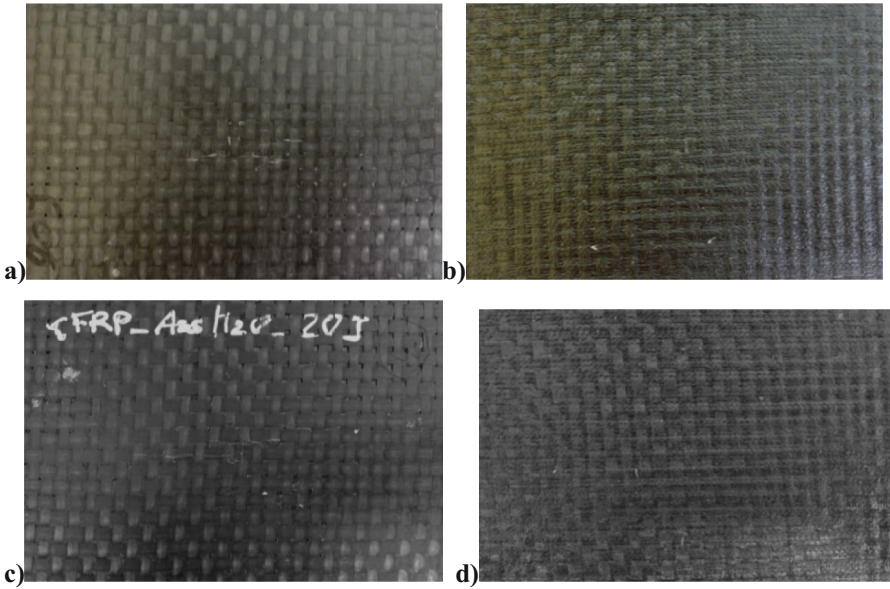


**Fig. 2.** Specimen subjected at impact at  $U = 20\text{J}$  (a) front dry sample (b) backside sample (c) wet front sample and (d) wet back sample.

In order to quantify the damage, Fig. 3 shows indentation depth,  $I$ , the footprint impressed by the impactor on the impacted side, correlated to the impact energy,  $U$ .

As expected, the indentation depth increases as the impact energy increase for dry and water wet systems indicating a non-significant effect of water absorption on the plastic deformation.

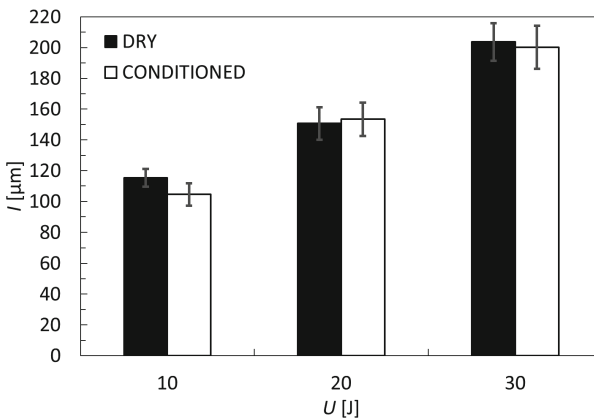


**Fig. 3.** Indentation depth,  $I$ , comparison between dry and wet samples ( $U = 10\text{J}, 20\text{J}, 30\text{J}$ )

So, further analyses were carried out by means of non-destructive testing showing a significant increase in in-plane damage extension rather than along the thickness of the specimens. These results were taken into account to pursue the additional investigation with the ESPI approach in order to calculate the delaminated area without any backscattering effect as for the ultrasonic non-destructive testing. In fact, with the ESPI technique, it is possible to evaluate in one shot the influence of the global damage extended both in-plane and in-depth.

Each specimen was clamped to avoid excessive perturbation, and for the same reason, the system was placed on an isolated table with the ESPI equipment. It was used as a thermal source to generate the external perturbation, and a correlation fringe pattern was recorded. In Fig. 4 are reported the ESPI acquisitions of the correlation fringe pattern for dry and wet specimens impacted at 30J. In addition, the respective unwrapped phase map was elaborated in order to highlight the impact damage (see right side in Fig. 4). The damaged area has a singular geometry characteristic of impacted laminates [26] identified by a circular impactor footprint and lateral longitudinal delamination.

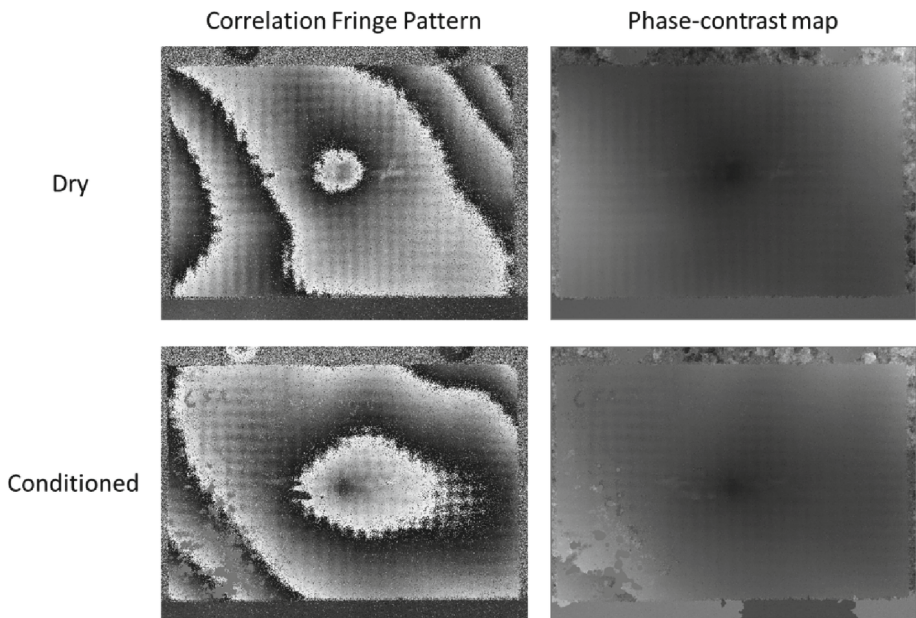


**Fig. 4.** ESPI images of dry and wet vinyl-ester laminates (front sides) after low-velocity impact test at an energy level equal to 30 J.

Figure 5 shows the damaged areas. The measurements were obtained by investigating both the impacted side and back.

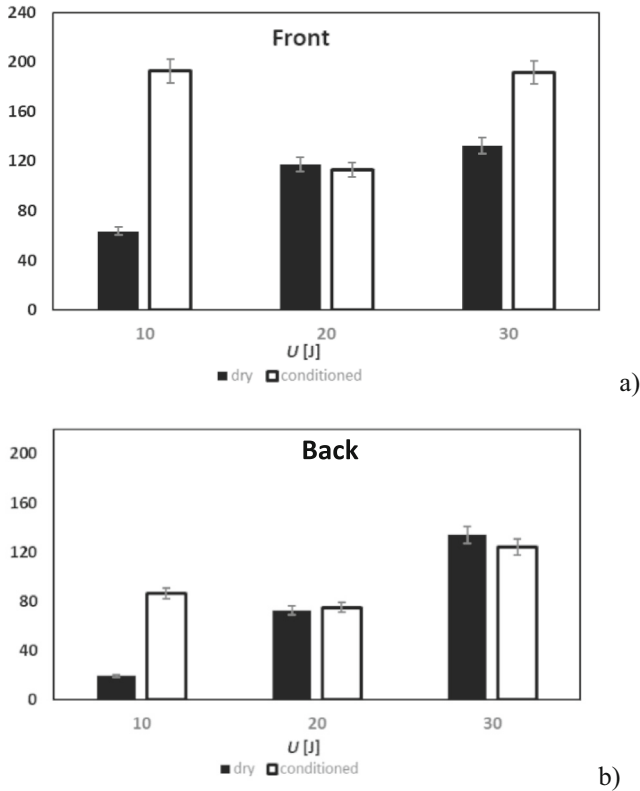


**Fig. 5.** Damaged areas for both the impacted side and back

There is an increase in the damaged area for the wet samples (except for the back 30J case) from the acquisitions, especially at low energy. This confirms the effect of conditioning in water, demonstrating the sensitivity, albeit minimal, to the period spent in an aggressive environment. In addition, the effect of water has weakened the interface bond between fiber and matrix, making the composite more sensitive to delamination.

## 4 Conclusions

The influence of water absorption ageing on the impact damage of wet carbon fiber/vinyl ester laminate was investigated by means of speckle interferometry. The results show that the effect of the process is detectable in terms of the damaged area. The trend is that the water absorption degrades the samples, and consequently, the damaged area increases.

**Acknowledgements.** The authors sincerely thank Eng. Giulia Leone and Eng. Gennaro D'Angelo for the scientific contribution in the elaboration of the ESPI images and Prof. Formisano Antonio for contributing to the material's saturation phase.

## References

1. Menail, Y., El Mahi, A., Assarar, M., Redjel, B., Kondrats, A.: The effects of water aging on the mechanical properties of glass-fiber and Kevlar-fiber epoxy composite materials. *Mechanika* **76**, 28-32A (2009)
2. Behera, A., Dehury, J., Thaware, M.M.: A comparative study on laminated and randomly oriented Luffa-Kevlar reinforced hybrid composites. *J. Nat. Fibers* **16**, 237–244 (2019)
3. Behera, A., Thaware, M.M., Ballal, A.: Effect of matrix crack generation on fatigue life of CFRP multidirectional laminates. *Mater. Today Proc.* **5**, 20078–20084 (2018)
4. Mouritz, A.P., Gellert, E., Burchill, P., Challis, K.: Review of advanced composite structure for naval ships and submarines. *J. Comp. Struct.* **53**, 21–41 (2001)
5. Williams, C.: Effect of Water absorption on the room temperature properties of carbon fiber and glass fiber reinforced polymer composites, DTRC-SME, December 1998
6. Sala, G.: Composite degradation due to fluid absorption. *J. Compos.* **31**, 357–373 (2000)
7. Bao, L.R., Yee, A.F.: Effect of temperature on moisture absorption in a bismaleimide resin and its carbon fiber composites. *J. Polym. Sci.* **43**, 3987–4399 (2002)
8. Nakamura, T., Singh, R.P., Vaddadi, P.: Effects of environmental degradation on flexural failure strength of fiber reinforced composites. *J. Exp. Mech.* **46**(2), 257–268 (2006). <https://doi.org/10.1007/s11340-006-6067-7>
9. Kumar, B.G., Sing, R.P., Nakamura, T.: Degradation of carbon fiber reinforced epoxy composite by ultraviolet radiation and condensation. *J. Compos. Mater.* **36**, 2713–2733 (2002)
10. Caprino, G., Lopresto, V.: The significance of indentation in the inspection of carbon fibre-reinforced plastic panels damaged by low-velocity impact. *Compos. Sci. Technol.* **60**, 1003–1012 (2000)
11. Shivakumar, K.N., Swaminathan, G., Sharpe, M.: Carbon/vinyl ester composites for enhanced performance in marine applications. *J. Reinf. Plast. Compos.* **25**, 1101 (2006)
12. Gellert, E.P., Turely, D.M.: Seawater immersion of ageing glass fiber reinforced polymer laminates for marine applications. *J. Compos. A* **30**, 1259–1265 (1999)
13. Lopresto, V., Langella, A., Papa, I.: Interaction of water with carbon fiber reinforced polymer laminates under dynamic loading conditions. *J. Mater. Eng. Perform.* **28**(6), 3220–3227 (2019). <https://doi.org/10.1007/s11665-019-03915-5>
14. Papa, I., Formisano, A., Lopresto, V., Cimino, F., Vitiello, L., Russo, P.: Water ageing effects on the mechanical properties of flax fibre fabric/polypropylene composite laminates. *J. Compos. Mater.* **54**(24), 3481–3489 (2020). <https://doi.org/10.1177/0021998320916546>
15. Berketis, K., Tzetzis, D.: Long-term water immersion ageing characteristics of GFRP composites. *J. Mater. Sci.* **44**(13), 3578–3588 (2009). <https://doi.org/10.1007/s10853-009-3485-9>
16. Lopresto, V., Langella, A., Papa, I.: Dynamic load on composite laminates in the presence of water. *Polym. Eng. Sci.* **57**(6), 613–620 (2017)
17. Garcia, R., Castellanos, A.G., Prabhacar, P.: Influence of Arctic seawater exposure on the flexural behavior of woven carbon/vinyl ester composites. *J. Sandwich Struct. Mater.* **21**(3), 1190–1208 (2017)
18. Dale, M., Acha, B.A., Carlsson, L.A.: Low velocity impact and compression after impact characterization of woven carbon/vinylester at dry and water saturated conditions. *Comp. Struct.* **94**, 1582–1589 (2012)



19. Kootsookos, A., Mouritz, A.P.: Seawater durability of glass and carbon polymer composites. *J. Comp. Sci. Tech.* **64**, 1503–1511 (2004)
20. Byars, E.A., Waldron, P., Dejke, V., Demis, S., Heddadin, S.: Durability of FRP in concrete - deterioration mechanisms. *Int. J. Mater. Prod. Technol.* **19**(1–2), 28–39 (2003)
21. Fischer, B., Sarasini, F., Tirillò, J., Papa, I., Lopresto, V., Ecault, R.: Impact damage assessment in biocomposites by micro-CT and innovative air-coupled detection of laser-generated ultrasound. *Compos. Struct.* **210**, 922–931 (2019). <https://doi.org/10.1016/j.compstruct.2018.12.013>
22. Russo, P., Pagliarulo, V., Bianco, V., Simeoli, G., Cimmino, F., Ferraro, P.: Characterization of ‘green’ composite laminates after flexural tests by speckle interferometry. *Opt. Eng.* **59**(10), 102416 (2020)
23. Pagliarulo, V., Russo, P., Leone, G., D’Angelo, G.A., Ferraro, P.: A multimodal optical approach for investigating 3D-printed carbon PEEK composites. *Opt. Lasers Eng.* **151**, 1068882022 (2022)
24. Gagliardi, F., et al.: Joining of thermoplastic structures by friction riveting: a mechanical and a microstructural investigation on pure and glass reinforced polyamide sheets. *Compos. Struct.* **204**, 268–275 (2018)
25. Papa, I., Formisano, A., Lopresto, V., Russo, P.: Mechanical degradation of carbon fiber/vinyl ester samples subject to marine environments. *J. Comp. Mat.* **55**, 2967–2974 (2021). <https://doi.org/10.1177/00219983211005006>
26. Donadio, F., et al.: Response of glass/carbon hybrid composites subjected to repeated low velocity impacts. *J. Comp. Mater.* **55**, 2789–2802 (2022)



# Speckle Interferometry Applied to the Detection of Defects in Stiffened Panel

Russo Pietro<sup>1</sup>, Ricci Fabrizio<sup>2</sup>, Monaco Ernesto<sup>2</sup>, Laurino Gianfranco<sup>2</sup>, Paturzo Melania<sup>3</sup>, D.'Angelo Gennaro<sup>3</sup>, and Pagliarulo Vito<sup>3</sup>(✉)

<sup>1</sup> CNR National Research Council, IPCB Institute for Polymers, Composites and Biomaterials, Via Campi Flegrei 34, 80078 Pozzuoli, NA, Italy

<sup>2</sup> Department of Industrial Engineering, University of Naples Federico II, Piazzale V. Tecchio 80, 80125 Napoli, Italy

<sup>3</sup> CNR National Research Council, ISASI, Institute of Applied Sciences and Intelligent Systems, Via Campi Flegrei 34, 80078 Pozzuoli, NA, Italy  
vito.pagliarulo@isasi.cnr.it

**Abstract.** In accordance with the Damage Tolerance (DT) approach, the structural components of the aircraft must be periodically maintained to improve the durability of airframes. This approach is applied to anticipated loads in the presence of fatigue, corrosion, or accidental damage until detection via inspections. To prevent the catastrophic growth of the damage, it is necessary to proceed with the replacement or repair of the piece itself. Due to the complex damage growth in composites, the DT approach is not as well-established as on metals. Furthermore, in the presence of a crack, its propagation is rapid and the scheduled inspections do not always cover the time from the crack creation to a critical damage size that is dangerous for the structural safety of the aircraft. In this work, it is proposed a non-destructive interferometric investigation technique to identify artificial defects in load-bearing structural parts in non-contact mode. Results have shown that the speckle technique was able to identify the Kapton sheet and other geometrical discontinuities in the structure.

**Keywords:** NDT · Stiffened Wing Panel · Composite · Automated Fiber Placement · ESPI

## 1 Introduction

Nowadays composites are widely used in aerospace and automotive to design high performance and lighter weight components, on the other hand they suffer of different problems due to their nature that require attention in the design and manufacture. In fact composite materials are susceptible to the formation of internal defects named Barely Visible Damages (BVID) which can reduce their performance in terms of rigidity, resistance and fatigue life. An important aspect is their vulnerability to low velocity impact events. The integrity of composite structural components can severely be reduced after an impact even if the visual damage is not so evident. This is mostly due to the non-homogeneous and anisotropic nature of the composite material, failing in a wide variety of damage modes like indentations, inter-laminar fractures caused by inter-laminar

stresses, fibers cracks and matrix cracks. It is very interesting the understanding of the damage initiation and propagation and the complex interaction between failure modes. Many efforts were already done [1, 2] to investigate the influence of the large number of parameters involved in dynamic phenomena on the different modes of impact failure.

It follows that, all structural components are inspected at regular intervals using a variety of complicated and costly Non-Destructive Techniques. In this work, it is proposed an interferometric investigation technique to identify defects in load-bearing structural parts without the use of coupling agent needed for UT [3, 4]. By the means of the Electronic Speckle Pattern Interferometry (ESPI) technique, it was possible to detect the presence of an artificial debonding in a stiffened wing panel. A Kapton foil was positioned between the stringer and the wing sheet made both in carbo-fibre epoxy-based matrix composite material by Automated Fibre Placement (AFP). Results have shown that the ESPI technique was able to identify the Kapton sheet and other geometrical discontinuities in the structure with high accuracy.

## 2 Experimental

### 2.1 A Materials and Manufacturing Description

In order to reproduce an artificial discontinuity between a primary thin-wall structure and its stiffener, a mono stringer panel was obtained by co-infusion manufacturing process in presence of an artificial disbonding. UD dry Tenax IMS65 E23 24K carbon fibers were placed by automated fibre placement (AFP) process and impregnated with resin liquid infusion (RLI) method in Cytec PRISM EP2400 epoxy resin. The skin of the stiffened panel was made of 14 plies with a layers sequence [45/-45/0/90/-45/45]<sub>S</sub>, measuring 950 mm in length and 480 mm in width. While, the T-shaped stringer was made of 10 plies with a layers sequence [90/0/0/-45/45]<sub>S</sub>, having a size of 450x170 mm. In order to allow the same thickness for the web and the foot of the stringer, a cap was placed with a layers sequence [90/0/0/-45/45] to create a symmetrical laminate with the stringer foot flanges, made of 5 plies each. Between the stringer foot and the cap interface, it was introduced the artificial disbonding simulated by the use of a folded Kapton foil measuring 70x50 mm and placed along the longitudinal axis of the stringer. The specimen is shown in Fig. 1.

The main advantages of the AFP technique are the repeatability and reliability of the process and the possibility to manufacture components with complex shapes.

### 2.2 Speckle Interferometry

ESPI non-destructive system was used to identify the artificial disbonding by means of a green laser source (532 nm). The holographic technique is based on the scattering of a coherent light source in order to analyse the out-of-plane displacements, deformations or vibrations of the detected specimen's surface. Any defect in the material, such as welding defects, inhomogeneity or void gaps, acts as an obstacle to the internal stress path interrupting it and provoking a discontinuity in the deformation recorded as a fringe pattern. Unlike the external stresses (thermal, mechanical, etc.) to which the material

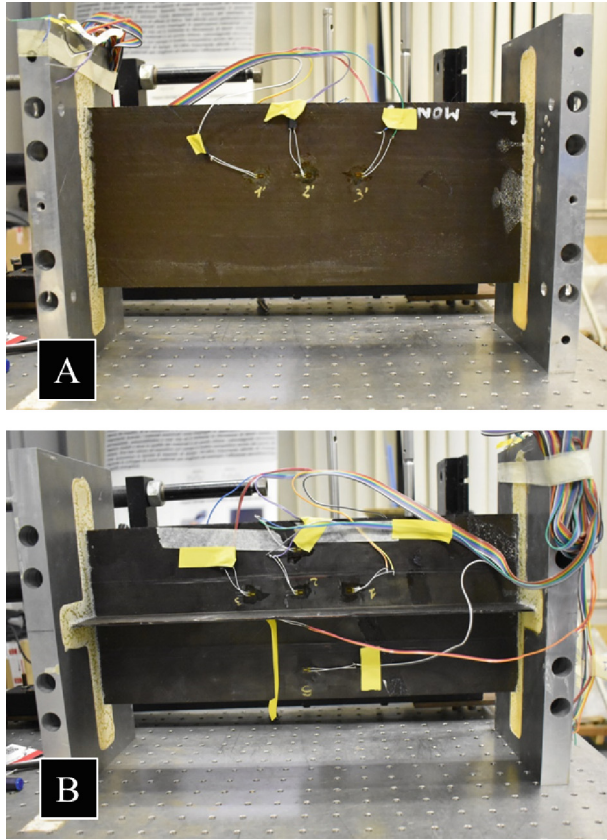


**Fig. 1.** (A) Front side and (B) back side of the stiffened wing panel.

is subjected, discontinuities or particular geometric pattern in the design of the fringes may occur. The ESPI equipment is installed on an optical table which works as an environmental vibration-isolation system and the entire set-up is described in previous work [5]. The coherent laser source generates a reference beam (RB) light and object one (OB), which is reflected by the investigated surface. The light waves of the RB and the reflected OB are coupled into a CMOS camera by means of an optical fiber. Then, they are processed into a speckle pattern by an image-processing computer as a result of the mathematical calculations based on interferometric phenomena. The intensity of the unperturbed speckle pattern is recorded with the intensity  $I_1$ , mathematically expressed as follows:

$$I_1 = I_0 + I_r + 2\sqrt{I_0 I_r} \cos(\theta) \quad (1)$$

where  $I_0$  is the light intensity scattered from the object,  $I_r$  is the light intensity of the reference beam and  $\theta$  is the phase angle.

Then, a thermal external perturbation produces stress into the specimen and the deformation of the sample surface brings to new speckle pattern. Thus, the reflected wave

front is slightly modified and recorded with a new perturbed speckle pattern intensity  $I_2$ :

$$I_2 = I_0 + I_r + 2\sqrt{I_0 I_r} \cos(\theta + \phi) \quad (2)$$

where  $\phi$  is the angle is related to the displacement, i.e. the deformation. The stored intensity  $I_1$  is digitalized by the ESPI system and then subtracted from  $I_2$ , resulting in a speckle fringes pattern  $I_{1-2}$ . The comparison between the recorded undisturbed and disturbed speckle patterns leads to a correlation fringe pattern time by time. Analytically, the subtraction of the fringe patterns is governed by the following equation:

$$I_{1-2} = 2\sqrt{I_0 I_r} [\cos(\theta) - \cos(\theta + \phi)] \quad (3)$$

The computer-aided subtraction of the deformed and the non-deformed patterns represents the out-of-plane displacement, i.e. the deformation that travel along with the sample. Any discontinuity in the fringe pattern can identify a discontinuity in the investigated material. Then, the correlation fringe pattern can be processed for contrast enhancement and noise removal, so the final phase-contrast map can be used to measure the displacement field with high accuracy [6].

### 3 Results

In this work, ESPI interferometric non-destructive technique was applied for the identification of an artificial defect that plays as a gap between the cap and the stringer foot. So, the presence of a Kapton sheet represents an inclusion that acts by reducing the structural capability of the wing, decreasing its performance. Previous investigation was considered employing a Phased Array Ultrasonic Testing (PAUT) in order to verify the presence of the Kapton foil with a standardized technique [7]. The UT technique was applied only on the front flat side due to the presence of the stringer on the back one. The results brought to light only part of the insert showing an overturned C-shaped inclusion. A possible cause of this result is that the resin has penetrated between the composite layers and the Kapton sheet, acting as a bridge for the ultrasonic waves that continued to travel undisturbed, passing the obstacle without returning any backscattering signal. Further analyzes were conducted with the aim to identify the foil and assess the penetration state of the resin between the layers. The ESPI technique was applied both on the front and on the back of the stiffened panel, and with the help of markers, the area of interest was centred on the defect. The ESPI correlation fringes image can be seen in Fig. 2 which examines the front of the panel (not stiffened side). The fringes have a symmetrical pattern with an X-shaped propagation whose centre corresponds to the position of the stringer arranged transversally. In detail, although the surface is stiffened free, the presence of the stringer on the back side is identified by the traverse line. It is possible to notice that the central area is darker due to the presence of the insert which, undergoing a different deformation from the neighbourhood, generates different out-of-plane displacements detected through the gray color chart. In fact, the horizontal fringes are assembled at the top and bottom of the image and they are stopped at the defect boundaries. Once the image has been processed, it is possible to obtain a phase-contrast map, of easier interpretation.

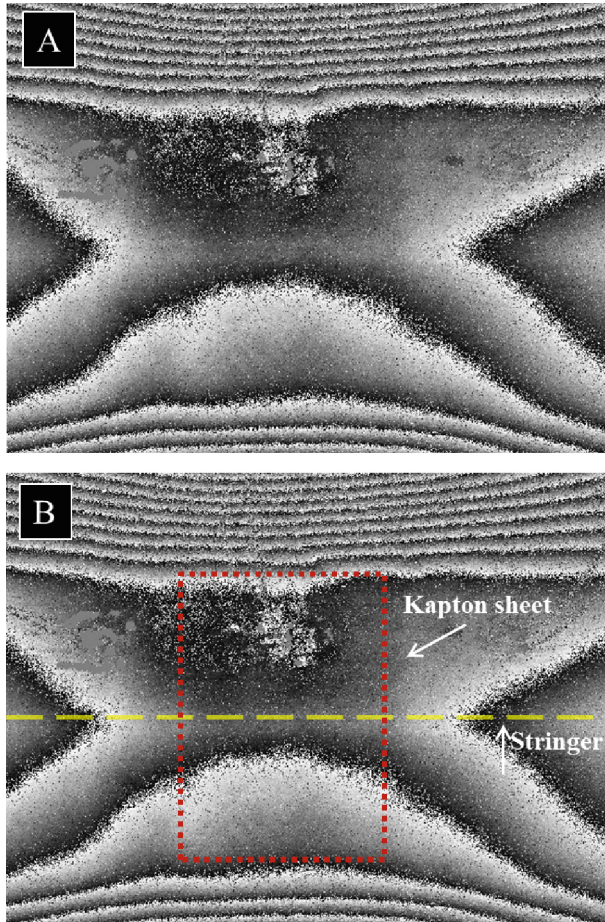


**Fig. 2.** (A) ESPI correlation fringe pattern of the front (not stiffened side) of the wing panel and (B) details. Transverse stringer in yellow and Kapton sheet in red.

Figure 3 shows the phase-contrast map of the back side of the panel (stiffened side). It is possible to distinguish the rectangular profile of the insert identified by a central dark profile. It is also observed that the central part of the rectangle is lighter than at the edge and in particular the right side. Probably, the resin has penetrated between the interface, as supposed before, and the resin has been acted as a vibration damper. It is also evident a horizontal central line representing the stringer. In addition to the presence of the insert, it is possible to notice that there is a gradient in the gray color along the vertical axis and, in detail, the colour change represents the position of the stringer edges. Thanks to the correlation between pixel and millimetres, it was measured the insert dimensions with an accuracy of 94% with the respect to the nominal size.

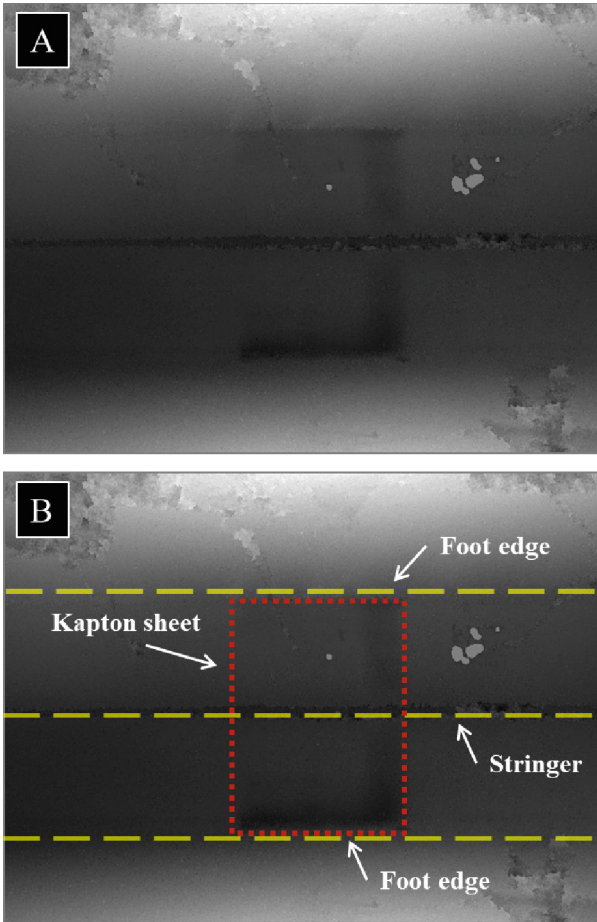


**Fig. 3.** (A) ESPI phase-contrast map of the back (stiffened side) of the wing panel and (B) details. Transverse stringer and foot stringer edge in yellow and Kapton sheet in red.

## 4 Conclusions

The experimental evidence of this research allows affirming that the ESPI technique can be applied to the study of stiffened composite panels without accessibility limits due to the presence of the stringers. In addition to the identification of the insert with a dimensional accuracy of 94%, the results show the presence of additional elements such as the foot of the stringer. It was also found out that during the infusion process, the resin penetrated between the composite layers and the Kapton sheet, hiding part of the insert under investigation due to its vibration damping properties. In any case, this technique goes so far as to identify the geometric rectangular profile, guaranteeing an easy interpretation of the artificial debonding despite manufacturing defects.

**Acknowledgements.** The authors sincerely thank Eng. Giulia Leone for the scientific contribution in the elaboration of the ESPI images.

## References

1. Schoeppner, G., Abrate, S.: Delamination threshold loads for low-velocity impact on composite laminates. *Comp. A* **31**, 903–915 (2000)
2. Papa, I., Langella, A., Lopresto, V.: CFRP laminates under low-velocity impact conditions: influence of matrix and temperature. *Polym. Eng. Sci.* **59**(12), 2429–2437 (2019)
3. Pagliarulo, V., Russo, P., Leone, G., D' Angelo, G.A., Ferraro, P.: A multimodal optical approach for investigating 3D-printed carbon PEEK composites. *Opt. Lasers Eng.* **151**, 106888 (2022)
4. Gagliardi, F., et al.: Joining of thermoplastic structures by friction riveting: a mechanical and a microstructural investigation on pure and glass reinforced polyamide sheets. *Compos. Struct.* **204**, 268–275 (2018)
5. Russo, P., Pagliarulo, V., Bianco, V., Simeoli, G., Cimmino, F., Ferraro, P.: Characterization of 'green' composite laminates after flexural tests by speckle interferometry. *Opt. Eng.* **59**(10), 102416 (2020)
6. Pagliarulo, V., Bianco, V., Memmolo, P., Distanto, C., Ruggiero, B., Ferraro, P.: Leaks detection in stainless steel kegs via ESPI. *Opt. Lasers Eng.* **110**, 220–227 (2018)
7. Boffa, N., Monaco, E., Ricci, F., Amoroso, F.: Investigation of manufacturing effects by strength assessment, NDI and guided waves based SHM in composite plates reinforced with bonded stringers. In: *Proceedings of SPIE*, vol. 10972, p. 109720Y-5 (2021)





# Use of an Innovative Methodology for the Characterization of Polymers in the Analysis of the UV-Light Radiation Effects

Andrea Genovese<sup>(✉)</sup> , Vincenzo Maria Arricale , Mario Barbaro, Luigi Marenga,  
Michele Sanfelice, and Guido Napolitano Dell'Annunziata 

Department of Industrial Engineering, University of Naples "Federico II", Via Claudio 21,  
80125 Naples, Italy  
andrea.genovese2@unina.it

**Abstract.** The mechanical behaviour of viscoelastic materials is typically investigated by means Dynamic Mechanical Analysis (DMA) carried out on standardized specimens suitable for laboratory conditions, which can be specifically produced for the test or extracted from a component, causing its destruction. Here, an innovative methodology, based on the instrumented indentation, is presented to assess the mechanical response of polymers' compound. The innovative device, called VESevo, provides a non-destructive and non-invasive testing procedure allowing the characterization of a material directly in-situ, without the destruction of a component to create a suitable sample. Taking advantage of this methodology, the aim of this work is the study of polymers' compound viscoelastic properties variations, caused by exposure to UV-rays. The analysis has been carried out on a polymers' compound designed to be used as a tire tread. UV radiations are usually employed to change properties of the polymers, but there are very few examples of UV-curing effects applied to tires compound as well as the monitoring of properties over time using non-destructive techniques. In order to assess the compound viscoelastic properties variation, a proper test bench has been set, adopting in a combined manner an UV-Lamp and the innovative device VESevo. After that, a dedicated test campaign has been carried out on a tire compound specimens tested in different conditions. The preliminary results highlighted: the ability of the proposed technique to measure the variation in the mechanical behavior of the material induced by exposure to UV rays; significant variations in viscoelastic properties induced on the compound as a function of the time of exposure to UV rays.

**Keywords:** Viscoelastic Properties · Tires · Polymers · Mechanical Characterization · Non-Destructive Test · UV-Rays

## 1 Introduction

Pneumatic tires are high-tech engineering products manufactured employing a wide range of materials with specific functions to obtain the required performance of the finished product. Particularly, the tire tread surface is based on styrene-butadiene-rubber

(SBR), the peculiar characteristics of which makes it one of the most important constituent materials in tire manufacturing. This elastomer, usually compounded with silica, carbon black and other functional fillers, exhibits unique viscoelastic behavior that allows to obtain high adhesion and grip capacity. Therefore, the investigation of the tire tread viscoelastic properties becomes a key factor in the development of proper contact mechanics models necessary to improve the prediction of the interactions between tire tread and road surface in order to achieve the desired features, in terms of tire performance and road safety [1, 2]. From this point of view, it is also essential to understand how chemical or physical treatments affect the viscoelastic response of polymer compounds. In this framework, the UV radiation effects have been widely investigated by exploring the main mechanisms underlying the polymers photodegradation phenomena [3–7]. Despite that, there no relevant studies in literature that deeply explore tire viscoelastic properties variations, strongly related to the tire maximum achievable grip, and chemical-physical characteristics changes induced by the UV. Adopting testing procedures that involve a non-invasive analysis plays an important role in preservation of the surface properties of polymeric materials providing the possibility to differentiate the effects induced by the characterization from the effect of the chemical or physical treatment to which the material is subjected. For this reason, an innovative device, based on a non-destructive indentation, known as VESevo (Viscoelasticity Evaluation System evolved), has been employed to investigate the effects of the UV radiation exposure on the viscoelastic properties of a polymer compound.

## 2 Non-destructive Viscoelasticity Evaluation: VESevo

The viscoelastic analysis of polymers, such as tire tread compounds, can be carried out with several characterization techniques although their mechanical behavior is typically investigated with dynamic experiments by means of Dynamic Mechanical Analysis [8, 9], which provides specific dynamic functions, known as Storage and Loss Moduli and Loss Factor that mathematically describe the viscoelastic behavior of the tested material and its attitude to recover and dissipate energy in a loading-unloading cycle [10–15]. Although DMA is capable of providing useful information on the viscoelastic properties of polymeric materials, it requires complex and very expensive equipment and the destruction of the pneumatic tires in order to obtain a suitable specimen with standardized dimensions. In this scenario, recent studies investigate different methodologies to characterize the polymer in non-destructive way [16, 17]. VESevo represents an alternative solution capable of overcoming the technical limitations of the conventional characterization methods. Developed by the Vehicle Dynamics Research Group of the Department of Industrial Engineering at the University of Naples Federico II, VESevo can be used to investigate different viscoelastic phenomena in a completely non-destructive and non-invasive way: from the characterization of viscoelastic properties to the evaluation of their variations in time due to wear or ageing phenomena [18]. In its prototypal design, VESevo consists of a rod-spring mechanism made of a steel rod and a semi-spherical indenter that, in free fall, impacts on the tread surface under analysis when a trigger is released. The rod displacement is measured with an optical laser sensor and, at the same time, an IR pyrometer monitors in real time the tread surface temperature. A generic raw displacement curve measured at a specific temperature is shown in Fig. 1(a).

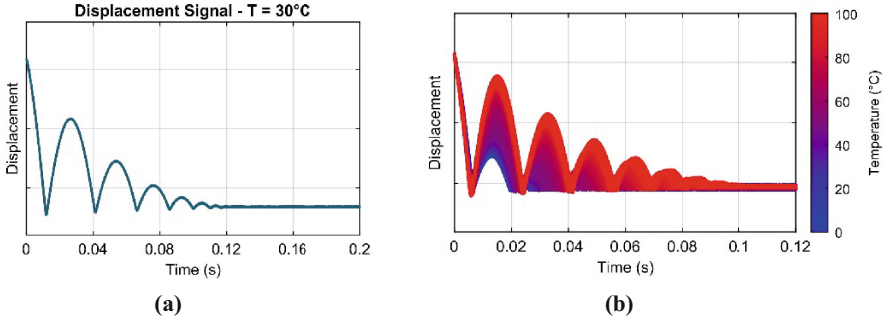


**Fig. 1.** (a) Raw signal of the rod displacement at a measured temperature of 30 °C; (b) Displacement curves at different temperatures of the tire tread surface.

Since the viscoelastic properties of polymeric materials are strongly temperature dependent, a typical VESevo test session consists of several acquisitions carried out following a standard testing procedure:

- Several acquisitions at ambient temperature;
- Cooling to about -20 °C employing a climatic cell and then performing VESevo acquisitions during the natural heating process up to ambient temperature;
- Forced heating up to 100 °C through a thermal blanket or a professional heating gun, and then carrying out acquisitions down to ambient temperature.

The displacement curves, acquired throughout the temperature range, are illustrated in Fig. 1(b). The bounce curves reflect the natural viscoelastic response of polymeric materials as a function of temperature: at low temperature, rebounds with small amplitude emerge because the material behaves as a glassy solid; conversely, at high temperature an increasingly smaller energy dissipation occurs with a resulting increase in bounces number and their amplitude because the material exhibits a rubbery behavior. In order to evaluate the viscoelastic properties, the displacement raw signals are processed with a data processing algorithm from which a series of temperature-dependent physical parameters are identified by modelling the dynamic response of the rod with a second order damped mass-spring system. Particularly, the Loss Factor can be defined with the following mathematical relationship [19]:

$$\tan \delta = \frac{\omega_s \sigma_c}{K_c} \quad (1)$$

where  $\omega_s$  is the frequency of the damped motion of the rod on the viscoelastic surface while  $K_c$  and  $\sigma_c$  represent the equivalent contact stiffness and damping coefficient, respectively.

### 3 Experimental Setup

The investigation of the UV rays effects on the viscoelastic properties of polymeric materials has been carried out by setting up a proper test bench for the characterization

of a specific polymer compound designed to be used as a tire tread. More specifically, the specimen under analysis, denoted as Compound A, is a SBR/BR rubber blend with a 85/15 blend ratio. In accordance with the ISO standard for the UV radiation exposure [20], the characterization tests have been performed in dry conditions ensuring that the specimen under analysis is not subjected to any applied stress and maintaining the same irradiation conditions throughout the entire exposure cycle. The UV-Gun houses a UV lamp that emits ultraviolet radiation with a UV peak at 395–400 nm. The UV curing lamp has been placed on a horizontal worktable and positioned at a distance of 56 cm from the specimen to be tested while an external IR pyrometer has been used for the real time monitoring of the specimen's temperature to verify eventual thermal heating (Fig. 2).



**Fig. 2.** Scangrip UV-Gun (on the left); Dual laser beam IR pyrometer (on the right).

## 4 Result Analysis

Before the UV treatment, the compound A has been tested in different days with the VESevo device. The VESevo outputs has highlighted that the specimen under analysis has maintained unchanged its viscoelastic properties over time in the entire acquired temperature range, thus proving its homogeneity, properties stability in time and the high repeatability of the device. After this preliminary analysis, the compound A has been cured with an exposure time of 10 min. During the UV radiation treatment, a negligible increase in the specimen surface temperature of about 10 °C has been measured by the external IR pyrometer.

The propagation of the UV curing phenomenon within the material has also been investigated by exposing to UV lamp only one side of the specimen under analysis. After one hour from the curing treatment, the cured side of the slab has been characterized with the VESevo device following the standard testing procedure explained in the previous section. The same test has been carried out after 24 h on both sides of the slab in order to verify if the effects of the UV curing treatment on the viscoelastic properties change over this time period. The overall results are shown in Fig. 3.

The results highlight that the UV curing treatment affects not only the surface properties but also the viscoelastic response of the polymer compound in the bulk. The most

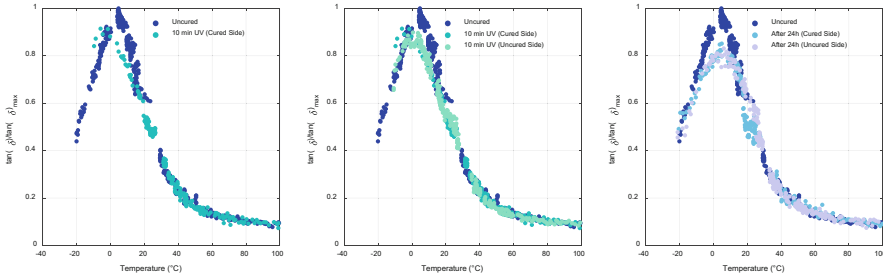


**Fig. 3.** Normalized Loss Factor curves for the Compound A.

significant variations are observed at low temperatures, close to the Loss Factor peak. Particularly:

- the exposure time of 10 min leads to a slight decrease of the Loss Factor peak; both the exposed surface and the uncured side are affected by this hardening phenomenon;
- the tests carried out 24 h after the UV radiation exposure show a more marked decrease of the Loss Factor on both specimen sides.

## 5 Conclusions

In this preliminary study, the effects of the UV radiation on the mechanical behavior of a polymer compound have been investigated by means of a non-destructive characterization methodology. The VESevo device has been able to capture differences in viscoelastic response of the compound after the curing treatment. The UV radiation exposure has been shown to have noticeable effects of the viscoelastic properties and an evident propagation of the UV curing effect within the material, as the VESevo outputs have highlighted. Since the UV curing process strongly depends on the exposure duration, future studies will be aimed at investigation of the exposure time effect on the viscoelastic properties of polymer compounds subjecting them to different UV exposure times. In addition, it will be necessary to carry out a very robust experimental test campaign in order to:

- Evaluate the UV susceptibility of the polymers compounds as the blend ratio changes;
- Find a correlation between the UV-induced chemical-physical properties variations and the viscoelastic properties changes measured by means of the VESevo device.

Finally, it should be noted that this preliminary work has been limited to the characterization of a unique polymer compound in the form of a slab although the VESevo technology has the potential to directly test the tire tread surface, thus extending the analysis of the UV radiation effects to the pneumatic tires.

## References

1. Genovese, A., Carputo, F., Ciavarella, M., Farroni, F., Papangelo, A., Sakhnevych, A.: Analysis of multiscale theories for viscoelastic rubber friction. In: Carcaterra, A., Paolone, A., Graziani, G. (eds.) AIMETA 2019. LNME, pp. 1125–1135. Springer, Cham (2020). [https://doi.org/10.1007/978-3-030-41057-5\\_91](https://doi.org/10.1007/978-3-030-41057-5_91)
2. Wang, Y., et al.: Tire road friction coefficient estimation: review and research perspectives. *Chin. J. Mech. Eng.* **35**, 1–11 (2022)
3. Rabek, J.F.: *Photodegradation of Polymers: Physical Characteristics and Applications*. Springer, Heidelberg (2012)
4. Aboelkheir, M.G., Filho, R.D.T., Souza Jr, F.G.: Study on vulcanized rubber degradation after exposure to ultraviolet irradiation (2019)
5. Alawais, A., West, R.P.: Ultra-violet and chemical treatment of crumb rubber aggregate in a sustainable concrete mix. *J. Struct. Integr. Maintenance* **4**, 144–152 (2019)
6. Ossola, G., Wojcik, A.: UV modification of tire rubber for use in cementitious composites. *Cement Concr. Compos.* **52**, 34–41 (2014)
7. Al-Tayeb, M.M., Bakar, B.A., Ismail, H., Akil, H.M.: Effect of partial replacement of sand by recycled fine crumb rubber on the performance of hybrid rubberized-normal concrete under impact load: experiment and simulation. *J. Clean. Prod.* **59**, 284–289 (2013)
8. Menard, K.P., Menard, N.R.: *Dynamic Mechanical Analysis*. CRC Press, Boca Raton (2020)
9. Cho, K.S.: *Viscoelasticity of Polymers: Theory and Numerical Algorithms*. Springer, Heidelberg (2016)
10. Lakes, R., Lakes, R.S.: *Viscoelastic Materials*. Cambridge University Press, Cambridge (2009)
11. Tschoegl, N.W.: *The Phenomenological Theory of Linear Viscoelastic Behavior: An Introduction*. Springer, Heidelberg (2012)
12. Ferry, J. D. *Viscoelastic Properties of Polymers* (John Wiley & Sons, 1980)
13. Shaw, M.T., MacKnight, W.J.: *Introduction to Polymer Viscoelasticity*. Wiley, Hoboken (2005)
14. Brinson, H.F., Brinson, L.C.: *Polymer Engineering Science and Viscoelasticity: An Introduction*. Springer, Heidelberg (2015)
15. Mark, J.E., Erman, B., Roland, M.: *The Science and Technology of Rubber*. Academic press, Cambridge (2013)
16. Genovese, A., Maiorano, A., Russo, R.: A novel methodology for non-destructive characterization of polymers' viscoelastic properties. *Int. J. Appl. Mech.* **14**, 2250017 (2022)
17. Genovese, A., Pastore, S.R.: A novel nondestructive procedure for tire tread viscoelastic characterization. *Tire Sci. Technol.* **50**, 61–77 (2022)
18. Farroni, F., Genovese, A., Maiorano, A., Sakhnevych, A., Timpone, F.: Development of an innovative instrument for non-destructive viscoelasticity characterization: VESevo. In: Niola, V., Gasparetto, A. (eds.) IFToMM ITALY 2020. MMS, vol. 91, pp. 804–812. Springer, Cham (2021). [https://doi.org/10.1007/978-3-030-55807-9\\_89](https://doi.org/10.1007/978-3-030-55807-9_89)
19. Genovese, A., Pastore, S.R.: Development of a portable instrument for non-destructive characterization of the polymers viscoelastic properties. *Mech. Syst. Signal Process.* **150**, 107259 (2021)
20. ISO 4892-3: *Plastics—Methods of Exposure to Laboratory Light Sources—Part 3: Fluorescent UV Lamps* (2016)



# Double-Double Laminate Composites for Unmanned Aerial Vehicles

F. Di Caprio<sup>1</sup>, A. Riccio<sup>3</sup>, S. W. Tsai<sup>2</sup>, A. Russo<sup>3</sup>(✉), A. Braco<sup>3</sup>, C. Leccia<sup>3</sup>,  
and A. Sellitto<sup>3</sup>

<sup>1</sup> C.I.R.A. (Italian Aerospace Research Centre), 81043 Capua, Italy

<sup>2</sup> Department of Aeronautics and Astronautics, Stanford University, Stanford, CA 94305, USA

<sup>3</sup> Department of Engineering, University of Campania “L. Vanvitelli”, via Roma, 29, 81031  
Aversa (CE), Italy

angela.russo@unicampania.it

**Abstract.** The successful combination of low weight and high strength is envisaged for an optimised aeronautical structure. The use of composite materials is particularly attractive to meet the required challenging weight saving. Nowadays, the use of these materials is established for many structural components of modern aircrafts, such as the Airbus A380 or the Boeing 787, while their adoption for Unmanned Aerial Vehicles (UAVs), such as drones, which is progressively increasing, especially for civil applications, such as fire prevention, emergency operations, surveillance, and research missions.

In this paper, the redesign of an aluminium drone components have been re-performed by using carbon fibre composite materials, with the aim to lighten the overall structure of the drone and to increase its strength. Conventional quasi-isotropic stacking sequence has been considered to study the performance of the structure under operational tensile and torsional loads. Later, a sensitivity analysis has been performed to find a new design configuration with Double-Double laminates [1–4]. The different materials and stacking sequences have been compared to find the best combination between performances and weight.

**Keywords:** double-double · drone · UAVs · composite materials · optimization

## 1 Introduction

The development of drones has started for military applications, but, nowadays, UAV are used more and more frequently for civil purposes, such as remote sensing, communications, emergency operations, surveillance, and rescue operations. Moreover, small cargo drones, used for commercial and consumer applications, are pushing design objectives toward the development of low weight and high strength and stiffness structures able to guarantee increased autonomy and payload [5, 6].

Carbon fibre reinforced composite materials have been widely used in transportation industries to manufacture lightweight structures and they are becoming widespread in the field of UAVs to design high-strength low-weight frames [7, 8]. The major limitation in the fibre reinforced composite materials structures employment is their damages

behaviour [9, 10], which is strictly correlated to the processing technologies, the geometry of the components and the layers arrangement. The geometry of the components often cannot be modified to optimise the damage resistance of a composite structure, because it also depends on other aspects, such as aerodynamics, connections, etc. Hence, modifications to the laminate layup are the preferred choice for the optimization of the performances in terms of stiffness, strength and, consequently, of the damage behaviour of the composite structures. Double-Double (DD) laminates [1–4], newly developed by Prof. S.W. Tsai, can enhance the standard layup design of laminated composites. DD permit to overcome the limitations of the quasi-isotropic stacking sequences, which are characterized by four fixed angles ( $0^\circ$ ,  $45^\circ$ ,  $-45^\circ$ ,  $90^\circ$ ) and balancing/symmetry requirements with respect to the midplane. DD laminates allow for using an unrestricted range of angles and for easily implementing homogenization.

In this paper, Double-Double laminates have been used to optimise the structural frame of a multicopter, with a maximum take-off mass of 10 kg. The main structure is composed by six beams, representing the drone's arms connecting rotor engines to the controlling unit. The redesign of the original aluminium alloy arms has been performed and the investigation has been focused on a single arm, for symmetry reasons. Section 2 briefly introduces Double-Double laminates, while Sect. 3 presents a comparison of the numerical results, in terms of mass, maximum displacement and first natural frequency, obtained for metallic and composite components, including quasi-isotropic stacking sequence and non-conventional DD plies angles.

## 2 Double-Double Laminates

Double-double laminates have disrupted the well-established composites manufacturing processes and rules, allowing to achieve lighter structures with improved stiffness. Indeed, since the 1960s, when composites first appeared in the aeronautical field, the quasi-isotropic laminates, made of  $0^\circ$ ,  $\pm 45^\circ$ ,  $90^\circ$  fibre-oriented plies, have been the only option for designing with composites. The quasi-isotropic major limitations are represented by the mid-plane symmetry, which allow to avoid warpage upon cooldown, the 10% rule, which requires that all the four orientations of the stacking sequence are represented in at least the 10% of the laminate.

Even if composites and their manufacturing processes have undergone developments and enhancement over time, the standard sub-laminate ( $0$ ,  $\pm 45$ ,  $90$ ) remained the same of the 60s, as a matter of convenience, with a number of limitations. Actually, quasi-isotropic laminates building blocks are constituted by a minimum of 8 plies, so the minimum thickness is 1 mm (considering symmetry about the midplane). As a result, design and manufacturing become very complex, and optimization process (for weight reduction) become even harder to perform. The use of DD laminates aims to overcome these issues. They consist of building block with  $[\pm\Phi, \pm\Psi]$  angle orientations, where all angles are considered feasible between  $0^\circ$  and  $90^\circ$ . The sub-laminate block is a 4-ply block and it can be simply homogenized to facilitate the manufacturing process. In this framework, the Tsai's modulus [2] becomes very important, as it allows to normalize the lamina stiffness matrix  $[Q]$  to satisfy the relationship in Eq. (1), where  $[A^*]$  is the extensional stiffness matrix and  $[D^*]$  is the bending stiffness matrix normalized by the



Tsai's modulus.

$$\text{Tr}[A^*] = \text{tr}[D^*] = \text{tr}[Q] \quad (1)$$

Homogenization of a laminate is reached when  $[A^*] = [D^*]$ , while  $[B] = 0$ , and it is more easily achieved when dealing with thin laminate blocks. On the contrary, for quasi-isotropic layups, it becomes difficult to obtain homogenization because its sub-laminates are thick and midplane symmetry is mandatory. This difference is crucial in composite laminates design and manufacturing. Moreover, laminates with taper can be produced to lighten the structure. Hence, DD-laminates with  $[\pm\Phi/\pm\Psi]$  layup allow for easy manufacturing, weight savings, reduction of production cost and time, and potential structural applications of composite materials not yet developed.

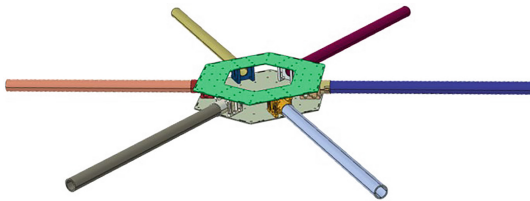
### 3 Numerical Results

In this section, the structural frame of a multicopter, with maximum take-off mass of 10 kg, has been modelled and analysed. Metallic and composite design solutions have been compared.

#### 3.1 The Numerical Test-Case

The drone structure, shown in Fig. 1, is composed of six beams, representing the drone's arms, a central support and six arms mounts. The starting configuration of the drone is made of aluminium alloy. The main purpose of the paper is to lighten the entire structure by replacing the metal alloy with Carbon Fibre Reinforced Polymer (CFRP) composites. Both quasi-isotropic and DD laminates have been considered. However, composite materials have been employed only for the drone's arms, representing most of the total structural mass. Indeed, the use of CFRP for the central support and the arms mounts has been considered not appropriated since it could lead to manufacturing difficulties, with a limited advantage in terms of weight or performances.

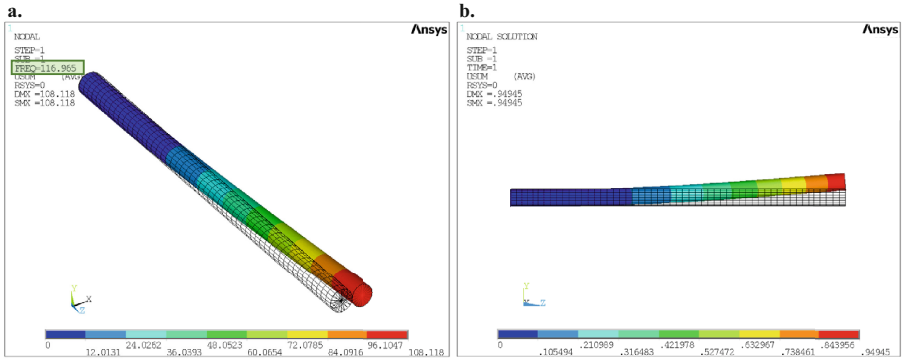
The material properties of the aluminium alloy and the CFRP are listed in Table 1.



**Fig. 1.** Numerical model of the multicopter.

**Table 1.** Materials properties.

Material	Young Modulus		Density	Shear Modulus	Poissons' ratio
	$E_{11}$ [MPa]	$E_{22}$ [MPa]	$P$ [Kg/m <sup>3</sup> ]	$G$ [MPa]	$\nu$
Aluminium	72500	–	2.8E–06	–	0.3
CFRP	141000	140800	1.6E–06	21073	0.3002

**Fig. 2.** Numerical results of the aluminium configuration: a) first natural frequency; b) displacement field.

### 3.2 Numerical Results and Discussion

The numerical study has been performed in the Ansys Mechanical environment by considering a single arm, for cyclical symmetry reasons. A transversal force of 42 N and a torque of 2.7 N have been placed at the end of the arm. Modal and static analyses have been carried out.

The first set of analyses have been performed on the aluminium configuration, with 3 mm thickness. Then, the arm has been modelled considering 24, 32 and 40 plies of a quasi-isotropic laminate, with a lamina thickness of 0.125 mm. Figure 2 shows the numerical results in terms of first natural frequency and displacement contour plots of the aluminium configuration. In Table 2, such results have been compared to the CFRP configurations outputs, obtained by considering different arm thicknesses (i.e. an increasing number of laminate plies).

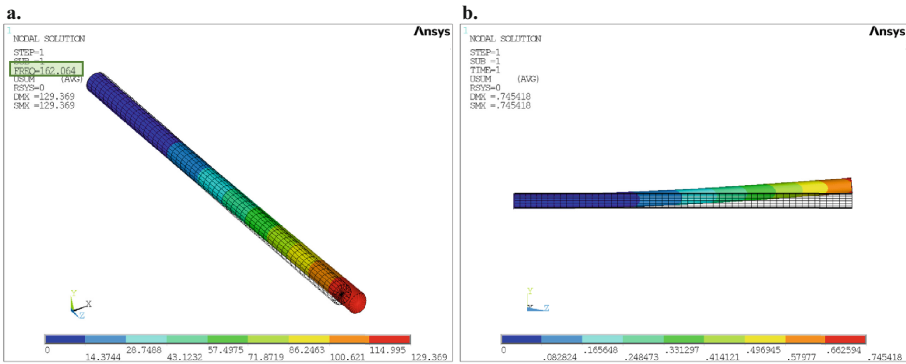
It is worth to notice that the quasi-isotropic composite material configurations lead to a reduction in terms of weight, even if the total arm thickness increases with respect to the aluminium one (e.g. with 32 and 40 plies). Moreover, the increase in the first natural frequency demonstrates that the total stiffness of the structure has been improved by using quasi-isotropic composite material. Indeed, the first vibration mode often defines the highest loads in a structure.

Among the considered quasi-isotropic CFRP configurations, the one characterized by 32 plies has been identified as the best possible choice, since the maximum displacement is very close to the one obtained for the metallic configuration, while the mass is reduced

**Table 2.** Summary of numerical analyses results.

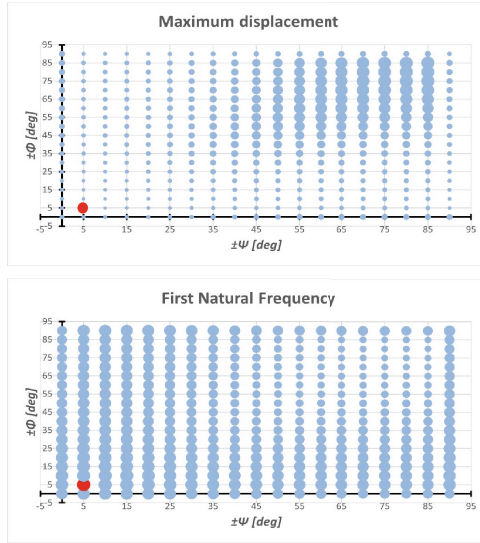
	Aluminium alloy	Quad (24 plies)	Quad (32 plies)	Quad (40 plies)
Mass [g]	377	191	255	319
Maximum displacement [mm]	0.949	1.44	0.745	0.485
First natural frequency [Hz]	117	131	162	181

and the first vibration mode increases. The first natural frequency and total resultant displacement contour plots of the 32 plies CFRP configuration are shown in Fig. 3.



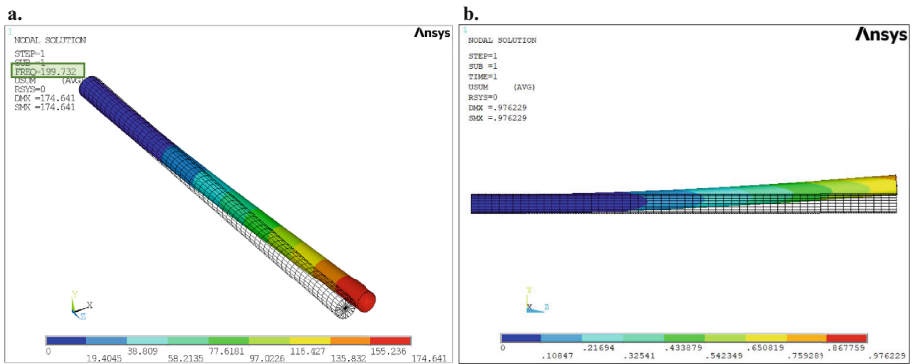
**Fig. 3.** Numerical results of the quasi-isotropic configuration: a) first natural frequency; b) displacement field.

Finally, the drone’s arm has been redesigned considering the novel DD laminates. The first step was to identify the best combination of  $[\pm\Phi/\pm\Psi]$  angles with the purpose of minimize the weight and maximize the performance. A sensitivity analysis has been performed, by considering different angles combinations, to finds the strongest DD laminate based on the set of inputs (e.g., material properties and loads). According to Fig. 4, the  $[\pm\Phi = 5^\circ, \pm\Psi = 5^\circ]$  configuration has been identified as the one which minimises the maximum tip displacement and maximises the first natural frequency. A 36 plies DD laminate has been used to model the structure, with an overall structural thickness of 2.25 mm, which includes 9 blocks of 4 plies, each of 0.0625 mm as is typical for these laminates.



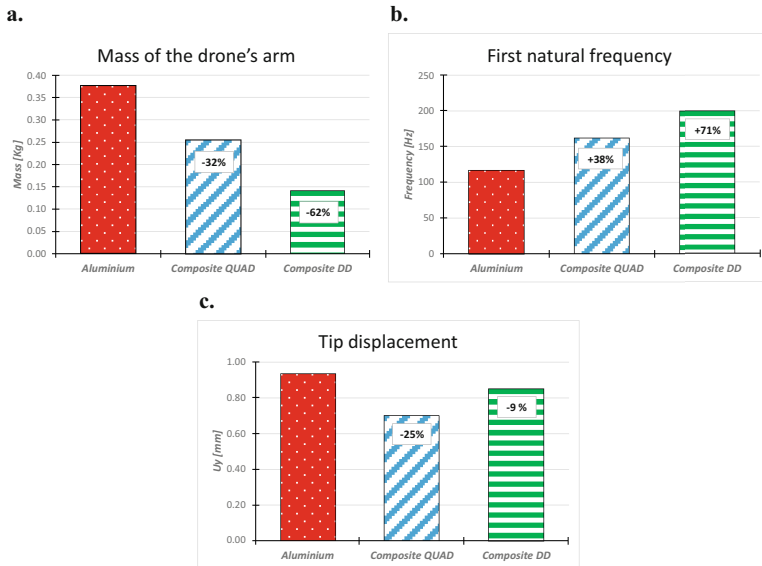
**Fig. 4.** Angles sensitivity analysis.

Figure 5 shows the numerical results in terms of first natural frequency and total resultant displacement contour plots of the DD configuration. Comparisons among metal, quasi-isotropic and DD configurations are shown in Fig. 6, in terms of bar charts.



**Fig. 5.** Numerical results of the DD configuration: a) first natural frequency; b) displacement field.

According to Fig. 6, the adopted DD layup provides excellent mass saving while maintaining the requirements in terms of stiffness and tip displacement of the arm.



**Fig. 6.** Numerical results comparison.

## 4 Conclusions

In this paper, the frame of an aluminium drone has been redesigned by considering composite material systems for replacement of the aluminium alloy. Both quasi-isotropic laminates and Double-Double (DD) laminates have been analysed, with the aim to reduce the overall weight of the structure, without reducing its stiffness and strength. As expected, the newly developed DD laminate family proves to be a real innovation for the design of lightweight high-performance structures. Indeed, a reduction of 62% of the total arms mass has been achieved with a 36-ply  $[\pm\Phi = 5^\circ, \pm\Psi = 5^\circ]$  layup, against the 32% mass reduction obtained with a standard 32-ply quasi-isotropic laminate.

## References

1. Shrivastava, S., Sharma, N., Tsai, S.W., Mohite, P.M.: D and DD-drop layup optimization of aircraft wing panels under multi-load case design environment. *Composite Struct.* **248**, art. no. 112518 (2020)
2. Vermes, B., Tsai, S.W., Riccio, A., Di Caprio, F., Roy, S.: Application of the Tsai's modulus and double-double concepts to the definition of a new affordable design approach for composite laminates. *Composite Struct.* **259**, art. no. 113246(2021)
3. Vermes, B., Tsai, S.W., Massard, T., Springer, G.S., Czigan, T.: Design of laminates by a novel "double-double" layup. *Thin-Walled Struct.* **165**, art. no. 107954 (2021)
4. Tsai, S.W.: Double-double: new family of composite laminates. *AIAA J.* **59**(11), 4293–4305 (2021)
5. Austin, R.: *Unmanned Aircraft Systems: UAVS Design, Development and Deployment*, 1st edn. Wiley, United States

6. Kontogiannis, S.G., Ekaterinaris, J.A.: Design, performance evaluation and optimization of a UAV. *Aerosp. Sci. Technol.* **29**(1), 339–350 (2013)
7. Alhammad, M., Avdelidis, N.P., Deane, S., Ibarra-Castanedo, C., Pant, S., Nooralishahi, P., Ahmadi, M., Genest, M., Zolotas, M., Zanotti-Fragonara, L., Valdes, J., Maldague, X.P.V.: Diagnosis of composite materials in aircraft applications: towards a UAV-based active thermography inspection approach. In: *Proceedings of the SPIE 11743, Thermosense: Thermal Infrared Applications XLIII*, p. 1174306 (2021)
8. Vasić, Z., Maksimović, S., Georgijević, D.: Applied integrated design in composite UAV development. *Appl. Compos. Mater.* **25**(2), 221–236 (2017). <https://doi.org/10.1007/s10443-017-9611-y>
9. Sellitto, A., Saputo, S., Russo, A., Innaro, V., Riccio, A., Acerra, F., Russo, S.: Numerical-experimental investigation into the tensile behavior of a hybrid metallic-CFRP stiffened aeronautical panel. *Appl. Sci. (Switzerland)* **10**(5) (2020)
10. Riccio, A., Palumbo, C., Acanfora, V., Sellitto, A., Russo, A.: Influence of failure criteria and intralaminar damage progression numerical models on the prediction of the mechanical behavior of composite laminates. *J. Compos. Sci.* **5**(12) (2021)



# Numerical Study on the Compressive Behaviour of Repaired Composite Panels

Aniello Riccio<sup>1</sup>, Andrea Sellitto<sup>1</sup>✉, Antonio Garofano<sup>1</sup>, Giancarlo Ingenito<sup>3</sup>,  
and Mauro Zarrelli<sup>2</sup>

<sup>1</sup> Department of Engineering, University of Campania “Luigi Vanvitelli”, 81031 Aversa, Italy  
andrea.sellitto@unicampania.it

<sup>2</sup> National Research Council of Italy (CNR), Institute for Polymers, Composite and Biomedical  
Materials (IPCB), 80055 Portici, Italy

<sup>3</sup> METItalia Srl, Via delle Fontane 78, 84012 Anghi, Italy

**Abstract.** Despite their attractive properties, composites are characterized by a high susceptibility to damage arising from impact loading. BVID may induce delaminations and further intra-laminar damages, due to intrinsic weakness of composite laminates in the out-of-plane direction, which can considerably reduce the stiffness and the strength of composite components. Impact damaged composite structures require component replacement or repair. Considering economic and environmental benefits, composite repair is preferred as the main and cost-effective approach able to fully restore the structural integrity of the damaged components. This work is aimed to numerically study the compressive behaviour of an impact damaged aeronautical composite stiffened panel undergoing repair. Two Finite Element based models have been developed in the ABAQUS FEM platform to numerically simulated the mechanical behaviour of the investigated composite structure: a model for the *pristine* configuration and a model for the *repaired* configuration. In the repaired configuration, a bonded stepped patch with an external ply for the skin’s external surface has been placed. According to the repair scheme, the replacement of six parts of carbon-fiber plies in concentric circles by new plies with increased radius, allowing plies overlapping, has been considered. Linearized buckling analyses and static non-linear buckling analyses have been performed to study the panels’ compressive behaviour and the effects of repair process on mechanical performances in terms of stiffness and deformed shapes evolution during compression, for the pristine and the repaired configuration.

**Keywords:** Composite Failure · Impact Damage · Bonded Stepped Repair · Finite Element Analysis

## 1 Introduction

Carbon fiber-reinforced polymer composite laminates are widely used for primary and secondary structures in aerospace, automotive, and wind energy production industries thanks to their high stiffness-to-weight and strength-to-weight ratios, and their high tailoring and moulding capabilities [1, 2]. However, due to their intrinsic weakness in

the out-of-plane direction, composite laminates are highly vulnerable to impact loading conditions. Additionally, their interacting failure mechanisms, which are very difficult to be predicted and can be critical for structural integrity, introduce significant difficulties in designing effective lightweight safe structures [3].

Low-velocity impacts due to drop tools during maintenance or debris encountered during take-off and landing phases may cause Barely Visible Impact Damage (BVID), which can be hardly detected using the standard visual inspections and require the use of Non-Destructive Inspection (NDI) techniques. BVIDs may induce delaminations and intra-laminar damages, due to the characteristic weakness of composite laminates in the out-of-plane direction. Such failure mechanisms can considerably reduce stiffness and strength of composite laminates [4, 5].

Damaged composite structures require replacement or repair of the damaged components. The intensive use of composites in primary load-carrying structures, in several industrial fields, raised their sustainability as a prevalent issue. The choice between replacement or repair of a damaged composite component can be related to several considerations on mechanical properties requirements, geometrical characteristic of the component and damage extension and location. However, considering economic and environmental benefits, composite repair is, usually, preferred as the main and cost-effective approach able to fully restore the structural integrity of damaged components [6, 7]. Therefore, efficient repair techniques are needed to re-establish mechanical performance of damaged composite structures.

Strength and stiffness reduction of composite structures, due to impact events, is of main concern under compression loading conditions. Indeed, impact damages may evolve, under compressive loading conditions, and lead to premature structural collapse well below the design limits [8]. Even for composite structures under compression loading conditions, structural repair can be the only feasible and cost-effective solution, if damage is not widespread. Refurbish strength and stiffness and restore original structural and operational effectiveness of a damaged composite part is the main target of any composite repair technique [9]. With these goals, mechanical joints and adhesive bonding are generally used as repair methods for composite damaged structures in aircraft maintenance [10].

In this paper, two Finite Elements based numerical model have been developed, in the ABAQUS FEM platform, to study the behaviour of an aeronautical composite omega stiffened panel subjected to a compressive loading condition: a model for the pristine configuration and a model for the repaired configuration. In the repaired configuration, a bonded stepped patch with an external ply for the skin's external surface has been placed. According to the repair scheme, the re-placement of six parts of carbon-fiber plies in concentric circles by new plies with increased radius, allowing plies overlapping, has been considered. Linearized buckling analyses and static non-linear buckling analyses have been performed to study the panels' compressive behaviour and the effects of repair process on mechanical performances in terms of stiffness and deformed shapes evolution during compression, for the pristine and the repaired configuration.



In Sect. 2, the developed Finite elements models for the pristine and repaired configurations are shown; while, in Sect. 3 numerical results are presented demonstrated the effectiveness of the adopted repair scheme and its influence on the mechanical behaviour of the analysed stiffened composite panel.

## 2 Numerical Application: FEM Models

The stiffened panel, analysed in the frame of the present paper, is fully representative of a structural component of the forward zone of a regional airplane's fuselage. The small effective curvature of a real fuselage panel has been neglected. This structural component is typically involved in composite repair processes on in-service airplanes. Among the other techniques, stepped bonded patch is one of the most used repair approaches in aeronautical application; this is the reason why, this technique has been selected in the frame of the performed numerical study on repaired composite structures.

The pristine analysed reinforced composite panel is made of a laminated skin stiffened by two longitudinal omega stringers. Details on the geometry are given in Fig. 1.

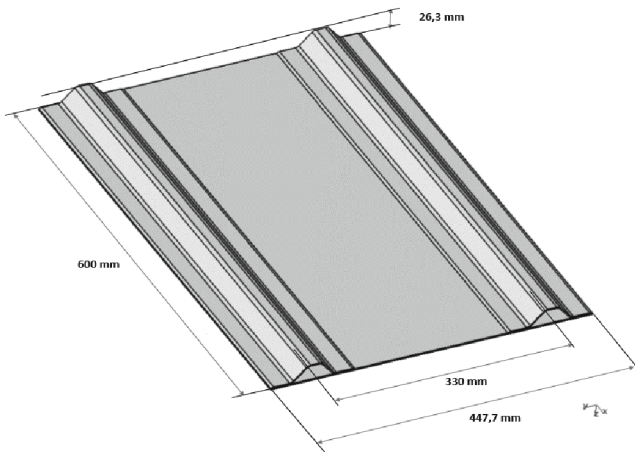


**Fig. 1.** Reference panel geometry and dimensions

In the repaired configuration, repair was simulated as a stepped bonded patch with an external ply on the skin's external surface as shown in Fig. 2a. Repair scheme involves six plies and has a circular shape. Circular patches have been placed at skin's centre starting from a 25 mm radius. The radius of the circular patches has been increased of 6 mm for each lamina moving toward the external surface, allowing plies overlapping (see Fig. 2b and 2c).

The FEM model has been discretized in Abaqus. The skin has been modelled by using 4-noded shell elements with a full integration scheme (S4); while stringers have been modelled by using reduced integration 8-nodes quadrilateral continuum shell elements

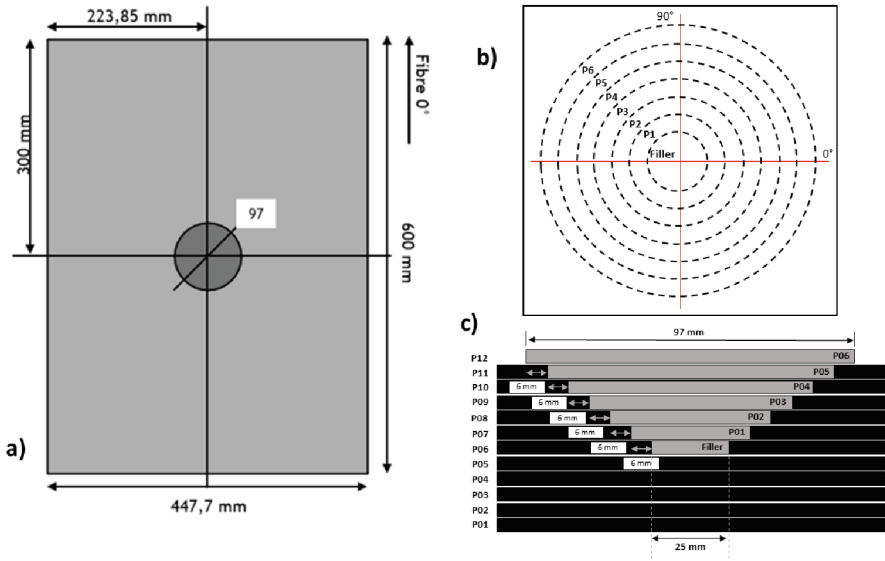


**Fig. 2.** a) Repair patch location; b) Patch scheme; c) Plies reference

with hourglass control (SC8R). In the patch region, discretization at ply-level has been used, where each ply has been modelled by considering concentric circles. Details on the repaired stiffened panel FEM model are presented in Fig. 3.

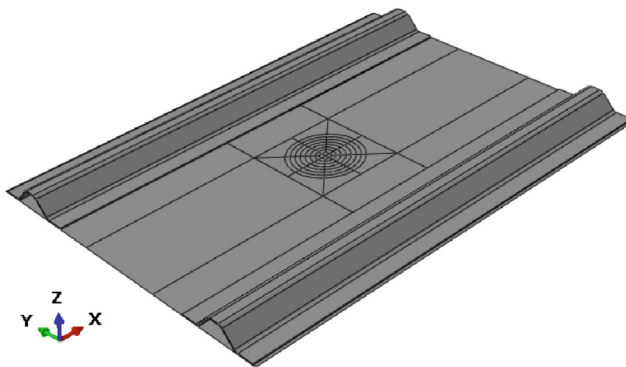


**Fig. 3.** Repaired stiffened Panel's FEM model

The stacking sequences, defined for skin, stringers and repair patch, are reported in Table 1. Material properties of the aerospace carbon/epoxy unidirectional tapes used for panel and the repair patch are presented in Table 2. The label MAT\_1 has been assigned to the material system CYCOM 977-2-34-24K IMS-196-T1-300 UD tape (IMS-977/2 PREPREG) used for the stiffened panel; the label MAT\_2 has been assigned the the material system SAERTEX U-C 204 g/m<sup>2</sup> 1220 mm UD tape/HEXCEL RTM6-2 infusion

resin used for repair patch. One edge of the panel has been clamped while compressive displacement has been applied on the opposite side.

**Table 1.** Stacking sequences of the stiffened panel's parts

PLY	STRINGER	SKIN	PATCH
1	90	0	90
2	-45	90	0
3	0	45	-45
4	45	-45	45
5	0	0	90
6	45	90	0
7	0	0	
8	-45	-45	
9	90	45	
10		90	
11		0	

### 3 Numerical Application: FEM Results

Linearized buckling analyses and static non-linear post-buckling analyses have been performed for both the pristine and the repaired configuration. In non-linear analyses, intra-laminar damage's onset and propagation have been evaluated using Hashin Failure Criteria, while Continuum Damage Mechanics Has been used as softening degradation process after damage's onset. Linearized buckling analyses have been performed on pristine and repaired panels to investigate the first buckling mode. Two very similar eigenvalues, as reported in Table 3, and buckling mode shapes have been found for the pristine and the repaired configuration. This demonstrated that the repair process did not affect the panel's critical instability load.

Non-linear static analyses under compressive loading condition Have been aimed to investigate the post-buckling compressive behaviour and damage onset during loading for both the pristine and the repaired configuration.

The numerically evaluated stiffness evolution trend, found for the two analysed panel's configurations are compared in Fig. 4.

According to Fig. 4, the stiffness evolution shows similar trends for the pristine and the repaired configuration. Both configurations experience a stiffness reduction due to the first mode skin panel's buckling and later, increasing the applied compressive load, due to the stringers' buckling. The analysis of the Stiffness's evolution trends points out that the repair process did not affect the global panel's stiffness.

The deformed shapes of the pristine and the repaired configuration at the maximum applied displacement are compared in Fig. 5.

**Table 2.** Composite mechanical properties: MAT\_1 for panel; MAT\_2 for repair patch

PROPERTIES	VALUE	
	MAT_1	MAT_2
Thickness	0.186 mm	0.200 mm
Orthotropic properties	E11 = 152310 MPa	E11 = 138000 MPa
	E22 = 8730 MPa	E22 = 7660 MPa
	E33 = 8730 MPa	E33 = 7660 MPa
	G12 = 3940 MPa	G12 = 3770 MPa
	G13 = 3940 MPa	G13 = 3770 MPa
	G23 = 2840 MPa	G23 = 2440 MPa
	$V_{12} = 0.34$	$V_{12} = 0.34$
	$V_{13} = 0.34$	$V_{13} = 0.34$
Strength	Xt = 2459.5 MPa	Xt = 2541.9 MPa
	Xc = 813.6 MPa	Xc = 726.3 MPa
	Yt = 87 MPa	Yt = 45.2 MPa
	Yc = 85.2 MPa	Yc = 131 MPa
	S = 99.9 MPa	S = 90.4 MPa
In-plane fracture energies	G1t = 91.6 kJ/m <sup>2</sup>	G1t = 91.6 kJ/m <sup>2</sup>
	G1c = 79.9 kJ/m <sup>2</sup>	G1c = 79.9 kJ/m <sup>2</sup>
	G2t = 0.8 kJ/m <sup>2</sup>	G2t = 0.6 kJ/m <sup>2</sup>
	G2c = 1.1 kJ/m <sup>2</sup>	G2c = 2.4 kJ/m <sup>2</sup>

**Table 3.** First mode buckling eigenvalues for pristine and repaired model

Model	Eigenvalue
Pristine	0.20352
Repaired	0.21252

Figure 5 shows that the presence of the circular patches, at the centre of the bay, varies the local stiffness nearby the repaired zone with a consequent variation of the deformed shape of the panel under compression. This happens, despite the patch has got the same stacking sequence of the removed plies from the pristine structure. Actually, the reduced material properties of the patches induce a variation in the panel's local mechanical performance and, consequently, in its deformed shape.

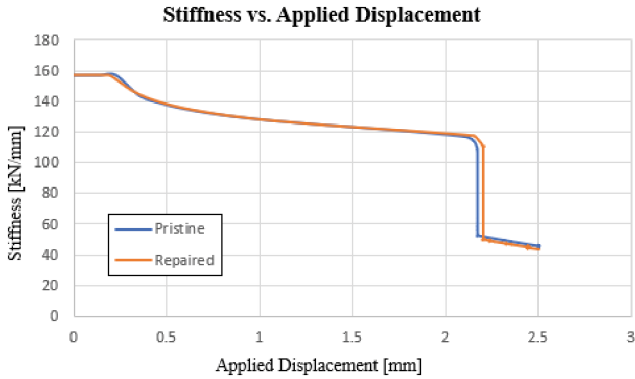


**Fig. 4.** Stiffness – Applied Displacement curve for pristine and repaired configuration

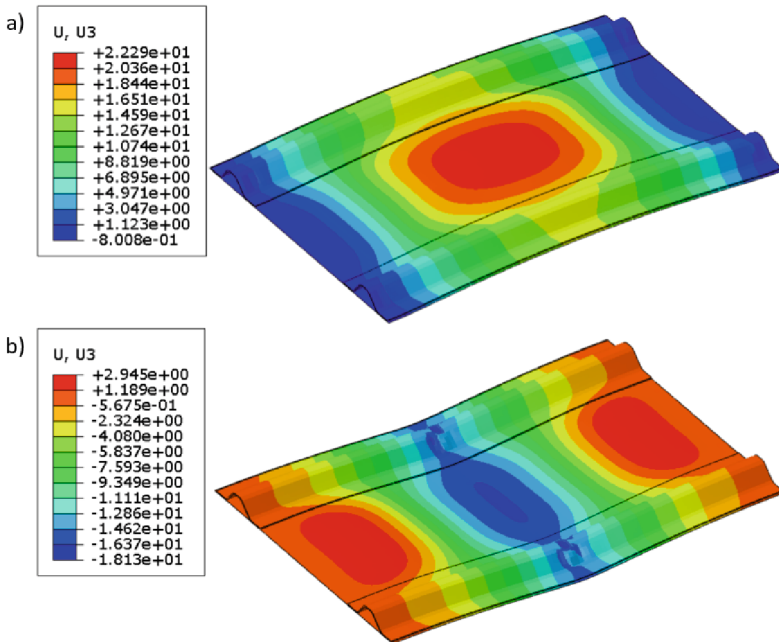


**Fig. 5.** Post-buckling panel’s deformed shapes – Out-of-plane displacement: **a)** pristine configuration; **b)** repaired configuration

Intra-laminar damages have been also evaluated for both the pristine and the repaired configuration. The numerical analyses, performed on the pristine panel, show intra-laminar damages for fiber and matrix failure nearby stringers’ edge, as shown in Fig. 6. The numerical analyses performed on the repaired panel, show intra-laminar damages with fiber and matrix failure at the center of the stringers, as shown in Fig. 7. No damage has been found in the patch’s zone. Differences in intralaminar damage location are related to the differences in stiffness distribution for the two analysed configurations.

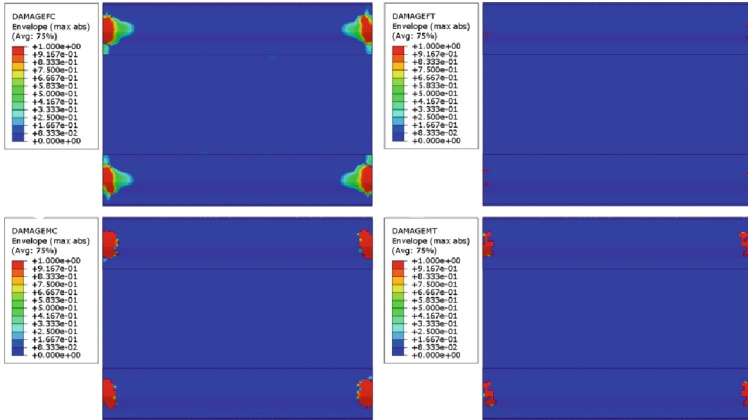


Fig. 6. Intra-laminar damages in pristine configuration

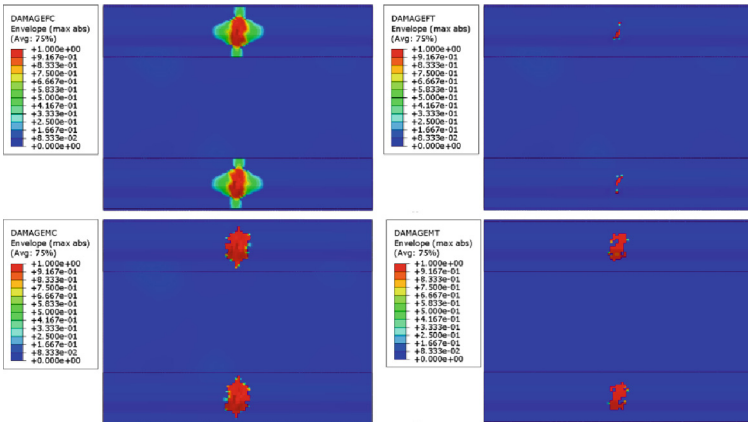


Fig. 7. Intra-laminar damages in repaired configuration

## 4 Conclusions

Repair revealed to be the most cost-effective approach to deal with composite damaged structural components by fully restore their structural integrity without reducing global stiffness and without replacing components. Actually, repairs contribute to reduce maintenance periods for aircrafts. In this work, the numerical evaluation of the compression behaviour of an omega stiffened composite panel, in pristine and repaired configuration, allowed to perform a preliminary study of the repair's effect on mechanical performances of an aeronautical composite component. The adopted repair scheme has been demonstrated able to correctly restore the initial global panel's stiffness and to preserve the global behaviour, in terms of stiffness evolution during the compressive loading phase. A variation of the local stiffness distribution has been found nearby the patch able to modify the deformed shape of the panel and consequently, the location of intralaminar

damage with respect to the pristine configuration. Patch's material properties and stacking sequence revealed to be key aspects for the effectiveness of a repair scheme finalised to restore mechanical performances of damaged composite components.

## References

1. Muffikhun, M., Yokozeki, T.: Experimental and numerical analysis of CFRP-SPCC hybrid laminates for automotive and structural applications with cost analysis assessment. *Composite Struct.* **263** (2016)
2. Yancey, R.: Challenges, opportunities, and perspectives on lightweight composite structures: aerospace versus automotive. In: Njuguna, J. (ed.) *Lightweight Composite Structures in Transport*, pp. 35–52. Woodhead Publishing (2016)
3. Katnam, K., Comer, A., Roy, D., Da Silva, L., Young, T.: Composite repair in wind turbine blades: an overview. *J. Adhesion* 113–139 (2015)
4. Psarras, S., Loutas, T., Galanopoulos, G., Karamadoukis, G., Sotiriadis, G., Kostopoulos, V.: Evaluating experimentally and numerically different scarf-repair methodologies of composite structures. *Int. J. Adhesion Adhesives* **97** (2020)
5. Goossens, S., Berghmans, F., Khodaei, Z., Lambinet, F., Karachalios, E., Saenz-Castillo D., Geernaert, T.: Practicalities of BVID detection on aerospace-grade CFRP materials with optical fibre sensors. *Composite Struct.* (**259**) (2021)
6. Nishino, M., Aoki, T.: Nonlinear analysis and damage monitoring of a one-sided patch repair with delamination. *Compos. Struct.* **73**, 423–431 (2006)
7. Andrew, J.J., Arumugam, V., Bull, D., Dhakal, H.: Residual strength and damage characterization of repaired glass/epoxy composite laminates using A.E. and D.I.C. *Composite Struct.* **152**, 124–139 (2016)
8. Azzam, A., Li, W.: The low-velocity impact damage resistance of the composite structures - a review. *Rev. Adv. Mater. Sci.* 127–145 (2015)
9. Sun, C., Zhao, W., Zhou, J., Altenaiji, M., Cantwell, W., Wang, Q., Guan, Z.: Mechanical behaviour of composite laminates repaired with a stitched scarf patch. *Composite Struct.* **255** (2021)
10. Sałaciński, M., Orzechowski, P., Chalimoniuk, M., Leski, A.: Analysis of bonding layer quality in repair process of aircraft composite structure after impact damage. *Composites Theory Pract.* 134–141 (2020)



# 3D Printed Carbon PEEK - Influence of Printing Strategy on Tensile Performances

Sara Varetti<sup>1</sup> (✉), Nicola Gallo<sup>2</sup>, Ignazio Scavo<sup>2</sup>, and Stefano Corvaglia<sup>2</sup>

<sup>1</sup> Leonardo Labs, Materials, Grottaglie, TA, Italy  
sara.varetti.ext@leonardo.com

<sup>2</sup> Leonardo Aerostructures, Grottaglie, TA, Italy

**Abstract.** Additive Manufacturing, also called 3D printing, plays an increasingly important role in various sectors, including aerospace. Among the most used additive technologies there is Fusion Deposition Modeling (FDM), which offers various opportunities in the printing of thermoplastic polymers by layer-by-layer deposition of the material. Currently, the technology is mainly exploited as rapid prototyping, but the goal in the near future is to use it for the production of mechanical components, especially with high-performance technopolymers, such as Ultem, PEEK and Carbon PEEK [1, 2]. To achieve this goal, process control and repeatability of parts must be increased. Furthermore, the process parameters have to be optimized in order to reduce defects and porosities and to increase the bonding between adjacent filaments within the same layer and between layers. The performances of parts produced in FDM are influenced by many process parameters, such as the material deposition speed, the printing strategy, the layer thickness, the nozzle and working chamber temperature. In the present work the printing strategies of the specimens in Carbon PEEK were studied and their influence on the mechanical tensile performance were evaluated [3]. The specimens were produced by a Roboze Argo 500 3D printer with four different filament deposition strategies (printing orientation: 0°, 90°, ±45°, 0/90°), nozzle temperature of 450 °C, chamber temperature of 180 °C, layer thickness of 0.225 mm, nozzle diameter of 4 mm and 100% infill.

**Keywords:** Thermoplastic materials · Tensile tests · Carbon PEEK · 3D printing

## 1 Introduction

Additive Manufacturing (AM) includes a series of technologies that allow the production of parts layer by layer, by deposition or solidification of the material only where it is necessary for the geometry of the component, with a great saving of waste. It allows to work with very complex shapes and different materials as metals, polymers, ceramics and composites [3–6]. The most widespread AM technology for the realization of polymeric components is Fusion Deposition Modeling (FDM), which works with thermoplastics. The technique consists in extruding a filament of the desired material through a nozzle: the filament is heated by a resistance beyond its softening point and pushed through the nozzle, which moves depositing the material layer by layer. The movement of the



deposition head is coordinated by a file (.gcode) that contains the information necessary to build the geometry of the component [7–9]. FDM technology is currently very common on the market, particularly in the area of competence of low-cost 3D printing machines for the production of prototypes and models, and can produce parts in some materials that are simple to process and inexpensive, such as PLA (polylactic acid) and ABS (acrylonitrile-butadiene-styrene) [10–12]. Although less common, there are FDM machines for industrial use, able to work on materials that are difficult to print such as PEEK (polyetheretherketone), Carbon PEEK (polyetheretheretherketone with short carbon fibers), PEI (polyetherimide) and Nylon. These materials have high mechanical performance and good resistance to high temperatures, therefore they are suitable for the production of finished mechanical parts and tools in various sectors of interest, including aerospace [13–16].

In the present work a mechanical characterization was carried out on C-PEEK specimens produced with a Roboze Argo500 machine in order to optimize the process parameters and verify which variable has a greater influence on the parts produced.

## 2 Materials and Methods

A campaign of C-PEEK specimens was carried out using a filament that incorporates 10% of carbon fiber reinforcement into a PEEK matrix for increase strength. The C-PEEK is very interesting for aerospace sector due to his long-term performance up to 240 °C and his exceptional chemical resistance. The samples were produced with the Roboze Argo500, a 3D printer that uses Fused Deposition Modeling (FDM) technology, focused on the production of technopolymers (as PEEK, C-PEEK, Ultem and others). The machine has a working chamber that can be heated up to 180 °C and with a volume of 500x500x500 mm<sup>3</sup>.

The test campaign consists of tension testing C-PEEK specimens produced with four different printing strategies (0°, 90°, ±45°, 0/90, using two machines for the production Argo500 and three batches of filament. The test matrix is shown in the Table 1, which lists the nominal dimensions of the specimens according with the reference standard (ASTM D3039), the number of batches and printers and the number of specimens. Each printer and batch combination has been identified by a different job, as shown in Table 2. All the specimens were produced flat on the building plate and the supports are removed by CNC machining. The tabs used are in Aluminium alloy, with dimension according to ASTM D3039, and were attached to the specimens through a two-component epoxy glue.

According with ASTM D3039, all specimens were subjected to tensile test with constant traverse speed of 2 mm/min by a MTS machine with a load cell of 250 kN. The Ultimate strength was calculated for all the specimens as maximum load on nominal cross section. The E modulus was calculated by extensometer for Job 1, 3, 4, 5 and 6, while for job 2 the E modulus and the Poisson ratio were calculated by Strain Gage (SG).

## 3 Results and Discussion

Figure 1 and Fig. 2 allow to analyze the results of Job 2 which was taken as a reference to compare the different printing strategies. The highest values of ultimate strength and

**Table 1.** Test matrix for Unnotched Tension (UNT).

Printing strategy [deg]	Nominal thickness [mm]	Nominal width [mm]	Nominal length [mm]	N. of batches	N. of printers	N. of specimens
0	4.05 (18 layers)	25.4	254	3	2	6
90	4.05 (18 layers)	25.4	254	3	2	6
$\pm 45$	4.05 (18 layers)	25.4	254	3	2	6
0/90	4.05 (18 layers)	25.4	254	3	2	6

**Table 2.** Jobs features.

Job 1	Job 2	Job 3	Job 4	Job 5	Job 6
Printer 1	Printer 1	Printer 1	Printer 2	Printer 2	Printer 2
Batch 1	Batch 2	Batch 3	Batch 1	Batch 2	Batch 3

elastic modulus  $E$  are for the specimens printed with a  $0^\circ$  strategy, with the filaments deposited in the same direction in which the load acts during the test. The mechanical strength is given by the contribution of the extruded filament and in part by the welding between the filaments within the same layer and between one layer and another. From the stress-strain curve (Fig. 1) it is possible to note the presence of a plastic deformation section of the specimen before breaking at the maximum load. The lowest ultimate strength and elastic modulus  $E$  values were instead recorded for the specimens with printing strategy at  $90^\circ$ , with respect to the direction of the tension load. In these samples the mechanical strength is given by the lateral welding of the deposited filaments, which is much weaker than the filament along the deposition direction. There is a net failure along the cross section and little deformation before breaking. The  $\pm 45^\circ$  and  $0/90^\circ$  printing strategies are the intermediate cases. The  $0/90^\circ$  specimens have a higher ultimate strength and modulus value than the  $45^\circ$  ones thanks to the contribution of the  $0^\circ$  oriented layers, but the breaking mechanism is similar to that of the  $90^\circ$  specimens: net failure along the cross section and little deformation before breaking. The  $45^\circ$  specimens, on the other hand, show a failure in several points and a greater plastic deformation before failure, which occurs at higher deformation values compared to the specimens of the other strategies.

Comparing the Poisson ratio values, it is possible to note that the most evident thinning occurs in the  $45^\circ$  specimens, thanks to the alignment of the filaments during the test, followed by the  $0^\circ$  specimens whose value is given by the thinning of the

single connected filaments between them by the intermediate weld. The 90° and 0/90° specimens exhibit low thinning during the test.

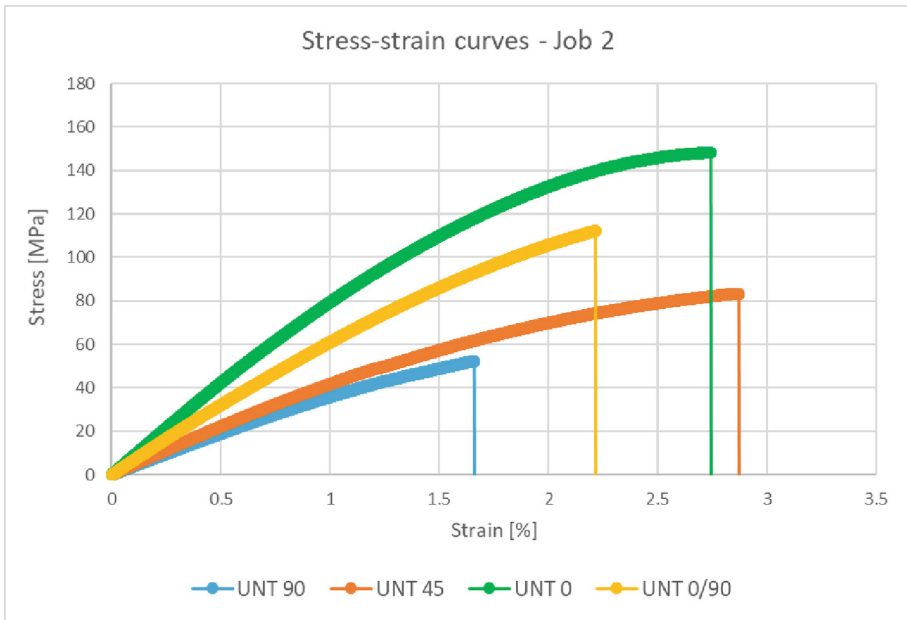


**Fig. 1.** Results of tensile tests on Job2 specimens in terms of a) Ultimate strength, b) elastic modulus.

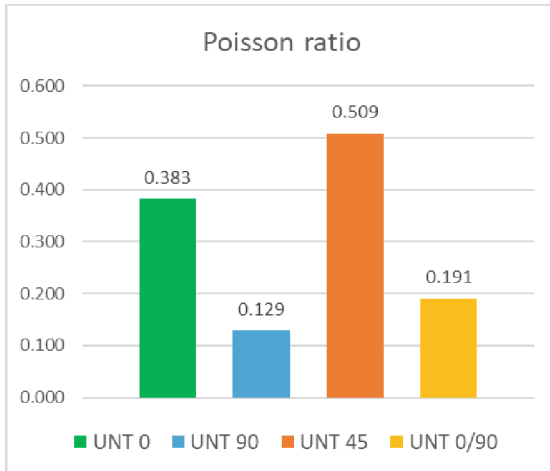


**Fig. 2.** Results of tensile tests on Job2 specimens in terms of Poisson ratio.

From the graph in Fig. 3 is possible to see that the tested samples printed at  $\pm 45^\circ$  have a low dispersion of the data within the same job (low standard deviation), while

the results are a little different between the jobs: the results from Job 6 are a little higher (average ultimate strength of 92 MPa) and for the Job 5 a little lower (average ultimate strength of 81 MPa). The data from Job 1, 2 and 3 (produced with printer 1, as shown in Table 2) seems more uniform compared to the data of the other three.

The graph in Fig. 4 concerns the tests on the specimens printed with the  $0^\circ$  strategy. The dispersion of data within the single job is higher than the dispersion at  $45^\circ$ , furthermore it can be noted that some specimens have much lower Ultimate Strength values than the total average. In particular, one of the specimens of Job 5 and all the specimens of Job 4 break at lower loads than the other jobs: the average value of Ultimate Strength for the specimens of Job 4 is 111 Mpa, while the average value for the Job 3 is 154 MPa. Also for  $0^\circ$  specimens the results from the Jobs 1, 2 and 3 seems more uniform and repeatable. All specimens that have broken at lower loads have a very high internal porosity and very marked surface roughness (Fig. 6a). The phenomenon may be due to the uneven deposition of material by the nozzle and the consequent release of lumps that are dragged by the nozzle, forming grooves in the specimen during the deposition of new material.

Finally, the graph in Fig. 5 shows the results for the specimens printed at  $90^\circ$ . The dispersion of data within the individual Jobs is higher than that seen for the other strategies. This is due to the fact that the breaking mechanism for the  $90^\circ$  specimens is given by the failure of the lateral welds between the filaments that are the least resistant area. Despite this variability of the results, a group of specimens has an Ultimate Strength above the average value: one of the specimens of Job 1 (81 MPa) and all the specimens of Job 4 (average of 78 MPa). These values are higher than Ultimate Strength of the other Jobs: for Job 3, for example, there is a failure at 51 MPa. This is due to good welds between filaments and to few defects (Fig. 6b), thus allowing the specimen to break at much higher loads. This improvement may be due to a higher effective extrusion temperature than the set one, which allowed the filament to better adhere to adjacent points.

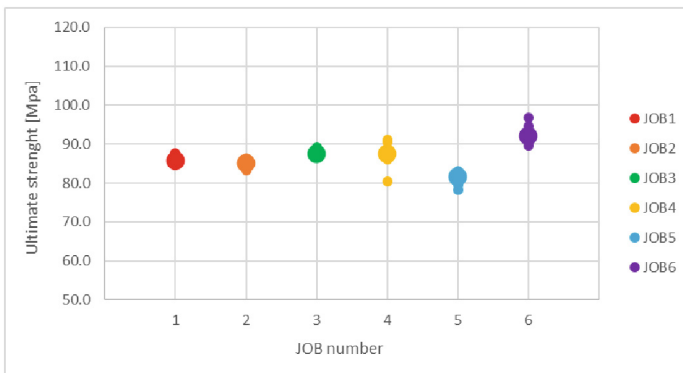


**Fig. 3.** Ultimate strength for  $\pm 45^\circ$  specimens.

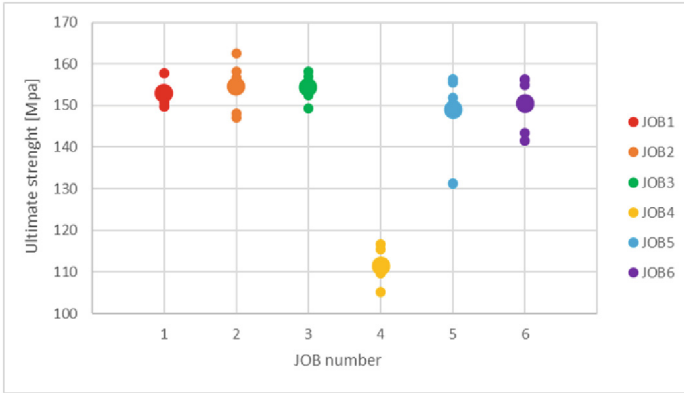


**Fig. 4.** Ultimate strength for 0° specimens.

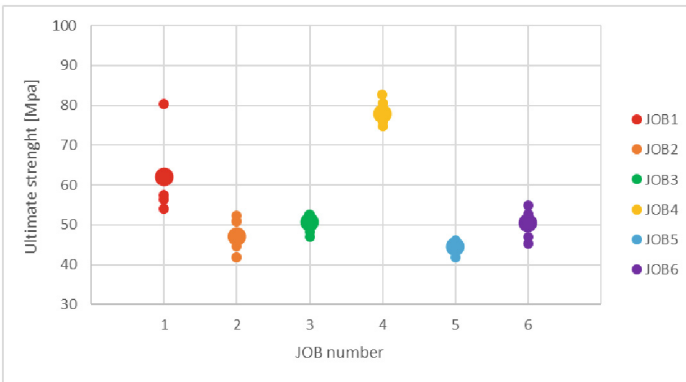
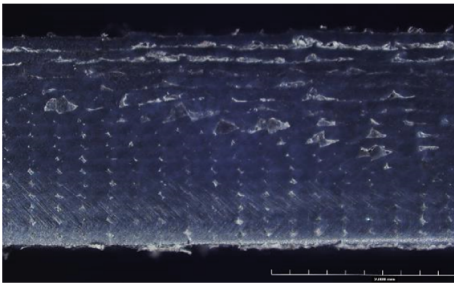
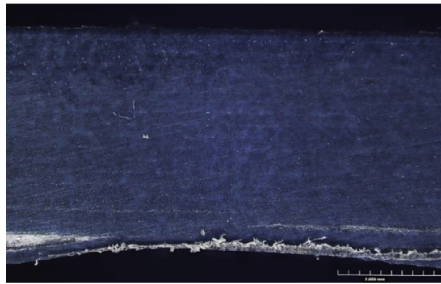


**Fig. 5.** Ultimate strength for 90° specimens.



a)



b)

**Fig. 6.** Cross-section images by Optical Microscope of the specimens from Job 4 printed with a) 0° strategy (Ultimate Strength of 105 MPa) and b) 90° strategy (Ultimate Strength of 81 MPa).

## 4 Conclusions

From this preliminary characterization of the Carbon PEEK printed with the Roboze Argo500 machine, it was possible to compare four different flat printing strategies of the specimens. The specimens with the best mechanical performance are those printed at  $0^\circ$ , followed by those with  $0/90^\circ$  stratification, at  $\pm 45^\circ$  and finally by those at  $90^\circ$ . The specimens were printed in six different Jobs by varying three batches of material and two machines of the same type, to observe the influence of these factors on mechanical tests. The greatest influence is given by the machine used: it seems that the specimens produced with Printer 1 (Jobs 1, 2 and 3) have less dispersed and more repeatable results than those of the specimens obtained with Printer 2 (Jobs 4, 5 and 6). This is especially visible for the specimens printed at  $0^\circ$  and at  $\pm 45^\circ$ . Some specimens printed at  $0^\circ$  showed lower Ultimate Strength than average value due to an anomalous presence of pores inside, which greatly reduced the resistant section. On the other hand, a group of  $90^\circ$  specimens showed above average results, thanks to a very dense internal structure and good welds between the filaments. Both of these results can be traced back to differences in the extrusion temperature and more generally to the machine hardware. Better process control would be required to ensure repeatability of results on all machines.

## References

1. Thiruchitrabalam, M., Bubesh Kumar, D., Shanmugam, D., Jawaid, M.: A review on PEEK composites – manufacturing methods, properties and applications. *Mater. Today: Proc.* **33**, 1085–1092 (2020)
2. Jafferson, J.M., Chatterjee, D.: A review on polymeric materials in additive manufacturing. *Mater. Today: Proc.* **46**, 1349–1365 (2021)
3. Dul, S., Fambri, L., Pegoretti, A.: Fused deposition modelling with ABS–graphene nanocomposites. *Composit. Part A* **85**, 181–191 (2016)
4. Lay, M., Thajudin, N.L.N., Hamid, Z.A.A., Rusli, A., Abdullah, M.K., Shuib, R.K.: Comparison of physical and mechanical properties of PLA, ABS and nylon 6 fabricated using fused deposition modeling and injection molding. *Composit. Part B* **176**, 107341 (2019)
5. Sheoran, A.J., Kumar, H.: Fused Deposition modeling process parameters optimization and effect on mechanical properties and part quality: Review and reflection on present research. *Mater. Today: Proc.* **21**, 1659–1672 (2020)
6. Liu, Z., Lei, Q., Xing, S.: Mechanical characteristics of wood, ceramic, metal and carbon fiber-based PLA composites fabricated by FDM. *J. Mater. Res. Technol.* **8**(5), 3741–3751 (2019)
7. Giri, J., Chiwande, A., Gupta, Y., Mahatme, C., Giri, P.: Effect of process parameters on mechanical properties of 3d printed samples using FDM process. *Mater. Today: Proc.* <https://doi.org/10.1016/j.matpr.2021.04.283>
8. Berretta, S., Davies, R., Shyng, Y.T., Wang, Y., Ghita, O.: Fused Deposition Modelling of high temperature polymers: exploring CNT PEEK composites. *Polym. Testing* **63**, 251–262 (2017)
9. Patil, P., Singh, D., Raykar, S.J., Bhamu, J.: Multi-objective optimization of process parameters of Fused Deposition Modeling (FDM) for printing Poly(lactic Acid) (PLA) polymer components. *Mater. Today: Proc.* **45**, 4880–4885 (2021)

10. Chen, K., Liguó, Y., Cui, Y., Jia, M., Pan, K.: Optimization of printing parameters of 3D-printed continuous glass fiber reinforced polylactic acid composites. *Thin-Walled Struct.* **164**, 107717 (2021)
11. Roy, R., Mukhopadhyay, A.: Tribological studies of 3D printed ABS and PLA plastic parts. *Mater. Today: Proc.* **41**, 856–862 (2021)
12. Gunasekaran, K.N., Vishaal Aravinth, C.B., Muthu Kumaran, K., Madhankumar, S., Kumar, P.: Investigation of mechanical properties of PLA printed materials under varying infill density. *Mater. Today: Proc.* **45**, 1849–1856 (2021)
13. Ding, S., Zou, B., Wang, P., Ding, H.: Effects of nozzle temperature and building orientation on mechanical properties and microstructure of PEEK and PEI printed by 3D-FDM. *Polym. Testing* **78**, 105948 (2019)
14. Chang, B., Li, X., Parandoush, P., Ruan, S., Shen, C., Lin, D.: Additive manufacturing of continuous carbon fiber reinforced poly-ether-ether-ketone with ultrahigh mechanical properties. *Polym. Testing* **88**, 106563 (2020)
15. El Magri, A., Vanaei, S., Vaudreuil, S.: An overview on the influence of process parameters through the characteristic of 3D-printed PEEK and PEI parts. *High Perform. Polym.* 1–19. <https://doi.org/10.1177/09540083211009961journals.sagepub.com/home/hip>
16. Jayaraghul, T.K., Karthik, K., Yaswanth, A., Venkatesan, M.: Nozzle flow characteristics of P.E.E.K (Poly-ether ether ketone) material used in 3D-printing. *Mater. Today: Proc.* **44**, 2963–2967 (2021)



# Influence of Process Parameters of 3D Printed PEEK on Crystallinity and Mechanical Performances

Valentina Trimini<sup>1,2</sup>(✉), Sara Varetto<sup>2</sup>, Gianluca Percoco<sup>1</sup>, Stefano Corvaglia<sup>3</sup>, Nicola Gallo<sup>3</sup>, and Ignazio Scavo<sup>3</sup>

<sup>1</sup> Dipartimento di Meccanica, Matematica e Management, Politecnico di Bari, Via E. Orabona 4, Bari, Italy

valentina.trimini@poliba.it

<sup>2</sup> Leonardo Lab, Materials, Grottaglie, TA, Italy

<sup>3</sup> Leonardo Aerostrutture, Grottaglie, TA, Italy

**Abstract.** Additive manufacturing of high-performance polymers has a great potential for future metal replacement due to several advantages that it offers [1]. Among the most used additive technologies there is Fusion Deposition Modelling (FDM), which offers various opportunities in the printing of thermoplastic polymers by layer-upon-layer deposition [2]. The FDM process of poly(ether ether ketone), PEEK, is a challenging task due to the need of high temperature of printing [3]. In the present work several printing parameters for PEEK specimens were studied and their influence on crystallinity and mechanical tensile performance was evaluated.

**Keywords:** Thermoplastic materials · tensile tests · thermal tests · PEEK · 3D printing

## 1 Introduction

Additive manufacturing (AM) has shown significant potential in reducing both the time and cost of product development. Among AM technologies, FDM is one of the most typically used for prototyping because it enables the production of complex geometries hard in achieving by subtractive manufacturing. Typically, the performances of parts produced with FDM are influenced by many process parameters, such as the material deposition speed, the orientation of the part, the layer thickness, the nozzle and working chamber temperature [4]. These issues are even more evident when the process is applied to high-performance polymers such as PEEK owing to their semicrystalline nature, high melting point and viscosity. Therefore, AM processing of these materials present limitations associated with large thermal gradients, residual stress buildup, and interlayer adhesion [5]. However, PEEK, due to its excellent mechanical strength, thermal stability and good chemical resistance, has attracted increased interest for weight savings and metal replacement in a wide range of fields, including aerospace, [6, 7] and automotive. [8] For these reasons, in the last years, several studies were carried out to understand



the process parameters to be optimized in order to obtain end-use FDM-printed PEEK parts. It's well known that the use of base plates and chamber heating are essential for the successful fabrication of ideal-performance PEEK components with good crystallinity, high interlayer adhesion and excellent mechanical properties [9–11]. Yang et al. reported that the crystallinity and the mechanical performance are highly dependent on the ambient temperature, that should be higher than glass transition temperature [12]. Wang et al. observed that the density and surface quality of printed PEEK parts can be improved by decreasing the layer thickness and printing speed. Furthermore, for the authors, the nozzle diameter should be, at least, 1.5 times the value of layer thickness to assure strong adhesion between printed polymer filaments [13]. Rahman et al. explored three different raster orientations and their results showed that the best orientation for PEEK printing is 0° (consistent with the longest edge) [14]. Generally, many studies reported that print at a nozzle temperature higher than 400 °C improves the adhesion between extruded filaments both inter- and intra-layer [10, 13, 15]. Starting from the results of the above mentioned works, in the present study we chose to keep printing orientation at 0°, layer thickness of 0.225 mm, nozzle diameter of 4 mm and 100% infill constant, and to vary printing speed, nozzle and chamber temperature in order to evaluate the changes in crystallinity and tensile properties of FDM-printed PEEK parts.

## 2 Materials and Methods

In this, the specimens were produced by using a Roboze PEEK filament with a diameter of 1,75 mm and a Roboze Argo 500 3D-printer. In particular, we decided to investigate two nozzle temperature (440 and 450 °C), three chamber temperature (25, 100 and 160 °C) and three printing speeds (1500, 2000 and 2600 mm/min).

The samples were 250 mm × 25 mm × 4mm specimens for tensile test according to ASTM D3039 standard. Tensile testing was carried out by using an MTS Landmark servo hydraulic tests system machine with a 250 kN load cell. Testing speed for all samples was 2 mm/min. The extensometer was used to calculate the Young's Modulus.

The thermal properties were studied by differential scanning calorimetry (PerkinElmer Diamond DSC). The degree of crystallinity ( $\chi$ ) of PEEK was calculated by the following equation:

$$\chi = \frac{\Delta H_m - \Delta H_{cc}}{\Delta H_m^{100\%}} \times 100 \quad (1)$$

where:  $\Delta H_m$  is the melting Enthalpy,  $\Delta H_{cc}$  is the cold crystallization Enthalpy and  $\Delta H_m^{100\%}$  is the melting Enthalpy of 100% crystalline PEEK (about 130 J/g).

## 3 Results and Discussion

### 3.1 Thermal Characterization

**Effect of Chamber Temperature on Crystallinity.** The effect of chamber temperature on the PEEK degree of crystallinity ( $\chi\%$ ) was first evaluated by keeping the nozzle

temperature constant at 450 °C. This temperature made it possible to print even at a chamber temperature of 25 °C without the risk of clogging the nozzle. It was chosen to study this effect at ambient temperature (25 °C) and at temperatures below and above the PEEK glass transition temperature ( $T_g \approx 145$  °C), 100 °C and 160 °C respectively. However, the print at 25 °C did not allow proper adhesion to the printing bed and the samples resulted embarked due to high residual stress.

The thermal properties of both virgin PEEK filament and printed specimens were evaluated by a DSC heating run (from 50 °C to 400 °C), under 50 ml/min nitrogen flow at a rate of 10 °C/min. To determine the crystallization temperature ( $T_c$ ) of virgin PEEK, an additional cooling step was carried out under the same nitrogen flow and scan rate. As a reference, all the characteristic transition temperatures and the calculated degree of crystallinity for virgin PEEK are reported in Table 1.

**Table 1.** Degree of crystallinity and transition temperatures of virgin PEEK filament corresponding to DSC heating and cooling scans.

$T_g(^{\circ}\text{C})$	$T_m(^{\circ}\text{C})$	$T_c(^{\circ}\text{C})$	$\chi\%$
149.4	332.4	288.5	27.5

The DSC scans of samples printed at the same nozzle temperature (450 °C) and printing speed (2000 mm/min) are reported in Fig. 1, to show the material thermal transitions as the chamber temperature changes. It is important to note that the samples printed at a chamber temperature of 25 °C and 100 °C exhibit a cold crystallization exothermic peak at around 170 °C. This phenomenon is a reordering of the molecular chains due to increased mobility during the heating step: this extra energy helps the formation of more crystalline regions. By means Eq. (1) it was possible to calculate the initial crystallinity of these samples (see Table 2). In all cases the chamber temperature has a greater influence on crystallinity than the printing speed: the higher the chamber temperature, the higher the PEEK degree of crystallinity is. This behaviour is due to a phenomenon called isothermal crystallization which occurs the closer the ambient temperature is to that of PEEK crystallization ( $\approx 290$  °C) [12]. In this process, the amorphous polymer chains have sufficient energy and time to crystallize in a degree close to the typical PEEK crystallinity (35%). In our case, by reducing the speed at 1500 mm/min and keeping the chamber at 160 °C, a degree of crystallinity of 33,3% was obtained.

**Effect of Nozzle Temperature on Crystallinity.** The effect of nozzle temperature was evaluated at two levels, 440 and 450 °C, for two chamber temperatures of 100 °C and 160 °C. The results, reported in Table 3, show that comparable degrees of crystallinity were obtained. Generally, the crystallinity decreases when the difference between the chamber and the nozzle temperature increases, due to the higher cooling rate of the extruded filament.

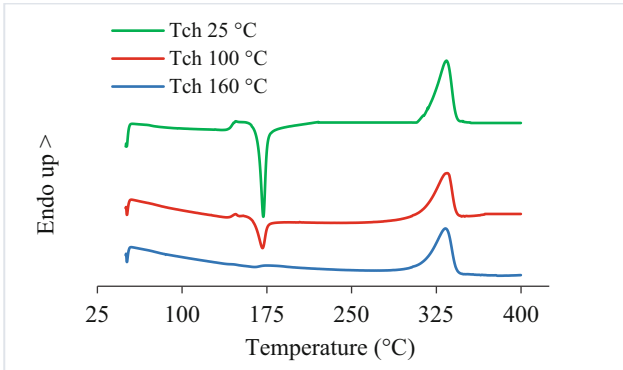


**Fig. 1.** DSC scans of samples printed at different chamber temperature.

**Table 2.** Degree of crystallinity of printed PEEK samples calculated from DSC heating scan.

Tnozzle = 450 °C			
T chamber (°C)	$\chi\%$ @ 1500 mm/min	$\chi\%$ @ 2000 mm/min	$\chi\%$ @ 2600 mm/min
25	16.7	15.1	13.9
100	24.5	24	19.9
160	33.3	29.5	27.5

**Table 3.** Degree of crystallinity of printed PEEK samples at different chamber and nozzle temperatures.

Tchamber = 100 °C			
T nozzle (°C)	$\chi\%$ @ 1500 mm/min	$\chi\%$ @ 2000 mm/min	$\chi\%$ @ 2600 mm/min
440	28.1	27.8	22.4
450	24.5	24	19.9
Tchamber = 160 °C			
T nozzle (°C)	$\chi\%$ @ 1500 mm/min	$\chi\%$ @ 2000 mm/min	$\chi\%$ @ 2600 mm/min
440	30.9	29.3	28.1
450	33.3	29.5	27.5

### 3.2 Mechanical Characterization

Tensile mechanical characterization was performed according to ASTM D3039 standard due to the similarity between the extruded filaments and unidirectional fibres in a composite when subjected to traction. Before to perform the tensile test, a sacrificial sample from each series was viewed in cross-section under the optical microscope (see Fig. 2). From these observations, it was evident the influence of the printing speed on the inter-

and intra-layer adhesion: the presence and the size of voids within the sample decrease by reducing the printing speed. Moreover, the adhesion is improved by increasing the nozzle temperature as well. All mechanical results are collected in Table 4. From these tests it was possible to notice that at a crystallinity lower than 25% the material becomes more ductile. In this work, the best tensile performances were obtained when the chamber temperature was at its maximum value and the printing speed at the minimum value tested, that allowed to obtain a degree of crystallinity higher than 30%.

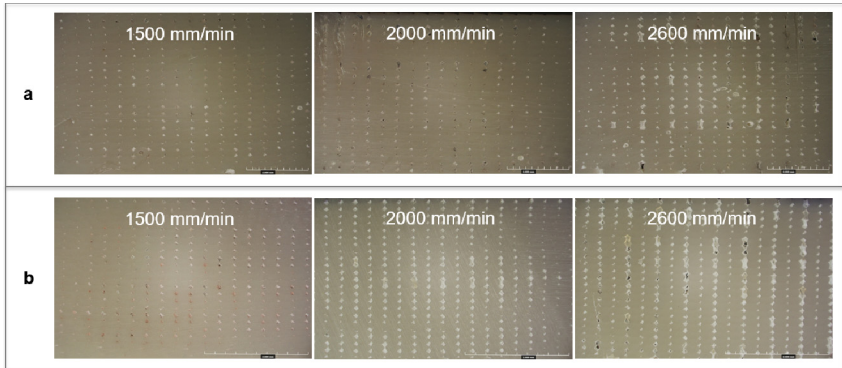


**Fig. 2.** Cross section of samples printed at a Tchamber of 160 °C and a Tnozzle of 450 °C (a) and 440 °C (b).

**Table 4.** Tensile test results.

Tnozzle (°C)	Tchamber (°C)	Sp (mm/min)	Average Tensile strength (Mpa)	Average Young Modulus E (MPa)	Average Elongaion at break (%)
450	160	1500	83.25 ± 0.62	3172.61 ± 22.10	4.95 ± 0.19
		2000	83.19 ± 1.19	3138.98 ± 8.20	5.15 ± 0.18
		2600	79.69 ± 0.87	3055.40 ± 12.91	4.96 ± 0.10
	100	1500	61.40 ± 0.20	2489.67 ± 6.52	5.13 ± 0.10
		2000	60.55 ± 0.89	2439.63 ± 41.12	5.12 ± 0.06
		2600	58.25 ± 0.51	2392.03 ± 41.98	5.05 ± 0.09
440	160	1500	80.87 ± 0.77	3042.45 ± 36.7	5.29 ± 0.04
		2000	79.92 ± 1.17	3011.59 ± 34.41	5.41 ± 0.08
		2600	76.76 ± 0.55	2904.02 ± 35.66	5.23 ± 0.05
	100	1500	59.64 ± 0.91	2423.70 ± 36.06	4.80 ± 0.08
		2000	59.60 ± 0.28	2415.35 ± 16.27	4.82 ± 0.06
		2600	56.62 ± 1.13	2272.50 ± 47.87	4.85 ± 0.12

## 4 Conclusions

In this work were studied the effects of printing parameters (nozzle and chamber temperatures and printing speed) on mechanical performances and crystalline characteristics. It was found that the chamber and the nozzle temperature are the most important parameters that can determine the crystallinity and the mechanical properties of PEEK. By changing these parameters, it is possible to obtain a more ductile or more rigid material according to its final application. Instead, the printing speed has a slight influence on the crystallinity, but it's very important its effect on the porosity and consequently on the mechanical performances of the final part. In the present study, the best tensile performances (tensile strength and Young's modulus of about 83 MPa and 3173 MPa respectively) and the higher degree of crystallinity (33,3%) were obtained by printing at nozzle temperature of 450 °C, chamber temperature of 160 °C and with a printing speed of 1500 mm/min. Probably, further improvements could be obtained by slightly increasing the nozzle temperature and reducing the printing speed.






## References

1. Holmes, M.: Additive manufacturing continues composites market growth. *Reinf. Plast.* **63**(6), 296–301 (2019)
2. Turner, B.N., Strong, R., Gold, S.A.: A review of melt extrusion additive manufacturing processes: I. process design and modeling. *Rapid Prototyp. J.* **20**(3), 192–204 (2014)
3. Rinaldi, M., Ghidini, T., Cecchini, F.: Additive layer manufacturing of poly(ether ether ketone) via FDM. *Composites 145 (Part B): Eng.* 162–172 (2018)
4. El Magri, A., Vanaei, S., Vaudreuil, S.: An overview on the influence of process parameters through the characteristic of 3D-printed PEEK and PEI parts. *High Perform. Polym.* **33**(8), 862–880 (2021)
5. Das, A., et al.: Current understanding and challenges in high temperature additive manufacturing of engineering thermoplastic polymers. *Additive Manuf.* **34**, 101218 (2020)
6. Murray, B.R., Doyle, A., Feerick, P.J., Semprimoschnig, C.O.A., Leen, S.B., 'O Br'adaigh, C.M.: Rotational moulding of PEEK polymer liners with carbon fiber/PEEK over tape-placement for space cryogenic fuel tanks. *Mater. Des.* **132**, 567–581 (2017)
7. Rival, G., Paulmier, T., Dantras, E.: Influence of electronic irradiations on the chemical and structural properties of PEEK for space applications. *Polym. Degrad. Stab.* **168**, 108943 (2019)
8. Pan, L., Liu, Z., Kızıltas, O., Zhong, L.: Carbon fiber/poly ether ether ketone composites modified with graphene for electro-thermal deicing applications. *Compos. Sci. Technol.* **192**, 108117 (2020)
9. Hu, B., Duan, X., Xing, Z.: Improved design of fused deposition modeling equipment for 3D printing of high-performance PEEK parts. *Mech. Mater.* **137**, 1–13 (2019)
10. Vaezi, M., Yang, S.: Extrusion-based additive manufacturing of PEEK for biomedical applications. *Virtual Phys. Prototyp.* **10**, 1–13 (2015)
11. Wu, W.Z., Geng, P., Zhao, J.: Manufacture and thermal deformation analysis of semicrystalline polymer polyether ether ketone by 3D printing. *Mater. Res. Innov.* **18**(5), 12–16 (2014)
12. Yang, C., Tian, X., Li, D.: Influence of thermal processing conditions in 3D printing on the crystallinity and mechanical properties of PEEK material. *J. Mater. Process. Technol.* **248**, 1–7 (2017)
13. Wang, P., Zou, B., Xiao, H.: Effects of printing parameters of fused deposition modeling on mechanical properties, surface quality, and microstructure of PEEK. *J. Mater. Process. Technol.* **271**, 62–74 (2019)

14. Rahman, K. M., Letcher, T., Reese, R.: Mechanical Properties of Additively Manufactured PEEK Components Using Fused Filament Fabrication. In: IMECE on Proceedings, ASME, Houston (2015)
15. Cicala, G., Latteri, A., Del Curto, B., Lo Russo, A., Recca, G., Farè, S.: Engineering thermoplastics for additive manufacturing: a critical perspective with experimental evidence to support functional applications. *J. Appl. Biomater. Funct. Mater.* **15**, 10–18 (2017)



# Machining Approach for Recycling of CFRP Laminates

Massimo Durante , Luca Boccarusso , Dario De Fazio ,  
Antonio Formisano  <sup>(✉)</sup>, and Antonio Langella 

Department of Chemical, Materials and Production Engineering, University of Naples Federico II, Piazzale Tecchio 80, 80125 Naples, Italy  
aformisa@unina.it

**Abstract.** The use of carbon fibre reinforced plastics (CFRPs) is gaining more and more importance in many industrial fields in which the structures must guarantee high performance and lightness. As a consequence, it is necessary to develop sustainable and efficient recycling solutions to manage them at the end of their life. In light of this, a machining approach for the recycling of CFRP laminates is presented in this work; in particular, the cutting strategies were investigated for the effective reuse of composite structures after their end of life. CFRP laminates were obtained by unidirectional carbon fibre prepregs and, then, were worked through the peripheral down-milling process for different spindle speed and feed rate values. The cutting power and the specific cutting energy were estimated through the recording of the cutting forces and the chips from the milling process were classified as a function of their dimensions. This study sets the stage for a later idea of using this recycling strategy for the manufacture of chip-based composite materials.

**Keywords:** Recycling · CFRP · Peripheral milling · Specific cutting energy

## 1 Introduction

The development of CFRPs is attracting relevant attention in recent decades because they combine excellent mechanical properties and lightness, due to the high strength-to-weight ratio of the carbon fibres (CF), which represent the load-carrying elements in the polymer matrix.

CFRP is frequently used in place of the most common metals and alloys [1] for the manufacture of components with applications in different industrial fields, like aerospace, automotive, construction, and energy [2]. On the other hand, the high demand for CF and CFRP generates a dramatical increase in the waste of them-based products; therefore, the management of these products at the end of their service life has been raising a strong interest [3]: for example, the European directive 2000/53/EC is oriented to the recovery, reuse, and recycling of almost all the total vehicle components at the end of their life cycle [4] and similar guidance also interests the aerospace industry [5].

The main strategies to manage the waste of CFRPs are three, i.e., disposal (land-filling), energy recovery (incineration) and recycling (e.g., mechanical, chemical, and

thermal methods). The recycling of CF-based products seems to have the potential to cover a significant role in a circular economy approach for this materials' family, compared to the other two strategies. In fact, incineration cannot be considered a sustainable solution for managing waste in the long term [6] because it releases large amounts of pollutants into the environment; concerning landfilling, despite being the most common and cheapest method of disposal, it is subjected to the restrictive legislation of US and EU authorities for the management of CFRP products [7, 8].

Mechanical recycling is a practical technique to manage the increasingly large volumes of CF-based waste: in fact, it guarantees the lowering of the emission of greenhouse gasses and energy usage and has characteristics of fast processing and facile scalability. This strategy is based on the reduction of CFRPs into small pieces, using shredding and milling/grinding [9]. The shredding of the components in pieces of 50–100 mm allows above all the removal of metal inserts and easier transport. Then, the chunks are ground into fragments of 50  $\mu\text{m}$ –10 mm through a cutting or hammer mill. Finally, cyclone machines and sieves separate the fragments [10].

The strategy can be very efficient when the recycling process is very difficult; just think about the thermoset-based composites, for which the heterogeneous nature does not help separate the fibres. Furthermore, it is possible to consider the CFRP waste as reinforcement in, for example, epoxy foams [11] or epoxy composites [12].

Considering the above, this work aims to employ the peripheral down-milling process for the recycling of CFRP laminates. The strategy was used for laminates made by unidirectional carbon fibre prepregs, by varying the spindle speed and the feed rate: the cutting forces were monitored, to evaluate the cutting power and the specific cutting energy; moreover, the chips from the milling process were classified based on their dimensions.

This research highlights the opportunity to machine components in their wholeness without cutting them before the milling, to set the cutting strategy depending on the chip dimensions and the geometry of the components and to use a common milling machine in a job shop scheme, making a shorter supply chain.

## 2 Materials and Methods

### 2.1 Materials

The CFRP laminates, with a  $[0/90]_s$  stacking sequence, thickness  $t = 4$  mm and fibre content of approximately 55% in volume, were obtained by unidirectional prepregs subjected to an autoclave curing process. The laminates were cut into 200 mm  $\times$  200 mm pieces for the milling tests.

### 2.2 Equipment and Cutting Strategy

The peripheral down-milling tests were carried out by HSS-PM three flute end mills (UOP, Series 14805), 20 mm in diameter, and a 5-axis vertical machining centre (C.B. Ferrari), equipped with a CNC control system.

Two different cutting strategies were considered, by varying the feed rate,  $f$ , and the spindle speed,  $s$ , but leaving unchanged the feed per tooth ( $f_z = 0.33$  mm); in detail,



the first strategy was  $s = 500$  rpm and  $f = 500$  mm/min, while the second one was  $s = 1000$  rpm and  $f = 1000$  mm/min. For both cases, a depth of cut of 3 mm was considered.

An example of the peripheral down-milling process and the representation of some features are reported in Fig. 1.

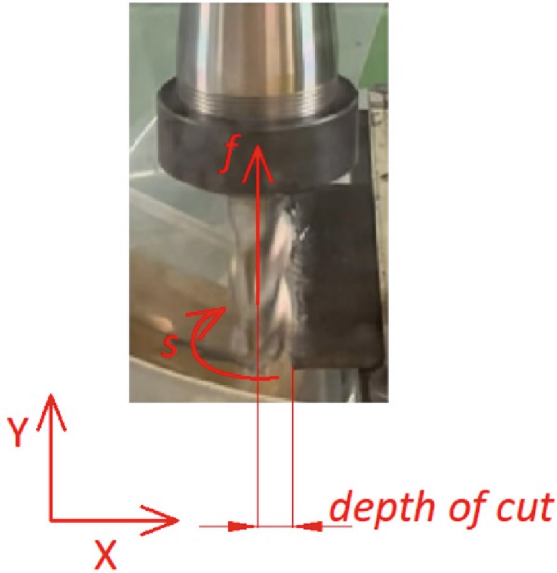


Fig. 1. Peripheral down-milling process.

### 2.3 Features Measured

The cutting forces were measured by a three-axis Kistler 9257A piezoelectric transducer, fixed on the CNC table. The signal was collected and amplified by a multi-channel amplifier and transferred to a National Instruments data acquisition card; then, the signal was sampled at 20 kHz.

The measurement of the cutting forces was used for the evaluation of the cutting power,  $P$ , and the specific cutting energy,  $E_{SP}$ . In particular,  $P$  was the sum of two contributions related to the rotational and the axis feed motion, depending on  $s$  and  $f$ . Concerning the specific cutting energy,  $E_{SP}$ , it was measured by the following equation:

$$E_{SP} = P / (MRR \times \text{material density}) \quad (1)$$

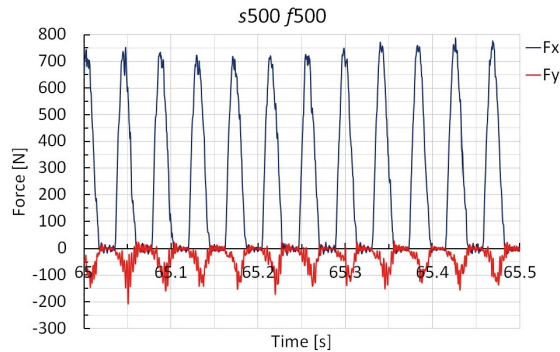
where  $MRR$  in Eq. 1 is the material removal rate, equal to:

$$MRR = f \times t \times \text{depth of cut} \quad (2)$$

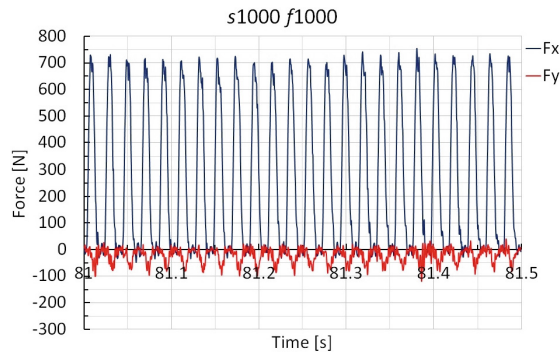
Moreover, the chips were separated by sieving and were classified into six ranges of dimension ( $d_c$ ):  $d_c > 3$  mm;  $2 \text{ mm} < d_c \leq 3$  mm;  $1 \text{ mm} < d_c \leq 2$  mm;  $0.5 \text{ mm} < d_c \leq 1$  mm;  $0.1 \text{ mm} < d_c \leq 0.5$  mm;  $d_c \leq 0.1$  mm.

### 3 Results

Figure 2 reports the stabilized trend of the two components of the cutting forces,  $F_x$  and  $F_y$ , for  $s = 500$  rpm and  $f = 500$  mm/min (Fig. 2a) and  $s = 1000$  rpm and  $f = 1000$  mm/min (Fig. 2b).  $P$  values were measured from the mean values of these forces; all the same, the  $E_{SP}$  was evaluated by Eq. 1. Both values of these two features are reported in Fig. 3.



(a)



(b)

**Fig. 2.** Trend of the cutting forces for (a)  $s = 500$  rpm and  $f = 500$  mm/min and (b)  $s = 1000$  rpm and  $f = 1000$  mm/min.

The last figure highlights that the cutting power is higher for the fastest strategy while, for this one, the specific cutting energy is slightly lower. Besides, compared to the recycling of CFRP components by hammer milling (for which  $E_{SP} = 2.03$  MJ/kg was estimated for a 10 kg/hr waste processing rate), the process seems to guarantee energy saving; consider, however, that the energy evaluation in this work is based on measures of forces and does not consider the energy losses of the process. Finally, the strategy shows economic and environmental benefits if compared to the embodied energy of virgin CF (183–286 MJ/kg) [13].

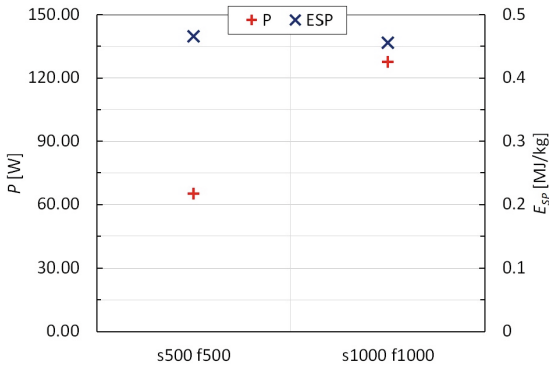


**Fig. 3.** Cutting power and specific cutting energy values

Figure 4 shows the separated chips depending on their dimensions (Fig. 4a) and their distribution (Fig. 4b). Figure 4b highlights that the investigated process parameters strongly influence the dimensions of the chips; then, the process parameters can be opportunely set to obtain different chip dimensions, and this can be used to manufacture chip-based composites with opportune chip size.

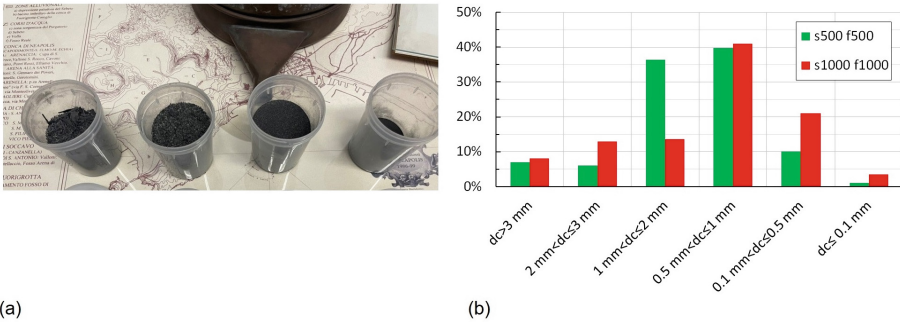


**Fig. 4.** (a) Separation of the chips and (b) distribution of the chip dimensions.

### 4 Conclusions

The present work furnishes some interesting results on the employment of conventional milling for the recycling of CFRP laminates. In particular, the evaluation of the specific cutting energy highlights that the method can replace hammer milling; then, it represents a viable way to reach economic and environmental benefits, compared to the production of virgin carbon fibres. Moreover, the dimensions of the chips are strongly influenced by the investigated process parameters.

Future works can provide for an extended experimental campaign and the morphological investigation of the chips, to carry out a deepened investigation of this recycling

strategy. Finally, it is possible to hypothesise the use of recycled chips as reinforcement of chip-based composites.

## References

1. Verma, S., Balasubramaniam, B., Gupta, R.K.: Recycling, reclamation and re-manufacturing of carbon fibres. *Current Opin. Green Sustain. Chem.* **13**, 86–90 (2018)
2. Stergiou, V., Konstantopoulos, G., Charitidis, C.A.: Carbon fiber reinforced plastics in space: life cycle assessment towards improved sustainability of space vehicles. *J. Compos. Sci.* **6**(5), 144 (2022)
3. Lin, L., Schlarb, A.K.: Recycled carbon fibers as reinforcements for hybrid PEEK composites with excellent friction and wear performance. *Wear* **432–433**, 20928 (2019)
4. La Rosa, A.D., Banatao, D.R., Pastine, S.J., Latteri, A., Cicala, G.: Recycling treatment of carbon fibre/epoxy composites: materials recovery and characterization and environmental impacts through life cycle assessment. *Compos. B Eng.* **104**, 17–25 (2016)
5. Vieira, D.R., Vieira, R.K., Chang Chain, M.: Strategy and management for the recycling of carbon fiber-reinforced polymers (CFRPs) in the aircraft industry: a critical review. *Int. J. Sust. Dev. World* **24**(3), 214–223 (2017)
6. Gharde, S., Kandasubramanian, B.: Mechanochemical and chemical recycling methodologies for the Fibre Reinforced Plastic (FRP). *Environ. Technol. Innov.* **14**, 100311 (2019)
7. Khalil, Y.F.: Comparative environmental and human health evaluations of thermolysis and solvolysis recycling technologies of carbon fiber reinforced polymer waste. *Waste Manage.* **76**, 767–778 (2018)
8. Tapper, R.J., Longana, M.L., Yu, H., Hamerton, I., Potter, K.D.: Development of a closed-loop recycling process for discontinuous carbon fibre polypropylene composites. *Compos. B Eng.* **146**, 222–231 (2018)
9. Oliveux, G., Dandy, L.O., Leeke, G.A.: Current status of recycling of fibre reinforced polymers: review of technologies, reuse and resulting properties. *Prog. Mater. Sci.* **72**, 61–69 (2015)
10. Pickering, S.J.: Recycling technologies for thermoset composite materials—current status. *Compos. A Appl. Sci. Manuf.* **37**(8), 1206–1215 (2006)
11. Song, W., Magid, A., Li, D., Lee, K.-Y.: Application of recycled carbon-fibre reinforced polymers as reinforcement for epoxy foams. *J. Environ. Manage.* **269**, 110766 (2020)
12. Thomas, C., Borges, P.H.R., Panzera, T.H., Cimentada, A., Lombillo, I.: Epoxy composites containing CFRP powder wastes. *Compos. B Eng.* **59**, 260–268 (2014)
13. Howarth, J., Mareddy, S.S.R., Mativenga, P.T.: Energy intensity and environmental analysis of mechanical recycling of carbon fibre composite. *J. Clean. Prod.* **81**, 46–50 (2014)



# Thermo-mechanical Modelling of the Directed Energy Deposition (DED) Process for the Optimization of Deposition Strategies

Marco Vallone<sup>1</sup> (✉), Massimo Damasio<sup>1</sup>, Eleonora Atzeni<sup>2</sup>, Mirna Poggi<sup>2</sup>,  
and Alessandro Salmi<sup>2</sup>

<sup>1</sup> Exemplar s.r.l., Corso Vittorio Emanuele II, 161, 10139 Torino, Italy  
marco.vallone@exemplar.com

<sup>2</sup> Department of Management and Production Engineering (DIGEP), Politecnico di Torino,  
Corso Duca degli Abruzzi, 24, 10129 Torino, Italy

**Abstract.** Directed Energy Distribution (DED) process involves a continuous and subsequent deposition of layers, by means of a laser heat source that melts the feedstock material supplied in form of powders or wires. Laser power, powder flow rate, travel speed affect temperature gradient distribution and residual stresses in components. Due to this, the main process parameters' influence on DED process was investigated, followed by a fine-tuning.

The main objective of this work was to compare four simulations with different scanning strategies for the to-be-printed component, focusing on deformation results. To achieve this objective, the 3DEXperience software was essential in simulating DED process accurately. Setting up the Finite Element Method (FEM) model, mesh type, material properties, and boundary conditions followed a strict procedure.

As final step, once the best case in terms of deformations from a production perspective has been highlighted, the component is subjected to post-processing machining to respect the designed dimensioning and tolerances.

**Keywords:** Additive Manufacturing · Directed Energy Deposition · FEM · Structural · Heat transfer

## 1 Introduction

Additive manufacturing comprises all manufacturing technologies that realize components by material addition, layer by layer, as opposed to traditional technologies that rely on material subtraction. In the early 1980s, it was known as rapid prototyping (RP) or 3D Printing because, as the name suggests, it was primarily employed to create prototypes [1]. Today, however, the scope is no longer limited to prototyping alone; it is feasible to produce components and entire products that may be launched directly to the market.

The AM processes can be classified by ISO/ASTM 52900-2015 into seven categories. One of this is the Directed Energy Deposition technique that permits the printing of components by melting feedstock material while depositing it on the substrate in a

layer-by-layer fashion. This additive manufacturing technique is mostly used with metal powders as feedstock material and laser as heat source, taking the name of Laser Powder Directed Energy Deposition (LP-DED) process. Some of the advantages of this process include the capability to process massive build volume exceeding one cubic meter, repair damaged parts, and changing the material composition throughout the building process, hence producing functionally graded materials.

The LP-DED is a layer wise technique in which a focused laser beam follows a specified scanning path, generated by a CAM software. Thus, the blown powder is melted and a metal bead is deposited layer by layer along the path during the deposition. A schematic representation of the LP-DED process is shown in Fig. 1.

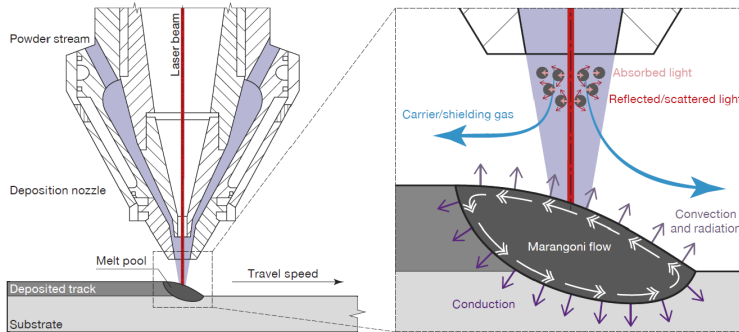


**Fig. 1.** Schematic of a typical laser powder LP-DED process [16].

Despite its benefits, this technique has some drawbacks, most of which stem from the process's physical complexity. The high temperature gradient and the dynamic cooling/heating rate of the LP-DED process lead to residual stresses and distortion of the final LP-DED component as a result of part's extreme temperature fluctuations. Thus, residual stress and deformation are highly influenced by process parameters, scanning pattern, the size, and the geometry of the component. At the end the deposited beads of metal, after solidification, will result in a tensile stress state (referring to the top layers) and in a compressive stress state for the inner and below layers [12]. Because of these aspects, the functionality of the components and the application they're used for could be compromise.

Moreover, the microstructure is significantly affected by the cooling rate, which in turn is affected by process parameters, such as laser power (tied to the melting pool formation and thus the temperature reached in that zone), travel speed (which determine how many time the heat source hit the previous beads so, it controls the transition of temperature gradient) and powder feed rate (it determines the amount of powder absorbed by the melt pool and consequently influences the temperature in that zone) (Table 1).

**Table 1.** Influence of process parameters on the cladding dimensions [12].

Parameters	Deposition height	Deposition thickness	Dilution
Laser Power	↓	↑	↑
Laser spot size	↑	↓	↓
Powder feed rate	↑	↑	↓
Scanning speed	↑	↓	↓

## 2 Direct Energy Deposition (DED) Process Simulation

### 2.1 The Main Role of the Simulations

The severe temperature gradients [2] make the defects like cracks or pores one of the principal problems once the printing is terminated, caused by residual internal stresses. From that is intuitive that the final quality suffers. The question is how to avoid these to a minimum? Many are the process parameters influencing the temperatures reached in melt-pool. Surely a parallel experimental work leads to understand how to tune these parameters, but this requires time and moreover it's a cost. So, instead to proceed by an experimental practice the better way is to tune the parameters by means of numerical simulation. Simulating the LP-DED process, a weakly coupled thermo-mechanical model is so required: the two models are described below.

### 2.2 Thermal Model

The first step in FEA analysis is to solve the thermal problem using the heat transfer energy governing balance (1), which permits the study of the transient thermal history [3]. From the results of the thermal history, an estimate of the solidification time of the manufactured model is derived.

$$\rho C_p \frac{dT}{dt} = -\nabla \cdot \mathbf{q}(\mathbf{r}, t) + Q(\mathbf{r}, t) \quad (1)$$

In the left-hand side  $\rho$  represent the density of the material,  $C_p$  the specific heat capacity,  $T$  the temperature, and  $t$  the time. The terms on the right-hand side include  $Q$ , the external heat source,  $\nabla \cdot$ , the divergence,  $q$ , the heat flux vector represented by the relative reference coordinates,  $r$ , and by the time  $t$ .

According to Fourier's law, the heat flux is expressed as a function of the temperature gradient (2), in which  $k$  is thermal conductivity which depends from the temperature in an isotropic way [13]:

$$Q(\mathbf{r}, t) = -k \nabla T \quad (2)$$

The requirements to solve the equations listed until now are:

- The initial conditions by setting the temperature of the entire model
- A heat flux input model which consists of an applied heat flux
- Thermal boundary conditions

### 2.3 Mechanical Model

To simulate and extrapolate the results of the mechanical problem, the solver employs a quasi-static model in which the explicit analysis benefits [4] are incorporate into the solution of the quasi-static problem and the inertia effects can be neglected. Using the weakly coupled solution method described before, the quasi-static equilibrium of stress is determined at each time step [13] after the thermal simulation has been conducted. The stress equilibrium governing technique (3) is described, with  $\sigma$  the stress:

$$\nabla \cdot \sigma = 0 \quad (3)$$

## 3 3D Experience Suite

### 3.1 Process Simulation Framework

The 3DEXperience (Dassault Systèmes) cloud suite provides a comprehensive platform of cutting – edge solutions that provide all the necessary skills to bring concept ideas to life. The suite strength lies in its roles, which permits its break down into a set of tools. Starting from the Assembly Design app (Fig. 2) with the CAD model, the simulation process passes through the Additive Manufacturing app performing a sequentially coupled thermal-stress analysis by solving first the transient heat transfer, then reading the temperature solution as a predefined field, and finally solving the structural analysis.

At its core is the toolpath-mesh intersection module, a powerful tool that takes the process toolpath data as input from the event series and activates the required elements of an arbitrary mesh by applying the proper thermal energy to the model.

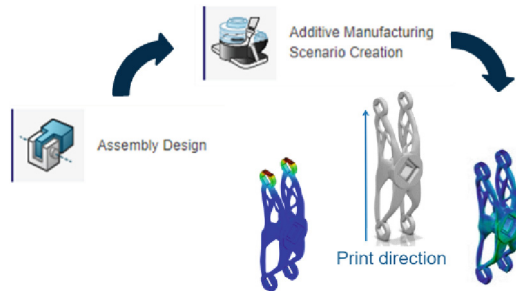


**Fig. 2.** 3DEXperience process simulation framework [7].

At the end of the simulation the 3DEXperience platform allows to post-process the analysis using the Physics Results Explorer app supplying a complete graphical suite to evaluate the results.



### 3.2 Thermomechanical Simulation in 3DEXperience for AM

Abaqus/Standard offers a general framework for thermomechanical simulations that guarantees the definition of adequate boundary conditions, interactions, loads, constraints, temperature-dependent material properties.

An AM process thermal-stress analysis:

- guarantee exact specification in space and time of the processing conditions, such as laser properties, laser scan path, material deposition sequence, and build environment;
- consents a precise control upon the fidelity of solutions for various simulation needs;
- can be followed by heat treatment applications, support removal, mechanical performance tests, etc.
- it is usually more accurate but more computationally expensive than an eigenstrain analysis.

Simulating an AM process, a sequential thermal-stress analysis consists of a transient heat transfer analysis of thermal loads introduced by the process on a printing part followed by a static structural analysis that is driven by the temperature field from the thermal analysis [4]. The analysis, if required, can also include support structures and a substrate where the part and/or the supports are built, considering their thermal conduction influences, part distortions, and residual stresses.

## 4 Experimental Validation

This section examines how experimental results were obtained. A brief description of the experimental setup is presented and elaborated upon, followed by sections on results, graphs, and concluding remarks.

Once the simulation setup can be defined as precisely as possible, as a result of an orthogonal experimental procedure validation of the process parameters, the results, such as the numerical model may be considered stable and truthful with a certain acceptable approximation from the experimental results. Further considerations on these can be analyzed in combinations with reflections about the influence of process parameters, scanning path on the mean temperature's distribution and the final deformations.

With this type of approach, a suitable design for a particular component or system can be conceived and directed from an engineering perspective, allowing for the realization of the designed component based on the application and, as a result, wisely tuning the process parameters to achieve the desired final result.

### 4.1 Experimental Setup

**Laserdyne® 430 LP-DED Machine.** The LP-DED machine used during this work is a Prima Additive (Torino, Italy) machine, the LASERDYNE® 430 (Fig. 3a): a laser melting deposition platform [9] with high accuracy, build rate and productivity suitable for three-dimensional fabrication, reworking and research and development applications.

**Laser Head.** The laser head used (Fig. 3b) is a multi-purpose laser head with 1kW laser source of 2mm spot and a reliable powder feeder [10].

**The Feeder.** The powder feeder (Fig. 3c), an Optomec (Albuquerque, NM, USA) system, allows the delivering of metal powders inside the machine through the inert shielding gas used to prevent the oxidation of the newly deposited bead [8].

**Mastercam.** The CAD/CAM software Mastercam has been used to generate the G-Code from the CAD file with the implementation of scanning path instructions, laser power, federate, accelerations, etc. [11].

**The Dial Indicator.** To measure the substrate's flatness a dial indicator has been mounted on a perfectly planar suitable base to get a fixed reference from which the difference in deformations between the initial and the final cases could be extrapolated.

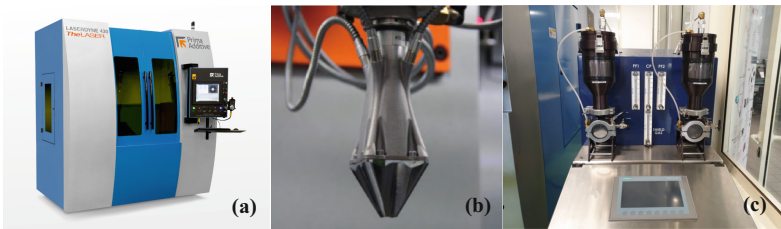


**Fig. 3.** (a) Prima Additive Laserdyne 430 [8], (b) tool laser head [10], (c) powders feeder [8].

**AISI 316L.** Ti6Al4V was one of the first material adopted in LP-DED due to the Powder Bed Fabrication experience gained over the years, and its extensive use in the aerospace, biomedicine and motorsport industries. In recent years, however, AISI 316L [5] has been widely adopted in LP-DED process for use in numerous industrial areas where an aggressive environment plays a central role. Hence, the literature provides studies of investigations conducted on numerous components printed with AISI 316L.

The thermal and mechanical properties of the AISI 316L, utilized in the 3DExperience software, can be summarized in (Fig. 4) and (Table 2): the set of data was shared by the researcher G. Piscopo of the “IAM center of the Politecnico di Torino” [15].

The latent heat of fusion is the change in the enthalpy of a material caused by the application to it of heat, at constant pressure, in order to change its state from solid to liquid.

During the melting process, the solidus temperature is the highest temperature at which an alloy is solid whereas the liquidus temperature is the temperature at which an alloy is completely melted. Between these two temperatures the alloy is in a state of partial melting.

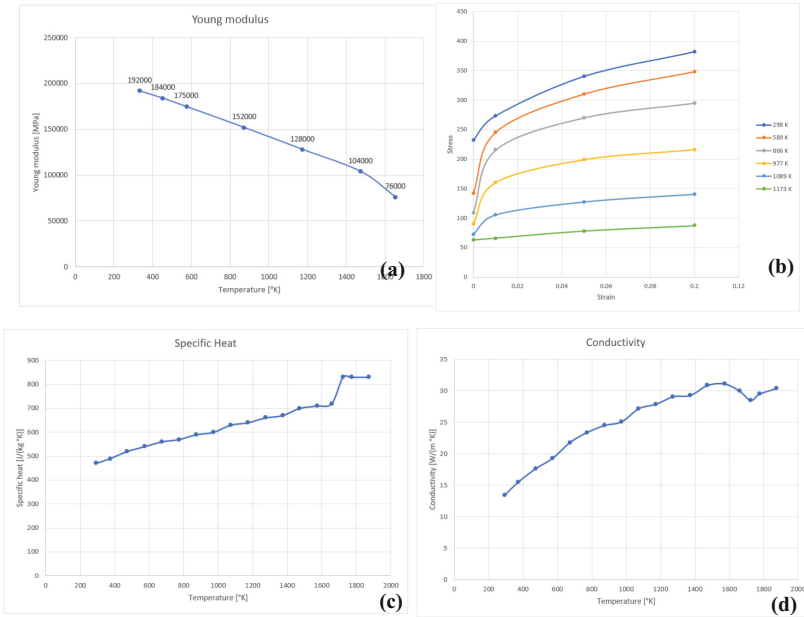


**Fig. 4.** AISI 316L elastic field plot (a), plastic field plot (b), specific heat plot (c), conductivity plot (d),

**Table 2.** AISI 316L thermal properties [7].

Latent heat [J/kg]	Solidus temperature [K]	Liquidus temperature [K]	Emissivity [–]	Absorption [–]
26000	1674	1697	0.6	0.4

### 4.2 Simulation Activity and Results

The primary objective of this work is to develop a suitable numerical model for the LP-DED simulation process, through an experimental validation. As other AM techniques (i.e., PBF in aerospace, medicine, motorsports, etc. industries) are well-established from an industrial production standpoint, whereas the LP-DED processes are not well-implement and reliable due to the numerous complexities involved. So, in comparison to what the literature provides (i.e., cube and thin wall), a few more complex models have been chosen: in particular, a shape (Fig. 5) encountered during the 3DEXperience training performed using AM applications was proposed.

The realization of the desired shape with LP-DED technology requires several steps post-processing, in which a first stage is necessary to divide the substrate from initial deposition through a Wire Electrical Discharge Machining (W-EDM) process, followed by a machining operation to obtain the final designed dimensions with a better surface



**Fig. 5.** First design idea (a): the designed component we want to obtain; deposition (b): redesigned component to take into account over metal compensation for post – processing machining.

finishing. Thus, to obtain the designed dimensions following the W-EDM and machining process, the printed part dimensions have been adjusted realizing a new CAD model.

After the CAD phase has been completed, the numerical simulations begin. Researching in the literature an order of magnitude of the main process parameters required for the LP-DED process simulation on 3DEXperience, the first analysis has been led to understand how to approach to the software for the simulations point of view and how it responds in terms of time required to get the solution, mean temperature distribution, deformations and consequently main residual stress.

In order to reach the goal, preliminary simulations on a thin wall and on a rectangular shape have been conducted. In addition to process parameters, the machine G-Code must be used to generate the event series, the input file for the simulations. After establishing the reliability and stability of the software and resolving the problem with the generation of the event series files, the scanning paths for the desired geometry have been explored. The objective is to highlight the key differences between them in terms of thermal history and deformation outcomes, in order to determine which one can be used to obtain the minimal deformations and manufacture the designed component, and which one highlights the maximum deformation. In particular, has been chosen the following scanning strategies described in (Fig. 6) and (Fig. 7):

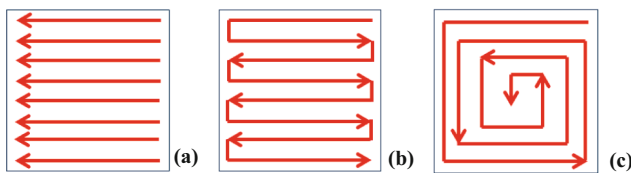


**Fig. 6.** (a) one way pattern: unidirectional parallel tracks, (b) zig – zag pattern: same as the one – way pattern but with alternated starting and final points, (c) spiral inward pattern: the laser doesn't power off and it follows a spiral – concentric path from the outside to the inside.

A preliminary simulation for the one – way pattern case applied to the test case has been conducted, to determine how to set up the various process parameters and the mesh size, incremental time step, etc., so that the optimal model can be constructed by extrapolating these first results (thermal history and final displacements).

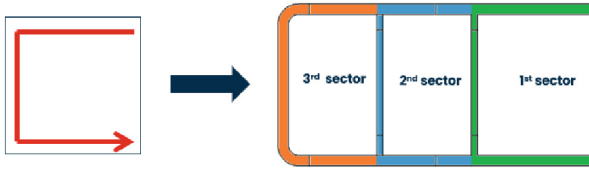


**Fig. 7.** C – sectors pattern: the cladding is manufactured following three C – shapes.

### 4.3 Experimental Activity

After extrapolating all these early results, the following step is to compare them with experimental results. This is a crucial step for aligning the simulations with the practical case, allowing subsequent simulations to be run and considered accurate without the help of additional experimental tests. To proceed with the printing of the designed geometry, some step was needed to set up in the correct way the machine operating in total safety and to be sure to extrapolate the deformation results. To ensure moderate deformations, in terms of some millimeters, the AISI 316L substrate (Fig. 8) has been first cut in dimensions 100 mm × 265 mm, then machined to get a substrate height of 10 mm. Due to the top surface was too shiny then a further step with abrasive paper has been led to mitigate the radiation losses of the laser. Some point was identified with a pencil for the next acquisitions with the dial indicator.

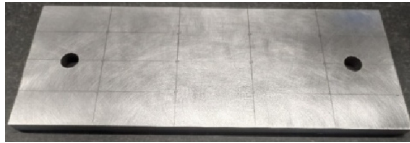


**Fig. 8.** Substrate AISI 316L plate for the LP-DED cladding process.

The planarity of the substrate has been computed through the aim of a dial indicator used as comparator. First of all, the substrate was clamped (Fig. 9) through some steel slab with the help of two bolted brackets.



**Fig. 9.** Comparator setup with the clamped substrate.

The results about the planarity before the LP-DED process are reported in (Fig. 10):

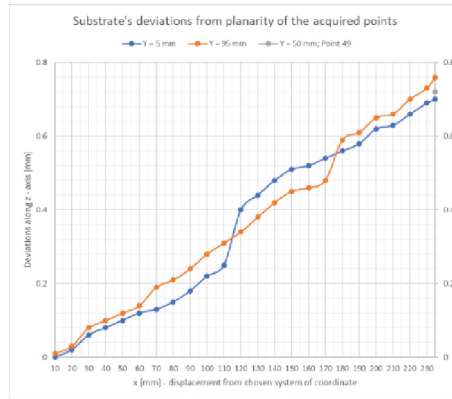


**Fig. 10.** Acquisitions of points' deviations from the ideal planarity.

Once the described planarity values were taken, some single-track e multi-track depositions were proposed to determine, using the initial process parameters, if there were failures in the attachment of the first printed layer, or if the powder was melted correctly. The thin walls machine code has been created by means of Mastercam using the following process parameters:

- Laser power: 500 W
- Travel speed: 700 mm/min
- Powder flow rate: 11.1 g/min

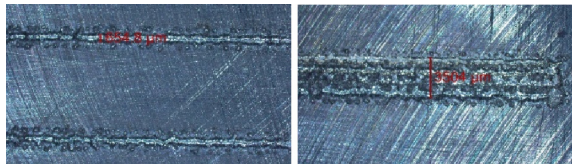


**Fig. 11.** Microscope acquisitions for bead width and process parameters evaluation.

As seen in (Fig. 11), the single and multi-tracks deposited are imperfect, due to mainly a sintering rather than a complete melting of the powder is realized. The tracks are not uniformly distributed, and the real bead width is about  $654.8 \mu\text{m}$ . Considering a fixed laser spot size of 2 mm, the obtained results are unsatisfactory and inadequate. Moreover, considering the four parallel patch of the multi-track deposition, can be highlight how the distance between them is huge such that a completed melted layer cannot be generated. So, it was clear that the energy provided to the substrate was not sufficient then a new set of process parameters has been chosen and tested:

- Laser power: 700 W
- Travel speed: 850 mm/min

- Powder flow rate: 11.8 g/min

With the revised process parameters, the beads are more homogenous, well distributed, and attached to the substrate (Fig. 12).



**Fig. 12.** Microscope acquisitions of the new deposited layers and bead width.

**Scanning Strategy Involving Maximum Deformations.** Before printing the design component, two different orientations (Fig. 13) of the cladding part were analyzed for each scanning strategy in the 3DEXperience suite to determine which emphasized the final deformations of the substrate:

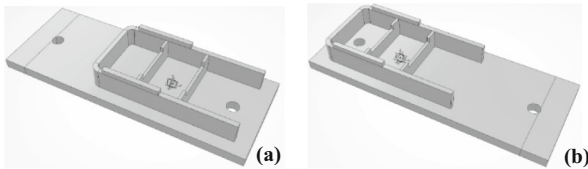


**Fig. 13.** (a) Case A: has the closed section facing the clamped part (b) Case B: vice versa.

To solve the analysis the entire substrate has been modelled with natural convection ( $10 \frac{W}{m^2K}$ ) except the cladding part with the forced convection ( $40 \frac{W}{m^2K}$ ) applied and the two clamped areas which involve conduction phenomena with the plates of the clamping system (Fig. 14).

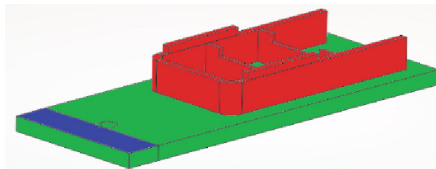


**Fig. 14.** Convection losses set up.

In all the simulations, the substrate with the single-track zig-zag pattern is the most distorted; hence, the first designed component to be printed employs this scanning strategy with the case B configuration.

Mastercam was used to generate the G-Code file, the substrate was cleaned, and clamp it in a cantilever beam configuration. A “homing” procedure has been followed by the machine for the  $x - y$  axes while for the  $z -$  axis, the zero was set manually: the laser head shift down slowly until it touches a paper sheet of 0,1 mm among the substrate and the laser head. Then the right focal height was set to 8 mm increasing the  $z$ -height of the laser head manually, this is the new  $z = 0$  mm. A first dry run, in which the laser and the feeder are both turned off, has been run to guarantee a correct execution of the G-Code steps.

So, once the set of process parameters has been chosen and tested:

- Laser power: 700 W
- Travel speed: 850 mm/min
- Powder flow rate: 11.8 g/min

And the scanning strategy for the maximum deformations results identified, the designed component has been manufactured (Fig. 15).

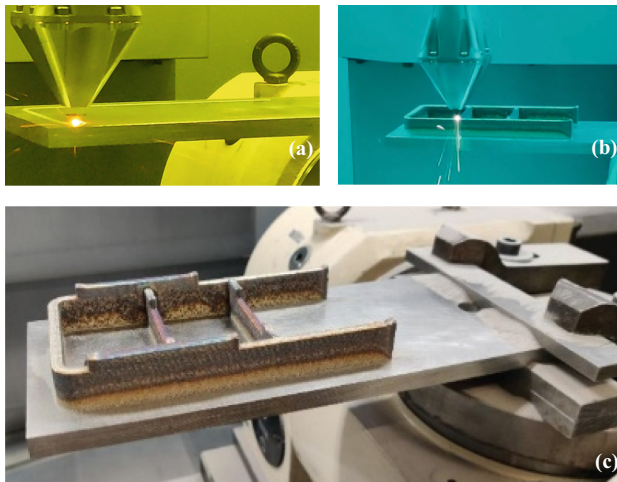


**Fig. 15.** First layer (a) and middle layer deposition of the designed component (b) – manufactured component (c).

Measurements were captured by Leica S9i (Wentzler, Germany) optical microscope to identify the actual bead width and the walls thickness, and to determine if the correct designed over-metal is respected in the three - dimensions. The bead width was computed, and a value about 1.8 mm was extrapolated. (Fig. 16) shows examples of microscope’s acquisitions:



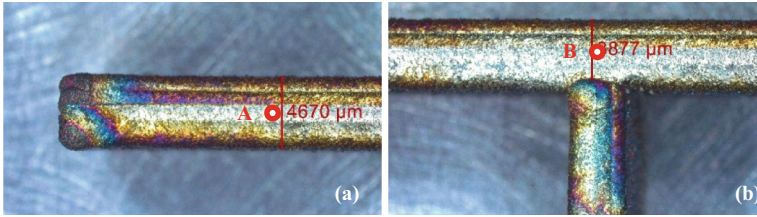


**Fig. 16.** Point A (a), Point B (b).

The final deformations (Fig. 17) of the substrate have been acquired with the comparator. The points are acquired every 10 mm along the lateral edges of the substrate, approximately 5 mm beside these. Considering the previously observed deviations from the planarity, these points have been considered as reference points for the comparison with the final numerical model.

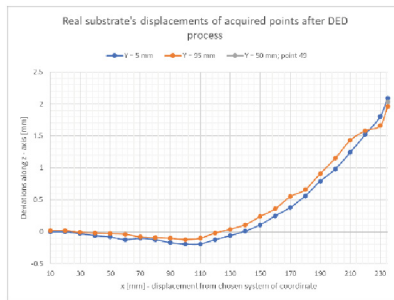


**Fig. 17.** Deviations trend after LP-DED manufacturing process.

**Time Step – Results Comparison.** Evaluation of the time step's effect on the thermal and displacements results is the next stage for the new numerical model. In the simulation using forced convection for both the substrate and deposition material, three distinct time steps have been explored and compared. In Abaqus, the time step contributes to the total load which is gradually applied during the simulation. It is fundamental to improve the simulation so that the final results and the computation time can be considered acceptable. For that reason, three different time steps were taken in account: 100 s, 25 s, and 5 s. Concerning the thermal history of an internal cladding point (Fig. 18), by varying the time step, then the mean temperature trend (the dotted lines) is almost the same, but with the finest time step the local thermal behaviour (red peak) is captured.

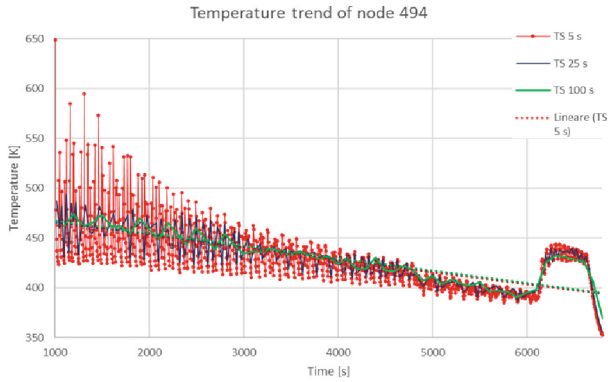


**Fig. 18.** Node temperatures with time steps trends comparison.

Considering the node with the highest final displacement, raising the time step also increases the approximation error, but with a reduction of the computation time (Fig. 19). The manufacturing process required two hours so, it makes no sense that the simulation takes more time. Thus, a compromise with the time step of 25 s has been chosen, finding the correct balance between accuracy in results and computational costs.

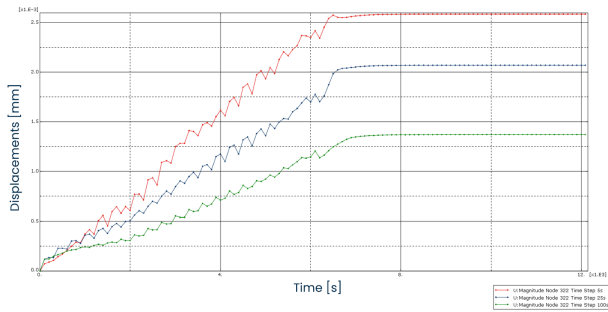


**Fig. 19.** Displacement node with time steps 5 s–25 s–100 s.

**Convection Model.** It remains to set a suitable convection model. On the entire model, natural convection, forced convection, and intermediate cases were considered. Following is a comparison between the simulated substrate displacements and the in – situ process displacements. Looking at the (Fig. 20) the three final points on the forced convection displacements curve have a decreasing trend, with the last point having the same displacement value of the other two cases. This could be caused by the continuous forced cooling condition set even during the deposition of the last layers, where the shielding gas doesn't influence the substrate in such way and during the final cooling phase, once the laser turn off.

Anyway, the model with the intermediate convection of  $25 \frac{W}{m^2K}$  has been chosen to take in account in part of the local forced convection losses.

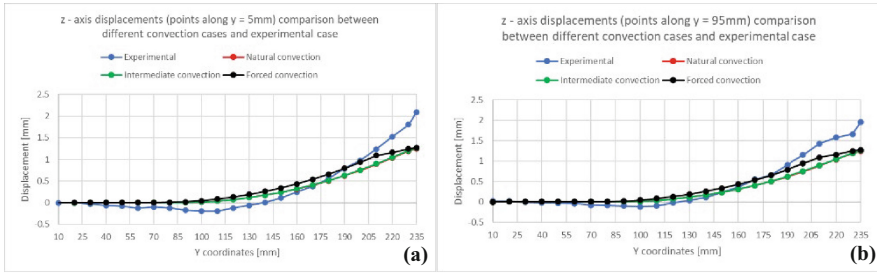


**Fig. 20.** Displacements comparison between different convection cases (time step 25 s) and experimental case, along the edge 5 mm (a) and 95 mm (b) far.

The shrinking along the z – axis (Fig. 21) is considered for some points and the comparison between the in – situ process, the simulation, and the theoretical height of the CAD model is proposed. The deviation of the in – situ process from simulation is negligible, while from the theoretical CAD model is about 1 mm.

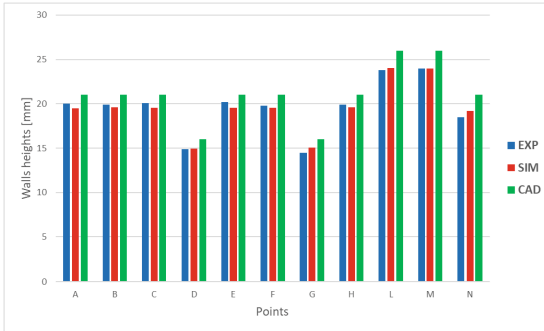


**Fig. 21.** Shrinking of wall’s height.

**Effect of Heating on Oxides’ Colors.** Also taken into consideration is the heating temperature dependence of oxides color. The heat – tint color is caused by the continuous oxide layer’s thickening, which causes the color change as the temperature rises. The level of oxygen in the atmosphere, the length of time that the heating persists, and the surface finishing are the primary factors that influence the oxidation level [14]. A comparison between the maximum temperature reached in the simulation, for a specific node, just before the oxidation with the maximum approximated temperature from the heat tint colour table for the same point, is provided. Considering the shadings varying from the dark purple to the dark blue, the order of magnitude is correctly esteemed (Fig. 22).

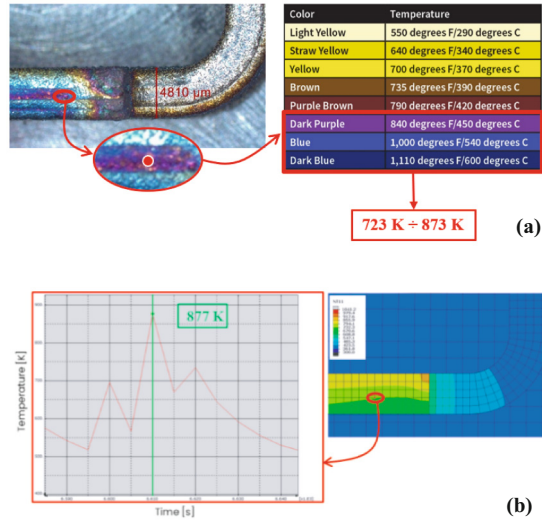


**Fig. 22.** Oxidation temperature reached during deposition (a); temperature of oxidation in numerical simulation (b).

**Manufactured and Simulated Test Case Comparison.** Some manufactured component views compared with the simulated ones to mark the excellent software prediction of the most deformed zones are figured out in (Fig. 23).

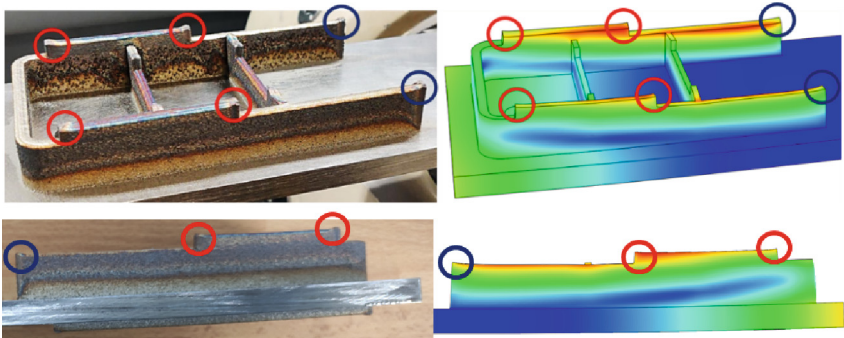


**Fig. 23.** Manufactured and simulated test case.

**Scanning Strategy Involving Minimum Deformations.** With the numerical model properly configured, considering the approximations done with the time step and the convection losses, the other scanning strategies are simulated to determine which one yields the smallest deformations for a given production aim. Consider a point on the last layer (Figs. 24 and 25): the C – sectors pattern gives less shrinking in the z – axis direction with a displacement value of  $-1.56$  mm which, considering the worst clamping

condition in a cantilever beam configuration and the bad positioning of the cladding, this is a great value.

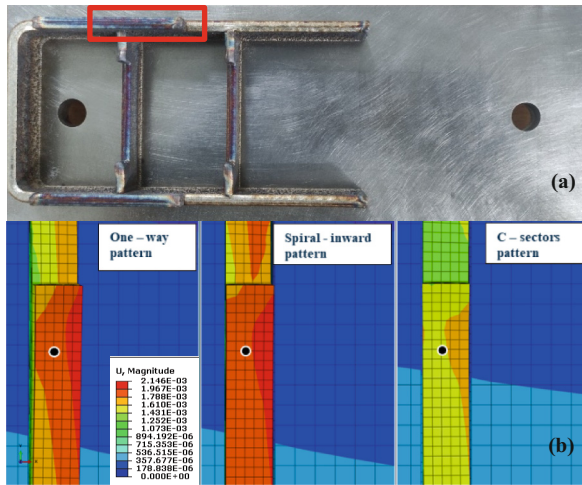


**Fig. 24.** Deposition zone analyzed in the numerical model (a); referring point for the displacement's comparison along z – axis (b).

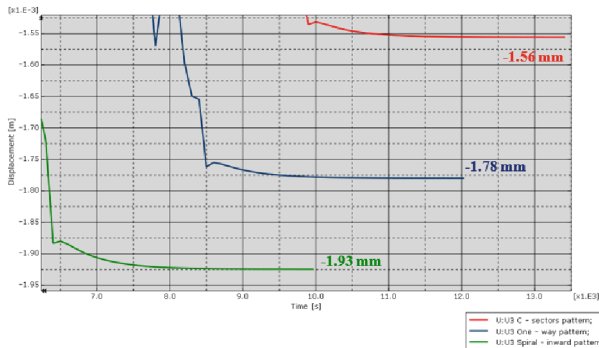


**Fig. 25.** Displacements along z – axis (shrinking) of the point figure out in the previous figure

## 5 Conclusions

The 3DEXperience allowed to set up the simulation of LP-DED manufacturing process and it guaranteed a friendly user interface using ABAQUS solver.

The strength is a cloud suite with various integrated apps where it is easy to switch between different environment (CAD, Additive manufacturing parameter setup, CAE simulation/Postprocessing results, etc.) remaining on the same platform.

Once the simulation process has been set up, it is possible to perform sensitivity analysis using simulation on different parameter (toolpath strategy, tool speed, laser power, component positioning) to predict the better setup in order to print the component avoiding printing test as much as possible. This is the target of DfAM (Design for Additive Manufacturing).

From this work, future aims might be achieved, such as doing a comprehensive investigation from metallurgic point of view in an effort to replicate the experimental melting pool temperatures in simulation as closely as feasible. In addition, a reverse engineering research can be conducted to get the desired component to minimize local deformations.

**Acknowledgement.** This work has been partially supported by the award “TESUN-83486178370409 finanziamento dipartimenti di eccellenza CAP. 1694 TIT. 232 ART. 6”, which was conferred by Ministero dell’Istruzione, dell’Università e della Ricerca and by the Interdepartmental Centre for Integrated Additive Manufacturing (IAM@PoliTo) at the Politecnico di Torino, Torino, Italy.

## References

1. Gibson, I., Rosen, D., Stucker, B.: Additive Manufacturing Technologies: 3D Printing, Rapid Prototyping, and Direct Digital Manufacturing. Springer New York, New York, NY (2015). <https://doi.org/10.1007/978-1-4939-2113-3>
2. He, K., Zhao, X.: 3D thermal finite element analysis of the SLM 316L parts with microstructural correlations. *Complexity* **2018**, 1–13 (2018). <https://doi.org/10.1155/2018/6910187>
3. Heigel, J.C., Michaleris, P., Reutzel, E.W.: Thermo-mechanical model development and validation of directed energy deposition additive manufacturing of Ti–6Al–4V. *Additive Manufac.* **5**, 9–19 (2015). <https://doi.org/10.1016/j.addma.2014.10.003>
4. <https://abaqus-docs.mit.edu/2017/English/SIMACAEGSARefMap/simagsa-m-Quasi-sb.htm>
5. Aversa, A., Marchese, G., Bassini, E.: Directed energy deposition of AISI 316L stainless steel powder: effect of process parameters. *Metals* **11**, 932 (2021). <https://doi.org/10.3390/met11060932>
6. Poggi, M., Vecchi, G.: Simulazioni Directed Energy Deposition Process. Politecnico di Torino, Torino
7. The 3DEXPERIENCE platform, a Game Changer for Business and Innovation | Dassault Systèmes (3ds.com)
8. Poggi, M., Pilagatti, A.N., Nonis, F.: Pianificazione degli esperimenti industriali. Politecnico di Torino, Torino

9. [https://www.primaathome.com/images/prima/macchine/laserdyne-430/Brochure\\_TheADDITIVE.pdf](https://www.primaathome.com/images/prima/macchine/laserdyne-430/Brochure_TheADDITIVE.pdf)
10. <https://www.primaadditive.com/en/technologies/direct-energy-deposition/real-ded-laser-head>
11. <https://www.mastercam.com/solutions/>
12. Miedzinski, M.: Materials for Additive Manufacturing by Direct Energy Deposition (2017)
13. Gouge, M., Michaleris, P., Denlinger, E., Irwin, J.: Thermo-Mechanical Modeling of Additive Manufacturing
14. [https://bssa.org.uk/bssa\\_articles/heat-tint-temper-colours-on-stainless-steel-surface-heated-in-air/](https://bssa.org.uk/bssa_articles/heat-tint-temper-colours-on-stainless-steel-surface-heated-in-air/)
15. <https://doi.org/10.1007/s11665-021-05954-3>
16. <https://doi.org/10.3390/ma12172819>



# AM Part Qualification by Meltpool, Material, and Grain Boundary Engineering

Mallikharjun Marrey<sup>1</sup>, Amirhossein Eftekharian<sup>1</sup>, Guan-Cheng Chen<sup>1,2</sup>,  
Dade Huang<sup>1</sup>, and Frank Abdi<sup>1,3</sup> (✉)

<sup>1</sup> AlphaSTAR Technology Solutions, Irvine, CA, USA

{arjun, amir, echen, huangd, fabdi}@alphastarcorp.com

<sup>2</sup> Mechanical Engineering Department, University of California Los Angeles, Los Angeles, CA, USA

<sup>3</sup> Imperial College London, London, UK

**Abstract.** Additive Manufacturing (AM) achieves significant cost savings and enables complex geometries that are otherwise impossible to fabricate using conventional manufacturing processes. 3D-printed parts produced by Laser Power Bed Fusion (LPBF) need to be qualified and may suffer from: (i) defects (micro, macro), (ii) net-shape warpage, (iii) high residual stresses, (iv) surface roughness, (v) inconsistent density, (vi) anisotropic microstructures, (vii) scatter in mechanical properties, and (viii) poor fracture and fatigue performance. AM defects (e.g., unfused powder, balling, humping, and keyholing) are affected by variations in power and speed as well as hatch spacing that result in pores, thermal cracks, rough surface finish and warping. The objective is to minimize the trial-and-error prints using a building block qualification strategy. An Integrated Computational and Material Engineering (ICME) tool is proposed to perform: 1) melt pool engineering (MPE) and predict the process thermal map and density map, as well as temperature time history to establish print road map, 2) Grain boundary engineering (GBE) to perform micro scale material modeling of alloy composition and predict the grain size, mechanical strength, fracture, fatigue crack growth properties due to defects and precipitates; and 3) thermal-structural analysis incorporating MPE and GBE to evaluate part quality. This includes: i) void prediction at the coupon level, ii) print error macro void calculations at element level along with scatter in material strength and allowables, iii) prediction of fracture control plan, iv) computing part distortion due to different print strategies, and v) net shape and warpage measurements.

**Keywords:** AM Part Qualification · Meltpool Engineering · Grain Boundary Engineering · Process and Void Map · Strength and Scatter · Warpage · Effect of Defects · ICME



# 1 Introduction

The Additive Manufacturing (AM) industry is interested in part qualification. Traditional manufacturing has used post-fabrication Non-Destructive Evaluations (NDE) to assess build quality for over a century. Recently, the AM community has sought the development of reliable ICME (integrated Computational Material Engineering) methodology, and *in-situ* sensing and monitoring technologies for metal AM processes to enhance the quality of builds. The motivation has been to support the production of critical and non-critical components while benefiting from the reduction in scrap rate, associated costs, and the need for post-built NDE. This information may be used in conjunction with a building block strategy and qualification criteria to ensure part acceptance. Table 1 describes ten qualification steps based on NASA STD 6030 document [1]. An Integrated Computational and Material Engineering (ICME) based methodology is proposed to minimize the trial-and-error part qualification [2].

## 1.1 Problems with AM qualification and Trial and Error Fabrication

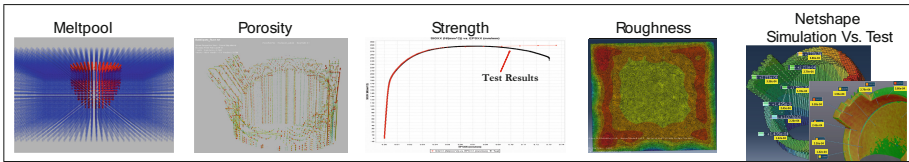
The key steps in qualification of AM parts are selection and optimization of the machine parameters (Table 2). Achieve the required tolerance level and net shape after base plate removal and obtain the mechanical properties (stress-strain curve), fracture and fatigue control plan, including scatter and uncertainty of yield and ultimate stresses such as shown in Table 1. A typical ICME calculations is shown in Fig. 1, it demonstrates AM Process thermal and material performance and the consequence on As-Built part performance. This applies to several AM machine modalities including: 1) Powder bed Fusion (PBF) including: Selective Laser Sintering (SLS), Selective Laser Melting (SLM), and Electron Beam Melting (EBM); and 2) Directed Energy Deposition (DED).

**Table 1.** AM Part Qualification Criteria

Qualification Category	Description
1-Micro defects	Micro voids/Density during thermal history, super melting sintering and solidification
2-Macro defects	Macro porosity: Printing error around hole and boundary
3-Surface roughness	Diffusional creep, Triaxial stress
4-Intergranular cracks	Diffusional creep, Biaxial stress
5-Scatter in material properties	Stress-strain relation (yield stress, ultimate/plastic strain) due to voids (micro/macro) and cracks
6-Fracture control plan	Characterization of fracture properties, fatigue crack growth, stress intensity curve
7-Warpage	Evaluation of support, Residual stress
8-Net shape	Residual stress, Baseplate removal
9-As-built performance	In-service loading
10-Post heat treatment	Grain growth, lower strain; thermal analysis

**Table 2.** Primary Machine Parameters

Item	Parameter	Description
1	Average Power, P	Total Energy Output of Laser
2	Scan Velocity, v	Velocity of laser across surface
3	Scan Spacing, Ss	Distance between neighboring passes
4	Scan Strategy	Pattern of laser scanning (spirals, zig-zag)
5	Deposition System Parameters	Recoater vel, pressure, recoater type, closing
6	Layer thickness, L	Height of single powder layer
7	Powder bed temperature, T <sub>p</sub>	Build temperature of powder bed
8	Oxygen level, %O <sub>2</sub>	Likely most important environment parameter
9	Gas flow velocity, v <sub>g</sub>	Influences convective cooling
10	Ambient Temperature, T <sub>inf</sub>	Affecting cooling, reheat, and residual stress

**Fig. 1.** Example of ICME Prediction of AM material and part consequences.

## 2 Methodology

The overall workflow for the **ICME** based Virtual Manufacturing (**VM**) and Virtual Testing (**VT**) approach is presented in Fig. 2. AlphaSTAR has implemented this six step **ICME** approach to qualify part and consider the uncertainty quantification. This includes materials model (i.e., Ti-6-Al-4V, AL-SI-10Mg, Steel), determine optimal machine parameters for component fabrication, predict build outcomes, assess quality of build results, and predict the performance of the as-built part subject to in-service loading, including durability and damage tolerance as related to available life.

The approach may be summarized as follows. *Step One* utilizes *thermo-physics modules for powder/wire morphology and microstructural alteration* that predict phase change, crystallization, lack of fusion, mass loss, void initiation, volume of solid, and roughness (Fig. 3). It should be noted that thermo-physics component addresses heating, melting, superheated melt, super-heated cooling, sintering-solidification, and cooling and develops a thermal card in support of material and thermal structural analysis. *Step one benefit:* powder to part performance as a function defects and effect of defects including parameter sensitivity. *Step Two* addresses *macro errors/defects related to print*

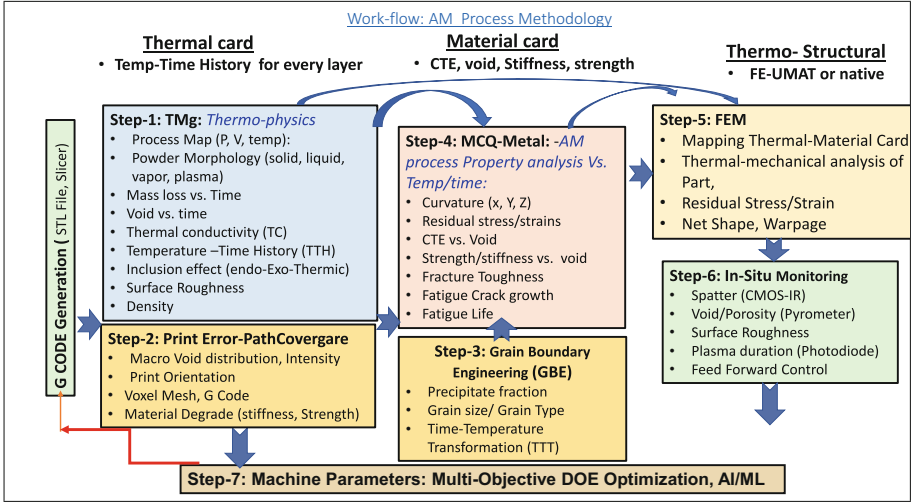


Fig. 2. Workflow: AM Process Methodology.

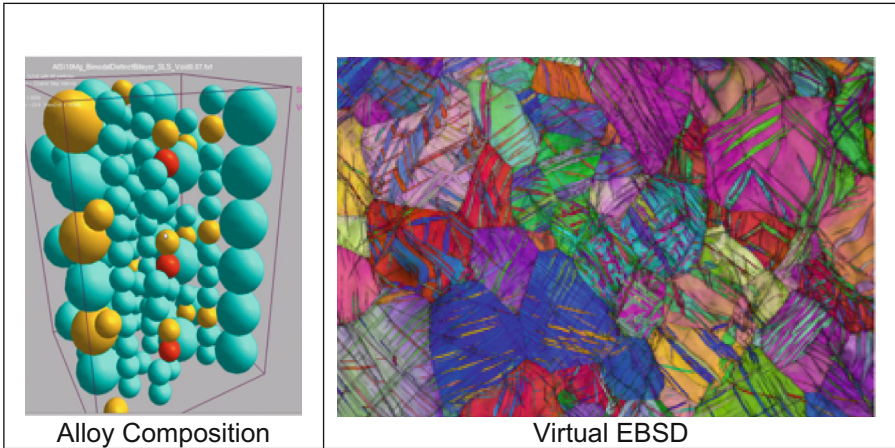


Fig. 3. Powder Morphology & Unit Cell.

path, orientation, and spacing, which manifest as a function of build plan and G-code parameter settings (i.e., speed, etc.). Macro defect may can lead to reduced performance and issues of net shape. *Step two benefit:* identification of inherent macro defects and related build impact. *Step Three supports material characterization and qualification (MCQ)* for development of a material card including determination of the impact of the effect-of-defects on the coefficient of thermal expansion as well as mechanical, fracture, fatigue crack growth and fatigue life properties. *Step three benefit:* mechanical properties, scatter (allowable), and fracture fatigued considering voids. Step Four addresses FEM based thermo-structural analysis of a printed part considering the effect-of-defects

with predictions related to net shape, (distortion, shrinkage, expansion), residual stress, surface roughness, density, mechanical strength, fracture control including toughness; fatigue life; warpage; and other anomalies as related to part qualification and acceptance. This includes determination of support structure location and design, where additional anomalies/macro defects may arise during build process. *Step four benefit: full AM process simulation with platform for optimization.*

*Step five describes the integration of ICME prediction with In-situ Monitoring to provide the foundation for Feed Forward and Feedback Control using real-time big data processing and data discovery for the identification of actionable information. Step five benefit: basis for feedback modification and foundation for intelligent g-code feed forward correction.* Finally, *Step Six describes the use of DOE optimization, meta surrogate modeling to perform single-criteria or multi-criteria decision making to determine optimal build print parameters in support of part qualification and generation of functions for artificial intelligence (AI) and machine learning (ML). Step six benefit: platform ready integration of AI, ML and optimization techniques for increased accuracy and surrogate meta modeling, HPC and emulation for increased speed and generation of actionable data.*

On closer examination, AlphaSTAR ICME thermos-physics tool, **TMg**, to generate a three-dimensional process map, which describes good/bad build parameter configurations in terms of power, speed, temperature, and other controlled machine parameters

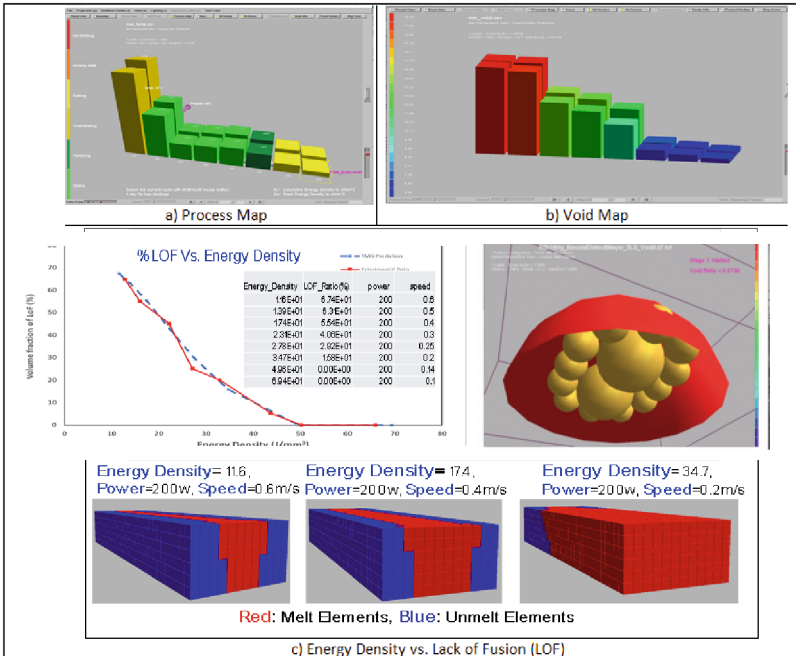


**Fig. 4.** Finding Machine Parameters.

(i.e., hatch spacing, layer thickness, etc.). These process maps, which include Time Temperature Transformation (TTT), Time Temperature Precipitation (TTP), and equally significant void maps, will identify stable and unstable (balling, overheating, humping, etc.) print regions as a function of process parameter settings. (Fig. 4).

In parallel to the process map, TMg will also utilizes safe print machine parameters, alloy composition and particle distribution to determine: (i) Meltpool size (depth, width), void vs. XCT (X-Ray Scan) measurement; (ii) grain size evolution of part (coarse vs fine); (iii) Conductivity vs. time/temp; (iv) mass loss vs. time/temp; (v) surface roughness; (vi) temperature time history (TTH). The prediction process is assisted by Design of Experiments (DOE) optimization, for efficient CPU usage estimation.

A grain boundary engineering model of polycrystalline materials is constructed to calculate the  $\alpha$  and  $\beta$  phase fractions,  $\alpha$  lath width, microhardness, and strength with incorporating TTH from Meltpool engineering. The  $\alpha$  and  $\beta$  fractions will change mechanical and fracture properties of the material. The workflow of this model is illustrated in Fig. 5.

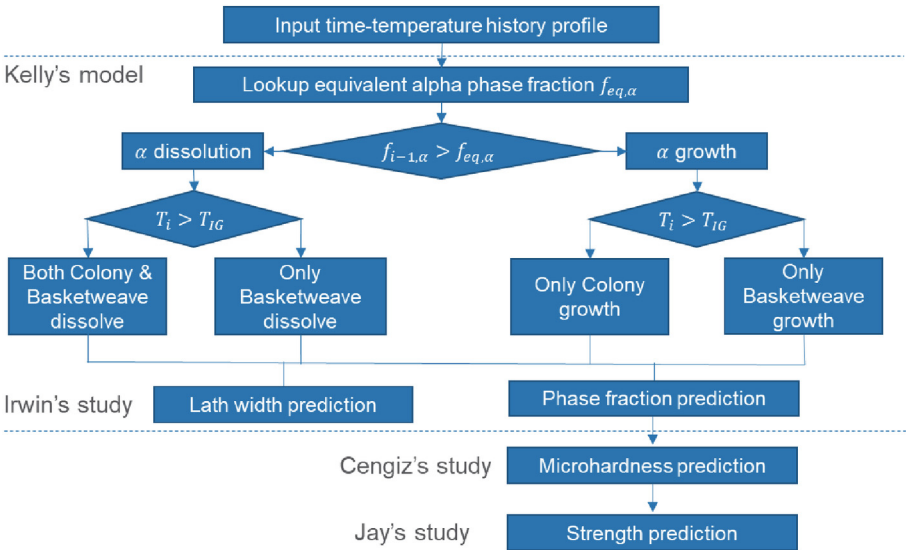


Fig. 5. Flowchart for the thermos-microstructural model.

### 3 Results and Discussion

Ti-6Al-4V metal-powder was characterized to determine the Thermal card, Material card, and strength mechanical properties. The simulation considered the uncertainty quantification to demonstrate the uncertainty quantification.

### 3.1 Meltpool Engineering

The Titanium Process map and void map is presented in Fig. 6. This includes the determination of safe and unsafe print regions considering variation of machine parameters such as power, speed, etc.)

Ti-6Al-4V metal-powder with the solid base plate in which the dynamic evolution of melt pool was validated against test with respect to melt pool size (depth and width). The laser was on for 1000  $\mu$ s assuming static laser condition (laser stationary case). Two different power cases (340 W and 520 W) were validated against the dynamic X-ray test data. Figure 7 and 8 show the comparison of the melt pool depth (on the left) and depth/width (on the right) between ZOM prediction and test data [3].

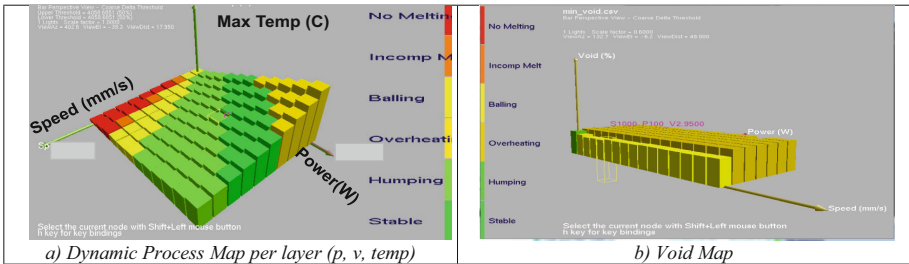


Fig. 6. GENOA 3DP Thermal Management (TMg) prediction of Dynamic Process and Void Map per layer depicting stable and unstable build regions.

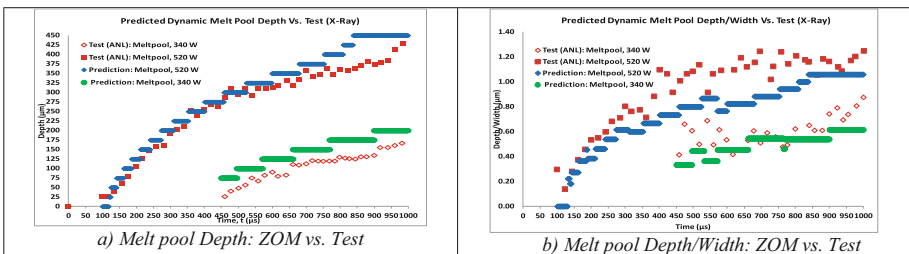
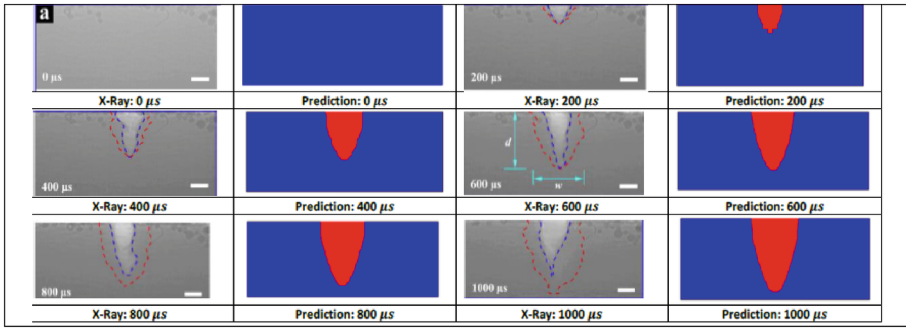


Fig. 7. Prediction/validation of ZOM vs. Argonne National Lab test data for Titanium.

### Grain Boundary Engineering

#### Phase Dissolution and Growth Prediction from Thermal History

With the thermal history of the AM process, phase changes in each time step are predicted based on the model and TTT diagram (Fig. 9a) developed by Kelly [6] and parameters improvement by Irwin [7] work. This model is validated by comparing Babu’s [8, 9] experiment results with the  $\alpha$  phase fraction predictions from this model as shown in Fig. 10. Moreover, microhardness value can then be captured using the rule of mixture of  $\alpha$  and  $\beta$  fractions [10]. Next, yield and tensile strengths can be estimated with linear regression equations from Jay’s strength-hardness relationship study in AM titanium alloys [5]. Figure 9 shows an example of the input time-temperature history and the



**Fig. 8.** Comparison of predicted melt pool size/shape (depth/width) at different time steps, laser is on for 1000  $\mu\text{s}$  (available experimental data for Titanium) [3].

output results from this model. The data in Fig. 9 (c) to (g) are used in next section of MCQ to predict mechanical strength and these results will be incorporated into thermal condition to consider the effect in time-temperature history.

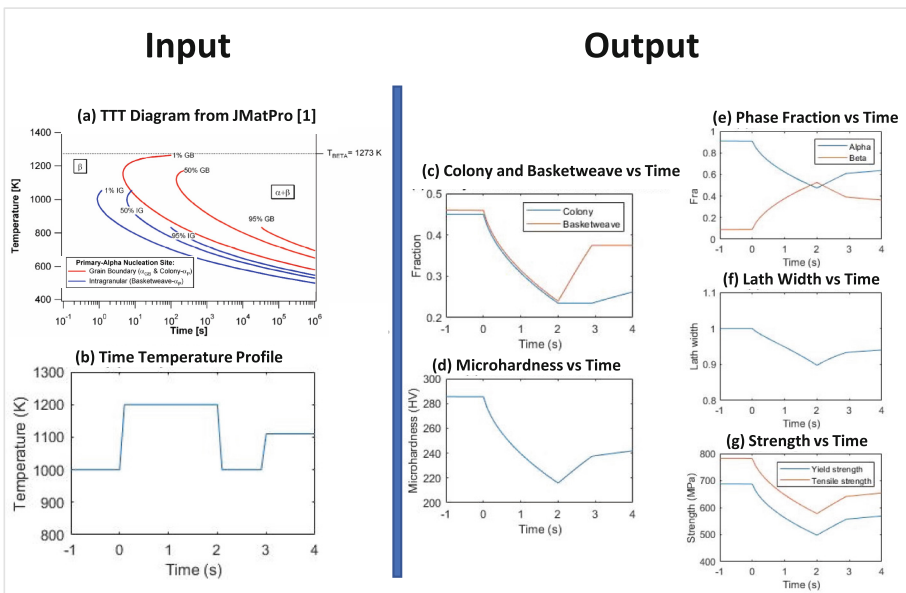


**Fig. 9.** (a) diagrams predicted by JMatPro for  $\alpha$  phases nucleation and growth [1], (b) Input time-temperature history, and output (c) colony and basketweave phase fraction, (d) microhardness, (e)  $\alpha$  and  $\beta$  phase fraction, (f) lath width, and (g) strength predictions from the model. [6, 7]

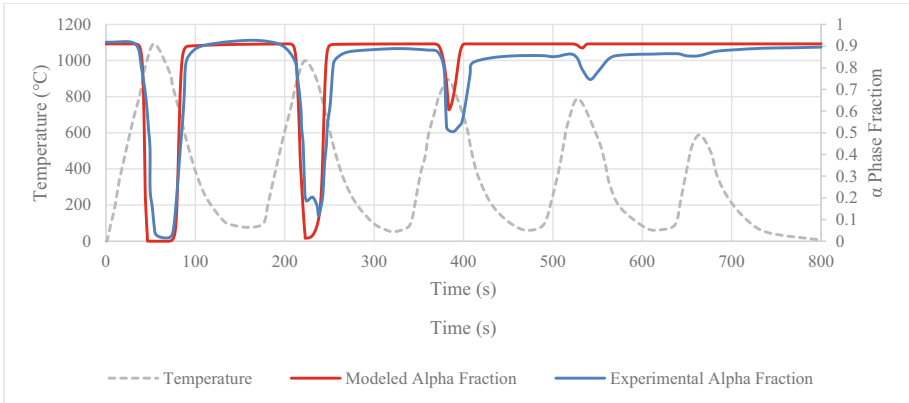


**Fig. 10.** Comparison of the predicted total  $\alpha$  phase fraction from this model with experimental data [3].

### 3.2 Mechanical and Fracture Property Prediction

Material Modeling utilizing the ICME was performed. MCQ software predicts material mechanical properties (stiffness, strength, and viscosity) at different temperatures, and the effect of scatter on material performance (yield, ultimate, strain). MCQ results was validated with Ti6Al4V to be able to predict static and fatigue DMLS printed metal properties and allowables at room and high temperature. The static properties were predicted by mixing Ti6Al4V base metal properties with bald spot percentages and compared to test (Fig. 11). The bald spot percentage, shape (ellipsoid shown) and aspect ratios are used as inputs to predict stiffness and strength in all directions. Depending on other options during the calculation the output can be isotropic, orthotropic, or anisotropic. The Wrought with Air Particles is the simulation curve, and the LENS is the tested printed material. The SS curve was idealized in black in the top right of Fig. 12 to be able to predict fracture toughness vs thickness. The plane strain fracture toughness is then fed into computations for fatigue crack growth determinations and the results of the MCQ metals prediction (FCG) are compared with test Ti6Al4V DMLS Milled. Furthermore, the  $da/dN$  vs  $dG$  curve is used as input to an FE model to determine the SN life of the part, which also accounted for additional observed surface roughness. The GENOA SN prediction matched the DMLS As Built test data which is a reduced life compared to milled specimens. Finally, room and high temperature (700°F, 371°C) allowables were generated using method discussed in Fig. 13 and are shown in Fig. 13.



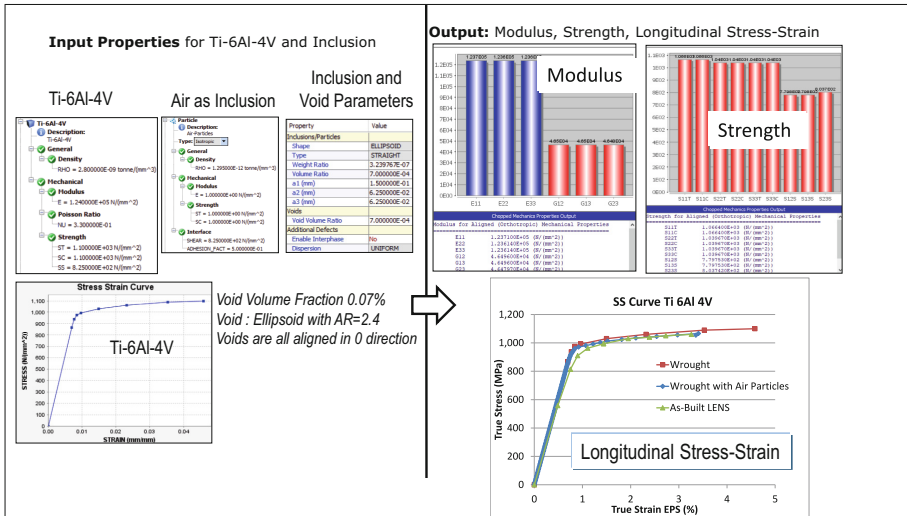


Fig. 11. 3D Printing SS Curve Prediction vs. Test.

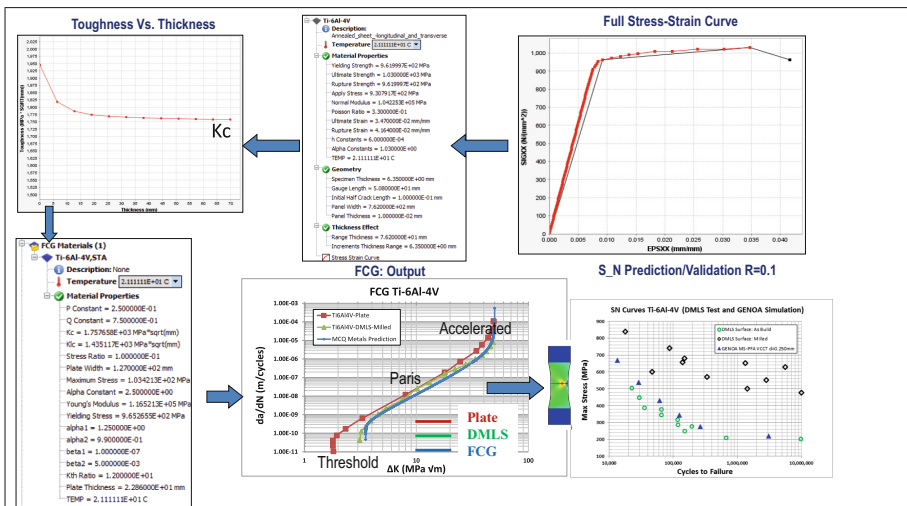


Fig. 12. 3D Printing Fatigue Prediction vs. Test.

## 4 Conclusion

An integrated solution is vital to predict AM process and it being with material modeling and ends with service loading. The ICME approach discussed showed In-Situ Monitoring and Visualization can be used to calculate of material performance during heating, melting, solidification, and cooling and can predict defects and map them to simulation models. Material modeling can predict material mechanical properties (stiffness,

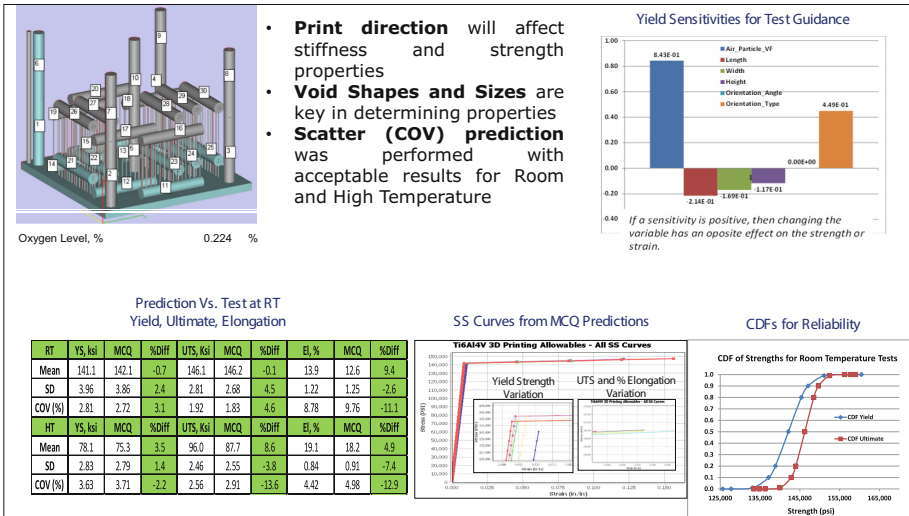


Fig. 13. Scatter in properties and sensitivity: Test vs Simulation.

strength, and viscosity) at different temperatures, void formation and roughness during diffusion creep, and the effect of scatter on material performance (yield, ultimate, strain) as shown for test validated case for Ti6Al4V. Process Modeling combined with the ABAQUS Thermal-Structural solution can predict residual stress and warpage due to thermal induced stresses. Service Loading of the As-Built 3D-printed part can support residual strength during loading for the as built part. This can be used to assess part qualification and certification.

## References

1. NASA-STD-6030: Approved: 2021-04-21, Additive Manufacturing Requirements for Spaceflight Systems. Approved for Public Release—Distribution Is Unlimited
2. Abdi, F., Miraj, R., Tam, C., Rios, I., Harik, V.: AM part qualification by ICME analysis and real time NDE monitoring, MBE Summit 2020, NIST-March 2020
3. Moazami, N., Kaviany, M., Baid, H., Hajiha, R., Godines, C., Abdi, F.: Microscale thermal management and effect of defects in fused deposition modeling of continuous carbon fiber PLA composite, TP19-0728. CAMX 2019, 23–25 September 2019, Anaheim, CA (2019)
4. Godines, C., DorMohammadi, S., Abdi, F., Huang, D., Roche, R.I.: 3D print -material and process model and effect of defects on part performance. In: Science in the Age of Experience Simulia User Conference, 18–21 June 218, Boston, MA (2018)
5. Abdi, F., Yavari, P., Harik, V., Godines, C.: Material allowable generation and AM process parameters effect on porosity. J. Coating (2020)
6. Kelly, S.M.: Thermal and Microstructure Modeling of Metal Deposition Processes with Application to Ti-6Al-4V, Ph.D. dissertation, Virginia Polytechnic Institute and State University, Blacksburg, VA (2004)
7. Irwin, J., Reutzler, E.W., Michaleris, P., Keist, J., Nassar, A.R.: Predicting microstructure from thermal history during additive manufacturing for Ti-6Al-4V. J. Manuf. Sci. Eng. **138**(11), 111007 (2016)

8. Babu, S., Kelly, S., Specht, E., Palmer, T., Elmer, J.: Measurement of phase transformation kinetics during repeated thermal cycling of Ti-6Al-4V using time-resolved X-ray diffraction. In: International Conference on Solid-Solid Phase Transformations in Inorganic Materials, pp. 503–508 (2005)
9. Cengiz, B., Oncu, A., Merve, T., Albert, C.T.: A process-microstructure finite element simulation framework for predicting phase transformations and microhardness for directed energy deposition of Ti6Al4V. *Addit. Manuf.* **35**, 101252 (2020)
10. Keist, J., Palmer, T.: Development of strength-hardness relationships in additively manufactured titanium alloys. *Mater. Sci. Eng. A* **693**, 214–224 (2017)



# AF-Challenges-Synthetic Materials (Polymer and Ceramic) Lfing Model Blind Test Validation

Harsh Baid<sup>1</sup>, Amirhossein Eftekharian<sup>1</sup>, Mohammedreza Bahadori<sup>1</sup>, Dade Huang<sup>1</sup>,  
Andrea Cantarutti<sup>1</sup>, and Frank Abdi<sup>1,2</sup>(✉)

<sup>1</sup> AlphaSTAR Technology Solutions, Irvine, CA, USA

{hkbaid, rbahadori, huangd, acantarutti, fabdi}@alphastarcorp.com

<sup>2</sup> Imperial College London, London, UK

**Abstract.** In recent years use of “virtual testing” has increased as an effort to evaluate new materials for structures earlier in the applications timeline. Virtual testing is made possible by conducting progressive failure analysis and combining it with available data to predict structure/component safety based on the physics of micro/macro mechanics of materials, manufacturing processes, and service environments. The US Airforce (AFRL) blind test lifing modeling challenges are described as virtual testing under In-service thermo-mechanical loading in two categories.

- 1) Polymer Matrix Composite (PMC) Durability Damage Tolerance (D&DT): (i) Static strength, (ii) Fatigue, and (iii) Retained strength after fatigue. This effort performed modeling of the high-performance aerospace PMC IM7-977-3 material, unnotched and notched specimens at Room Temperature (RT)
- 2) Ceramic Matrix Composite (CMC) D&DT and lifing: (i) Static strength, (ii) Fatigue, (iii) Creep; and (iv) Retained strength and crack growth. This effort performed modeling of two CMC material systems: SiC/SiC based S200 and GEA, unnotched and notched specimens at Room and Elevated Temperatures (RT/ET)

The overall objective of these two efforts was to evaluate the best class invited computational models for accuracy and speed of simulations and to provide a theoretical prediction for damage and fracture evolution for a set of unnotched and notched laminated composites.

Integrated Computational Material Engineering (ICME) and Computational Structural Mechanics (CSM) by Multiscale Progressive Failure Analysis (MS-PFA) were used to address the predictive evaluation of PMC and CMC materials using a building block validation strategy. ICME model considers nano-micro-mechanics coupled with Multi-scale progressive failure De-homogenized analysis to track damage/fracture evolution of laminated composites including: **a**) crack density formation in matrix, **b**) fiber damage and interphase/interface bridging, **c**) delamination, and **d**) crack initiation and propagation. Verification, Validation, and Accreditation (VVA) predictions for: **1**) for the PMC IM7-977-3, static and fatigue simulation results were 12.8% and 11.9% within the test data for quasi static, soft and hybrid laminated composites; and **2**) for the CMC material systems (S200 and GEA), multiple layups were tested for both unnotched and notched configurations

at room and elevated temperatures. Calibration of fiber and matrix properties was performed using in-plane test data. The static, fatigue, and creep recalibration simulations of strength and stiffness showed an average error of less than 7% between simulation and the test data. Retained strength vs. damage and crack growth pattern compared well with test data.

The proposed method is consistent and follows a building block simulation approach which can serve as a foundation for analysis of more complex structures considered by the industry.

**Keywords:** Virtual Testing · Static/Fatigue/Creep Test · Multi-Scale Progressive Failure Analysis · ICME · CMC · PMC · Fiber/Matrix Interphase · Micro Crack Density · ASTM Open Hole Test · Building Block Validation Strategy

## 1 Introduction

The objective of this effort is to determine and evaluate the GENOA software Durability and Damage Tolerance (D&DT). This objective came on request by the Air Force for advance composite benchmarks to compare results under static, fatigue, and creep service loading for notched and unnotched mixed layups [1]. Designers of composite structures need accurate computer codes for cost-effective and light-weight design of components and structures. There is an increasing interest in numerical and analytical models that can use a simulation and testing building block approach, without knowledge of test data, to (1) verify/calibrate/reverse engineer constituents using five simulated in-plane ASTM tests, (2) validate using next-level ASTM tests (3Pt Bend, DCB, ENF, other applicable test), and (3) predict further tests such as mixed layups, open hole, filled hole, element/components, and full structure. This merger of simulation and tests helps reduce the amount of testing performed in (3) by being able to blindly predict when test is not available. The focus is to show the ability to blindly predict test results, which is a high priority item in the composite D&DT community.

Composite D&DT models have to be validated and benchmarked to provide a high level of confidence in their use. It is largely against this background that a series of activities [2] have recently been conducted with the aim of assessing the predictive capabilities and boundaries of applicability of current models and design methodologies from selected companies across the globe. Some of the selection criteria proposed by AFRL was: progressive damage, residual strength and fatigue accuracy in blind predictions, maturity and extensiveness of capability, and the user interface (ease of use), integration with FE software, and commercial availability/software support and documentation. This paper is one of the contributions to those activities in which the authors provide details of their micromechanics based Multi-Scale Progressive Failure Analysis (MS-PFA) methodology incorporated in GENOA, a widely recognized Durability and Damage Tolerance (D&DT) software for modeling damage and failure in composites including effects of defects due to manufacturing process (e.g. fiber waviness, void shapes and size effect, laminate thickness effect, residual stresses, gaps, curing, resin rich pockets, etc.).

GENOA's enhanced PMC and CMC environmental model was used to compute crack density formation, fiber rupture (creep) behavior, low cycle fatigue, and interphase mechanics for several composite systems at both room and elevated temperatures. The detail of these different phenomenon is described in the methodology section.

## 2 Methodology

Durability and Damage Tolerance (D&DT) of a structure can be assessed for complex structures by performing a Progressive Failure Analysis and investigating what type of damage initiates and how it propagates and leads to fracture and failure of the structure. Knowledge of these items can lead to better designs by delaying damage or altering damage paths (e.g. away from stringers/stiffeners). This can be performed in many ways – changing material, layup, structure, manufacturing process (voids, curing, residual stresses).

### 2.1 Multi Scale Progressive Failure Analysis

The General Optimizer Analyzer (GENOA) code is able to accurately simulate structural damage process under static, dynamic, impact, creep, stability, thermal, low and high cycle fatigue, random power spectral density loads (PSD), and random thermal acoustic fatigue service loadings for small- and large-scale models. It includes the effects of uncertainties in material properties, loading, and manufacturing. It distinguishes between “as-is” and “as-designed” structures through elaborate defect modeling for composite (void, initial delamination, fiber waviness, gaps, etc.).

The code integrates: 1) finite element structural analysis with nonlinear stress-strain and plasticity considerations; 2) composite micro-mechanics; 3) material characterization routines (MCQ) to scale up the effects (de-homogenized) of local damage mechanisms to the structure level to evaluate overall performance and integrity; 4) fracture mechanics; 5) damage progression tracking; 6) probabilistic risk assessment; and 7) minimum damage design optimization. The GENOA module performs automated re-meshing of FE software and damage convergence checks to zoom in on critical points and track the initiation and growth of cracks of any size.

Micro-mechanics composite analysis is integrated with finite element analysis and damage and fracture tracking to perform MS-PFA. The capability is integrated in the GENOA software system [3]. Traditionally, failure is assessed at the lamina or laminate scale. This assessment is inconsistent with the physical behaviour of the composite material since damage occurs at a lower scale, that is the fiber, matrix or interface level. The methodology presented in this paper augments FEA analysis, with a full-hierarchical modeling that decomposes FE stresses, strains, and curvatures to the micro-scale of sub-divided unit cells composed of fiber bundles and their surrounding matrix. Every time the load is increased or equilibrium is being established an updated finite element input file with the degraded stiffness locally is generated for the FE solver by GENOA. The damage tracking is decomposed from global structural level to micro-scale level; the GUI can show fiber, matrix and if included interphase damage for each element. Displacements, stresses, and strains derived from the structural scale FEA solution at

a node or element of the finite element model are passed to the laminate and lamina scales using laminate theory. Stresses and strains at the micro-scale are derived from the lamina scale using micro-stress theory. Micro stresses are interrogated for damage using a set of damage/failure criteria. This analysis is performed progressively, enabling the determination of damage initiation and progression which includes fracture initiation and propagation on a micro level as well as structural level. The approach evaluates damage and failure mechanics caused by matrix and fiber failure (interphase, if applicable). The damage mechanisms account for matrix cracking under transverse, compressive, and shear loading. The ply fracture mechanisms include fiber failure under tension, compression (crushing, micro-buckling and de-bonding), and delamination. It allows: 1) use of commercial finite element solvers for user ease of use and selected CPU time and accuracy; 2) selection of 2D or 3D architectural details (through-the-thickness fibers), resin rich layers between weave plies, fiber volume ratio, void shape, size and location, cure condition, etc.; 3) any desired loading type static, fatigue, creep, thermal, impact, combined (thermo-mechanical), or spectrum loading; 4) quick micromechanics interaction with FE for full scale structural capability; and 5) control of degradation of material properties and new mesh by sequentially writing new solver decks at increased loading/cycles based on detected damage to overcome convergence issues.

## 2.2 Micro-Crack Density in Matrix Using Simulations

This precursor to damage can be evaluated by predicting crack density in the matrix. ATS's in-house Material Characterization and Qualification (MCQ) Composite software comes with the capability to predict such micro-mechanical behavior. The crack density prediction capability in MCQ Composite software gives the entire profile of the crack density distribution through the structure during the loading process. At each location of the structure, the crack density is obtained at the ply level.

Prediction of the crack density in the laminate matrix in MCQ Composites includes three parts, **1**) the onset of cracks in the matrix, **2**) the multiplication of cracks in the matrix, and **3**) the degradation of composite properties due to the existence of cracks. The computational procedure in crack density prediction is shown in Fig. 1.

The onset of cracks in the matrix is predicted by the transverse tensile failure criterion. It occurs when

$$\sigma_{22} \geq \sigma_{22T} \quad (1)$$

In Eq. 1,  $\sigma_{22}$  is the ply transverse tensile stress and  $\sigma_{22T}$  is the ply transverse tensile strength. Alternately, even when the inequality of Eq. (1) is not satisfied, transverse tensile failure may occur according to the modified distortion energy failure criterion due to combined stresses.

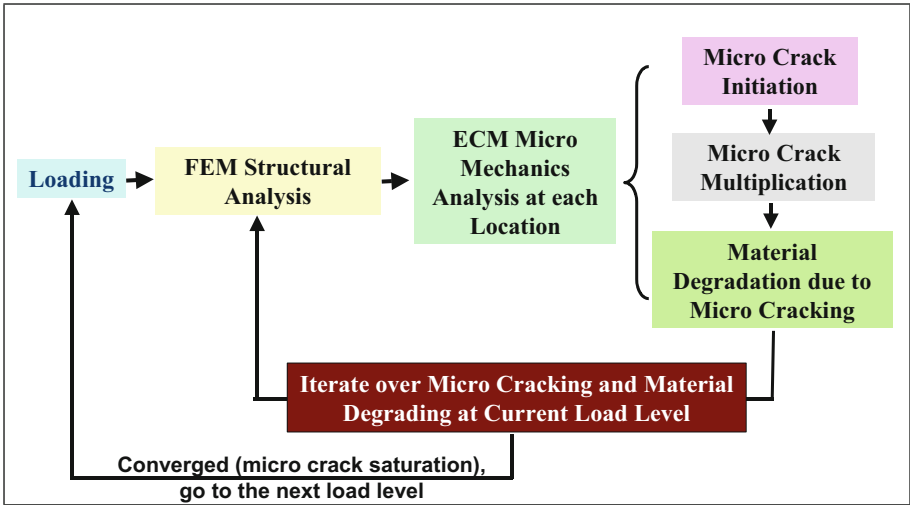


Fig. 1. Computational procedure in crack density prediction

### 2.3 Effect of Interphase on Composite Mechanics [4]

Interphase regions between the fiber and matrix phases are present in several types of composite structures. For example, in SiC/SiC ceramic matrix composites, fibers are usually coated with a weak interphase to prevent the propagation of matrix cracks into fiber fractures. Interphase is able to consider delamination type (tension, and shear) between fiber and matrix. Assume a square packed array of fibers in a unidirectional lamina. Each fiber will have a square region of matrix with side  $a$  surrounding it as shown in Fig. 2.

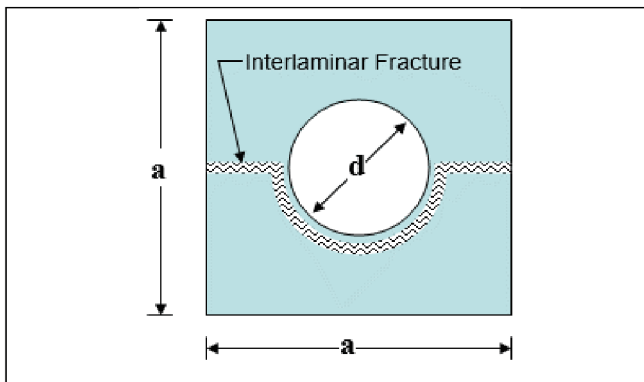


Fig. 2. Interlaminar fracture path for square-packed unidirectional composite



### 3 Results and Discussion

#### 3.1 Tensile Behavior of GEA SiC/SiC with a Unique Layout

##### 3.1.1 Problem Description

Perform blind predictions of stress versus strain behavior for a tension test specimen of GEA SiC/SiC with the unique layout at 23 °C (73 °C), 816 °C (1500°F), and 1316 °C (2400 °F).

##### 3.1.2 Material Parameters

**Input:** The fiber and matrix properties are shown in Fig. 3. The micro crack density parameters (varies for different temperature), fiber matrix interphase properties (varies for different temperature) and the degradation factors are shown in Fig. 4. The micro crack density parameters were calibrated based on the test data. **Assumption:** The material input included linear matrix, micro crack density parameters and fiber matrix interphase for mixed layout. The stress-based damage/fracture criteria are shown in Fig. 5.

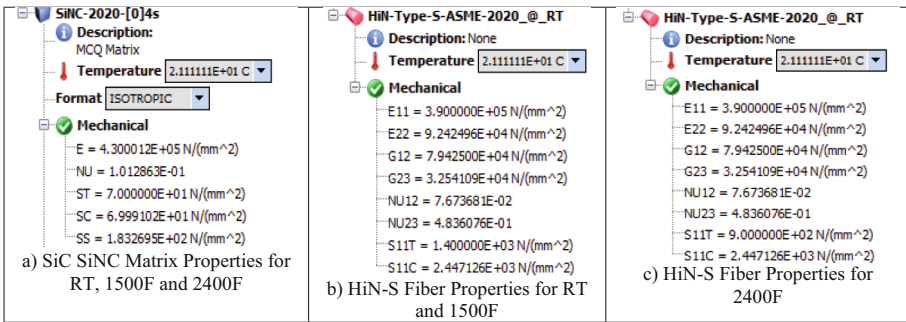


Fig. 3. Linear Matrix and Fiber Properties (GEA SiC/SiC)

<b>Crack Density Parameter</b>	<b>RT</b>	<b>1500 F</b>	<b>2400 F</b>
Stiffness Degradation Parameter	1	1	1
Crack Density Incremental Parameter	20	10	1.25
Correction Factor for Material Degradation	20	10	1.25
Maximum Number of Iteration	5	5	5
(a) Micro Crack Density Parameter			
<b>Fiber/Matrix/Interphase Properties</b>	<b>RT</b>	<b>1500 F</b>	<b>2400 F</b>
FACES	0.01	1.8	1.45
FACET	1.5	1.5	1.15
FACETHICK	0.1	0.1	0.2
FACEE	0.2	1	0.14
FACENU	1	1	1
(b) Fiber-Matrix Interphase			
<b>Post Damage Degradation</b>	<b>RT</b>	<b>1500 F</b>	<b>2400 F</b>
Damage Factor Tension (DFACTT)	1E-5	1E-5	1E-5
Damage Factor Tension (DFACTT)	1E-5	1E-5	1E-5
Damage Factor Tension (DFACTT)	1E-5	1E-5	1E-5
Damage Factor Tension (DFACTT)	0.25	1E-3	1E-3
(c) Degradation Factor			

**Fig. 4.** a) Micro Crack Density Parameters, b) Fiber-Matrix Interphase, and c) Degradation Factors

Name	Damage	Failure
<b>Maximum Stress Based Failure Criteria</b>	<b>Yes</b>	<b>Yes</b>
<b>Fiber Failure Criteria</b>		
(S11T) Longitudinal Tensile	Yes	Yes
(S11C) Longitudinal Compressive	Yes	Yes
(F11C) Fiber Micro-Buckling	Yes	No
(R11C) Fiber Crush	Yes	No
(D11C) Delaminations	No	No
<b>Matrix Failure Criteria</b>		
(S22T) Transverse Tensile	Yes	No
(S22C) Transverse Compressive	Yes	Yes
(S33C) Normal Compressive	Yes	Yes
(S12S) In-Plane Shear	Yes	No
<b>Delamination Failure Criteria</b>		
(S33T) Normal Tensile	Yes	Yes
(S23S) Transverse Normal Shear	Yes	Yes
(S13S) Longitudinal Normal Shear	Yes	Yes
(RROT) Relative Rotation	Yes	Yes

Room Temperature

**Note:** For Elevated Temperature In-Plane share was also considered as part of failure.

**Fig. 5.** Stress Based Criteria

### 3.1.3 Computational Considerations

The computational models utilized GENOA Progressive Failure Analysis (PFA) with ABAQUS as solver. The FEM Model consisted of solid elements (C3D8) with details shown in Fig. 6. After calibration, when performing damage and fracture using FEA, the fracture criteria must be adjusted to those actually splitting the CMC’s apart, the final pull.

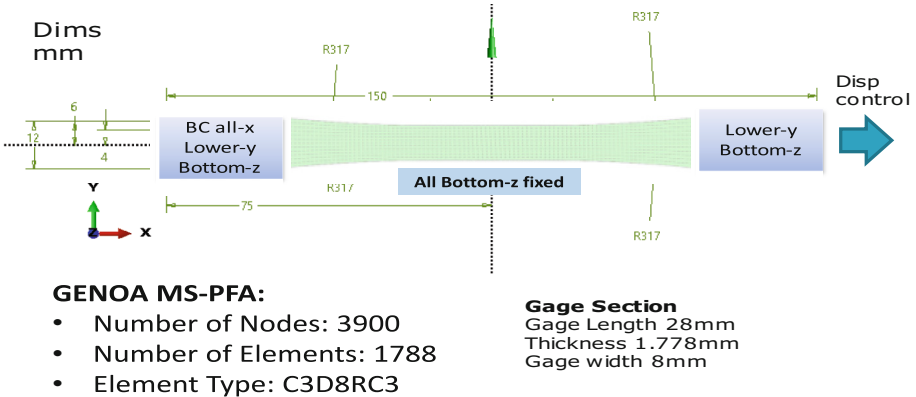


**Fig. 6.** GENOA-PFA FEM Model Dimensions, Boundary Conditions, and Displacement Application

### 3.1.4 Predictions

The stress strain plot from FEM driven GENAO-PFA software and tested data for the GEA SiC/SiC system at RT is shown in Fig. 7. As shown in Fig. 7 matrix damage initiates in the damage in 90° ply (Location A) which results in initiation of micro crack density in 90° ply as well. Next micro cracks initiates in 60° ply followed by initiation in 30° ply. At Location B damage in Fiber initiates thus degrades the stiffness of fiber to 20% of initial value. At Location C elements get removed due to delamination from relative rotation (Kaddour et al., 2013) which results in laminate failure. The simulation took approximately 4 h. The stress strain curves are calculated by selecting two nodes on the center of the model having a distance of 25.9 mm and extracting load displacement. The selected nodes were in the center of the specimen. The strain value is calculated by taking the difference in the displacement value of these two nodes and dividing by the initial distance of 25.9 mm. The stress value is calculated by dividing the load by cross sectional area.

### 3.1.5 Tabulated Tensile Properties

The tabulated data for the GENOA-PFA predictions and test at the three temperatures are shown in Table 1.

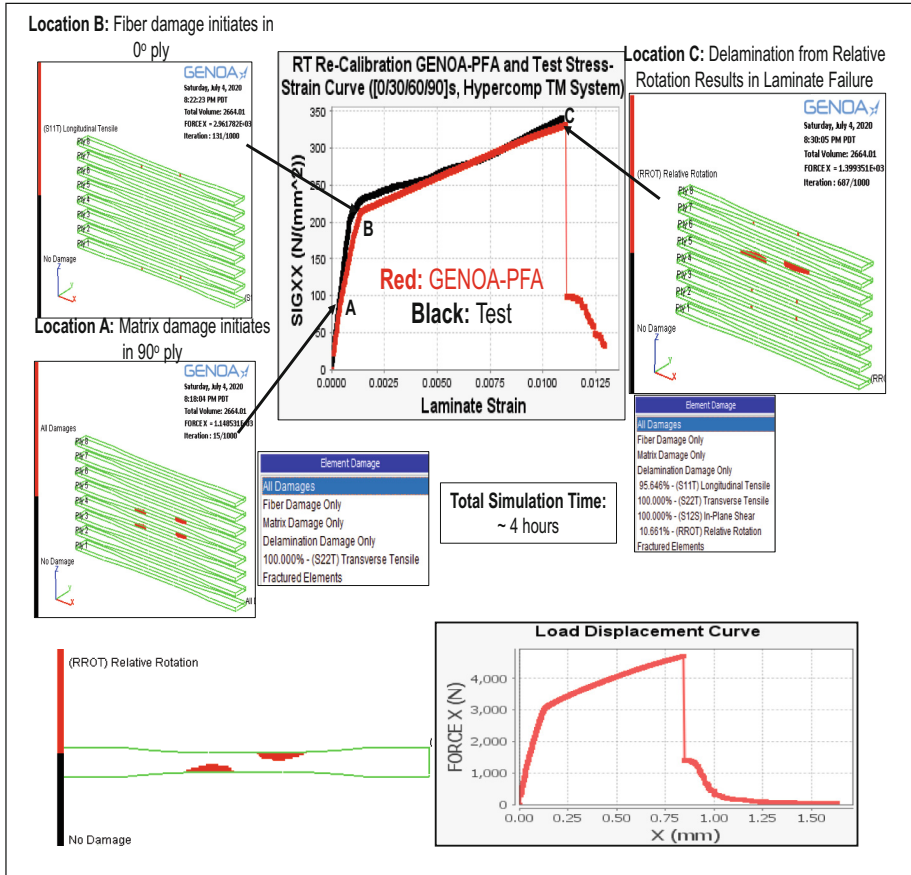


**Fig. 7. GENOA-PFA (Numerical) and Test Result for Room Temperature**

**Table 1. Tabulated Tensile Properties from GENOA-PFA (Numerical) Predictions vs. test**

Challenge #	Analysis Type/Output	Temp (C)	Analysis	Test	%Error
1 (GEA Sic/SiC)	Tensile Unique Layup/UTS (MPa)	23	33128	35173	-5.81
		816	284.5	300.05	-5.18
		1316	200.1	198.66	0.72
	Tensile Unique Layup/Strain-to-Failure (%)	23	110	11	0.00
		816	0.72	0.77	-6.49
		1316	0.38	0.31	

### 3.2 Tensile Behavior of S200H With Features

#### 3.2.1 Problem Description

Perform blind predictions of net section stress versus extensometer displacement behavior for a tension test specimen of S200H with a unique feature at 23 °C, 982 °C and 1200 °C. The unique feature will be two staggered holes.

#### 3.2.2 Computational Considerations

The computational models utilized GENOA Progressive Failure Analysis (PFA) with ABAQUS as solver. The FEM Model consisted of solid elements with details shown in Fig. 8. After calibration, when performing damage and fracture using FEA, the fracture criteria must be adjusted to those actually splitting the CMC’s apart, the final pull. The damage/fracture criteria in the predictive FE model is also shown in Fig. 8.

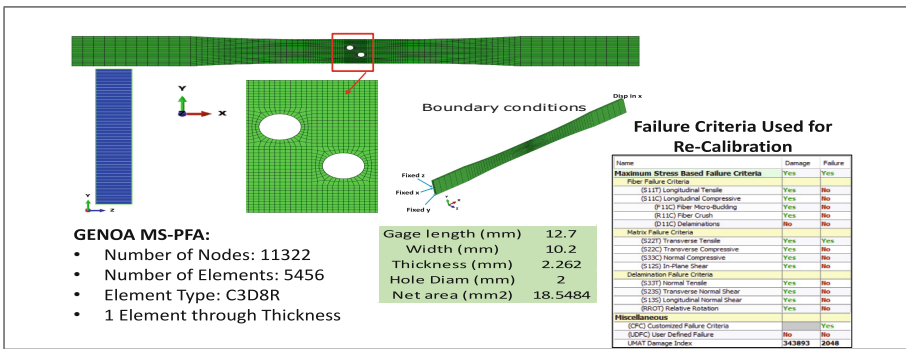


**Fig. 8.** GENOA-PFA (Numerical) FEM Model Dimensions, Boundary Conditions, Displacement Application, and Failure Criteria

#### 3.2.3 Damage Evolution

As shown in Fig. 9 Damage initiates in 90° plies as matrix damage (Longitudinal Tension) at Location A. At Location B entire failure of 90° plies is observed due to Matrix Failure as well as Transverse Compression. In-Phase Shear Failure is also observed in 0° Plies.

### 3.2.4 Fracture Path

The fracture path for the nodal based approach compared with the test results are shown in Fig. 10. The fracture path appears close comparison to the test.

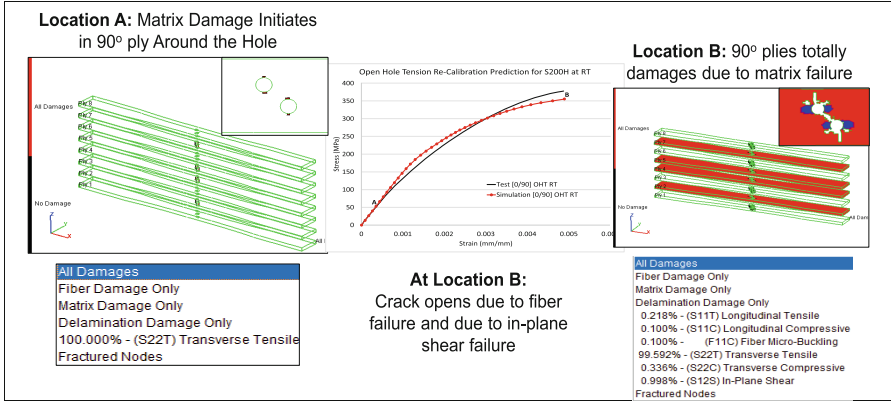


Fig. 9. Details of the damage evolution captured by simulation at RT

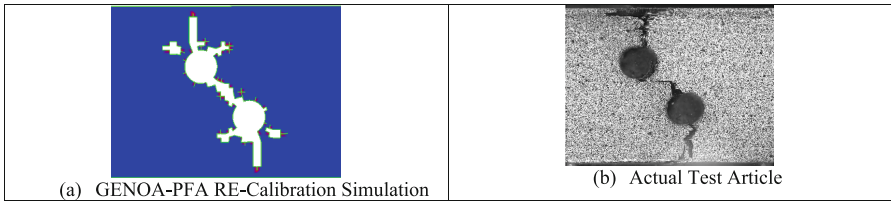


Fig. 10. Fracture Path Compared with Test Results (RT)

### 3.3 PMC Material Blind Test Predictions, Recalibration Predictions, and Test Data

Quasi isotropic static test case was chosen to show the blind prediction results as well as the recalibration results. Failure criteria selected were strength, and strain based: a) trans-laminar (fiber, matrix); b) interlaminar (shear, tension, relative rotation); and c) interactive. The results of blind prediction (labeled as submittal) and the recalibration results are shown in Fig. 11.

During the recalibration, no FE modeling changes were made. The FE models were kept simple (shells, consistent boundary conditions, test grips were not modeled). This paves the way for attainable solutions for large structures. Based on extensive experience with Alpha Star staff and consultants, FE models with solid elements are not practical in component, sub assembly, and full vehicle models.

There were several modeling improvements made: 1)  $X_c = 1,680$  MPa from reference was used as approved by LM Aero. Same MCQ Calibration approach performed.

2) Matrix anisotropy was removed from the prediction. 3) Fiber waviness was taken into account for mixed layups (this required the use of one additional quasi iso layup test to calibrate to (CC-25). CC-25 stiffness was matched using fiber waviness parameters (theoretically accounts for waviness and gap effects in micromechanics equations). Fiber waviness is only active during a compressive stress state; 4) Analysis will check for tension and compression based on stress state and activated fiber waviness for compression in the lamina; 5) Analysis switch from Updated Lagrangian to Total Lagrangian (with stress redistribution after damage) after a global stiffness reduction falls under 20% across three consecutive equilibrium load step iterations; and 6) Same set of inputs and damage/fracture criteria were used for all tension and compression cases. Figure 9 shows Blind (Submittal) and Re-calibrated Prediction of Quasi Static [0/45/90/-45]<sub>s</sub> Un-notched and Openhole Specimens under tension and compression load.

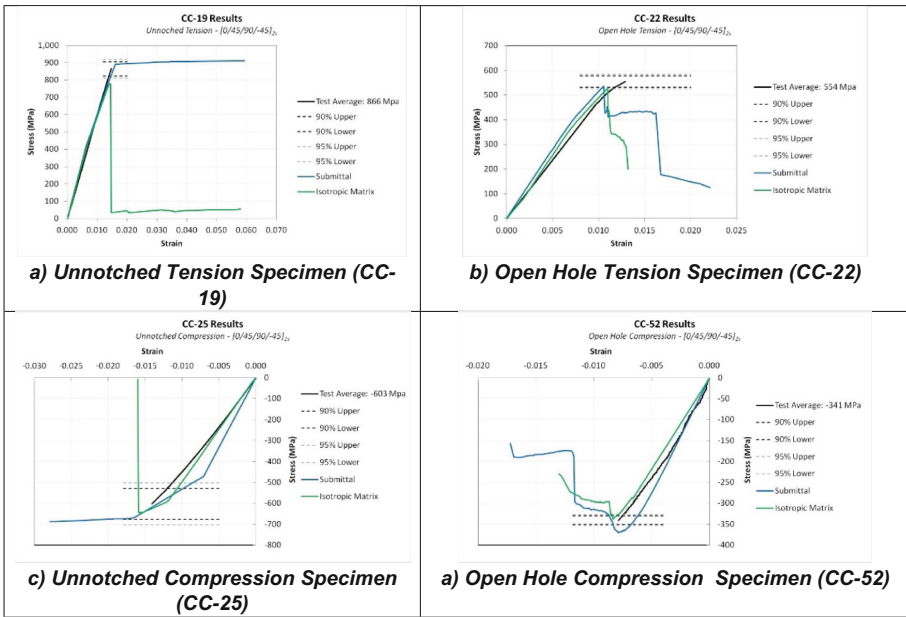


**Fig. 11.** Blind Prediction (Submittal), Re-Calibrated Prediction, and Test Data of Quasi Static [0/45/90/-45]<sub>s</sub> Un-notched and Openhole Specimens under tension and compression load

## 4 Conclusion

The CMC model includes linear matrix, micro crack density, SN and ET curves for matrix/fiber and fiber matrix interphase for both material systems. For S200H material system the model also includes 8 HS fiber architecture considering out of plane fiber orientation. For both the predictions for three temperatures were made with re-calibrated properties. MCQ analysis showed excellent comparison to the test with detailed physical interpretation. GENOA-PFA analysis also showed good comparison with test. It also

showed detailed physical interpretation of the analysis as well. For PMC material system both blind and recalibration phases incorporate single layered shell element using GENOA MS-PFA and FE NASTRAN solvers. The simulation time for MCQ material model and unnotched was within minutes, while un-notched and open hole specimens took 2 h. The blind prediction of quasi-isotropic specimen was predicted within 10%. The recalibration phase improvements to match test data incorporated effect of defects such as fiber waviness, and removal of matrix anisotropy were performed primarily to improve the other layup predictions.

## References

1. Baid, H., Abdi, F., Huang, D.: Integrated computational material science engineering lifing model of CMC coupons using nano-micromechanics based multiscale progressive failure analysis. *Int. J. Multiscale Comput. Eng.* **19**(6) (2021)
2. Chamis, C.C., et al.: Micromechanics-based progressive failure analysis prediction for WWFE-III composite coupon test cases. *J. Compos. Mater.* **47**, 2695–2712 (2013)
3. Abdi, F., Surdenas, J., Munir, N., Housner, J., Keshavanarayana, R.: Computational approach toward advanced composite material qualification and structural certification, virtual testing and predictive modeling. In: Farahmand, B. (eds.) *Virtual Testing and Predictive Modeling*, pp. 137–185. Springer, Berlin (2009). [https://doi.org/10.1007/978-0-387-95924-5\\_6](https://doi.org/10.1007/978-0-387-95924-5_6)
4. Minnetyan, L., Su, X., Abdi, F.: Fiber-matrix interphase effects on damage progression in composite structures, AIAA-2008-1732, Chicago, IL, April 2008





# Reduction of Slamming Damage on GFRP Panels in Dry/Wet Conditions in Hulls of High-Speed Boats

A. Pollastro<sup>1</sup> (✉), V. Lopresto<sup>1</sup>, P. Townsend<sup>2</sup>, and J. C. Suarez-Bermejo<sup>3</sup>

<sup>1</sup> Dipartimento di Ingegneria Chimica, dei Materiali e della Produzione Industriale, Università degli studi di Napoli Federico II, Naples, Italy

<sup>2</sup> Facultad de Ingeniería Marítima y Ciencias del Mar, ESPOL, Guayaquil, Ecuador

<sup>3</sup> Material Science Department, Universidad Politécnica de Madrid, Madrid, Spain

**Abstract.** In this work we investigated slamming impact damages on symmetric GFRP for high-speed boats' hulls, and two ways to reduce it, the first one consisting in inserting a Kevlar's layer, while the second one consists in putting a 3D-printed sacrificial viscoelastic panel on top of the composite. Both the solution showed good reduction in impact damage and in energy absorption, but 3D-printed layers showed a consistent reduction in energy absorption even at higher energy levels.

**Keywords:** Slamming impact · GFRP · Aramidic fiber · 3D-printed layer

## 1 Introduction

Slamming is a significant event during navigation that occurs as a sudden force that strikes the vessel vertically on the bow and generates energy by the impact of a boat's hull on the free surface of the water. This force results in pulses of short duration (typically on the order of a few milliseconds) that act on a small surface and give rise to high-pressure peaks. The severity of such impacts and the resulting damage to the vessel are so unpredictable that operators proceed cautiously and slowly to avoid additional damage during voyages, a situation that is aggravated in the case of high-speed crafts [1].

In the case of GFRP vessels, slamming is unique in that the impact of the sea is converted into energy that is dissipated in a composite material, producing different levels of damage, which makes studying it very complex. This phenomenon has become one of the most important in ship design directly affecting the cost, capacity, and comfort [2].

In this work, we investigated two ways to reduce the slamming damage, the first one consisting in inserting a Kevlar's layer in the middle of the composite, while the second one consists in putting a 3D-printed sacrificial viscoelastic panel on top of the composite.

## 2 Experimental Methods

For the slamming tests,  $100 \times 100$  mm GFRP panels were prepared from 0–90 woven fabric and +45/–45 biaxial fabric, and polyester resin, using RTM technology. The panels have been left in vacuum bags for 24 h at ambient temperature, and then put in oven at 60°C for 2 h. The lamination configuration was  $[0/90, +45/ - 45, 0/90]_s$ .

We also prepared  $250 \times 250$  mm panels to be put in a salt spray chamber to analyse the effect of aging. The spray was made by 3,5% in weight of salt, and unmodified and kevlar-modified panels were left in the chamber for a period of 200, 400, 600, 800 and 1000 h and then tested under slamming impact. To choose the impact energy, some preliminary impact tests were made on  $250 \times 250$  mm dry panels, and then we took the impact energy in which the response was the most elastic, identified at 45,5 J for unmodified panels, and 40,3 J for the kevlar-modified panels. The panels with the viscoelastic layer were not put into the salt spray chamber because that kind of structure is very less sensitive to this kind of aging.

For the manufacture of the viscoelastic layers, a 3D Ultimaker-3 printer with two independent extruders was used to avoid contamination between the two polymers used, and the film was printed on a 200 mm x 300 mm hot bed by sequentially printing layers of molten material. The mechanism for energy dissipation is based on the incompressibility of a material with a Poisson coefficient close to 0.5, as most elastomers have. In this case, the elastomer (Thermoplastic Polyurethan TPU) is surrounded by cell walls of a stiffer material (Nylon). After receiving the impact, the elastomer is forced to deform but it is in confined by the rigid walls that impede the deformation. Forced in a state of volume invariance, the elastomer responds increasing its apparent stiffness modulus.

The viscoelastic layer is made of a periodic repetition of TPU hexagonal structures on the  $z$  plane, surrounded by Nylon. The section on the  $z$  axis of the TPU structure is also hexagonal. This structure has a nylon core, also hexagonal, as shown in Fig. 1. The largest corner of the TPU hexagon measure 5.60 mm.

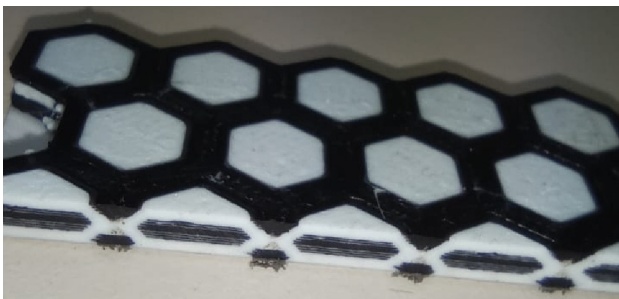


**Fig. 1.** Section of a viscoelastic layer. Is possible to identify hexagonal structures of TPU (in white) and of nylon (in black)

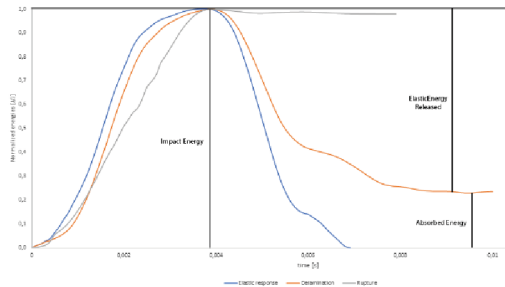
The Kevlar-modified specimens were prepared with the same lamination configuration of the unmodified panels, but right in the middle a hybrid fabric layer, made of aramidic woven and glass fibers mat, was inserted. So, the final configuration was [0/90, ±45, 0/90, Kevlarlayer, 0/90, ±45, 0/90].

To simulate the slamming impact, i.e. an impulsive force on the specimens, a low velocity drop weight test was conducted. The impactor head is launched by gravity, guided on two rails. The specimen is installed and clamped on the base. The anti-rebound system is designed to be activated with a laser reader, avoiding repeated impacts. Changing the height and weight of the impactor, we changed the energy of the test. Additionally, an acceleration sensor or single-axis accelerometer was installed. The accelerometer sends the information to a data acquisition system to record acceleration versus the time of impact. From these accelerations we evaluated the energy that the panels received during the impact, and the value of the energy absorbed in delamination, cracking and in general damage processes, as suggested in a previous work [3].

An ultrasonic inspection of each of the specimens was conducted to evaluate damage after LVI. For this purpose, an immersion tank manufactured by Tecnitest was used with a motorized head to sweep the entire surface with an accuracy of 0.1–0.2 mm at a maximum inspection speed of 100 mm/s, and the apparatus was connected to a Masterscan 335 data acquisition and management system, showing the results in a C-scan representation with a color scale indicating the differences in ultrasonic attenuation in each zone of the panel.

### 3 Results

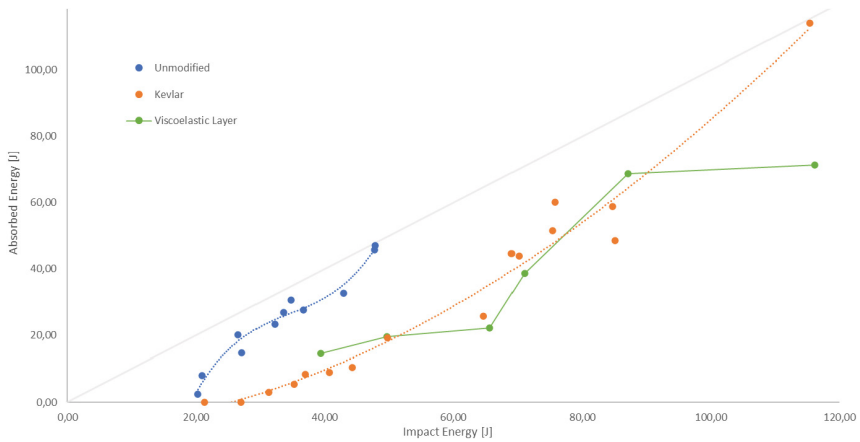
Impact tests gave different kind of response. At low impact energies, the response was totally elastic. At higher energies the panels start absorbing some energy. Finally, at rupture, all the energy is absorbed. This is shown in picture 2. We evaluated the absorbed energies for all the samples, as shown in the Table 1. We plotted the absorbed energy against the impact energy, obtaining the results shown in Fig. 3 (Fig. 2).



**Fig. 2.** Examples of normalized energies for GFRP panels with different response: totally elastic response (blue), partially elastic response with a certain amount of energy absorbed in delaminations and crackings (orange), and complete penetration into the specimen, where all the energy is absorbed (grey)

**Table 1.** Impact energy and absorbed energy for every specimen.

Unmodified			Kevlar			Viscoelastic Layer		
Spec.	E_imp	E_abs	Spec.	E_imp	E_abs	Spec.	E_imp	E_abs
1u	20,34	2,35	1k	21,38	0,00	1_vl	39,37	14,53
2u	20,95	8,02	2k	27,09	0,00	2_vl	49,69	19,70
3u	26,59	20,10	3k	31,27	2,99	3_vl	65,65	22,25
4u	27,12	14,82	4k	35,22	5,34	4_vl	71,09	38,74
5u	32,23	23,27	5k	37,00	8,48	5_vl	87,16	68,66
6u	33,59	26,87	6k	40,69	8,95	6_vl	116,09	71,28
7u	34,71	30,72	7k	44,31	10,52			
8u	36,68	27,66	8k	49,73	19,16			
9u	42,90	32,66	9k	64,73	25,74			
10u	47,75	45,79	10k	69,03	44,72			
11u	47,85	47,11	11k	70,20	43,90			
12u	66,40	66,40	12k	75,43	51,49			
			13k	75,76	60,16			
			14k	84,73	58,81			
			15k	85,15	48,58			
			16k	115,39	113,90			

**Fig. 3.** Absorbed energies in LVI by different kind of specimens: unmodified (blue), with kevlar (orange) and with a viscoelastic layer (green)

As we can see, both unmodified and Kevlar-modified panels present a complete elastic behaviour at low energy, while the specimens with the viscoelastic layer present, even at low energies, a certain amount of absorbed energy, due to resin debonding near the viscoelastic layer. At higher energies, unmodified panels reach quite fast the rupture point, identified at almost 50 J, while all the other specimens present just delamination (more or less severe) but without complete rupture. At high energies, i.e. around 70 J, Kevlar-modified specimens start presenting severe delamination and fiber rupture, while those modified with the viscoelastic layer show less severe delamination and small fiber rupture. Finally, at 120 J, Kevlar-modified panels reach rupture absorbing all the energy,

while the viscoelastic layer still preserve the panel, even if there is a severe delamination and some fiber rupture. Normalizing this plot respect to areal density (weight [kg] / surface [m<sup>2</sup>]), we obtain the same results, as shown in Fig. 4.

Ultrasounds analysis show even better results, as shown in Fig. 5. Unmodified specimens and Kevlar-modified specimens present the same behaviour, even if at different energy levels: the damaged surface grows with the impact energy because of delamination processes, until the point in which fiber rupture start, at which delamination processes stop leaving places to fiber rupture processes. Specimens modified with viscoelastic layer show a similar behaviour, but at energies way higher. Only the last specimen, at 116 J, present fiber rupture. In general, visual inspection confirm this hypothesis.

The specimens put in the salt spray chamber showed an interesting response to the effect of aging, according to Zong’s and Joshi’s previous work [4]: the more the panels remain in the chamber, the most elastic the response to the slamming impact. This can be attributed to the absorption of humidity, that made the polyester resin more plastic and flexible [4]. Unmodified specimens showed this effect in a more gradual way than kevlar-modified specimens, as showed in Figs. 6a and 6b.

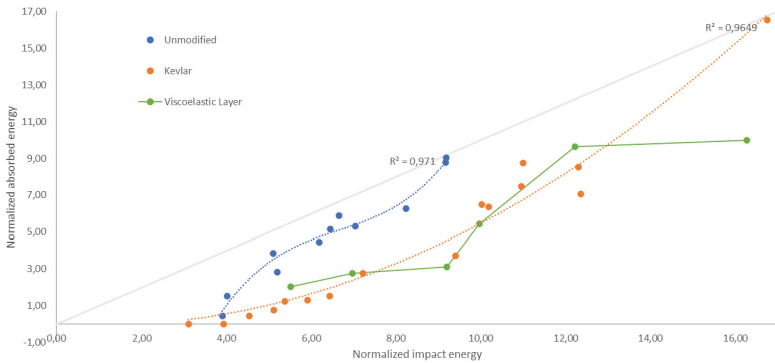


**Fig. 4.** Energies absorbed by different kind of specimens normalized with areal density: unmodified (blue), with kevlar (orange) and with a viscoelastic layer (green)

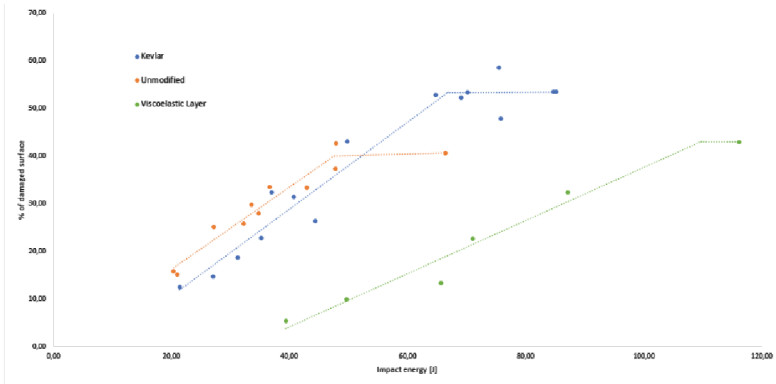


**Fig. 5.** Percentage of damaged surface for different kinds of specimens, measured with ultrasounds analysis.

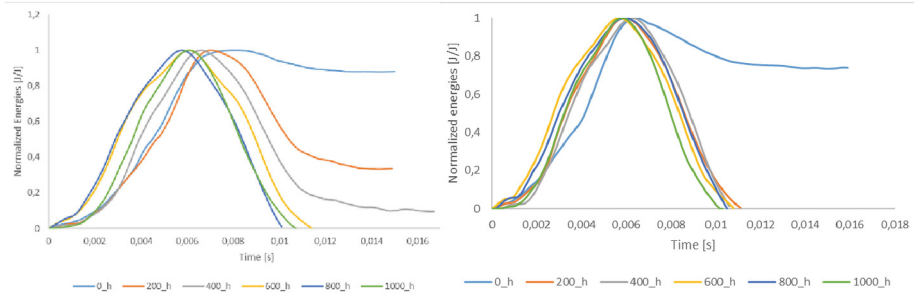


**Fig. 6.** Absorbed energies in LVI for aged specimens. In 6a are shown unmodified specimens, put in the chamber for 0, 200, 400, 600, 800 and 1000 h, while in 6b are shown the kevlar-modified specimens, aged in the same way.

## 4 Conclusions

Investigation of impact damage showed how both solutions (i.e., with a Kevlar layer and with a viscoelastic layer) resist better to slamming impacts, with a range of energy absorption without rupture way wider than the unmodified specimens. For the range of 50 J–75 J, specimens modified with the viscoelastic layer show a more elastic behaviour than Kevlar-modified specimens and present a very smaller delaminated surface. At high energies Kevlar-modified specimens reach rupture (i.e., with impactor penetration) while the specimens with the viscoelastic layer are still resisting well to the impact, just with a little bit of fiber rupture. The salt spray chamber showed how, in the beginning of the aging process, the humidity absorption made the composite panels more compliant.

## References

1. Townsend, P., Suárez-Bermejo, J.C., Sanz-Horcajo, E., Pinilla-Cea, P.: Reduction of slamming damage in the hull of high-speed crafts manufactured from composite materials using viscoelastic layers. *Ocean Eng.* **159**, 253–267 (2018)
2. Suárez, J.C., Townsend, P., Sanz, E., de Ulzurum, I.D., Pinilla, P.: The effect of slamming impact on out-of-autoclave cured prepregs of GFRP composite panels for hulls. *Procedia Eng.* **167**, 252–264 (2016)
3. Munoz, N., Townsend Valencia, P., Suárez-Bermejo, J.: Viscoelastic layer insertion to reduce the propagation of energy by vertical impacts on GFRP laminates (2020). <https://doi.org/10.18687/LACCEI2020.1.1.78>
4. Zhong, Y., Joshi, S.C.: Impact behavior and damage characteristics of hygrothermally conditioned carbon epoxy composite laminates. *Mater. Des. (1980–2015)* **65**, 254–264 (2015)



# Characterization of the Viscoelastic Properties of Tires Through Non- Destructive Tests

D. D.'agostinis Rinaldi<sup>(✉)</sup>, F. Farroni, and A. Genovese

University of Naples Federico II, Piazzale Tecchio 80, 80125 Naples, Italy  
davide.dago2000@gmail.com

**Abstract.** The design of a vehicle, whatever it is, is strongly influenced by the characteristics of the tire: it is important to understand how this determines the driveability, safety, performance, efficiency and comfort of the vehicle. The tire supports the weight of the vehicle and allows the forces of interaction with the road to be exchanged. It is one of the main examples of viscoelastic material for which the evaluation of the viscoelasticity of tires is a fundamental issue that aims at the development of polymers for innovative compounds, for the optimization of vehicle performance and road safety. The viscoelastic properties of tires are commonly determined by destructive methods among which dynamic mechanical analysis (DMA) is the most widespread. However, this method has several disadvantages, including the need to produce samples to be tested in the laboratory. In the automotive sector, on the other hand, the need to safeguard the entire structure is often dictated by regulations: it is therefore important to study alternative methods of analysis. In this work, a specific innovative and non-destructive device is presented to determine the dynamic characteristics of the compound of a tire. Specifically, the activity is aimed at developing experimental tests, carried out with the device, on different tire compounds to determine their viscoelasticity. The need to develop prototypes, which allow non-destructive analysis of the material, thus benefiting the analysis of a tire from a temporal point of view and from an economic point of view, is spreading in the world panorama of the development of racing and road tires.

**Keywords:** tire · viscoelasticity · dynamic load · non-destructive analysis

## 1 Introduction

In the nineteenth century, the physicists James Clerk Maxwell, Ludwig Boltzmann, Woldemar Voigt worked on models of viscoelasticity by studying the phenomena of creep (also called “creep”) and recovery of various materials, including: glass, metals and rubber [1]. The phenomenon of viscoelasticity was further elaborated at the end of the twentieth century on the synthesis of the first synthetic polymers, which show viscoelastic behavior. Viscoelasticity is a phenomenon expressed through mathematical models, which describes a material that behaves in an intermediate way between an elastic solid and a fluid [2]. Although some materials follow Newton’s law or Hooke’s law quite well, all materials show a marked deviation from elastic behavior and purely



viscous behavior, so from a practical point of view all materials are viscoelastic [1]. Some striking examples of viscoelastic materials include: amorphous polymers, semi-crystalline polymers, biopolymers, high temperature metals, and bituminous materials.

The tire of a vehicle is the contact element between the vehicle and the road and is the most important component in vehicle dynamic. The performance of the vehicle is strongly influenced by the characteristics of the tire: it effects handling and comfort, it supports the weight of the vehicle and, in particular, it allows the forces of interaction with the road to be exchanged [4].

The tire is one of the main examples of viscoelastic material so the evaluation of the viscoelasticity is a fundamental issue for the optimization of vehicle performance and road safety. The viscoelastic properties of tires are commonly determined by destructive methods among which dynamic mechanical analysis (DMA) is the most widespread [3, 5, 6]. However, this method has several disadvantages [3]. In this work, a specific innovative and non-destructive device is presented to determine the dynamic characteristics of the compound of a tire. Specifically, the activity is aimed at developing experimental tests, carried out with the device, on the tire to determine their viscoelasticity. The need to develop prototypes, which allow non-destructive analysis of the material, thus benefiting the analysis of a tire from a temporal point of view and from an economic point of view, is spreading in the world panorama of the development of racing and road tires [7].

## 2 Methods, Materials and Equipment

In the automotive sector, the need to characterize the tire compound thanks to non-destructive tests, to safeguard the entire structure, means that these tests are progressively developing and spreading. From 2021, among the non-destructive methods of tire compound characterization, the automotive world can also count on VESevo: “Viscoelasticity Evaluation System Evo”: a specific innovative and non-destructive device for determining the dynamic characteristics of a tire compound [8–10]. The tests were carried out directly on the tires. The tire used for the experimental tests is a traditional passenger tire compound [3] that represents the contact element between the vehicle and the road and it is the most important component in vehicle dynamic. The performance of the vehicle is strongly influenced by the characteristics of the tire: it effects handling and comfort, it supports the weight of the vehicle and, in particular, it allows the forces of interaction with the road to be exchanged [4].

The activity is aimed at the development of experimental tests, carried out with this device to determine their viscoelasticity.

### 2.1 Device

The VESevo device was designed [3] taking into consideration a gun-shaped handle; therefore, the ergonomics of the instrument, practical and functional, allows a high number of tests with satisfactory repeatability (Fig. 1).

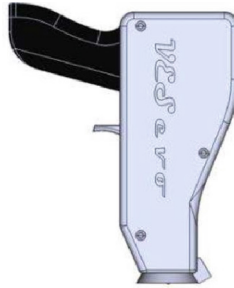


**Fig. 1.** VESEVO device [3]

The device is internally characterized by a steel rod with a hemispherical indenter. The rod is free to bounce on the surface of the tire by sliding inside a special guide, thus neglecting the phenomenon of damping during the movement of the rod. The system features a spring to ensure minimum preload and a magnet that ensures that the movement of the rod always starts from the same starting position: this magnet is mounted on a special cursor and can hold the upper plate of the rod. During each test it is necessary to analyze the displacement of the rod starting from the initial position with respect to the surface of the compound. A displacement sensor with a high response frequency is used to acquire the displacement signal. Since the temperature is a parameter that influences the behavior of a material, the temperature of the compound must also be acquired together with the displacement data during a single test. Therefore, an IR pyrometer was chosen and positioned at the end of the device to analyze the signals corresponding to the different viscoelastic behaviors of the sample of interest in the different test conditions [3].

## 2.2 Test

Pressing the “trigger” positioned on the handle activates the test allowing the indenter, present at the end of the steel rod, to impact the surface of the tire. In a single acquisition that takes place thanks to a National Instruments data logger and a software created in the Lab-View environment, the rebound of the rod has three different phases that are essential for the evaluation of the indices related to the viscoelastic behavior. The first is characterized by the impact of the sensorized rod on the surface of the tire; this first phase coincides with the minimum point of the curve acquired and reported in Fig. 2. During the second phase, the rod bounces up to the maximum point of the curve due to its interaction with the outer rubber layer of the tire; in particular, after the first one, different rebounds could occur depending on the surface temperature and the starting position. The last phase is characterized by a displacement value of the rod corresponding to the damping of the bar at the end of the reciprocal dynamic action.

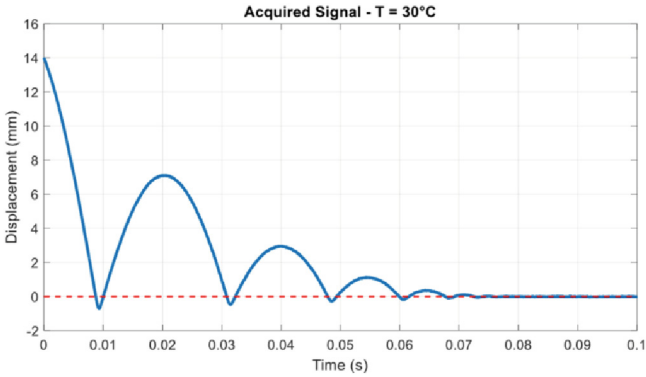


**Fig. 2.** Signal acquired at 30° [3]

### 2.2.1 Temperature

During a test session the tread surface is cooled and heated without degrading the material until its temperature stabilizes: the temperature plays a fundamental role in the study of tires. For the complete characterization of a tire it is necessary to study it in a range of temperatures according to the needs suitable for the use. Special devices such as heat guns or coolant sprays are used which modify the thermal conditions of the tire. Considering the typical shape of the signals provided by the VESevo, it is possible to estimate a set of indicators of the viscoelastic behavior of the material for the time-temperature characterization [3].

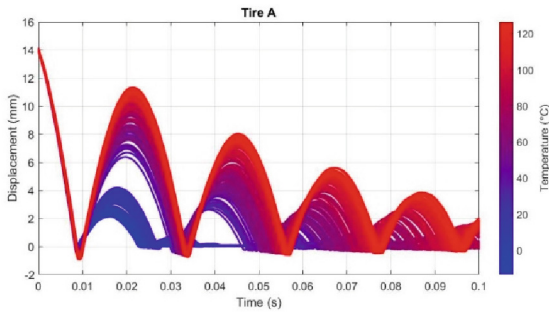


**Fig. 3.** Time-temperature characterization [3]

It can be seen in Fig. 3, which shows the data acquired on a tire compound, how these data vary as the temperature varies. As the temperature increases, the movement of the rod changes due to the different responses of the material. The signal is characterized by small amplitudes and a reduced number of bounces at low temperatures; on the contrary, at high temperatures there are more rebounds with higher amplitude values. This phenomenon is strictly dependent on the variations in viscoelasticity because of temperature: at lower

temperatures, the strain energy loss peak decreases and the bar cannot reach its maximum amplitude during return phase, vice versa at higher temperatures.

### 3 Comparison and Validation

Beyond the reasons presented at the beginning on the practical aspects of the described non-destructive methods compared to the destructive ones, it is possible to conclude that the results are completely in agreement: the glass transition temperature values, estimated through VESevo acquisitions, are compared with those obtained through D.M.A. shown in the Table. As clear, the results are very similar to demonstrating the goodness of the non-destructive method [4].

Tested Tire	Tg (D.M.A.)	Tg (VESevo)
Tire A	-26.8°C	-27.02°C
Tire B	-45.2°C	-46.42°C
Tire C	-25.5°C	-26.01°C

### 4 Conclusions

In this paper, the importance of non-destructive tests for determining the dynamic characteristics of a tire compound was highlighted and an interesting device, VESevo, that allows to carry out numerous experimental tests directly on the entire tire in a practical, simple and fast way to determine its viscoelasticity under varying conditions such as temperature, loading speed and composition of the compound, was presented. Given the importance of tires for the safety and efficiency of a vehicle and the need, sometimes dictated by regulations, not to destroy the structure, the prototypes that allow non-destructive analysis of the material, with consequent advantages both from a point of both temporal and economic, are the basis of research in recent years and will be the subject of future ones.

### References

1. Brukner, S., et al.: *Scienza e Tecnologia dei Materiali Polimerici* (2016)
2. Farroni, F., Russo, R., Timpone, F.: Experimental investigations on rubber friction coefficient dependence on visco-elastic characteristics, track roughness, contact force, and slide velocity (2017)
3. Farroni, F., Genovese, A., Maiorano, A., Sakhnevych, A.: Development of an innovative instrument for non-destructive viscoelasticity characterization: VESevo. In: Niola, V., Gasparetto, A. (eds.) *Advances in Italian Mechanism Science*, vol. 91, pp. 804–812. Springer, Cham (2020). [https://doi.org/10.1007/978-3-030-55807-9\\_89](https://doi.org/10.1007/978-3-030-55807-9_89)
4. Dongiovanni, C.: *Sviluppo di un modello numerico per il controllo automatico di un banco sperimentale per prove su pneumatici*, tesi (2019)

5. Menard, K.P., Menard, N.: Dynamic mechanical analysis. In: *Encyclopedia of Analytical Chemistry*, pp. 1–25. Wiley, Chichester (2017)
6. van Krevelen, D.W.: *Properties of polymers : their correlation with chemical structure ; their numerical estimation and prediction from additive group contributions*. Elsevier (1997)
7. Farroni, F., Sakhnevych, A., Timpone, F.: Physical modeling of a dynamic dial indicator for the non-destructive evaluation of tire tread viscoelastic characteristics. *Lecture Notes in Engineering and Computer Science* (2016)
8. Grosch, K.A.: The rolling resistance, wear and traction properties of tread compounds. *Rubber Chem. Technol.* **69**(3), 495–568 (1996)
9. Farroni, F., Sakhnevych, A., Timpone, F.: Physical modelling of tire wear for the analysis of the influence of thermal and frictional effects on vehicle performance. *Proc. Inst. Mech. Eng. Part L: J. Mater.: Des. Appl.* **231**, 151–161 (2017)
10. Maghami, S., Dierkes, W.K., Tolpekina, T.V., Schultz, S.M., Noordermeer, J.W.M.: Role of material composition in the construction of viscoelastic master curves: silica-filler network effects. *Rubber Chem. Technol.* **85**(4), 513–525 (2013)

# **Dynamic Behaviour of Lightweighting and Natural Composites**



# OAK Wood Chemical Densification: Microstructure Changes and Perspectives

L. Sansone<sup>1</sup>✉, C. Cigliano<sup>2</sup>, V. Lopresto<sup>2</sup>, I. Papa<sup>2</sup>, P. Russo<sup>1</sup>, V. Antonucci<sup>1</sup>,  
and M. R. Ricciardi<sup>1</sup>

<sup>1</sup> Institute for Polymers, Composites and Biomaterials, National Research of Council, P.le E.  
Fermi, 80055 Portici, Italy

lucia.sansone@ipcb.cnr.it

<sup>2</sup> Department of Chemical, Materials and Production Engineering, University of Naples  
“Federico II”, P. le Tecchio 80, 80125 Naples, Italy

**Abstract.** Wood is a versatile material used for various purposes due to its good properties, such as its aesthetic properties, acoustic properties, mechanical properties, and thermal properties, although its poor dimensional stability and low natural durability are the main obstacles that limit its use in mechanical applications. Therefore, modification is needed to improve these properties. Wood densification improves mechanical and physical properties by compressing the porous structure under steam, heat, and pressure. The wood’s lignin, cellulose, and hemicelluloses are polymers that behave similarly to the artificial polymers and are bonded together in wood. However, lignin differs from the other two substances by its highly branched, amorphous, three-dimensional structure. Under appropriate conditions, the lignin incorporated in the wood softens at about 100 °C, allowing its molecules to deform in the cell walls.

This paper proposes an eco-friendly and cost-effective method based on the hydrothermal modification of wood, as potential substitute of conventional chemical techniques for the densification of wood. The chemical structure and mechanical properties of wood cell walls were modified by the traditional alkali method and new hydrothermal treatments and experimentally characterized. This study provides a facile strategy by means of the facile green hydrothermal method for the development of new wood nanotechnology and various functional wood-derived materials.

**Keywords:** hydrothermal modification · thermal treatment · wood modification

## 1 Introduction

Wood densification is one of the effective techniques to improve the strength of low-density wood species and expand wood product applications due to the enhanced density of surfaces or the whole wood. The improvement of wood’s physical and mechanical properties has been performed through thermal treatments and impregnation or densification processes. Among these processes, densification is obtained by compressing wood in a transverse direction [1–3]. The increased wood density should then translate

into increased wood mechanical performances [4–9]. Densification by compression can be preceded by heating at high temperatures [10], softening it with hot steam [11] or by chemical treatments [12] or impregnation with resins [13, 14].

Song et al. [15] proposed a wood densification process based on a water solution of sodium hydroxide (NaOH) and sodium sulfite ( $\text{Na}_2\text{SO}_3$ ) to remove a part of cellulose, hemicellulose, and lignin. After a chemical bath in the water solution, wood is compressed to reduce its volume up to 80%, increasing its density and improving its mechanical properties compared to non-treated wood. The authors explain the high values of strength parameters of the treated material and its high resistance to punctures, not only by the tissue densification but also by the increased order and compression of cellulose nanofibers, that contributes to the creation of new hydrogen bonds. The reduction in the content of the components forming the matrix of the cellulose structure results in a significant reduction in elastic recovery. In lignocellulosic materials, hemicellulose is responsible for shape stabilization, while lignin plays a major role in quasi-elastic recovery (shape memory effect).

The hydrothermal modification of wood in different media, using a variety of temperatures and pressures, is one of the most prominent methods among thermal treatment techniques [16–18]. In addition, it can be performed in the presence of steam or liquid water under pressure or vacuum at various temperature levels. The hydrothermal modification reduces the equilibrium moisture content of treated wood samples, which subsequently leads to the enhancement of dimensional stability. The reduction in the equilibrium moisture content is caused by heat-induced factors, namely, hydroxyl groups reduction [19]. In hydrothermal modification in buffered media, treated wood is more hydrophobic, as water absorption into wood is limited and fungal growth is prevented. Durability has also improved with minimal lowering of strength properties [20–22]. Thus, several types of wood modification methods are available to enhance wood properties (i.e. heat, oil heat, chemical treatment, and hydrothermal modification).

In this study, a new hydrothermal method has been investigated. It is based on treatment of oak wood slices in a Teflon-lined stainless steel autoclave in a water/ethanol solution at temperature of 195 °C for 80 min, followed by hot-pressing, leading to the total collapse of cell walls and the complete densification of the natural wood with highly aligned cellulose nanofibres. The effects of hydrothermal modification on wood's morphological, physical, mechanical and chemical properties have been explored and compared to the alkali modification method.

## 2 Experimental

### 2.1 Materials and Processing

#### Materials

Oak (*Quercus*) wood slices of size 10 × 10 cm with a thickness of 1 cm, were used in this study.

Sodium hydroxide (NaOH), sodium sulfite ( $\text{Na}_2\text{SO}_3$ ), ethanol 99% v/v, and other chemical reagents were purchased from Merck Life Science (Milano, Italy). All reagents were used as received.



## Densification of Wood

### Alkaline Process

Oak wood blocks (sample size  $10 \times 10$  cm) were immersed in a boiling aqueous solution of mixed 2.5 M NaOH and 0.4 M Na<sub>2</sub>SO<sub>3</sub> for 7h, followed by immersion in boiling deionized water several times to remove chemicals<sup>15</sup>. Then, the wood blocks were pressed at 100 °C under a pressure of about 50 bar for about 1 day to obtain the densified wood (see Fig. 1).

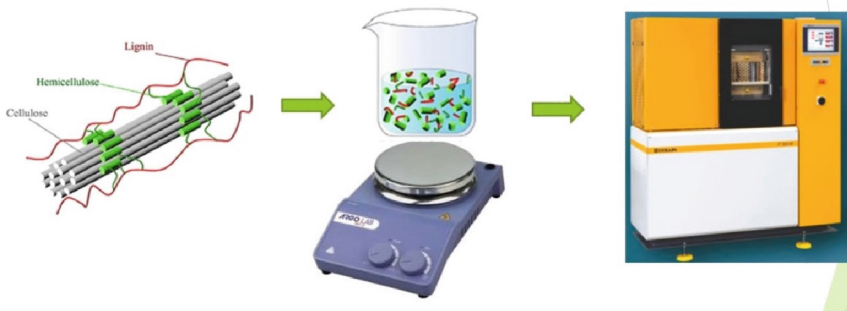


**Fig. 1.** Scheme of the Alkali process.

### The Green Process

Oak wood blocks (sample size,  $10 \times 5$  cm) were immersed in a water/ethanol solution 10% v/v and were transferred to a Teflon-lined stainlesssteel autoclave, which was sealed and maintained at 195 °C for 80 min, followed by immersion in deionized water several times to remove the chemicals and residues. The wood blocks were pressed at 100 °C under a pressure of about 50 bar for about 1 day to obtain the densified wood (see Fig. 2).



**Fig. 2.** Scheme of the eco-friendly process

## 2.2 Testing

Several experimental techniques have been used to evaluate both structural/morphological properties and thermodynamic/functional properties of oak wood before and after densification treatments.

### Scanning Electron Microscopy and X-ray Microanalysis (SEM-EDX)

The morphology of oak wood was investigated by scanning electron microscopy (SEM) using a field emission instrument Quanta 200 FEG. The sample was covered with a layer of gold/palladium alloy in a high-resolution metallizer Emitech K575X. X-Ray microanalysis was carried out by EDX Inca Oxford 250 instrument.

### Thermogravimetric Analysis

The specimens were scanned by a TA Instruments Q500 TGA (TA Instruments, New Castle, Delaware, USA) under air atmosphere.

### Fourier-Transform Infrared Spectroscopy

Fourier-transform infrared spectroscopy (FTIR) measurements on the wood samples, have been performed with Perkin Elmer FTIR-NIR Spectrum Frontier ((System 2000 FT-IR, Perkin-Elmer, Waltham, MA, USA) to estimate principal chemical bonds present on the samples and to verify any changes induced by the processes.

### Dynamic Mechanical Analysis (DMA)- Three Point Bending

The Dynamic Mechanical Analyzer (DMA) instrument detect these viscoelastic properties by either applying a small oscillating strain to the sample or measuring the resulting stress or by applying periodic stress and measuring the resulting strain. Samples are analyzed by a TA Instruments 2980 Dynamic Mechanical Analyzer (TA Instruments, New Castle, Delaware, USA).

## 3 Results and Discussion

The approach involves partial removal of lignin/hemicellulose from bulk natural oak wood followed by hot-pressing. Natural oak wood contains many channels (see Figs. 3 a) and c)). Chemical treatment leads to substantial reduction of lignin/hemicellulose content in natural wood, the wood becomes more porous and less rigid (see Fig. 3 b)). Upon hot-pressing at 100 °C perpendicular to the wood growth direction, the porous wood cell walls collapse entirely, resulting in a densified piece of wood reduced in thickness to about 23% (see Fig. 3 c)). Most of the densified wood consists of well-aligned cellulose nanofibres, which greatly enhance hydrogen bond formation among neighboring nanofibres. Hydrothermal treatment leads to a densified porous structure with small pores compared to chemical treatment (see Fig. 3 e)). The hot pressing causes the collapse of the porous wood cells (see Fig. 3 f)) and the densified wood shows a reduction thickness of about 67%, compared to the alkali treatment.

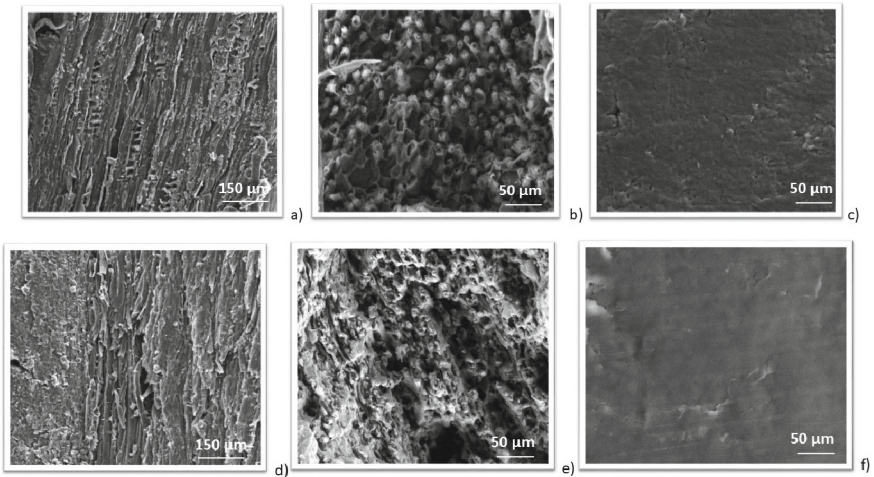


**Fig. 3.** Morphological analysis by SEM of a) untreated oak; b) porous oak after alkali method; c) Oak after pressing treatment; d) untreated oak; e) porous oak after green method; f) Oak after pressing treatment.

To understand the changes of wood cell wall polymers during the densification process, the infrared spectra were collected and are shown in Fig. 4. The bands at  $3378\text{ cm}^{-1}$  and  $2900\text{ cm}^{-1}$  were attributed to O–H and C–H stretching vibration in cellulose, hemicellulose and lignin. The two discussed methods analyzed some characteristic bands in untreated and densified wood. The absorption band at  $1733\text{ cm}^{-1}$  is attributed to C = O stretching vibration in unconjugated ketones, a characteristic hemicellulose band. The disappearance of this band in the densified wood was caused by the deacetylation in hemicellulose, indicating that the two methods entirely dissolved hemicellulose. The band in the range of  $1593\text{--}1650\text{ cm}^{-1}$  appeared to be a shoulder absorption peak in the pristine wood but turned into a sharp peak only at  $1593\text{ cm}^{-1}$  (C = C stretching vibration on benzene ring) in the densified wood spectrum. It was indicated that the polar functional groups conjugated with benzene ring caused some changes. In addition, the lignin molecular structure may be changed from vitreous to high-elastic, and the band changes at  $1240\text{ cm}^{-1}$  (C–H of guaiacyl ring in lignin) indicated that lignin unit may be changed [23].

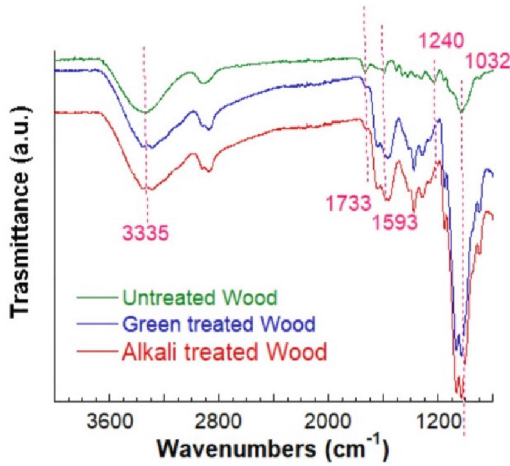


**Fig. 4.** FTIR Spectra of oak wood compared to the alkali-treated wood and green oak treated wood

Moreover, the thermal stability of the untreated oak wood compared to treated one was also investigated by DTA. From DTA curves in Fig. 5, it can be observed that the weight loss of untreated oak wood takes place at two stages: the first one (from 70 °C to 140 °C) is probably caused by water loss of wood, while the other (from 200 °C to 400 °C) is probably induced by the degradation of wood. The thermal degradation of alkali-treated oak wood is from 200 to 330 °C, compared to untreated and green-treated samples, probably due to the chemicals that modify the chemical wood structure.

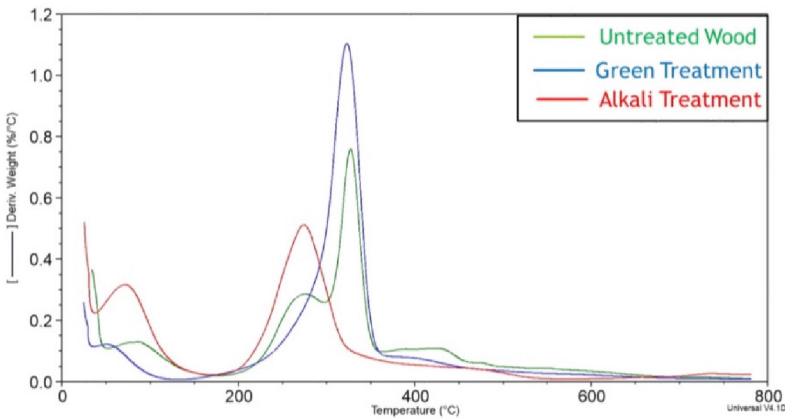


**Fig. 5.** DTA curves of untreated wood compared to alkali treated oak and green treated wood

Storage modulus is a crucial property to measure the energy storage capability of material after elastic deformation. Figure 6 shows the storage modulus of treated and untreated wood specimens.

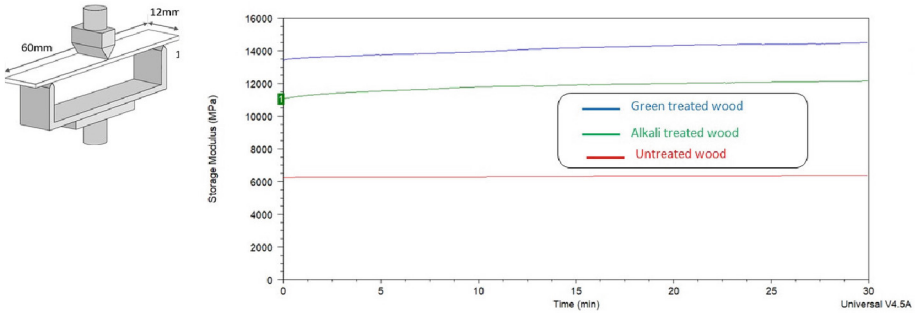


**Fig. 6.** DMA curves of untreated wood compared to alkali treated oak and green treated wood

Storage modulus decreased as temperature increased, depending on the increased chain mobility of the polymeric components of the wood cell walls at higher temperatures. Storage modulus of alkali treated and green treated wood sample significantly increased compared to the untreated sample (see Table 1). The increase of storage modulus demonstrates that the chemical and temperature-pressure treatments enhance the elastic properties of the wood samples and reduce their brittleness, probably due to high cross-linkage between the celluloses and acidic hydrolysis or degradation of cell walls under high acidity and high temperature.

**Table 1.** Storage modulus of untreated wood compared to alkali treated oak and green treated wood

Samples	Storage Modulus (MPa)
Untreated Sample	6000
Alkali treated Sample	11280
Green treated Sample	13500

## 4 Conclusion

This study proposes an eco-friendly hydrothermal method to densify oak wood. This method is based on treating oak slices in a Teflon Teflon-lined stainless steel autoclave, which was sealed and maintained at 195°C for 80 min, followed by immersion in deionized water several times to remove the chemicals and residues. Then, the wood blocks were pressed at 100 °C under a pressure of about 50 bar for about 1 day to obtain the densified wood. Experimental results show that the mechanical properties of treated wood by hydrothermal method significantly improved over treated wood with alkali treatment and untreated wood due to the increase of cross-linked bonds in the crosslinking network, by increasing elasticity and reducing degradation in the wood cell walls. DTA analysis showed that alkali-treated wood samples have lower stability than the untreated

sample and treated samples with the green method, in particular, the last samples showed high stability. In conclusion, after hydrothermal modification, wood shows interesting improved properties and is suitable for different material applications.

**Acknowledgment.** The authors would like to thank F. Docimo and M. R. Marcedula for their support of the experiments, Valerio Di Giulio the wood craftsman, Ph.D. Leandro Maio, and Vittorio Memmolo of the Industrial Engineering Department of the University of Study Federico II for their support of getting oak wood.

## References

1. Bekhta, P., Proszkyk, S., Krystofak, T.: Color in short-term thermomechanically densified veneer of various wood species. *Eur. J. Wood Wood Prod.* **72**(6), 785–797 (2014). <https://doi.org/10.1007/s00107-014-0837-1>
2. Kutnar, A., Kamke, F.A., Sernek, M.: The mechanical properties of densified VTC wood relevant for structural composites. *Holz. Roh. Werkst.* **66**(6), 439–446 (2008)
3. Laine, K., Belt, T., Rautkari, L., Ramsay, J., Hill, C.A.S., Hughes, M.: Measuring the thickness swelling and set-recovery of densified and thermally modified Scots pine solid wood. *J. Mater. Sci.* **48**(24), 8530–8538 (2013). <https://doi.org/10.1007/s10853-013-7671-4>
4. Blomberg, J., Persson, B., Blomberg, A.: Effects of semi-isostatic densification of wood on the variation in strength properties with density. *Wood Sci. Technol.* **39**(5), 339–350 (2005). <https://doi.org/10.1007/s00226-005-0290-8>
5. Kutnar, A., Kamke, F.A., Sernek, M.: Density profile and morphology of viscoelastic thermal compressed wood. *Wood Sci. Technol.* **43**(1–2), 57–68 (2009). <https://doi.org/10.1007/s00226-008-0198-1>
6. Rautkari, L., Properzi, M., Pichelin, F., Hughes, M.: Properties and set recovery of surface densified Norway spruce and European beech. *Wood Sci. Technol.* **44**(4), 679–691 (2010). <https://doi.org/10.1007/s00226-009-0291-0>
7. Laskowska, A.: The influence of process parameters on the density profile and hardness of surface-densified birch wood (*Betula pendula* Roth). *BioResources* **12**(3), 6011–6023 (2017)
8. Pelit, H., Budakçı, M., Sönmez, A.: Density and some mechanical properties of densified and heat post-treated Uludağ fir, linden and black poplar woods. *Eur. J. Wood Wood Prod.* **76**(1), 79–87 (2018). <https://doi.org/10.1007/s00107-017-1182-y>
9. Sandberg, D., Haller, P., Navi, P.: Thermo-hydro and thermo-hydromechanical wood processing: an opportunity for future environmentally friendly wood products. *Wood Mater. Sci. Eng.* **8**(1), 64–88 (2013)
10. Pelit, H., Sonmez, A., Budakci, M.: Effects of ThermoWood® process combined with thermo-mechanical densification on some physical properties of scots pine (*Pinus sylvestris* L.). *BioResources* **9**(3), 4552–4567 (2014)
11. Fang, C.H., Mariotti, N., Cloutier, A., Koubaa, A., Blanchet, P.: Densification of wood veneers by compression combined with heat and steam. *Eur. J. Wood Wood Prod.* **70**(1–3), 155–163 (2012)
12. Ugovšek, A., Kamke, F.A., Sernek, M., Kutnar, A.: Bending performance of 3-layer beech (*Fagus sylvatica* L.) and Norway spruce (*Picea abies* (L.) Karst.) VTC composites bonded with phenol-formaldehyde adhesive and liquefied wood. *Eur. J. Wood Wood Prod.* **71**(4), 507–514 (2013)
13. Laine, K., Segerholm, K., Wålinder, M., Rautkari, L., Hughes, M.: Wood densification and thermal modification: hardness, set-recovery and micromorphology. *Wood Sci. Technol.* **50**(5), 883–894 (2016). <https://doi.org/10.1007/s00226-016-0835-z>

14. Lykidis, C., Moya, R., Tenorio, C.: The effect of melamine formaldehyde impregnation and hot-pressing parameters on the density profile of densified poplar wood. *Eur. J. Wood Wood Prod.* **78**(3), 433–440 (2020). <https://doi.org/10.1007/s00107-020-01515-y>
15. Song, J., et al.: Processing bulk natural wood into a high performance structural material. *Nature* **554**(7691), 224–228 (2018)
16. Ilanidis, D., Stagge, S., Jönsson, L.J., Martín, C.: Hydrothermal pretreatment of wheat straw: effects of temperature and acidity on byproduct formation and inhibition of enzymatic hydrolysis and ethanolic fermentation. *Agronomy* **11**, 487–507 (2021)
17. Endo, K., Obataya, E., Zeniya, N., Matsuo, M.: Effects of heating humidity on the physical properties of hydrothermally treated spruce wood. *Wood Sci. Technol.* **50**(6), 1161–1179 (2016). <https://doi.org/10.1007/s00226-016-0822-4>
18. Song, B., Lin, R., Lam, C.H., Wu, H., Tsui, T.H., Yu, Y.: Recent advances and challenges of inter-disciplinary biomass valorization by integrating hydrothermal and biological techniques. *Renew. Sustain. Energy Rev.* **135**, 110370 (2021)
19. Jamsa, P., Jämsä, S., Viitaniemi, P.: Heat treatment of wood better durability without chemicals. In: Rapp, A.O. (ed.) *Special Seminar: Environmental Optimization of Wood Protection*. COST: Bruseless, Belgium, Antibes, France, 17–22 (2001)
20. Saliman, M.A.R., et al.: Hydrothermal treatment of oil palm wood: effect of treatment variables on dimensional stability using response surface methodology. *J. Oil Palm Res.* **29**, 130–135 (2017)
21. Talaei, A., Karimi, A.: Compression strength, hardness and shear strength of heat treated beech (*Fagus Orientalis*) wood in buffered mediums. *Int. J. Mech. Prod. Eng.* **3**, 6–9 (2015)
22. Ebadi, S.E., Ashaari, Z., Late Masoumi, H.R.F., Soltani, M., Naji, H.R., Vaysi, R.: Evaluation of bending strength of hydrothermally treated oil palm wood in various buffered media using response surface methodology. *J. Trop. For. Sci.* **31**, 151–161 (2019)
23. Lehto, J., Louhelainen, J., Kłosińska, T., Drożdżek, M., Alén, R.: Characterization of alkali-extracted wood by FTIR-ATR spectroscopy. *Biomass Convers. Biorefin.* **8**(4), 847–855 (2018). <https://doi.org/10.1007/s13399-018-0327-5>



# Hybridization of Thin Laminates with Natural Fibers: A Comparison Study Between Hemp and Flax

L. Boccarusso<sup>1</sup>(✉), M. Durante<sup>1</sup>, D. De Fazio<sup>1</sup>, K. Myronidis<sup>2</sup>, M. Meo<sup>2</sup>,  
and F. Pinto<sup>2</sup>

<sup>1</sup> Department of Chemical, Materials and Production Engineering, University of Naples  
“Federico II”, P.le Tecchio 80, 80125 Naples, Italy  
luca.boccarusso@unina.it

<sup>2</sup> Department of Mechanical Engineering, Material Research Centre, University of Bath, Bath,  
UK

**Abstract.** In recent years, the rapid growth of interest in the use of natural fibers (NFs) as reinforcement for composites, due to their reduced environmental impact and low-cost, generated several research studies aimed at the study of manufacturing processes of natural fibers polymeric composites and their innovative applications.

However, composite reinforced by natural fibers like hemp or flax are currently mainly used for non-structural applications because of their high variability in mechanical properties, lower mechanical performances if compared to synthetic fibers and susceptibility to humidity. Consequently, a possible method for overcoming these problems and expanding NF applications also for structural components, could be their use in hybrid systems. In particular, the development of hybrid panels characterized by a combination of two different reinforcements, guarantees higher tailorability of the structure, alleviating the inherent drawbacks of each of the different fibers while keeping the benefits of both, and at the same time enables synergistic effects that can lead to properties that neither of the constituents possesses, leading to the extension of the application fields for some materials that alone do not possess the required properties.

Therefore, this paper is focused on the study of the production and mechanical characterization in terms of impact performances of hybrid thin sandwich panels consisting in CFRP skins and a thin hemp and flax bigrid as core that was manufactured with an ad hoc continuous manufacturing process.

**Keywords:** Hybridization · Composite · Sandwich · Hemp · Flax · LVI

## 1 Introduction

Fiber-reinforced plastics (FRPs) composites are a family of materials consisting of a polymer matrix reinforced by fibers with diameters ranging from a few micrometers to several tens of micrometers. Their unique characteristics such as high specific mechanical



properties, good chemical resistance and low thermal expansion, have made over the last 40 years FRPs attractive to a number of industrial sectors, including the aerospace, naval, automotive, construction and sporting goods industries [1].

FRPs materials are characterized by an interesting freedom design not only concerning the type and dimension of reinforcement and matrix, but also in the orientation of the fibers, their content fraction and stacking sequence. Based on these considerations, appeared to be promising to incorporate within the same matrix system, two or more fiber types in order to combine their characteristics and obtain a final product with unique properties. The materials resulting from such interaction are known as fiber-hybrid composites (FHCs) and their main advantages are to alleviate the inherent drawbacks of each of the fiber types while keeping the benefits of both, while enabling synergistic effects that can lead to properties that neither of the constituents possess [1–3]. Nowadays, considering the environmental awareness, depletion of petroleum resources, disposal problems after use, and introduction of new rules and regulations by legislative authorities to satisfy the demands of the society, the new products must minimize the environmental impact; therefore in this context appeared to be interesting the use of vegetable fibers as reinforcing phase in hybrid composite systems. However, if on one hand the use of vegetable fibers is connected with several environment advantages, on the others it has to be considered that the lower mechanical properties can sometime limit their application for structural components.

In this context, the hybridization between vegetable and syntenic fibers in FHC systems, appeared to be an interesting way to overcome this limitation.

Carbon/vegetable fiber hybrid composites can have some role especially for the possible combination of properties: vegetable fiber composites might allow different mechanisms of damage propagation and energy dissipation and possibly even have some mitigating effect on the inherent brittleness (limited toughness) of carbon fibre composites. Vegetable fibers exhibit nonlinear behavior when subjected to external loads, resulting in a more efficient energy dissipation mechanism that, in turn, can lead to better performance of components where vibration damping is anticipated [1, 4].

Among various kinds of natural fibers, hemp and flax appeared to be the most attractive ones due to their interesting properties like the low density, high specific stiffness, high vibration damping performance, thermal isolation, impact response and so on [5–7].

Therefore, aiming to extend the use of these vegetable fibers also for structural components for primary, the focus of this work is to combine the ductility of hemp and flax fibers with the strength of carbon fibers developing a hybrid system. In detail, it was studied the possibility to produce thin laminates in sandwich configuration with a midplane vegetable layer and skins in carbon fibers. Two type of laminates that differ in the type of vegetable layer (hemp or flax) are produced and the impact properties at 2 and 5 J were investigated.

## **2 Materials and Methods**

### **2.1 Materials and Manufacturing**

The thin composite laminates under investigation consisted in three layers, two in carbon fibers and one in vegetable fibers (hemp or flax) in a sandwich configuration where the

vegetable layer were located in the midplane. In the next of the text, the sample reinforced with flax will be labelled as F and the one reinforced with hemp as H.

For this purpose, bio-epoxy system (Super Sap® 100 Epoxy provided by Entropy Resins) and woven hemp and flax fabric having an areal density (GMS) of 380 g/m<sup>2</sup> (supplied by Fidia), were used to produce the bio composite plies used in the midplane of the hybrid laminates. Before impregnation, hemp and flax fabrics were dried in an oven for 12 h at 60 °C and a relative humidity of 20% [8].

Woven carbon fabric with an areal density of 200 g/m<sup>2</sup> (supplied by Toray international Srl) were impregnated with SX10 epoxy resin (supplied by d by Mates Srl) to produce top and bottom thin composite plies.

All composite laminates were manufactured in two steps: first the production of the vegetable composite layers by using an ad-hoc manufacturing process and after the impregnation of carbon layers and then the final stacking. In details, the production system used to produce the bio-based vegetable layer [8, 9] is schematized in Fig. 1 and it is divided in the following steps:

- Impregnation
- Resin content reduction
- Resin absorption
- Cutting
- Polymerization

In the first step, a caterpillar apparatus localized at the end of the production system pulls and forces the vegetable fabric in a resin bath, where tension rolls squeeze the fibers in order to obtain a good impregnation. At this point, the impregnated fabric passes under an air jet flow that blows through the mesh of the fabric and then, between a couple of rolls covered with absorbent paper layers; thanks to the large mesh that characterizes both the flax and hemp fabric, the air flow is able to remove the excess of resin between the spaces reaching the desired fiber content. By controlling the amount of resin in the resin bath and by tailoring the resin removal process, the ratio between the weight of the impregnated and unimpregnated layers was kept constant to 2.5 and the fiber weight fraction content of each layer at almost 40%. Finally, the impregnated fabric is cut in layers 300 × 300 mm<sup>2</sup>.

After this step, all composite laminates were manufactured by the combination of hand lay-up and vacuum compression molding technique. Carbon fabrics were manually impregnated with the epoxy resin and placed in a sandwich configuration with the previous vegetable fibers produced in a mold sized 300 × 300 mm<sup>2</sup> by hand layup technique. At the end of the stratification phase the mold with the uncured laminates were sealed in an elastomeric bag under vacuum and placed in a hydraulic press under a pressure of 8 bar at 55 °C for 2 h, then the laminates were left to cure at room temperature under a pressure of 8 bar for 24 h. The final thickness for both H and F sample type were equal to 0.25 mm. In Fig. 2, a representation of the vegetable fibres used and of the produced laminate are reported.

Impact tests were carried out using a home-made falling drop weight machine, equipped with an impactor tip of 16 mm diameter and an impactor mass of 2.66 kg [1]. Moreover, in order to avoid possible further impacts, the impactor rig is equipped

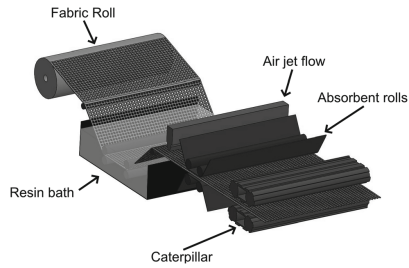


**Fig. 1.** Schematization of the production system.

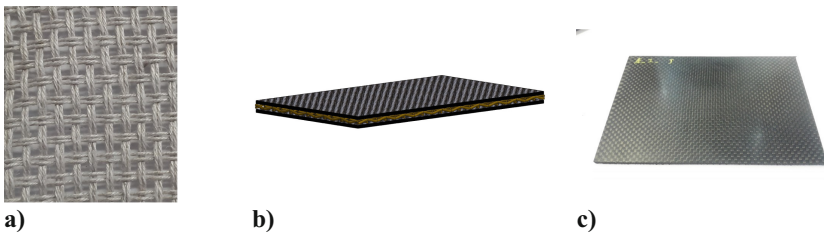


**Fig. 2.** Vegetable impregnated fabrics (a), schematization of sample type (b) and example of produced laminate (c).

with an anti-rebound system that hold the shuttle after the first impact. The impact tests were performed according to ASTM D7136 standard. The impacts were carried out on a total number of 5 specimens for each sample typology. Rectangular specimens 100 mm × 150 mm in dimension were cut according to the ASTM standard and clamped between two steel plates using bold serrated by hand in order to avoid any movement of the samples. Impact test at 2 and 5J of energy were conducted. Finally, thermography ND technique were used to analyze the damage. Below the thermography setup:

- The generator is a Hensel TRIA 6000 S rated at 6000 J energy
- The 2 flash heads (50% each of the total energy) were Hensel EH Pro 6000 S
- IR Camera was a Longwave IR Xenics Bobcat 640 GigE, resolution 640 × 512 pixels with a max frame rate of 50 Hz Software used Xeneth that comes with the camera First Section

### 3 Results and Discussion

Figure 3 shows the typical force vs displacement curves and thermography images related to samples impacted at 2J.

From the comparison appeared that the sample type having hemp in the midplane (H sample) are able to react with a slightly higher force and rigidity respect to F sample type (reinforced with flax fibres). Both sample types when the displacement was around 5.5 mm showed a load drop due to the starting of damage of the carbon skins top layer. However, from both the plot and thermography images it is possible to observe that H

type are more prone to damage when reach this value of displacement than F sample type. Looking at table it is possible to observe that H sample type are able to absorb more energy than F (Table 1).

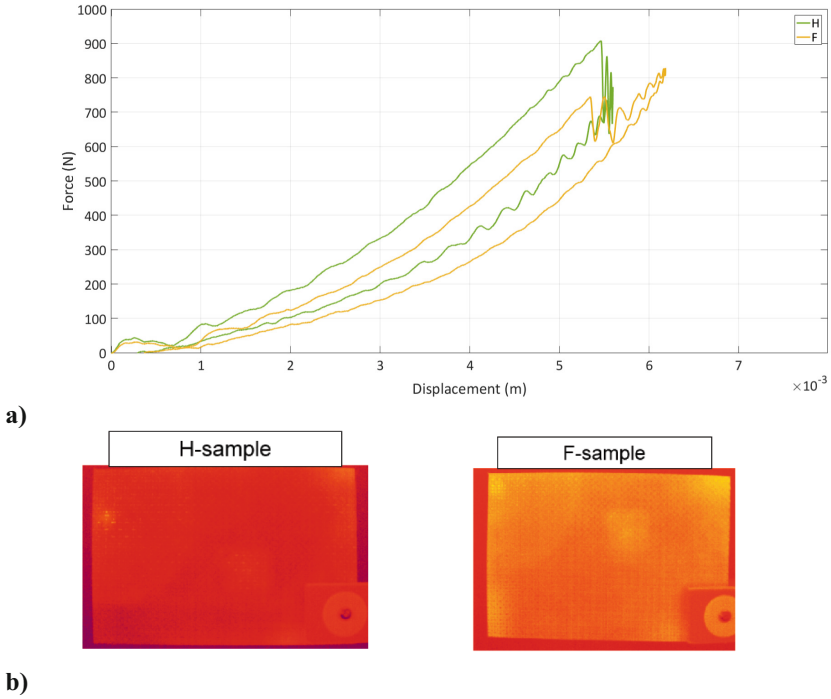
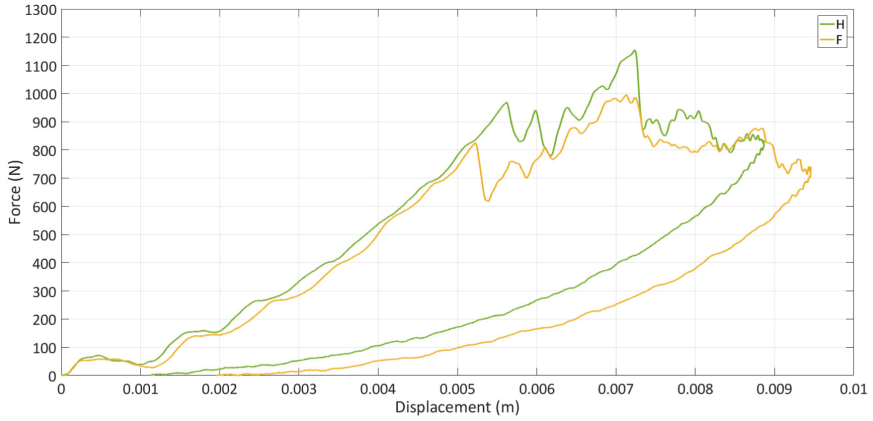


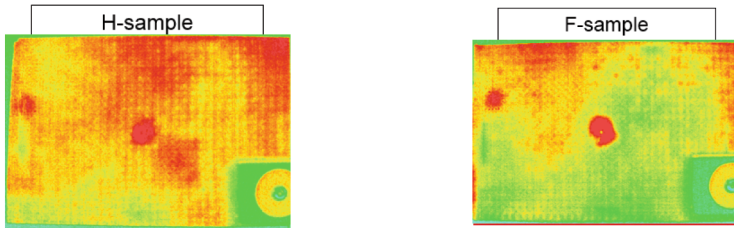
**Fig. 3.** Typical impact curves (force versus displacement) for H and F samples impacted at 2J (a) and thermography images of tested samples (b).

Looking at Fig. 4, it is possible to note that when the impact energy was raised to 5J, no significative differences in terms of rigidity and maximum force between H and F were detected and both sample type showed damages.

Therefore, differently from impact test at 2J, at higher impact energy the flax was able to highlight its better properties, indeed as reported in Table 2, the absorbed energy is higher than H samples.



a)



b)

**Fig. 4.** Typical impact curves (force versus displacement) for H and F samples impacted at 5J (a) and thermography images of tested samples (b).

**Table 1.** Results of impact tests carried out at 2J.

Sample	Max Force (N)	Max Displacement (mm)	Absorbed Energy (J)
H	907.0	5.6	0.70
F	827.5	6.1	0.56

**Table 2.** Results of impact tests carried out at 5J.

Sample	Max Force (N)	Max Displacement (mm)	Absorbed Energy (J)
H	1154.2	8.9	3.14
F	998.3	9.5	3.49

## 4 Conclusions

Natural fibers are an eco-friendly and sustainable resource for the manufacturing of composites and they constitute a green alternative to traditional materials. In this preliminary work, hemp, flax and carbon fibers were used to produce thin hybrid laminate, 0.25 mm in thickness. Since the aim was the production of thin laminates in sandwich configuration with the vegetable layer lightness as possible and located in the midplane, the choice to use ad-hoc manufacturing process for the production of the vegetable layer appeared to be suitable.

The results showed that under low values of impact energy, i.e. 2J, the samples with the hemp fibers showed slightly higher mechanical performances in terms of absorbed energy but with a more evident damage. Instead, at higher impact energy, i.e. 5J, the flax fibers were able to highlight their higher mechanical performances. Future work based on these results can include an extended experimental campaign including the production of different samples characterized by different density of the vegetable layer and additionally impact tests at different energy levels.

## References

1. Pinto, F., Boccarusso, L., De Fazio, D., Cuomo, S., Durante, M., Meo, M.: Carbon/Hemp bio-hybrid composites: effects of the stacking sequence on flexural damping and Impact properties. *Compos. Struct.* **242**, 112148 (2020)
2. Swolfs, Y., Gorbatikh, L., Verpoest, I.: Fibre hybridisation in polymer composites: a review. *Compos. A* **67**, 181–200 (2014)
3. Visweswaraiyah, S.B., Lessard, L., Hubert, P.: Interlaminar shear behaviour of hybrid fibre architectures of randomly oriented strands combined with laminate groups. *Compos. Struct.* **176**, 823–832 (2017)
4. Flynn, J., Amiri, A., Ulven, C.: Hybridized carbon and flax fiber composites for tailored performance. *Mater. Des.* **102**, 102–121 (2016)
5. Awais, H., Nawab, Y., Anjang, A., Akil, H.M., Abidin, M.S.Z.: Mechanical properties of continuous natural fibres (Jute, Hemp, Flax) reinforced polypropylene composites modified with hollow glass microspheres. *Fibers Polym.* **21**(9), 2076–2083 (2020). <https://doi.org/10.1007/s12221-020-2260-z>
6. Manian, A.P., Cordin, M., Pham, T.: Extraction of cellulose fibers from flax and hemp: a review. *Cellulose* **28**(13), 8275–8294 (2021). <https://doi.org/10.1007/s10570-021-04051-x>
7. Hernandez-Estrada, A., Müssig, J., Hughes, M.: The impact of fibre processing on the mechanical properties of epoxy matrix composites and wood-based particleboard reinforced with hemp (*Cannabis sativa L.*) fibre. *J. Mater. Sci.* **57**, 1738–1754 (2022)
8. Boccarusso, L., Durante, M., Langella, A.: Lightweight hemp/bio-epoxy grid structure manufactured by a new continuous process. *Compos. B Eng.* **146**, 165–175 (2018)
9. Boccarusso, L., et al.: Design, manufacturing, and characterization of hybrid carbon/hemp sandwich panels. *J. Mater. Eng. Perform.* **31**(1), 769–785 (2021). <https://doi.org/10.1007/s11665-021-06186-1>



# On the Damage Sensitivity of Guided Wave SHM System Under Different Loading Conditions

Donato Perfetto, Alessandro De Luca<sup>(✉)</sup>, Giuseppe Lamanna, Aldo Minardo, Raffaele Vallifuoco, and Francesco Caputo

Department of Engineering, University of Campania “L. Vanvitelli”, Via Roma 29, 81031 Aversa, Italy

alessandro.deluca@unicampania.it

**Abstract.** Guided wave based Structural Health Monitoring (SHM) systems are a reliable and non-invasive approach to monitor structures in several fields. They provide indication about the occurrence of damage, but their large-scale industrial application is still challenging due to some aspects such as the operating loads affecting the structures. Actually, equipping damage tolerant structures with SHM systems can allow the continuous monitoring providing several benefits in terms of conditioned maintenance and repairing operations. This paper presents a numerical modelling technique, based on the Finite Element (FE) method, for the simulation of guided waves in a composite panel affected by loads. Guided wave propagation mechanisms have been analyzed also on a loaded damaged configuration of the panel, in order to investigate the damage sensitivity of the proposed SHM system. The combination of both damage and load allowed considering a scenario closer to the operating conditions of the structure, providing a contribution towards the implementation of SHM in industrial applications.

**Keywords:** Guided waves · Finite Element Method · Operating loads · Damage detection · Structural Health Monitoring

## 1 Introduction

Guided wave (GW) propagation is a well-recognized technique for the Structural Health Monitoring and damage detection in real isotropic and composite structures, because of their ability to travel long distances with low power consumption [1, 2]. GW based SHM approach is essentially based on the generation and sensing of elastic waves using mainly piezoelectric transducers (PZT) that can be surface-mounted or embedded in the to-be-monitored structure. By means of a low number of sensors, a large portion of the structure can be easily inspected using one or more excitation sources (actuators) and the pulse-echo or pitch-catch sensing approach. This way, it is possible to continuously and quickly monitoring primary and secondary plate-like components, preventing sudden failures. As a consequence, it is possible to further improve the design of damage tolerant structures, with great benefits in terms of weight savings and maintenance costs [3, 4].

In fact, the quasi-real time control of deficiencies through continuous monitoring provides greater safety and reduced repairing costs in both the medium and long term

[5, 6]. Nevertheless, one of the major challenges when dealing with GWs is that they are multi-modal (different modes of different order are superimposed) and dispersive (each mode propagates with different speed depending on the excitation frequency) [7]. Additionally, in composites, GWs exhibit a fiber-related characteristic: the dependence of speed on the propagation angle (slowness phenomenon). Thus, the post-processing phase is crucial to extract the most useful information about the actual state of the structure (presence of the damage). Detection of damages is often accomplished by comparing actual signal dataset to a baseline one, recorded in the reference (undamaged) state of the structure.

GW SHM systems can find applications in the aerospace components, storage vessels, ships etc. For this reason, their damage detection robustness and accuracy can be easily threatened by additional undesired effects, the so-called environmental (temperature, humidity...) and operational (load, initial stress-strain state...) conditions (EOCs) parameters [8, 9]. For the mentioned applications, loadings may be unavoidable in the in-situ environment and induce initial stress-strain states into the components affecting the incident propagating wave, thus reducing the useful signal strength to interrogate any damage.

In order to cut experimental campaign costs, Finite Element Analysis (FEA) can be effectively used [10, 11] to simulate the GW propagation in real components, characterized for instance by geometrical complexity and subjected to EOCs. The explicit method is widely used for the simulation of GW since it is a dynamic phenomenon [12]. However, to accurately model the wave propagation in a loaded component, three approaches can be used, also depending on the type of load. For dynamic loads, the explicit formulation of the FE method can be used. For quasi-static loads, two modelling approaches can be used: the explicit formulation, by defining the loading and the boundary conditions following the well-recognized steps for the definition of a quasi-static simulation, and the implicit scheme. The former was investigated also by De Luca *et al.* in [9]. Authors proved that when a load affects a complex composite component, the GW speeds may be altered: the load determines an increase/reduction of the wave speed, depending on the propagation angle and on the stress-strain state. Relatively to the latter approach, Aslam *et al.* presented a comparative study of different FE procedures for wave propagation modeling in simple and unloaded plates: implicit scheme, explicit and implicit-explicit co-simulation. According to authors' results, the co-simulation model is more reliable and efficient compared to the other two models [13]. However, with respect to quasi-static loads, the use of the explicit formulation for GW simulation can cause some numerical issues: i.e., the stress-strain field induced by a quasi-static load, modeled according to both implicit and explicit (quasi-static) schemes, when imported as a predefined field in the GW simulation step, is treated by the solver as initial condition for the plate, becoming a time-dependent load. As a result, in this paper, the effects of the load on GW propagation mechanisms are treated according to the implicit formulation. A first step of the manuscript has been addressed to simulate GW propagation through numerical simulations via both explicit and implicit formulations in a simple plate made of carbon fiber reinforced plastic (CFRP) material. The modelling aspects in each case are detailed in subsequent sections. Simulations are carried out using the commercially available software package Abaqus® CAE 2021. Mode shapes obtained



from the simulation schemes are compared for a specific frequency. Then, the effect of a quasi-static tensile load on GW has been investigated. In particular, for that purpose, the implicit scheme has been adopted to model both the load step and the GW propagation step. Results are reported again in terms of mode shapes and compared to the ones recorded at the unloaded configuration of the panel. Finally, a damage configuration has been investigated in the unloaded and preloaded plates in order to assess the damage sensitivity of the proposed SHM system.

## 2 FE Modelling of the Test Article

The objective of this work is to propose a modelling approach to analyze the effect of the load on GW dispersion behavior in a composite panel. As first step, the implicit and explicit formulations for the modelling of GW propagation have been investigated. Analyses have been performed by means of Abaqus® CAE module.

The test article investigated in this work consists of a flat panel characterized by a square shape ( $310 \times 310 \text{ mm}^2$ ), Fig. 1. It has a thickness of 1.5 mm and it is made up of 8 CFRP plies with a stacking sequence of  $[0, 90, +45, -45]_s$ . Lamina mechanical properties are listed in Table 1. A network of 5 piezoelectric transducers has been modelled on the upper surface of the plate, to generate and sense the diagnostic GW signal. The thickness and the radius of the PZT disk are  $t_{\text{PZT}} = 0.25 \text{ mm}$  and  $d_{\text{PZT}} = 10 \text{ mm}$ , respectively, while their mechanical properties are reported in Table 1. As visible from Fig. 1, the mapped area is square-shaped, with the actuator in a central position and the 4 receivers at a 100 mm distance along the diagonals. This configuration permits the investigation of the slowness phenomenon.

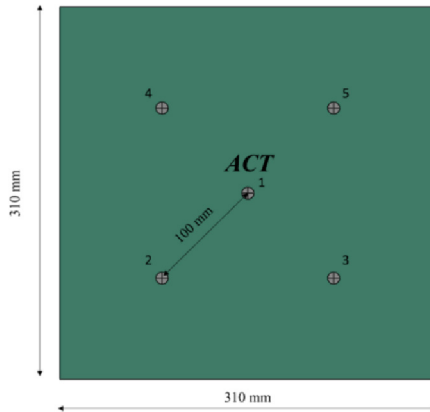


**Fig. 1.** Geometry of the investigated panel.

Two different modelling approaches have been used to model the plate and the PZTs: C3D8R solid elements have been chosen for plate and sensors modelling in the explicit formulation, according to the work [15], whilst C3D8I and C3D8E finite elements have

**Table 1.** Material properties of CFRP composite lamina and PZT (PIC255) sensors.

Material Properties	Symbol	Units	CFRP Lamina	PZT
Mass density	$\rho$	[kgm <sup>-3</sup> ]	1, 534	7, 850
Young's modulus	E	[GPa]	–	76
Longitudinal Young's modulus	E <sub>11</sub>	[GPa]	105.125	–
Transversal Young's modulus	E <sub>22</sub>	[GPa]	7.7	–
Transversal Young's modulus	E <sub>33</sub>	[GPa]	7.7	–
Shear modulus	G	[GPa]	–	29
Shear modulus	G <sub>12</sub>	[GPa]	3.6	–
Shear modulus	G <sub>13</sub>	[GPa]	3.6	–
Shear modulus	G <sub>23</sub>	[GPa]	2.7	–
Poisson's ratio	$\nu$	–	–	–
Poisson's ratio	$\nu_{12}$	–	0.36	–
Poisson's ratio	$\nu_{13}$	–	0.36	–
Poisson's ratio	$\nu_{23}$	–	0.4	–
Dielectric constant	K <sub>3</sub>	–	–	1, 280
Piezoelectric charge constant	d <sub>31</sub>	[10 <sup>-9</sup> mmV <sup>-1</sup> ]	–	–180

been used for plate and sensors in the implicit scheme, respectively [14]. In particular, C3D8E elements include the piezoelectric coupling by defining the piezoelectric coefficient and the dielectric matrices.

Plates and sensors have been discretized with an average element size of 1.0 mm and 0.4 mm, respectively. These values allow discretizing 20 NPW (nodes per wavelength) at 200 kHz carrier frequency, as reported in [12, 15]. To ensure the contact between sensors and plate, the tie constraints approach available in Abaqus® has been employed at the contact interfaces to simulate the adhesive layer between sensors and plate (not here modelled).

Concerning the GW propagation, radial displacements, calculated through the in-house code pre-processing phase, have been applied on the actuator upper edge [10, 15] for the explicit simulation. Whilst, for the implicit formulation, a voltage has been applied at the upper and lower surfaces of the actuator. In both cases, a 200 kHz carrier tone burst Hanning windowed excitation signal has been used in order to inspect the structure. Finally, the four corners of the plate have been constrained.

In the implicit method, there is no limit on the timestep size as it is unconditionally stable. However, a maximum increment of T/10 (where T is the analysis period) was chosen to obtain reasonable results [14]. On the other hand, explicit method is conditionally stable. Hence, the time step is chosen considering the wave speed and the minimum element length [15, 16].

### 3 Implicit vs. Explicit Formulation for GW Simulation

Results for both implicit and explicit formulations are herein discussed. Extracted signals have been firstly compared to highlight the differences between the two simulation schemes in a reference (no load) configuration of the investigated component.

Predicted signals at the sensor positions have been calculated as the average of the in-plane strains measured at all nodes defining each sensor [12] and then converted through the own post-process code.

The central sensor of Fig. 1 has been used as actuator, while the others ones acted as receivers. The normalized signals, recorded in both formulation schemes under a 200 kHz carrier frequency test, are shown in Fig. 2. For the sake of brevity, only the response of PZT4 and PZT3, located at opposite sides of the actuator, are reported: all signals are very similar each other because of the quasi-isotropy of the plate. The need to focus on signals from faced sensors derives from the very purpose of this paper: highlighting the effects on GW propagation of a non-symmetrical stress-strain state generated by a load, as described in the following.

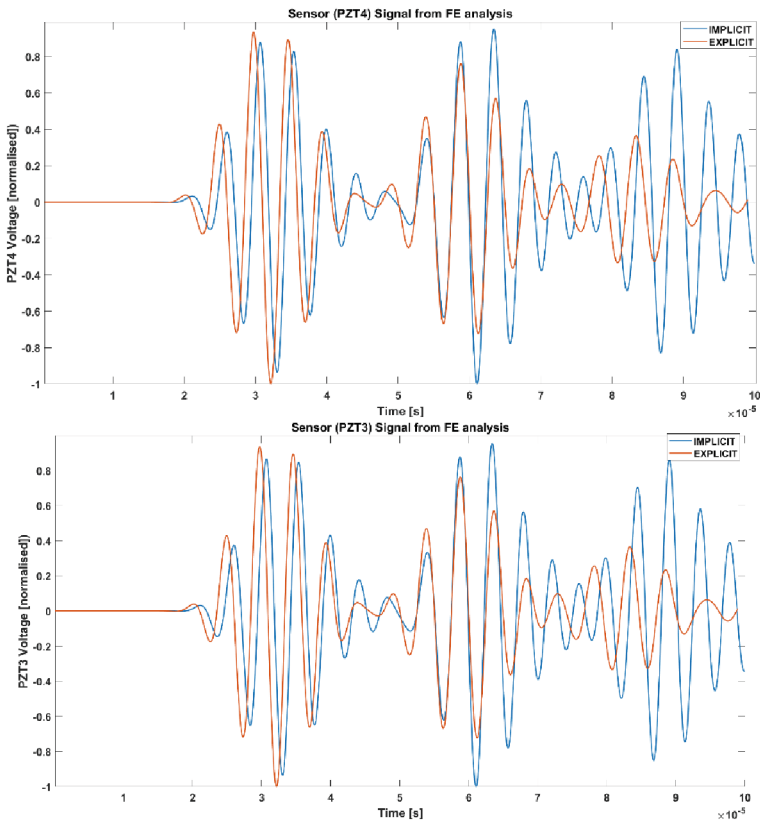


**Fig. 2.** Comparison of the recorded signals in the implicit (blue lines) and explicit (red lines) formulation schemes.

From Fig. 2, a slight difference between the signals predicted by the two simulation approaches can be noticed. In particular, the implicit modelling introduces a delay of the S0 mode with respect to the explicit one, whilst the A0 wave packets are almost overlapped. This delay was also found in [13]. The explicit formulation also has been widely validated against experiments, as reported in [12, 15], and it allows considerably reduced computational efforts and costs. However, despite such misalignment, the implicit scheme can be used to simulate the GWs in the pristine, damaged and loaded configurations. The damage detection is carried out by comparing quantitatively the signals predicted at different configurations of the plate, in a such way to extract features linked to both loads and damage and compensate the misalignment. As a result, the observed delay will not have any effect on the accuracy of the results. Also, with respect to the extraction of the group velocities, the delay between the explicit and the implicit schemes will not have any effect on their accuracy, since they are calculated based on the time spent by the specific GW mode to travel from the actuator to the receiver. In the implicit scheme, both actuation and receiving signals are affected by the same delay, so the latter is automatically compensated in the calculation of the Time of Flight (ToF).

### 4 Load Effect on GW Propagation

The study of GW propagation in a loaded structure is fundamental to assess the SHM system sensitivity for damage detection in actual in-service scenarios of the structure.

Starting from the reference (i.e., no load) configuration of the investigated panel (see Sects. 2 and 3), the load has been introduced focusing on the implicit formulation of the problem. A quasi-static tensile load, equals to 10 MPa, has been applied on the right side of the plate, whilst the left side has been fully constrained, introducing a not symmetric condition, see Fig. 3. Displacements field induced by guided waves assumes an order of magnitude of about  $10^{-6}$  mm– $10^{-7}$  mm, which is much smaller than the displacements field corresponding to the load. So, to facilitate the comprehension of the propagation mechanisms as well as the signals post-processing, the actuation signal has been numerically amplified by a factor of  $10^5$ . This procedure does not affect the accuracy of the FE model since the received signals are normalized in the post-processing phase to enhance the damage detection sensitivity.

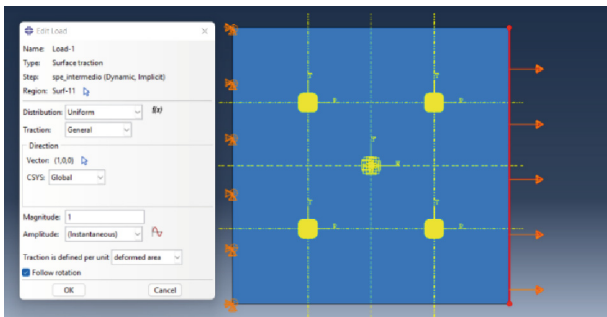
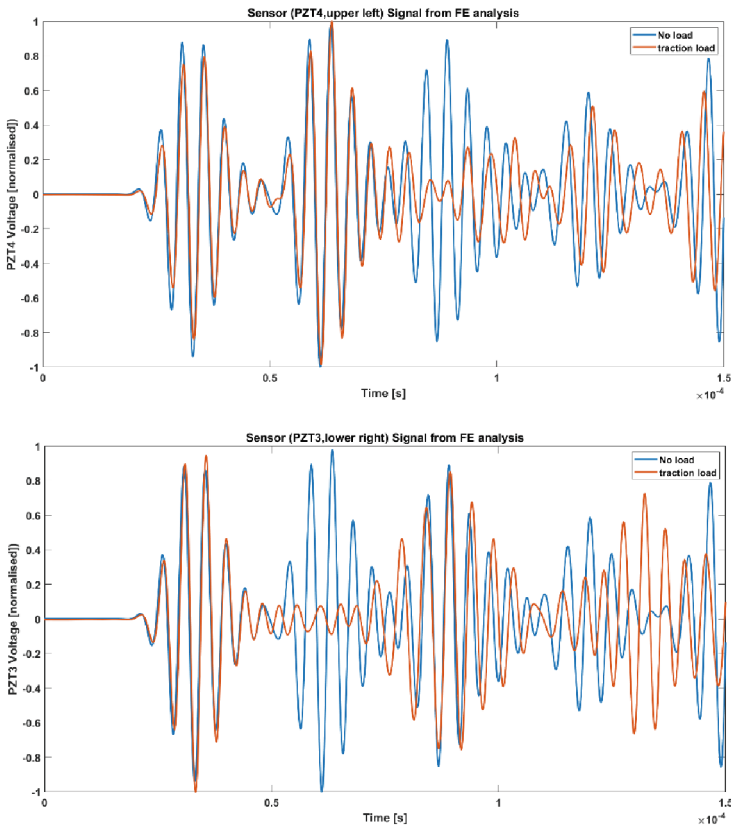


Fig. 3. Loaded configuration.

In a loaded structure, the presence of an initial stress-strain state on the guided wave propagation path may produce distinct changes in the amplitude, waveform and ToF.

The most efficient method to evaluate such effect is comparing the signal recorded in the actual (loaded) configuration against the baseline one, achieved in a pristine unloaded configuration of the test case. Again, the central sensor of Fig. 1 has been used as actuator, while the other ones acted as receivers. The normalized signals, simulated according to the implicit formulation under a 200 kHz carrier frequency test, are shown in Fig. 4. For the sake of brevity, only the response of PZT4 and PZT3, located at the opposite sides of the actuator, are reported.

As visible from the results in Fig. 4, the load affects the wave propagation mechanisms: the signals recorded by the sensors placed at the right side of the actuator, i.e., nearer to the load, are perfectly overlapped relatively to the S0 mode, whilst the A0 mode (PZT3 in Fig. 4) is highly affected. It can be clearly noticed that the presence of the initial stress-strain state causes slight variations in signals A0 mode amplitude for the loaded configuration, and this effect is more evident for sensors near to the load application zone.



**Fig. 4.** Comparison of the recorded signals in the reference (blue lines) and loaded (red lines) configuration of the structure – implicit formulation.

In order to investigate the damage detection of the developed SHM system under an operating load, a damage has been modeled by means of a through-thickness square notch [17] within the unloaded and preloaded plates, see Fig. 5. Subsequently, the damage detection algorithm proposed by authors in [9] has been used to identify the damage location.

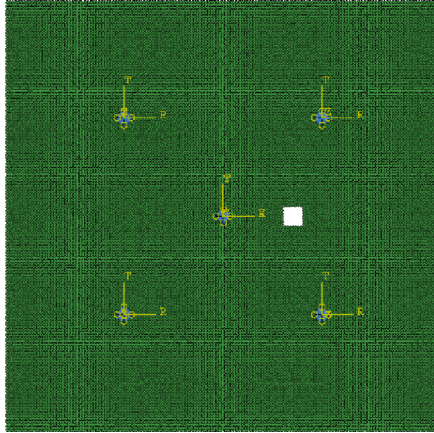


Fig. 5. Damaged plate.

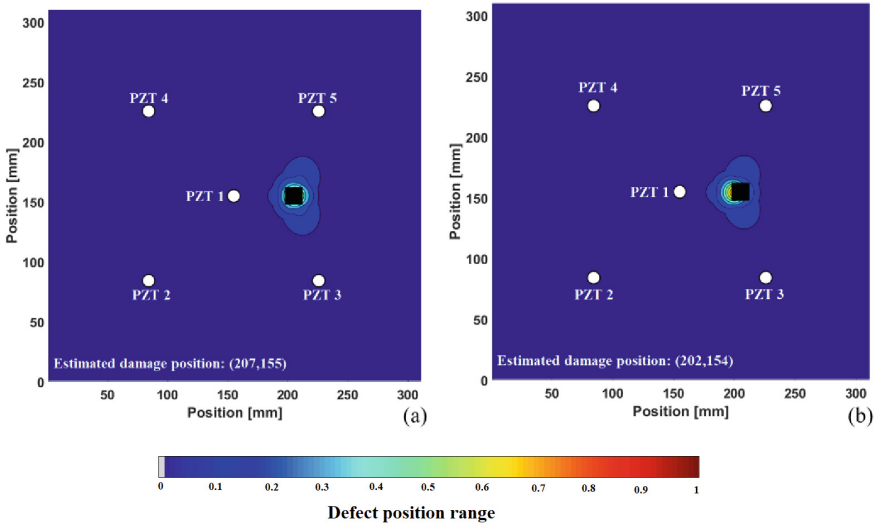


Fig. 6. Damaged detection in: (a) unloaded and (b) loaded plate configurations.

According to Fig. 6, although the presence of the initial stress-strain state causes variations in signals, the damage detection algorithm appears capable to compensate

such effects, providing a good level of accuracy. The compensation of the load is carried out automatically by the damage detection algorithm, just by focusing on the S0 waves packet.

## 5 Concluding Remarks

In this paper two modelling techniques have been compared, both based on the FE method, to analyze the differences in GW propagation mechanisms in a composite flat panel. In particular, the implicit and explicit formulations have been investigated. Then, the effect of a uniaxial traction load, which characterizes for example aircrafts, tanks, pipes, etc. in actual in-service scenarios, on GW propagation mechanisms has been investigated.

Specifically, the simulations in the two schemes highlighted a slight variation of the S0 mode propagation velocity for the implicit formulation, compared to the explicit one. In particular, the implicit modelling introduces a delay of the S0 mode with respect to the explicit one, whilst no difference has been observed for the A0 wave packets. Relatively to the loaded configuration of the component, it can be stated that the presence of an initial stress-strain state causes slight variations in signals A0 mode amplitude with respect to the reference (unloaded) configuration, and this effect is more evident for sensors near the load application zone. Vice versa, no difference has been detected for the S0 wave packets. By taking advantage of such aspect, the damage detection algorithm pointed out to be very accurate in terms of damage location identification despite the load effects.

**Acknowledgements.** This research was funded by the University of Campania “Luigi Vanvitelli” in the framework of “SAFES—Smart pAtch For active Shm” funded research project, as part of V: ALERE 2020 program.

## References

1. Rocha, H., Semprinoschnig, C., Nunes, J.P.: Sensors for process and structural health monitoring of aerospace composites: a review. *Eng. Struct.* **237** (2021). <https://doi.org/10.1016/j.engstruct.2021.112231>
2. Gorgin, R., Luo, Y., Wu, Z.: Environmental and operational conditions effects on Lamb wave based structural health monitoring systems: a review. *Ultrasonics* **105**, 106114 (2020). <https://doi.org/10.1016/j.ultras.2020.106114>
3. Rose, J.L.: A baseline and vision of ultrasonic guided wave inspection potential. *J. Pressure Vessel Technol.* **124**, 273–282 (2002). <https://doi.org/10.1115/1.1491272>
4. Su, Z., Ye, L.: *Identification of Damage Using Lamb Waves*. Springer, London, London (2009)
5. Perfetto, D., Lamanna, G., Manzo, M., Chiariello, A., di Caprio, F., di Palma, L.: Numerical and experimental investigation on the energy absorption capability of a full-scale composite fuselage section. *Key Eng. Mater.* **827**, 19–24 (2019). <https://doi.org/10.4028/www.scientific.net/KEM.827.19>
6. Caputo, F., Lamanna, G., Perfetto, D., Chiariello, A., Di Caprio, F., Di Palma, L.: Experimental and numerical crashworthiness study of a full-scale composite fuselage section. *AIAA J.* **59**, 700–718 (2021). <https://doi.org/10.2514/1.J059216>

7. Wilcox, P.D.: A rapid signal processing technique to remove the effect of dispersion from guided wave signals. *IEEE Trans. Ultrason. Ferroelectr. Freq. Control* **50**, 419–427 (2003). <https://doi.org/10.1109/TUFFC.2003.1197965>
8. Salmanpour, M.S., Sharif Khodaei, Z., Aliabadi, M.H.: Airborne transducer integrity under operational environment for structural health monitoring. *Sensors* **16**, 2110 (2016). <https://doi.org/10.3390/s16122110>
9. De Luca, A., Perfetto, D., Caputo, F., Petrone, G., De Fenza, A.: Numerical simulation of guided waves propagation in loaded composite structures. In: *AIP Conference Proceedings*, pp. 020029 (2020)
10. De Luca, A., Perfetto, D., De Fenza, A., Petrone, G., Caputo, F.: Guided wave SHM system for damage detection in complex composite structure. *Theoret. Appl. Fract. Mech.* **105**, 102408 (2020). <https://doi.org/10.1016/j.tafmec.2019.102408>
11. De Luca, A., Perfetto, D., De Fenza, A., Petrone, G., Caputo, F.: Guided waves in a composite winglet structure: numerical and experimental investigations. *Compos. Struct.* **210**, 96–108 (2019). <https://doi.org/10.1016/j.compstruct.2018.11.048>
12. de Luca, A., Perfetto, D., Lamanna, G., Aversano, A., Caputo, F.: Numerical investigation on guided waves dispersion and scattering phenomena in stiffened panels. *Materials*. **15**, 74 (2021). <https://doi.org/10.3390/ma15010074>
13. Aslam, M., Nagarajan, P., Remanan, M.: Numerical procedures for simulation of wave propagation in plates. In: Singh, R.M., Sudheer, K.P., Kurian, B. (eds.) *Advances in Civil Engineering*. LNCE, vol. 83, pp. 741–749. Springer, Singapore (2021). [https://doi.org/10.1007/978-981-15-5644-9\\_58](https://doi.org/10.1007/978-981-15-5644-9_58)
14. ABAQUS: Abaqus 6.14 (2014)
15. Perfetto, D., de Luca, A., Perfetto, M., Lamanna, G., Caputo, F.: Damage detection in flat panels by guided waves based artificial neural network trained through finite element method. *Materials*. **14**, 7602 (2021). <https://doi.org/10.3390/ma14247602>
16. Perfetto, D., De Luca, A., Lamanna, G., Caputo, F.: On the prediction of guided wave dispersion curves in plates for health monitoring applications. *Macromol. Symp.* **396**, 1–4 (2021). <https://doi.org/10.1002/masy.202000333>
17. de Luca, A., Perfetto, D., de Fenza, A., Petrone, G., Caputo, F.: A sensitivity analysis on the damage detection capability of a Lamb waves based SHM system for a composite winglet. *Procedia Struct. Integrity*. **12**, 578–588 (2018). <https://doi.org/10.1016/j.prostr.2018.11.061>





# Impact Response of Carbon Fiber Composites: Comparison Between Epoxy and Bio-Based Epoxy Matrices

R. Ciardiello<sup>(✉)</sup>, C. Boursier Niutta, A. Tridello, and D. S. Paolino

Department of Mechanical and Aerospace Engineering, Politecnico di Torino, Corso Duca degli  
Abruzzi 24, 10129 Turin, Italy  
raffaele.ciardiello@polito.it

**Abstract.** The elastic properties and the impact response of composite laminates made of carbon fibres (CFRP) and two different matrices, epoxy and bio-based epoxy, has been experimentally assessed with the Impulse Excitation Technique (IET) and with drop dart tests. Eight carbon twills ( $2 \times 2$ ) have been used to prepare the composite laminates with a traditional epoxy resin and an epoxy-based resin with 31% of bio content (glycerol in place of petroleum-based propylene).

The elastic properties of the two investigated composite plates have been found to be slightly different, if assessed with the IET. Similarly, the resin type has been found to not influence the impact response, for impact energy equal to 15 J (dart rebound) and to 30 J (dart penetration). For the range of investigated impact energies, it can be concluded that the bio-based resin can be used in place of a commonly used epoxy resin.

**Keywords:** Drop dart · sustainable resin · energy absorption · Impulse Excitation Technique

## 1 Introduction

The use of composite materials is extremely important to reach specific lightweight goals in different industrial fields (e.g., the aerospace or the automotive fields), such as reducing fuel consumption/emission or increasing the autonomy of electric vehicles.

However, the last challenge for the transportation industry is the design of new components by considering the Life Cycle Assessment and so reduce the overall carbon footprint [1]. Accordingly, new thermoplastic and bio-based resins have been developed and are currently commercially available and can substitute traditional resins that cannot be recycled. However, in order to ensure the structural integrity of components, the mechanical properties of composite made with bio-based resin should be experimentally assessed and compared to those of commonly used epoxy resin composite laminates. Among these, the assessment of the impact response is fundamental for composite materials. Indeed, technical literature has widely investigated the tolerance of composite materials to impact damage. Pursuing metal approaches, the residual load-bearing capability has been the first concern. However, the prediction of the post-impact

load-bearing capability of a damaged composite structure is more difficult than in metals, as the damage zone is generally complex in nature. Great efforts have been thus made to improve the impact resistance of fibre composites, by focusing on the governing parameters related to the constituents. Another approach looks at the energy absorption aptitude of the composite structures.

Energy balances approaches particularly allow to evaluate the level of damage accumulation of composites during impact events. The manner in which composite materials respond to impact loading and dissipate the incident kinetic energy,  $E_i$ , is very different to that of metals. For low and intermediate impact energy, metals absorb energy through elastic and plastic deformation, whose consequences on the load-carrying capability are usually limited. At high energy, perforation may occur, and its effects can be predicted through fracture mechanics principles. In composites, whose plastic deformation is very limited if not null, the impacting energy  $E_i$  is dissipated both through elastic deformation and by fracturing. Net of the elastic energy  $E_{el}$ , whereby the impactor rebounds, the residual part of the incident energy is absorbed in creating large areas of fracture. Impact damages are thus strictly correlated to the absorbed energy  $E_{abs}$ , which can be in turn interpreted as a measure of the material damage [2].

This work aims at assessing the elastic properties and the impact response of two composite laminates made with carbon fibers and an epoxy resin and a bio-based epoxy resin commercially available. The two resins present a similar cost. The elastic properties have been assessed with the Impulse Excitation Technique [3]. Free fall drop dart impact tests at increasing impact energies have been carried out to assess the impact response. The peak force and absorbed energy have been compared in order to assess if the bio-based resin affects the impact response of the investigated composite laminates.

## 2 Materials and Methods

In the Section, the tested materials and the experimental setup are described. In Sect. 2.1, details on the preparation of the two tested composite laminate types are provided. In Sects. 2.2 and 2.3, the Impulse Excitation Technique (IET) employed for comparing the elastic properties and the testing configuration for assessing the impact response are described, respectively.

### 2.1 Materials

Composite laminates made of carbon fibres have been prepared with two different epoxy resins: a traditional commercially available epoxy resin IN2 (EasyComposite, UK) and an epoxy resin with 31% of bio content IB2 (EasyComposite, UK). The bio-content of the bio-based resin is due to the glycerol, plant derived, in place of petroleum-based propylene.

The two resins present similar mechanical properties that are reported in Table 1.

**Table 1.** Tensile and flexural properties of IN2 and IB2 resins

	IN2	IB2
Tensile strength [MPa]	68.5	65
Flexural strength [MPa]	118	107
Flexural modulus [GPa]	3.3	2.8
Elongation at break [%]	7.0	5.3

Composite laminates, 2mm thick (8 layers), were obtained by using vacuum infusion technique. The fabric is a 210 g and  $2 \times 2$  carbon twill (Mitsubishi, JP). The fabric is characterized by a maximum tensile strength of 4120 MPa, a tensile modulus of 240 GPa and a maximum elongation of 1.8%. The two resins were degassed in a vacuum chamber before the infusion and cured for 24 h at room temperature and post-cured in the oven at 100 °C for 3 h.

## 2.2 Impulse Excitation Technique

The elastic properties of the epoxy-based and bio-based resin composites are determined through the Impulse Excitation Technique (IET). The IET allows to characterize the elastic response specifically of the impacted plates and, in addition, its degradation after the impact.

In this work, the IET is used to compare the material properties of the two composites. It is assumed that the elastic properties of the two principal directions are equal, the plate is perfectly square, and the in-plane material principal directions are aligned to the edges of the plate. Under these assumptions, the equation  $\frac{a}{b} = \left(\frac{E_{11}}{E_{22}}\right)^{\frac{1}{4}}$  is satisfied, being  $a$  and  $b$  the plate dimensions and  $E_{11}$  and  $E_{22}$  the in-plane Young's moduli. Therefore, the O and X modes can be properly excited and used to determine the elastic properties together with the torsional mode. Figure 1 depicts the modes here considered.

Following the methodology proposed by McIntyre and Woodhouse [4], the in-plane shear modulus  $G_{12}$  can be calculated from the torsional mode as:

$$G_{12} = 0.822 \frac{f_T^2 \cdot \rho \cdot a^4}{h^2} \quad (1)$$

where  $f_T$  is the measured torsional frequency,  $\rho$  the material density and  $h$  the plate thickness.

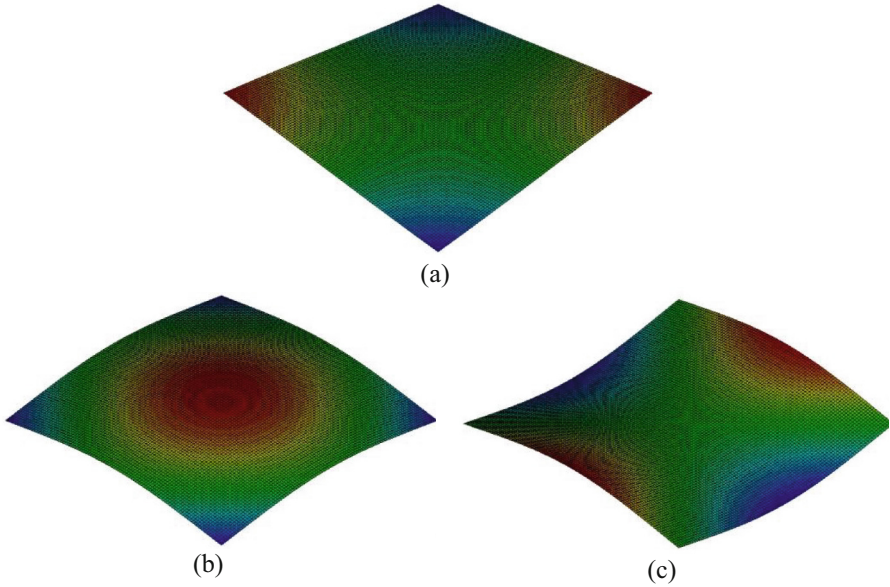


**Fig. 1.** Mode shapes for the assessment of the elastic properties: a) torsional mode; b) O mode; c) X mode

The in-plane Young’s moduli,  $E_{11}$  and  $E_{22}$ , and Poisson’s ratio,  $\nu_{12}$ , can be obtained from the O and X modes. The approximated formulas for the O and X frequencies were derived by McIntyre and Woodhouse [4] as:

$$\begin{aligned}
 f_O^2 &\cong \frac{h^2}{\rho \cdot a^4} \left( 13 \cdot \sqrt{D_{11} \cdot D_{22}} + 4.4 \cdot D_{12} \right) \\
 f_X^2 &\cong \frac{h^2}{\rho \cdot a^4} \left( 13 \cdot \sqrt{D_{11} \cdot D_{22}} - 4.4 \cdot D_{12} \right)
 \end{aligned}
 \tag{2}$$

where

$$\begin{aligned}
 D_{11} &= \frac{E_{11}}{12 \cdot (1 - \nu_{12}\nu_{21})} \\
 D_{22} &= \frac{E_{22}}{12 \cdot (1 - \nu_{12}\nu_{21})} \\
 D_{12} &= 2 \cdot \nu_{12} \cdot D_{22} = 2 \cdot \nu_{21} \cdot D_{11}
 \end{aligned}
 \tag{3}$$

Considering that the elastic properties of the two principal directions are equal, we can compute  $D_{11}$ ,  $D_{22}$  and  $D_{12}$  as:

$$\begin{aligned}
 D_{11} = D_{22} &= \left( f_O^2 + f_X^2 \right) \frac{\rho \cdot a^4}{26 \cdot h^2} \\
 D_{12} &= \left( f_O^2 - f_X^2 \right) \frac{\rho \cdot a^4}{8.8 \cdot h^2}
 \end{aligned}
 \tag{4}$$

from which the Young's moduli and the Poisson's ratios can be calculated through Eqs. (3).

The experimental setup is shown in Fig. 2.

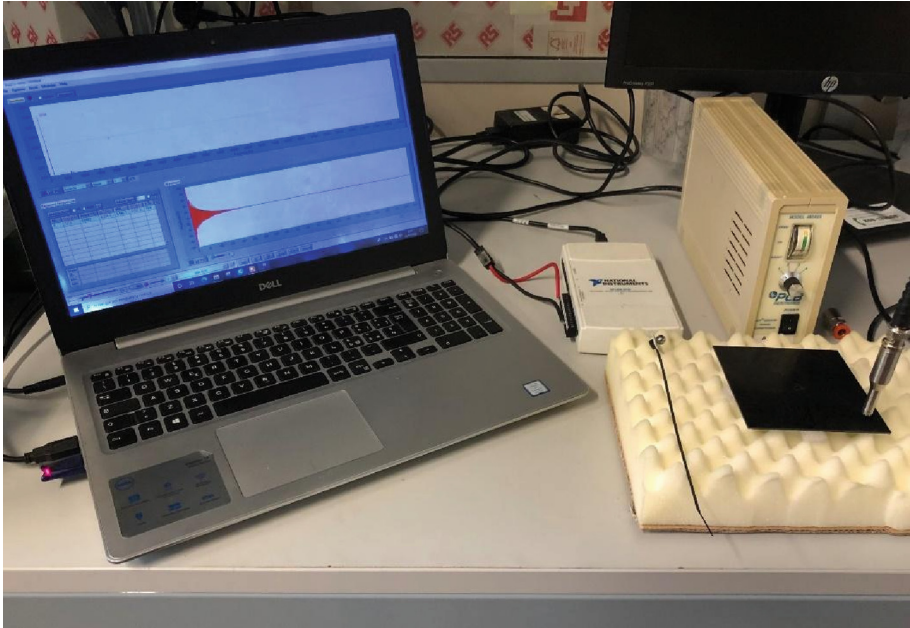


**Fig. 2.** Experimental setup for the IET tests

The plate was excited by impulse in accordance with the IET and the mechanical vibrations were measured through a microphone. The frequencies of interest were excited by properly providing the impulse and accordingly disposing the microphone for the acquisition. For example, for the O mode, the plate has been excited in the center and the vibrations have been acquired in correspondence of one of the corners.

The NI USB-6210 system was used for the analogic-to-digital conversion of the signal. In Buzz-o-sonic® environment, the fundamental resonant frequency was calculated through a FFT of the signal.

### 2.3 Impact Test Configuration

Impact tests have been carried out by using free fall drop dart testing machine (CEAST 9350 FRACTOVIS PLUS), which allows to assess the out of plane impact response of laminates in a speed range 0.77–24 m/s and with impact energy between 1J and 1800J. For a fixed impact speed, the impact energy is varied by changing the impact mass. A hemispherical impact tup with 20 mm diameter has been used. 100 × 100 mm squared plates have been used for the impact tests, with a 76 mm diameter circular unclamped region, in agreement with the recommendations of the ASTM standard [5]. The force

signal during the impact tests has been acquired with a piezoelectric load cell (203B by PCB Piezotronics), located behind the impactor tup, at a sample rate of 1 MHz. The signal is thereafter amplified and acquired by using a National Instrument acquisition system. Furthermore, the impact speed just before the impact is measured with an optoelectronic device, which is also used as a trigger to start the acquisition of the force signal. For each test, therefore, the impact velocity and the force-time signal are acquired. The force-time signal has been moreover smoothed with a moving average filter to minimize the acquisition noise.

Figure 3 shows a schematic image of the impact test configuration and of the clamping system, which ensures a uniform pressure distribution on the clamped region.

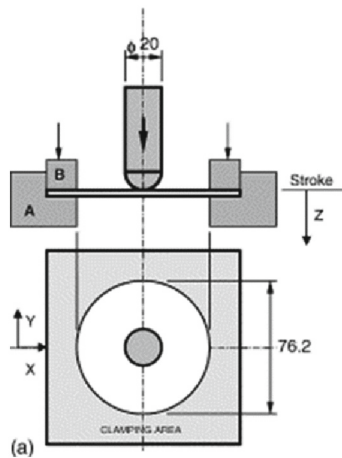


Fig. 3. Schematic image of the clamping system [6].

Impact tests were carried out with a mass of 15.9 kg and two impact speeds, namely at 1.4 m/s and 2 m/s, corresponding to impact energies of 15 J and 30 J. These two impact energies have been selected to analyze the response of the tested laminates without perforation (impact energy of 15 J) and when perforation occurs (impact energy of 30 J). Three repetitions for each configuration have been carried out. However, for an impact energy of 15 J and the composite with epoxy resin, only two valid tests are available.

### 3 Experimental Results

In this Section the experimental results are analyzed. In particular, the elastic properties assessed with the IET are compared in Sect. 3.1, whereas the results of the impact tests are analyzed in Sect. 3.2.

#### 3.1 Elastic Properties Assessment

The elastic properties of the composite plates have been determined through the IET and the methodology described in Sect. 2.2. The use of the IET allows to assess the elastic

properties of each impacted plate, which can be then correlated to the impact response. In addition, the material degradation after the impact can be quantitatively assessed. In this regard, it is worth noticing that the damage would be consistently involved in the O mode vibration, as the plate is impacted in the center, thus affecting in turn its resonant frequency [7].

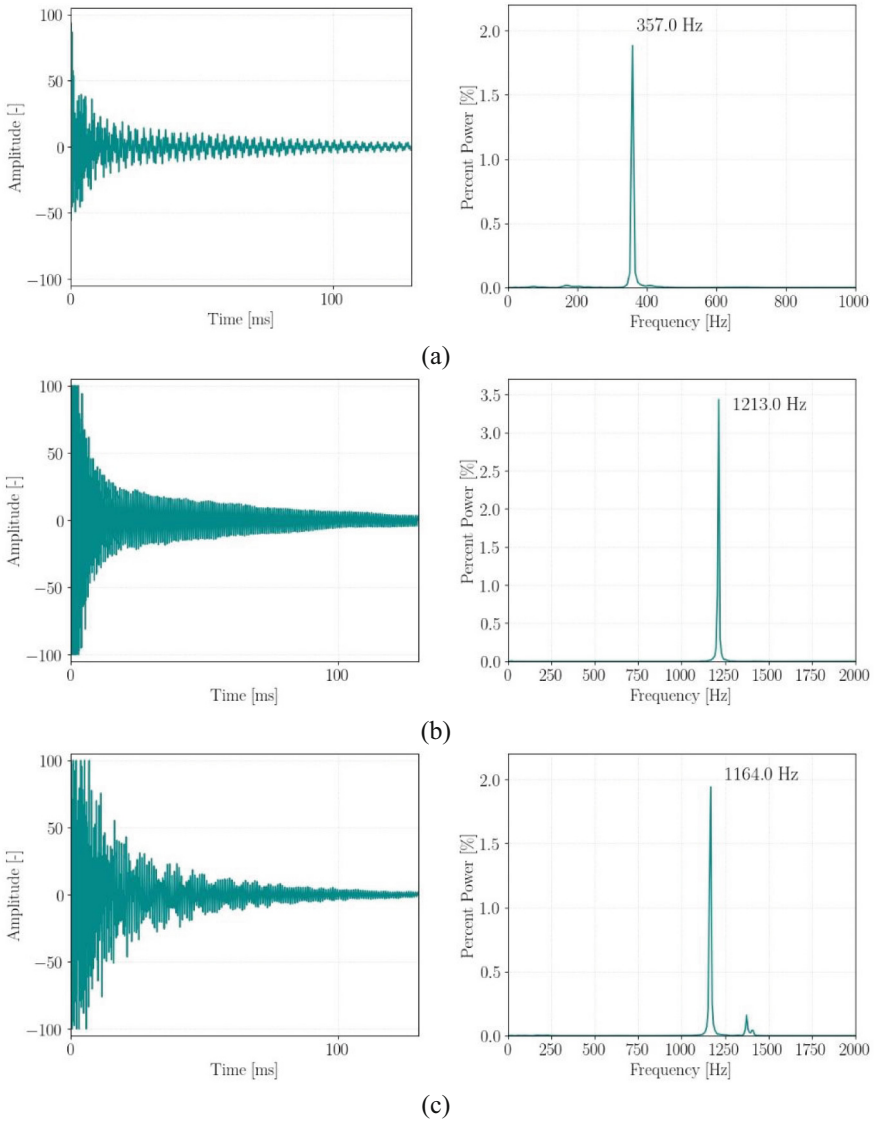


**Fig. 4.** Signals in time and frequency response functions of the retained modes for the epoxy-based composite: a) torsional mode; b) O mode; c) X mode

Figure 4 shows typical signals in time and the corresponding frequency response functions (FRFs) of the three retained modes.

These FRFs particularly refer to an epoxy-based plate. In all cases, the resonant pick is clearly recognizable and well distinguished from the other resonances of the plate.

In Table 2, the determined elastic properties are reported for the epoxy and bio-based epoxy composites.

**Table 2.** Material properties of the tested materials obtained through IET tests

Material	$E_{11}$ [GPa]	$E_{22}$ [GPa]	$G_{12}$ [GPa]	$\nu_{12}$ [-]
Epoxy resin composite	$46.0 \pm 1.6$	$46.0 \pm 1.6$	$3.6 \pm 0.3$	$0.054 \pm 0.02$
Bio-based epoxy resin composite	$44.9 \pm 1.8$	$44.9 \pm 1.8$	$3.15 \pm 0.2$	$0.047 \pm 0.01$

The elastic properties of the two materials are very similar, being those of the bio-based epoxy laminate slightly lower than the corresponding ones of the epoxy composite. Also, the confidence intervals are similar, being the same the manufacturing process. For a better comparison, a thermogravimetric analysis (TGA) could reveal the fiber volume fraction of the composites.

### 3.2 Impact Test Response Analysis

In this Section, the impact properties are analyzed and compared. Figure 5 shows one representative acquired force-time curve for the epoxy and the bio-based composite laminates at an impact energy of 15 J (Fig. 5a) and 30 J (Fig. 5b).

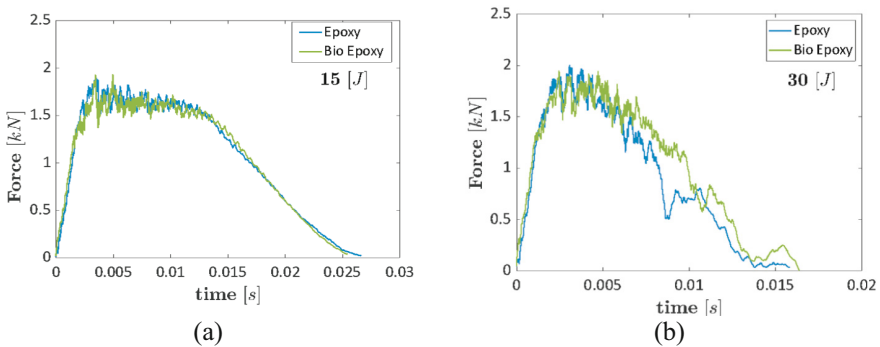


**Fig. 5.** Representative force-time curves for the epoxy and the bio-based composite laminates: a) impact energy of 15 J; b) impact energy of 30 J.

Figure 5 illustrates that the composite obtained with the epoxy and the bio-based resins shows the same impact response with respect to time. However, for a proper analysis of the absorbing capabilities, the force-displacement curves and the absorbed



energy should be compared. The displacement has been obtained through a double integration of the acceleration signal, obtained from the acquired force signal, with respect to time [8]. Figure 6 compares the force-displacement curve for impact energy of 15 J (Fig. 6a) and 30 J (Fig. 6b).

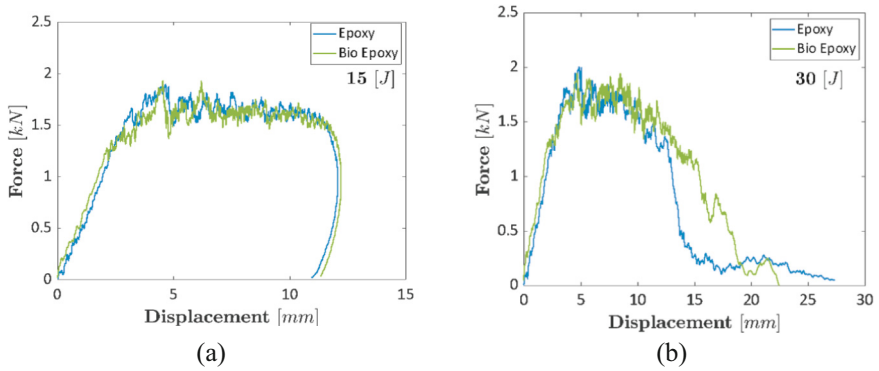


**Fig. 6.** Force with respect to displacement curves for the epoxy and the bio-based composite laminates; a) impact energy of 15 J; impact energy of 30 J.

Figure 6 shows that the resin type does not influence the impact response of the tested composite laminates. For an impact energy of 15 J, the laminates are not perforated, with the curves showing a rebound of the dart of about 1 mm. An impact energy of 15 J is not enough to induce a complete failure with perforation. The slope in the first region and the peak forces are the same. On the other hand, with an impact energy of 30 J, the perforation is achieved, with the displacement continuously increasing during the test. Even for this impact energy inducing a perforation of the composite laminates, the resin type does not influence the impact properties. Figure 7 shows an image of the tested composite laminates after the impact tests: Fig. 7 for an impact energy of 15 J, whereas Fig. 7 b for an impact energy of 30 J. Similar fracture surface morphologies have been found for the epoxy and the bio-based composite plates.

Figure 7a confirms that an impact energy of 15 J does not induce a complete perforation of the laminate, with cracks starting to propagate from the impact area along the horizontal and vertical directions. On the other hand, at 30 J, the signs of the perforation are clear (Fig. 7b), with cracks propagating from the region where the impact has occurred.



**Fig. 7.** Composite plates after the impact tests: a) impact energy of 15 J; b) impact energy of 30 J.

Table 3 finally compares the impact response of the two tested composite laminates. In particular, the peak force and the impact energy are considered. The average value (between the three tests) and the standard deviation (within round brackets) are reported.

**Table 3.** Comparison of the energy absorbing properties of the two investigated laminates

	Epoxy resin		Bio-based epoxy	
	15 J	30 J	15 J	30 J
Peak force [N]	1891	1988 ( $\pm 27$ )	1882 ( $\pm 42$ )	1902 ( $\pm 75$ )
Absorbed energy [J]	16.8	21.3 ( $\pm 1.3$ )	16.7 ( $\pm 0.1$ )	23.1 ( $\pm 2.7$ )

According to Table 3, the peak force increases with the impact energy and the increment is larger for the epoxy resin. The peak force is, moreover, slightly larger for the epoxy resin composite at the two investigated impact responses, but the difference is limited. On the other hand, the absorbed energy is the same for impact energy of 15 J, whereas it is larger for the bio-based resin at the impact energy of 30 J. However, due to the larger experimental scatter at this energy level, the difference between the absorbed energy of the epoxy resin composite and the bio-based resin composite cannot be considered significant.

To conclude, for the range of investigated impact energy, the impact response of the epoxy and the bio-based resin is the same.

## 4 Conclusions

In the present work, the elastic properties and the impact response of two composite laminates made by 8 layers of woven carbon fibres with epoxy and bio-based epoxy resins commercially available were investigated.

The elastic properties were assessed through the Impulse Excitation Technique (IET) directly on the square plate subjected to impact test. The torsional mode, O mode and X

mode have been used to determine the elastic properties through a methodology derived from McIntyre and Woodhouse [4]. Results showed that the elastic properties of the two materials are very similar, being those of the bio-based epoxy laminate slightly lower than the corresponding ones of the epoxy composite. Even though the manufacturing process was the same, a thermogravimetric analysis (TGA) will be considered in the future for a better comparison of the material properties.

The impact response was experimentally assessed with free-falling dart impact tests at two impact energies, 15 J (rebound of the dart) and 30 J (perforation of the laminates). For the range of investigated impact energies, it was experimentally found that the CFRP laminates prepared with the two resins are characterized by a similar impact response, with the peak forces and the absorbed energies showing almost the same values.

According to the analyses carried out in the paper, it can be concluded that the investigated commercially available bio-based resins can be used in place of the epoxy resin since it does not affect its elastic properties, measured with the IET, and the impact response.

## References

1. Ciardiello, R.: The mechanical performance of re-bonded and healed adhesive joints activable through induction heating systems. *Materials* **14**(21), 6351 (2021)
2. Belingardi, G., Cavatorta, M.P., Paolino, D.S.: A new damage index to monitor the range of the penetration process in thick laminates. *Compos. Sci. Technol.* **68**(13), 2646–2652 (2008)
3. ASTM E1876-21. Standard Test Method for Dynamic Young's Modulus, Shear Modulus, and Poisson's ratio by Impulse Excitation of Vibration (2015)
4. McIntyre, M.E., Woodhouse, J.: On measuring the elastic and damping constants of orthotropic sheet materials. *Acta Metall.* **36**, 1397–1416 (1988)
5. ASTM D5628-10. Standard Test Method for Impact Resistance of Flat, Rigid Plastic Specimens by Means of a Falling Dart (Tup or Falling Mass). ASTM International: West Conshohocken (2010)
6. Elmarakbi, A., et al.: Effect of graphene nanoplatelets on the impact response of a carbon fibre reinforced composite. *Mater. Today Commun.* **25**, 101530 (2020)
7. Boursier Niutta, C.: Residual elastic response in damaged woven laminates through local Impulse Excitation Technique. *Compos. Struct.* **293**, 115723 (2020)
8. Belingardi, G., Vadori, R.: Low velocity impact tests of laminate glass-fiber-epoxy matrix composite material plates. *Int. J. Impact Eng* **27**(2), 213–229 (2002)



# Analysis of the Behavior of Fiberglass Composite Panels in Contact with Water Subjected to Repeated Impacts

A. C. Omaña<sup>1</sup>(✉), J. M. Arenas<sup>1</sup>, and J. C. Suarez<sup>2</sup>

<sup>1</sup> ETS de Ingeniería y Diseño Industrial- Universidad Politécnica de Madrid, Rda. de Valencia, 3, 28012 Madrid, Spain

anabeliscarolina.omana.lozada@alumnos.upm.es,  
josemanuel.arenas@upm.es

<sup>2</sup> Department of Materials, ETS de Ingenieros Navales – Universidad Politécnica de Madrid, Av. de la Memoria, 4, 28040 Madrid, Spain

juancarlos.suarez@upm.es

**Abstract.** The slamming phenomenon process frequently occurs during the fast navigation of vessels and consists of a force that cyclically strikes the hull of the vessel as a result of its impact against the free surface of the water. This force is translated into short duration pulses acting on a very small surface area causing high pressure peaks. The magnitude of this impact and its possible damage to the hull are difficult to foresee and, therefore, the maximum sailing speed of the ship is usually limited so as not to suffer additional damage during voyages. This situation is more pronounced in the case of high-speed gliders. Given the importance of this effect on the safety and integrity of the ship during navigation, it is necessary to know the technical behavior of the materials used in the hull against this effect. Cyclic impact and shear tests are presented together with the methodology followed to evaluate the damage by means of destructive and non-destructive analysis techniques.

**Keywords:** Slamming · Damage · Composite Materials · Bioinspired

## 1 Introduction

Slamming is an important event during ship navigation and presents itself as a sudden force that strikes vertically at the bow and generates energy by the impact between the hull of a vessel and the free surface of the water [1]. This force translates into pulses of very short duration (typically on the order of a few milliseconds) acting on a very small surface area and resulting in high pressure peaks. [2]. The severity of this impact and its damage to the ship is so unpredictable that operators are very cautious and reduce speed to avoid further damage during crossings, a situation that is aggravated in the case of high-speed gliders. The complexity of the phenomenon is due to the fact that the bottom of the ship enters the water through the angular difference between the surface of the body and the sea surface, causing the contact region to expand at high-speed independent of the speed of the ship [3].

## 2 Methodology

### 2.1 Materials

For the slamming test, compacted panels of  $22 \times 22$  cm were made with 4 layers of unidirectional fiberglass oriented in 4 directions ( $0^\circ/90^\circ/\pm 45^\circ/\pm 45^\circ/90^\circ$ ), the first layer being the one in contact with the cam, with polyurethane matrix. To manufacture the panels, they were laminated on a Teflon tool to be vacuum sealed, and polyethylene bag. Inside, the breathing cloth was included at the top, the peelable on both sides and the impermeable cloth at the end so that the resin flow does not cover the breathing valve that was placed to maintain the vacuum with a pump.

### 2.2 Test Equipment

The slamming reproduction equipment, which is shown in Fig. 1, consists of a water tank, a specimen fixation system and an eccentric cam.

The hydraulic system of the machine consists of the following main elements: accumulator tank, water pump, pressure tank, pressure gauge, pressure line and drain chamber. The water required for the test is stored in the accumulator tank. The pump takes the water from the tank through a pipe. This pump, thanks to the pressure tank and a three-way valve, drives the water through another pipe with the preset flow rate and pressure to its inlet at the bottom of one end of the pressure line.



**Fig. 1.** Slamming Playback Equipment with built-in eccentric cam

The specimen fixation system is located on the outside face of the support plate and consists of a flat rubber ring joint, the specimen to be tested and a metal plate that firmly and securely fixes the four sides of the panel to be tested and the rubber joint so that when the eccentric cam hits the panel it does not detach from the fixture or cause water leakage, as shown in Fig. 2.

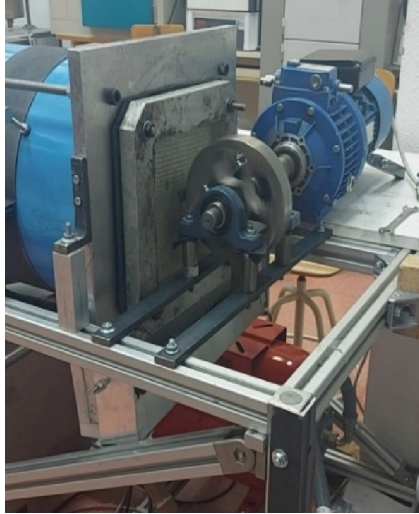


**Fig. 2.** Cam detail and panel location

The eccentric cam is composed of a variator-electric motor assembly, which was connected by means of a shaft supported on two bearings, the steel cam that is keyed to the shaft had lightening in its mass to be balanced with the center of the shaft and avoid inertial loads due to its eccentric shape. The variator installed allows the motor to work at a frequency of 200 to 320 RPM, values at which the set is more efficient and the vibrations produced by the equipment when rotating do not affect the assembly of the parts. Rubber gaskets were placed on the bases of the bearings supporting the shaft to dissipate the reaction energy of the cam against the panel so that this lateral load does not affect the motor-drive assembly. The cam design causes the deformation and relaxation of the panel to gradually press on the contact face and hammer blow loads are avoided.

The ultrasonic inspection of each of the manufactured specimens was necessary, for which a Tecnitest immersion tank was used, a motorized head with a reader with a scanning accuracy of 0.1 to 0.2 mm at a maximum inspection speed of 100 mm/sec, and all connected to the Masterscan 335 integrated data acquisition and management equipment, as shown in Fig. 3.

The equipment is both emitter and receiver at the same time, the waves sweep over the entire material to cover the surface and look for imperfections, in which the discontinuity may be a porosity, a crack, a delamination or a defect that changes the density of the material, causing the wave to return early, testing the equipment the location of the fault.

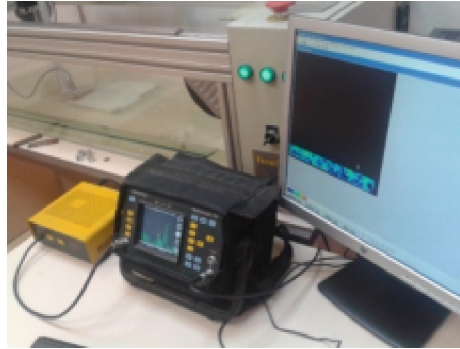


**Fig. 3.** Ultrasound reproduction equipment

In order to determine the residual strength of the damaged panels and to establish a comparison, Iosipescu [4] tests were carried out, which allows obtaining stiffness and strength values, its main use is to obtain the shear modulus of a composite sheet, for this purpose, the test tries to reproduce at the interface a uniform tangential stress distribution by means of external shear solicitation, so that if we mount two strain gages at  $45^\circ$  with the loading direction and perpendicular to each other, we can obtain the values of  $\gamma_{12}$ , as shown in Fig. 4. However, the existence of a shear stress causes the occurrence of a bending moment and, therefore, the presence of normal stresses that make it difficult to obtain the shear modulus correctly. Iosipescu proposes a model in which the central section of the specimen presents a state of uniform shear and zero bending which is illustrated in Fig. 5.



**Fig. 4.** Iosipescu test device view



Fig. 5. View of the break

### 3 Results and Discussion

#### 3.1 Untested Panels

Ultrasound tests were performed on panels without being subjected in the slamming machine, to verify that the amount of damaged bits is not higher than 5% by the manufacturing and drying process, as shown in Fig. 6 and 7, which proceeded to perform the tests.

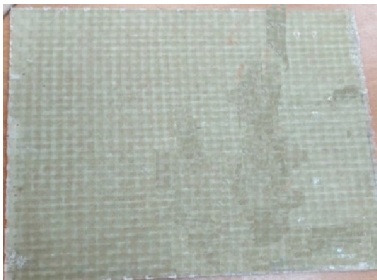


Fig. 6. Untested panel

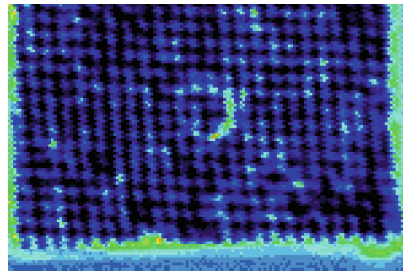


Fig. 7. Ultrasound untested panel

#### 3.1.1 Panels Tested on the Slamming Machine

The tested panels reached 85% of damage in the area of contact with the slamming machine and the cam, it was observed that the first micro-cracks appeared at 200 impacts, and were already very visible at 1000 cycles. The first damages observed as slight white shadows were located in the areas where they touch the sides of the cam, and then aligned towards the center of the contact surface as shown in Fig. 8.

The images obtained in 32 colors were converted to black and white using ImageJ software to separate the bits greater than 18 decibels and to quantify the damage. Figure 9 shows the image of a panel damaged with ultrasound and its corresponding black and white binary image showing the damaged areas after one of the tests.



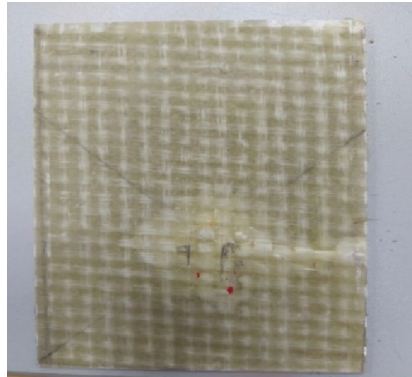


**Fig. 8.** Panel tested on slamming reproduction machine

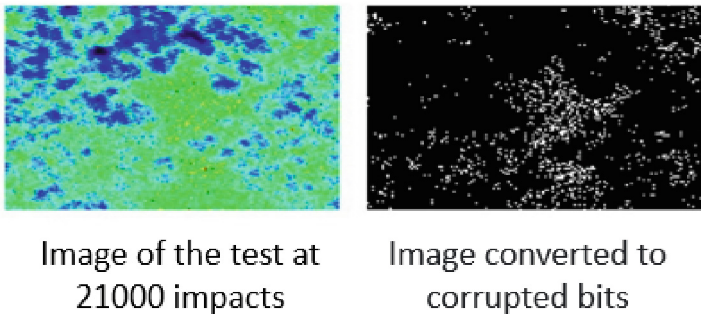


**Fig. 9.** 32-bit to 2-bit image conversion from a tested panel

This result establishes the direct relationship between the change in flexibility of an untested panel and the slamming pressure. Visual observation of the damaged surface within the cam contact area after a number of impact cycles served to check the proportion of damage related to the stress values that exceeded the damage threshold by becoming microcracks.

### 3.2 Shear Test Results

From the panel without being impacted, 10 specimens were cut as shown in Fig. 10, the maximum dimension is 22.22 mm wide by 97.16 mm long, being the cross section 2 mm thick, the narrowest section 4 mm. The Iosipescu notch was made by means of a milling machine, the specimen was fixed to the clamp with an angle of  $45^\circ$  and the milling cutter was passed through the interface, which produced an angle of  $90^\circ$ .

Figure 11 shows the Iosipescu test graphically, the shear force as a function of displacement (stroke) for one of the specimens, with a displacement of 2.0415 mm as a function of the force of 1.139531KN, where the maximum breaking strength is observed, which reflects the deformed zone.



Fig. 10. Specimens used in the shear test

The result obtained indicates that the maximum shear stress of the specimen is 558.183MPa, the result of the other specimens was similar to this test.

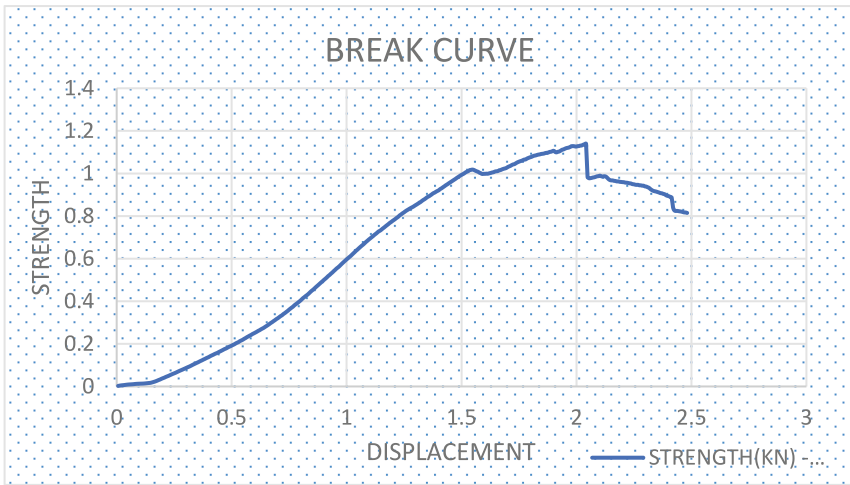


Fig. 11. Losipescu trial results

The present investigation, the panels that make up the hull of a ship built with fiber-glass composite material, effectively mitigate the damage produced by the slamming phenomenon by reproducing the impacts under controlled laboratory conditions. The damage protection presented allows damping the destructive energy dissipation protecting the hull structure and increasing its service life. This brings a new perspective to ship design as it changes the way in which stress concentrations are distributed in the hull of vessels. The equipment built to reproduce slamming impacts was sufficient to observe the evolution of the damage produced by this phenomenon at the level of micro-cracks, which joined together to form easily observable delamination surfaces.

## 4 Conclusions

1. The proposed methodology, is a reproducible way to assess damage during navigation, according to the slamming pressures recorded on the bottom of a vessel's hull.
2. The use of the observation of the damage quantified by the ImageJ software after scanning the specimens with submerged ultrasound, allows to know how the damage tendency changes in the material with the impacts, as well as to quantify its behavior for damages not visually observable during the slamming tests.
3. The equipment is suitable to perform low energy slamming impact tests in which the microcracks are aligned in an interlaminar way to medium energy level impacts in which the interlaminar damage also produces intralaminar damage.
4. This work will be complemented with additional shear tests of the specimens subjected to the slamming test in order to make a quantitative comparison with the untested specimens.

## References

1. He, W., Wu, J., Lu, Y.: Numerical investigation of dynamic response and failure mechanisms for composite lattice sandwich structure under different slamming loads. *Appl. Compos. Mater.* **28**(5), 1477–1509 (2021). <https://doi.org/10.1007/s10443-021-09919-6>
2. Ki, W.K., Heung, S.K.: Strength reduction behavior of honeycomb sandwich structure subjected to low- velocity impact. *Mater. Sci. Eng. A, China* **483–484**, 333–335 (2008)
3. Hassoon, O.H., Tarfaoui, M., El Moumen, A., Qureshi, Y., Benyahia, H., Nachatne, M.: Mechanical performance evaluation of sandwich panels exposed to slamming impacts: comparison between experimental and SPH results. **220**, 776–783. France (2019)
4. Barroso, A., Mantic, V., París, F.: *Int. J. Fract.* **119**, 1–23 (2003)
5. Lopresto, V., Langella, A., Papá, I.: Dynamic loading on composite laminates in the presence of water. *Polym. Eng. Sci.* **57**, 613–620 (2017)
6. Aktay, L., Johnson, A.F., Holzapfel, M.: Prediction of impact damage on sandwich composite panels. *Comput. Mater. Sci. Germany* 252–260 (2005)
7. Arias, A., Zaera, R., López-Puente, J., Navarro, C.: Numerical modelling of the impact behavior of new particulate loaded composite materials. *Compos. Struct.* **61**, 151–159 (2003)
8. Balci, O., Coban, O., Bora, M.O.: Experimental investigation of single and repeated impacts for repaired honeycomb sandwich structures. *Mater. Sci. Eng. A, Istanbul* 23–30 (2017)
9. Akatay, A., Bora, M.O., Coban, O.: The influence of low velocity repeated impacts on residual compressive properties of honeycomb sandwich structures. *Compos. Struct.* **125**, Istanbul 425–433 (2015)
10. Shams, A., Zhao, S., Porfiri, M.: Water Impact of Syntactic Foams, pp. 1–15. Department of Mechanical and Aerospace Engineering, New York (2017)
11. Zouari, R., Benhamida, A., Dumontet, H.: A micromechanical iterative approach for the behavior of polydispersed composites. *Int J. Solids Struct.* **45**, 3139–3315 (2008)



# Crash Testing of Polymer Matrix Composites Using Flat Specimens

Lorenzo Vigna<sup>1</sup>(✉), Valentina Lopresto<sup>2</sup>, Ilaria Papa<sup>2</sup>, Pietro Russo<sup>3</sup>,  
Andrea Calzolari<sup>4</sup>, Giuseppe Galizia<sup>4</sup>, Davide Salvatore Paolino<sup>1</sup>,  
and Giovanni Belingardi<sup>1</sup>

<sup>1</sup> Department of Mechanical and Aerospace Engineering, Politecnico di Torino, Corso Duca degli Abruzzi, 24, 10129 Turin, Italy  
lorenzo\_vigna@polito.it

<sup>2</sup> Department of Chemicals, Materials and Production Engineering, University of Naples “Federico II”, P.le Tecchio 80, 80125 Naples, Italy

<sup>3</sup> Institute for Polymers, Composites and Biomaterials, National Research Council, via Campi Flegrei 34, 80078 Pozzuoli, NA, Italy

<sup>4</sup> ITW Test And Measurement Italia S.r.l. - Instron CEAST Division, via Airauda 12, 10044 Pianezza, TO, Italy

**Abstract.** The industry’s use of polymer composite materials is continuously increasing because of their excellent mechanical properties and light weight. However, among the multiple structural applications whose performance can be improved using composites, crashworthiness is one of the less common but with good perspectives for the future, thanks to the high level of energy absorption of these materials.

In the present work, the crash behavior of three composite materials (a carbon/epoxy, a hybrid glass-carbon/vinyl ester and a carbon/vinyl ester laminate) was studied by performing in-plane compression tests of flat plates in impact conditions using a drop tower. The testing setup required a fixture to hold the specimen in vertical position and avoid buckling when loaded in in-plane direction. Two different versions of the testing fixture were compared. The first one requires a plate to transmit the load from the falling mass to the specimen, while in the second version the falling mass gets directly in contact with the specimen.

The specimen crashed under the impact load, and the main failure mechanism was splaying with fronds. Both fixture versions worked effectively to crash the specimens and measure the Specific Energy Absorption (SEA) of the three materials. The carbon/epoxy and hybrid laminate showed a similar crash force, with the second having higher SEA because of the lower density. The carbon/vinyl ester material showed higher crash stress and SEA.

**Keywords:** Crashworthiness · Specific Energy Absorption · Impact testing · Polymer matrix composites

## 1 Introduction

The good performances of composite materials for crashworthiness are well known in the literature. They are due to the high level of energy absorption during failure combined with the low density. Many composite materials can exceed the performances of metals in similar applications, making them good candidates for metal substitution to get lighter and safer vehicles [1]. Today several applications have been implemented in motorsport and aerospace. Still, some issues are slowing down the diffusion of composites for crashworthiness applications in standard automotive mass production, mainly due to a trial-and-error approach adopted to design these structures, which makes the design process long and expensive. This is mainly due to the multiple failure modes of composites that result in very different energy absorption levels and can be induced by different structure geometries and production processes, even for the same material [2]. This means that the prediction of the behavior of a composite structure during crash is difficult even through finite element modeling, and expensive prototype testing is required to make comparisons with simulation results. Furthermore, the parameters of the material model need to be tuned to have good matching with experimental results [3].

Another issue related to evaluating the energy absorption capabilities of composites is the absence of an adequate standard to run crashworthiness tests at coupon level [4]. Existing standards for material characterization (tensile, compression, shear, bending, matrix toughness, puncture, compression after impact, Charpy etc.) cannot describe the energy absorption capabilities of the material during failure in crash conditions. For this reason, the typical approach requires performing crash compression tests on material samples in quasi-static, high strain rate or impact conditions. Due to the absence of a standard testing procedure, several approaches have been adopted in the last decades. They can be found in literature with different specimen geometries as shown in Fig. 1 [5–12]. Due to the effect of the specimen geometry on the failure modes and energy absorption level of the material, the comparison between results obtained by studies carried out testing specimens with different geometries is not possible [13]. For this research, a flat specimen was chosen to avoid the effect of the curvature on the energy absorption during failure.

An in-plane compression test on a flat specimen requires a fixture to clamp the specimen and avoid buckling. Several fixtures with this aim have been proposed in literature, but none is today recognized as a standard setup for crashworthiness tests on composites [6, 11, 14–16]. In this research, an innovative fixture, optimized for testing in a drop weight machine, has been used to compare the Specific Energy Absorption (SEA) of three different laminates [17]. Two different testing setups are compared to identify the most effective one.

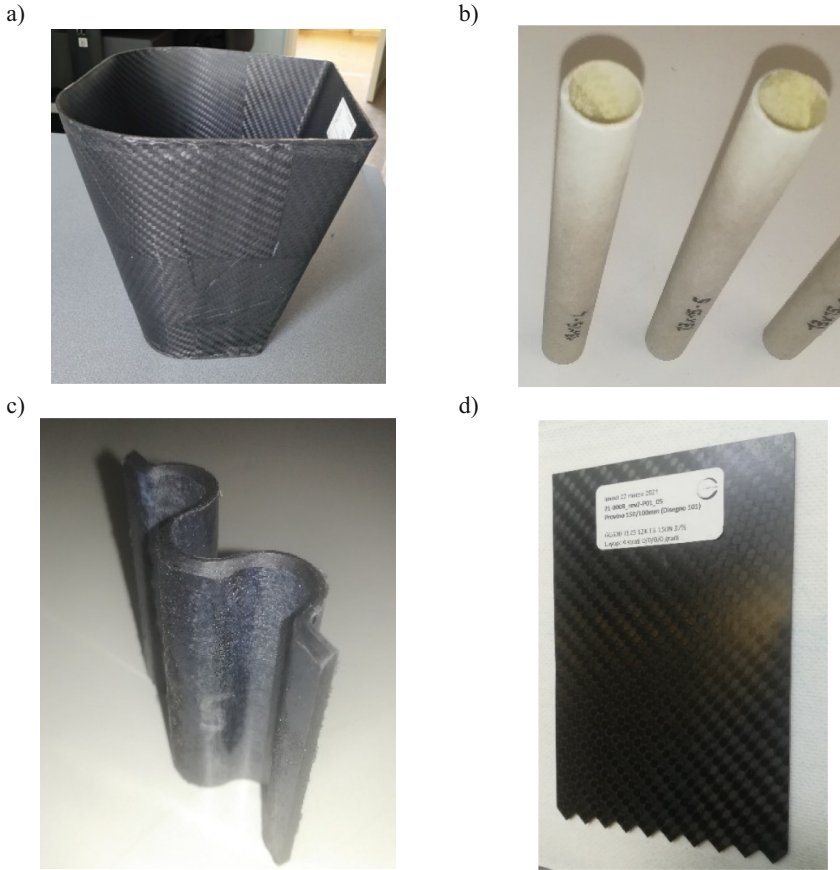


**Fig. 1.** Different specimen geometries for crashworthiness test: a) full scale crash box, b) closed section self-supporting specimen, c) open section self-supporting specimen, d) flat specimen.

## 2 Materials and Methods

Three different laminates have been produced with different layups:

**Carbon/Epoxy.** A carbon/epoxy laminate has been produced using 14 plies of  $0^\circ/90^\circ$  T700 carbon fabric with a weight of  $300 \text{ g/m}^2$  coated with a SX 10 epoxy resin by Mates Italy using a vacuum infusion process. The obtained laminate has a 48% fiber volume content and a thickness of 3.7 mm.

**Hybrid.** A hybrid laminate has been produced alternating a  $0^\circ/90^\circ$  carbon fiber fabric with a weight of  $320 \text{ g/m}^2$  by Mike Composites and a  $0^\circ/90^\circ$  glass fiber fabric with a weight of  $300 \text{ g/m}^2$  by Castro Composites. The stacking sequence alternated two layers of glass fabric (total 10 layers) to one of carbon fabric (total 5 layers). The fibers were coated by means of a resin transfer molding process using a Crystic VE 679PA vinyl ester resin at IMDEA, Madrid, within the SMP financially supported by Office of Naval

Research (ONR). The nominal thickness of the laminate was  $3.5 \pm 0.25$  mm with a fiber volume fraction of 58%.

**Carbon/Vinyl Ester.** A Carbon/vinyl ester laminate was produced with 14 plies of  $0^\circ/90^\circ$  T700 carbon fabric with a weight of  $300 \text{ g/m}^2$  coated by a DION® FR 9300 vinyl ester resin, a brominated fire-retardant epoxy-based resin for marine applications with high physical and chemical properties. A vacuum infusion process produced the plates and the resulting laminate has a 50% fiber volume fraction and a nominal thickness of 4 mm.

The cured laminates were cut into rectangular specimens having dimensions of  $100 \text{ mm} \times 150 \text{ mm}$ . On one of the 100 mm-long sides, a saw tooth geometry was machined to trigger a splaying failure of the material and avoid a possible sudden failure in the central part of the specimen.

The three laminates were tested using a fixture designed by some authors to carry out in-plane compression tests in a drop tower testing machine (Fig. 2). The specimen is clamped between two plates with a controlled force of 4 kN. It is pushed vertically by the dropped mass. Three columns on each plate (two longer, one shorter to avoid interference with the impactor) are in contact with the specimen and have been coated with a PTFE spray layer to reduce the friction force to a minimum in order to avoid a possible overestimation of the crash force, and thus of the energy absorption capabilities of the specimen [18]. The failure happens in the lower part of the specimen, where the trigger has been positioned. An unsupported height of 10 mm was left to allow the formation of two fronds of material and obtain the desired failure mode (splaying). Two different versions of the testing fixture are compared in this paper. The first one (Fig. 2a) requires a steel plate positioned on the specimen to distribute the load of the impact mass on the upper side of the specimen; the second one (Fig. 2b) allows direct contact between the impact mass, equipped with a striker with the larger contact surface, and the specimen.

Impact tests were performed by a Instron 9450 drop tower with an impact energy of 550 J, corresponding to a mass of 50.4 kg and an impact velocity of 4.7 m/s. The crash force is acquired using a striker equipped with a strain gauge load cell with maximum load range of 222 kN and sampled at a frequency of 1 MHz. A double integration of the force signal allowed to calculate the displacement of the impacted mass, corresponding to the specimen's crushed length. The integral of the force-displacement curve corresponds to the energy absorbed by the material during failure. The acquired data evaluated many results:

- Peak force, typically due to the first contact between the falling mass and the specimen
- Average crash force  $F_m$ , calculated considering the stable crash area in an interval between 40% and 90% of the maximum displacement
- Average crash stress as the ratio of average force and cross section of the specimen
- Specific Energy Absorption (SEA) as

$$SEA = \frac{E}{\rho A \delta} = \frac{\int F dx}{\rho A \delta} \quad (1)$$

Where  $E$  is the energy absorbed during stable crash (from 40% to 90% of the maximum displacement [17]),  $F$  the force signal,  $\rho$  the material density,  $A$  the cross section of the specimen,  $\delta$  the considered curve length in mm (i.e., from 40% to 90% of the maximum displacement).

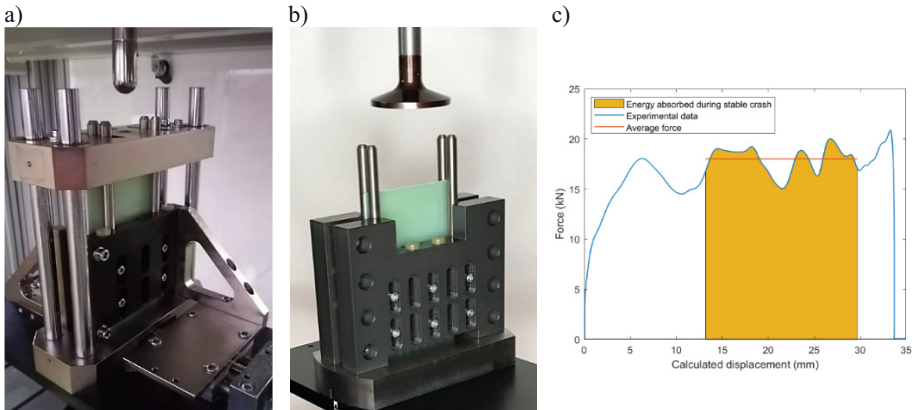


**Fig. 2.** a) Fixture for crashworthiness test on flat composite specimens: first setup with upper crash plate, b) fixture for crashworthiness test on flat composite specimens: second setup for direct contact between specimen and impactor, c) typical force-displacement curve obtained from a crashworthiness test with direct contact between specimen and impactor (second setup).

### 3 Results

All the specimens tested showed the expected splaying failure mode, which consists of delamination in the mid plane of the laminate with formation of two fronds that bend in opposite directions. In addition, delamination between many layers is visible in the two fronds, and fragmentation of the matrix occurs with the formation of many debris and powders during the test. An example of failure for each configuration is reported in Fig. 3, where it is possible to note that each laminate has a different failure depending on the material, but no effect of the two testing setups appears visible.

Stress-displacement curves (Fig. 4) have very different trends caused by the two testing setups. In the first one (Fig. 4a) the striker gets in contact with the upper steel plate, whose inertia causes an initial stress peak followed by a drop to zero (the contact is lost) and a second peak followed by strong oscillations. The second testing setup (Fig. 4b), thanks to the direct contact between the specimen and the striker, causes lower initial peaks and a lower level of oscillations. Crash curves obtained from the second setup give a better understanding of the real behavior of the material. In contrast, the oscillating behavior observed with the first testing setup is mainly related to the setup rather than the material.

The carbon-vinyl ester laminate shows significantly higher crash stress that causes lower curve length because of the same impact energy used in all the tests. The crash stress



for hybrid and carbon/vinyl ester is similar. Still, the hybrid laminate shows a slightly higher initial peak, probably due to a material effect that slows down the initiation of the stable crash failure. The average results obtained are reported in Table 1. Comparing average stress and SEA obtained from the two different testing setups, the agreement is good for carbon/epoxy and carbon/vinyl ester. Hybrid specimens showed a higher difference in the two testing setups, probably due to higher scatter and the low number of repeated tests.

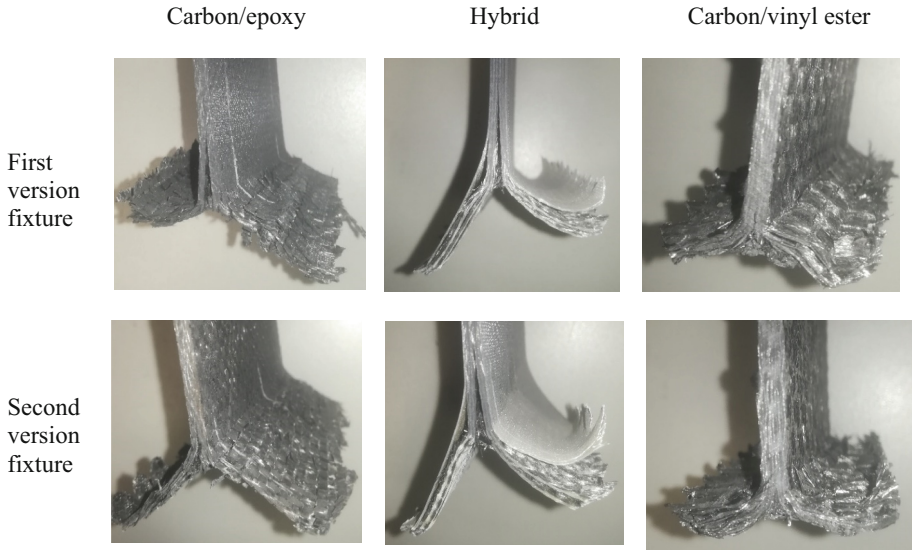


**Fig. 3.** Splaying failure mode found on specimens after the crashworthiness test.

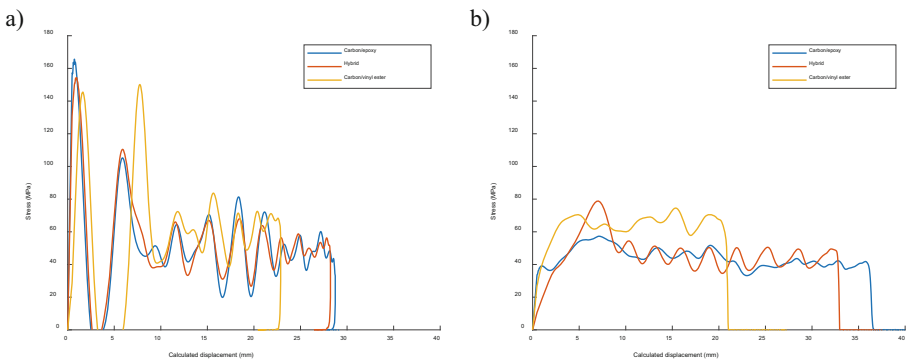


**Fig. 4.** a) Force-displacement curves acquired during crashworthiness tests using the first version of the fixture with upper plate, b) Force-displacement curves acquired during crashworthiness tests using the second version of the fixture with direct contact between specimen and dropped mass.

Considering all the tests carried out with the two testing setups, the three plots in Fig. 5 describe the main results of the crashworthiness tests. The carbon/vinyl ester material showed better mechanical properties, while the carbon/epoxy and the hybrid laminates showed similar crash force and stress. Considering the density to evaluate the SEA, the carbon/epoxy material has a better performance than the hybrid due to the lower density of the carbon fibers with respect to glass fibers present in the hybrid laminate. As a result, carbon/vinyl ester shows the higher SEA with an average value of 42.5 kJ/kg.

**Table 1.** Average results of crashworthiness tests.

Material	Fixture	Average force (kN)	Average stress (MPa)	SEA (kJ/kg)
Carbon/epoxy	First version	15.9	44.1	34.6
	Second version	17.1	46.8	34.1
Hybrid	First version	18.4	49.7	30.5
	Second version	14.0	37.0	23.1
Carbon/vinyl ester	First version	25.4	58.6	43.1
	Second version	24.6	57.9	42.2

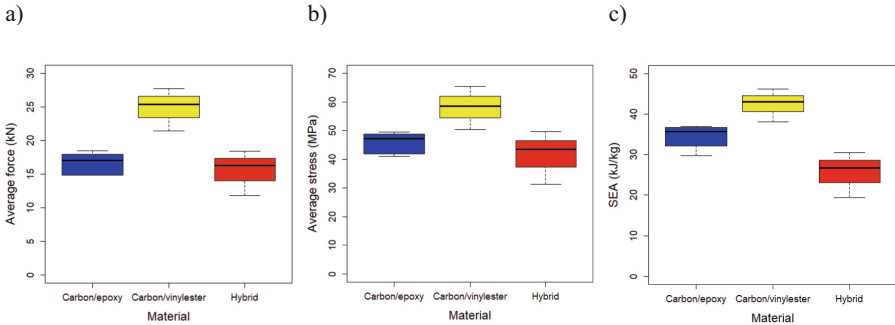


**Fig. 5.** Results of crashworthiness tests a) average crash force, b) average crash stress, c) Specific Energy Absorption

## 4 Conclusions

Crashworthiness tests were carried out on three different composite flat laminates using an anti-buckling fixture designed to carry out in-plane compression tests in impact conditions. The fixture proved to work effectively for all the composite samples and obtained good results. Of the two testing setups compared, the second one is the most suited for these tests thanks to the direct contact between the specimen and the falling mass,

which allows obtaining curves with lower oscillations where it is easier to understand the behavior of the material.

The carbon/vinyl ester was the most effective for crashworthiness applications due to the higher SEA between the three laminates compared. The Carbon/epoxy laminate showed significantly lower crash stress and SEA than carbon/vinyl ester, indicating a strong effect of the matrix on the energy absorption in this kind of test. The hybrid carbon/glass laminate showed lower performance in terms of energy absorption, in particular if the higher density of glass fibers is taken into account for the SEA calculation. However, a hybrid layup can be a good choice if other properties are needed, like a higher damage resistance in case of impacts.

The proposed testing procedure proved to be useful for providing a quantitative evaluation of the energy absorption capability of composite laminates under crash failure. To provide a complete characterization of the material behavior, considering different failure mode, further developments of the testing setup are needed and a comparison with results obtained with specimens with different geometries should be carried out.

## References

1. Lukaszewicz, D.H.-J.A.: Automotive composite structures for crashworthiness. In: Elmarakbi, A. (ed.) *Advanced Composite Materials for Automotive Applications: Structural Integrity and Crashworthiness*, pp. 99–127. Wile, Chichester, UK (2013)
2. Farley, G.L., Jones, R.M.: Energy-Absorption Capability of Composite Tubes and Beams. NASA Technical Memorandum 101634 (1989)
3. Cherniaev, A., Montesano, J., Butcher, C.: Modeling the axial crush response of CFRP tubes using MAT 054, MAT058 and MAT262 in LS-DYNA. In: 15th International LS-DYNA Users Conference (2018)
4. Feraboli, P., Deleo, F., Garattoni, F.: Efforts in the standardization of composite materials crashworthiness energy absorption. American Society for Composites - 22nd Technical Conference of the American Society for Composites 2007 – Composites Enabling a New Era Civil Aviation, vol. 1, pp. 741–759 (2007)
5. Feraboli, P.: Development of a corrugated test specimen for composite materials energy absorption. *J. Compos. Mater.* **42**, 229–256 (2008). <https://doi.org/10.1177/0021998307086202>
6. Feraboli, P.: Development of a modified flat-plate test specimen and fixture for composite materials crush energy absorption. *J. Compos. Mater.* **43**, 1967–1990 (2009). <https://doi.org/10.1177/0021998309343025>
7. Obradovic, J., Boria, S., Belingardi, G.: Lightweight design and crash analysis of composite frontal impact energy absorbing structures. *Compos. Struct.* **94**, 423–430 (2012). <https://doi.org/10.1016/j.compstruct.2011.08.005>
8. Boria, S., Scattina, A., Belingardi, G.: Axial energy absorption of CFRP truncated cones. *Compos. Struct.* **130**, 18–28 (2015). <https://doi.org/10.1016/j.compstruct.2015.04.026>
9. Hull, D.: A unified approach to progressive crushing of fibre-reinforced composite tubes. *Compos. Sci. Technol.* **40**, 377–421 (1991)
10. Dalli, D., Varandas, L.F., Catalanotti, G., et al.: Assessing the current modelling approach for predicting the crashworthiness of Formula One composite structures. *Compos. Part B Eng.* **201**, 108242 (2020). <https://doi.org/10.1016/j.compositesb.2020.108242>
11. Lescheticky, J., Barnes, G., Schrank, M.: System level design simulation to predict passive safety performance for CFRP automotive structures. SAE Technical Paper 2 (2013). <https://doi.org/10.4271/2013-01-0663>

12. Heimbs, S., Strobl, F.: Crash simulation of an F1 racing car front impact structure. In: 7th European LS-DYNA Conference 1–8 (2009)
13. Feraboli, P., Wade, B., Deleo, F., Rassaian, M.: Composites : part A Crush energy absorption of composite channel section specimens. *Compos. Part A* **40**, 1248–1256 (2009). <https://doi.org/10.1016/j.compositesa.2009.05.021>
14. Lavoie, J.A., Morton, J.: Design and Application of a Quasistatic Crush Test Fixture for Investigating Scale Effects in Energy Absorbing Composite Plates. NASA Contractor Report 4526 (1993)
15. Cauchi Savona, S., Hogg, P.J.: Investigation of plate geometry on the crushing of flat composite plates. *Compos. Sci. Technol.* **66**, 1639–1650 (2006). <https://doi.org/10.1016/j.compscitech.2005.11.011>
16. Duong, A.V., Rivallant, S., Barrau, J.J., et al.: Influence of speed on the crushing behavior of composite plates. In: 7th Asian-Australasian Conference on Composite Materials 2010, pp 678–681. ACCM 2010. Taipei, Taiwan (2010)
17. Vigna, L., Babaei, I., Garg, R., et al.: An innovative fixture for testing the crashworthiness of composite materials. *Frat ed Integrità Strutt* **15**, 76–87 (2021). <https://doi.org/10.3221/IGF-ESIS.55.06>
18. Vigna, L., Calzolari, A., Galizia, G., et al.: Effect of friction on a crashworthiness test of flat composite plates. *Forces. Mech.* **6** (2022). <https://doi.org/10.1016/j.finmec.2021.100070>



# Green Composites Surface Modification Regarding Fibre/Resin Compatibility: An Approach from an Engineering and Chemistry Perspective

Neffer A. Gomez<sup>1</sup>(✉), Martin Muscat<sup>1</sup>, Claire DeMarco Muscat-Fenech<sup>1</sup>,  
Duncan Camilleri<sup>1</sup>, Emmanuel Sinagra<sup>2</sup>, and Sandro Lanfranco<sup>3</sup>

<sup>1</sup> Department of Mechanical Engineering, University of Malta, Msida 2080, MSD, Malta  
NefferA.Gomez@gmail.com

<sup>2</sup> Department of Chemistry, University of Malta, Msida 2080, MSD, Malta

<sup>3</sup> Department of Biology, University of Malta, Msida 2080, MSD, Malta

**Abstract.** The current work involves the analysis of the fibre-polymer adhesion characteristics in green composites aiming to improve the compatibility between the natural fibres and the polymer resin. Adhesion properties depend on the type and material properties both of the fibre and the resin. In order to have a better understanding of how to improve fibre/resin adhesion, it is important to explore the chemical interaction between the two. The document considers several aspects related to chemical bonding and physical attraction forces.

**Keywords:** Green Composite · Natural Fibre · surface modification · polymer matrix · reinforcement

## 1 Introduction

Composites are the combinations of two or more materials having different properties. The two materials are the reinforcement and the matrix. The composites' material mechanical, physical, thermal, and electrical properties are distinct from each other. After being combined, composites have a synergetic behaviour, improving or obtaining new properties which are difficult to obtain with the base material alone [1]. Due to the awareness of increasing global environmental concerns, recent research in green composite materials has gained momentum. Green composites are eco-friendlier than their synthetic counterparts mainly because of their potential biodegradability. The reinforcing materials are mainly based on fibres, which are obtained directly from natural resources such as agave plants. Natural fibres have remarkable characteristics, and these make them applicable to many different areas. Advantageous properties of such natural fibres are biodegradability, low density, low-cost of extraction, and abundance in nature [2, 3]. Natural fibres have shown excellent physicochemical and mechanical properties, similar properties to synthetic fibres, and at the same time as alternatives to petroleum-based products. However, there are still some disadvantages because of fibre's hydrophilic

properties, which result in poor adhesion with the polymer matrix. The methods to improve fibre/resin compatibility usually looks at changing the polarity properties of the fibre or resin. Nevertheless, it is necessary to consider which polymer matrix should be used to fabricate the composite. The final material behaviour would depend on the chemical groups present in the polymer resin matrix. These groups would be interacting with the fibre. The present work, which is part of the DLANComp (Developing Local Agave Natural Fibre composites) project, aims to help and clarify knowledge used by researchers working on green composites regarding fibre/resin compatibility. In this work, the study of surface modification in natural plant fibres will be considered from a chemical point of view. It would clarify the understanding of some important and relevant concepts such as hydrogen bonding, chemical and physical interaction, natural polarity, and potential active modification points. The authors would like to acknowledge the project from which DLANComp is being funded: 'Setting up of transdisciplinary research and knowledge (TRAKE) complex at the University of Malta (ERDF.01.124)' which is being co-financed through the European Union through the European Regional Development Fund 2014–2020.

## 2 Natural Fibres

Fibres are an important component in polymer composites and are the constituents that give mechanical strength to the composite. In recent years there have been several attempts to replace synthetic fibres with natural fibres in fibre reinforced composites due to increasing environmental awareness and depletion of oil resources. These materials have some advantages such as lower environmental impact, high strength and are renewable and biodegradable. However, natural fibres have shown some drawbacks such as degradation, irregular mechanical properties, low thermal stability, moisture absorbance, and poor surface interaction with the matrix [4–6]. None the less, cellulosic fibres in micro and nano scale are attractive to replace man-made fibres as reinforcement to make environmentally friendly green products.

Natural fibres from plant sources are classified as primary fibres. They are made up of cellulose (40–75%), hemicellulose (10–25%) and lignin (5–15%), which have complex structures as show in Table 1. Cellulose is enclosed in soft lignin, while hemicellulose forms the ancillary layer of the fibre.

There are a number of reasons why researchers have started to evaluate the influence of treatment on the fibre surface in order to determinate the modification of their properties. According to Ahmad R et al. [6], there are a number of parameters that affect the extent the surface properties of fibres can be modified. These parameters include the morphology of the fibre, chemical composition, processing condition, and the type of plant from which the fibres are extracted. Natural fibres are harvested from plants and crops so have inherently different lengths, cross-sectional areas, and structural defects that affect the fibres' mechanical properties, and which dictate the type of interaction that could occur with the polymer matrix. The extraction processes such as pressing, rolling, machine decortication or biological retting also has an effect on the composite's mechanical properties [7, 8]. Fibre processing especially fibre drying is an important step since moisture content directly affects the quality and adhesion of the fibres to the matrix [8, 9].

**Table 1.** Chemical constitution of some selected plants [10]

Fibre	Cellulose	Hemicellulose	Lignin
Sisal	40–75	10–25	4–12
Flax	27–70	60–81	2–3
Jute	26	45–84	5–26
Kenaf	6–53	37–72	9–21
Bamboo	11–17	26–43	21–30

### 3 Composites

In the composite structure, the matrix is a continuous component, while the fibre is discontinuous. Both materials have different chemical, physical, electrical, and thermal properties. These properties have a synergic behaviour (combined action) and produce new properties which would be difficult to obtain from one material. Due to this, these materials have been used in different applications. Polymer composites are heterogeneous components with properties governed by the composition of the individual components. The application of composite materials depends on the transfer of the stress from the matrix to the fibres. The stress transfer is limited by the compatibility of the materials used in the composite fabrication, which leads to interphase between both individual components [3, 11].

Natural Fibre composites were some of the earliest materials used by man. In 1930 H Ford explored different natural fibres as reinforcement for composites used as part of a car's body [12]. The second world war paved the way for fibre composites used in the aero industry. Of particular note is the use of a new flax fibre composite in the construction of a spitfire fuselage [13]. During the second half of the 20th century the East German car 'the Trabant' used a composite 'Duroplast' composed of a phenol resin reinforced with cotton fibres for its interior and body parts [14]. As a result, the use of natural fibre composites in the automotive sector found a good application [15]. The use of natural fibre composites has now spread into other markets such as sports and marine goods like yachts and pleasure craft, surfboards, kayaks, bicycles, and helmets [16].

### 4 Polymer Resin

Polymer materials have different properties depending on their chemical structure. There are two common types known as thermoplastic and thermosetting. The former can be reprocessed again at elevated temperatures while the latter cannot be re-processed as such [17]. Thermosetting polymer resin materials form a lot of cross-links after the curing process, which is the reason why the material is resistant to high temperatures [18]. Resins have been largely used in the fabrication of advanced composites aiming to attain good specific properties. Nevertheless, resins such as epoxy have some disadvantages and limitations. These disadvantages and weaknesses are overcome by incorporating fibres and using fillers [19].

## 5 Fibre Modification

The use of natural fibre applied as reinforcement to polymer materials requires looking for the most efficient process which could improve the interaction between the fibre and the matrix. A better understanding of the factors that determine the compatibility of the materials would help to obtain a better result for the final mechanical properties of the composite.

It is important to understand how the compatibility between the filler and the matrix work to give a better and clearer overview of the observed failures in composites. Most of the failures are due to poor interfacial interaction in the composite and poor resistance to moisture absorption. These can develop stress concentration regions and produce fracture initiation sites in the composite.

A strong interaction between fibre and matrix helps to transmit the stress applied from the matrix to the fibre. The interaction is achieved by intermolecular interaction between the chemical groups on the fibre surface binding the chemical groups located in the matrix. Nevertheless, if the adhesion between both parts in the composite exhibit poor compatibility, the ability to transfer the stress is low, decreasing the mechanical properties of the composite [6, 20, 21].

The interaction between the polymer matrix and the fibres can vary from mere physical interfacial to chemical interaction, such as covalent bonds or secondary forces such as Van der Waal forces or hydrogen bonds amongst the components, electrostatic forces, and mechanical interlocking [10].

Surface modification processes are used on natural fibres to improve the fibre morphology, moisture absorption, thermal degradation, wear, mechanical properties, and mechanical processing parameters [20, 21]. These modifications can improve interfacial bonding, wettability of the fibre by the matrix, the roughness of the fibre surface, decrease the moisture absorption of the material, and so also the swelling of the composite [6].

The polymer matrix is essentially hydrophobic. This is the reason why these materials have low compatibility with natural fibre, which has a strong hydrophilic character.

To attempt to improve the poor interface interaction between hydrophilic fibres and hydrophobic matrices, different methods have been tried by modifying the surface of the fibre, using chemical, physical and biologic treatments [4].

The chemical constitution of the fibre consists of cellulose, hemicellulose, lignin and pectin [6]. According to Komal, et al. [22], in order to improve the fibre it is necessary to increase its percentage of cellulose. The percentage of cellulose determines the usefulness of the fibre, because it is responsible for increasing the mechanical properties of the fibre giving rigidity to the material. The characteristics of the cellulosic fibre are modified with the presence of lignin and the non-cellulosic constituents [6, 23].

Cellulose is a linear polymer naturally constituted by monomers of glucose. It has a hydrophilic nature because of the polar groups in the cellulose and the large number of hydroxyl groups present in every monomer of glucose.

To enhance the compatibility between the fibre and the matrix, the chemical treatment is best focused on the modification and functionalization or activation of the hydroxyl groups located on the surface, reducing the inherent hydrophilic nature of the fibre or by introducing a third material aiming to increase the fibre reactivity due to the activation of its structure [6]. These groups have some elements which can interact with



the matrix, changing the composition of the material. The replaced new elements with hydrophobic properties would improve the interaction with the non-polar polymer matrix [6]. Different chemicals have been used in the fibre modification, such as alkali, silane, water-repelling agents, peroxides, and permanganates, among others [4, 6, 13, 24].

One of the most common methods used on natural fibres is the alkali treatment or mercerization. This methodology increases the cellulose content and aims to make the weak amorphous fraction of the fibre, such as hemicellulose and lignin, soluble by breaking the existing interaction between cellulose and lignin. These weak compounds develop poor surface wetting and reduce the interaction bonding in the composite.

The mercerization process removes impurity components such as wax and oils, cleaning the surface of the fibre, making it more porous so that the resin can enter inside the fibrils of the fibre during the curing process leading to a mechanical interlocking. Moreover, the fibre becomes sticky, increasing the roughness and the surface area, which would be in contact with the matrix. In addition, cleaning the surface contributes to increasing the number of cellulose (crystalline) exposed on the fibre surface. It results in a lower moisture absorption capacity and minimized thermal and biological degradation because of a more ordered physical structure. The use of alkaline treatment increases the concentration of exposed hydroxyl groups located on the surface of the fibre, thus having more potential to change the nature of the fibre by chemical modification [4, 23–26].

NaOH, KOH, Ba(OH)<sub>2</sub> and Ca(OH)<sub>2</sub> are alkaline chemicals that have been used in the treatment of the fibre surface. Time and chemical concentration of the alkaline product influence the final fibre behaviour. According to Ahmad R et al. [6] the use of alkali concentration above 10% NaOH result in weakening or damaging the fibre.

The use of coupling agents takes advantage of the chemical structure of molecules which have two polar functions. The first fraction reacts with the hydroxyl groups located on the wall of the fibre [6] and the second reacts with the functional groups located on the matrix. Coupling agents such as silane are a way to enhance the interfacial interactions between the fibre and the matrix due to the formation of chemical bonding promoting adhesion to hydrophilic composites [4, 6]. In this case, the coupling agent links the oxide groups on the fibre surface and the polymer molecules. The chemical structure for the silane coupling agent is based on an alkoxy and alkyl bridge connected to the silicon atom and with the presence of an organic functionality. These groups form silanols which are adsorbed on to the fibre-matrix surface [24, 27].

Treatments such as silanization, creates stable covalent bonding between the chemical and the hydroxyl group of the fibre in the interface, the crosslinked structure that is formed decreases the swelling of the composite. However, it has been observed that a large added coupling molecule reacts with hydroxyl groups, which would destroy the cellulose packing chain leading to decrease the crystallinity. But both tensile and flexural strengths increased [6, 28].

Graft copolymerization is an effective methodology to improve the compatibility of the fibre-polymer matrix even though these would have a polarity difference. In this treatment a functional group reacts with the chemical groups in the fibre, mainly with the reactive position (actives cites) C2, C3, and C6 hydroxyls and C-H groups located in the cellulose structure, which get involved in an ionic or condensation polymerization

[28] (Fig. 1). Dai D. et al. observed that the organic material acts as a bridge between the hydrophilic reinforcement and the hydrophobic matrix by the induction of covalent bond formation and physical interaction because of condensation reaction or hydrogens bonds [23, 25, 29, 30].

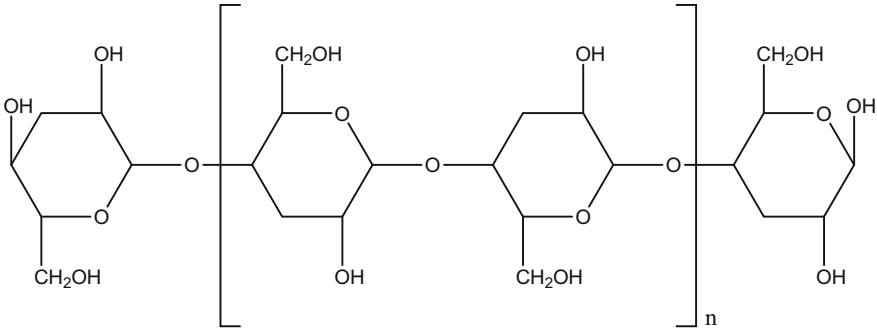


**Fig. 1.** Schematic representation of cellulose structure.

## 6 Conclusion

As have been observed in the present document, the surface treatments of the fibre have been used by different authors aiming to improve the fibre/resin compatibility. To increase the adhesion in the composite it is necessary to change the chemical structure of the fibre and introduce reactive groups on the surface, leading to the production of important modifications in the physicochemical and mechanical properties which can be analyzed by different methodologies. The modification process aims to improve the adhesion between the fibre and the epoxy polymer matrix achieving a favorable wettability, a mechanical interlocking and better interaction by chemical bonding. The treatments improve the interface by modifying the chemical structure of the fibre and increasing the contact area of the reinforcement and the polymer compound. This modification prioritizes the hydroxyl groups located on the fibre surface. These groups are modified to decrease the hydrophilic nature of the fibre and increase its adhesion, so that this improves the compatibility with the hydrophobic polymer matrix.

**Acknowledgements.** The authors would like to acknowledge the University of Malta for the financial support of the DLANComp project.

**Conflict of Interest.** None.

## References

1. Reddy, K.H., Reddy, R.M., Ramesh, M., Mohana Krishnudu, D., Reddy, B.M., Rao, H.R.: Impact of alkali treatment on characterization of tapsi (*sterculia urens*) natural bark fibre

- reinforced polymer composites. *J. Nat. Fibres* **18**(3), 378–389 (2021). <https://doi.org/10.1080/15440478.2019.1623747>
2. Syduzzaman, Md., Al Faruque, M.A., Bilisik, K., Naebe, M.: Plant-based natural fibre reinforced composites: a review on fabrication, properties and applications. *Coatings* **10**(10), 973 (2020). <https://doi.org/10.3390/coatings10100973>
  3. Varghese, A.M., Mittal, V.: Surface modification of natural fibres. In: *Biodegradable and Biocompatible Polymer Composites: Processing, Properties and Applications*, pp. 115–155. Woodhead Publishing Limited (2017). <https://doi.org/10.1016/B978-0-08-100970-3.00005-5>
  4. Cruz, J., Figueiro, R.: Surface modification of natural fibres: a review. *Procedia Eng.* **155**, 285–288 (2016). <https://doi.org/10.1016/j.proeng.2016.08.030>
  5. Kalia, S., Vashistha, S.: Surface modification of sisal fibres (agave sisalana) using bacterial cellulose and methyl methacrylate. *J. Environ. Polym. Degrad.* **20**(1), 142–151 (2012). <https://doi.org/10.1007/s10924-011-0363-8>
  6. Ahmad, R., Hamid, R., Osman, S.A.: Physical and chemical modifications of plant fibres for reinforcement in cementitious composites. *Adv. Civ. Eng.* **2019**, 1–19 (2019). <https://doi.org/10.1155/2019/5185806>
  7. Zuccarello, B., Zingales, M.: Toward high performance renewable agave reinforced biocomposites: optimization of fibre performance and fibre-matrix adhesion analysis. *Compos. B Eng.* **122**, 109–120 (2017). <https://doi.org/10.1016/j.compositesb.2017.04.011>
  8. Hulle, A., Kadole, P., Katkar, P.: Agave Americana leaf fibres. *Fibres* **3**(1), 64–75 (2015). <https://doi.org/10.3390/fib3010064>
  9. Ortega, Z., et al.: Characterization of agave americana L. plant as potential source of fibres for composites obtaining. *SN Appl. Sci.* **1**(9), 1–9 (2019). <https://doi.org/10.1007/s42452-019-1022-2>
  10. Owonubi, S.J., Agwuncha, S., Anusionwu, C., Revaprasadu, N., Sadiku, R.: Fibre-matrix relationship for composites preparation. *Renewable and Sustainable Composites*, 13–15 (2019). <https://doi.org/10.5772/intechopen.84753>
  11. Camargo, P.H.C., Satyanarayana, K.G., Wypych, F.: Nanocomposites: synthesis, structure, properties and new application opportunities. *Mater. Res.* **12**(1), 1–39 (2009). <https://doi.org/10.1590/S1516-14392009000100002>
  12. Donald, V.R., Marlene, G.R., Dominick, V.R.: Concise encyclopedia of plastics. Springer (2000). <https://doi.org/10.1007/978-1-4615-4579-8>
  13. Pocius, A.V.: Adhesives. In: *Physical Properties of Polymers Handbook*, pp. 479–486. Springer, New York (2007). [https://doi.org/10.1007/978-0-387-69002-5\\_27](https://doi.org/10.1007/978-0-387-69002-5_27)
  14. Fortea-Verdejo, M., Bumberis, E., Burgstaller, C., Bismarck, A., Lee, K.Y.: Plant fibre-reinforced polymers: where do we stand in terms of tensile properties? *Int. Mater. Rev.* **62**(8), 441–464 (2017). <https://doi.org/10.1080/09506608.2016.1271089>
  15. Yan, L., Chow, N., Jayaraman, K.: Flax fibre and its composites - a review. *Compos. B Eng.* **56**, 296–317 (2014). <https://doi.org/10.1016/j.compositesb.2013.08.014>
  16. Ansell, M.P.: Natural fibre composites in a marine environment. In: *Natural Fibre Composites: Materials, Processes and Applications (Issue 1972)*, pp. 365–375. Woodhead Publishing Limited (2014). <https://doi.org/10.1533/9780857099228.3.365>
  17. Krehula, L.K., Katancić, Z., Siročić, A.P., Hrnjak-Murgić, Z.: Weathering of high-density polyethylene-wood plastic composites. *J. Wood Chem. Technol.* **34**(1), 39–54 (2014). <https://doi.org/10.1080/02773813.2013.827209>
  18. Schmidlin, P.R., Stawarczyk, B., Wieland, M., Attin, T., Hämmerle, C.H.F., Fischer, J.: Effect of different surface pre-treatments and luting materials on shear bond strength to PEEK. *Dent. Mater.* **26**(6), 553–559 (2010). <https://doi.org/10.1016/j.dental.2010.02.003>
  19. Becker, C.M., Dick, T.A., Wypych, F., Schrekker, H.S., Amico, S.C.: Synergetic effect of LDH and glass fibre on the properties of two- and three-component epoxy composites. *Polym. Testing* **31**(6), 741–747 (2012). <https://doi.org/10.1016/j.polymertesting.2012.04.009>

20. Haque, R., Saxena, M., Shit, S.C., Asokan, P.: Fibre-matrix adhesion and properties evaluation of sisal polymer composite. *Fibers and Polymers* **16**(1), 146–152 (2015). <https://doi.org/10.1007/s12221-015-0146-2>
21. Gupta, M.K., Srivastava, R.K.: Properties of sisal fibre reinforced epoxy composite. *Indian J. Fibre Text. Res.* **41**(3), 235–241 (2016)
22. Komal, U.K., Verma, V., Ashwani, T., Verma, N., Singh, I.: Effect of chemical treatment on thermal, mechanical and degradation behaviour of banana fibre reinforced polymer composites. *J. Nat. Fibres* **17**(7), 1026–1038 (2020). <https://doi.org/10.1080/15440478.2018.1550461>
23. Gañan, P., Garbizu, S., Llano-Ponte, R., Mondragon, I.: Surface modification of sisal fibers: effects on the mechanical and thermal properties of their epoxy composites. *Polym. Compos.* **26**(2), 121–127 (2005). <https://doi.org/10.1002/pc.20083>
24. Li, X., Tabil, L.G., Panigrahi, S.: Chemical treatments of natural fibre for use in natural fibre-reinforced composites: a review. *J. Environ. Polym. Degrad.* **15**(1), 25–33 (2007). <https://doi.org/10.1007/s10924-006-0042-3>
25. Gurunathan, T., Mohanty, S., Nayak, S.K.: A review of the recent developments in biocomposites based on natural fibres and their application perspectives. *Compos. A Appl. Sci. Manuf.* **77**, 1–25 (2015). <https://doi.org/10.1016/j.compositesa.2015.06.007>
26. Behera, S., Gautam, R.K., Mohan, S., Chattopadhyay, A.: Dry sliding wear behavior of chemically treated sisal fiber reinforced epoxy composites. *J. Nat. Fibres* **19**(13), 6134–6147 (2021). <https://doi.org/10.1080/15440478.2021.1904483>
27. Aravindh, M., et al.: A review on the effect of various chemical treatments on the mechanical properties of renewable fibre-reinforced composites. *Adv. Mater. Sci. Eng.* **2022**, 1–24 (2022). <https://doi.org/10.1155/2022/2009691>
28. Kalia, S., Kaith, B.S., Kaur, I.: Pretreatments of natural fibres and their application as reinforcing material in polymer composites-a review. *Polym. Eng. Sci.* **49**(7), 1253–1272 (2009). <https://doi.org/10.1002/pen.21328>
29. Dai, D., Fan, M.: Wood fibres as reinforcements in natural fibre composites: structure, properties, processing and applications. In: *Natural Fibre Composites: Materials, Processes and Applications*, pp. 3–65. Woodhead Publishing Limited (2013). <https://doi.org/10.1533/9780857099228.1.3>
30. El Oudiani, A., Msahli, S., Sakli, F.: In-depth study of agave fibre structure using Fourier transform infrared spectroscopy. *Carbohydr. Polym.* **164**, 242–248 (2017). <https://doi.org/10.1016/j.carbpol.2017.01.091>



# Strain-Rate Dependent FDEM Simulation of the Perforation Behaviour of Woven Composites Subjected to Low-Velocity Impact

M. Rezasefat<sup>1</sup>, A. A. X. da Silva<sup>2</sup>, S. C. Amico<sup>2</sup>, M. Giglio<sup>1</sup>, and A. Manes<sup>1</sup> (✉)

<sup>1</sup> Politecnico di Milano, Dipartimento di Meccanica, via La Masa 1, 20155 Milano, Italy  
andrea.manes@polimi.it

<sup>2</sup> PPGE3M, Federal University of Rio Grande do Sul, Porto Alegre, RS, Brazil

**Abstract.** The mechanical behaviour of composite materials during perforation during high but also low-velocity impacts is of interest in many engineering fields. Perforation of composites is a very complex event that yields a multi-mode failure, making numerical modelling very challenging. This paper presents a novel approach to study the perforation of composites under low-velocity impact, aided by the recording of the response during impact tests and by a comprehensive validation campaign in quasi-static conditions. The performance of S2-glass fibre reinforced polymer (GFRP) composites under low-velocity impact with energies higher than their penetration limit is experimentally and numerically investigated. A strain-rate dependent cohesive model is developed and implemented in the FE solver using a user-defined material model. The cohesive model is used in the proposed numerical framework based on the Coupled Finite Element-Discrete Element Method (FDEM). Strain-rate dependent mechanical properties, such as tensile and fracture toughness, are used as inputs of the cohesive model to describe failure and perforation. The results showed that the new approach is accurate in predicting the damage morphology of perforated woven composites subjected to low-velocity impacts. The coupling between interlaminar and intralaminar failure modes led to a more accurate prediction of the delamination area by considering the rate sensitivity effect on the latter.

**Keywords:** Perforation behaviour · Woven composite · Low-velocity impact · Strain-rate · FDEM

## 1 Introduction

In the past decade, a lot of attention has been paid to the simulation of composite laminates subjected to low-velocity impacts due to their susceptibility to out-of-plane impact and the possible barely visible impact damage caused by it. Macro-heterogeneous Finite Element (FE) models based on Continuum Damage Mechanics (CDM) have been widely used to simulate those events [1]. The smeared crack approach is normally used to represent damage following the CDM, although it cannot predict discrete local discontinuities observed in experiments [2].

Cohesive Zone Modeling (CZM) has been used to overcome these issues [3–6]. With CZM, a hybrid simulation approach, based on inserting 2D cohesive elements between 3D solid elements, adds additional degrees of freedom to the model in identifying potential crack paths. In such a model, the global behaviour is controlled by the solid elements while the cohesive elements control damage initiation and propagation. Joosten et al. [3] simulated the discrete cracking in notched composites using cohesive interface elements. Cao et al. [4] used zero thickness cohesive elements with a bi-linear traction separation formulation between elements and between plies for the prediction of matrix cracks and delamination in L-shaped cross-ply laminates. Cohesive elements were also used for low-velocity impact simulations in Hongkarnjanakul et al. [5] and Soto et al. [6] resulting in better predictions of matrix cracking and delamination and also indicating that these elements can be used to simulate multi-mode failure in a more complex load case.

In this work, a novel Coupled Finite Element-Discrete Element Method (FDEM) is proposed for simulating perforation in woven glass fibre/epoxy laminates subjected to low-velocity impacts. A user-defined material model is developed to constitute strain-rate dependent bilinear traction separation law for the cohesive elements. Three different models were developed, in which rate sensitivity was considered to follow different assumptions of rate-dependent fracture energy, and they were verified by comparison with experimental data in terms of damage response and morphology.

## 2 Numerical Model

The schematic of the coupled finite element-discrete element method is shown in Fig. 1. Each layer was simulated by a combination of zero-thickness cohesive elements inserted between two adjacent solid 3D elements. The global response of the layer was controlled by the solid elements, which follow an elastic orthotropic behaviour, while the initiation and propagation of intralaminar damage were controlled by the cohesive elements, which follow a bi-linear traction separation law. The adjacent plies in the laminate were also connected with cohesive elements, to account for delamination [7]. The interlaminar and intralaminar cohesive elements represented all potential crack paths in the impact event.

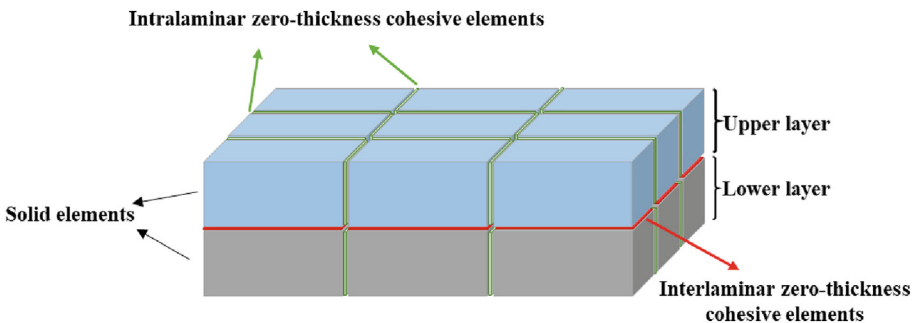


**Fig. 1.** Schematic of the coupled finite element-discrete element method.

## 2.1 Strain-Rate Dependent Cohesive Zone Model

Strain-rate significantly influences the simulation results of laminates subjected to impact. In this paper, the strain-rate sensitivity for the intralaminar cohesive elements was taken into account by adding the rate sensitivity to the bi-linear traction separation law of Abaqus/Explicit using a VUSDFLD subroutine. The behaviour of the cohesive law is the same for normal and shear loading i.e., mode I and mode II. The damage initiates at the displacement ( $\delta_i^0$ ) following Eq. (1),

$$\delta_i^0 = \frac{\sigma_i^0}{K_i} \quad (1)$$

where  $i = n, s$  (for normal and shear modes, respectively),  $K_i$  is the element stiffness and  $\sigma_i^0$  is the maximum traction (cohesive strength). Final failure separation ( $\delta_i^f$ ), indicating final decohesion, is obtained using Eq. (2),

$$\delta_i^f = \frac{2G_i}{\sigma_i^0} \quad (2)$$

where  $G_i$  is the mixed-mode fracture toughness.

A quadratic stress failure criterion (Eq. (3)) is used for the initiation of damage [8]. The damage propagation follows the mixed-mode fracture energy laws of Benzeggagh and Kenane (B-K) [8] according to Eq. (4).

$$\frac{(\sigma_n)^2}{N^2} + \frac{\sigma_s^2}{S^2} + \frac{\sigma_t^2}{S^2} = 1 \quad (3)$$

$$G_n^C + \left(G_s^C - G_n^C\right) \left\{ \frac{G_s}{G_T} \right\}^\eta = G^C \quad (4)$$

To include the effect of strain rate, the effective strain rate at each time increment is calculated using Eq. (5) inside the VUSDFLD subroutine. The Vgetvrm routine is used to acquire the necessary strain components at each time increment.

$$\dot{\varepsilon} = \frac{\sqrt{\dot{u}_n^2 + \dot{u}_s^2 + \dot{u}_t^2}}{t_e} \quad (5)$$

where  $\dot{u}_i^2$  is the velocity corresponding to the normal and shear separations and  $t_e$  is the element thickness. The strain-rate dependent normal strength is calculated using Eq. (6),

$$\sigma_n^0(\dot{\varepsilon}) > \begin{cases} (\sigma^0)_{ref} & \text{for } \dot{\varepsilon} \leq \dot{\varepsilon}_{ref} \\ (\sigma^0)_{ref}(\dot{\varepsilon})^b & \text{for } \dot{\varepsilon} \geq \dot{\varepsilon}_{ref} \end{cases} \quad (6)$$

where  $\sigma^0$  is the quasi-static tensile strength.

## 2.2 Determination of Cohesive Law Parameters

In this work, the strain-rate effect is only considered for the cohesive elements used for predicting intralaminar damage. The strain-rate dependent normal strength data is taken from mesoscale simulations of [9] on woven fabric GFRP composites, shown in Fig. 2 along with the fitted curve based on Eq. (6).

Two different approaches are considered for the estimation of fracture energy following the assumptions of [10]:

- (i) Constant fracture energy (CE) during damage evolution for different rate-sensitive yield strengths, resulting in lower failure displacements at higher strain-rates.

$$G_c = \int_0^{\delta^f} \sigma d\delta = \frac{1}{2} \sigma^0 \delta^f \quad (7)$$

- (ii) Constant in-elastic failure displacement (CD) calculated following Eq. (8), resulting in higher fracture energies at higher strain-rates.

$$\delta_{in,i}^f = \delta_i^f - \delta_i^0 \quad (8)$$

A third model, without the effect of rate sensitivity (NRS), was also investigated.

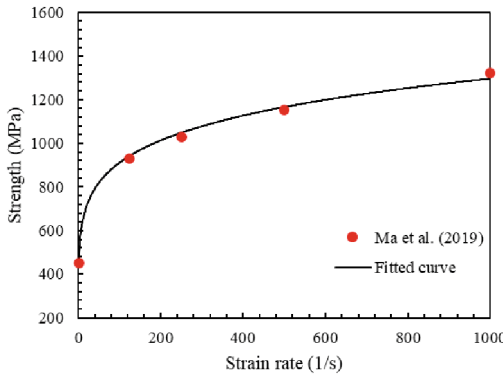


**Fig. 2.** The effect of strain-rate on normal strength for glass fibre woven composites. Data from mesoscale simulations of [9].

## 2.3 Finite Element-Discrete Element Model Setup

The 3D FDEM model of the low-velocity impact is shown in Fig. 3. Cohesive elements were used between solid elements in the fine mesh region near the impactor/laminate contact area. The solid elements followed elastic behaviour with properties reported in Table 1, from tensile and in-plane shear tests.



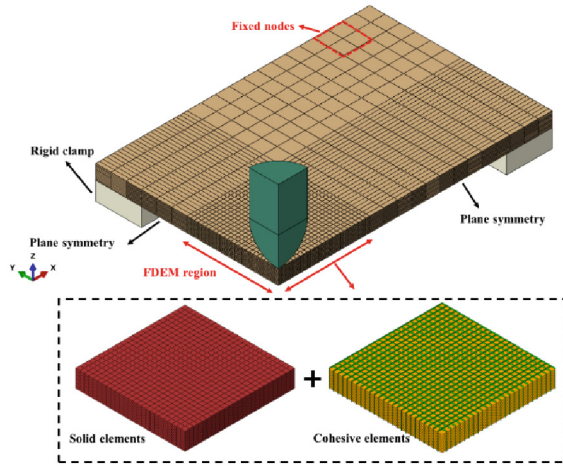


**Fig. 3.** FDEM model setup.

**Table 1.** Mechanical properties of the GFRP composite and the interlaminar cohesive elements.

Lamina properties	Symbol [unit]	Value	Interlaminar cohesive	Symbol [unit]	Value
Elastic moduli	$E_{11}, E_{22}$ [GPa]	26.5	Strength	$N$ [MPa]	45.9 [11]
Elastic modulus	$E_{33}$ [GPa]	11.8		$S$ [MPa]	49.5 [11]
Poisson's ratio	$\nu_{21}$	0.12	Fracture toughness	$G_n^C$ [N/mm]	0.98 [11]
Shear modulus	$G_{12}$ [GPa]	1.80		$G_s^C$ [N/mm]	3.71 [11]

### 3 Results and Discussions

In order to verify the implementation of the strain-rate sensitive bi-linear traction separation law, a simple tensile load case of a single zero-thickness cohesive element between two rigid solid elements was subjected to tensile loading at different rates (see Fig. 4 for the geometry). The results of both methods, i.e., CE and CD, are compared with the mesoscale simulations of [9]. A good correlation between the predicted rate-dependent normal strengths and the results from [9] was observed. Meanwhile, significant differences in estimated fracture energy can be observed between the two methods, i.e., the CD predicted higher fracture energies for higher strain-rates, whereas the CE predicted similar fracture energies.

The comparison of low-velocity impact response from simulation and experiment at an impact energy of 109.7 J is shown in Fig. 5 a-c. The details of low-velocity impact tests and results were previously reported in [12]. Perforation of the projectile was experimentally observed at this energy and the dominant damage mechanisms were fibre breakage, delamination and matrix cracks [12]. The fibre cracks initiated at the backside of the specimen and propagated towards the impact side leading to a sudden

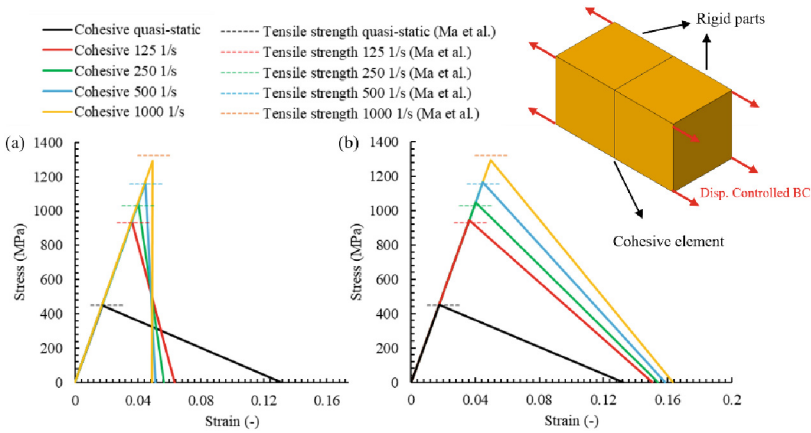


**Fig. 4.** Simple loading test at different strain-rates for: (a) Constant fracture energy (CE), (b) Constant in-elastic failure displacement (CD).

drop in the force-displacement curve shown in Fig. 5. The laminate was unable to absorb all the impact energy resulting in a residual impact velocity after perforation and an open force-displacement curve. As for the numerical results, the three models were able to predict perforation as well as the open force-displacement curve.

In Fig. 5 a-b, it can be seen that without the strain-rate effect, the model was unable to give accurate predictions of peak force, bending stiffness and impact resistance. As expected, the CD assumption led to higher peak forces and impact resistance compared to the CE model due to the higher fracture energies and strain-rates of the former. In all cases, some of the impact energy was absorbed by the laminate as in-elastic energy. The model without rate sensitivity performed poorly in predicting the absorbed energy, with a calculated error of  $-45.1\%$ , while the CD and CE models achieved better agreement, with  $-1.23\%$  and  $-8.7\%$  error, respectively.

Besides, due to the coupling between intralaminar and intralaminar failure modes, the strain-rate has a significant effect on the predicted delamination area and shape. The comparison of cross-section images in Fig. 6 shows larger contact gaps between the delaminated layers for the NRS model as well as larger in-plane damage at different laminate interfaces. The experimental and numerical results of the total projected delamination area are compared in Fig. 7. Both elliptical [13] and rhombus-like [14] damage patterns have been reported in the literature for the damaged area of woven fabric composites. The predictions from the CD and CE models have a more elliptical pattern, while the NRS model better correlated the experimental observation, with a more rhombus-like pattern. The CD and the NRS models predicted a delamination area of  $984 \text{ mm}^2$  (representing a  $23.9\%$  error) and  $1228 \text{ mm}^2$  (error of  $54.6\%$ ), respectively. As observed, the lower intralaminar fracture energies at high strain-rates of the CE model compared to CD one resulted in a larger delamination area.

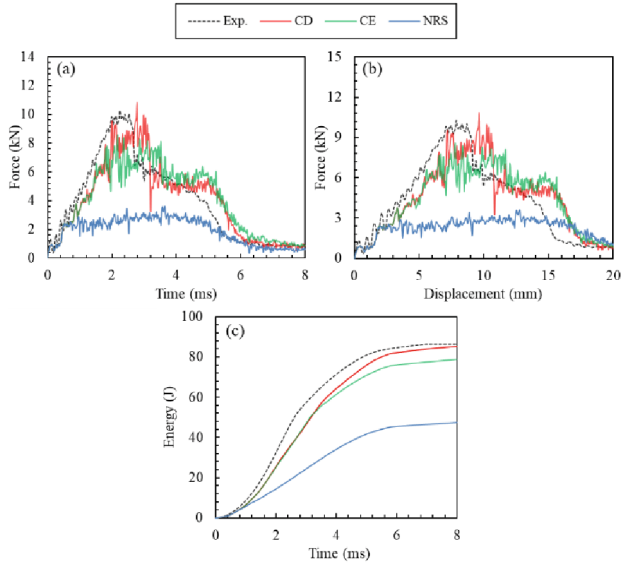


**Fig. 5.** Comparison of low-velocity impact responses: (a) Force-time curve, (b) Force-displacement curve, (c) Energy-time curve.

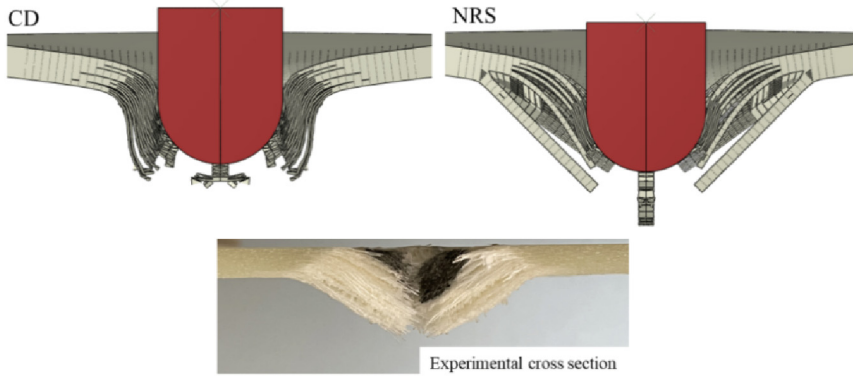


**Fig. 6.** Comparison of cross-section images from numerical and experimental observations.

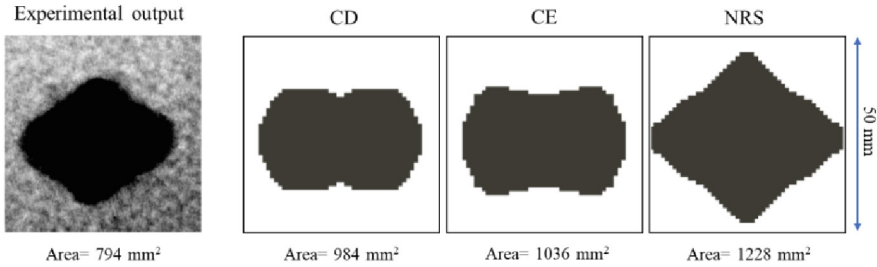


Fig. 7. Comparison of experimental and numerical delamination areas.

## 4 Conclusion

This paper presented a novel Coupled Finite Element-Discrete Element Method (FDEM) model for the simulation of perforation during the low-velocity impact of woven fabric GFRP laminates. The model considered different intralaminar and intralaminar failure modes and the strain-rate sensitivity was included via a user-defined material model. Validation of the model was performed by comparing numerical and experimental force-time, force-displacement, and energy-time curves.

Perforation was experimentally observed and the laminate was unable to absorb all the impact energy (109.7 J). All three models were able to predict perforation, as well as an open force-displacement curve. Nevertheless, disregard of the strain-rate effect led to inaccurate predictions of peak force ( $-45.1\%$ ), with a severe underprediction of laminate stiffness and impact resistance. On the other hand, the two models that considered strain-rate sensitivity better correlated with the experimental results, with errors of only  $-1.23\%$  (CD) and  $-8.7\%$  (CE).

Finally, the coupling between intralaminar and interlaminar failure modes led to a more accurate prediction of the delamination area when considering the rate sensitivity for the intralaminar failure mode. The non-rate sensitive model (NRS) showed larger contact gaps between the delaminated layers as well as larger in-plane spread of damage at different laminate interfaces.

## References

1. Rezasefat, M., Gonzalez-Jimenez, A., Giglio, M., Manes, A.: An evaluation of Cuntze and Puck inter fibre failure criteria in simulation of thin CFRP plates subjected to low velocity impact. *Compos. Struct.* **278**, 114654 (2021). <https://doi.org/10.1016/j.compstruct.2021.114654>
2. Rezasefat, M., Gonzalez-Jimenez, A., Giglio, M., Manes, A.: Numerical study on the dynamic progressive failure due to low-velocity repeated impacts in thin CFRP laminated composite plates. *Thin-Walled Struct.* **167**, 108220 (2021). <https://doi.org/10.1016/j.tws.2021.108220>
3. Joosten, M.W., Yang, Q.D., Blacklock, M., Wang, C.H.: A cohesive network approach for modelling fibre and matrix damage in composite laminates. *Compos. Struct.* **206**, 658–667 (2018). <https://doi.org/10.1016/J.COMPSTRUCT.2018.08.087>
4. Cao, D., Duan, Q., Hu, H., Zhong, Y., Li, S.: Computational investigation of both intralaminar matrix cracking and inter-laminar delamination of curved composite components with

- cohesive elements. *Compos. Struct.* **192**, 300–309 (2018). <https://doi.org/10.1016/J.COMPSTRUCT.2018.02.072>
5. Hongkarnjanakul, N., Bouvet, C., Rivallant, S.: Validation of low velocity impact modelling on different stacking sequences of CFRP laminates and influence of fibre failure. *Compos. Struct.* **106**, 549–559 (2013). <https://doi.org/10.1016/J.COMPSTRUCT.2013.07.008>
  6. Soto, A., González, E.V., Maimí, P., Mayugo, J.A., Pasquali, P.R., Camanho, P.P.: A methodology to simulate low velocity impact and compression after impact in large composite stiffened panels. *Compos. Struct.* **204**, 223–238 (2018). <https://doi.org/10.1016/j.compstruct.2018.07.081>
  7. Rezasefat, M., Giglio, M., Manes, A.: Numerical investigation of the effect of open holes on the impact response of CFRP laminates. *Appl. Compos. Mater.* **29**, 1555–1578 (2022). <https://doi.org/10.1007/s10443-022-10031-6>
  8. ABAQUS 2016 Documentation. ABAQUS Theory Manual (2017). n.d
  9. Ma, D., Manes, A., Amico, S.C., Giglio, M.: Ballistic strain-rate-dependent material modelling of glass-fibre woven composite based on the prediction of a meso-heterogeneous approach. *Compos. Struct.* **216**, 187–200 (2019). <https://doi.org/10.1016/J.COMPSTRUCT.2019.02.102>
  10. Xin, S.H., Wen, H.M.: A progressive damage model for fiber reinforced plastic composites subjected to impact loading. *Int. J. Impact Eng.* **75**, 40–52 (2015). <https://doi.org/10.1016/J.IJIMPENG.2014.07.014>
  11. Perillo, G., Jørgensen, J.K.: Numerical/experimental study of the impact and compression after impact on GFRP composite for wind/marine applications. *Procedia Eng.* **167**, 129–137 (2016). <https://doi.org/10.1016/J.PROENG.2016.11.679>
  12. Rezasefat, M., et al.: Experimental study on the low-velocity impact response of inter-ply S2-glass/aramid woven fabric hybrid laminates. *Thin-Walled Struct.* **177**, 109458 (2022). <https://doi.org/10.1016/J.TWS.2022.109458>
  13. Wu, E., Chang, L.C.: Woven glass/epoxy laminates subject to projectile impact. *Int. J. Impact Eng.* **16**, 607–619 (1995). [https://doi.org/10.1016/0734-743X\(95\)00001-Q](https://doi.org/10.1016/0734-743X(95)00001-Q)
  14. Subadra, S.P., Griskevicius, P., Yousef, S.: Low velocity impact and pseudo-ductile behaviour of carbon/glass/epoxy and carbon/glass/PMMA hybrid composite laminates for aircraft application at service temperature. *Polym. Test* **89**, 106711 (2020). <https://doi.org/10.1016/J.POLYMERTESTING.2020.106711>

**Design and Manufacturing of New  
Generation Composite Materials  
for Aerospace Sector**



# On the Use of Double-Double Laminates to Improve and Innovate the Design of an All-Composite Wing Box

Aniello Riccio<sup>1</sup>✉, Francesco Di Caprio<sup>2</sup>, Steven W. Tsai<sup>3</sup>, and Andrea Sellitto<sup>1</sup>

<sup>1</sup> Department of Engineering, University of Campania “Luigi Vanvitelli”, 81031 Aversa, Italy  
aniello.riccio@unicampania.it

<sup>2</sup> C.I.R.A. (Italian Aerospace Research Centre), 81043 Capua, Italy

<sup>3</sup> Department of Aeronautics and Astronautics, Stanford University, Stanford, CA 94305, USA

**Abstract.** This work focuses on the study and application of an innovative design philosophy for composite structures, specifically suitable, but not limited, for aeronautical applications. Recent studies have shown that some classes of fibre-reinforced composite materials can be treated almost in the same way as isotropic materials, regarding the number of variables to be taken into account in the design phases. This is made possible by the definition of the Tsai’s Modulus and the concept of the Master ply. The new laminate families resulting from the application of these two concepts have been named Double-Double. These new design methodologies have been applied to a regional jet composite wing-box test case to evaluate their flexibility and robustness as well as their benefit in terms of structural mass reduction.

**Keywords:** Tsai’s modulus · Double-Double laminate · Lightweight structures · wing-box · CFRP · Master ply

## 1 Introduction

Due to lightweight requirements, the use of laminate composite structures, especially in the aerospace industry, has strongly increased in the last years [1–4].

Since the 1960s, when boron and carbon composites were first adopted, they have found increasing application in the aerospace field; in particular, they were used in the form of laminates with the basic four ply orientations: 0,  $\pm 45$ , and 90 (Quad-Laminates). To adapt some specific characteristics to the laminates, researchers focused their efforts on the influence of the ply angles on the mechanical properties of the laminate.

An important limitation of traditional quad-laminates is related to design/production rules and issues, such as the need to have a symmetrical stacking sequence to avoid out-of-plane deformation during the curing process. Consequently, sub-laminates with any degree of orthotropy are typically made of building block of six to ten plies. These configurations can be hardly tapered and lead to over-dimensioning of composite components which are extremely out-of-plane weak and prone to delamination [5].

In this work, a different approach to the standard design rule for composite laminates has been proposed. This new approach is based on the Tsai modulus and the double-double laminate ( $[\pm\Phi/\pm\Psi]$  with angles  $\Phi$  and  $\Psi$  arbitrarily chosen in the range  $[0^\circ-90^\circ]$ ). This family of laminates is simpler to manufacture and more homogenized if compared the quasi-isotropic quad laminates [6, 7]. Recently, a research group led by Prof. S.W. Tsai has developed tools to help the composite designers understanding the high potential of Double-Double laminates and their implementation in new designed composite structures. In order to find the best laminate under multiple load conditions, software such as Lam search (Stanford University) and DD-Design tool (CIRA-University of Campania-Stanford University) can be used [8–10].

The research work reported in this paper aims to investigate the capability of this new design approach with composites by the application to a composite wing-box test-case. In particular, an entire regional jet wing-box has been redesigned with DD laminates, while maintaining the strength, critical load, and stiffness requirements.

In Sect. 2, an overview on Double-Double laminates is introduced. Then, in Sect. 3, the numerical wing box test-case is presented and the proposed methodology, applied to redesign the composite material part, improving the lightweight characteristics considering the strength, critical load, and stiffness requirements, is described.

## 2 Double-Double Laminate: An Overview

In this section, the strategies to design and select laminates with improved characteristics (in terms of strength, toughness, ease of design, fabrication and tapering, weight, costs, and other constraints), if compared to traditional quad-axial laminates, are described. A new approach based on double bi-axial angles ( $[\pm\Phi/\pm\Psi]$ ), thus the name double-double (DD), will be proposed that will open new opportunities with respect to the classical quad-laminates. The selection of laminates is based on building up sub-laminates starting from these four ply angles (chosen in the range of  $[0^\circ-90^\circ]$  oriented plies). First, a four plies laminate is selected, where the plies are oriented according to each of the four ( $[\pm\Phi/\pm\Psi]$ ) angles. The angles are then changed according to strength requirements by checking the Tsai Modulus (Lamsearch tool). Then more plies are added until failure criteria are satisfied in the frame of an optimization process (DD Design tool). Iterations are performed to decrease the thickness of the laminate reducing the margins related to the failure criteria and obtaining an optimized laminate. DD laminates are naturally homogenized avoiding symmetry constrain and delaminations, in addition to other advantages such as faster layup, simpler design, easier tapering through single ply drops, and easier merging or transition with different sub-laminates in adjacent zones. Having thinner sub-laminates will reduce the minimum gage of composites plate.

### 2.1 DD Laminate

The historically most adopted stacking sequence (traditional laminates) are based on a collection of  $0, \pm 45$ , and  $90$  ply angles. There were also rules governing the use of these angles. The better-known rules are:



- Laminates must have mid-plane symmetry (to avoid warpage during curing process);
- A 10% rule that requires each of four ply orientations to be at least 10% of the total laminate.
- In order to reduce delaminations, laminates have to not exceed more than three layers with the same orientation for each plies group. Hence, for a ten-ply sub-laminate, if the desired load carrying orientation is  $0^\circ$ , The maximum possible number of  $0^\circ$  oriented plies is seven, because for the 10% rule, at least one ply at  $90^\circ$ , one ply at  $45^\circ$  and one ply at  $-45^\circ$  need to be places in the stacking sequence. These plies can be divided into three blocks of  $0^\circ$  oriented plies (for example, one of two layers, one of two layers and the last of three layers), and between each block of  $0^\circ$  oriented plies a ply oriented at  $90^\circ$ , a ply oriented at  $45^\circ$  and a ply oriented at  $-45^\circ$  must be placed.
- Ply drop must maintain the required mid-plane symmetry (drop symmetrically).
- To guarantee the balancing of laminates,  $45^\circ$  and  $-45^\circ$  oriented plies must be balanced, in other words, additional two plies oriented at  $45^\circ$  and  $-45^\circ$  must be added on the other side of the midplane. In terms of matrix components, it means  $A_{16}$  and  $A_{26}$  are zero.

As a result, sub-laminates that are used to build the total laminates become thicker in order to achieve desired directionality and respect the design rules. DD laminates are able to change this design process, leading to lighter and more optimized laminates.

In DD laminates, the  $[\pm\Phi, \pm\Psi]$  angles are continuous and form a field rather than a collection of discrete laminates in the legacy quad. The ply angles must compete to be selected. Angles do not get a *free pass*, for symmetry, balancing and other design rules, as in the case of the legacy quad family. A comparison between the two approaches is shown in Fig. 1, where the adimensionalised  $A_{11}$  stiffness matrix terms is shown. The top graph shows a table of legacy quad with its tabulated Master ply [8] values for  $A_{11}$ , and a plot of its discrete member laminates. This plot is often referred to in the US as “carpet plot” as the triangular shape looks like a stack of carpets for sale in stores. At the bottom of this Fig. 1, the double-double with its continuous values of  $A_{11}$ , and its field appearance is shown. There are 36 laminates in the quad family, and no limit on the DD. At  $10^\circ$  increments in Fig. 1 corresponds 100 members (65 independent) of DD. But smaller angle increments can be used, resulting in many member laminates as desired, in hundreds if not thousands. Zooming is limited in the legacy quad without having laminate with very large minimum gage.

The basic building blocks of sub-laminates in legacy quad ranges from 12- to 20-ply thick (with mid-plane symmetry imposed). There is no scaling, and no optimization. The double-double, on the other hand, is at most four-ply thick in its building block. When thin plies are used, it can be two or one-ply thick. There are immediate benefits with such thin ply assembly, as can be derived in the application section.

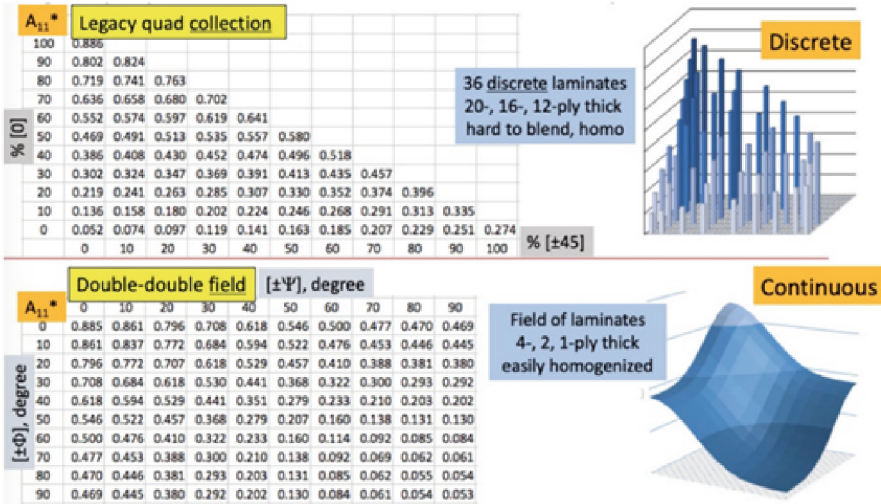


Fig. 1. Master ply  $A_{11}$  in legacy quad collection versus double-double field.

### 3 Numerical Test Case: Composite Wing Box

In this section, the re-design of the regional aircraft wing box test case according to the new Double-Double approach is presented. The presented geometric support model is equipped with suitable parameters for the definition of the geometric and topological characteristics of the wing, and for the quality control of the computational grid in terms of mesh density and relative distortions (angular, taper and elongation). The main target is to evaluate the possible weight reduction and the manufacturing simplification due to the new DD approach, taking into account the requirement in terms of strength, critical load, and stiffness.

#### 3.1 Numerical Test Case Description

The geometrical model of the analyzed wing-box is shown in Fig. 2, while, in Table 1, the corresponding dimensions are listed.

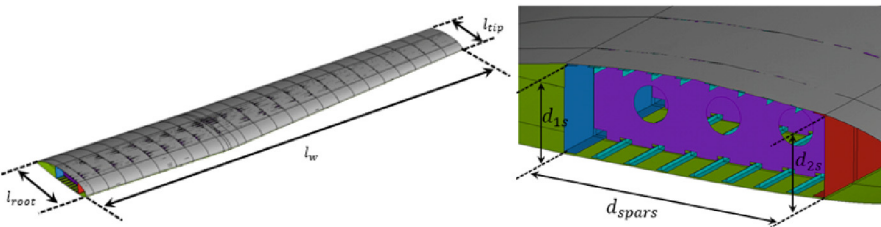
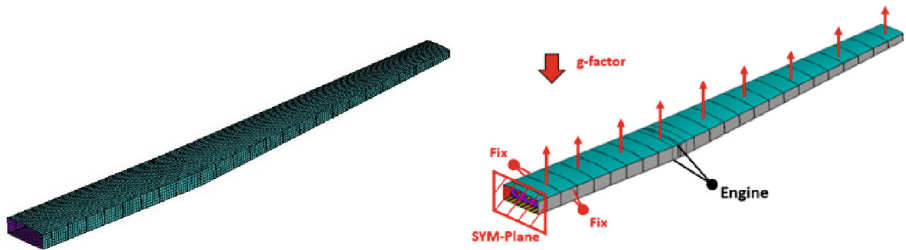


Fig. 2. Test case description.

**Table 1.** Test case dimensions.

Symbol	Dimension	Description	Value
$l_w$	<i>mm</i>	Length of wingspan	14370
$l_{root}$	<i>mm</i>	Length of wing root	3100
$l_{tip}$	<i>mm</i>	Length of wing tip	1912
$d_{1s}$	<i>mm</i>	Distance between the top and the bottom skin surface at the trailing edge of the wing	432
$d_{2s}$	<i>mm</i>	Distance between the top and the bottom skin surface at the leading edge of the wing	406
$d_{spars}$	<i>mm</i>	Distance between the spars	1364
$N_{s,top}$	-	Number of upper stringers	8
$N_{s,bottom}$	-	Number of lower stringers	7
$N_r$	-	Number of ribs	24
$N_{sp}$	-	Number of spars	2

The wing box has been modelled by using a macro in Ansys Parametric Design Language (APDL) [11], using linear layered shell elements with four nodes and six degrees of freedom per node (SHELL 181). The resulting numerical model and the applied boundary conditions are shown in Fig. 3. Two different load conditions have been analyzed. The first one is related to the landing phase and the second one to the taxiing phase. Both load conditions must respect the stiffness and buckling requirements of the wing. The load has been applied to the parametric model, along the wingspan, at 14 stations.

**Fig. 3.** Wing box numerical model and applied boundary conditions.

The model has been divided into cells and zones. Each zone is characterized by a specific DD-Layup, therefore all cells belonging to that zone will have the same DD-Layup but a specific thickness. In Fig. 4, four zones are shown, namely, the upper and lower skin surface and the front/rear spar of the wing box. Each zone has been divided into 27 cells, as shown, as an example, in Fig. 4 for zone 1.

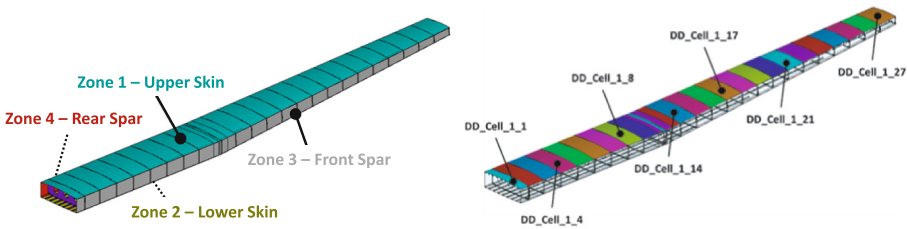


Fig. 4. Wing box zones and cells.

### 3.2 Optimization Procedure

The main workflow of the entire optimization process is reported in Fig. 5 [9].

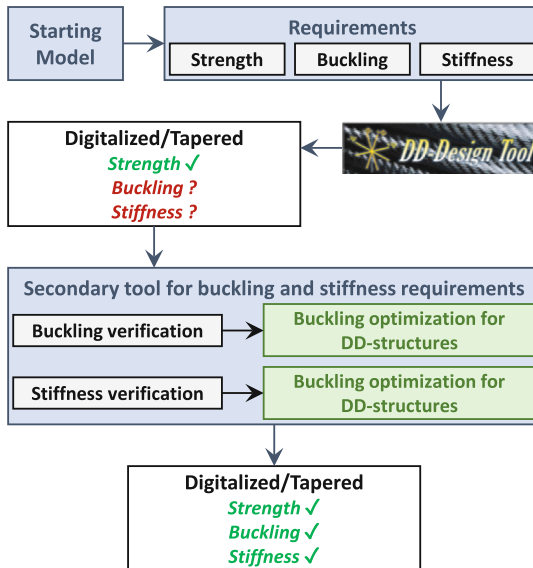


Fig. 5. Optimization workflow.

Optimization is performed according to three sequential steps. A first optimization step is performed to choose DD layout in the different zone to achieve the desired strength requirements. Then a further optimization for buckling constraints is performed by locally increase the thickness of the cells (it is possible to define any buckling threshold, but in this case the threshold is set equal to 1). Finally, the last optimization, finalized to stiffness requirements, is performed by locally increase the thickness of specific zones.

### 3.3 Numerical Results

The DD-Design tool is able to generate the best solution in terms of strength requirements. Then, this solution serves as input for the buckling and stiffness optimization procedures. The results of each optimization step are reported in Table 2. The final mass saving is about 51% (261.7 kg) but at the same time the maximum displacement has been reduced up to the one of starting model (1476.64 mm).

**Table 2.** Comparison of the mass/displacement values of the initial configuration vs. the optimized configurations corresponding to the DD regions.

	Starting Model	Strength requirements	Buckling opt.	Stiffness Opt.
Wing Mass [kg]	508.7	84.1	154.7	247.0
Skin Upper Mass [kg]	203.9	25.3	36.2	82.8
Skin Lower Mass [kg]	171.4	40.9	42.3	87.6
Frontal Spa Mass [kg]	65.9	8.7	40	40.2
Rear Spar Mass [kg]	67.5	9.2	36.2	36.4
Buckling eigenvalue [-]	1.54	0.001	1	1
Tip displacement [mm]	1477	2879	2345	1477

The max displacement evolution is reported in Fig. 6. The starting value is equal to 1477 mm and at the end of the process the max global displacement goes back to the starting value. Obviously, any other requirement can be defined in the stiffness optimization process. Moreover, Fig. 7 shows the thickness evolution. The starting value is equal to 15.2 mm and at the end of the process the max thickness is reduced to 7.25 mm.

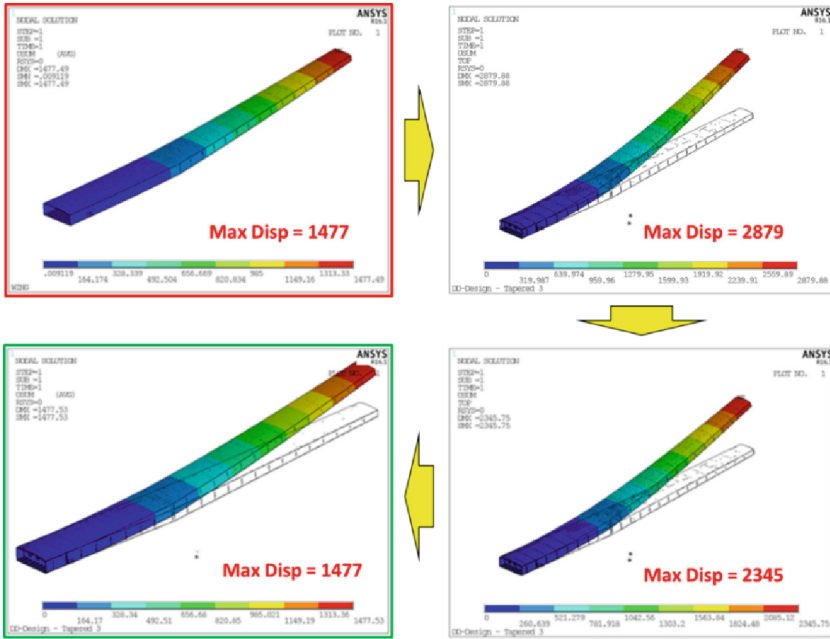


Fig. 6. Maximum displacement evolution.

As expected, the adopted method provides excellent results in terms of mass reduction, maintaining the requirements that the wing box must meet in terms of strength and stiffness.

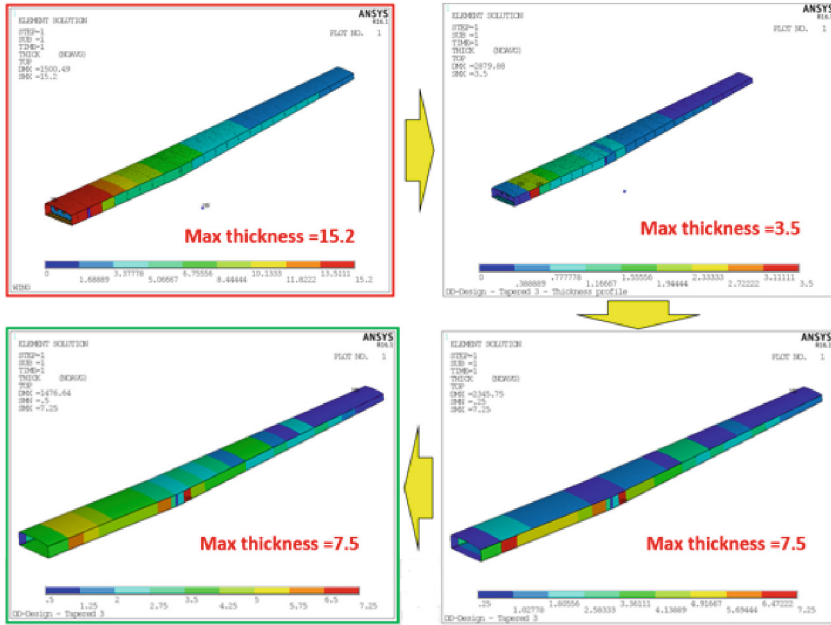


Fig. 7. Maximum thickness evolution.

## 4 Conclusion

In the present work, an innovative design approach for composite structures to be applied, but not limited, to aerospace engineering design field, has been presented. The investigated methodologies are based on recent studies performed by an international research group coordinated by Prof. S.W. Tsai which have demonstrated how it is possible to scale the fundamental parameters of composite laminates by introducing a new family of laminates: double-doubles. A regional jet composite wing box test case has been used to evaluate the possible weight savings related to the adoption of the DD approach respect to the ones currently adopted for the design and manufacturing of composite.

According to the presented study, the introduction of DD can make the quad-laminates obsolete and can removes many constraints in composite usage. In order to have a proper term of comparison, the test article was first designed with a quad-layup. Then the quad design was compared to the DD-Design. This comparison showed a reduction of mass of or more than 50%, with the satisfaction of the same constraints in terms of strength, buckling and stiffness.

## References

1. Zhang, H., Fan, X., et al.: A simple and green strategy for preparing flexible thermoplastic polyimide foams with exceptional mechanical, thermal-insulating properties, and temperature resistance for high-temperature lightweight composite sandwich structures. *Compos. Part B Eng.* **228**, 109405 (2022)

2. Xiong, J., Li, Z., et al.: Advances in aerospace lightweight composite shell structure [航空航天轻质复合材料壳体结构研究进展]. *Fuhe Cailiao Xuebao/Acta Materiae Compositae Sinica* **38**(6), 1629–1650 (2021)
3. Zhang, S., Zhao, D.: *Aerospace Materials Handbook*, 1st ed. CRC Press (2016)
4. Stefan, A., Pelin, G., et al.: Manufacturing process, mechanical behavior and modeling of composites structures sandwich panel. *INCAS Bull.* **13**(1), 183–191 (2021)
5. Sellitto, A., et al.: Numerical–experimental correlation of impact-induced damages in CFRP laminates. *Appl. Sci.* **9**(11), 2372 (2019). <https://doi.org/10.3390/app9112372>
6. Tsai, S.W.: Double–double: new family of composite laminates. *AIAA J.* **59**(11), 4293–4305 (2021)
7. Vermes, B., Tsai, S.W., Massard, T., Springer, G.S., Czigany, T.: Design of laminates by a novel “double–double” layup. *Thin-Walled Struct.* **165**, 107954 (2021). <https://doi.org/10.1016/j.tws.2021.107954>
8. Arteiro, A., Sharma, N., et al.: A case for Tsai’s Modulus, an invariant-based approach to stiffness. *Compos. Struct.* **252**, 112683 (2020)
9. Vermes, B., Tsai, S.W., Riccio, A., Di Caprio, F., Roy, S.: Application of the Tsai’s modulus and double-double concepts to the definition of a new affordable design approach for composite laminates. *Compos. Struct.* **259**, 113246 (2021). <https://doi.org/10.1016/j.compstruct.2020.113246>
10. Zhang, Z., Zhang, Z., di Caprio, F., Gu, G.X.: Machine learning for accelerating the design process of double-double composite structures. *Compos. Struct.* **285**, 115233 (2022)
11. Ansys® Academic Research Mechanical, Release 18.1





# Thermal and Morphological Evaluation of the Composite Manufactured with Carbon Epoxy Prepreg via Hot Compression Molding

Samia Danuta Brejão de Souza<sup>1</sup>(✉), Nicola Gallo<sup>2</sup>, Ignazio Scavo<sup>2</sup>, and Stefano Corvaglia<sup>2</sup>

<sup>1</sup> Leonardo Labs, Materials, Grottaglie, TA, Italy  
danuta.brejao@leonardo.com

<sup>2</sup> Leonardo Aerostrutture, Grottaglie, TA, Italy

**Abstract.** The manufacturing process for composite via autoclave has an expensive cost and take a long cycle time until the piece is ready and it is possible to open the autoclave. Instead, hot compression molding is a fast process, that does not require a long process time and the quality of the part is similar to the parts made in autoclave [1, 2]. The hot compressing molding is a process considered out-of-autoclave (OOA) cured process [2]. OOA is widely used due to be faster and cheaper process in relation to autoclave, beyond to be possible to manufacture complex shaped parts and reduce secondary stages [2]. For this study, it was used a prepreg made with epoxy-carbon fiber, that is used for autoclave process, however, it has been used for OOA process, to see if it is possible to reach similar or better results compared with the samples from autoclave. The laminate was manufactured via hot compression molding instead the usual process for this material, as autoclave. DSC tests were carried out to analyze the  $T_g$  (glass transition temperature) in order to verify if there was still some polymerization process to finish and verify the combination of parameters that was proposed in the work plan. The morphological tests were made in order to verify if there was porosity in the composite, due to the manufacturing process, and verify if the layers were well compacted.

**Keywords:** Composite materials · Hot Compression Molding · Out-of-autoclave · PEEK · Prepreg

## 1 Introduction

The process manufacturing for composite materials most used for aerospace applications has been the autoclave, however is limited to aerospace companies due to the high cost of production, and an alternative is the out-of-autoclave (OOA) manufacturing process, which can be reduce the costs and the time. The pieces manufactured using OOA process presenting similar properties in relation to the pieces made with the autoclave. There are already developed special prepreg for OOA manufactured process, including also certified prepreg for aerospace field [2].

The goal using OOA is to remove the high-pressure curing, resulting in a machine with more cost-effective equipment with a modest maintenance and operational cost [2, 3].

With the OOA manufacturing process (oven curing process) is possible to reduce the secondary processes, decrease the quantity of bagging material, increase the possibility to manufacture complex shaped parts beyond to improve the surface finish of the final part. The surface finish obtained in OOA is very similar the one from the autoclave, where the porosity was reduced and consequently decreased the time for post-operation for other steps, as example painting [2].

What distinguishes the autoclave and OOA manufacturing process is how the vacuum works in these process. For the autoclave, the whole chamber is under vacuum and the composite piece in under vacuum also since it is inside the vacuum bag [2, 4].

The concept for transfer the heat in oven and autoclave manufacturing processes is based on convection heating, however, there is a difference in the medium of the heat transfer, for the autoclave is used compressed nitrogen and for oven curing is used normal air. A slow ramp to increase the temperature is more indicated due to decrease the risk of exothermic reactions [2–4].

The OOA manufacturing process for thermoset composites applied in aerospace field is used mainly to reduce costs, due to the use of low pressure and the ability to use automation. Nonetheless, with this manufacturing process there is a tendency to form voids in relation to the autoclave process, due to the absence of high pressure. For OOA is important to recognize the parameters that can cause the voids and eliminates them [5–7].

One of this parameters can be the resin impregnation, which is not enough to wet the prepreg fibers, and this occurs as a consequence of the low transverse permeability. Another parameter can be the vacuum pathway, that is related to the removal of air inside the laminate before to consolidate and permit the whole saturation of the resin into the fibers [4, 5, 8].

For the OOA process (oven curing process), the degree of impregnation needs to control for to trap the air, because when it is used a low viscosity resin, the flow can lock some routes and not allowed the air stays there [2, 5, 9].

## 2 Materials and Methods

The material used in the study is a prepreg made with epoxy resin and woven carbon fabric from Solvay. The prepreg is indicated for autoclave manufacturing process and the objective of the study is to use this material for hot compression molding (Fig. 1).

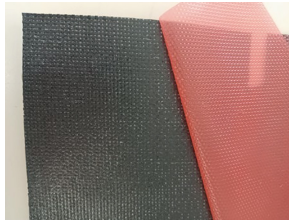


**Fig. 1.** It is shown the prepreg used in the study.

The samples were made with 15 layers, with the dimension 100 x 100 mm. The press machine used is a Fluid Press - 4C-PR 10 ton. The parameters used in the hot compression molding is shown in Table 1:

**Table 1.** Parameters for hot compression molding.

Layers	Heating (°C)	Pressure (bar)	Holding time (min)	Cooling (°C/min)
15	180.0	3.0	30	60
15	180.0	3.0	60	60

To analyze the  $T_g$  (glass transition temperature) and verify if the polymerization process was finished, it was used two DSC (Differential scanning calorimetry): Diamond DSC and DSC 8000, both from Perkin Elmer. The parameters for DSC are in the Table 2.

**Table 2.** Parameters for DSC analysis.

Heating range (°C)	Ramp (°C/min)	Inert atmosphere (ml/min)
25.0 – 230.0	10.0	40

Before performing the DSC tests, the edges of the laminate were cut and then 3 samples were taken from each corner and 3 samples were taken from the center of the laminate. In this way, each region of the laminate was analyzed three times, and in this way it was possible to verify if all regions of the laminate provided similar properties after processing via hot compressing molding.

The morphological analysis was used to verify the existence of porosity inside the laminate and if the layers were compacted well. For this, it was used the optical microscopy Hirox – MXB-2500REZ.

## 3 Results

### 3.1 Laminate Manufacturing Process and Thermal Analysis (DSC)

It was manufacture two laminates with different processing time, as shown in previous section (Table 1) and both presented the same surface finish, for example, fibers were not

burned and the borders did not present a lack of resin. In Fig. 2a is shown the laminate inside the press machine and in Fig. 2b is shown the laminate already cured.

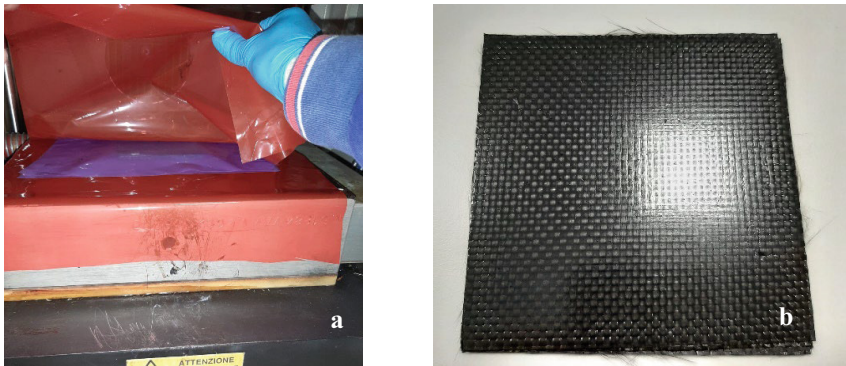


**Fig. 2.** It is shown the laminate inside the press machine.

In Fig. 3 is presented the samples for the thermal analysis and how it was cut. In Fig. 3a, the samples for DSC analysis were cut in the edge and in the middle of the laminate. For each region described were cut three samples for the thermal analysis. With the DSC results shown in Table 3 (Sample 1 (30 min)), it was possible to verify that the polymerization process did not finish, due to the difference between the results acquired and the datasheet from Solvay, in which is presented 177 °C for the autoclave cure temperature.



**Fig. 3.** Both laminates are with 15 plies, for [a] was used 30 min and [b] 60 min in the press machine

In this way, it was decided to manufacture another laminate and use 60 min as hold time. For this laminate, it was cut the edge and it was used 3 samples from each corner and for the center, as shown in Fig. 3b.

In Table 3 is also shown the DSC results for this laminate. It is possible to verify that there was an increase in the  $T_g$  average but there are differences between the regions analyzed in the laminate, as example, between the brown corner and the orange corner

the difference is 11.31 °C. Perhaps the polymerization process did not complete yet and due this, it was decided to leave inside the oven both laminates, during 2 h at 180 °C. After this, it was done once again the DSC analysis.

**Table 3.** DSC results – laminates manufactured in the pressing machine.

Sample 1 (30 min)	Tg (°C) average
Intern	166.03
Extern	157.93
Sample 2 (60 min)	Tg (°C) average
Center	190.59
Brown corner	181.95
Green corner	186.86
Orange corner	193.26
Blue corner	191.19

Figure 4 shows both laminates after remain 2 h at 180 °C inside the oven. These laminates are the same that were used for the previous DSC analysis. From each colored region and from the center were taken three samples for the thermal analysis.

From the results showed in Table 4, it is possible to verify that the temperatures are more homogeneous for each side of the sample (as example, orange and green corner are in the same side of the sample) and the difference between the colored regions are small (as example, the difference between pink and green regions).

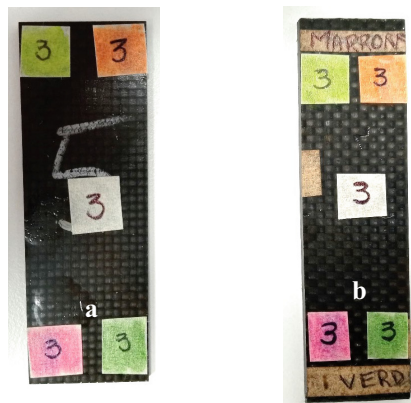


**Fig. 4.** Both laminates after remain inside the oven for 2 h at 180 °C: [a] Sample 1 (30 min) and [b] Sample 2 (60 min)

Comparing the Tg average with the Tg from the datasheet (Solvay), it exists a difference between them around 20 °C. This can be due the use the prepreg in a different manufacturing process recommended for it.

**Table 4.** DSC results after remain inside the oven.

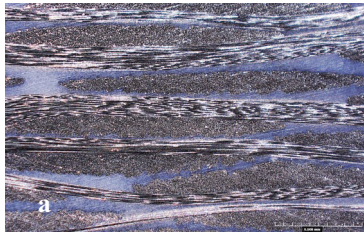
Sample 1 (30 min)	Tg (°C) average
Yellow corner	197.12
Orange corner	196.63
Pink corner	195.98
Green corner	196.93
Center	197.43
Sample 2 (60 min)	Tg (°C) average
Yellow corner	193.83
Orange corner	195.85
Pink corner	195.10
Green corner	193.58
Center	198.28

### 3.2 Microscopy Analysis

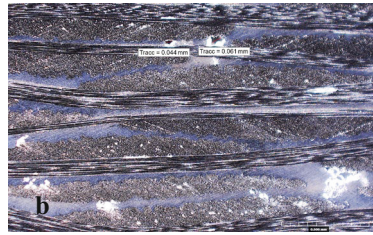
Figure 5 shows the microscopy for both laminates. The analysis was done in the inner side of the laminates and it was used 140X magnification for all of them. For the sample 1, that remained 30 min in the press machine, it was found some very small porous, as shown in Fig. 5b. The measures of the porous are 0.044 nm and 0.061 nm. This kind of porosity was found in the region of the edges and very few inside the laminate.

For the sample 2, that remained 60 min in the press machine, it was not found any kind of porosity, just on the edges, but normally this area is discarded in the production. It is possible to visualize that does not have an accumulation of resin, fibers present a good impregnation and the layers are well compacted.

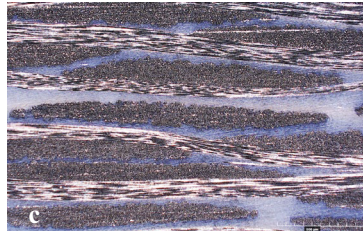
Nonetheless, the study continues, it is still necessary to find the right combination of the parameters, study the mechanical properties and evaluate the possibility to use the prepreg for the hot compressing molding manufactured process for 3D shapes.



Sample 1 (30 min) - 140X



Sample 1 (30 min) - 140X



Sample 2 (60 min) - 140X

**Fig. 5.** Microscopy images: [a] Sample 1 (30 min), [b] Sample 1 (30 min) and [c] Sample 2 (60 min)

## 4 Conclusion

Although, there were made a small amount of analysis from this study, they are relevant, due to the possibility to observe that the layers are well compacted and the  $T_g$  average from all regions are more homogeneous in the whole laminate, as the manufacturing cycle was changed.

There is the difference between the glass transition temperature from the datasheet and from the analysis, however, this could have happened due to the manufacturing process used is different from the recommended and perhaps, due this changing, the polymerization process can complete with a higher temperature.

## References

1. Nadlene, R., et al.: Chapter 15 - out-of-autoclave as a sustainable composites manufacturing process for aerospace applications. *Design for Sustainability*, 395–413 (2021)
2. Shaik, F., Ramakrishna, M., Varma, P.D.: A review on fabrication of thermoset prepreg composites using out-of-autoclave technology. *INCAS Bull.* **13**(2), 133–149 (2021)
3. Rudd, C.D., Long, A.C., Kendall, K.N., Mangin, C.G.E.: *Liquid Moulding Technologies*. SAE International, Woodhead Publishing, Cambridge (1997)
4. International Thermal Systems. <https://www.internationalthermalsystems.com/2018/06/composite-curing-ovens-autoclave-tutorial/>. last accessed 2019/03/13
5. Cender, T.A., Gangloff, Jr., J.J., Simacek, P., Advani, S.G.: Void reduction during out-of-autoclave thermoset prepreg composite processing. In: *Society for the Advancement of Material and Process Engineering*, SAMPE, Seattle (2014)

6. Ralf, E., Rizqullah, I., Kilian, B., Niklas, A., Klaus, D.: Thermoset prepreg compaction during automated fiber placement and vacuum debulking. *Procedia CIRP* **85**, 153–158 (2019)
7. Vasileios, M.D., James, C.S., Charalambos, C.D.: Curing pressure influence of out-of-autoclave processing on structural composites for commercial aviation. *Adv. Mater. Sci. Eng.* **2013**, 1–14 (2013)
8. Hubert, P., et al.: Out-of-autoclave prepreg processing. *Comprehensive Composite Materials II*, 2, pp. 63–94 (2018)
9. Barbara, A.M.: Fabrication methods and costs for thermoset and thermoplastic composite processing for aerospace applications. Massachusetts Institute of Technology, Massachusetts (1988)





# Application of Recycled Carbon Fibers in Aircraft Windows Frame

S. Minosi<sup>1</sup>(✉), G. Buccoliero<sup>2</sup>, M. Araganese<sup>2</sup>, U. Raganato<sup>2</sup>, A. Tarzia<sup>2</sup>,  
S. Corvaglia<sup>3</sup>, and N. Gallo<sup>3</sup>

<sup>1</sup> Leonardo Labs, Via per Monteiasi 83, 74023 Grottaglie, Italy  
stefania.minosi.ext@leonardo.com

<sup>2</sup> Advanced Materials and Processes Consulting Department, CETMA, Brindisi, Italy

<sup>3</sup> Leonardo Aerostructures, Via per Monteiasi 83, 74023 Grottaglie, Italy

**Abstract.** In recent years, carbon fibres have been widely used in an increasing number of industrial sectors. The use of large quantities of CFRPs creates significant environmental and economic problems related to waste disposal and consumption of non-renewable resources. Recently, European legislation has imposed more controls on composite materials waste management from both manufacturing processes and end-of-life products. In this context, the development of technological know-how that enables the recovery of added-value of waste, instead of its simple disposal. Among the most promising recycling methods are thermal processes that include pyrolysis. Pyrolysis is the only process implemented on an industrial scale in Europe because of its economic viability and technical feasibility. The challenge is to develop production processes for composites reinforced with recycled fibres that compete with virgin CFRP both economically and in terms of mechanical properties. CETMA and Leonardo Aerostructure have used Prepreg Compression Molding to produce a windows frame with non-woven fabrics of recycled carbon fibres impregnated with a fast-curing resin. The pyrolysis-recycled fibres were treated with a sizing previously developed by CETMA and compatible with fast-curing epoxy resin.

**Keywords:** Composite materials · Recycling · Pyrolysis · Compression molding

## 1 Introduction

In recent years, carbon fibers (CF) have been widely used in increasing number of industrial sectors [1, 2]. The CF industry is constantly growing, as it has conquered markets that involve the massive production of carbon fiber reinforced composites (CFRP), often as a replacement for metal components [3]. Large quantities of CFRPs used creates significant environmental and economic problems related to waste disposal and consumption of non-renewable resources. CFRP wastes are mainly composed of production off-cuts, up to 40%, and end-of-life products, which are expected at 20 tons per year by 2025. Currently, the wastes are landfilled or incinerated, reducing the value of carbon fibers [4, 5]. Recently, European legislation has imposed more controls on composite materials waste management from both manufacturing processes and end-of-life products [6]. In

this context, the development of technological know-how that enables the recovery of added-value of waste, instead of its simple disposal, is a process crucial to promoting the application of EU requirements and the realization of a circular economy model. There are several methods for recycling composite materials and can be divided into four three: mechanical, chemical, and thermal recycling [2, 7, 8]. Actually, thermal recycling, in particular pyrolysis, is the only process implemented on an industrial scale in Europe because of its economic viability and technical feasibility [9]. The challenge is to develop production processes for composites reinforced with recycled fibers that compete with virgin CFRP, both economically and in terms of mechanical properties [7]. A suitable process for manufacturing components, including for the aerospace industry, reinforced with recycled carbon fibers could be prepreg compression molding.

## 2 Prepreg Compression Molding

Prepreg Compression Molding (PCM) involves the compression molding of prepregs. This process is possible by using fast curing resins that have short curing times, even less than 3 min. Materials produced with this process have physical and mechanical properties comparable to those produced in an autoclave [10, 11]. The first step in the PCM process involves preforming. The prepreg is cut, either manually or automatically, and placed inside the preforming tool. The tool is heated to aid material deformation during the preforming process. After preforming, the final component is molded. The preform consolidates by applying temperature and pressure through the mold. At the end of the curing process, the mold is cooled down to allow for demolding and trimming operations [10, 12]. Each operation can be automated to reduce the production time cycle of the single component and ensure a more reproducible and reliable process.

## 3 Experimental Part

CETMA and Leonardo Aerostructures have studied and optimized the PCM process for nonwoven fabric reinforced prepreg of recycled carbon fibers (rCFs). The final aim is the production of a window frame for aviation applications. In this work, ELG supplied the recycled fibers in the form of nonwoven fabric. The fabric used was Carbon Fibre Ltd (Carbisio™) M with the areal weight of 200 g/m<sup>2</sup>. The nonwoven was impregnated by Technologycom with an epoxy fast curing resin, with an expected cure time of 3 min. The prepreg produced has 65 wt% of resin areal weight of 570 g/m<sup>2</sup>. The recycled fibers were treated with sizing before the fabric fabrication to increase the mechanical properties of the final composite. The sizing used was formulated by CETMA and is specific for recycled fibers via pyrolysis and to be integrated into epoxy resin. The study of sizing formulation started within funded projects and private research contracts focused on the recycled fiber used as reinforcement for polymer matrix composites [13]. The specific sizing formulation used in this work is intended to provide enhanced adhesion between recycled fibers and matrix, better handling, and processability of the fibers during fabric production and prepreg production. Two flat panels were fabricated from prepreg of nonwoven fabric with recycled fibers with and without sizing to evaluate the effect of the treatment. Samples were extracted from these panels for physical and mechanical characterization.

### 3.1 Production of Flat Panels

Two flat panels were produced, one with sizing and one without, having 10 plies of prepreg oriented at  $0^\circ$ . The preform composed of prepreg layers is loaded inside the heated mold to produce a single panel. Mold has a temperature of  $150^\circ\text{C}$  and is closed after the prepreg layers loading. A consolidation pressure of 50 bar is constantly applied during the curing process. After the 3-min curing, the mold is cooled down to a temperature lower than  $110^\circ\text{C}$ , which is the glass transition temperature of the resin. When the mold is cooled down, the panel can be demolded. The mold used for the flat panels was designed to have tight control on the perimeter flow of exceeding resin, and to ensure the constant volume of fibers compared to the epoxy matrix. Samples were extracted from the panels for micrographic analysis with an optical microscope, constituent analysis via acid digestion, and mechanical characterization through tensile and compression tests. The section of some samples analyzed by optical microscope does not give evidence of the presence of porosity, defects, or delamination. Micrographs of panels, with and without sizing, can be appreciated in Fig. 1. The analysis of the constituents for each panel was performed via nitric acid digestion technique according to ASTM D3171. The results are consistent with the theoretical values defined during the design of the laminate. The panels produced have an average reinforcement volume percentage of 42%, which is higher than typical values for composites made from recycled carbon fibers.

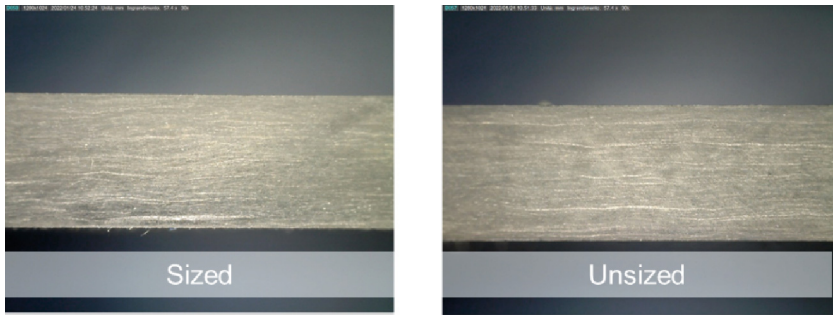


**Fig. 1.** Cross-section micrograph of flat panels: sized on the right and unsized on the left

Tensile and compression tests were performed according to ASTM D3039 and ASTM D3410 standards, respectively. The tests were conducted on samples from both panels, with and without sizing. The Samples were manufactured from the panels to test the mechanical properties along two main directions of the composite named  $0^\circ$  and  $90^\circ$ . The directions tested are shown in Fig. 2.

Figure 3 shows the results of mechanical test. The test campaign proves that the mechanical properties along the  $90^\circ$  direction are much higher than the  $0^\circ$  direction. Tensile properties for  $90^\circ$  direction increase by 20% when sizing is applied, while compression strength increases by approximately 15% in both directions.

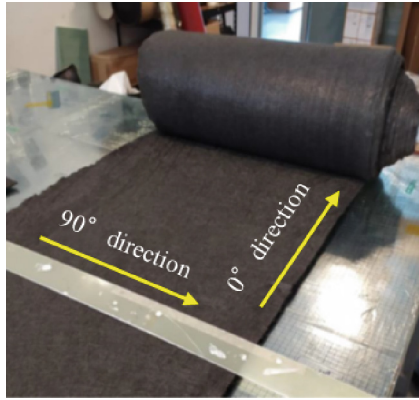


Fig. 2. Tested directions

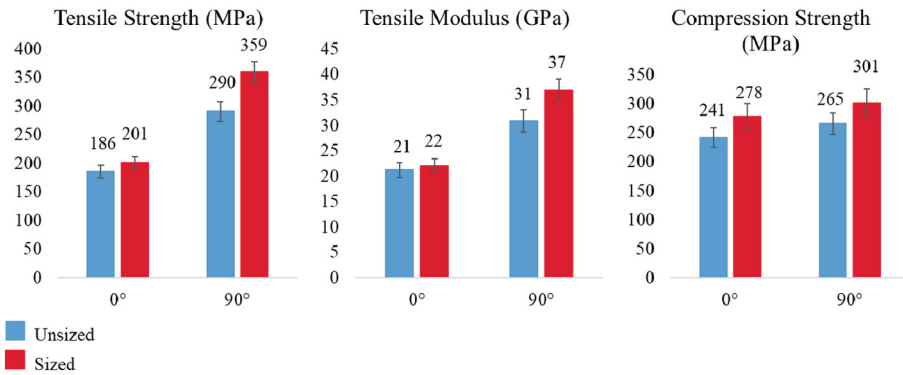


Fig. 3. Mechanical test results

### 3.2 Production of a Window Frame

Currently, aircraft window frame manufacturing involves the SMC process of composite materials with mechanical properties and cycle times comparable to ones of the innovative material presented in this study [14, 15]. The prepreg with recycled carbon fibers processed through PCM has the advantage of using recycled fibers instead of virgin fibers, in addition to the possible cost reduction triggered by the employment of secondary raw materials. In addition to coupon-level characterization, a prototype aircraft window frame was manufactured to demonstrate the applicability of the proposed material and process. Sized carbon fibers and process parameters used for prototype manufacture are the same as flat panels. The preform was realized manually in the laboratory environment. The performing step could also be automatized, further reducing the production time of the final component. After curing and demolding, the component was cleaned and trimmed. The final product is shown in Fig. 4.



**Fig. 4.** Windows frame prototype

## 4 Conclusion

This study proves that carbon fibers recycled via pyrolysis can be used to manufacture an aircraft window frame. This purpose is achieved by exploiting prepreg compression molding for processing non-woven fabric prepreg realized from recycled carbon fibers. The work also shows that the sizing formulation developed by CETMA for this application improves the mechanical performance of the composite. The mechanical properties of the composite with sized fibers are comparable with those of SMC composite currently used for aircraft window frames. The prepreg developed for PCM is a viable alternative to the materials traditionally used to produce the window frames since it has the advantage of using recycled fibers. The employment of fibers recovered from waste materials could reduce the cost of the component and ensure equal mechanical performance and production rate.

## References

1. Gopalraj, S.K., Kärki, T.: A review on the recycling of waste carbon fibre/glass fibre-reinforced composites: fibre recovery, properties and life-cycle analysis. *SN Appl. Sci.* **2**(3), 1–21 (2020). <https://doi.org/10.1007/s42452-020-2195-4>
2. Giorgini, L., et al.: Recovery of carbon fibers from cured and uncured carbon fiber reinforced composites wastes and their use as feedstock for a new composite production. *Polym. Compos.* **36**, 1084–1095 (2015)
3. Sun, H., et al.: Recycling of carbon fibers from carbon fiber reinforced polymer using electrochemical method. *Compos. A Appl. Sci. Manuf.* **78**, 10–17 (2015)
4. Zhang, J., Chevali, V.S., Wang, H., Wang, C.-H.: Current status of carbon fibre and carbon fibre composites recycling. *Compos. B Eng.* **193**, 108053 (2020)
5. Qazi, H., Subiantoro, A., Lin, R., Jayaraman, K.: Prediction model of optimised process parameters for recycling carbon fibre composites. *Thermal Sci. Eng. Progress.* **33**, 101344 (2022)
6. Utekar, S., Suriya, V.K., More, N., Rao, A.: Comprehensive study of recycling of thermosetting polymer composites – driving force, challenges and methods. *Compos. Part B Eng.* **207**, 108596 (2021)

7. Pickering, S.J., Liu, Z., Turner, T.A., Wong, K.H.: Applications for carbon fibre recovered from Composites. *IOP Conf. Ser. Mater. Sci. Eng.* **139**, 012005 (2016)
8. Oliveux, G., Dandy, L.O., Leeke, G.A.: Current status of recycling of fibre reinforced polymers: review of technologies, reuse and resulting properties. *Prog. Mater. Sci.* **72**, 61–99 (2015)
9. Pimenta, S., Pinho, S.T.: Recycling carbon fibre reinforced polymers for structural applications: technology review and market outlook. *Waste Manage.* **31**, 378–392 (2011)
10. Pasco, C., Kendall, K.: ACCE SPE 2016. In: Characterisation of the Thermoset Prepreg Compression Moulding Process (2016)
11. Wulfsberg, J., Herrmann, A., Ziegmann, G., Lonsdorfer, G., Stöß, N., Fette, M.: Combination of carbon fibre sheet moulding compound and prepreg compression moulding in aerospace industry. *Procedia Eng.* **81**, 1601–1607 (2014)
12. Introduction of new large tow carbon fiber products and PCM\* Technology. <http://www.alumag.com/wp-content/uploads/2013/11/RCOM11.2011MitsubishiLecture.pdf>
13. Passaro, A.: New sizing formulation for recycled carbon fibres (2020)
14. HEXMC carbon fibre/epoxy moulded parts for Boeing 787. <https://www.jeccomposites.com/news/hexmc-carbon-fibre-epoxy-moulded-parts-for-boeing-787/>
15. User guide - hexcel | composite materials and structures. [https://www.hexcel.com/user\\_area/content\\_media/raw/HexMC\\_UserGuide.pdf](https://www.hexcel.com/user_area/content_media/raw/HexMC_UserGuide.pdf)



# Experimental Investigation on Fracture Toughness of Open Hole Coupons Under Tension Load

R. Cumbo<sup>1</sup>(✉) and A. Baroni<sup>2</sup>

<sup>1</sup> Leonardo Labs, Via dell'Aeronautica, 80038 Pomigliano d'Arco, Italy  
roberta.cumbo.ext@leonardo.com

<sup>2</sup> Leonardo Aerostructures, Via per Monteiasi 83, 74023 Grottaglie, Italy

**Abstract.** The failure of a composite material is identified by a stress or energy criterion which is function of the ratio between the critical length of the crack and the characteristic size of the tested specimen. Experimental evidence shows that a net-fracture is observed for open-hole specimens under tension and even if the critical length can be evaluated analytically, it is difficult to find an experimental validation as the crack occurs instantaneously. The fracture toughness of an open hole coupon shows the same experimental difficulties. Usually this value is considered as an intrinsic property of the material and it is experimentally evaluated with ad-hoc tests, e.g. Double Cantilever Beam or Compact Tension test. An analytical approach has been proposed in literature for the evaluation of the critical fracture toughness of a general laminate with mixed plies starting from the knowledge of the fracture toughness obtained through a Compact Tension test. The approach has been tested for specimens with center-crack. However, some assumptions behind this method are not experimentally validated as for example the hypothesis of same critical length for all the laminates. This contribution presents a small experimental campaign aimed to verify the mentioned hypothesis and the validity of the relation between fracture toughness of plies at  $0^\circ$  with the one of a general stacking sequence.

**Keywords:** Composite laminates · Mechanical properties · Fracture toughness · Open hole test

## 1 Introduction

The failure of a composite laminate is determined by two main factors: the brittleness of the material and the ratio between the crack (if any) and the characteristic size of the tested specimen. When dealing with extreme cases of null or large crack, a stress or energetic criterion is considered respectively. For intermediate cases, both failure criteria should be considered. Cornetti et al. [1] proposed a coupled Finite Fracture Mechanics (FFM) criterion by introducing the crack extension  $l$  as a structural variable, differently from other standard FFM approaches which consider this quantity as a material constant.

By combining the stress and the energy criterion, the following set of equations yields:

$$\begin{cases} \frac{1}{l_{cr}} \int_a^{a+l_{cr}} \sigma_y(x) dx = \tilde{\sigma}_{um} \\ \frac{1}{l_{cr}} \int_a^{a+l_{cr}} K_I^2(x) dx = K_{IC}^2 \end{cases} \quad (1)$$

where  $l_{cr}$  is the critical length, i.e. process zone,  $a$  is the characteristic length of the initial crack,  $\tilde{\sigma}_{um}$  is the ultimate strength of the same specimen in un-notched conditions,  $K_I$  is the stress intensity factor and  $K_{IC}$  is the fracture toughness. The reference system  $xy$  is shown in Fig. 1.

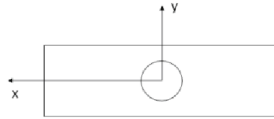


Fig. 1. Reference system of the open hole specimen.

Equation (1) presents two unknowns: the stress field and the stress intensity factor. For sufficiently large  $W/a$  ratio<sup>1</sup>, they can be approximated as:

$$\sigma_y(x) = \frac{\sigma_\infty x}{\sqrt{x^2 - a^2}} \quad (2)$$

$$K_I(x) = \sigma_\infty \sqrt{\pi x} \quad (3)$$

where  $\sigma_\infty$  is the value of the remote stress applied to the notched specimen. The value of the ratio  $W/a$  suggested by ASTM D5766 satisfies this hypothesis. The authors of ref. [1] explain Eq. (1) as “fracture is energy driven but a sufficiently high stress field must act in order to trigger crack propagation”. This failure criterion for notched specimen has been verified in ref. [1] for a side crack on a three-point bending test. For the case of a center-cracked specimen, more considerations should be done. Ref. [2] shows through experimental evidence that a net-fracture is observed for open-hole specimens under tension and even if the critical length can be evaluated analytically, it is difficult to find an experimental validation as the crack occurs instantaneously (Fig. 2). In this case indeed, the hypothesis of brittle material should be considered and only the stress criterion holds.

However, refs. [3, 4] apply the failure criteria presented in ref. [1] for specimen with open hole in tension. The fracture toughness is a physical parameter which is difficult to be retrieved experimentally for different stacking sequences. Usually this value is considered as an intrinsic property of the material and it is experimentally evaluated with ad-hoc tests, e.g. Double Cantilever Beam or Compact Tension test. Ref. [5] proposes an analytical approach for the evaluation of the fracture toughness of a general laminate with mixed plies starting from the knowledge of the fracture toughness obtained through a CT test. The approach has been tested for specimens with center-crack. However, some assumptions made in ref. [5] are not experimentally validated as:

1. The critical length of a laminate is not varying with the stacking sequence and/or is negligible if compared with the size of the hole;



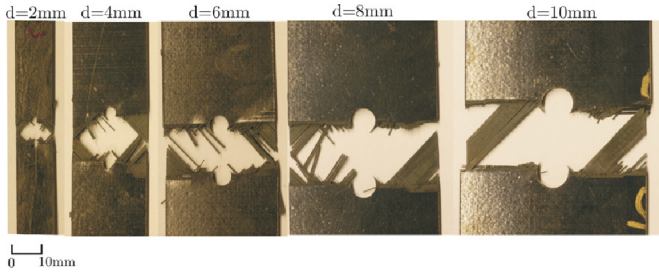


**Fig. 2.** Net-fracture observed for some open hole specimen with same w/d ratio from ref. [2].

2. The experimental validation has not been carried out on different notches but only limited to a general center-crack specimen;
3. The different geometry correction factor for a CT and Open Hole Tension (OHT) specimen is not considered and not justified in any work.

This contribution aims thus to perform an experimental validation of the approach proposed in ref. [5] giving an explanation to the mentioned assumptions and verify its applicability on open hole specimens.

**1.1 Analytical Model of Mode I Fracture Toughness – Ref. [5]**

Considering a sub-laminate (i), i.e. all plies with same orientation different from 0°, and a 0° notched laminate, the ratio between the remote stresses is:

$$\Omega_0^i = \frac{\sigma_\infty^{(i)}}{\sigma_\infty^0} \tag{4}$$

which can be retrieved from lamination theory. For a general cracked specimen, the stresses can be expressed as:

$$\sigma_\infty^{(i)} = \frac{K_{IC}^{(i)}}{X^{(i)} Y^{(i)} \sqrt{\pi(a^{(i)} + l_{cr}^{(i)})}} \tag{5}$$

where  $Y = f(W, a)$  is the geometric correction factor, X is function of the elastic properties of the ply material and indicates the degree of orthotropy, W and a are the width and the initial crack sizes of the specimen. By combining Eqs. (4), (5) and considering the first assumption explained in Sect. 1:

$$K_{IC}^{(i)} = \frac{X^{(i)} \Omega_0^{(i)}}{X^0} K_{IC}^0 \tag{6}$$

Equation (6) relates the fracture toughness of a general laminate of plies equally oriented to that of 0° plies. The energy release rate  $G_{IC}^L$  of a laminate with mixed orientations can be then expressed as:

$$G_{IC}^L = \frac{\sum_i^N \frac{K_{IC}^{(i)2}}{E_{eq}^i} t^{(i)}}{t^L} = \frac{\sum_i^N G_{IC}^{(i)} t^{(i)}}{t^L} \tag{7}$$

where  $N$  is the number of sub-laminates, equal to the number of orientations in the laminate,  $t$  is the thickness and  $E_{eq}$  is an elastic property which can be retrieved from lamination theory.

## 2 Experimental Investigation on OHT

Some observations can be made on the analytical approach of ref. [5] as it has been presented with lack of explanations and experimental evidence. Equation (6) is obtained by considering that:

$$X^{(i)} = X^0 \quad (8a)$$

$$l_{cr}^{(i)} = l_{cr}^0 \quad (8b)$$

The assumption of Eq. (8a) is valid as long as the two laminates (i) and  $0^\circ$  have the same geometry. In ref. [5], it is unclear if the authors tested the relation on CT specimens sub-laminates assuming then that the laminate fracture toughness is the same for OHT and CT specimens. Equation (8b) assumes instead that the critical length of the crack has the same value for all the sub-laminates. The authors of ref. [5] underline that this assumption can not be experimentally verified and the results show anyhow good correlations with experimental data. Without any simplification, Eq. (6) would be:

$$K_{IC}^{(i)} = \frac{X^{(i)} Y^{(i)} \sqrt{a^{(i)} + l_{cr}^{(i)}}}{X^0 Y^0 \sqrt{a^0 + l_{cr}^0}} \Omega_0^{(i)} K_{IC}^0 \quad (9)$$

This contribution aims to study the influence of the critical length on the evaluation of fracture toughness for different stacking sequences. Two layups were manufactured in Cycom977-2 IMS65 as listed in Table 1 and tested in notched and un-notched configuration under tensile loading. The measured strength values are then used to solve the first of Eq. (1) in order to obtain the value of  $l_{cr}$ . Notched and un-notched laminates with plies at  $0^\circ$ ,  $90^\circ$  and  $45^\circ$  have been also tested in order to collect sub-laminates (i) strength properties. The ratio  $W/d$  is equal to 6 for all the open hole specimens. The geometries of all the manufactured coupons are as specified by ASTM D3039 and D5766 for UNT and OHT respectively. Each test is repeated on 5 specimens and Figs. 3, 4 show the failed notched specimens after the tensile tests.

The same study has been also performed on numerical data (layup listed in Table 2) obtained with FE simulation. The material IM7/8552 is considered for this study even if no FE validation with respect to test data has been performed. The model is defined from the knowledge of constituent's properties.

**Table 1.** Test matrix on Cycom977–2 IMS65. – nominal ply thickness = 0.186 mm

ID	Layup	Width [mm]	D [mm]
<b>OHT</b>			
OHT1_1	[+45/0/-45/90]2s	36	6
OHT1_2	[+45/0/-45/90]2s	48	8
OHT1_3	[45/0/-45/90]2s	60	10
OHT2_1	[45/90/-45/0/90/0/90/0/45/-45/0/90/0/90/0/-45/90/45]	36	6
OHT2_2	[45/90/-45/0/90/0/90/0/45/-45/0/90/0/90/0/-45/90/45]	48	8
OHT2_3	[45/90/-45/0/90/0/90/0/45/-45/0/90/0/90/0/-45/90/45]	60	10
OHT0	[0]6	38.4	6.4
OHT45	[45]12	38.4	6.4
OHT90	[90]11	38.4	6.4
<b>UNT</b>			
UNT1	[45/0/-45/90]2s	25	
UNT2	[45/90/-45/0/90/0/90/0/45/-45/0/90/0/90/0/-45/90/45]	25	
UNT0	[0]6	25	
UNT45	[45]12	25	
UNT90	[90]11	25	

**Table 2.** UNT/OHT FEM test matrix on IM7/8552 – nominal ply thickness = 0.131 mm

ID	Layup
FE1	[45/90/-45/90]2s
FE2	[45/0/-45/90/90/-45/45/90]s
FE3	[45/0/-45/90/90/-45/0/45]s
FE4	[45/0/-45/90/-45/0/45/0]s
FE5	[45/0/-45/-45/0/45/0/0]s
FE6	[45/0/-45/90/90/-45/45/90/-45/45/90/90]s
FE7	[45/0/-45/90/90/-45/0/45/90/-45/45/90]s
FE8	[45/0/-45/90/90/-45/0/45/-45/0/45/0]s
FE9	[45/0/-45/90/-45/0/45/-45/0/45/0/0]s



Fig. 3. Failed specimens OHT0, OHT45, OHT90 (from left to right).



Fig. 4. Failed specimens OHT1\_1, OHT2\_1 (from left to right).

Experimental data of ultimate UNT/OHT strength of specimens listed in Table 1 are reported in Table 3 together with the value of  $l_{cr}$  evaluated by solving the first of Eq. (1). From these results, the following considerations can be made:

- $l_{cr}$  is not influenced by the specimen size (for fixed ratio  $W/d$ );
- $l_{cr}$  is varying with the stacking sequence of the laminate;
- The value of  $l_{cr}$  is not negligible if compared with the radius of the notch;
- The specimen OHT45 shows a high and unfeasible value of  $l_{cr}$ .

The last observation could be explained by the values of experimental strength in notched and un-notched conditions. Indeed, these values are comparable because for a laminate with all plies oriented at  $\pm 45^\circ$  with respect to the loading direction, the loads path is comparable as schematically shown in Fig. 5. Indeed, if the specimen is un-notched, the load will be equally distributed between plies at  $+45^\circ$  and  $-45^\circ$ . Similarly, the notched specimen presents a load distribution crossing around the hole in

a direction parallel to plies at  $+45^\circ$  and  $-45^\circ$ . In this case it is thus difficult to evaluate the applicability of Eq. (1).

**Table 3.** Values of experimental strength, process zone and fracture toughness.

ID	Strength ratio( $\sigma_{\text{UNT}}/\sigma_{\text{OHT}} - 1$ )	$l_{cr}$ [mm]	$K_{IC}$ [MPa $\sqrt{\text{m}}$ ]– Eq. (1)	$G_{IC}$ [J/m <sup>2</sup> ]
OHT1_1	0.45	5.4	71.0	0.088
OHT1_2	0.58	5.3	70.3	0.087
OHT1_3	0.69	5.3	70.3	0.087
OHT2_1	0.87	2.4	65.7	0.074
OHT2_2	0.81	3.5	79.0	0.106
OHT2_3	0.95	3.5	79.6	0.108
OHT0	0.53	4.8	221.9	0.913
OHT45	0.03	99.4	—	0.219
OHT90	1.10	1.8	2.9	$5e-4$

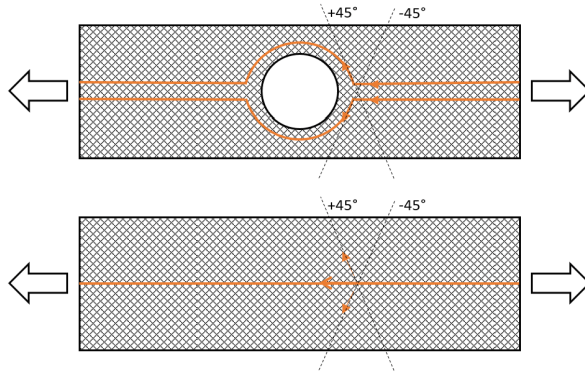


**Fig. 5.** Load path for notched and un-notched tensile test.

For this reason, the value of fracture toughness for specimen OHT45 is not reported in Table 3. The sub-laminates approach of Eq. (7) has also been adopted in order to evaluate the energy release rate for the two laminates OHT1 and OHT2, resulting respectively in 0.24 and 0.31 J/m<sup>2</sup>, differently from the values shown in Table 3 obtained through the direct approach.

As additional analysis, Fig. 6 shows the results of Eq. (1) in terms of fracture toughness and process zone for the simulated specimen listed in Table 2. Same conclusions about  $l_{cr}$  can be made.

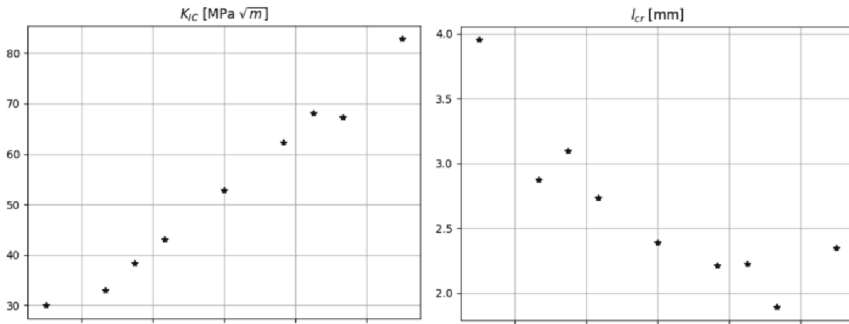


Fig. 6.  $K_{IC}$  and  $l_{cr}$  of simulated specimens.

### 3 Conclusions

An experimental investigation on the applicability of FFM equations for open hole specimens is presented in this work for the definition of the laminate fracture toughness. The proposed study aims to validate some assumptions made behind the analytical framework in object which allows to evaluate the laminate fracture toughness of a notched specimen starting from the knowledge of the one associated to a specimen with plies at  $0^\circ$ . The results showed that the effect of the process zone (which is normally not possible to measure experimentally) is not negligible on the tested layups and specimens and the investigated failure criteria gives unfeasible value of process zone for specimens with plies  $\pm 45^\circ$ . The applicability of the whole process remains also unclear for open hole specimens under tensile loading because the failure normally occurs with a net-crack. Moreover, the sub-laminates approach predict an incorrect value of the fracture toughness of the tested laminates. This means that the current procedure can not be applied directly on open hole specimens and CT test is strictly needed in order to retrieve these quantities.





The presented work does not intend to criticize the validity of the analytical framework but aims to underline that more experimental validation on different layups, specimens and materials should be carried out from the authors in order to clarify the investigated aspects that still remain unclear.

### References

1. Cornetti, P., Pugno, N., Carpinteri, A., Taylor, D.: Finite fracture mechanics: a coupled stress and energy failure criterion. *Eng. Fract. Mech.* **73**(14), 2021–2033 (2006)
2. Camanho, P.P., Maimí, P., Dávila, C.G.: Prediction of size effects in notched laminates using continuum damage mechanics. *Compos. Sci. Technol.* **67**(13), 2715–2727 (2007)
3. Camanho, P.P., Catalanotti, G.: On the relation between the mode I fracture toughness of a composite laminate and that of a 0 ply: analytical model and experimental validation. *Eng. Fract. Mech.* **78**(13), 2535–2546 (2011)
4. Furtado, C., et al.: A methodology to generate design allowables of composite laminates using machine learning. *Int. J. Solids Struct.* **233**, 111095 (2021)
5. Camanho, P.P., Erçin, G.H., Catalanotti, G., Mahdi, S., Linde, P.: A finite fracture mechanics model for the prediction of the open-hole strength of composite laminates. *Compos. A Appl. Sci. Manuf.* **43**(8), 1219–1225 (2012)



# Influence of Laser Texturing on Mechanical Performances of CFRP Single Lap Bonded Joint

Gianluca Parodo<sup>1</sup> , Wilma Polini<sup>2</sup> , Luca Sorrentino<sup>2</sup> ,  
and Sandro Turchetta<sup>2</sup> 

<sup>1</sup> Department of Industrial Engineering, University of Salerno, 84084 Fisciano, SA, Italy  
gparodo@unisa.it

<sup>2</sup> Department of Civil and Mechanical Engineering, University of Cassino and Southern Lazio,  
03043 Cassino, FR, Italy

**Abstract.** Nowadays polymer composites have found increasing use especially in those areas where high mechanical performance is required with the lowest possible weight. For example, often the parts have complex geometries difficult to achieve with a single forming step, so in the industrial field there is the tendency to make more parts of simpler geometry to be assembled later. The use of structural adhesives makes it possible to avoid drilling and the use of bolts, significantly reducing the weight of the joint and the risk to damage the fibers. However, it is often necessary to pretreat the surfaces for manufacturing a reliable joint. For this reason, composite adherends are generally degreased and/or sanded before bonding; this technique presents problems related to the presence of solvents and large volume of dust produced during the process that must be controlled by means of hoods. The use of laser sources for pretreatment can be a valid replacement of these processes. In this work the effectiveness of a pretreatment made with a CO<sub>2</sub> laser on CFRP adherends constituting a lap shear bonded joint is investigated. In order to define the treatment parameters for avoiding damages of the laminates, the treated surfaces were analyzed using conoscopic holography and optical analysis. The obtained experimental results show that the joints' strength is higher than that obtained with degreasing process. Moreover, it represents a sustainable process to prepare the adherend's surface to bonding, reducing the volume of removed material and limiting dust production.

**Keywords:** Adhesive Bonding · Single Lap Joint · Laser Surface Texturing · Experimental Tests

## 1 Introduction

In the last decades, polymer composites have found increasing use especially in those areas where high mechanical performance is required with the lowest possible weight. Often the parts have complex geometries difficult to achieve with a single forming step, so in the industrial field there is the tendency to make more parts of simpler geometry to be assembled later. Traditional methods as bolting and riveting needs the drilling of the parts to be assembled, which can lead to delaminations. The use of structural adhesives

can avoid this problem. However, often the parts to be bonded need a surface treatment before bonding in order to produce a reliable joint [2, 3]. Generally, abrasive processes as sanding and grit blasting can be adopted in order to increase the roughness of the adherends. Nevertheless, some contaminations as oil and release agents could remain on the surface or, in some cases, accumulate in the crevices [3]. For this reason, cleaning treatments as degreasing with solvents can be used as alternative [4]. More recently, the use of laser systems shows the potentiality of removing the first vitreous layer of FRP without damaging the underlying reinforcement [5, 6]. Laser systems have some advantages respect mechanical techniques: they are non-contact processes so there is no tool wear and further cleaning process are not necessary [7]. The ablation mechanism in the case of processing on CFRP depends on the wavelength of the laser beam used. In case of wavelengths on the IR, the ablation is of thermal type: the beam raises the temperature locally increasing the average kinetic energy of the polymer molecules to lead to the breakdown of molecular bonds, leading to the ablation of the resin [8]. Respect other types of reinforcements, carbon fibers dissipate more heat generated during process due to the high conductive coefficient, so this phenomenon is more accentuated [9, 10]. In case of UV-wavelength, the energy of the photons of the beam is such as to directly break the molecular bonds: for this reason the use of UV-lasers allows to significantly reduce the size of the Heat Affected Zone (HAZ) [11, 12]. However, IR-lasers, such as CO<sub>2</sub> lasers, are widespread in the industrial sector due to their beam quality, efficiency and flexibility, in addition to the range of powers that can be used [13].

In this work, the effectiveness of a laser texturing pretreatment, made with a CO<sub>2</sub> laser system on lap shear bonded joints (SLJs), is experimentally evaluated. In particular, preliminary tests have been carried out to define the laser pretreatment in order not to generate thermal damage on the laminate and ensuring an increase in the roughness of the treated surface. Subsequently, SLJ bonded joints were manufactured and tested using a degreasing treatment with acetone and the laser texturing optimized with the preliminary tests. The results showed the effectiveness of developed laser pretreatment.

## 2 Materials and Methods

The laminates were produced through vacuum bagging technique using a unidirectional carbon prepreg system known as CYCOM 751-42%-HM-170-350. The layup adopted was [0<sub>2</sub>/90/0<sub>2</sub>/90/0]<sub>s</sub>, while the cure cycle consisted in a dwell of 2 h at 125 °C. The produced laminates were subjected to surface treatments prior bonding. The treatments adopted in this work were two: one consisted in degreasing using acetone and the other in a laser texturing carried out with a Giotto CO<sub>2</sub> Laser System manufactured by Sei S.p.A. (TEM<sub>00</sub>). Preliminary tests were realized in order to investigate the optimal process parameters for the laser texturing. The first step consisted in identify an approach of laser texturing that avoids thermal degradation of the adherends, removing the first surface vitreous layer without the damage of the reinforcement. Initially, the laser texturing consisted in etched lines on the bonding area (Fig. 1a). In this case, texturing was defined as a function of the distance between two consecutive lines (offset).

In order to assess the thermal damage to the laminate, laser etchings were observed with Leica VMM 200 optical microscope and a non-contact measuring system (based



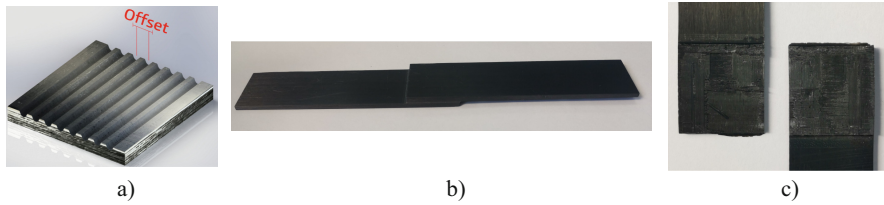


**Fig. 1.** Laser texturing based on linear etching: a) Scheme of texturing; b) Lap shear specimen; c) Fiber tear failure of treated lap shear specimens.

on conoscopic holography) called Conoscan 3000 and produced by Optimet Optical Metrology Ltd. However, this type of texturing showed either excessive thermal damage, or insufficient etching depth to observe an increase in roughness compared to the untreated surfaces. Therefore, the parameters have been defined to have appreciable roughness increase compared to untreated surfaces, so preliminary lap shear tests have been carried out to evaluate their effectiveness. Unfortunately, in accordance with the ASTM D5573 standard, fiber tear failure (Fig. 1b) has been observed, meaning that the adherends, damaged thermally, were the cause of failure of the joint, with lower mechanical resistance compared to degreasing treatments with acetone. For this reason, a different texturing has been adopted based no longer on linear etching but on dimples in square grid (Fig. 2). The first step consisted in the definition of the process parameters for the realization of the single dimple, so the grid size was used to evaluate different treatment densities  $\rho$  defined in Eq. (1).

$$\rho = \frac{\pi D^2}{4G_d^2} \times 100 \quad (1)$$

where  $D$  was the dimension of the dimple and  $G_d$  was the grid dimension. Fixing the dimension of dimple ( $D$ ), the density of treatment varied only as a function of the grid dimension ( $G_d$ ). The obtained optimal laser parameters for realizing a single dimple consisted in a power of 11 W, a frequency of about 25 kHz, a laser fluence equal to 1.44 J/cm<sup>2</sup>, a writing speed of about 6 m/s, a pulse duration of 18  $\mu$ s and a laser spot diameter equal to 200  $\mu$ m. As a results of the optical and conoscopic analysis, a density of 20% has been chosen because it guarantees an increase of surface roughness minimizing the thermal effect on the adherend surface. In fact, it was chosen to produce the bonding with a density treatment of 20% because lower values showed a reduced roughness increase, while higher values showed a higher HAZ and elliptic dimples, with the largest size along the direction of the underlying reinforcement [14]. Once the laser texturing treatment was defined, the degreasing treatments with acetone and laser texturing were carried out, so the bonding was realized. The adopted adhesive was the EA9309.3NA, which is a two-part epoxy resin manufactured by Hysol. It has been chosen this adhesive because it is widely used for bonding various types of materials for structural application [15–18]. The polymerization of the adhesive took place in five days at room temperature. After the polymerization of the adhesive, lap shear specimens were manufactured according to ASTM D1002 and ASTM D5868 (Fig. 1b), while the

speed of the crosshead was set to 1.3 mm/min during tests. For clarity, the experimental test plan is given in Table 1.

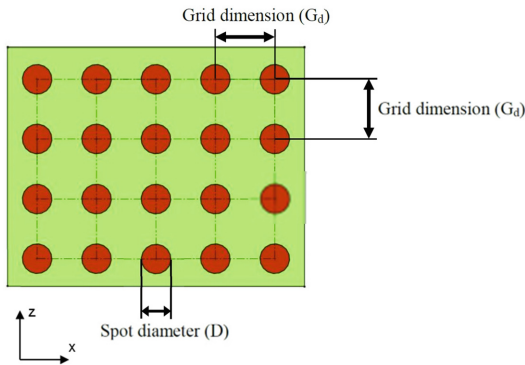


**Fig. 2.** Scheme of the texturing based on dimples in square grid.

**Table 1.** Experimental plan.

Factors	# Level	Levels
Surface treatment	2	<ul style="list-style-type: none"> <li>• Degreasing with acetone</li> <li>• Laser texturing (<math>\rho = 20\%</math>)</li> </ul>
Replication	5	

### 3 Results and Discussions

Optical observation of the laser treated surfaces showed an influence of the direction of the underlying reinforcement on the morphology of the etching. In fact, linear texturing has shown difficulty in making etchings with a constant and repeatable size in transverse direction respect the underlying reinforcement. In fact, the heat generated in the process area was conducted in the direction of the reinforcement, leading to a variation of the HAZ essentially linked to the position of the underlying reinforcement with respect to the free surface of the laminate. Treatments with linear texturing parallel to the reinforcement have not shown this problem, however they have resulted in a thermal damage of the laminate also confirmed by preliminary test lap shear (Fig. 1c). The adoption of texturing based on dimples in square grid showed problems of excessive size of HAZ only for values of density of treatment above the 35%.

The load-displacement median curves obtained from the lap shear tests are given in Fig. 3a. Lap shear tests showed an increase in performance of about 39% compared to samples degreased with acetone. In accordance with ASTM D5573, the failure surfaces were of the light fiber tear type for degreased and laser-treated specimens (Fig. 4). This highlights the good bonding for both types of treatment and confirms the efficiency

of laser pretreatment. In conclusion, the developed laser pretreatment presents a valid solution for the bonding of structural CFRP parts. Future developments will investigate how the performance of laser treated joints varies under cyclic thermal shock conditions, assessing its durability in harsh operating conditions.

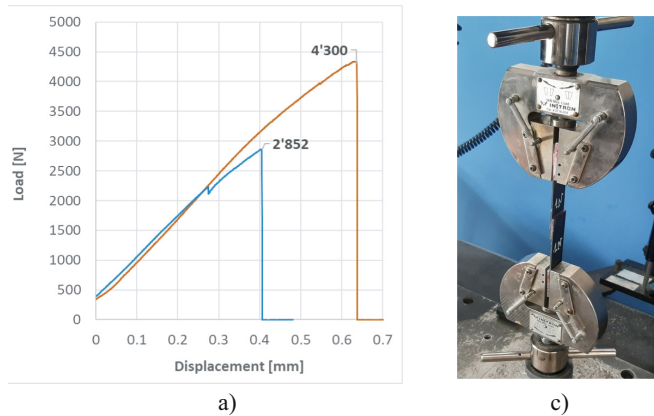


**Fig. 3.** Lap shear test results for laser treated (orange) and degreased (blue) specimens: a) Load – displacement median curves; b) Image of a specimen during test. (Color figure online)

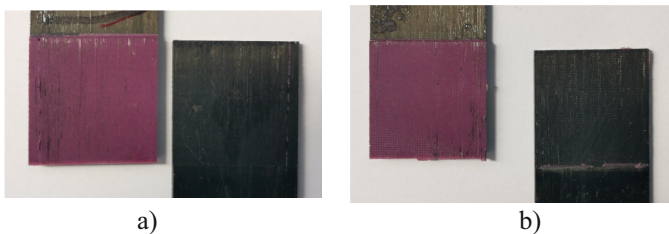


**Fig. 4.** Failure surfaces of a specimen subjected to: a) degreasing with acetone; b) laser texturing based on dimples in square grid.

## 4 Conclusions

In this work a laser texturing pretreatment on CFRP has been defined and its effectiveness on the mechanical resistance of bonded lap shear joints (SLJ) evaluated. The optimal texturing for this purpose was found to be based on square grid dimples. A treatment density has been defined as a function of the grid size and, through optical and holographic analysis on treated laminated surfaces, an optimum density of treatment for the realization of the joints was defined equal to 20%. The experimental results showed a 39% increase in mechanical performance compared to joints made degreasing treatment with acetone. From the analysis of the fracture surfaces, it has been confirmed the

goodness of the pretreatment as there have been no ruptures by tearing of the adherends. Future works will investigate the effect of cyclic thermal shocks on the reliability and durability of the joints, in order to assess the reliability of the developed pre-treatment over time and under severe working conditions.

## References

1. Tao, R., Alfano, M., Lubineau, G.: In situ analysis of interfacial damage in adhesively bonded composite joints subjected to various surface pretreatments. *Compos. Part A Appl. Sci. Manuf.* **116**, 216–223 (2019)
2. Sorrentino, L., Polini, W., Bellini, C., Parodo, G.: Surface treatment of CFRP: influence on single lap joint performances. *Int. J. Adhes. Adhes.* **85**, 225–233 (2018)
3. Pocius, A.V.: *Adhesion and Adhesives Technology*. Carl Hanser Verlag (2012)
4. Da Silva, L.F.M., Ferreira, N.M.A.J., Richter-Trummer, V., Marques, E.A.S.: Effect of grooves on the strength of adhesively bonded joints. *Int. J. Adhes. Adhes.* **30**, 735–743 (2010)
5. Sorrentino, L., Marfia, S., Parodo, G., Sacco, E.: Laser treatment surface: an innovative method to increase the adhesive bonding of ENF joints in CFRP. *Compos. Struct.* **233**, 111638 (2020)
6. Sorrentino, L., Parodo, G., Turchetta, S.: Influence of laser treatment on end notched flexure bonded joints in carbon fiber reinforced polymer: experimental and numerical results. *Materials (Basel)* **15**, 910 (2022)
7. Sathiyamurthy, R., Duraiselvam, M.: Selective laser ablation of CFRP composite to enhance adhesion bonding. *Mater. Manuf. Process.* **34**, 1296–1305 (2019)
8. Wu, C.W., Wu, X.Q., Huang, C.G.: Ablation behaviors of carbon reinforced polymer composites by laser of different operation modes. *Opt. Laser Technol.* **73**, 23–28 (2015)
9. Sorrentino, L., Turchetta, S., Parodo, G.: Drilling of glare laminates: effect of cutting parameters on process forces and temperatures. *Int. J. Adv. Manuf. Technol.* (2022)
10. Parodo, G., Rubino, F., Sorrentino, L., Turchetta, S.: Temperature analysis in fiber metal laminates drilling: experimental and numerical results. *Polym. Compos.* **43**, 1–16 (2022)
11. Reitz, V., Meinhard, D., Ruck, S., Riegel, H., Knoblauch, V.: A comparison of IR- and UV-laser pretreatment to increase the bonding strength of adhesively joined aluminum/CFRP components. *Compos. Part A Appl. Sci. Manuf.* **96**, 18–27 (2017)
12. Leone, C., Papa, I., Tagliaferri, F., Lopresto, V.: Investigation of CFRP laser milling using a 30 W Q-switched Yb:YAG fiber laser: Effect of process parameters on removal mechanisms and HAZ formation. *Compos. Part A Appl. Sci. Manuf.* **55**, 129–142 (2013)
13. Graf, S., Staupendahl, G., Kramer, A., Muller, F.A.: High precision materials processing using a novel Q-switched CO<sub>2</sub> laser. *Opt. Lasers Eng.* **66**, 152–157 (2015)
14. Sorrentino, L., Parodo, G., Turchetta, S.: CFRP laser texturing to increase the adhesive bonding: morphological analysis of treated surfaces. *J. Adhes.* 1–14 (2020)
15. Kim, K.S., Yi, Y.M., Cho, G.R., Kim, C.G.: Failure prediction and strength improvement of uni-directional composite single lap bonded joints. *Compos. Struct.* **82**, 513–520 (2008)
16. Sorrentino, L., Parodo, G., Giuliano, G.: Lightweight structures: an innovative method to uniform the thickness of metal sheets by patchwork blanks. *Int. J. Light. Mater. Manuf.* **5**, 20–28 (2022)
17. Sacco, E., Marfia, S., Parodo, G., Sorrentino, L.: Experimental study and numerical modeling of ENF scheme: comparison of different beam approaches. *Eng. Fract. Mech.* **262**, 108230 (2022)
18. Giuliano, G., Parodo, G., Sorrentino, L.: Uniformity of thickness of metal sheets by patchwork blanks: potential of adhesive bonding. *Frat. ed Integrità Strutt.* **14**, 166–176 (2020)



# Preliminary Sizing of a Hybrid-Electric Aircraft with Structural Batteries

Salvatore Corcione, Gennaro Di Mauro, Vincenzo Cusati<sup>(✉)</sup>, Valerio Marciello, Michele Guida, and Fabrizio Nicolosi

Industrial Engineering Department, University of Naples Federico II, 80125 Naples, Italy  
vincenzo.cusati@unina.it

**Abstract.** This research work aims to evaluate the potential benefits the structural batteries have on the fuel burn for an 11-seat commuter aircraft. According to the envisaged technologies (structural batteries), this work will focus on the determination of the best hybridization factors determining the energy requirements for the typical mission of a commuter aircraft.

The reference is a flying aircraft made of metallic material, and through a domestic tool, the initial sizing was performed by changing the material to a composite material, that can be easily adopted for the realization of structural batteries (SB), a new technology that can simultaneously store energy and support loads. This solution makes it possible to think of a hybrid-parallel power train to perform various flight phases, approaching the requirements of environmentally friendly aviation.

**Keywords:** Structural Batteries · Multifunctional Materials · Hybrid-Electric Aircraft · Aircraft Design

## 1 Introduction

Aviation is nowadays demanded to unite environmental sustainability and economic growth [1]. These needs resulted in policy roadmaps in Europe and led to consistent long-term research efforts. In 2019, the European Green Deal [2] set the ambitious goal of achieving by 2050 climate neutrality in all sectors of the EU economy, including air transport. One of the main strategies to limit in-flight pollutant emissions is the increased use of electrical energy onboard aircraft for both non-propulsive and propulsive purposes, leading to the concepts of “More Electric Aircraft” (MEA), “Hybrid Electric Aircraft” (HEA) [3, 4], and “All-Electric Aircraft” (AEA).

As of today, some all-electric aircraft have been designed and flown and a short list of models is provided by Riboldi [5]. Those models are electrified versions of existing gliders, or very light machines, inspired by a corresponding conventionally powered aircraft in the Light Sport Aircraft (LSA) category. Concerning hybrid-electric propulsion, fewer specimens exist, and currently, there are no designs available on the market. However, today research is active in this field.

Despite modern electric motor drivers are more efficient in converting stored energy into mechanical power with respect to conventional Internal Combustion Engines (ICE),

the main limit to electric propulsion is represented by the limits of energy storage systems, i.e. batteries, which do not offer sufficient energy-to-mass and energy-to-volume densities [6] without a relevant negative impact on aircraft maximum take-off weight and in turn on the payload or aircraft size. As a result of nowadays research efforts toward the improvement of such performance indices, it is possible to design and fly an electrically propelled aircraft, as demonstrated by some existing examples, in the categories of ultra-light and general aviation [7].

Whatever the selected aircraft configuration is, a hybrid electric solution based on conventional battery technology to store the required electrical power will be affected by the addition of extra weight, represented by the batteries themselves. The battery mass will trigger the detrimental “snowball” effect on the aircraft weight: the more the demand for electric power, the higher the battery mass is and in turn the aircraft maximum take-off weight.

To break or at least mitigate such detrimental loop on the aircraft weight an alternative approach can be adopted, which consists in combining energy storage and load-bearing capabilities in structural batteries (SB), which have come to the forefront of research since the late 1990s. Structural batteries are hybrid and multifunctional composite materials that can provide electrical energy storage (like conventional Lithium-ion batteries) being at the same time a structural element carrying loads. Based on [8], structural batteries can be embedded (Fig. 1 left), being multifunctional structures where lithium-ion battery cells are efficiently embedded into a composite structure or more often sandwich structure; and laminated structural electrodes where the electrode material possesses an intrinsic load bearing and energy storage function (Fig. 1 right). A more detailed classification of SBs can be found in [9].

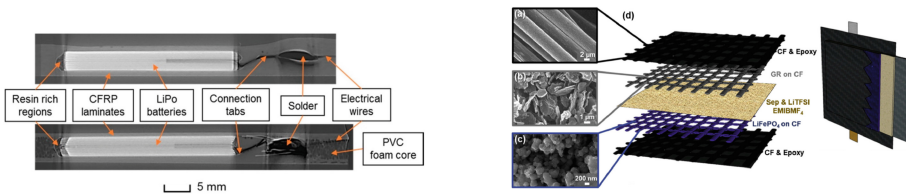


**Fig. 1.** Schematic of an embedded (left) and laminated (right) structural battery [9].

The schematic of the proposed SB concept is illustrated in Fig. 2. Considering the current state of the state of the art, to maximize mechanical properties, carbon fiber with twill architecture is used to get both the SB anode and the cathode (functionalizing it with *LiFePo4*). The separator between the electrodes is made of glass fiber. A Solid battery electrolyte should be used to achieve better mechanical performance. As it regards the binder’s material, copper & aluminum foils (respectively for anode and cathode) are used to avoid galvanic corrosion.

This paper wants to investigate the potential benefits in terms of fuel burn reduction achievable through integrating an under-development concept for a structural battery into the hybridization process of a 11-seat commuter aircraft. Starting from a conventional reference aircraft with an all-aluminum alloy structure, this work will address the

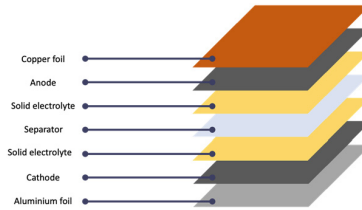


**Fig. 2.** Schematic of the proposed SB concept.

potential structural mass that can serve as SB and will estimate the potential energy and power demand to fulfill the design mission of the reference aircraft. The best hybridization strategy to fulfill the Top-Level Aircraft Requirements (TLARs) and the design mission with the minimum MTOW will be identified and the benefits in terms of fuel burn reduction will be shown.

## 2 Hybridization Process of the Reference Aircraft and Results

Starting from the inspiring work performed by Riboldi et al. [10], this paper wants to move a step further into applying the SB technology on a larger scale of aircraft. The selected reference aircraft is like the 11-seater Tecnam P2012 Traveller. The aircraft is an all-metal structure, high wing, twin-engine, unpressurized, piston aircraft with fixed tricycle landing gear. The P2012 maximum takeoff weight short field performance provides takeoff and landing run as low as 564 m (1849 ft) and 365 m (1198 ft) respectively. Cruise speed up to 194 kts and range up to 1760 km (950 NM) are accompanied by excellent fuel economy at any altitude thanks to the turbocharged piston engines which don't suffer the low-level high fuel consumption of turboprops.

The hybridization process has been accomplished by means of an in-house developed tool named HEAD (Hybrid Electric Aircraft Design tool). This tool starts from the initial sizing of a conventional aircraft according to the assigned TLARs. The design mission considered is 600 NM with 100 NM of alternate (diversion) plus 30 min of loiter, take-off and landing distances must be lower than 600 m and 400 m respectively. The above-mentioned workflow is adopted to fulfill the initial sizing for a conventional as well as for a hybrid-electric aircraft. After a preliminary sizing of a conventional platform accomplished by means of statistical data to fulfill the provided TLARs, the real sizing process is started. According to the provided design mission and all the TLARs a converging loop is performed about masses, aerodynamics, weight, balance, and mission analysis. The initialization of a conventional aircraft is needed to estimate the energy and/or the power needed to fulfill the design mission sizing the powerplant and in turn the fuel needed. Moreover, by deriving the energy profile along the mission, it is possible to understand the key flight phases that could benefit from a hybridization process. Concerning the weight breakdown for the conventional reference platform, the overall MTOW is about 3710 kg and the estimated fuel needed to fulfill the design mission is about 588 kg, the structural mass is about 1122.5 kg. The latter has been estimated assuming an all-aluminum alloy structure. Particular attention must be focused on the wing and fuselage structural masses that are equal to 339.3 kg and 430.5 kg respectively.

The structural elements of the wing and the fuselage will be the vessels of the structural batteries.

The energy history along the mission profile of both design and typical mission profiles is shown in Fig. 3. The total energy consumption is about 6700 kWh and 3500 kWh at 600 and 200 NM. To fulfill the hybridization process there is the need to assess the potential battery mass storable in the structure in form of SB. The idea behind this work is not to design a new aircraft rather than convert in a retrofitting fashion the existing P2012 conventional aircraft. Thus, the aircraft sizing would not be changed a part for the weight breakdown.

The use of SB in the fuselage does not raise issues bound to stress limits, due to their comparatively limited aerodynamic loading, the specific load resistance of SB is a primary matter of concern when it comes to placing them in the wings. To estimate the amount of structural mass that can host SB the same assumption made by Riboldi et al. [10] has been considered.

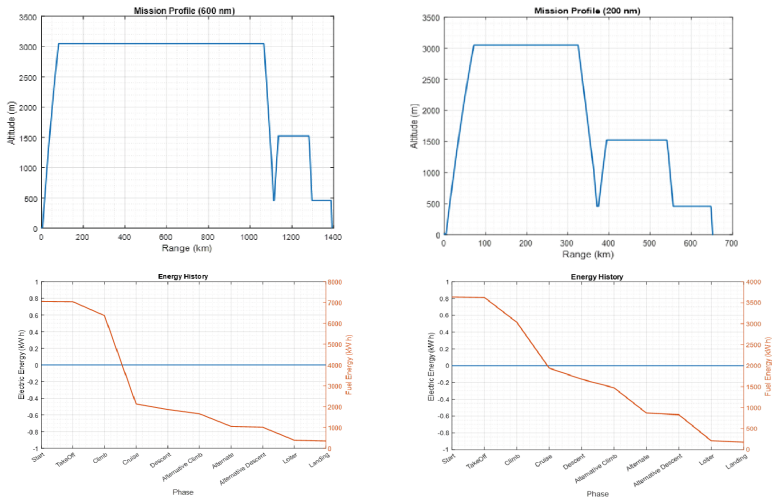


Fig. 3. Tecnam P2012 energy history for the missions of 600 NM (left) and of 200 NM (right).

To avoid areas of heavy compression loads wing upper skin panels and the whole empennage surface will be not considered as suitable for hosting SB. The lower wing skins panels, the wing leading and trailing edges, and the whole fuselage structures have been assumed as suitable components to host structural batteries.

Starting from the estimation of critical flight loads according to CS23/FAR23 [11], the effective structural masses have been estimated and compared with the conventional all aluminum alloy reference aircraft. By considering wing and fuselage structures made of CFRP plus SB (only for the specified part of the wing and fuselage), the overall structural weight is increased by 10% with respect to the conventional all-aluminum alloy structure.

Once the estimation of the structural masses is available it is possible to calculate the amount of SB installed onboard the aircraft. The overall SB mass that can be hosted



in the selected structural components is about 551 kg which is the sum of 38% of wing structural mass equipped with SB and 75% of the fuselage structural mass hosting the SB technology. Thus, by assuming the gravimetric energy density of 75 Wh/kg the overall electric energy storable onboard is about 41 kWh. This value is only a very small fraction of the required energy to fulfill the design mission of the selected aircraft. The latter confirms that with SoTA SBs it is still not possible to fly in full electric mode.

However, a hybridization strategy can be defined to exploit the potential 41 kWh of electric energy that can be stored in the aircraft structures. The selected powerplant is characterized by a parallel hybrid architecture, in which there are two parallel propulsion shafts, powered by combustion and electric sources (Motor/Generator), which are mechanically coupled. Battery-powered EM and ICE shafts are both coupled to a shaft that drives the propeller, so either or both can provide propulsion. This hybrid architecture may also allow charging the batteries when the ICE drives the propeller and the EM through the coupling. In this case, the EM operates as an electric generator. Differently from series and series-parallel, there is no electric generator on the ICE's shaft, and machines may be sized smaller since the propelling power is provided by both, with corresponding weight reduction [12]. The disadvantages of this configuration are the extra mass by the mechanical coupling, and the need for a more sophisticated propulsion control system. Additionally, the ICE's operation may be less optimal in different flight stages than in a series configuration since it is involved in thrust generation [13].

The overall hybridization factor is fixed by the amount of the battery mass that is possible to install onboard, in this exercise a 17% of "gross" hybridization factor is available. The electric power will be used only for the two key phases of take-off and climb, where the power demand on the ICE can be reduced by exploiting the available electric energy. The latter will help into scaling the maximum power of the ICE leading to a lighter ICE powerplant and lower fuel consumption. The splitting strategy between thermal and electrical power is defined by means of the power supply ratios being the ration between the electrical power over the total power needed for a specific flight phase. The best strategy in splitting the total amount of electric and thermal power has been found being 8% for the take-off and 4% in climb when the design mission of 600 NM is considered and 8% and 5.8% for take-off and climb respectively in the case of the typical mission. The energy histories of the hybrid-electric solution are shown in Fig. 4 for both the considered mission profiles.

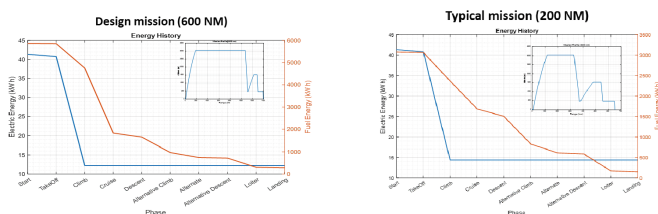


**Fig. 4.** Hybrid-electric P2012 like aircraft: energy profile for design and typical missions.

The selected hybrid-electric configuration leads to a fuel saving of about 18% on the design mission and 20% for the typical mission with respect to the conventional P2012

like aircraft (353 kg HEA vs. 433 kg of the conventional and 132 kg HEA vs. 166 kg of the conventional aircraft).

Since the overall structural mass of the HEA solution has been increased by 10%, part of the fuel saving comes from the scaling of the thermal engine since there is the augmentation of the electric motor drive. In fact, the overall powerplant system of the HEA is about 630 kg whereas for the conventional architecture was about 770 kg. The other part of the fuel saving comes from the lower thermal power used for both the take-off and climb leading to lower specific fuel consumption (for the climb phase).

### 3 Conclusions

This paper assessed a preliminary evaluation of the potential benefits of installing a SB concept on a 11-seaters aircraft like the P2012 Traveller.

A potential of 38% and 75% of wing and fuselage structural mass hosting the SB technology has been estimated. According to the current SoTA gravimetric energy density of SB of 75 Wh/kg and the estimated amount of available structural battery mass it has been demonstrated that an AEA solution is not viable. However, SB is still an intriguing enabling technology for the hybridization of such an aircraft.

By adopting a hybrid parallel power train in which the electric energy is used to augment the ICE during the takeoff and climb phase, a potential of 18–20% of the fuel burn has been achieved. Deeper investigations about the structural sizing of wing and fuselage are needed for the most reliable estimate of the SB mass available on the aircraft.

Structural battery is a promising enabling technology towards near zero emissions aircraft. But by the materials point of view, the SB cell net energy density needs to be increased to fit aeronautical needs. SB integration concepts for aeronautic applications need to be developed to optimize the position, shape, and distribution of SB cells within the structure to minimize the onset of damage. Moreover, reliable electrical wiring and connections will need to be integrated into the structure. Finally, a comprehensive understanding of the influence of SB integration on mechanical properties needs to be assessed both at a material and aeronautic structures level by developing characterization and testing methods to assess the multifunctional performance of aeronautic structural battery composite elements in complex-load cases.

### References

1. European Commission: Clean Sky Benefits. <https://www.cleansky.eu/benefits>. Accessed 13 July 2022
2. European Commission: Communication from the Commission—The European Green Deal. <https://eur-lex.europa.eu/legal-content/EN/TXT/?uri=COM%3A2019%3A640%3AFIN>. Accessed 13 July 2022
3. Friederich, C., Robertson, P.A.: Hybrid-electric propulsion for aircraft. *J. Aircr.* **52**(1), 76–89 (2015)
4. Riboldi, C.E.D., Trainelli, L., Mariani, L., Rolando, A., Saluzzi, F.: Predicting the effect of electric and hybrid-electric aviation on acoustic pollution. *Noise Map.* **7**, 35–56 (2020)
5. Riboldi, C.E.D., Gualdoni, F.: An integrated approach to the preliminary weight sizing of small electric aircraft. *Aerosp. Sci. Technol.* **58**, 134–149 (2016)

6. Ozawa, K.: *Lithium-ion Rechargeable Batteries*, 1st edn. Wiley–VCH, Weinheim (2009)
7. Pistoia, G.: *Electric and Hybrid Vehicles*, 1st edn. Elsevier (2010)
8. Leif, E.A., Johansson, M., Lindbergh, G., Xu, J., Zenkert, D.: Structural battery composites: a review. *Funct. Compos. Struct.* **1**(4), 1–19 (2019)
9. Kühnelt, H., et al.: Structural batteries for aeronautic applications - state of the art. *Res. Gaps Technol. Dev. Needs Aerosp.* **9**(1), 1–24 (2021)
10. Riboldi, C.E.D., Trainelli, L., Biondani, F.: Structural batteries in aviation: a preliminary sizing methodology. *J. Aerosp. Eng.* **33**(4), 1–15 (2020)
11. European Aviation Safety Agency (EASA): CS-23 Normal, Utility, Aerobatic and Commuter Aeroplanes (2012). <https://www.easa.europa.eu/sites/default/files/dfu/agency-measures-docs-certification-specifications-CS-23-CS-23-Amdt-3.pdf>. Accessed 14 July 2022
12. Wall, T., Meyer, R.T.: Hybrid electric aircraft switched model optimal control. *J. Propul. Power* **36**, 488–497 (2020)
13. Schömann, J.: *Hybrid-electric Propulsion Systems for Small Unmanned Aircraft in München*, Technical University, Dissertation (2014)



# Low-Velocity Impact Response of a Composite Structural Battery

Gennaro Di Mauro<sup>1</sup>(✉), Pietro Russo<sup>2</sup>, and Michele Guida<sup>1</sup>

<sup>1</sup> Department of Industrial Engineering, Università degli studi di Napoli Federico II, Naples, Italy

[gennaro.dimauro@unina.it](mailto:gennaro.dimauro@unina.it)

<sup>2</sup> Institute for Polymers, Composites and Biomaterials, National Research Council, Pozzuoli-Naples, Italy

**Abstract.** Recently, ambitious targets have been set out in various branches of transportation to restrict pollutant emissions and combat environmental degradation. In this frame, with specific reference to the aeronautic field, new designs incorporating electric or hybrid-electric propulsion systems face the problem of penalizing battery characteristics, in terms of energy density and power density. A new technology, with the potential to overtake such limitations, is constituted by structural batteries. These are multi-functional structural components, capable of both replacing stress-supporting parts and storing electrical energy.

In the literature, structural batteries can be classified into two categories: multifunctional structures and multifunctional materials. In the first case, different materials within the structural battery perform a single function (energy storage or load bearing), however, the overall composite is multifunctional, whereas in the latter all materials adopt multiple functions.

The purpose of this work is to establish the response of a composite structural battery in presence of a low-velocity impact. In this paper, the process used to manufacture a structural battery model is described. The experimental activity is performed by a customized drop tower. By following the ASTM D7136 standard, a ground frame is used to fix the specimen, whose acceleration time history at the impact is recorded by using a piezo-electric accelerometer. A load cell embedded into the hemispherical dart impacting the specimen is used to capture the load time history.

Drop test results are then compared to numerical ones, obtained by simulating numerically the impact test scenario using the explicit finite element code LS-DYNA.

**Keywords:** Structural battery · Multi-functionality · Drop tower · Impact test

## 1 Introduction

Nowadays there are several reasons to study alternative propulsion systems. As reported in [1], civil aviation within Europe is responsible for 13.2% of CO<sub>2</sub> emissions in the transport sector. The European Aviation Environmental Report 2019 shows a relative

increase of 16% in CO<sub>2</sub> emissions compared to the reference year of 2005 to 2017. A further increase of 42% is expected according to current models.

Besides that, the amount of oil is limited, and its price is progressively increasing. A resolution to these outcomes has been made by the European Flightpath, which set ambitious environmental goals for civil aviation. By 2050, the technologies are expected to reduce both CO<sub>2</sub> and NO emissions per passenger kilometer respectively by 75% and 90%. About aviation, hybrid and all electric aircraft represent higher steps toward environmentally friendly air transport. As of today, some all-electric aircraft have been designed and flown [2]. Most of them are basically electrified versions of existing gliders, others are very light machines, inspired by a corresponding conventionally powered aircraft in the light-weight sport aircraft category.

Concerning batteries, lithium-based are the preferred ones, since they have better performances in terms of energy density and volumetric energy density. Despite that, such battery parameters are exactly the limiting aspects for electrification in aircraft applications, especially when high-weight categories of aircraft are considered. Based on [3], once the energy amount is fixed, a lithium battery weighs about 60 times more and is about 18 times bigger than a kerosene system. Given such problems, all-electric aircraft might be successfully developed if a limited range is acceptable, which is currently the only feasible solution, but it is not the most attractive one; if significantly increased specific energy levels are reached, but estimations coming from battery developers give their availability within the next 10–20 years; if unconventional structures are developed, which is the most interesting roadable solution.

## 2 Structural Battery: A Promising Solution

Structural composites stand out as a possible solution to the problems mentioned before since they are capable to perform both the load bearing and the energy storing functions. In literature [4, 5], SB (Structural Battery) concepts are classified into 4 categories, based on the degree of integration parameter, which is used as a measure for the proportion by which a battery is integrated into a fiber-reinforced structure.

### 2.1 Integrated Conventional Storage (Type I)

The integration of commercial lithium batteries into a dedicated structural element, as shown in Fig. 1, represents the lowest degree of integration. It was the first and remains the most widely investigated approach. Weight savings are achieved by replacing the battery cover with a composite fiber material to get integration.

The mechanical and electrochemical performance depends on how many batteries are incorporated into the structure. A general trend is that the more batteries are incorporated, the higher the achieved energy density, but the lower the mechanical properties. Therefore, the main challenge remains to find the right compromise between the reduction of mechanical properties and the achievable energy density [7].

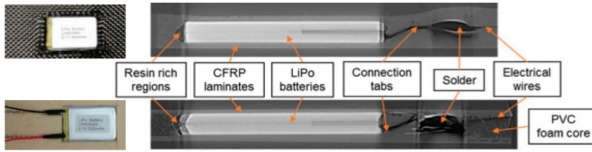


**Fig. 1.** Type-I SB examples: (top) composite laminate and (bottom) sandwich composite [6].

## 2.2 Integrated Thin-Film Energy Storage (Type II)

Integrating thin-film batteries into structural elements has the advantage of minimizing the impact of the battery on the mechanical properties of the composite structure. Unfortunately, very low energy densities have been reached with this approach and in addition, higher costs are expected since thin-film batteries are significantly more expensive than conventional cells.

## 2.3 Single-ply Functionalization (Type III)

Type-III structural batteries represent the first step toward true multifunctionalization. The idea behind this approach is to substitute the passive components of the conventional battery, with load-bearing elements, as shown in Fig. 2.

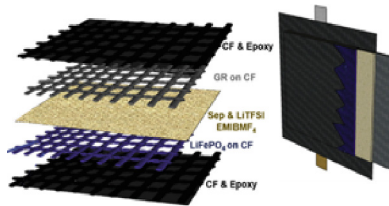


**Fig. 2.** Example of type-III SB [6].

Therefore, the cathode is usually prepared from conventional laminate electrodes or functionalizing carbon fibers with active materials like  $\text{LiFePO}_4$ . Carbon fibers can be also used for the anode, as they show similar performances to conventional graphitic materials. The separator can be obtained by a glass-fiber weave. Concerning the electrolyte, conventional liquid carbonates are still employed due to the lack of alternative highly conducting electrolytes with good mechanical and structural properties [8]. Working SBs belonging to this category have shown specific energies of  $12 \div 58$  Wh/kg and elastic or tensile modulus in the GPa range.

## 2.4 Constituent Functionalization (Type IV)

For type-IV SBs two different setups are proposed from the state of the art, the coaxial and layered ones. The coaxial approach envisions a fiber-shaped battery, which is composed of a carbon fiber core onto which an electrolyte layer is deposited; afterward, the fibers

are immersed into a matrix acting as the cathode material [9]. In the layered approach, carbon fibers act as the anode material as well, with coated carbon fibers acting as the cathode material. They are aligned to form electrode bands, separated by a thin layer of electrolyte [10]. Unfortunately, no functional type-IV structural battery offering significant energy storage and load-bearing capabilities has yet been demonstrated.

### 3 Numerical - Experimental Impact Test for a Structural Battery Model

#### 3.1 Experimental Activity

The purpose of the tests was to verify the behavior of laminates after a low-velocity impact test. The focus was on the evaluation of differences between laminated panels with and without an embedded battery, thus referring to a Type I SB. To simulate the presence of the embedded battery from a mechanical point of view, a through-the-thickness discontinuity was needed, thus a Teflon layer has been inserted between the plies of the laminate during the manufacturing. A single panel is created, then cut to obtain 4 specimens: 2 of them with the embedded Teflon layer and the other two without it (Fig. 3). A hand-lay-up process has been applied, impregnating the dry carbon fabric with epoxy resin. A  $200 \text{ g/m}^2$  plain fabric has been used, for a total of 12 plies. Teflon is applied between the 6<sup>th</sup> and 7<sup>th</sup> plies of the laminate during the manufacturing process, performed by both controlling pressure and temperature respectively with a vacuum pump and an oven.



**Fig. 3.** Laminated specimens with (right) and without (left) the embedded Teflon layer.

Once realized, the specimens were subjected to impact tests, thanks to the availability of a small-customized free fall drop tower. The sample to be tested is fixed with the aid of ground support. It consists of a metallic frame, which is characterized by a rectangular hole (whose dimensions are given by ASTM D7136 requirement [11]), enabling the deflection of the sample subjected to the impact test. To obtain the desired boundary conditions, four clamps are mounted on the ground frame to make it possible to lock the sample on the edges.

The drop tower is instrumented with a set of sensors that allow measuring force and acceleration: a piezoelectric accelerometer is used to measure the acceleration on the impacted sample, while a quartz piezoelectric force sensor is directly exposed to the force at impact and with a stiffness required to measure high impact force with fast rise time. Figure 4 shows the general set-up for the performed tests.

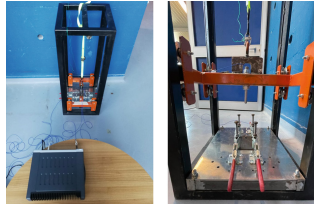


**Fig. 4.** Test set-up.

### 3.2 Modeling Procedure

The SB type-I model has been performed in LS-DYNA, considering the corresponding experimental test. A rectangular 150 mm × 100 mm laminate (3.6 mm thick) has been modeled by using solid squared elements. The dimensions of the mesh elements have been set to have a right compromise between computational time and the accuracy of the expected results. The same considerations are valid also for the spherical dart. The laminate is clamped at the edges, and the dart is given a mass of 13.4 kg (to account for the whole falling frame weight) and a velocity constant profile with 0.7 m/s magnitude.

In order of having a safer model validation, it was initially chosen to consider the structure without a Teflon layer through the thickness. After that, the addition of a Teflon layer simulating the presence of the battery has been performed. The solid element has been inserted between the 6<sup>th</sup> and 7<sup>th</sup> plies of the laminate.

LS-DYNA has several stress-based composite continuum damage mechanics (CDM) material failure models, implemented as standard in the software package. The adopted material model is the model MAT-22, used for orthotropic-elastic material models meshed through solid elements.

### 3.3 Experimental-Numerical Correlation

In the considered application, the drop tower falling frame is dropped from a height of 3 cm. The experimental results have been compared with the numerical simulation outputs, both the acceleration evaluated on the specimen and the force at the impact (Fig. 5). Notice that the outputs of the experimental tests have been averaged and treated by a Gaussian filter. Another aspect to consider concerns the absence of an anti-rebound system for the drop tower, thus only the first peak value of each curve is considered.

Notice that the numerical model effectively reproduces the impact dynamics and time history of the impact force and acceleration, but the FE model is to be improved with more experimental tests. The main purpose of such a global analysis is to try to gain an understanding of the behavior of vibro-impacting systems and the situation, thanks to this preliminary experimental test, it is clear cut. Besides that, a comparison between the two numerical considered tests has been performed. Figure 6 shows the comparison between the vertical directed stresses for the two laminates, with and without the embedded teflon layer. The introduction of the battery into the laminate determines the onset of stress concentration zones between the ply of the laminate with possible delamination creation.

Such a result is confirmed also from an experimental point of view. A careful scan of impacted specimens has been performed to assess possible damage after the impact



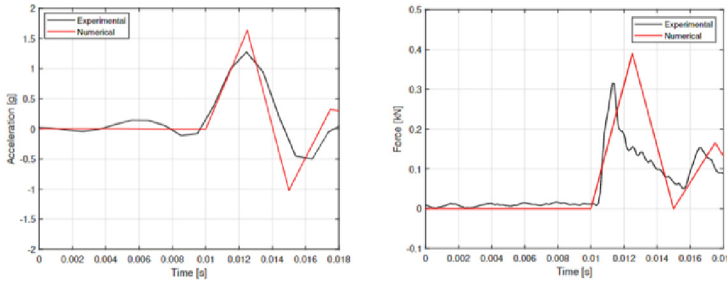


**Fig. 5.** Numerical-experimental comparison of acceleration and force on the specimen.

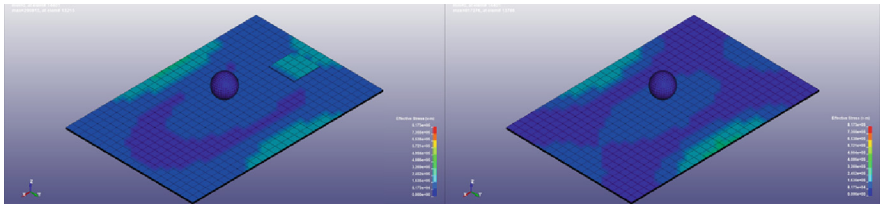


**Fig. 6.** Comparison of the vertical directed stresses for the laminate with (left) and without (right) the embedded teflon layer.

tests. An Omniscan SX from Olympus equipped with a 64-element inline, 5 MHz flat phased array probe has been used. It results, as shown in Fig. 7, that a small discontinuity is created at the teflon layer location for the SB model, which is not the case for the panel without the Teflon disk.

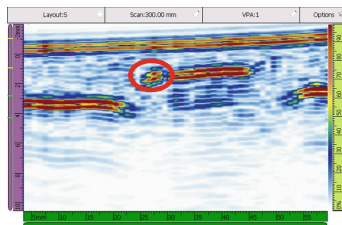


**Fig. 7.** Delamination onset after the impact for the laminate with the embedded teflon layer.

## 4 Conclusions

The main points concerning applications of multifunctional SB in the aeronautic field, arising from the most relevant state-of-the-art literature available publications have been presented and discussed. A focus on type I SB has been performed, through the realization of a composite laminate in which a teflon layer was embedded to create a discontinuity. Impact tests were chosen to prove the damage tolerance of the manufactured type-I

structural battery model. The numerical analysis, performed by the LS-DYNA software, confirms that the most critical area for the SB model is the one involving the embedded battery itself. Such a result is confirmed also from the experimental side by C-SCAN analysis on impacted specimens. Thus, it results that the area to be taken into account for type-I SBs, at least from a damage tolerance point of view, is the one involving the battery embedding, given the deviation and/or the interruption of the fiber in that location.

## References

1. Schefer, H., et al.: Discussion on electric power supply systems for all electric aircraft. *IEEE Access* **8**, 84188–84216 (2020)
2. Riboldi, C., et al.: Structural batteries in aviation: a preliminary sizing methodology. *J. Aerosp. Eng.* (2020)
3. Rohacs, J.: Conceptual design method adapted to electric/hybrid aircraft developments. *Int. J. Sustain. Aviat.* **5**, 175 (2019)
4. Adam, T.J., et al.: Multifunctional composites for future energy storage in aerospace structures. *Energies* **11**, 335 (2018)
5. Kühnelt, H., et al.: Structural batteries for aeronautic applications - state of the art, research gaps and technology development needs. *Aerospace* **9**(1), 1–24 (2021)
6. Asp, L.E., Johansson, M., Lindbergh, G., Xu, J., Zenkert, D.: Structural battery composites: a review. *Funct. Compos. Struct.* **1**(4), 042001 (2019)
7. Ladpli, P., et al.: Multifunctional energy storage composite structures with embedded lithium-ion batteries. *J. Power Sources* **414**, 517–529 (2019)
8. Snyder, J., et al.: Electrochemical and mechanical behavior in mechanically robust solid polymer electrolytes for use in multifunctional structural batteries. *Chem. Mater.* **19**, 3793–3801 (2007)
9. Xu, J., et al.: Multiphysics modeling of mechanical and electrochemical phenomena in structural composites for energy storage: single carbon fiber micro-battery. *J. Reinf. Plast. Compos.* **37**, 701–715 (2018)
10. Carlstedt, D., et al.: Conceptual design framework for laminated structural battery composites. In: *Proceedings of the 18th European Conference on Composite Materials, Athens, Greece*, pp. 24–8 (2018)
11. ASTM International. ASTM D7136, 2017: Standard Test Method for Measuring the Damage Resistance of a Fiber-Reinforced Polymer Matrix Composite to a Drop-Weight Impact Event (2017)



# Impact Dynamics of Different Cabin Solutions of Small Airplanes

Gennaro Di Mauro, Giuseppe Maurizio Gagliardi<sup>(✉)</sup>, Michele Guida,  
and Francesco Marulo

Department of Industrial Engineering, University of Naples “Federico II”, Via Claudio, 21,  
80125 Naples, Italy

[giuseppemaurizio.gagliardi@unina.it](mailto:giuseppemaurizio.gagliardi@unina.it)

**Abstract.** An important matter concerning small airplanes is the crashworthiness of the vehicle impacting the ground, thereafter the parachute opening. The current regulations for the emergency landing dynamic conditions CS 23.562 expect that seat design satisfies the requirements in vertical and horizontal test conditions. This work aims to compare two different aircraft configurations: a low-wing metallic and a high-wing composite one. Both the airplanes are two-seaters and single-engine equipped. The target of the analysis is the check of the compliance with human tolerance to injury criteria by the seats and the restraint system, and the determination of the possible strikes of the occupants inside the habitable space as a consequence of the impact loads. Finite element analysis of a partial section of the fuselage for both the configurations has been performed utilizing the commercial solver LS-Dyna. A parametric analysis is performed in order to find out the best impact angle in terms of the lumbar loads and the loads transmitted by the belts as a consequence of the contact between the aircraft and the ground, so to improve the level of safety. The performed investigation could be an important indication for the parachute system design.

**Keywords:** Impact · Emergency Landing · Composite Material ·  
Crashworthiness · Finite Element Analysis

## 1 Background

The safety of General Aviation (GA) remains a challenging issue, as evidenced by the persistently high accidental mortality [1, 2]. Various factors are associated with lethal outcomes, including flight phase, meteorological conditions, terrain, and pilot characteristics [3]. Fatal accidents are usually high-energy events due to flight speed, impact force, and impact angle. During a fatal impact, deceleration occurs when hitting the ground, resulting in a transfer of force that is often beyond human biomechanics. Studies have shown that the speed and elevation angle of an aircraft during impact affects survivability [4]. Efforts to reduce fatalities have focused on pilot training and reducing impact force transmission through the implementation of energy-absorbing structures. These efforts include a Federal Aviation Administration (FAA)-approved pilot safety

course, crash fuselage, shoulder harnesses, energy-absorbing seats, and airbags. More recently, Ballistic Parachute Recovery Systems (BPRS) have been incorporated into GA aircraft as a method to improve crash survival. Two major operational changes occur with a deployed BPRS: pilot control is no longer necessary for the aircraft descent and the speed is reduced before impact occurs [5, 6]. Nowadays Cirrus company equips many of their aircraft with this recovery system, which they named Cirrus Airframe Parachute System (CAPS) [7–9]. An exhaustive study about the design, manufacturing, testing, and operation procedure of parachute recovery systems can be found in [10].

An important matter concerning the parachute emergency landing is the crashworthiness of the vehicle impacting the ground, thereafter the parachute opening. The current regulations for the emergency landing dynamic conditions CS 23.562 expect that seat design satisfies the requirements in lumbar and shoulder loads: 680 kg and 794 kg respectively. The target of this work is the check of the compliance with human tolerance to injury criteria by the seats and the restraint system, and the determination of the possible strikes of the occupants inside the habitable space as a consequence of the impact loads. The main aim is to define the best impact angle in terms of lumbar loads and loads transmitted by the belts during the contact between the aircraft and the ground, to improve the level of safety. In this manner, it is possible to properly design the parachute ropes to have the impact on the ground at the best elevation angle in terms of occupants' safety. This work aims to compare two different aircraft configurations (low-wing metallic and high-wing composite) and evaluate their differences in terms of crashworthiness.

## 2 Finite Element Analysis

The FE analysis is addressed to investigate the behavior of a light airplane during an emergency landing by parachute. The attention is dedicated to the problem of fuselage crashworthiness so to define the limit loads transmitted on passengers. The main aim is to define the best impact angle in terms of the lumbar loads and loads transmitted by the belts for the two aircraft configurations and make a comparison between them. Finite Element analysis of a partial section of the fuselage has been performed using the LS-Dyna software. The models include seats, restraints, dummies, and the structural elements that could intercept the trajectory of the passengers during the crash events. The models are shown in Fig. 1.

The model consists of:

- **Fuselage:** a truss and skin-based model in the first case and a shell model for the second case.
- **Ground:** it has been modeled as a rigid plate.
- **Seats:** the seat and the back are modeled as two plates.
- **Dummy:** two hybrid III dummies are imported to investigate the human evolution during the impact. Surface-to-surface contact algorithms assigned to model the interaction between the dummies, the cushions and the structures are considered. For the simulations, two different parameters have been considered: lumbar loads and loads transmitted in the proximity of the interaction between the belt and the shoulder.
- **Belt:** The material is polyester, and two attachment points are considered directly connected to the seat structure.

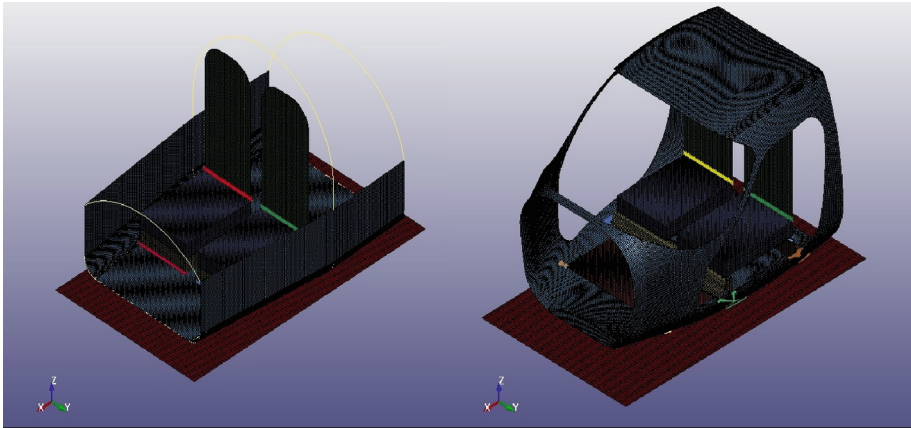


**Fig. 1.** Low-wing metallic (left) and high-wing composite (right) FE Models.

- **Cushion:** the square seat cushions have been realized in Polyurethane DAX 26 foam, commonly in use in aircraft seats manufacturing, with a density of 38 kg/m<sup>3</sup>, and a Young Modulus of 0.5 GPa.

In this study, the attention is focused on the fuselage frame, so not including the landing gears, wings, vertical and horizontal rudders. This solution guarantees to evaluate the ability of the fuselage and the seats to absorb the energy during the emergency landing.

### 3 Sensitivity Analysis

A sensitivity analysis has been performed for both configurations by varying the impact angle. Since both the aircraft have forward-located engines and propellers, the center of gravity lies quite ahead. At the same time, it is not possible to locate the parachute attachment too forward. Consequently, the airplane has a negative elevation angle during the impact on the ground. Properly designing the parachute strips, it is only possible to make minor changes in the impact angle. Thus, angles between 9° and 21° have been simulated. From the numerical model point of view, the variation in the impact angle has been simulated by inserting the two vertical and horizontal components of the velocity vector. The magnitude of the velocity vector is the same for all the tests: 30 ft/s (9.14 m/s). Only its direction has been changed to properly consider the impact angle.

### 4 Results

This research study is to explore the safety differences when using the aluminum and fiber reinforced composite as material for the fuselage of light aircraft under a crash landing. The overall safety zone of the carbon fiber reinforced composite is higher than that of the aluminum fuselage.

The aircraft are not comparable because the carbon fiber is applied on the high wing configuration, differently the aluminum alloy is considered in the low wing aircraft, but

for the samples in this study, in the process of crashing to the ground, the kinetic energy is the same and for both configurations decreased gradually and tended to be stable after the collision, whereas the internal energy increased with time and finally the total energy is conserved.

This study puts in evidence how the problem of the attenuation of both the compressive force transmitted to the spinal column of the occupant of a light aircraft and the shoulder hardness for the seatbelt, are two critical aspects in the evaluation of crashworthiness performances. Figure 2 reports the comparison between these values for all the impact angles about the low-wing aluminum aircraft. This allows for investigating the angle of attack in terms of peak and duration of the load transmitted along the shoulders. All the analyzed configurations present peaks quite below the limit (7.94 kN). However, among all the curves, the best condition is 15°.

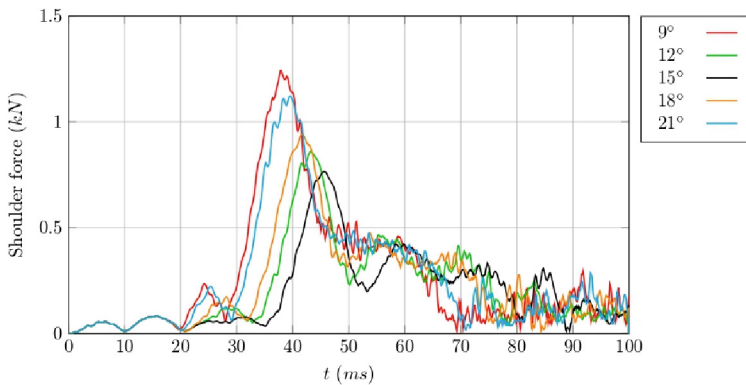


**Fig. 2.** Loads transmitted by the belt for various impact angles, low-wing aluminum aircraft.

A similar approach is considered for the loads transmitted in the lumbar zone (Fig. 3), where the better condition is again 15°. In this case, this represents the limit of the regulation, but the margin is enough high, also in terms of angle. Even if the optimal angle is not obtained, the curve is still under the limit.

Concerning the composite aircraft, the shoulder loads are increased, due to the higher stiffness of the cabin (Fig. 4). Looking at the lumbar curves, higher forces with respect to the aluminum case are evaluated. Moreover, only the optimal case (15°) is below the limit. Therefore, a very low range in terms of angles is obtained. Consequently, the application of a parachute on a composite aircraft must be properly evaluated. In addition, the tolerance of the impact angle must be increased with the use of other devices, such as shock-absorbing seats.

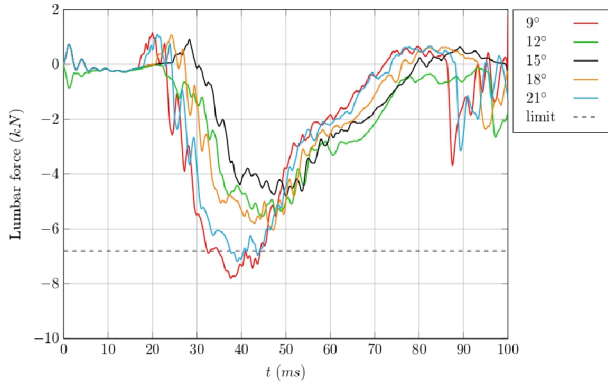


**Fig. 3.** Loads transmitted in the lumbar zone for various impact angles, low-wing aluminum aircraft.

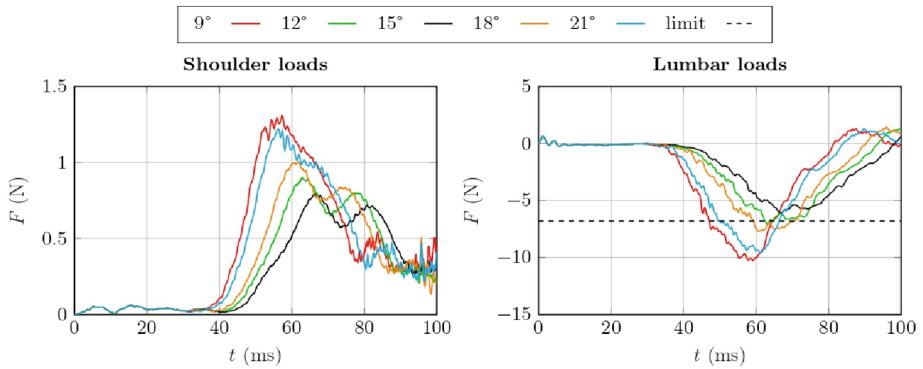


**Fig. 4.** Shoulder and lumbar loads for various impact angles, high-wing composite aircraft.

## 5 Conclusions

In this paper the parachute emergency landing problem and the current state-of-art on this topic have been defined. Attention was dedicated to the loads transmitted to the occupants on two light aircraft configurations: a low-wing in aluminum alloy material and a high-wing composite one. A FE Model of the cabin for both the configurations has been made up to perform a parametric analysis and find the best impact angle for the occupants' safety. The impact angle information is an important design indication for the parachute ropes. The analysis of the lumbar and shoulder loads verified compliance with the CS-23 requirement and possible strikes of the occupant in the habitable space have been evaluated. This work showed the possibility of equipping a composite aircraft with a parachute. The analyses revealed higher shoulder and lumbar loads and a very low margin with respect to the limitation for the last case. Therefore, the equipment of a composite aircraft with a parachute system has to be properly evaluated and additional devices have to be utilized.

## References

1. NTSB. Review of U.S. civil aviation accidents, calendar year 2011. National Transportation Safety Board (NTSB), Washington (DC); Report No.: NTSB/ARA-14/01 (2014)
2. Veronneau, S.J., Ricaurte, E.M.: Aircraft accidents: investigation and prevention. In: Davis, J.R., Johnson, R., Stepanek, J., Fogarty, J.A. (eds.) *Fundamentals of Aerospace Medicine*, pp. 560–566. Lippincott Williams & Wilkins, Philadelphia (2008)
3. Wiegmann, D.A., Taneja, N.: Analysis of injuries among pilots involved in fatal general aviation airplane accidents. *Accid. Anal. Prev.* **35**(4), 571–577 (2003)
4. NTSB. Safety report, general aviation crashworthiness project: phase two – impact severity and potential injury prevention in general aviation accidents. National Transportation Safety Board (NTSB), Washington (DC). Report No.: NTSB/SR-85/01 (1985)
5. Alaziz, M., Stolfi, A., Olson, D.M.: Cirrus airframe parachute system and odds of a fatal accident in Cirrus aircraft crashes. *Aerosp. Med. Human Perform.* **88**(6), 556–564 (2017)
6. Thomas, R., Thomas, D.: Design analysis of an aircraft parachute recovery system for very light jets. In: *The 26th Congress of ICAS and 8th AIAA ATIO* (2008)
7. Yeakle, J., Lingard, J., Underwood, J., Gudmundsson, S.: Computer simulation of a whole-aircraft parachute recovery system. In: *20th AIAA Aerodynamic Decelerator Systems Technology Conference and Seminar* (2009)
8. Overend, S., Underwood, J., Yeakle, J.: Testing of a two-stage reefed 27 m polyconical parachute for the Cirrus Jet. In *21st AIAA Aerodynamic Decelerator Systems Technology Conference and Seminar* (2011)
9. Winter, S.R., Fanjoy, R.O., Lu, C.T., Carney, T.Q., Greenan, J.P.: Decision to use an airframe parachute in a flight training environment. *J. Aviat. Technol. Eng.* **3**(2), 28 (2014)
10. Knacke, T.W.: *Parachute recovery systems design manual*. Naval Weapons Center, China Lake, CA (1991)





# Design of Controlled Rupture Structure for Safe Vector Ejection

Aniello Smarrazzo<sup>1</sup>, Michele Guida<sup>1</sup> (✉), Francesco Marulo<sup>1</sup>, M. Coppola<sup>2</sup>,  
and R. Moliterno<sup>2</sup>

<sup>1</sup> Department of Industrial Engineering, Università degli Studi di Napoli, Federico II, Naples,  
Italy

michele.guida@unina.it

<sup>2</sup> MBDA ITALIA, Via Carlo Calosi, 1, Bacoli, 80070 Naples, Italy

**Abstract.** The design of controlled-fracture structures is of interest to both civilian and military industries, and the definition of design guidelines and criteria may be useful for future design configurations. In the automotive, aerospace, and defense industries, study solutions can be useful to meet stringent requirements for lightness and safety, and recent studies on composites and associated fracture micromechanics can help achieve these goals. Emphasis is placed on evaluating the element cancellation after excessive deformation and the behavior of the structure when it breaks at high velocity into controlled and tightly distributed fragments around one or more specific dimensions. The research activity is focused on numerical analysis to design a potential component for new ship gunnels. In particular, the design of a new tailgate configuration was investigated, taking into account the correct fragmentation of the structure to ensure a clear ejection while reducing the weight of the panels by exploiting the properties of the composite material. The complex geometry of the tailgate, the high impulse load, the energy transferred to the tailgate during missile impact, and how to safely break large panel flaps are elements that characterize the sizing of the composite material to meet the stringent ejection requirements in the life cycle of a missile during takeoff.

**Keywords:** Progressive failure · Composite material · FE non linear Analysis

## 1 Introduction

A missile canister protects the missile from foreign object intrusion, shock, and weather effects such as rain and waves, and facilitates smooth ejection during launch. The preferred canister cover is usually the rupture-type, which is easily manufactured and provides excellent handling. However, if the missile canister cover does not break during launch, it could potentially compromise the adjacent structure. An innovative concept for a hatch, consisting of a single carbon fiber composite laminate, is investigated, and by varying the geometric configuration, it is possible to optimize the fracture path and the contact force. In particular, in order to trigger the fracture, some areas without fibers

called carvings, were formed to delineate triangular fragments, which were named petals. The aim is to design a suitable tailgate shape that improves reliability and ensures safe launch and good protection during the life of the missile. The goal of this work is to develop a scientific and methodological approach to the study of the controlled fracture structure for the design and optimization of the missile tailgate. The sea canister is the enclosure that contains the missile on the deck of the ship and is the only protection from external impact. The canister is usually made of metal, while the cover is made of polymer or ceramic materials. To prevent damage to the missile tip, in some cases a sabot is inserted between the missile and the cover to reduce the impact force.



**Fig. 1.** Examples of similar applications for canisters (Marte ER and Aster system).

Usually, the type of tailgate varies according to size, velocity envelopes and environment. Small size missile covers consist of flexible or breakable tabs, while medium and large size missile tailgates have a mechanical opening or are rupture-type which have a programmed break. Common configurations have a four-pavilion dome, and the missile is placed on a trolley in the canister as shown in the figures below.

In the left of the Fig. 1, there is the application about the Marte ER, one of the most successful missiles produced by MBDA, has a four-pavilion configuration with an internal stiffener at the tip which puts in contact the missile tip and the tailgate top. The stiffeners and the tailgate design provide proper tailgate fragmentation, reducing contact force and accelerating the petals.

## 2 Best Practices for the Design of Rupture-Controlled Structures

There are several studies and discussions on the design of structures involved in crash events. The goal is to lead us to a strategic design of the structure by establishing guidelines and design criteria. For this purpose, it is very important to determine the probable impact conditions, considering impact velocities and angular velocities. The following concept map (Fig. 3) presents a possible workflow for designing a structure that achieves all objectives. Once the impact scenario and boundary conditions are determined, the impact force is estimated, and the allowable motions are defined. These represent the spatial structure design criteria and the hardness design criteria. If both requirements are met, a structure can be idealized in the first attempt, but weight is still a constraint. By iterating the procedure, the structure will meet all the targets.

Failure criteria for composite materials are often classified into two groups:

- *non-interactive failure criteria* (associated with failure modes) or limit criterion is defined as one having no interactions between the stress or strain components. In detail, it means that the failure criterion evaluates failure based on a single stress component and does not take into consideration a multi-axial stress state in the structure and how the combination of different stress components affects the failure initiation in a ply;
- *interactive failure criteria* (associated with failure modes and not) involves interactions between stress or strain components. The objective of this approach is to allow the fact that failure loads, when a multi-axial stress state exists in the material, may well differ from those when only a uniaxial stress is acting. Interactive failure criteria splits into three categories: polynomial theories, direct mode determining theories, and strain energy theories. The strain energy theories are based on local strain energy levels determined during nonlinear analysis (Fig. 2).

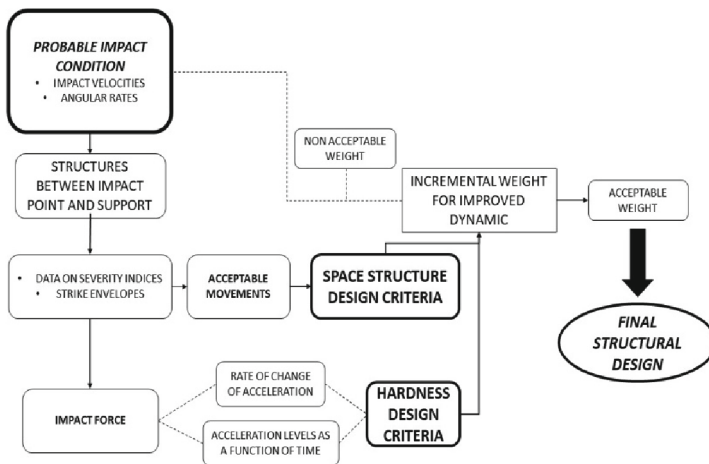


Fig. 2. Concept Map: Design of Rupture-Controlled Structures Flow Chart.

The LS-DYNA software has in its library several material models (constitutive law and failure criteria) specifically designed for composite materials when they are simulated exploiting a macro homogenous approach. In this case, the fibre and matrix are not reproduced separately but in a unique assembly. Therefore, it is fundamental to have a reliable criterion that allow mimicking both the constitutive behaviour and the failure mechanisms. MAT54 is designed specifically to simulate orthotropic materials with greatly differing properties in the longitudinal and transverse directions, such as unidirectional (UD) composite laminates and not fabric materials. For this reason, it implements a matrix-specific failure criterion in the transverse direction that would not be appropriate to evaluate a fiber-dominated material. Nevertheless, MAT54 has been used to simulate fabric composite structures in crash simulations.

MAT54 - MAT\_ENHANCED\_COMPOSITE\_DAMAGE is based on the Chang – Chang failure criteria for the damage onset and has a linear elastic behaviour before reaching the materials strength. Therefore, before the damage occurs, the model has a linear elastic behaviour. When the maximum stress is reached, the damage initiates. Basically, this model assumes three different in-plane failure modes: matrix cracking, fibre-matrix shearing, and fibre breakage. In addition to this, for material model 54 a compressive failure is considered.



**Fig. 3.** Chang-Chang Failure Criteria.

The minimum time step is defined by the highest distorted element. The parameters listed above are useful not only because they are necessary for deleting the elements but also because it is possible to tune the post damage behaviour. Regarding the contacts, it was noticed that the contact between plies is a critical aspect regarding composite modelling since inter-laminar behaviour is complex to model and it plays a fundamental role in impacts events.

### 3 Tailgate Design

The design of a breaking path begins with the analysis the impact scenario, focusing on the geometric shape, materials and their speed envelopes.

The tailgate has a square shape which can be considered planar to a first approximation. This is useful to observe the stress distribution between the impact point and the support, and several simulations were performed varying the material, geometry and configuration. The numerical finite element simulations were performed using the commercial code LS/Dyna with its explicit and implicit formulation; however, the implicit code works until the onset of fragmentation, then numerical instability and difficulties in managing contacts affect the performance of the simulation. The simulation has been performed using a rigid spherical impactor of radius 95 mm at 94 mm from the plate accelerating at  $150 \text{ m/s}^2$  (about 15 g), which is like a speed envelope of naval missile during the ejection. The sphere strikes the plate at a velocity of  $5,3 \text{ m/s}^2$  after 0,035 s. To reduce the computational time the sphere has been placed at 10 mm with an initial velocity of 5,025 m/s. After studying the isotropic material behaviour as reference case, the attention was dedicated on the composite material to satisfy the lightness requirement, and it has been chosen a carbon/epoxy laminate.

Initially, it was considered the analysis of a planar hatch with 4 petals and cruciform carvings, but to meet the design requirements, the concept of asymmetric impact must be introduced. The latest missile configurations have a low nose, so the contact between

the tailgate and the missile tip is not centred, which could compromise fragmentation and does not ensure safe ejection. For the simulation it has been considered that the contact is at the 66,5% of one edge while on the other side it is symmetric. In this case the lower petal, which is the largest one, is divided into two smaller triangular petals by introducing a carving along the height of the triangle (Fig. 4).

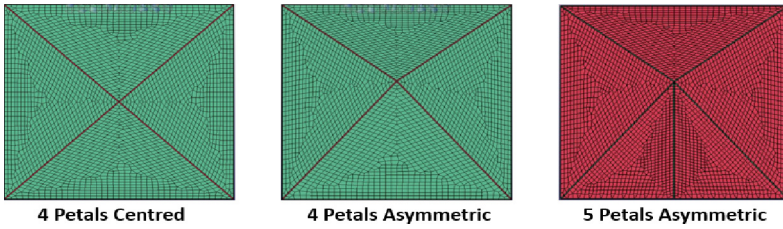


Fig. 4. Planar Tailgate configuration.

As a result, in the asymmetric solution with 4 petals, catastrophic failure occurs and fragmentation is not completed, the upper petals detach from the tailgate, but the lower petals do not, and this can be an obstacle to the launch because the debris is too large. The asymmetric configuration with 5 petals achieves a good breaking path, but the stresses are too high, and the petals detach at the same time, hindering launch (Figs. 5 and 6).

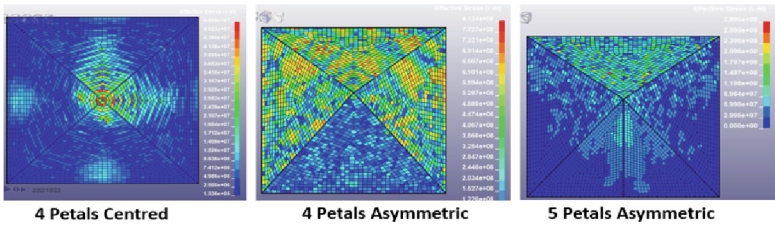


Fig. 5. Planar Tailgates: Stress Distribution.

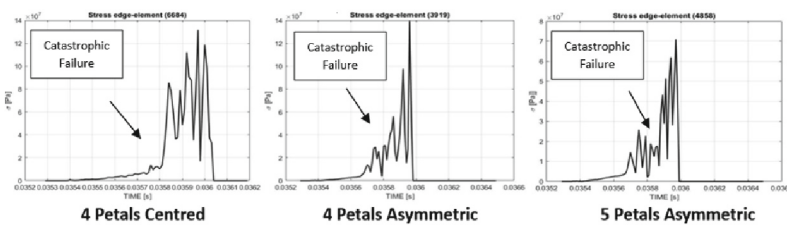


Fig. 6. Planar Tailgates: Contact Force.

An angled impact helps to exploit the constant acceleration profile and the angle to reach a higher rotational speed of petals around the sides during the impact and therefore a greater kinetic energy. Other two configuration were investigated: a pyramidal multifaced

and a pavilion dome to improve the fracture behaviour and the load distribution (Figs. 7, 8 and 9).

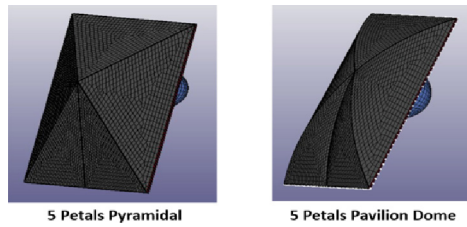


Fig. 7. Pyramidal and Pavilion Dome Tailgate configuration.

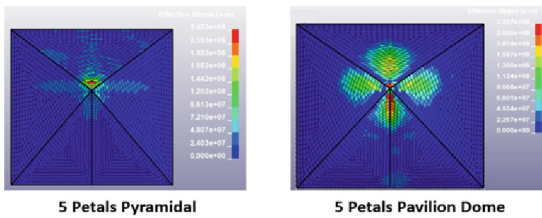


Fig. 8. Pyramidal and Pavilion Dome Tailgate configuration: Stress distribution.

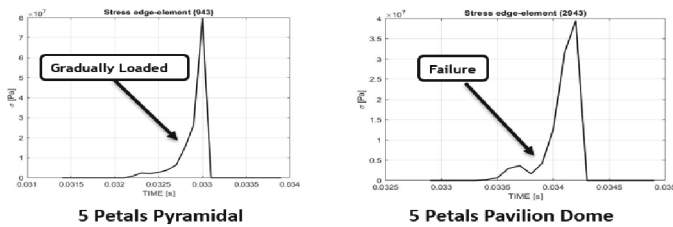


Fig. 9. Pyramidal and Pavilion Dome Tailgate configuration: Contact Force.

## 4 Conclusion

The five simulation models consist of three shapes configurations (planar, pyramidal, dome) respecting the overall dimensions and the weight limitations. The best solution for the static requirement is the pavilion dome because in addition to supporting the static “wave load”, it allows to manage the breakage by pressure load, but this aspect must be further studied.

The following table is a summary of all the results collected:

Configuration	Time	Breakage Time	Von Mises Stress	Weight
Planar 4 Petals Centred	0,035 s	$7 \times 10^{-4}$ s	131 MPa	2,02 kg
Planar 4 Petals Asymmetric	0,035 s	$6 \times 10^{-4}$ s	139 MPa	2,10 kg
Planar 5 Petals Asymmetric	0,035 s	$6 \times 10^{-4}$ s	70 MPa	2,08 kg
Pyramidal Multifaced	0,032 s	$1,4 \times 10^{-3}$ s	79 MPa	2,80 kg
Pavilion Dome	0,033s	$1 \times 10^{-3}$ s	39 MPa	3,17 kg

Planar configuration are lighter, but it has a faster and more sudden breakage, and this can lead to the uncorking of the tailgate or damaging the missile tip. The stresses are very high in both symmetric and asymmetric impact but introducing carvings can mitigate the peak of stress by having a progressive failure.

The introduction of an impact angle due to multifaced pyramidal and dome structures exhibited a smoother behaviour, but for the pyramidal one, the contact force is more concentrated, causing indentations while the pavilion dome exhibits a softer and more gradual contact.

## References

1. Guida, M., Marulo, F., Meo, M., Riccio, M.: Analysis of bird impact on a composite tailplane leading edge. *Appl. Compos. Mater.* **15**, 241–257 (2008)
2. Grimaldi, A., Sollo, A., Guida, M., Marulo, F.: Parametric study of a SPH high velocity impact analysis a birdstrike windshield application. *Compos. Struct.* **96**, 616–630 (2013). <https://doi.org/10.1016/j.compstruct.2012.09.037>
3. Tsartsaris, N., Dolce, F., Polimeno, U., Meo, M., Guida, M., Marulo, F.: Low velocity impact behavior of fibre metal laminates. *J. Compos. Mater.* **45**(7), 803–814 (2011). <https://doi.org/10.1177/0021998310376108>
4. Choi, W., Jung, S.: Launch Performance degradation of the rupture-type missile canister. *Appl. Sci.* **9**(7), 1290 (2019). <https://doi.org/10.3390/app9071290>



# Design of a VLA Vertical Control Surface with LRTM Technology

Massimo Viscardi<sup>(✉)</sup> 

Industrial Engineering Department - Aerospace Division, University of Naples “Federico II”,  
Via Claudio, 21, 80125 Naples, Italy  
massimo.viscardi@unina.it

**Abstract.** The present work is connected to a research project that faces the study of low-cost manufacturing technologies and processes of aeronautical structures made of composite material, referring to aircraft belonging to General Aviation (GA). In the specific, the main purpose of this work consists in the design and manufacturing of the vertical control surface of an aircraft belonging to the VLA class using Light Resin Transfer Moulding (LRTM). Starting from the geometrical characteristics of the control surface and the peculiarities of the related aircraft, the relative load distribution has been calculated according to the requirements expressed in Appendix B of CS-VLA regulations. Using a numerical simulation software for finite element analysis, the load, calculated by the procedure in question, has been used as input to the FEM model for the purpose of structural design, i.e. for the choice of the materials and of an appropriate stacking sequence. Once the model has been completely defined, it has been possible to design and to fabricate the moulds for the following phase, which consists in the production of the prototype.

Following the production process, the last part of the work focuses on the preparation and the implementation of an experimental campaign that aims at verifying the quality of the infusion process (C-Scan) and of the structural properties of the component, paying attention to the comparison with the previously obtained numerical results.

**Keywords:** Aviation · Composite · LRTM · FEM · Structural Testing

## 1 Introduction

Great attention has been given, within the last decade, to the use of composite materials in aeronautical field; in fact, the interest for composite airframe structures is common to very light airframe (VLA), CS23 aircrafts (up to *Commuters*), and airliners. However, this has made it necessary to develop new certification and to afford new operational problems through analytic and experimental study.

The study of new materials and processes aims to the design and production of prototypes in order to modify already existing aircraft components or to introduce innovative elements.



Cost impact is of fundamental importance, starting from storage up to final inspection; however, especially for VLA category aircrafts, the final customer can often ask for specific requirements that can be onerous in terms of costs and certifications. It is the case, for example, of specific electronic equipment that, in order to be installed, needs to respond to IRF requirements. Maintenance features are linked to manufacturing and inspection processes that constitute part of the program object of study; in fact, the use of composites can be an advantage in some respects, such as corrosion features, but there are some other parameters of fundamental importance (such as repair issues, thermal behaviour and inspection features) that must be considered and accurately studied when producing a composite aircraft. Because of this, the program is based on a *concurrent engineering* approach defining material characteristics, processing and inspection technologies to be set up in an iterative loop to support structural design from the beginning of aircraft development.

Unless otherwise indicated, main airframe structures involved in the study are made of carbon fibre reinforced composites, while fibreglass is a support material for interfaces and secondary aerodynamic shape parts or system installation.

The present activities have been developed within the TABASCO research program [4]. The project focuses on low-cost technologies and manufacturing processes for *General Aviation* (GA) airframe structures. The acronym stands for “*Tecnologie e Processi di Produzione A BASSo Costo per Structure in COmposito per Velivoli Avanzati*” (*Low Cost Technologies and Manufacturing Processes for Advanced Aircraft Composite Structures*). The funder of the project is the *Campania Aerospace Technological District* (DAC S.c.a.r.l.) and the partnership is composed by aircraft manufacturers, SME and Consortium Companies operating in GA.

The main purpose of TABASCO is to develop new technologies to support applications for GA aircrafts, in particular in terms of: design, manufacturing, inspection and test, certification and maintenance.

The specific target of the reference subtask is the design of a typical VLA component (generally made of aluminium alloys 20XX, 70XX, and 60XX) by the use of carbon fibre with special focus of the manufacturing technologies and tool's chain costs that needs to remain very low to open real market opportunities.

For this reason, special attention has been paid to LRTM process. Light resin transfer moulding is a variation of RTM, although it is very similar to VIP (*Vacuum Infusion Process*). Due to its low tooling costs, it is recently becoming one of the most used closed moulding processes for low or medium applications, displacing conventional RTM process in many applications requiring two finished sides and close dimensional tolerances.

One of the main advantages of LRTM is due to its efficiency; in fact, it is possible to use a single mould in conjunction with multiple moulds, allowing to increase production rates. This results in high productivity and low labour costs. Because of this, and because of the optimum surface finish, LRTM can be an improvement for pieces generally manufactured by open mould process.

LRTM has some also disadvantages too: its use is limited to the production of small components; it is not suitable for parts with negative draft; and part thickness is fixed at the time of mould construction.

## 2 Definition of the Component and Design

The aim of this work consists in the design and the manufacturing of the vertical control surface (*rudder*) of a *Very Light Aircraft* (VLA). With respect to TABASCO program, it has been decided to make a structure that could meet the requirements of EASA CS-VLA.

The first part of the work, that goes from the concept creation up to the definition of the design, can be summarized in several phases. First, a model has been created; the part geometry is based on an already existing 2D model. Secondly, an average operating load has been calculated. Then the selection of the materials has been made. At least, to complete the sizing of the design, it has been necessary to make a *Finite Element Model* (FEM model) using a FEA software (Femap) and perform the relative static and dynamic analysis.

### 2.1 Conceptual Design

Classically, the wing structure responsible for absorbing stresses is the wing box. It is made up of skin, ribs, stringers and spars. The pressure load generated by the aerodynamic forces on the wing is initially absorbed by the skin; then, this load it is transmitted through plate (bending) and membrane (in-plane) actions to the ribs and the stringers. In particular, ribs and stringers also help to absorb compression loads and, consequently, to prevent buckling. The spar web absorbs the shear stresses generated by shear and torsional loads, while the spar caps contribute to the absorption of the bending loads.

In order to meet the program requirements of lightweight structure and low-cost material and processes, the final part to be produced consists in a rudder whose internal structure (the wing box) is replaced by a foam core and whose skin is made from carbon fibre composite material. So, the resistance to loads must be fully supplied by the skin and core.

It has been necessary to make two cavities, one at the tip and one at the root of the part, in order to opportunely locate the metal inserts that will substitute the hinges. Figure 1 shows the basic profile: it has been extruded in a direction that is sloped of  $11^\circ$  with respect to the vertical; then the obtained solid has been cut as shown in Fig. 1. The centres of the holes are exactly at the centre of the fillet of the leading edge and the line that connect these two points is the hinge axis. Lengths are expressed in millimetres. Figure 2 shows an isometric view of the 3D drawing.

### 2.2 Load Calculation: EASA CS-VLA

EASA CS-VLA is the *European Aviation Safety Agency Certification Specification for Very Light Aircraft*: it includes *airworthiness codes* (Book 1) and *acceptable means of compliance* (Book 2) for very light aeroplanes and for engines and propellers. It entered into force on 14 November 2003. This airworthiness code is applicable to aeroplanes with a single engine (spark- or compression-ignition) having not more than two seats, with a Maximum Certificated Take-off Weight of not more than 750 kg and a stalling speed in the landing configuration of not more than 83 km/h (45 knots) (CAS), to be approved for day-VFR only.

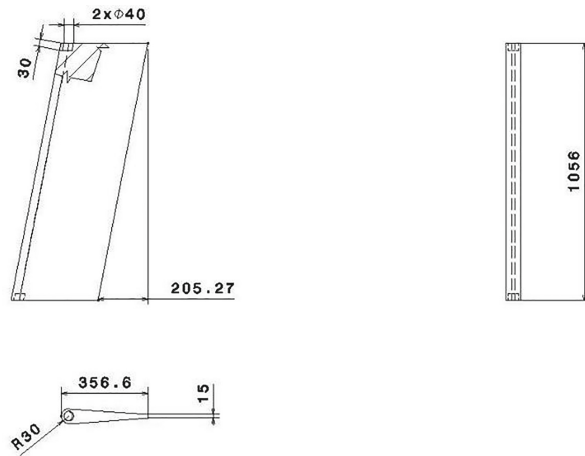


**Fig. 1.** CAD drawing of the component

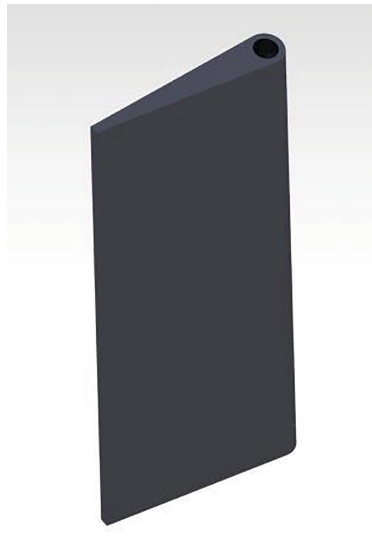


**Fig. 2.** 3D model of the Rudder

In connection with this thesis work, CS-VLA have been consulted to calculate an approximate load for the purpose of design; in particular, this value has been entered in a numerical simulation software for finite element analysis in order to select proper materials and evaluate the stacking sequence. Since the data were not enough to follow the procedure for vertical control surface indicated in Subpart C, it has been considered appropriate to follow the simplified procedure indicated in Appendix A. By the use of the technical procedure the average pressure acting on the rudder is  $\bar{P} = 1279.2$  Pa. The

load varies linearly from  $P = 2 \bar{P} = 2558.4$  Pa at the rudder hinge to  $P = 0$  Pa at the trailing edge and is constant along the rudder span.

### 2.3 Material Selection

Materials selection process for the rudder has taken into account TABASCO research program requirements: lighter and less expensive materials that can be processed using low-cost technologies and tooling without keeping the expected standard of product properties. Because of this, materials selection process has included materials that are not typically of aeronautical interest. A balancing between costs, required mechanical characteristics of the part and required manufacturing process (LRTM) has been done, in order to select the proper materials.

As a result of these observations, the following materials have been chosen:

- a composite material made of NUVOCRYL® FR 60–100 unsaturated acrylate-based resin and METYX® fabric of carbon fibres for the outside skin;
- a PVC foam having density equal to  $80 \text{ kg/m}^3$  for the inside.

A specific test campaign has been realised on biaxial specimen of the composite material (reinforcement in carbon  $400 \text{ g/m}^2$ ) in order to acquire the mechanical characteristics of the material, which have subsequently been entered in the FEA software.

### 2.4 FEM Modeling

Different combinations of lay-up have been studied to fulfill the strength requirement when the pressure load previously described is applied.

Next pictures show the mesh (Fig. 3) and the load distribution (Fig. 4).

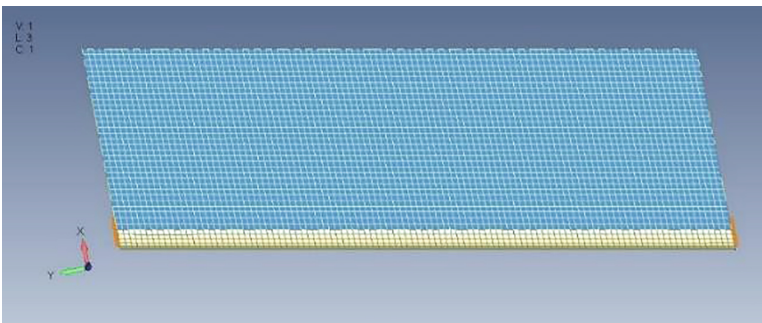


**Fig. 3.** Structural mesh

Following pictures, shot the Tsai-Wu failure index contour, zoom among the most stressed areas and the deflection contour for the selected lay-up configuration (2 plies  $400 \text{ g/m}^2$ ) (Figs. 5 and 6).

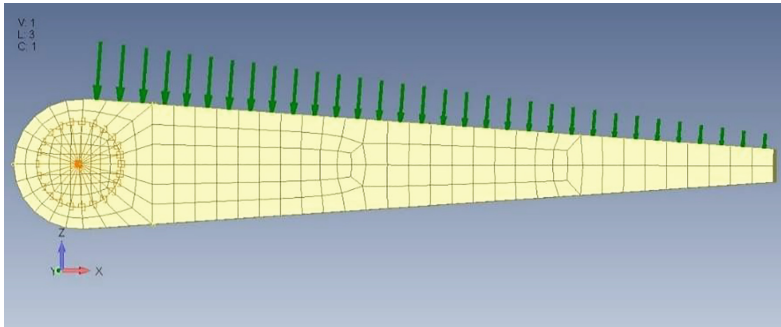


**Fig. 4.** Load distribution

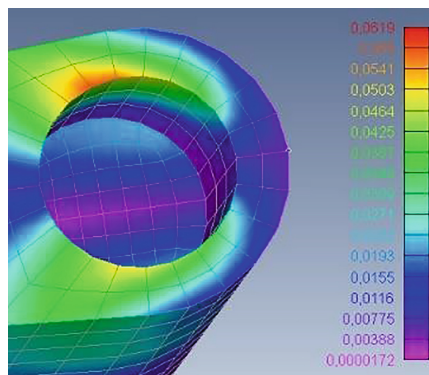


**Fig. 5.** Tsai-Wu failure index contour

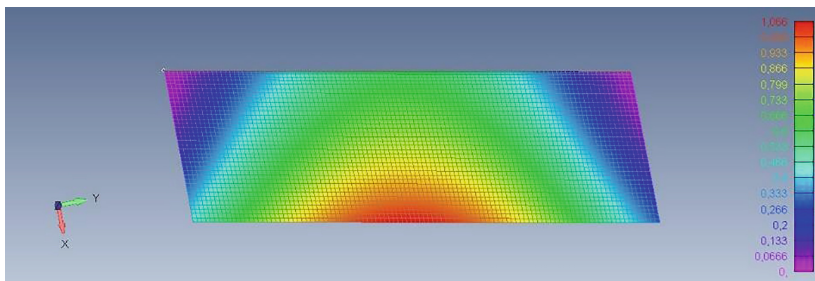


**Fig. 6.** Deflection contour.

### 3 Conclusions and Further Activities

The aim of this work has been the study of low-cost techniques to manufacture composite material aircraft structures. In particular, it has been realized the design of the vertical control surface of a VLA class aircraft and a prototype has been produced by Light Resin Transfer Moulding.

Once an approximate reference load has been calculated, a FEM model has been defined. The study has involved four different cases for the static analysis, each with a different stacking sequence, and two cases among these for modal analysis. Static analysis results have highlighted that none of the cases lead to failure. All the maximum values of principal stresses are far below the limit stresses and also the failure indices are less than 1. Because of this, the final choice of the stacking sequence has been done basing on total weight and structural deformation. In all four cases the most stressed areas are, as expected, those near the cavities, where there are the fixed constraints.

These results have allowed to proceed with the manufacturing process. Unfortunately, due to external factors, up to now, it has not been possible to complete the infusion process. The future developments of this work will be the completion of the manufacturing process with the infusion and the start of an experimental campaign to validate the numerical model.

## References

1. Campbell, F.C.: *Manufacturing Technology for Aerospace Structural Materials*. Elsevier (2006)
2. Bannister, M., Herszberg, I.: Advanced reinforcements. In: Kruckenberg, T., Paton, R. (eds.) *Resin Transfer Moulding for Aerospace Structures*, pp. 83–111. Springer, Netherlands (1998)
3. Campbell, F.C.: *Structural Composite Materials*. ASM International (2010)
4. DAC S.c.a.r.l, Progetto di ricerca TABASCO
5. EASA Certification Specifications for Very Light Aeroplanes, 14 November 2003
6. Groover, M.P.: *Fundamentals of Modern Manufacturing: Materials, Processes and Systems*, 4th edn. Wiley (2010)
7. Kabir, Md.E., Saha, M.C., Jeelani, S.: Tensile and fracture behaviour of polymer foams. *Mater. Sci. Eng. A* **429**(12), 225–235 (2006)
8. Kostopoulos, V., Vavouliotis, A.: Epoxy resins. In: Nicolais, L., Borzacchiello, A. (eds.) *Wiley Encyclopedia of Composites*, vol. 2, 2nd edn. Wiley (2012)
9. McIlhagger, A., Archer, E., McIlhagger, R.: Manufacturing processes for composite materials and components for aerospace applications. In: Irving, P.E., Soutis, C. (eds.) *Polymer Composites in the Aerospace Industry*, pp. 53–75. Woodhead Publishing (2015)
10. Sorrentino, L., Iannace, S.: Foamed cores. In: Nicolais, L., Borzacchiello, A. (eds.) *Wiley Encyclopedia of Composites*, vol. 2, 2nd edn. Wiley (2012)



# An Open Thinking for a Vision on Sustainable Green Aviation

Antonio Ficca<sup>1</sup>, Francesco Marulo<sup>2</sup>(✉), and Antonio Sollo<sup>3</sup>

<sup>1</sup> Mitsubishi Heavy Industries, Montreal, Canada

<sup>2</sup> University of Napoli Federico II, Napoli, Italy  
francesco.marulo@unina.it

<sup>3</sup> Piaggio Aerospace, Villanova d'Albenga (SV), Italy

**Abstract.** This paper has the main goal to look for the future of aviation considered as a leader discipline which will be able to improve the respect for the nature, to mitigate the polluting effects of the human activities, to setup admissible requirements which allow safe and enjoyable progress of the human being on the planet Earth.

Developing visions for the future is always a complex matter, but it is become even more difficult during these times which are worldwide attacked by a sanitary emergency followed by an unbelievable development of a war. One of the main reasons of this paper is just to show that there are still rooms for reflecting on the clean technological developments.

Green and environmentally sustainable aviation, in our opinion, can be achieved with continuous improvements of multiple parallel paths, ramp up of SAF (Sustainable Aviation Fuel) production, and of course, breakthrough technologies. The latter will require a significant amount of research, testing and probably mistakes need to be made before reaching the level of transportation efficiency and mission safety obtained with traditional propulsion, but these drawbacks should only encourage scientists, engineers, politicians and visionaries to strongly pursue the objectives of a new eco-aviation.

New technologies should probably be introduced into smaller aircraft segments first then migrate into the larger segments as the technologies mature. We should expect a first electric and hydrogen fuel cell commuter aircraft entry into service by the end of this decade, with hydrogen combustion-powered narrow bodies around 2040.

This paper will try to summarize the most important aspects which drive the vision for a sustainable green aviation and a possible roadmap for reaching the goal following a pathway which is not distracted by unwanted or even tragic events.

## 1 Introduction

The airplane evolution and progress is strongly related to the development and improvement of its propulsive system. The history of aviation is primarily the history of the aircraft engines, from the propeller to the high bypass ratio engines installed on modern widebodies like A350 and B777, [1].

The contribution of aviation to society, human development, prosperity, and growth is unquestionable and, moreover, aviation is a challenging business, where technical,

regulatory, financial aspects – just to name a few – must be evaluated for any development or change implementation. The demanding regulatory environment in which aviation operates ensures that a remarkable safety record is maintained. This makes aviation a difficult-to-abate business.

The driving factor for such new, still not available, aircraft is the stringent requirement for an environmentally sustainable aviation. Many institutions worldwide are addressing the environmental impact as one of the principal requirement for the next decades.

In Europe, the guidelines are set by the European Commission in association with the Advisory Council of Aviation Research (ACARE), under Vision 2020, now through Flightpath 2050 and the corresponding strategic research and innovation agenda [2, 3]. Environmentally Responsible Aviation N + series programs sponsored by the National Aeronautics and Space Administration (NASA) lead the guidelines and performance goals for the civil aviation industry in the USA [4]. The key aspect of these goals is to make the fleet operation more energy-efficient, reliable, and to reduce the emission and community noise. Many technology paths are being explored for improvements in the airframe and structural designs, in the propulsion system, and of the air-traffic management system to achieve such ambitious expected targets, [5, 6].

Current research guidelines are aligned towards the use of sustainable aviation fuel (SAF), the conversion toward more electric power in propulsion system, the implementation of hydrogen combustion, the application of hydrogen fuel cell, the combination of hybrid solutions, [7–11].

The sustainable aviation roadmap has the goal to achieve the target of net zero carbon in commercial aviation by 2050, considering how the new technologies will impact the commercial aircraft fleet and simultaneously key industry stakeholders. This paper will focus, based on the authors' perspectives, on the analysis of market trends, aircraft design evolution, sustainability developments, technology maturity, operators' requirements, and public acceptance.

Increasing viable industrialization and efficient production of SAF appears to be, at moment, the most effective way to reduce the carbon impact of commercial aviation and therefore procedures for accelerating production, incentivizing the use, and reducing the cost should be prioritized.

New technologies should be introduced into smaller aircraft segments first to be used as experimental platform, [12, 13], then migrate into the larger segments as the technologies mature. It could be expected to see the first electric and hydrogen fuel cell small commuter aircraft enter into service this decade, with hydrogen combustion-powered narrowbodies around 2040.

The enormous investment required to validate and certify a new program dictates a cautious approach to novelty. Regional aviation provides a vital service to smaller communities ensuring connectivity and supporting the economy. A rapid roll-out of clean, quiet technologies in the smaller aircraft segments will be crucial to supporting growth in these markets, [14].

Acting now to improve efficiency is vital. Despite reductions in air travel demand due to COVID-19, the aviation industry forecast is for a still strong growth propelled by increased GDP and propensity to travel. Aviation decarbonization will require strategies both in near term improvements in aircraft fuel efficiency and long-term propulsive



switching which will encompass transdisciplinary research. It will be crucial to have a coordinated and synchronized effort by all of those involved including airlines, airports, manufacturers, governments, certification authorities, and fuel suppliers, among others, [15–18].

In the near future significant improvements toward green transportation (land and sea) are expected and cross-fertilization of the outcomes are foreseen to affect also air transportation for the application of such new technologies, [19–21].

One of the motivations of this paper is also for recalling the attention of scientists, researchers, technicians and social managers on the real challenges required for a better quality of life and for finding solutions for using environmentally sustainable energies. The knowledge and the intelligence should be used for progressing along the respect of the nature, instead of regressing back to the instinct actions and rules of the animal world.

## 2 Strategies to Lower Chemical Pollution

Several different approaches currently available may be adopted to reduce the impact of greenhouse gas production, from simple already available operational changes, even though with small impact, to complete re-designs of aircraft and their related infrastructure that will have a large impact on emissions which, unfortunately will require many years for the technology to become mature and to be implemented. Achieving sustainability will necessarily involve a combination of these technologies. Civil aviation is always on an improved efficiency path per year, which translates directly into several advantages including lower carbon emissions, [22].

Each generation of aircraft design represents a stepwise improvement in efficiency. While the absolute CO<sub>2</sub> emissions have increased in line with the growth of the global fleet, significant improvements in aircraft efficiency have limited the impact.

Aerodynamics and structural solutions are other topics which are improved generation by generation. New materials, lighter airplanes with additive manufacturing components, new winglet designs (Sharklets, Split Scimitar), higher aspect ratio wings, folding wingtips are examples of improvements for increasing the efficiency which generally translates in pollution mitigation. Future developments include greater use of laminar flow surfaces, morphing wing surfaces, or more extreme arrangements such as truss-braced wings and blended wing body configurations which could also lead to innovative cabin configurations.

Aircraft systems also contribute to improved efficiency, and they can have a direct impact on fuel burn. Improvement of the operational efficiency, and the best use of the airspace design can also have a significant impact on the improved sustainability. However, continuous improvement alone will not be enough to achieve the target of Net Zero carbon by 2050 and it will be necessary to look for additional solutions to close the gap.

One of the potential first priority is the increased use of SAF which is obtained from renewable sources (biomass, electricity or hydrogen).

Today almost all flights are powered by kerosene, a petroleum product made from refining crude oil which, when burned, produces CO<sub>2</sub>, NO<sub>x</sub>, soot and other pollutants

that impact the environment. The production and the use of SAF may result in a 50%-80% net reduction of aircraft CO<sub>2</sub> emissions. SAF also burns cleaner than kerosene since it does not contain sulphur and other pollutants.

Strong benefits for the environment are expected from hydrogen combustion which offers many desirable attributes over carbon-based fuels, most importantly it does not generate CO<sub>2</sub> when burned. Hydrogen can be produced by several different methods which are categorized based on their sustainability impact. Green Hydrogen is produced on a CO<sub>2</sub>-neutral basis through the electrolysis of water using electricity generated from renewable energy sources such as wind energy, hydropower or solar energy.

For hydrogen combustion, the conventional turbofan or turboprop engine is modified to burn hydrogen gas instead of kerosene fuel. This approach maintains the conventional engine design with systems adapted for the unique properties of hydrogen. The biggest challenge involves the onboard storage of hydrogen. Unlike kerosene, which is a liquid and can be stored in the wings of the aircraft, hydrogen is a gas and must be stored in tanks under pressure. In order to minimize the volume, cryogenic liquid hydrogen is used, which is cooled to 21K (−253 °C). Even at this low temperature, hydrogen has a volumetric efficiency 1/4 that of kerosene, which means that it requires 4 times the volume of hydrogen for an equivalent amount of energy. These super-cooled storage tanks are located in the fuselage and take up space that would otherwise be allocated to passengers or cargo.

At this stage, the long-term outcome of hydrogen combustion is less clear. While the potential is definitely massive, being the only zero-carbon fuel source that is likely to deliver the performance required for jet-powered aircraft for the foreseeable future, it will also require massive investments to bring it to market and overcome the challenges of hydrogen storage.

Similar to hydrogen combustion, hydrogen fuel cells use hydrogen as a fuel source. The big difference is that instead of burning hydrogen, fuel cells use a chemical reaction to generate electricity, like a battery. Hydrogen fuel cells have been available for many years and are used for warehouse logistics, standby power and trucking. Newer technology is increasing the power density and reliability of these systems, making them more suitable for aviation applications. In addition to the hydrogen storage issues, a fuel cell-powered aircraft requires an entirely new electric powertrain and electric systems. The new design also brings new opportunities such as distributed propulsion, higher redundancy and more efficient systems. The weight and volume of the fuel cell, including its cooling system, limits the application to smaller aircraft today; however, developments that increase power output and reduce the amount of cooling required will lead to more compact systems in the future.

Today, the production cost of green hydrogen is about 5 times that of kerosene and the higher volume required increases the transportation cost. Sources of renewable electricity are expected to grow four-fold by 2030, which means that local production of hydrogen could be feasible, even on-site at the airports, which will dramatically reduce its cost.

The electrification of the propulsion system is expected to strongly change the propulsion system design, with merits and associated bottlenecks. A full electric system relies upon a battery or some other means of electrical energy source. Turboelectric configurations maintain fuel as main source converting the chemical energy of the fuel into electrical power, fully or partially, to drive the propulsor. Hybrid electric stands for more than one type of energy sources and consequent powertrain arrangement. The use of battery-electric propulsion is diffusely used in the automotive world and the research in the field may be beneficial for aviation industry, too. One example are the new Advanced (or Urban) Air Mobility projects which are based on battery electrical propulsion.

Batteries provide greater flexibility in aircraft design; they can be located almost anywhere. Additionally, the weight does not decrease during the flight as the energy is consumed, which means that there is no impact on the aircraft center of gravity either. The batteries can be located close to the electric motors to reduce the amount of wiring required and distributed propulsion systems can improve efficiency and add redundancy. Electric motors and systems tend to be very reliable and require less maintenance than combustion-based alternatives. An electric propulsor also weighs less than the turbine equivalent.

Weight is a major factor limiting the penetration of battery technology in aviation. With a system energy density of about 1/15 that of kerosene, battery-powered aircraft end up weighing significantly more than kerosene-powered models, which limits the payload and range capabilities.

The replacement of older narrowbodies with new generation aircraft, combined with operational efficiency improvements will be the major contributors. Furthermore, a ramp-up of SAF availability with several airlines, committing to 10% SAF use by 2030, is expected. By the next decade the implementation of the most promising technology that is under development today should become operative at high TRL. New engine technologies will deliver a further 20% efficiency improvement along with the potential to burn alternative fuels such as hydrogen. Electric systems are expected to increase their efficiency, leveraging the development of electric powertrains mainly on smaller aircraft. More radical aerodynamic improvements, such as truss-braced wings and higher aspect ratio wings, will be introduced on new models. SAF will become widely available and take over as the primary contributor to reducing greenhouse gases. New aircraft designed for taking advantage of hydrogen fuel cells and hydrogen combustion are expected to enter into service, Fig. 1.

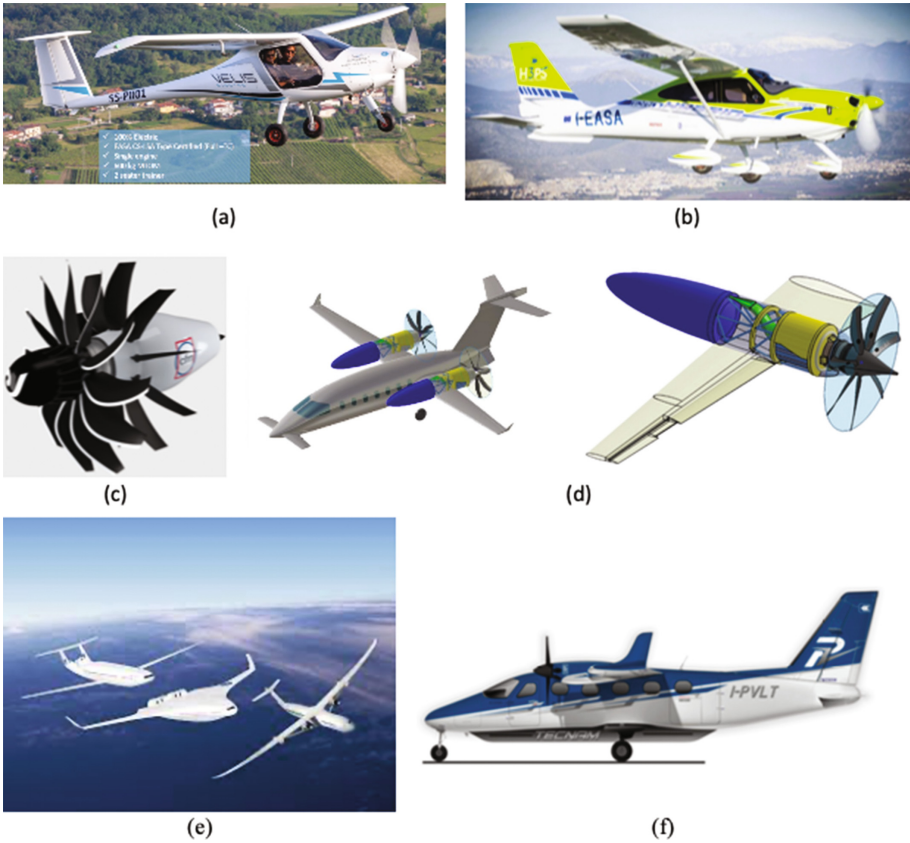


**Fig. 1.** Flying and potential design evolution for green aviation (a) Pipistrel Velis Electro; (b) Tecnam P2010 H3PS Hybrid; (c) CFM RISE Engine; (d) Future Full Electric Propulsion Concept for P180; (e) NASA Studies for Next Generation Hybrid/Electric Aircraft; (f) Tecnam Concept for Electric Powered Small Commuter P-Volt

### 3 Impact on the Infrastructure and Supply Chain

Sustainability challenge in aviation requires a tremendous effort by all impacted stakeholders and a strong support from the government of high-technology countries. The nature of the aviation business is highly complex with many competing requirements and limitations such as: aircraft performance, safety, reliability, regulatory, economic, financial, and so on. Each actor will have its own role and responsibility.

Airlines are probably the most impacted by the need of sustainability, being the direct public interfaces with the aviation business. They should optimize their operations, improve their fleet, engage passengers and get prepared for the future.

Airports will play an important role in the sustainability of aviation both directly and indirectly. As new fuel sources such as SAF and hydrogen are introduced to the aviation market, airports will need to develop the necessary support infrastructure.

Design and manufacturing of an airplane is not the commitment of a sole company. Each aircraft program is supported by hundreds of Tier 1 and thousands of sub-tier suppliers working together and depending on each other. Aircraft design is likely to change due to new requirements for fuel storage, new powerplant configurations and aerodynamic step-changes. Details are still under development; however, it is foreseen that these designs will require greater integration of aircraft and engine systems than actual supply chains. Aircraft and engine manufacturers, along with system providers, will have to work even more collaboratively and intimately to achieve the necessary optimization.

Governments need to provide the leadership, guidance, and vision to support sustainability. Considering the near-term challenge to increase the availability of SAF, subsidies for investment into production industrialization are the most effective path to meet the current need and provide a long-term supply. Nevertheless, there is a great opportunity in developing markets where investments will also serve to stimulate the local economy.

The adoption of new technologies will require a reworking of certification and operational standards, starting with commuter and regional aircraft. Aircraft and engine certifications, airline operating rules and manuals, flight and ground procedures, maintenance procedures, all will have to be adapted to reflect new requirements.

Many other stakeholders in the aviation ecosystem will be impacted to a greater or lesser degree by the actions toward sustainable aviation. Actually, petroleum producers provide over 300Mt of kerosene per year for commercial aviation. A switch to SAF will redefine their business model. Other stakeholders – such as financiers, lessors, airlines, airports, etc. – will have to define or adapt their policies with a focus on operating newer, greener aircraft. This is increasingly becoming a must to attract financing, satisfy investors and secure new business.

## 4 Some Examples

Airplanes which may claim to be fully environmentally sustainable are not available so far, but it is possible to list some examples of existing airplanes which for their special characteristics and performances have resulted best in the class for fuel consumption and reduction of CO<sub>2</sub> emissions. One of these airplanes is the Piaggio P180, a revolutionary airplane developed in the 70's, during the global energetic crisis, with an unconventional design which was considered the only viable solution for a very demanding challenge: to define an airplane with jet speed and significantly low fuel consumption, [23]. And nowadays, Avanti EVO, the last P180 version, is already approved to operate under blended use of SAF (Biofuel). It is also interesting to highlight in these times how important has been the unconventional design for complying with the requirement. Unconventional design will be required for future airplane to meet the sustainability objectives.

Other examples are the coming NASA X-57, the Tecnam Green P2010 resulting from a European funded project H3PS, the Pipistrel Velis Electro, first certified full electric two-seat aircraft.

As anticipated in this paper, first applications of the new technologies are in the small airplane sector, which should pave the way for the bigger commuter vehicles and subsequently the narrowbody and widebody configurations.

Novel configuration concepts are under exploration. In the near term the potential of electrical powerplant based on current available technology as far as battery is concerned drives toward the eP180 or the Tecnam P-Volt which, together with X-57 appear to be concept studies for being prepared for the coming technological achievements. Industrial maturity for production appears still far to get, Fig. 2.



**Fig. 2.** Evolution of airplanes for greener solutions (a) P180 EVO; (b) NASA/Tecnam X-57

## 5 Conclusions

It is possible for commercial aviation to achieve Net Zero by 2050, but it is a very demanding objective. It will require the cooperation of all the stakeholders: airlines, governments, aircraft manufacturers, airports, air traffic management and fuel suppliers, just to name a few. There are simple operational improvements that can be implemented today allowing immediate results even if in a small quantity. New technologies can be incorporated incrementally as older aircraft are retired and substituted by new more aerodynamically efficient and less fuel burn engine using increased percentage of SAF. It is expected that these new technologies will be applied first on local and regional flights and these small aircraft will be the incubators for battery-electric and hydrogen fuel cells that mature the technology for broader implementation.

However, it is the industrialization of SAF that will achieve the biggest impact for a fast decarbonization, because it can be used with existing in-service aircraft and is the only solution for narrowbody and widebody aircraft in the short term. Since these aircraft are responsible for the majority of the carbon emissions in the commercial aviation, the increased production and the broader use of SAF is going to be the priority for the aviation industry.

**Acknowledgements.** The authors would like to acknowledge Prof. Valentina Lopresto for offering the opportunity to open a window on the topic of the sustainable aviation which, in general, requires an effort of all the scientific and technological worldwide community. We do hope that the future will be driven by the challenges highlighted in the paper to efficiently solve them for the benefit of all of us, instead of pushing mankind to its self-destruction for the benefit of nobody.

## References

1. Pascale, L.: L'avvento della "Jet-Age" – dal Douglas DC-3 al Jumbo Jet. Seconda Università degli Studi di Napoli, Maggio (2013). (in Italian)
2. Busquin, P., Arguelles, P., Lumsden, J., Bishoff, M.: European Aeronautics: A Vision for 2020. European Community, Bruxelles (2001)
3. European Commission: Flightpath 2050: Europe's Vision for Aviation-Report of the High Level Group on Aviation Research. European Commission, Luxembourg (2011). <https://doi.org/10.2777/50266>. [https://www.acare4europe.org/sites/acare4europe.org/files/document/Flightpath2050\\_Final.pdf](https://www.acare4europe.org/sites/acare4europe.org/files/document/Flightpath2050_Final.pdf). Accessed 14 May 2022. ISBN 978-92-79-19724-6
4. NASA: Strategic implementation plan 2017 update, NP-2017-01-2352-HQ (2017). <https://www.nasa.gov/sites/default/files/atoms/files/sip-2017-03-23-17-high.pdf>. Accessed 14 May 2022
5. IATA: Aircraft technology roadmap to 2050. <https://www.iata.org/contentassets/8d19e716636a47c184e7221c77563c93/Technology-roadmap-2050.pdf>. Accessed 14 May 2022
6. Ashcraft, S.W., Padron, A.S., Pascioni, K.A., Stout, G.W., Jr., Huff, D.L.: Review of Propulsion Technologies for N+ 3 Subsonic Vehicle Concepts; NASA/TM—2011-217239. NASA Glenn Research Center, Cleveland (2011)
7. Developing sustainable aviation fuel (SAF). IATA. (n.d.). <https://www.iata.org/en/programs/environment/sustainable-aviation-fuels/>. Accessed 14 May 2022
8. Hydrogen fuel cells, explained. Airbus. (n.d.). <https://www.airbus.com/en/newsroom/news/2020-10-hydrogen-fuel-cells-explained>. Accessed 14 May 2022
9. Rolls-Royce and Tecnam join forces with Widerøe to deliver an all-electric passenger aircraft ready for service in 2026 – Tecnam Aircraft. <https://www.tecnam.com/rolls-royce-and-tecnam-join-forces-with-wideroe-to-deliver-an-all-electric-passenger-aircraft-ready-for-service-in-2026/>. Accessed 30 April 2022
10. World first hydrogen-electric passenger plane flight. ZeroAvia, 25 September 2020. <https://www.zeroavia.com/press-release-25-09-2020>. Accessed 1 Feb 2022
11. Embraer Energia: Embraer Commercial Aviation Sustainability, 23 November 2021. <https://embraercommercialaviationsustainability.com/concepts/>. Accessed 1 Feb 2022
12. Stückl, S., van Toor, J., Lobentanz, H.: VOLTAIR—the all electric propulsion concept platform—a vision for atmospheric friendly flight. In: Proceedings of the 28th International Congress of the Aeronautical Sciences (ICAS), Brisbane, Australia, 23–28 September 2012
13. Vratny, P.C., Forsbach, P., Seitz, A., Hornung, M.: Investigation of universally electric propulsion systems for transport aircraft. In: Proceedings of the 29th International Congress of the Aeronautical Sciences, St. Petersburg, Russia, 7–12 September 2014
14. Royal Netherlands Aerospace Centre, SEO Amsterdam Economics: Destination 2050—A route to net zero European aviation, Amsterdam, The Netherlands (2021)
15. Airbus: fello'fly Wake-energy retrieval to boost environmental performance (2021). <https://www.airbus.com/en/innovation/disruptive-concepts/biomimicry/fellofly>
16. Boeing: Sustainability and Innovation for the Future—Introducing the Boeing eco Demonstrator Program (2021). <https://www.boeing.com/principles/environment/ecodemonstrator>
17. Eurocontrol: A-CDM Airport Collaborative Decision-Making (2021). <https://www.eurocontrol.int/concept/airport-collaborative-decision-making>
18. ASTM Standards: Standard Specification for Aviation Turbine Fuel Containing Synthesized Hydrocarbons, ASTM D7566-21 (2021)
19. Sollo, A.: Piaggio Aerospace Vision for Green Aviation, Piaggio Aerospace, 10 May 2022
20. IEA: Net zero by 2050 – A Roadmap for the Global Energy Sector. IEA, May 2021. <https://www.iea.org/reports/net-zero-by-2050>. Accessed 31 Jan 2022

21. Aviation Benefits Beyond Borders. Aviationbenefits.org., September 2020. [https://aviationbenefits.org/media/167517/aw-oct-final-atag\\_abb-2020-publication-digital.pdf](https://aviationbenefits.org/media/167517/aw-oct-final-atag_abb-2020-publication-digital.pdf). Accessed 8 Feb 2022
22. Mitsubishi Heavy Industries Group: MHIRJ Sustainable Aviation Roadmap, April 2022
23. Sollo, A.: P.180 Avanti: An Iconic Airplane and the Achievement of an Historical Milestone – AerotecnicaMissili e Spazio, December 2020





# On the Crashworthiness Behaviour of Additive Manufactured Sandwich Panels

V. Acanfora<sup>(✉)</sup>, F. Baldieri, A. Garofano, F. Fittipaldi, and A. Riccio

Department of Engineering, University of Campania “L. Vanvitelli”, Via Roma, 29, 81031 Aversa (CE), Italy

valerio.acanfora@unicampania.it

**Abstract.** This paper explores the advantage introduced, in terms of load dissipation during a crash test, of additive manufactured composite sandwich panels. A numerical investigation has been performed on a small electric bus by comparing the results obtained by explicit crash test simulations with and without composite sandwich panels as shock absorption systems.

To assess the crashworthy behaviour of the investigated structures, detailed numerical simulations with 3D formulation based finite element models have been performed within the ABAQUS Explicit FEM environment. The proposed sandwich panels configuration has been obtained by combining carbon reinforced skins with a polymeric core. This kind of hybrid structure has been considered suitable to dissipate large amounts of impact energy both by plasticisation and by fibre and matrix breakage due to the interaction between the ductility of the polymeric core with the brittle behaviour of the CFRP skins.

In addition, the proposed sandwich panels are expected to exhibit a considerably high absorbed energy to mass ratio due to use of the additive manufacturing technique to produce the polymeric core. This manufacturing technique allow the definition of complex microstructures, such as lattice microstructures, characterised by significant energy absorption capabilities with a considerable mass reduction.

Hence, the research study presented in this paper is aimed to prove that, for the analysed small electric bus configuration, the considered combination of innovative materials and processes can help to develop compact and highly efficient shock absorber sandwich panels capable to reduce both stress and energy distribution on the chassis structure.

**Keywords:** Composite Materials · Finite Elements Models · Crashworthiness · Additive Manufacturing · Hybrid Shock Absorber

## 1 Introduction

The assessment of the crashworthiness properties of a structure is becoming more and more an important step in structural design [1–4]. A significant contribution to the improvement of the crashworthiness properties of transport vehicles is provided by the introduction, at specific key points, of shock absorbing systems. Examples of shock

absorbers can be found in [5, 6]. In [6], by adopting a combination of ductile polymers and composite material systems, it is possible to increase the capability of impact absorption systems to dissipate energy. This is possible because these hybrid sandwich shock absorbers can dissipate the impact energy both by plasticising the core [7–9] (with a properly designed core microstructure) and by intralaminar breakages in the composite skins.

Recent developments in the state of the art of shock absorbers prove that, to maximise the energy absorption capacity of the core while minimising its mass and volume, the Additive Manufacturing techniques can be adopted [8, 10–12]. Indeed, additive techniques allow to considerably lighten the core by introducing complex microstructures (e.g. latex domains) with increased void volume, while preserving energy absorption capabilities [12].

An attempt to evaluate the effectiveness, under service conditions, of these innovative hybrid shock absorbers is presented in this paper. In detail, in the frame of the research activity presented in this paper, numerical data in terms of stress state, deformations and energy, resulting from numerical crash test simulations has been analysed. Indeed, crash test simulations have been performed on the chassis structure of a minibus. Comparisons between numerical results from the simulations with and without hybrid shock absorbers, characterised by a core microstructure designed for Additive Manufacturing in [12], have been made.

The adopted sandwich panel configuration consists of a Polypropylene (PP) core and internal skin and carbon fibre reinforced polymers as external skins. This configuration allows to combine the ductility of the polymeric core with the lightness and strength of the external CFRP skins.

The explicit Finite Element Model (FEM) [[14, 15] of the bus chassis and the shock absorbers has been created with elements characterised by 3D formulation (C3D8R and SC8R) and the numerical simulation included the evaluation of the materials' failure mechanisms and material properties degradation. In particular, the prediction of the initiation and evolution phase of the intralaminar damage mechanisms of the composite skin component has been performed by means of the Hashin's theory and Continuum Damage mechanics theory [15–19], while the ductile behaviour of the steel chassis has been evaluated by means of the Johnson–Cook criteria [20–24]. Finally, the elastoplastic behaviour of the polypropylene has been considered in computations by implementing the sigma-epsilon material curve in the numerical material model [26].

FE models used for the crash simulations are presented in Sect. 2, while the comparison between the numerical results from minibus models with and without shock absorbers are introduced in Sect. 3.

## 2 Explicit Finite Element Models: Minibus Numerical Benchmark

This work has the main objective to assess the benefits introduced by the integration, in a typical minibus chassis, of hybrid (polymer-composite) sandwich panels acting as shock absorber systems with core microstructure designed to be produced by Additive Manufacturing techniques. Therefore, two minibus chassis configurations have been defined: a first one, without shock absorbing systems and a second one, with the proposed

hybrid sandwich panels as shock absorbing systems positioned on the front module. The main chassis geometrical parameters are shown in Fig. 1. As depicted shown in Fig. 1-d, it consists of tubes with a 40 mm × 60 mm rectangular section and internal thickness of 2 mm made in ASTM A-36 steel.

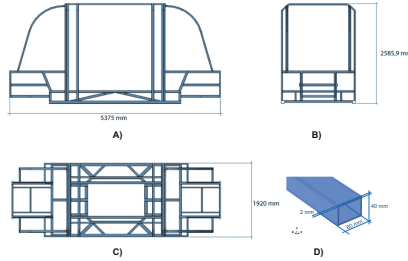


**Fig. 1.** Geometry of the minibus chassis. A) lateral view, B) frontal view; C) top view; D) section of the tubes

The mechanical properties of ASTM A-36 steel, listed in Table 1, were extracted from the literature reference [24]. In particular, the terms A, B, C and m of Table 1 are constants and identifies the yield stress of the material (A), the strain hardening constant (B), the strengthening coefficient of strain rate (C) and, the thermal softening coefficient (m). Moreover,  $\dot{\bar{\epsilon}}_0$  is the equivalent plastic strain rate, the terms  $d_1 - d_5$  are the damage model constants and, finally,  $\eta$  is the stress triaxiality. The nondimensional parameters m, Melting Temperature and Transition Temperature, were set to 0 to neglect, in the numerical analysis, the temperature strain rates' dependence.

**Table 1.** Mechanical properties of ASTM A36 steel used for the chassis structure [24]

	Value	Units
Density	$7.89 \times 10^{-9}$	t/mm <sup>3</sup>
Young's Modulus	200'000.00	MPa
Poisson's ratio	0.26	
A	286.10	MPa
B	500.10	MPa
$\eta$	0.2282	
m	0	
Melting temperature	0	
Transition temperature	0	
C	0.0171	
$\dot{\bar{\epsilon}}_0$	1	

(continued)

**Table 1.** (continued)

	Value	Units
$d_1$	0.403	
$d_2$	1.107	
$d_3$	-1.899	
$d_4$	0.00961	
$d_5$	0.3	
Reference Strainrate	1	

An isometric view of the two compared configurations, highlighting the shock absorbing system-chassis locations, is presented in Fig. 2.

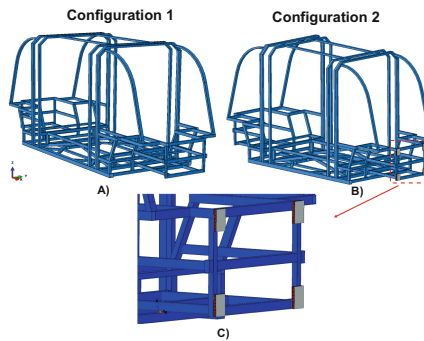


**Fig. 2.** Investigated chassis configurations: a) without shock absorbers; b) with shock absorbers; c) shock absorbers location detail

In Fig. 2-B and 2-C, configuration 2 is characterised by the presence of four shock absorber sandwich panels. According to Fig. 3, where geometrical and material details of the sandwich panels are presented, these panels are 23 mm thick. The total mass of the shock absorbing system is 0.792 kg.

As shown in Fig. 3, the sandwich panels have been obtained by combining two materials: Polypropylene (PP Roboze – coloured in red) and CFRP Composite Material (IM7/977-2 – coloured in light grey). This combination of materials give to the panels the ability to dissipate energy both by polymeric plasticisation and by fibre and matrix breakage.

For the extremely thin-wall structure of the honeycomb core, made by additive manufacturing, a thickness of 1 mm has been chosen. This small thickness gives to the structure a high flexibility, thus maximising its energy absorption capacity.

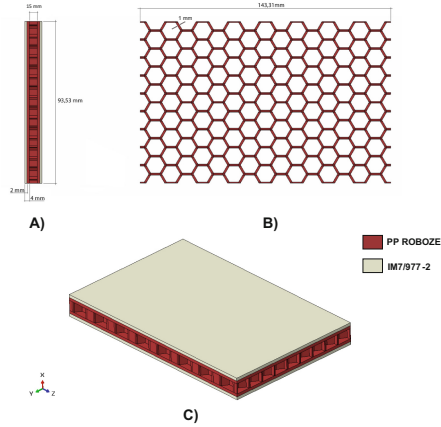


**Fig. 3.** Geometrical details of the shock absorber. A) lateral view, B) top view; C) isometric view

The mechanical properties of the adopted composite material (IM7/977–2) skins and polypropylene corer are detailed in Table 2 and Table 3, respectively.

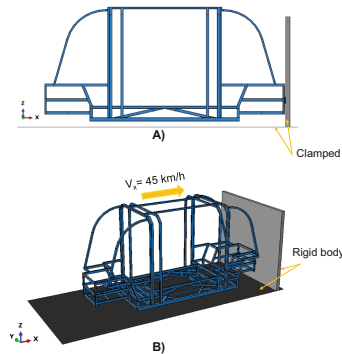
**Table 2.** Mechanical properties of IM7/977–2

	Value	Units
Density	$1.58 \times 10^{-9}$	t/mm <sup>3</sup>
$E_1$	153,050.00	MPa
$E_2 = E_3$	10,300.00	MPa
$G_{12} = G_{13}$	6000.00	MPa
$G_{23}$	3700.00	MPa
$\nu_{12} = \nu_{13}$	0.30	
$\nu_{23}$	0.40	
Longitudinal , Tensile Strength	1250.00	MPa
Longitudinal Compressive Strength	850.00	MPa
Transverse Tensile Strength	65.00	MPa
Transverse Compressive Strength	200.00	MPa
Longitudinal Shear Strength	75.00	MPa
Transverse Shear Strength	35.00	MPa
Longitudinal Tensile Fracture Energy	15.00	kJ/m <sup>2</sup>
Longitudinal Compressive Fracture Energy	7.00	kJ/m <sup>2</sup>
Transverse Tensile Fracture Energy	0.5	kJ/m <sup>2</sup>
Transverse Compressive Fracture Energy	4	kJ/m <sup>2</sup>

**Table 3.** Mechanical properties of polypropylene

	Value	Units
Density	$1.09 \times 10^{-9}$	t/mm <sup>3</sup>
Young's Modulus	1620.00	MPa
Poisson's ratio	0.35	
Tensile strength(at breakage)	20.10	MPa
Elongation at breakage	16.21	MPa

A road section and a rigid wall have been modelled to perform the frontal crash test simulations. The road has been modelled as a  $7000 \times 3000$  mm rectangular planar shell part and discretised by using S4R elements. The rigid wall has been modelled as a  $3000 \times 2500 \times 100$  mm solid extrusion part and discretised by using C3D8R elements. Both the road and the rigid wall have been considered as rigid bodies by creating two reference points for assigning the correct boundary conditions. Figure 4 shows the crash test simulation set-up assembly. To perform the crash test simulations, the reference points of both the road and the rigid wall have been clamped, while a 45 km/h initial velocity has been assigned to the chassis in the x-positive direction, according to the maximum speed achievable by the electric city minibus due to design constraints. Moreover, the gravity acceleration has also been assigned to the whole model. This acceleration, together with the density associated to materials, makes it possible to consider the gravitational effects in the simulations.

**Fig. 4.** Crash test set-up. A) lateral view, B) isometric view

### 3 Numerical Results

The effect of the introduction of the shock absorbing system on the dynamic behaviour of the minibus chassis' structure under crash test conditions, is discussed in this section.

Numerical results are compared in terms of Von Mises stresses (Fig. 5 and Fig. 6), energy in the chassis' safety cage (Fig. 7), and force–time graph (Fig. 8).

As illustrated in Fig. 5, the introduction of the shock-absorbing system has a significant effect on the stress state within the chassis. Indeed, by comparing the maximum Von Mises value of the stress between the investigated configurations, a reduction of the maximum von mises stress of about 24% has been found for configuration 2.

Indeed, as detailed in Fig. 5, in Configuration 1 the maximum Von Mises stress is 794.6 MPa while in Configuration 2 a maximum value of 604.1 MPa has been found.

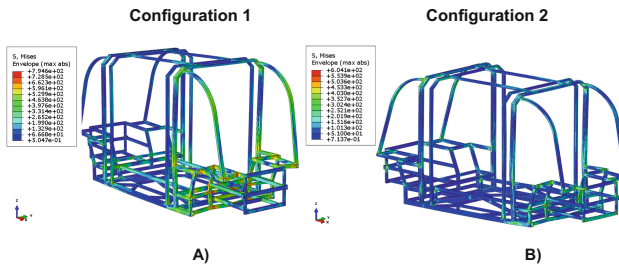


**Fig. 5.** Comparison in terms of Von Mises's stress between Configuration 1 (A) and Configuration 2 (B)

In both the numerical simulations (with and without shock absorbers), the von mises stress exceeds the allowable stress limit value set to 400 MPa. Figure 6 shows the areas where the allowable stress limit is exceeded. In configuration 2 the areas where the allowable stress limit is exceeded are reduced if compared to the configuration 1. Indeed, in configuration 2 these critical areas are limited to a few points, located at the multiple frame intersections. In addition, an enlargement of the absorber-chassis area is depicted in Fig. 6-C and Fig. 6-D in order to visualize the deformed shape obtained after the crash test.

In Fig. 7, comparisons are made between the impact energy transmitted to the safety cage (which is the most critical area of the chassis as it houses the passengers). As can be seen in Fig. 7, the shock absorption system contributes to absorb about 7 kJ. Indeed, in Configuration 1, the energy transmitted to the safety cage is 56.08 kJ, while in Configuration 2, it is 49.16 kJ.

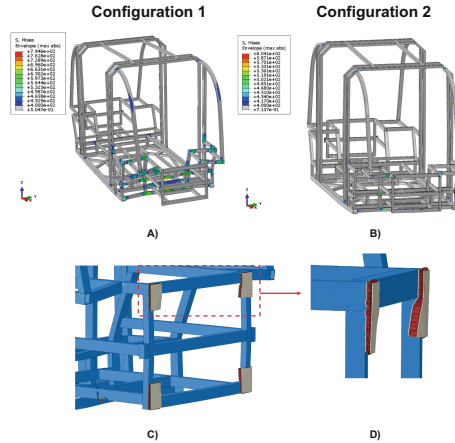


**Fig. 6.** Comparison with stress exceeding 400 MPa (A-B) and deformed shapes (C-D)

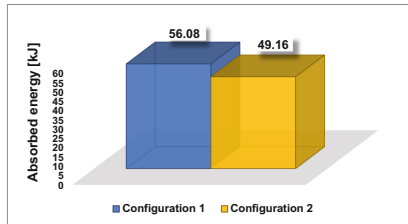


**Fig. 7.** Comparison of energy detected in the safety cage

From an energy point of view, the shock-absorbing systems also introduce another important effect, which can be deduced from the comparison of the force–time curves reported in Fig. 8.

Indeed, as can be seen in Fig. 8, in the time interval from 0 s to 0.005 s, the blue curve, representing the Configuration 1, exhibits a sudden collapse. This is because, since there is no damping (other than that due to the plastic effect of the steel of the chassis) the phenomenon immediately triggers the catastrophic failure of the structure. This effect is prevented equipping the shock absorbing systems. Indeed, at the same time interval, the chassis reinforced with shock absorbers is characterised by a reduced force (acceleration) peak and an horizontal trend. Indeed, the maximum load achieved by shock-absorber-reinforced configuration is 6.51% lower than the one found for configuration 1. These two effects (maximum peak force reduction and horizontal trend at peak) significantly improve the crashworthiness behaviour of the structure, resulting in a reduced experience of impact acceleration by the passengers and therefore an increase in their safety.

Finally, the result of the impact on a representative sandwich panel of the shock absorbing system is shown in terms of deformed shapes (Fig. 9-A to Fig. 9-B) and intralaminar damage of the composite, evaluated according to the Hashin failure criteria (Fig. 9-D).



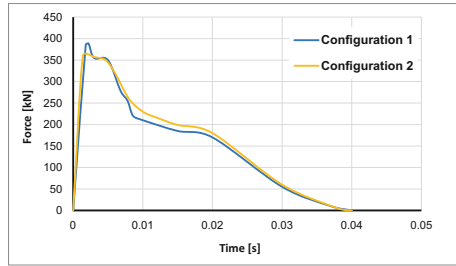


Fig. 8. Force–time graph

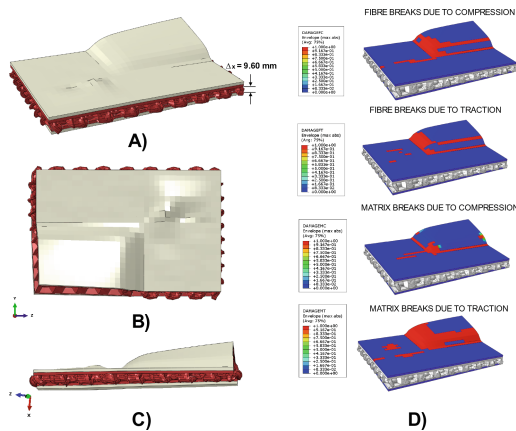


Fig. 9. Shock absorbers’ deformed shape (A-C) and intralaminar damages in the upper composite skin (D)

From Fig. 9, the contribution of the shock-absorbing system to the crashworthiness behaviour of the chassis, in terms of energy dissipation by plastic deformation and by intralaminar damage evolution, can be appreciated. Indeed, after the crash test simulation, a permanent deformation of 9.60 mm has been found on the absorber. This deformation is concentrated in the core of the sandwich panel. On the other hand, as shown in Fig. 9-d, the skins contribute to the dissipation of impact energy through fibre and matrix breakage. Due to their positioning on the chassis, the damages are mainly located in the area of the connection between the panel and the chassis’ structure.

### 4 Conclusions

This paper assesses the effectiveness, in terms of energy dissipation, of a Polypropylene/CFRP composite shock absorber, designed for Additive Manufacturing, under real service conditions.

In particular, the effects of the presence of shock absorbers on the maximum stress (Von Mises sigma) reached on the chassis of minibuses subjected to 45 km/h crash test simulation, are evaluated. The performed research work shows that the introduction of

absorbers can reduce the maximum Von Mises stress on the chassis by about 24.0%. Furthermore, by comparing the energies transmitted to the safety cage, the force–time graphs and the damage mechanisms arisen in the composite shock absorbers, the effectiveness of the energy dissipation system has been assessed. The chassis with shock absorbers can dissipate more energy produced during the crash test and reduce the maximum peak of the resulting load.

## References

1. Lulu, L., Zhenhua, Z., Wei, C., Gang, L.: Ballistic impact behaviour of stiffened aluminium plates for gas turbine engine containment system. *Int. J. Crashworthiness* **22**, 467–478 (2017)
2. Guntur, H.-L., Hendrowati, W., Budiarto, T.: Modeling and analysis of hybrid shock absorber for military vehicle suspension. *Appl. Mech. Mater.* **493**, 315–320 (2014)
3. Tao, X., Xiaoming, S., Tianyi, Z., Huan, L., Xiao, L., Ao, D.: Development and validation of dummies and human models used in crash test. *Appl. Bionics. Biomech.* **2018**, 3832850 (2018)
4. Daehn, G.S.: *Sustainable Design and Manufacture of Lightweight Vehicle Structures*. Richard Folkson (2014)
5. Guida, M., Marulo, F., Montesarchio, B., Bruno, M.: Innovative anti crash absorber for a crashworthy landing gear. *Appl. Compos. Mater.* **21**, 483–494 (2013)
6. Acanfora, V., et al.: Application of an additive manufactured hybrid metal/composite shock absorber panel to a military seat ejection system. *Appl. Sci.* **11**(14), 6473 (2021)
7. Li, M., Deng, Z.-Q., Guo, H.-W., Liu, R.-Q., Ding, B.-C., Li, M., Deng, Z.-Q., Guo, H.-W., Liu, R.-Q., Ding, B.-C.: Optimizing crashworthiness design of square honeycomb structure. *J. Central South Univ.* **21**, 912–919 (2014)
8. Acanfora, V., Castaldo, R., Riccio, A.: On the effects of core microstructure on energy absorbing capabilities of sandwich panels intended for additive manufacturing. *Materials* **15**(4), 1291 (2022)
9. Boonkong, T., et al.: The low velocity impact response of curvilinear-core sandwich structures. *Int. J. Impact Eng* **93**, 28–38 (2016)
10. Astori, P., Zanella, M., Bernardini, M.: Validation of numerical models of a rotorcraft crashworthy seat and subfloor. *Aerospace* **7**(12), 174 (2020)
11. Özen, İ., et al.: Low-energy impact response of composite sandwich panels with thermoplastic honeycomb and reentrant cores. *Thin-Walled Struct.* **156**, 106989 (2020)
12. Acanfora, V., Zarrelli, M., Riccio, A.: Experimental and numerical assessment of the impact behaviour of a composite sandwich panel with a polymeric honeycomb core. *Int. J. Impact Eng.* **171**, 104392 (2022)
13. Sun, J.S., Lee, K.H., Lee, H.P.: Comparison of implicit and explicit finite element methods for dynamic problems. *J. Mater. Process. Technol.* **105**(1–2), 110–118 (2000)
14. Zhang, B., et al.: A virtual experimental approach to estimate composite mechanical properties: modeling with an explicit finite element method. *Comput. Mater. Sci.* **49**(3), 645–651 (2010)
15. Sellitto, A., et al.: Numerical–experimental correlation of impact-induced damages in CFRP laminates. *Appl. Sci.* **9**(11), 2372 (2019)
16. Riccio, A., et al.: Modelling the simulation of impact induced damage onset and evolution in composites. *Compos. Part B: Eng.* **66**, 340–347 (2014)
17. Di Caprio, F., et al.: Experimental and numerical study of composite omega stringer–skin debonding under flexural loading conditions. *Multiscale and Multi. Mod. Exp. Des.* **2**(2), 105–118 (2019)

18. Riccio, A., et al.: Influence of failure criteria and intralaminar damage progression numerical models on the prediction of the mechanical behavior of composite laminates. *J. Compos. Sci.* **5**(12), 310 (2021)
19. Dassault System Abaqus 2016 User's Manual; Dassault Systèmes Simulia Corp.: Providence, RI, USA (2016)
20. Johnson, G.R., Cook, W.H.: Fracture characteristics of three metals subjected to various strains, strain rates, temperatures and pressures. *Eng. Fract. Mech.* **21**(1), 31–48 (1985)
21. Abaqus analysis user's manual. version 6.10 (2010)
22. Wang, X., Shi, J.: Validation of Johnson-Cook plasticity and damage model using impact experiment. *Int. J. Impact Eng.* **60**, 67–75 (2013)
23. Littlewood, D.J.: Simulation of dynamic fracture using peridynamics, finite element modeling, and contact. In: *ASME International Mechanical Engineering Congress and Exposition*. vol. 44465 (2010)
24. Seidt, J.D., et al.: High strain rate, high temperature constitutive and failure models for EOD impact scenarios. In: *Proceedings of the SEM Annual Conference & Exposition on Experimental and Applied Mechanics*. vol. 15. Society for Experimental Mechanics (2007)
25. Genikomsou, A.S., Polak, M.A.: Finite element analysis of punching shear of concrete slabs using damaged plasticity model in ABAQUS. *Eng. Struct.* **98**, 38–48 (2015)
26. Sümer, Y., Aktaş, M.: Defining parameters for concrete damage plasticity model. *Challenge J. Struct. Mech.* **1**(3), 149–155 (2015)

# Author Index

## A

Abdi, Frank 205, 217  
Acanfora, V. 86, 401  
Ameduri, Salvatore 36, 51  
Amico, S. C. 307  
Antonucci, V. 245  
Apuleo, G. 58  
Araganese, M. 337  
Arenas, J. M. 282  
Arricale, Vincenzo Maria 142  
Astarita, Antonello 99  
Atzeni, Eleonora 186

## B

Bahadori, Mohammedreza 217  
Baid, Harsh 217  
Baldieri, F. 401  
Barbaro, Mario 142  
Baroni, A. 343  
Belingardi, G. 3, 75, 290  
Bernasconi, A. 75  
Boccarusso, L. 180, 254  
Boursier Niutta, C. 271  
Braco, A. 148  
Buccoliero, G. 337

## C

Calzolari, Andrea 290  
Camilleri, Duncan 299  
Canegrati, A. 75  
Cantarutti, Andrea 217  
Caputo, Francesco 261  
Caputo, Gabriella 106  
Carrino, Luigi 106  
Cestino, E. 43  
Chen, Guan-Cheng 205  
Ciardiello, R. 271  
Cigliano, C. 245  
Ciminello, M. 36, 51, 58  
Concilio, A. 36, 58  
Coppola, M. 377

Corcione, Salvatore 357  
Corvaglia, S. 165, 173, 329, 337  
Cozzolino, Ersilia 99  
Cumbo, R. 343  
Cusati, Vincenzo 357

## D

da Silva, A. A. X. 307  
D.'agostinis, Rinaldi, D. 237  
Damasio, Massimo 186  
De Caro, Daniele 3  
De Fazio, D. 180, 254  
De Luca, Alessandro 261  
De Nicola, F. 86  
de Souza, Samia Danuta Brejão 329  
Dell'Annunziata, Guido Napolitano 142  
Di Caprio, F. 86, 148, 319  
Di Mauro, Gennaro 357, 364, 371  
Donadio, Federica 106  
Durante, M. 180, 254

## E

Eftekharian, Amirhossein 205, 217  
Epasto, Gabriella 116  
Ernesto, Monaco 135  
Esposito, Marco 20, 28

## F

Fabrizio, Ricci 135  
Fanteria, Daniele 67  
Farroni, F. 237  
Ficca, Antonio 391  
Fittipaldi, F. 401  
Fiumarella, D. 75  
Formisano, Antonio 180  
Frulla, G. 43  
Fusco, Giorgio 20

## G

Gabellone, Davide 3

Gagliardi, Giuseppe Maurizio 371  
 Galasso, B. 58  
 Galasso, Bernardino 36  
 Galizia, Giuseppe 290  
 Gallo, N. 165, 173, 329, 337  
 Garofano, Antonio 156, 401  
 Gennaro, D.'Angelo 135  
 Genovese, A. 142, 237  
 Gherlone, Marco 20, 28  
 Gianfranco, Laurino 135  
 Giglio, M. 307  
 Giusto, G. 86  
 Gomez, Neffer A. 299  
 Guida, Michele 357, 364, 371, 377

**H**

Huang, Dade 205, 217

**I**

Iannone, Vincenzo 67  
 Ingenito, Giancarlo 106, 156  
 Inverno, Michele 51

**K**

Karachalios, Evangelos 20, 28, 67  
 Kressel, I. 58

**L**

Lamanna, Giuseppe 261  
 Lanfranco, Sandro 299  
 Langella, Antonio 106, 180  
 Leccia, C. 148  
 Lopresto, V. 99, 106, 116, 125, 230, 245, 290

**M**

Manes, A. 307  
 Marciello, Valerio 357  
 Marena, Luigi 142  
 Marrey, Mallikharjun 205  
 Martulli, L. M. 75  
 Marulo, Francesco 371, 377, 391  
 Mastinu, G. 75  
 Mattone, Massimiliano 20, 28  
 Melania, Paturzo 135  
 Meo, M. 254  
 Mercurio, U. 58  
 Merola, U. 86  
 Minardo, Aldo 261

Minosi, S. 337  
 Moliterno, R. 377  
 Monaco, Ernesto 67  
 Muscat, Martin 299  
 Muscat-Fenech, Claire DeMarco 299  
 Myronidis, K. 254

**N**

Napolitano, Francesco 99  
 Nicolosi, Fabrizio 357  
 Nicolosi, G. 43  
 Niutta, Carlo Boursier 3  
 Nola, Nicola 20

**O**

Omaña, A. C. 282

**P**

Paolino, D. S. 3, 271, 290  
 Papa, I. 99, 106, 116, 125, 245, 290  
 Parodo, Gianluca 351  
 Pellone, L. 58  
 Percoco, Gianluca 173  
 Perfetto, Donato 261  
 Pinto, F. 254  
 Plano, Stefano 3  
 Poggi, Mirna 186  
 Polini, Wilma 351  
 Polla, A. 43  
 Pollastro, A. 230  
 Prentzas, Vasilios 20, 28

**R**

Raganato, U. 337  
 Rezasefat, M. 307  
 Ricciardi, M. R. 245  
 Riccio, A. 86, 148, 156, 319, 401  
 Romano, Fulvio 13, 20, 28, 36, 51, 67  
 Russo, A. 86, 148  
 Russo, P. 116, 125, 135, 245, 290, 364

**S**

Salmi, Alessandro 186  
 Sanfelice, Michele 142  
 Sansone, L. 245  
 Scattina, A. 75  
 Scavo, Ignazio 165, 173, 329  
 Sellitto, A. 148, 156, 319  
 Shoham, S. 58

Sinagra, Emmanuel 299  
Smarrazzo, Aniello 377  
Sollo, Antonio 391  
Sorrentino, Assunta 13, 51  
Sorrentino, Luca 351  
Sorrentino, Romualdo 51  
Squillace, Antonino 99  
Suarez, J. C. 230, 282

**T**

Tarzia, A. 337  
Tedesco, Michele M. 3  
Towsend, P. 230  
Tridello, A. 3, 271  
Trimini, Valentina 173  
Trinchese, Antonio 20

Tsai, S. W. 148, 319  
Turchetta, Sandro 351

**V**

Vallifuoco, Raffaele 261  
Vallone, Marco 186  
Varetti, Sara 165, 173  
Vigna, Lorenzo 290  
Viscardi, Massimo 384  
Viscusi, Antonio 106  
Vitiello, Libera 116  
Vito, Pagliarulo 125, 135

**Z**

Zarrelli, Mauro 156